Improved Prediction Methods for Finned Tube Bundle Heat Exchangers in Crossflow

by

Stuart Russell McIlwain B.Eng (Hons)

A Thesis submitted to University of Strathclyde
for the degree of Doctor of Philosophy

Department of Mechanical Engineering

December 2003

This thesis is dedicated to all the people who never understand why I do things, but simply nod and smile politely.

Acknowledgments

I wish to thank the following for all their help and encouragement:

Dr. Asaad Kenbar my NEL supervisor for putting up with my endless rambling questions, arguments and suggestions and ultimately trusting me to come up with answers to some fairly difficult problems.

Dr. Chee-Kong Lee, my Strathclyde supervisor, for asking awkward questions and driving me to consider things in different ways.

The technicians and staff of N.E.L, especially Paul Farrant, Tom Brisbane, Neil Barton, Amanda Brown, Brendan Robson, Tom Gallagher, and Kenny Mclleland.

HTFS (Heat Transfer and Fluid flow Service) for funding the project.

The HTFS Crossflow and Furnaces and Fired Heaters review panels for enduring hours of my technical presentations.

My pet rats, Apollo for providing endless hours of entertainment and Prandtl, who didn't quite make it to the end.

Abstract

Previous methods for predicting the heat transfer and pressure drop performance of crossflow heat exchangers with finned tubes have concentrated on developing correlations. These correlations have been based on the researchers observations of what geometric parameters may affect the performance, and then dimensionless groups developed to allow a correlation to be developed. This work shows that many of these models are limited either by design or by their databases, and often are not general enough to cater for air-cooled heat exchangers as well as the generally larger scale heat recovery bundles.

The most recent prediction methods have been developed as more aerodynamically based models, although these still encompass an element of empiricism to account for effects that are not readily understood. This new work develops from these physically based models.

An improved method for the prediction of the pressure drop of staggered finned tube bundles is presented, based on high quality test data and the results of a CFD (Computational Fluid Dynamics) study. This is shown to perform better than previous models, and also correct a defect in the formulation of a previous method.

A new prediction scheme for inline finned tube bundles is also presented. Experimental work was performed on nine inline air coolers to determine their performance characteristics and, along with open literature data, develop a reliable databank for prediction method development. The models incorporate a new approach to the pressure drop prediction using a sophisticated gap flow model, and a multiple term heat transfer model, that considers heat transfer and flow mixing between the main flow streams. This method is shown to significantly improve on previous methods.

Experiments were conducted on an isothermal staggered air-cooler bundle that allowed differing wall sealing devices (corbels) to be used, or allow a bypassing lane. Flow visualization tests were performed on this bundle, and observations of the flow patterns compared with a simple two-dimensional CFD model. From the test results a new method

of predicting the pressure drop performance of staggered bundles with various corbels was developed.

Using the bypassing air-cooler data and new data taken from a heat recovery bundle an iterative method to predict the pressure drop when a bypassing lane is present is presented. This method is shown to be both simple and computationally cheap, and is used in conjunction with the new staggered bundle pressure drop method.

The experimental inline air cooler results were used in conjunction with CFD to provide data to investigate the effect on heat transfer with an increasing number of rows through the bundle. It was found that the key factors in determining this are turbulence and the temperature difference between the tubeside and crossflow fluids, and also that the fin frequency plays a key role. A model is presented to predict the local heat transfer coefficient, which uses sub-models to express the two contributory factors. The results of this approach are shown to be very good, and promote better understanding of tube row heat transfer duty than previously developed models.

Table of Contents

Nomenclature

A_B	Bypass area for all bypass lanes	m^2
A_{BTrow}	Area of bare tube per row (base tube area)	m^2
A_{bl}	Blockage in heat exchanger duct	m^2
A_{Bundle}	Face area of the finned tube bundle	m^2
A_{Bypass}	Total face area of the bypass lanes	m^2
A_d	Area of duct	m^2
A_{Face}	Face area of the duct	m^2
A_{Fin}	Exposed area of fins on one tube row	m^2
A_{oT}	Airside surface area of the bare tubes	m^2
A_{ox}	The total airside surface area for heat transfer	m^2
A_r	Ratio of extended surface area to the area of the base tube	m^2
A_{TotRow}	Total outside surface area of the row	m^2
A_{Tube}	Exposed tube area per row, with fins in place (bare tube area)	m^2
C_A	Augmented Mass Transfer Coefficient	-
C_p	Specific heat capacity of gas at bulk conditions	J/kg K
$C_{p\ Local}$	Local specific heat of air at constant pressure	J/kg K
C_{Row}	Row correction factor	-
c_i	Sensitivity coefficient	-
D_e	Equivalent diameter	m
D_e	Tube annulus equivalent diameter (D_i – tube core diameter)	m
D_{eq}	Equivalent diameter of tubes used in CFD model	m
D_f	Fin tip diameter	m
D_r	Tube diameter	m
D_i	Tube inside diameter	m
D_{Point}	Point on fin radius where flow length is calculated	m
F	Sensitivity coefficient vector	-
F^T	Transposed sensitivity coefficient vector	-
FG_l	Gap between fins on CFD model	m
FFM	Fin Frequency Function	-
f	Darcy friction factor	-
f_B	Friction factor for bundle calculated from $\dot{M}_B$	-
f_{bypass}	Bypass friction factor	-
f_C	Fanning friction factor for bundle calculated from $\dot{M}_C$	-
G_A	Gap allowance term for staggered tubes	m
G_D	Diagonal gap between staggered tubes	m
G_{Entry}	Length from entry section to first fin on CFD model	m
G_{Exit}	Length from last fin to exit section on CFD model	m
G_{Fin}	Gap from edge of domain to fin ($W-0.5s_f$)	m

G_T	Transverse gap between staggered tubes	m
GR_{eff}	Effective gap ratio	-
GR_T	Transverse gap area ratio	-
g	Gravitational acceleration	m/s^2
H_{bypass}	Height of bypass lane	m
H_{CC}	Height from the duct wall to the centre of the tube nearest the wall	m
H_{co}	Height of corbel	m
H_{Duct}	Height of duct	m
H_{Fin}	Fin height	m
h	Overall HTC based on the total outside surface area per row	W/m^2K
I	Turbulence intensity	-
IAP	Inline arrangement parameter	-
IT_{Pred}	Turbulence intensity prediction	-
$IT_{PredCorr}$	Turbulence intensity prediction for low fin frequencies	-
j	Colburn j factor	-
K_B	Total Bundle loss coefficient (staggered bundles)	$m^{0.3}/s^{0.3}$
K_B	Total Bundle loss coefficient (inline)	$m^{0.44}/s^{0.44}$
K_{Bypass}	Bundle loss coefficient	$^{0.714}/s^{0.714}$
K_{fins}	Fin skin loss coefficient (staggered bundles)	$m^{0.3}/s^{0.3}$
K_{fins}	Fin skin loss coefficient (inline)	$m^{0.44}/s^{0.44}$
K_{ft}	Combined Fin skin and tube loss coefficient (staggered bundles)	$m^{0.3}/s^{0.3}$
K_{ft}	Fin and tube loss coefficient (inline)	$m^{0.44}/s^{0.44}$
K_{gap}	Gap loss coefficient (staggered bundles)	$m^{0.3}/s^{0.3}$
K_{gap}	Gap loss coefficient (inline)	$m^{0.44}/s^{0.44}$
K_{row}	Row effect coefficient	-
K_{tube}	Tube loss coefficient (staggered bundles)	$m^{0.3}/s^{0.3}$
K_{tube}	Tube loss coefficient (inline)	$m^{0.44}/s^{0.44}$
k	Coverage factor	-
k	Turbulent kinetic energy	m^2/s^2
L_B	The bypass lane width = 0.0373	m
L_{Bundle}	Length of bundle on CFD model	m
L_{Entry}	Length of entry section to bundle on CFD model	m
L_{Exit}	Length of exit section from bundle on CFD model	m
L_{mf}	Fin length along tube top line	m
L_T	Tube length	m
L_{tf}	Fin length along tube top region	m
$LMTD_{Row}$	Logarithmic mean temperature difference over a tube row	K
$\dot{M}_B$	Flow through bypass lane	kg/s
$\dot{M}_C$	Flow through bundle	kg/s
$\dot{M}_c$	Condensate mass flow rate	kg/s

M_{Max}	Mass flux through minimum flow area between the fins	kg/sm^2
$\dot{M}_T$	Total flow through bundle	kg/s
$\dot{m}_{Max}$	Mass flux through minimum flow area between the fins.	kg/sm^2
$\dot{m}_{MaxC}$	Mass flux through minimum flow area between the fins based on $\dot{M}_C$	kg/sm^2
m_f	Fin heat transfer number	1/m
mfr	Mass flow rate of air through bundle	kg/s
mfr_B	Mass flow rate through the bypass lanes	kg/s
mfr_B	Mass flow rate through the bypass lanes	kg/s
mfr_{Total}	Mass flow rate through the duct	kg/s
N_G	Number of gaps between rows in flow direction	-
N_R	Number of rows in flow direction	-
N_T	Number of tubes in the first rube row	-
Nu	Nusselt number	-
n_f	Fin frequency	1/m
n_{Row}	Local row number	-
Q_{lat}	Latent heat duty	W
Q_{row}	Duty per row	W
Q_{sup}	Superheat duty	W
Q_{sub}	Subcooling duty	W
Q_t	Steam side heat transfer rate	W
Q_x	Airside heat transfer rate	W
P_{In}	Static Pressure at approach to a tube row	N/m^2
P_L	Longnitudinal pitch	m
$P_{LocalRow}$	Static pressure at mean conditions over a tube row	N/m^2
P_{Out}	Static Pressure at exit to a tube row	N/m^2
Pr	Prandtl number at bulk gas conditions	-
P_T	Transverse pitch	m
R_{BL}	Ratio of fin gap to the thickness of boundary layer on the fins	-
Re_B	Reynolds number of flow through bypass lane based on $\dot{M}_B$	-
Re_{bypass}	Reynolds number based on the superficial bypasss velocity and bypass lane width	-
Re_C	Reynolds number of flow through bundle based on $\dot{M}_C$	-
Re_c	Reynolds number of condensate through tubes	-
Re_{Do}	Reynolds number of bulk fluid based on the mean superficial velocity and tube diameter	-
Re_{fin}	Reynolds number based on the fin velocity and base tube diameter	-
Re_{gap}	Reynolds number based on the gap flow velocity and base tube diameter	-
Re_{IF}	Reynolds number based on the tube centreline velocity and base	

	tube diameter	-
Re_{MF}	Reynolds number based on the tube top velocity and L_{mf}	-
Re_{max}	Reynolds number based on the maximum mass flux and base tube diameter	-
Re_{TF}	Reynolds number based on the tube top velocity and L_{tf}	-
RTC	Row Turbulence Coefficient	-
s_f	Mean fin thickness	m
Sh	Sherwood number used in Sung et.al's studies	-
S_{min}	Minimum bundle flow area	m^2
St	Stanton number	-
S_X	Covariance matrix	-
$T_{AirFace}$	Mean temperature at approach to a bundle	K
T_{In}	Gas temperature at inlet to a tube row	K
$T_{LocalRow}$	Temperature at mean conditions over a tube row	K
T_{Out}	Gas temperature at exit	K
T_{Tube}	Temperature of single pass tube side fluid at inlet	K
T_{TubeIn}	Temperature of tube side fluid at inlet	K
$T_{TubeOut}$	Temperature of tube side fluid at outlet	K
T_{tin}	Temperature at tubeside inlet	K
T_{tout}	Temperature at tubeside outlet	K
T_{xin}	Temperature at airside inlet	K
T_{xout}	Temperature at airside outlet	K
U	Overall heat transfer coefficient based on total surface area	W/m^2K.
U_c	Combined expanded uncertainty	-
U_i	Instrument's expanded uncertainty	-
U_m	Measurement expanded uncertainty	-
U_{Row}	Overall HTC based on the total outside surface area per row	W/m^2K.
u_B	Bypass velocity	m/s
u_{bypass}	Bypass lane velocity	m/s
u_{fin}	Inter-fin velocity	m/s
u_i	Instrument standard uncertainty	-
u_m	Measurement standard uncertainty	-
u_o	Mean superficial velocity	m/s
V_{ref}	Reference velocity for turbulence intensity (face velocity)	m/s
W	Width of CFD model	m

Greek

α	Uncorrected airside bundle heat transfer coefficient	W/m^2K
α_c	Corrected airside bundle heat transfer coefficient	W/m^2K
α_{Local}	Row specific, local, corrected heat transfer coefficient	W/m^2K

α_{ox}	Measured airside coefficient referred to the total surface area	W/m^2K
α_{oxc}	Corrected value of α_{ox} referred to the outside surface are	W/m^2K
α_{Row}	Air side Heat transfer coefficient	W/m^2K
α_{tube}	Tubeside heat transfer coefficient	W/m^2K
α_{Wall}	Tube wall heat transfer coefficient	W/m^2K
α_x	Measured airside coefficient	W/m^2K
β	HTFS2 fin tip clearance parameter	-
δ_{Mean}	Mean thickness of boundary layers on fin surface	m
δ_{IF}	Maximum thickness of boundary layers on fin surface on tube centerline	m
δ_{MF}	Maximum thickness of boundary layers on fin surface on tube top line	m
δ_{TF}	Maximum thickness of boundary layers on fin surface on fin top line	m
ΔP	Frictional pressure drop across bundle	N/m^2
ΔP_B	Frictional pressure drop across bypass lanes	N/m^2
ΔP_{by}	Pressure drop in bypassing lane	N/m^2
ΔP_C	Frictional pressure drop across bundle with reduced mass flow	N/m^2
ΔP_{co}	Pressure drop in bundle with corbels	N/m^2
ΔP_{Total}	Total pressure drop in bundle with corbel correction factor applied	N/m^2
ΔT_{lm}	Log mean temperature difference	K
Δx_i	Increment value	-
ε_f	Fin efficiency	-
ϕ	Total fin surface area per unit approach area	-
ϕ_f	Corrected fin height for fin efficiency	m
γ	Surface effectiveness	-
η	Airside dynamic viscosity at bulk conditions	N/sm^2
η_c	Dynamic viscosity of the condensate	N/sm^2
η_g	Dynamic viscosity of the steam	N/sm^2
λ	Thermal conductivity of gas at bulk conditions	W/mK
λ_c	Condensate thermal conductivity	W/m K
λ_f	Fin thermal conductivity	W/m K
λ_t	Tube thermal conductivity	W/m K
θ	Pitch angle of subsequent tubes	rad
θ	Angle of tubes from horizontal	rad
ρ	Density of bulk air/gas	kg/m^3
ρ_c	Condensate density	kg/m^3
ρ_s	Steam density	kg/m^3
σ	Ratio of approach area to minimum flow area	-

CHAPTER 1

Introduction

1.0 Introduction

This chapter introduces the background to the project, and explains some of the basics of modelling crossflow finned tube heat exchangers, and the limitations to the work presented in the thesis.

1.1 Crossflow heat exchangers

By the principle of conductive heat transfer it was found many years ago that using a fluid one could add/remove heat from another fluid by passing it over a bank of tubes. The tubes would act as a barrier between the fluid streams. In terms of crossflow heat exchangers three cases can exist:

1. Air cooling; the air is the low economic value fluid cooling a high value fluid in the tube
2. Gas cooling; the gas is the high economic value fluid and is being cooled by the low value fluid in the tube.
3. Heat Recovery: the gas is the low economic value fluid and is passing heat to the high value fluid in the tube.

It can be seen that 2 and 3, although different from an economic point of view, are essentially the same process, therefore two processes will be regarded in the subsequent sections of this thesis: Air Cooling and Heat Recovery.

It is known that by increasing the velocity of the gas more heat can be removed from/added to the tubeside fluid. However this incurs two penalties: Large gas pumping losses and high-speed flow induced structural vibrations that could lead to exchanger failure. To overcome this the tube heat transfer surface can be extended. In the case of this study this will be done with circular fins attached to the tubes. These fins help conduct heat from/to their carrying tube by presenting a larger area on the gas side. This benefits the process, as typically the tubeside fluid is a liquid with a relatively large heat transfer coefficient on the small tube internal area, whereas the gas has a significantly lower coefficient.

Typically there are two arrangements of finned tube banks; staggered and inline, as shown in Figure 1.1.

The staggered arrangement is normally employed to maximise the heat transfer for a given exchanger unit volume/plan area. Inline is often chosen in applications that suffer heavy fouling and require regular cleaning.

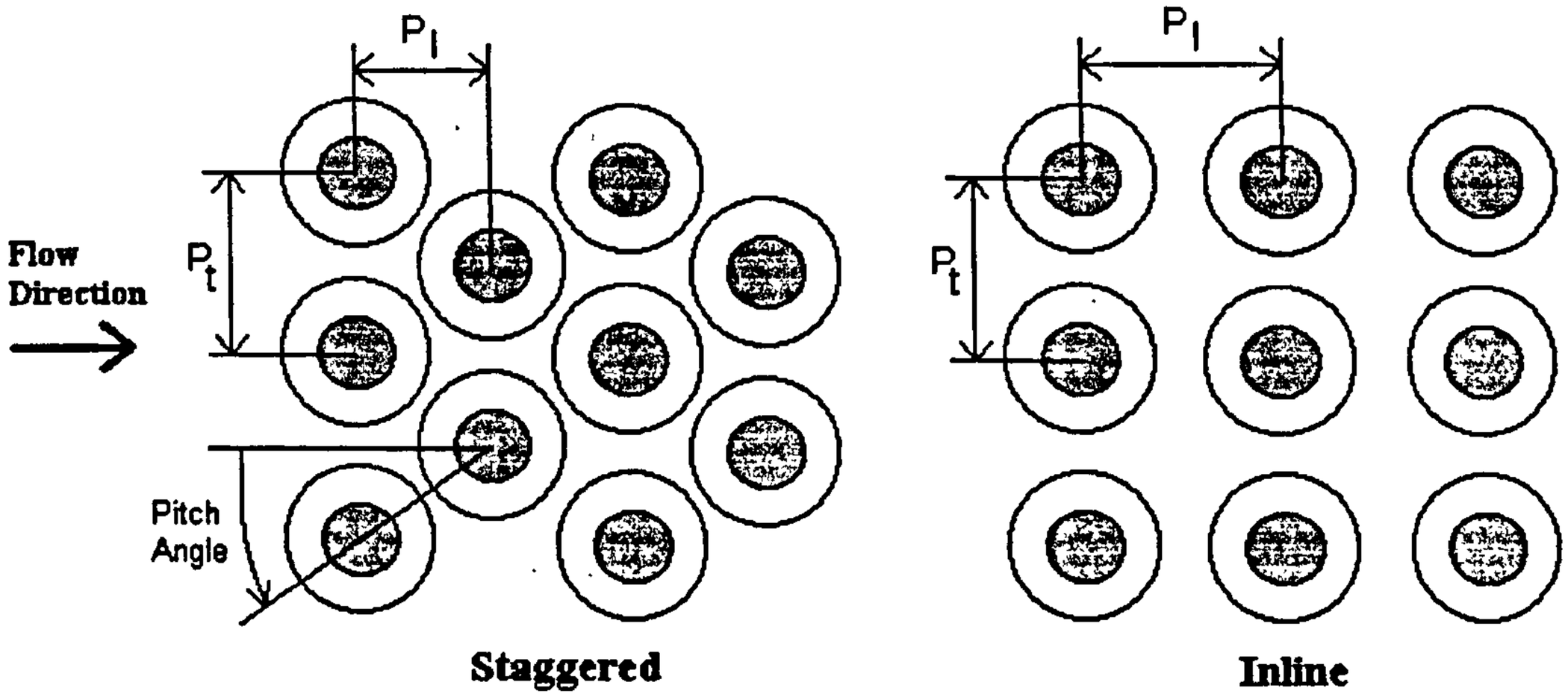

Figure 1.1: Tube bank arrangements, showing the pitch parameters

It is not appropriate to indicate here the influence of geometric parameters such as the layout angle of staggered bundles and the density of tube finning on bundles performance, all of which is a task for the design engineer. The influence of some parameters, however, will be explored in this thesis as appropriate.

1.2 Crossflow heat exchanger modelling

There are two main methods of modelling crossflow finned tube heat exchangers:

- Local (tube by tube or row by row) calculations that must be cumulatively considered to determine a bundle's overall thermal and pressure head loss. This would typically be carried out by finite volume methods such as CFD, but can be both expensive and time consuming.
- Bulk (averaged) calculations that are performed over an entire bundle to provide total thermal and head loss prediction. These may then be reduced to local values if necessary.

This study is largely concerned with the latter, for two reasons:

- Local measurements to help in the development of these local calculations are difficult and extremely expensive to perform.

- Industrial interest in heat exchangers is largely concerned with the overall performance.

The general objective of this thesis is to develop new algebraic models for the prediction of the heat transfer and pressure drop of various tube arrangements that can be used simply and quickly by process engineers.

1.3 Framework for PhD project

This project was carried out under the framework of the UK DTI (Department of Trade and Industry) PTP (Postgraduate Training Partnership) scheme. In this scheme the postgraduate researcher is placed at a RTO (Research and Technology Organisation) under the auspices of a University. The RTO for this project was the National Engineering Laboratory (NEL) in East Kilbride, Scotland. The University of Strathclyde, Glasgow, Scotland was the associated university.

The work contained in this thesis was carried out at the behest of HTFS, the Heat Transfer and Fluid flow Service. Through their industrial sponsorship the experimental heat exchanger bundles were provided, as well as access to a large databank of heat exchanger data and the HTFS research network, Symposium reports and industrial processes and methods handbook.

1.4 Limitations of the project

Before progressing to outline the work covered during the project, it is prudent to explain the limitations of the materials that will be shown and discussed:

1. The models all refer explicitly to the air/gas side of the heat exchanger bundle.
2. The types of heat exchangers used in the testing and method development in this report are all of circular tubes with circumferential, plain, high fins of medium to high fin frequency. The models are not explicitly or implicitly valid for any other type of heat exchanger.
3. The methods (unless stated) are bulk models that predict the overall performance of the total heat exchanger bundle, these methods ***do not*** predict on a tube-by-tube or row-by-row basis.

4. The methods are only valid within the limits of the databases from which they are developed. Extrapolation beyond these limits, while reasonably allowed for in the model construction, would be at the end users own risk.

5. All the models consider a single-phase dry air or gas passing across the finned tube surface.

CHAPTER 2

Review of previous work

2.0 Introduction

This chapter presents a review of previous work conducted by other research programmes in order to provide a starting point for the new research presented in this thesis. The topics examined are listed below:

1. Prediction methods for staggered tube layout heat exchangers
2. Prediction methods for inline tube layout heat exchanger
3. Staggered bundles with various sealing devices at the duct wall, and prediction methods to model this
4. Staggered bundles with bypassing flow between the bundle and duct wall and performance prediction methods
5. The row-by-row heat transfer of inline finned tube bundles
6. A review of finned tube bundle modelling in CFD

2.1 Staggered bundle performance prediction methods

2.1.1 Correlations

Correlations are equations mostly derived from dimensional analysis of suspected influences and regression of one form or another performed on experimental data to find a compact solution usually presented in the form (or a variation) of:

$$W = X * Y^Z$$

where Y could be a flow parameter such as Reynolds number, Z is an experimentally or statistically determined value, X is a correlation constant and W is the desired property result.

The largest uncertainty in the gas crossflow heat exchange process is in describing the flow of the gas through the bundle. This is normally attempted through a correlation method based on a few geometric parameters such as number of tube rows, and tube diameters. These methods have been very successful, but have been found to be limited in geometries such as inline tubes and bundles with bypass channels.

As will be shown most workers have found that the Reynolds number based on the mass velocity through the minimum flow area of the bundle is a good basis for a correlation.

This is referred to as the maximum Reynolds number through the minimum flow area defined as

$$\mathrm{Re} = \frac{M_{Max} D_r}{\eta_g}$$

where M_{Max} is mass flow rate per unit of minimum flow area through the bundle (kg/m^2s), D_r is the bare tube diameter (m) and η_g is the dynamic viscosity of the gas (Ns/m^2).

In industry, to provide direct comparison between heat exchanger surfaces, the dimensionless parameters j (Colburn j factor) and f (friction factor) are used to denote the heat transfer and pressure drop performance, respectively. These are normally plotted against the Reynolds number above to provide characteristic curves for designers to work from. However it would be impractical to test every heat exchanger geometry, and hence mathematical methods of predicting the heat transfer and pressure drop performance are required to allow designers to estimate the behaviour of a design when no test information is available.

2.1.2 Correlation methods

Kleinschmidt and Parsons [1] tested a number of extended surfaces excluding plate type fins for aeronautical cooling applications They developed a wind tunnel which drew air through the test exchangers by a large axial fan. Measurement of drag over the exchangers was performed using a mechanical load cell, which saw the exchanger balanced by weights via a fulcrum when no wind load was applied. When the wind loading was applied the movement of the exchanger from its reference point was read and, from the known calibration of the fulcrum, the drag force acting on the exchanger could be determined. They then attempted to develop a generalised correlation for the power absorbed by the cores. This is shown in Equ.2.1.

$$H.P. = c\left(R + \frac{w}{5.4}\right)V \qquad \text{(Equ.2.1)}$$

where H.P. is the horsepower necessary to overcome the resistance of the test bundle, c is a constant of a conversion factor (1/375), R is the measured pressure loss of the bundle in lb/ft^2, w is the weight of the test core in lb/ft^2 and V is the free air speed approaching the bundle in miles/hr.

It can be seen that this method contains three elements, two of which must be known to calculate the other. It must be made clear that this method was developed around what were standard exchanger cores at the time, so as such was a very limited design correlation.

Kays and London [2] presented prediction methods for various types of heat exchanger surfaces. They performed many tests on staggered finned tube bundles and presented a method of determining the heat transfer and pressure drop performance. They showed a very good treatment of the pressure drop problem and stated that the total static pressure drop for air coolers was the sum of:

- Entrance effects (ΔP_{In})
- Exit effects (ΔP_{Out})
- Gas acceleration (ΔP_{Acc})
- Bundle drag friction (ΔP_{Fric})

This was presented in the form given in Equ.2.2.

$$\Delta P_{Total} = \Delta P_{In} + \Delta P_{Fric} + \Delta P_{Acc} + \Delta P_{Out} \qquad \text{(Equ.2.2)}$$

In the more developed model shown, the entry and exit losses were considered part of the overall bundle calculation and included with the bundle friction model, provided the flow was normal to the bundle entrance. The resultant model had a heavy reliance on correction factors taken from charts.

Essentially, Kays and London were the originators of unified performance predictions for crossflow heat exchangers, but their methods relied too heavily on empirical corrections outside of the method itself, and as such were not considered complete by subsequent researchers. However, almost every study featured in this review cites them as a reference.

Briggs and Young [3] developed predictions for heat transfer from data collected from air coolers. They used data from twelve air coolers with six tube rows in the flow direction, all of an equilateral triangular pitch arrangement. From this they presented a detailed mathematical treatment providing details of their data reduction and determination of important parameters influencing heat transfer and pressure drop. They reduced the measurement data into a series of correlations each detailing the different

aspects of the individual bundles they tested. They used this step-by-step analysis to present a full correlation for the j factor, as shown in Equ.2.3.

$$j = 0.134\,\mathrm{Re}^{-0.319}\left(\frac{SF}{H}\right)^{0.2}\left(\frac{SF}{TF}\right)^{0.1134} \qquad \text{(Equ.2.3)}$$

where Re is the maximum Reynolds number based on the mass flux through the smallest flow area of the bundle, SF is the spacing between fins, H is the fin height and TF is the fin thickness.

Their treatment of pressure loss was *not* a unified correlation, but rather an example of a correlation for a specific tube bank in their databank. They cited that most friction factor predictions showed standard deviations of approximately ±40% and hence the notion of developing a correlation was not appropriate.

Schmidt [4] used his measurements and the data of Jameson [5], Brauer [6] [7] [8] [9] [10], Kays and London [2] and Hirschberg [11] to develop a heat transfer prediction method. Analysing this data he found that the amount of extended surface had a direct effect on the heat transfer performance; the more extended surface the higher the heat transfer. He characterised this with the area ratio, which related the extended surface to the bare tube area. His equation for the j factor is given in Equ.2.4.

$$j = 0.45\,\mathrm{Re}^{-0.375}\left(\frac{A_t}{A_b}\right)^{-0.375} \qquad \text{(Equ.2.4)}$$

where A_t is the total gas side heat transfer area and A_b is the area of the bare tube.

He determined that his correlation had an accuracy of approximately 10-25%. He attributed this to the varying effects of flow turbulence on the heat transfer from the different wind tunnel measurements. Until Schmidt's study, turbulence was not dealt with, and has since not been treated fully by researchers.

Robinson and Briggs [12] studied the pressure drop characteristics of fifteen air cooler tube banks with six tube rows with Reynolds numbers from 2000 to 50000. They presented many correlations that they used to show the effects of longitudinal and transverse pitch spacing and gave a thorough mathematical explanation of how they arrived at each correlation. They concluded by presenting a simple correlation for the

friction factor that covered all of their data within a ±6.6% error. This correlation is shown in Equ.2.5.

$$f = 18.93 \mathrm{Re}_r^{-0.316} \left(\frac{P_T}{D_r} \right)^{-0.927} \qquad \text{(Equ.2.5)}$$

where Re_r is the Reynolds number based on the mass flow rate at the minimum cross sectional area through the bundle, P_T is the transverse pitch of the bundle and D_r is the tube diameter.

This method appears to be the first to characterise the pressure drop data using the bare tube diameter, moving away from an equivalent diameter (often referred to as the hydraulic diameter) approach of previous methods. In their discussion they mentioned that the overall loss in finned tube bundles is due to two components: fin skin drag and tube form drag. They do not attempt to develop this into a multi component model however.

PFR [13] is considered one of the most successful attempts to produce pressure drop and heat transfer predictions, as it was based on a wide range of data. It was the recommended method of HTFS, is currently the recommended method of HTRI (Heat Transfer Research Incorporated), a large American conglomerate, and is used by many independent heat exchanger design consultancies. It is based on 30 different data sources and includes many arrangements of air cooler and some heat recovery data. They presented a suite of models including corrections for inline bundles and bundles with serrated fins. Their j factor correlation for plain fins is shown in Equ.2.6.

$$j = 0.29 \mathrm{Re}^{-0.367} \left(\frac{A_t}{A_b} \right)^{-0.17} \qquad \text{(Equ.2.6)}$$

It would appear that the PFR correlation layout draws on Schmidt [4], but there is no reference made to him in their report, indicating that they independently drew a similar conclusion with regard to the ratio of extended surface to the bare tube area.

Their friction factor method used a 'hydraulic equivalent diameter', which was an attempt to characterise the bundle as a single structure. It was calculated from Equ.2.7.

$$DH = 4L \frac{A_{\min}}{A_t} \qquad \text{(Equ.2.7)}$$

where L is the overall length of the bundle in the flow direction, A_{min} is the minimum gas flow area through the bundle and A_t is the total heat transferring area.

The Reynolds number (Re_h) would then be calculated from this and, the maximum mass flow through the minimum flow area. The friction factor could be calculated from either Equ. 2.8 or 2.9. If the ratio of the longitudinal pitch to the hydraulic diameter exceeds 4, then Equ.2.8 would be used, otherwise Equ.2.9 is used.

$$f = \left(150\,\mathrm{Re}_h^{-1} + 1.8\,\mathrm{Re}_h^{-0.2}\right)\left(\frac{P_L}{DH}\right)^{0.35} \qquad \text{(Equ.2.8)}$$

$$f = 13.6\,\mathrm{Re}_h^{-0.3}\left(\frac{P_L}{DH}\right)^{-0.42} \qquad \text{(Equ.2.9)}$$

where P_L is the longitudinal pitch.

While the PFR approach for friction factor is mathematically acceptable it does indicate that the model is not accurately reflecting any of the flow processes occurring in the bundle, although that is the nature of correlations.

The approach of Weierman [14] was to use multiple correction factors, similar to that of Kays and London [2]. His studies centred on large diameter heat recovery tubes with steel fins. In this respect his study is unique amongst the previously presented methods. His models were suitable for bundles with more than six tube rows, but he included correction factors for bundles with less than five tube rows. He presented his original model in 1976, but quickly revised it, removing a term and re-presenting it nearly a year later. His revised j factor correlation is given in Equ.2.10.

$$j = C_1 C_3 C_5 \left(\frac{D_F}{D_r}\right)^{0.5}\left[\frac{T_g + 273.15}{T_F + 273.151}\right]^{0.25} \qquad \text{(Equ.2.10)}$$

where C_1 is a flow term, a function of Reynolds number, C_3 is a correction factor relating the fin height and the fin thickness, C_5 is the row correction factor, T_g is the bulk gas temperature and T_F is the fin temperature.

The terms used by Weierman were an attempt to create a model that had physical significance by deliberately separating the flow and geometry effects. It was still a correlation, but the emphasis was on examining the individual elements with sub-models. This was also reflected in his pressure drop correlation, given in Equ.2.11.

$$f = 4C_2C_4C_6\left(\frac{D_F}{D_r}\right)^{0.5} \qquad \text{(Equ.2.11)}$$

where C_2 is a flow term, a function of Reynolds number, C_4 is a correction factor relating the transverse pitch and the bare tube diameter and C_6 is the row correction factor.

His models were particularly good for large diameter tubes, but were found to be unreliable for air cooler geometries. This has indicated that the method was not a complete prediction method, suggesting that his correction factors were biased towards his data set.

Rabas et.al [15] presented methods for both the j factor and friction factor of staggered bundles. It was developed from their own experimental work and the published results from five other studies to ensure a broad range of applicability. Their predicted j factor model was a correlation based on a number of physical parameters that they had shown to be effective in altering heat transfer performance. Their correlations were valid for Reynolds numbers (Re_{max}) between 1000 and 25000. Equ.2.12 shows this correlation.

$$j = 0.29\,\mathrm{Re}^{n}\left(\frac{s}{D_f}\right)^{1.115}\left(\frac{s}{h_f}\right)^{0.257}\left(\frac{t_f}{s}\right)^{0.666}\left(\frac{D_f}{D_r}\right)^{0.473}\left(\frac{D_f}{t_f}\right)^{0.772}\psi_h\psi_N \qquad \text{(Equ.2.12)}$$

where s is the fin spacing, h_f is the fin height, t_f is the fin thickness, ψ_h is the heating or cooling correction factor and ψ_N is the heat transfer bundle row number correction. The index, n, is defined as a function of the fin diameter and the fin spacing as given in Equ.2.13

$$n = -0.415 + 0.0346\ln\left(\frac{D_f}{s}\right) \qquad \text{(Equ.2.13)}$$

The friction factor was calculated from a similar formulation, and is shown in Equ.2.14

$$f = 3.805\,\mathrm{Re}^{-0.234}\left(\frac{s}{D_f}\right)^{0.251}\left(\frac{h_f}{s}\right)^{0.759}\left(\frac{D_r}{D_r}\right)^{0.729}\left(\frac{D_r}{S_T}\right)^{0.709}\left(\frac{S_T}{S_L}\right)^{0.379} \qquad \text{(Equ.2.14)}$$

where S_T is the transverse tube pitch and S_L is the longitudinal tube pitch.

Their use of the 'n' parameter was designed to describe the effects of altering the fin density. As the fin density increased, a negative value of n was achieved, therefore the

characteristics of their correlation changed to match the results they had found from testing. This was a good attempt to provide a more physical approach to developing a prediction method.

ESDU [16] presented a set of correlations for heat transfer and pressure drop. Their data set however was limited to only a few low finned bundles but their model was valid for a Reynolds number range of 1000 to 800000, or 100000 if the number or tubes per row exceeded 10.
Equ.2.15 shows the ESDU j factor correlation.

$$j = 183\,\mathrm{Re}^{0.3}\,\mathrm{Pr}^{0.027}\left(\frac{s}{H_f}\right)^{0.36}\left(\frac{H_f}{D_f}\right)^{0.11}\left(\frac{S_T}{D_f}\right)^{0.06}\phi_T\phi_N \qquad \text{(Equ.2.15)}$$

where Pr is the Prandtl number of the bulk fluid in the exchanger, ϕ_T is a temperature dependent factor to indicate heating or cooling and ϕ_N is the correction term for the number of rows in the bundle.

The friction factor was calculated from Equ.2.16

$$f = 4.71\,\mathrm{Re}^{-0.286}\left(\frac{S_T}{D_r}-1\right)^{-0.36}\left(\frac{H_f}{s}\right)^{0.51}\left(\frac{S_T-D_r}{S_L-D_r}\right)^{0.536} \qquad \text{(Equ.2.16)}$$

ESDU found it necessary to include a bundle pitch term in their f factor correlation. Compared to the other methods this is unusual, but was backed up by the data used for the development. The performance of these methods was shown to be poor for geometries outside of the limited database.

Chu [17] undertook a large review of all heat transfer and pressure drop material available in the open literature, and from HTFS test results for staggered bundles. With this information he postulated that, as there was no scheme for mathematical analysis that adequately described the heat transfer and pressure drop around a finned cylinder, the best approach should be an empirical equation. The geometry of a bundle is normally known and fluid properties can be found or derived, so a regression analysis was performed aimed at producing a correlation solidly based on these quantities.

His final correlations were based on the following method:

- Using an appropriate Reynolds number a rough equation of dimensionless groups (the G terms) was built in the form

$$f(x) = b\,\mathrm{Re}^{n}\, G_1^{a,1} G_2^{a,2} \ldots\ldots G_i^{a,i}$$

- The heat transfer equation was then converted to a linear form using logarithms:

$$\log_{10} Nu_{0b} = \log_{10} b + n\log_{10}\mathrm{Re} + \tfrac{1}{3}\log_{10}\mathrm{Pr} + a_1 \log_{10} G_1 + \ldots\ldots\ldots a_i \log_{10} G_i$$

- The pressure drop equation was converted into a log form where the dimensionless groups (G terms) were multiplied together for a fin skin drag Re and a tube form drag Re with a single constant:

$$f = b(a_0 G_1^{a,1} G_2^{a,1} \ldots G_i^{a,i}\,\mathrm{Re}^{-1} + c_0 G_1^{c,1} + G_2^{c,2} \ldots G_i^{c,i}\,\mathrm{Re}^{-0.2})^{m} G_1^{e,1} G_2^{e,2} \ldots . G_i^{e,i}$$

- Least squares regression analysis was then performed on the equations to determine the constants.

The ultimate correlations from this strategy were Equ.2.17 for the j factor

$$j = 0.0652\,\mathrm{Re}^{-0.327}\left[\frac{P_f}{D_r H^{0.7} s^{0.3}}\right]^{0.264}\left[\frac{L_f}{N_T P_t}\right]^{0.212} \qquad \text{(Equ.2.17)}$$

where P_f is the spacing between the fins, H is the fin height, s is the fin thickness, L_f is the length of the bundle in the flow direction, N_T is the number of tubes per row and P_t is the transverse pitch.

The friction factor is given by Equ.2.18

$$f = 13.295\left[\frac{P_f}{H}\right]^{-0.39}\left[\frac{P_t}{D_R}\right]^{-0.73}\mathrm{Re}^{-0.29} \qquad \text{(Equ.2.18)}$$

Chu asserts that a physical property calculation in the form of Petukhov's [18] relation for high temperature difference flow in a pipe is necessary. This is because the correlations assume a temperature difference of less than 100°C. This relation was not tested and as such was not included in the presented equation. This meant that the suitability of the correlation for heat recovery applications could be questioned.

As part of his study Chu evaluated the models of Briggs and Young [3], Schmidt [4], PFR [13] and Weierman [14]. His model and the PFR model outperformed all the other

methods but his conclusion was that while his new model accounted for the correct physics and showed a very good prediction in terms of scatter, the method of PFR [13] was statistically superior and hence was the recommended prediction method for HTFS applications.

2.1.3 Physically based models

Henry [19] studied the effects of the fin frequency and tube pitch and proposed a set of theoretical models that attempted to look at flow in bundles by systematically altering parameters to examine the effect of each of them on overall pressure drop and local effects. He used a small-scale isothermal model, which could be fitted with different finned tubes and had allowances for varying transverse and longitudinal pitches. This was important work as his research had revealed that previously published work had been built on a purely empirical basis of ratios and assumed relationships.

His findings were:

- Pressure drop was found to be proportional to the gas velocity raised to the power of 1.7 for finned and plain tube bundles. This finding was wholly experimental and did not appear to have a theoretical basis.
- The dependency of pressure loss on fin frequency was nearly linear.
- As transverse pitch increases (no change in longitudinal pitch) the pressure drop decreases.
- For a high fin frequency the change of transverse pitch has a much larger effect on pressure loss than was previously found.

From these conclusions Henry presented a proposed modelling scheme based on physical flow characteristics. Using fin tips touching as a baseline (no gap flow) he proposed that, in agreement with Chu [17], the loss could be attributed to the skin drag and form drag of the base tube. The derivation of this came from testing plain tubes and measuring the pressure drop for a given pitch arrangement, then retesting with finned tubes with 236 fins/m followed by 433 fins/m. The limiting case and the more practical case are shown in Figure 2.1.

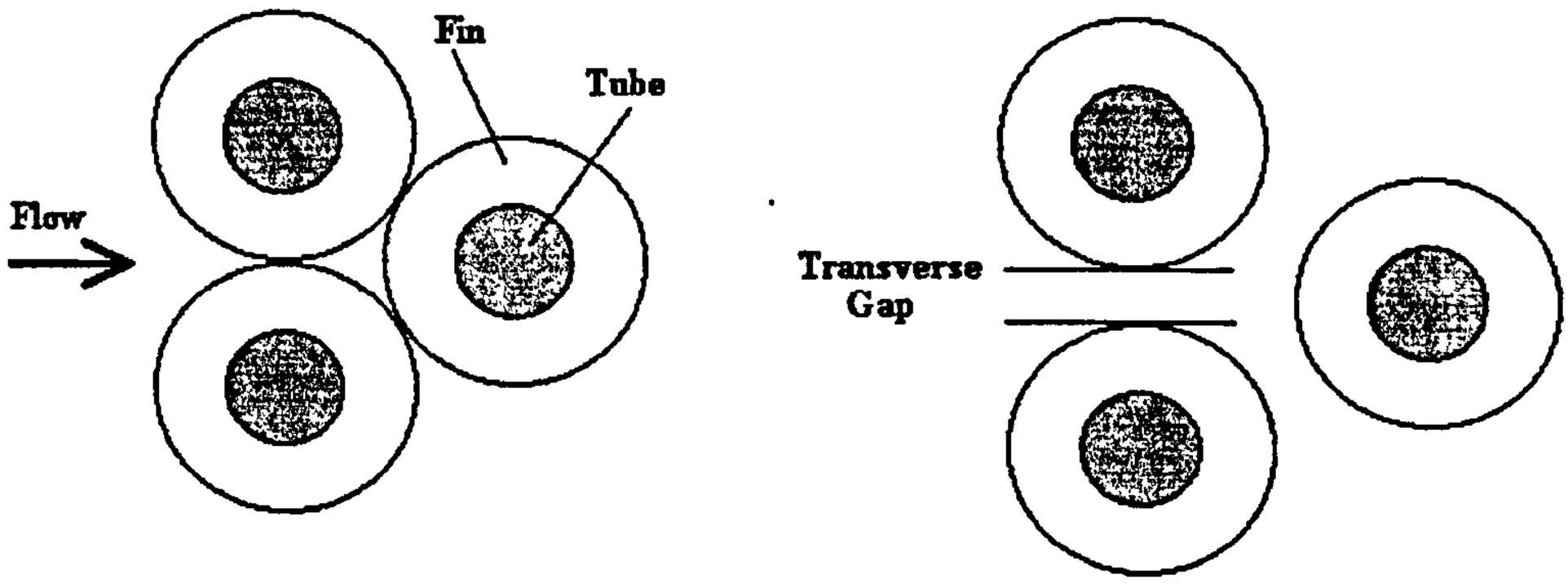

Figure 2.1: Highest pressure drop case (left) and more practical case (right)

Henry then discussed a function to predict the decrease in pressure drop that he attributed to the gaps that open up as the pitches increase, but only went as far as describing how it may work.

The skin drag contribution was then calculated as a function of Reynolds number, a ratio of fin surface area to approach area (to be proportional to the fin frequency) and the flow area ratio. The derivation of this came from the testing of the plain tubes and measuring the pressure drop for one pitch arrangement, then retesting with the finned tubes. A friction factor describing fin skin drag was presented that was to be used with a tube drag function. The tube drag function was developed from data presented by ESDU [20].

Essentially Henry did not present a usable model for pressure drop prediction, but provided a good basis for further study.

Ralston et al. [21] reviewed the work of Henry and assembled a databank of heat transfer and pressure drop data using HTFS data sources and published results for both air coolers and heat recovery applications. They used the relationship of the air velocity raised to the power of 1.7 and devised a new method of calculating the pressure drop based on a variation of the standard equation for aerodynamic drag force given below:

$$F_{Drag} = \frac{1}{2}\rho V^2 C_d A$$

where ρ is the freestream density, V is the freestream velocity, C_d is a drag coefficient and A is the frontal area of the body under investigation.

This standard relation was transformed into Equ.2.19

$$\Delta P = K_B \rho u_o^{1.7} \qquad \text{(Equ.2.19)}$$

where K_B is a bundle loss coefficient, ρ is the mean density of the fluid in the bundle and u_o is the mean velocity through the bundle.

The bundle loss coefficient was developed from the following approach:

- The pressure drop will be highest when the fin tips are touching, so the total resistance will be attributable to the fins and the base tube.
- A gap between the fins will allow flow to pass through, lowering the overall pressure drop.

By examining the HTFS databank a pressure loss coefficient for the base tubes was found from the plain tube bundle data of ESDU [20]. The fin contribution was determined from a function based on the ratio of the approach area to the minimum flow area (σ) and the total fin surface area per unit approach area (ϕ), which were calculated from Equs.2.20 and 2.21 respectively.

$$\sigma = \frac{D_f}{D_f - \left(D_o + n_f s_f \left(D_f - D_o\right)\right)} \qquad \text{(Equ.2.20)}$$

$$\phi = \frac{\pi\left(D_f{}^2 - D_r{}^2\right) n_f N_R}{2D_f} \qquad \text{(Equ.2.21)}$$

The fin skin drag was then calculated from Equ.2.22.

$$K_{fins} = 2.65 \cdot 10^{-2} \phi \sigma^{1.7} \qquad \text{(Equ.2.22)}$$

The total tube and fin friction was then calculated by summing the tube loss coefficient and the fin skin coefficient to give a maximum pressure loss coefficient (K_{ft}).

The gap loss coefficient was found from Equ.2.23.

$$K_{gap} = (N_R - 1)\left(1 - 0.65 \tanh(28(P_T - D_f))\right) \qquad \text{(Equ.2.23)}$$

The assembled bundle loss coefficient, when there is a fin gap, was presented as Equ.2.24. Otherwise the bottom line collapsed to unity and the loss coefficient was simply K_{ft}.

$$K_B = \frac{K_{ft}}{\left[\frac{D_f}{P_T} + \left(\frac{K_{ft}}{K_{gap}}\right)^{\frac{1}{1.7}}\left(1 - \frac{D_f}{P_T}\right)\right]^{1.7}} \qquad \text{(Equ.2.24)}$$

This bundle loss coefficient was substituted into Equ.2.19 and a correlation constant defined over the contents of the databank to give the final pressure loss prediction shown in Equ.2.25

$$\Delta P = 1.3 K_B \rho u_o^{1.7} \qquad \text{(Equ.2.25)}$$

This loss coefficient took the method away from previous methods of using a friction factor (f-factor) approach. The loss coefficient recognises the physical aspects of the flow, as the K_{ft} term is derived from separate tube loss and a fin loss coefficients.

The heat transfer correlation was also approached from a more physical angle, with the driving flow parameter identified as the Reynolds number over the fins. A balance of the pressure loss over the bundle showed that the product of the velocity over the fin combined with its loss coefficient would equal the loss of the whole bundle and the relationship was described as

$$K_B u_o^{1.7} = K_{ft} u_f^{1.7}$$

which allowed the calculation of the fin velocity as shown in Equ.2.26

$$u_f = \left(\frac{K_B}{K_{ft}}\right)^{\frac{1}{1.7}} u_o \qquad \text{(Equ.2.26)}$$

Ralston et al. believed that the heat transfer could all be attributed to the fin region and so developed a j-factor equation based on the Reynolds number, based on this fin velocity. This is shown in Equ.2.27

$$j = 0.215\,\mathrm{Re}_f^{-0.405}\,A_r^{-0.088} \qquad \text{(Equ.2.27)}$$

After testing this model it was found that while the new model outperformed Chu [17], which had been shown to outperform previous methods, both its pressure drop and heat transfer predictions were not as accurate as those of PFR [13] for some larger tube diameter bundles.

Due to this performance, Ralston and Chu [22] re-examined the Ralston et al. method using all the available data and revised the model. The tube loss coefficient remained as it was but a new parameter was devised, β, to define the fin tip clearance. This parameter was used in both the new fin loss and gap loss equations. The re-evaluated loss coefficient was as shown in Equ.2.28 and 2.29.

$$K_{fins} = 21.87\phi^{(0.44+1.41\beta)}\sigma^{1.7} \qquad \text{(Equ.2.28)}$$

$$K_{gap} = (N_R - 1)\left[1 - 9.72\tanh(-0.79\beta)\right]\left(\frac{\phi}{N_R}\right)^{0.31} \qquad \text{(Equ.2.29)}$$

The structure of the overall bundle loss coefficient was as shown in Equ.2.24, so the new pressure loss equation was as shown in Equ.2.30

$$\Delta P = 0.024 K_B \rho u_o^{1.7} \qquad \text{(Equ.2.30)}$$

In an attempt to characterise the interaction between the gap and fin flow a twin Reynolds number approach was investigated to develop a new correlation for the heat transfer. They added the maximum Reynolds number as this is based on the minimum flow area of the bundle and was thought to represent gap flow. This led to Equ.2.31 below.

$$j = 0.22\,\mathrm{Re}_{fin}^{\;0.04}\,\mathrm{Re}_{\max}^{\;-0.368}\,A_r^{\;-0.15} \qquad \text{(Equ.2.31)}$$

After presenting the updated model they went on to compare it with the best previous model, that of PFR [13] and showed that

- The level of data prediction was superior to that of PFR
- That PFR performed poorly for heat recovery applications in comparison

However it was later revealed that this model could severely undepredict pressure drop performance for bundles with a large number of tube rows (deep bundles) and very small fin gaps. This accounts for a reasonable amount of air cooler bundles and hence cast doubt over the method.

2.1.4 Conclusions

- Total bundle pressure drop is the sum of gas acceleration effects as well as the frictional pressure loss.

- The earliest model, Kays and London, was deduced from physical behaviour but its effectiveness was diminished by its difficulty of use. Subsequent models simplified the prediction process, but at the expense of understanding. Gradually models became more sophisticated, blending physical observations and behaviour with mathematics and statistics.

- Devising a general correlation that suits both types of heat exchangers (heat recovery and air coolers) is very difficult and requires a number of considerations as to the similarities and dissimilarities.

- Reliable data is required to develop an effective and general prediction method.
- The best available previous method was found to have a serious deficiency, and needs to be addressed.

2.2 Inline Bundles

The most common tube arrangement used in heat exchangers is the staggered layout mentioned previously. The lesser-used layout is the inline arrangement. As the name suggests the tubes are arranged inline with each other in one of the arrangement shown in Figure 2.2

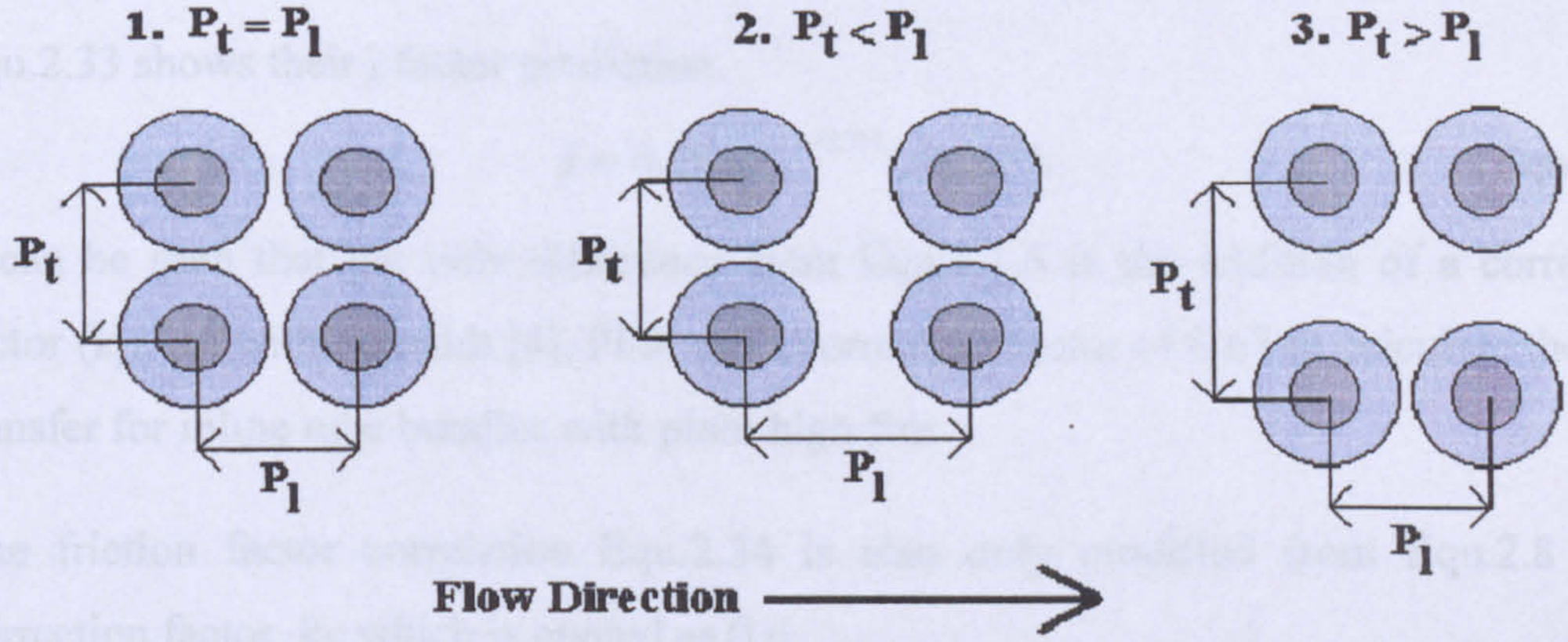

Figure 2.2: Finned tube bundle pitch arrangements

As the tubes lie directly behind each other the area presented to the gas-side flow is reduced and thus the frictional pressure drop is reduced. This also means that the subsequent tubes lie in the wake of the previous tubes and the heat transfer performance is reduced when compared with a comparable staggered bundle.

2.2.1 Correlation methods

Schmidt [4] analysed his experimental heat transfer data and data presented by Brauer [6] [7] [8] [9] [10] to develop a prediction method for the heat transfer performance of inline bundles. Equ.2.32 shows his j factor prediction.

$$j = 0.3\,\mathrm{Re}^{-0.375}\left(\frac{A_t}{A_b}\right)^{-0.375} \qquad \text{(Equ.2.32)}$$

It can be seen with reference to Equ.2.1.4 that he used the same layout of variables, and even the same exponents, which indicates that instead of performing a new analysis on the inline data he used his observation that for a given face area an inline bundle will transfer approximately 66% of the heat of a staggered bundle.

His statements of the prediction accuracy described in Section 2.1.2 applied to inline bundles as well, as does his assertion that inlet turbulence has affected the scatter of the prediction against his data. This method did not appear to be well received, as it appears to be rarely quoted in other publications.

PFR [13] presented correlations valid for $400<\mathrm{Re}<10^4$, and as with their staggered method these are used by HTFS, HTRI and many independent companies.

Equ.2.33 shows their j factor prediction.

$$j = 0.29\,\mathrm{Re}_D^{-0.367}\,Ar^{-0.17}k_j \qquad \text{(Equ.2.33)}$$

It can be seen that the only difference from Equ.2.1.6 is the addition of a correction factor (k_j). As with Schmidt [4], PFR use a correction factor of 0.67 to calculate the heat transfer for inline tube bundles with plain high fins.

The friction factor correlation Equ.2.34 is also only modified from Equ.2.8 by a correction factor, k_f, which is quoted as 0.6.

$$f = 150\mathrm{Re}_h^{-1} + 1.8\mathrm{Re}_h^{-0.2}\left[\frac{P_l}{D_h}\right]^{0.35} k_f \qquad \text{(Equ.2.34)}$$

PFR did state that they did not have enough inline data to properly derive an inline method; hence the reason why they used a constant based on observations of the slope of the j and friction factors for inline bundles when compared with otherwise similar geometry staggered bundles.

Weierman [14] made a concerted effort to characterise the inline heat recovery bundles in his databank. His basic equations were those presented in Equ.2.10 and 2.11, but the correction factors were altered to reflect his data specifically for inline bundles.

There have been many experimental studies on inline bundles published but few presented a performance prediction method, and as shown those that did tend to treat the inline models as being secondary to the, admittedly more popular, staggered arrangement. On this basis they are not presented here.

2.2.2 Physically based models

Chu and Ralston [23] proposed a set of models that predict inline bundle performance. To determine these they drew from the published results of Brauer [7] [8] [24] and Schmidt [4]. Using the same principles as they developed for staggered arrangements shown in Section 2.1.2 they examined the gap and fin loss coefficients and found that the adjustment to K_{fins} was the removal of the fin tip clearance exponent, to a format more like that of Ralston et.al. This is shown in Equ.2.35.

$$K_{fins} = 0.049\phi\sigma^{1.7} \qquad \text{(Equ.2.35)}$$

They found that the gap loss could be reduced to a simple function of the number of rows, to characterise the longitudinal gaps between tube rows. This is given in Equ.2.36.

$$K_{gap} = N_R - 1 \qquad \text{(Equ2.36)}$$

The overall bundle loss coefficient structure was the same as that shown in Equ.2.24, so the assembled pressure loss model, with its correlation coefficient was as given in Equ.2.37.

$$\Delta P = 0.67 K_B \rho u_O^{1.7} \qquad \text{(Equ.2.37)}$$

On the basis that the models would work in the same way as those of Ralston and Chu [22], they again used multi dimensional regression analysis on their heat transfer prediction to produce this equation (Equ.2.38):

$$j = 0.29 \,\mathrm{Re}_{fin}^{\;0.136}\, \mathrm{Re}_{\max}^{\;-0.525}\, Ar^{-0.391} \qquad \text{(Equ.2.38)}$$

When they compared their predictions against other methods it was found that the new models did not perform as well as those of PFR [13]. They acknowledged the relatively poor data that they had used was likely the cause of this, and stated that this new model could be developed as further if more test data was available.

2.2.3 Conclusions

- There are significantly fewer inline bundle prediction methods available than staggered methods.

- Inline methods have often been treated almost as an afterthought when studies have been conducted. This can be seen in Schmidt and PFR where the heat transfer and pressure drop are treated as a constant fraction of that of staggered bundles, although flow patterns differ substantially.

- Inline bundles present a notably different problem in terms of flow features when compared with that of staggered bundles.

- If new data became available the method of Chu and Ralston [23] could provide a basis for a new prediction method.

2.3 Use of Corbels as wall sealing devices

In research, heat exchangers are almost always tested with inactive (non-heat transferring) half tubes (corbels) placed at the bundle top and bottom walls to prevent the crossflow from bypassing the tubes, as shown in Figure 2.3.

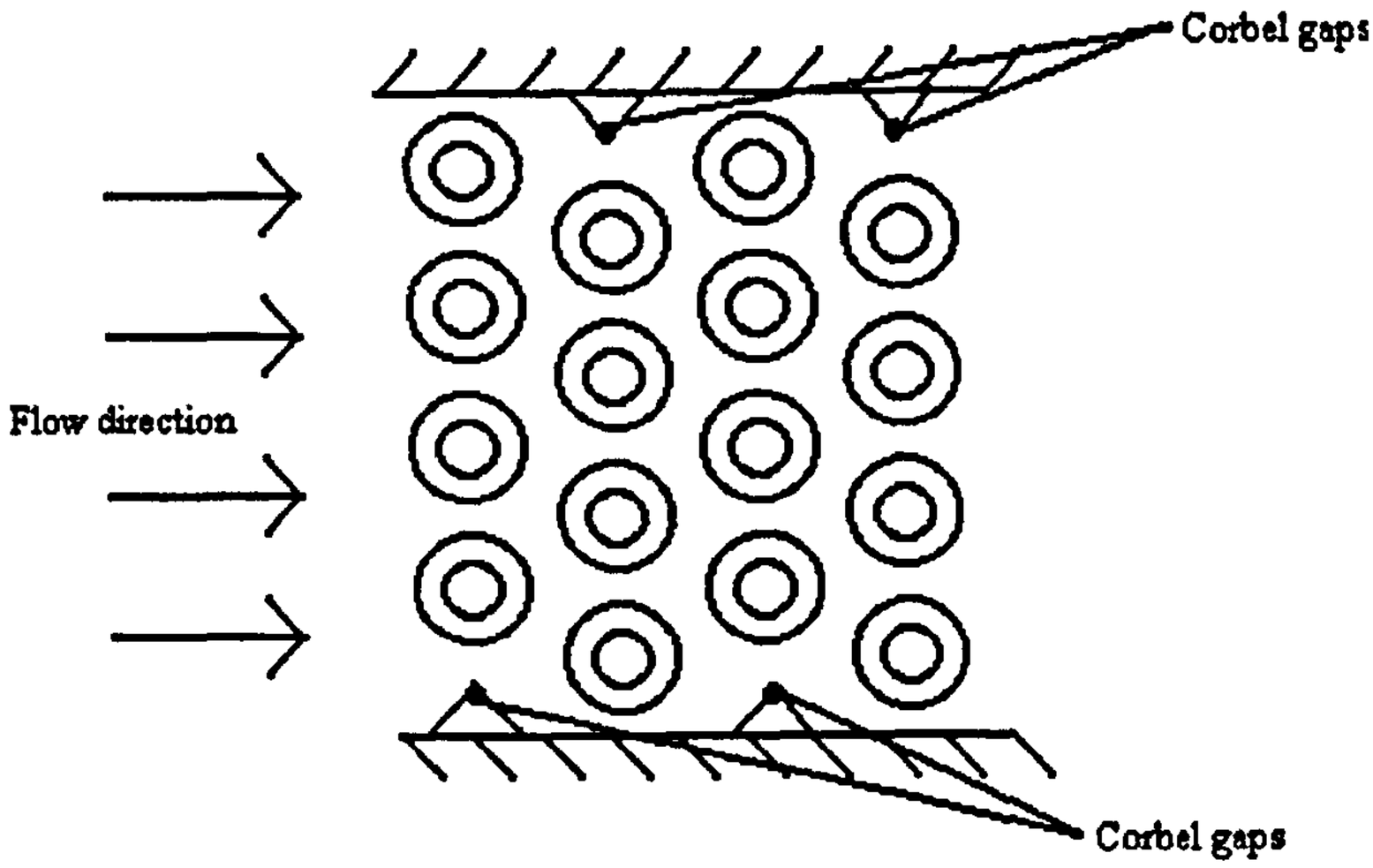

Figure 2.3: Staggered arrangement and corbel positioning

Ideally these corbels would be a complete half section of the finned tubes being used in the active section of the bundle. In practice, however, designers usually avoid finned half tube, as it is cheaper to use other shapes based on more readily available sections. Since the shapes are variable the flow patterns and resistance to flow will vary thus influencing the bundle pressure drop. Figure 2.4.shows diagrams of typical sections available.

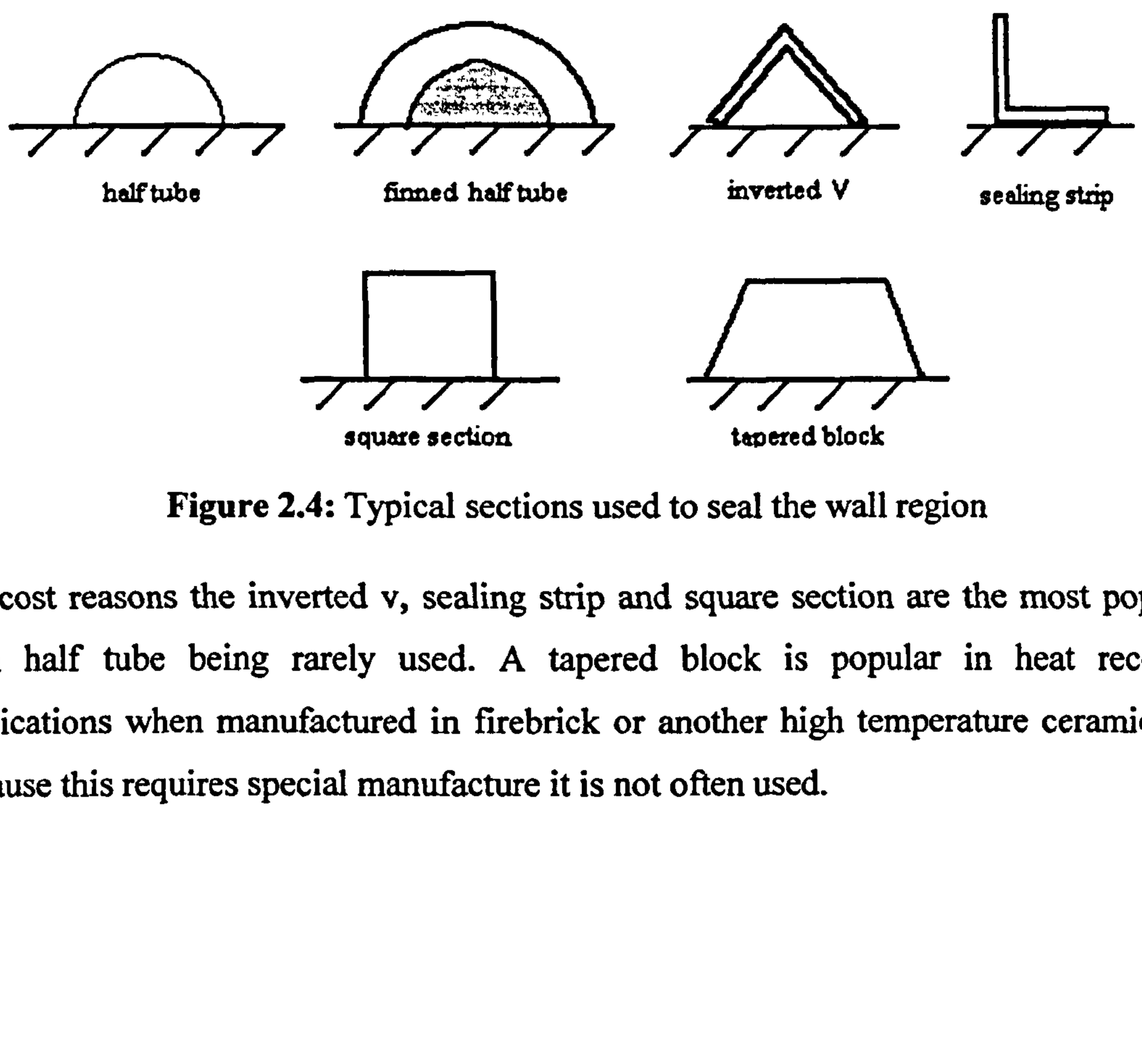

Figure 2.4: Typical sections used to seal the wall region

For cost reasons the inverted v, sealing strip and square section are the most popular, with half tube being rarely used. A tapered block is popular in heat recovery applications when manufactured in firebrick or another high temperature ceramic, but because this requires special manufacture it is not often used.

It is expected that the influence of corbels on bundle performance diminishes as the number of tubes per row in the bundle increases. In heat recovery bundles the number of tubes per row is usually much less than that used in air cooler applications since the tube diameter used is normally bigger. Therefore the influence of corbel presence and shape will be more pronounced.

In a survey of the open literature there was little information about testing of sealing devices.

2.3.1 Results

The study by Jameson [5] was one of the earliest reported that used corbels. He explored the effect of the flow that bypassed a finned tube bundle and reported that by using angle baffles (sealing strips in Figure 2.4) the heat transfer could be increased by up to 15% over his bypassing bundle.

Robinson and Briggs [12] describe all their test bundles as having finned half tube corbels enabling them to state that the flow through their equipment is of a perfect flow pattern, however no further mention was made of them.

Weierman [14] made reference to wall sealing devices in his list of assumptions and limitations to his prediction method. A worked example of his prediction method for a staggered bundle with segmented fins notes the usage of inverted v corbels, but made no mention of their effects on pressure drop or thermal performance. Similarly in a further study Weierman noted that all his test data for plain and segmented fins was recorded with half tubes on the roof and floor of the ducts, but it is not clear whether they were plain half tubes, or finned half tubes, similar to the ones used in the individual tests.

Rabas and Eckels [25] showed results for a bundle with different sealing methods. They used sealing strips and a wavy plate wall, as shown in Figure 2.5.

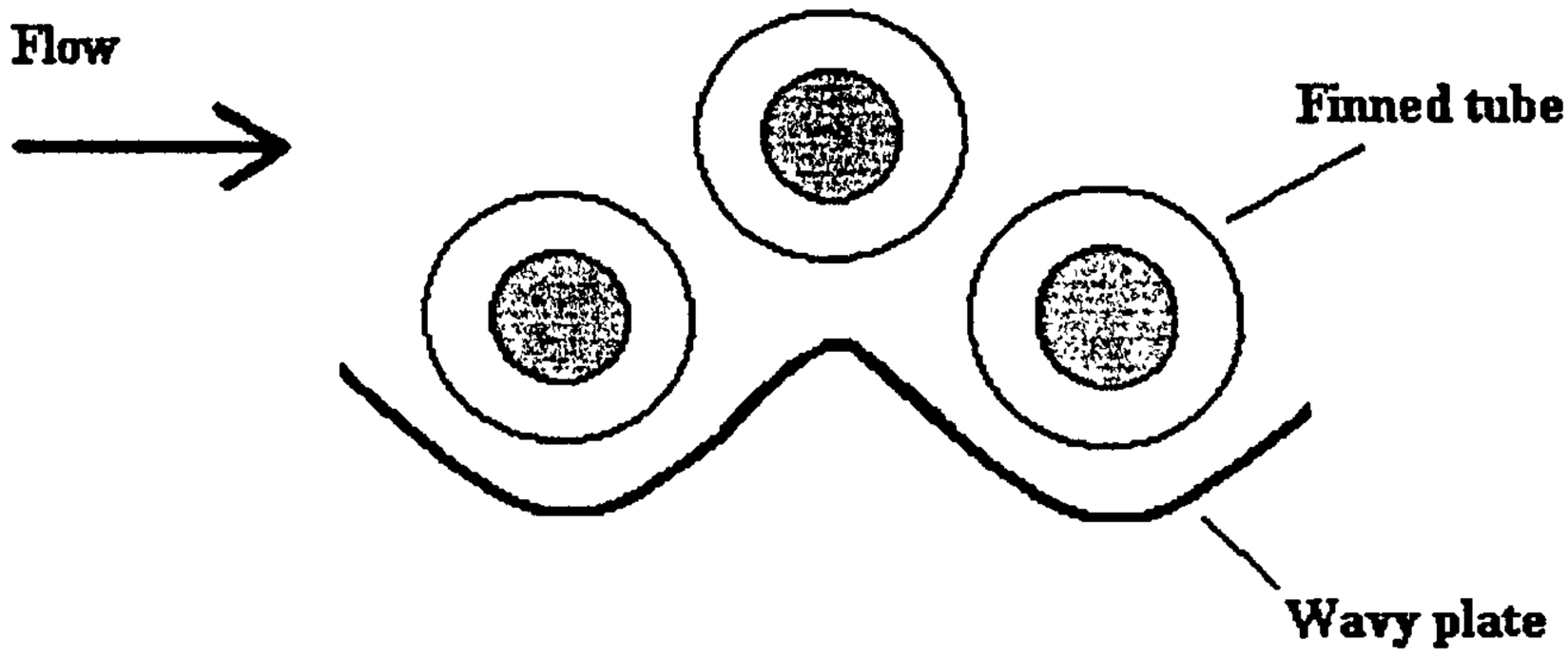

Figure 2.5: Wavy plate corbels of Rabas and Eckels [25]

The corrugated plate was an approximation of the inverted v corbel and showed surprisingly poor thermal performance. Their conclusion was that the thermal performance remained approximately the same as with bypassing, but the pressure drop increased substantially. This is perhaps why wavy plate was not found in any other study.

Their testing of a 14-row corbelled bundle yielded the following results:

- If half tubes are used the heat transfer increases as does the pressure drop over the bypassing case.
- Two sealing strips, at the 6^{th} and 10^{th} rows, yield the same performance as a complete set of half tubes.
- Sealing strips in each alternate row give the highest thermal performance and pressure drop
- If cost is a key factor, sealing strips in every second row will produce results similar to half tubes in each row.

Their conclusions were that corbels are an important design consideration, however, no effort was made to characterise the effects other than a very small presentation of results for friction factor and j factor, which exhibited a lot of scatter, and no effects prediction model was presented.

Eckels and Rabas [26] tested a three row hot-water heated bundle with five tubes per row, and took the unusual step of using active half tubes at the wall by connecting the hot water supply to their bundles into full finned tubes, and then filling the duct up with

epoxy resin to create a floor and roof with half tubes embedded into them. After the initial mention of this no discussion was made on the effects of doing this.

Kroger [27] made great efforts to achieve a perfect bundle in his study of the pressure drop and heat transfer of various bundles. He tested a four row staggered bundle, and used plaster to fill in the tubes nearest that wall to create perfect flow conditions. However no mention is made of the effects of this is made as he develops his method, other than reference to having perfect flow and thermal bundles.

2.3.2 Conclusions

It can be seen from the above that little attention is paid to the wall sealing devices, yet most presented prediction methods always make a vague statement that their data was taken with something in place to prevent bypassing. It is also clear that no one has presented a calculation method that takes account of the effects of corbel shape on bundle thermal and hydraulic performance

2.4 Bypassing flow prediction methods

Bypassing occurs in tube bundles when the flow at the edge of the bundle passes straight between the duct wall and the tubes/fins. This would typically occur because half tubes or other corbels have not been fitted to the duct wall.

2.4.1 Plain tube bundle studies

ESDU [28] presented a method of calculating the pressure loss and heat transfer over plain tube banks that was based on adding a correction factor to their tube bundle calculations. It was based on a ratio of the area of the bypass lane to the minimum flow area through the tube bank. This method is summarised below:

- Calculate the frontal areas of the bypass lanes and tube bank.
- Determine a bypass coefficient and an unexplained factor, q, from curves using the geometric ratio of bypass lane width to tube diameter, Reynolds number and the longitudinal pitch to diameter ratio.
- Determine the bypass correction factor from a relating equation.
- Multiply the ESDU crossflow pressure loss coefficient equation by this correction factor and proceed to calculate the pressure drop.

The stated accuracy of the method was very low and due reference was repeatedly made to the lack of data, and poor understanding of the phenomena.

The HTFS method [29] recommended for bypassing in plain tube banks was an amalgam of that of ESDU [28] and Russell and Wills [30]. The method was built on the simple principle of pressure drop equality in the bypass lane and the tube bundle:

$$\Delta P_{crossflow} = \Delta P_{bypass}$$

This assumes that the pressure drop in the tube bundle is equal to that of the bypass lane(s), that there is no mass transfer between the tube bundle and the bypass lane and also has the added assumption based on the Russell and Wills [30] study that the approximate mass flow split will be 70:30, bundle to bypass, at the exit of the exchanger, regardless of the geometry. This approximation was queried by Martin et al. [31]. The method was also not valid for tube bundles with less than six tube rows.

Martin et al. [31] performed isothermal experiments on a plain tube bundle with half tubes at one wall, and bypass at the other. The plain wall had a variable height mechanism and allowed the amount of bypass to be altered. By measuring the amount of mass flow in the bypass lane at the exit they determined that the mass flow that would be lost from the tube bundle was a function of the bypass width. Their conclusions were:

- The amount of bypass flow and bundles crossflow at entry could be approximated by the geometric areas of the two regions.
- The flow splits at the outlet were not related to the geometric area.
- The percentage of mass flow increase to the bypass lane from the bundle was not linear with the percentage increase in bypass lane width.

They tested the ESDU prediction method on their experimental data and found that for staggered bundles the pressure drop was overpredicted. They also tested a method presented by Bell [32] and found it to underpredict. No values of the levels of over and underprediction were presented, as the authors stated that the data would be presented in a future publication.

2.4.2 Finned tube bundles

Rabas and Taborek [33] presented a review of forced convection processes and their conclusions of a study that examined half tubes (corbels) and angle strips (sealing strips) [25]. They propose that correlations based on corbelled bundles are simply not satisfactory for bypassing bundles, as they will overpredict the thermal performance, and the pressure drop will be overpredicted, leading to a particularly under specified bundle.

Mueller and Chiou [34] reviewed flow maldistribution in many types of heat exchangers. They concluded that in experimental testing with bypass lanes the recorded outlet temperatures, and thus the bundle temperature difference, heat transfer coefficient and other parameters, will be incorrect. They explained that the logarithmic mean temperature difference (LMTD) for a bundle tested with bypass flow must be modified with a correction factor. The correction method they showed was that of Fisher and Parker [35].

The Fisher and Parker [35] method was based on shell and tube heat exchanger designs and was presented in a graphical form. It showed that for a given leakage ratio (the amount of bypassing flow to the overall flow) and number of sealing devices (baffles in shell and tube terminology), the 'F' correction factor could be found. This could then be applied to the determined LMTD for a given bundle.

2.4.3 Conclusion

Many studies have been conducted on bypassing flow in plain tube banks and methods are available for their prediction performance.

Finned tube bundles with bypass have been studied by a few workers, and despite this no open literature method for the prediction of pressure drop or heat transfer was presented.

There are a few available studies of shell and tube exchangers with bypassing, but these are mostly concerned with cylindrical shells, and share no common features with the exchanger types discussed in this thesis.

2.5 Development of heat transfer over an increasing number of tube rows

Note: Heat transfer coefficient will be abbreviated to HTC in the following sections to avoid repetition.

The heat transfer duty of the individual tube rows will vary with increasing row number as the flow passes through the bundle. This is due to two main factors:

- The temperature difference between the crossflow and the tubeside fluids
- Turbulence; both inherited from the freestream and generated in the flow as it passes over the exchanger tubes

The following presents a review of the limited literature on the subject of finned tube bundles. The reasons to concentrate on the lesser used inline bundles will become clear in Chapters 10.

2.5.1 Approach to experiments in row effect

Zukauskas and Ulinskas [36] explained that there are two methods of determining the row effect in experimental studies:

- Alter the number of rows in the bank and measure overall performance
- Constant number of tube rows and the heat transfer is measured in every row

Using a bundle with many tube rows leads to fully developed flow. This is the establishment of a pattern where no extra turbulence is generated due to a generation/dissipation cancellation effect as noted by the isothermal studies on plain tube banks by Pearce [37, 38], Zdravkovich [39], Lam and Fang [40] and others. To measure this with heat transfer a test bundle would need to be instrumented with many thermocouples. This would incur a great deal of complication, expense and could interfere with the flow, which is why it has been rarely done.

Neal and Hitchcook [41] conducted studies on a large scale staggered finned tube bundle with nine tube rows. The arrangement, however, was barely representative of normal tube bundle, as each row consisted either of two half tubes at the walls, or a single full tube. The method they used for collection of heat transfer data was peculiar, as their half tubes and full tubes were manufactured from wood, with only one metal, heated, finned tube. This single heated tube was moved from row to row and a

measurement taken. It is believed that this method of studying the row effect is not valid, as the only row affected quantity of the flow will be the turbulence. There will be no temperature difference from previously heated flow, so the measurements will be skewed with turbulence effects.

Hashizume [42] presented heat transfer and pressure drop data for staggered and inline finned tube banks, and he conducted his experiments in the same manner. Therefore his conclusions are believed to be invalid for the same reasons as those of Neal and Hitchcook above.

2.5.2 Results of plain tube inline bundle studies

ESDU [43] presented a method to calculate the heat transfer of a specific tube row in banks of plain tubes. The ESDU method is based on calculating the average HTC for a bundle from a formula based on flow physical properties and three correction factors; number of rows, tube inclination to flow direction and a tube wall temperature correction. The local row correction factor is then applied from a lookup table to find the individual row's HTC. The row correction factors given for inline plain tube banks are shown in graphical form as in Figure 2.6.

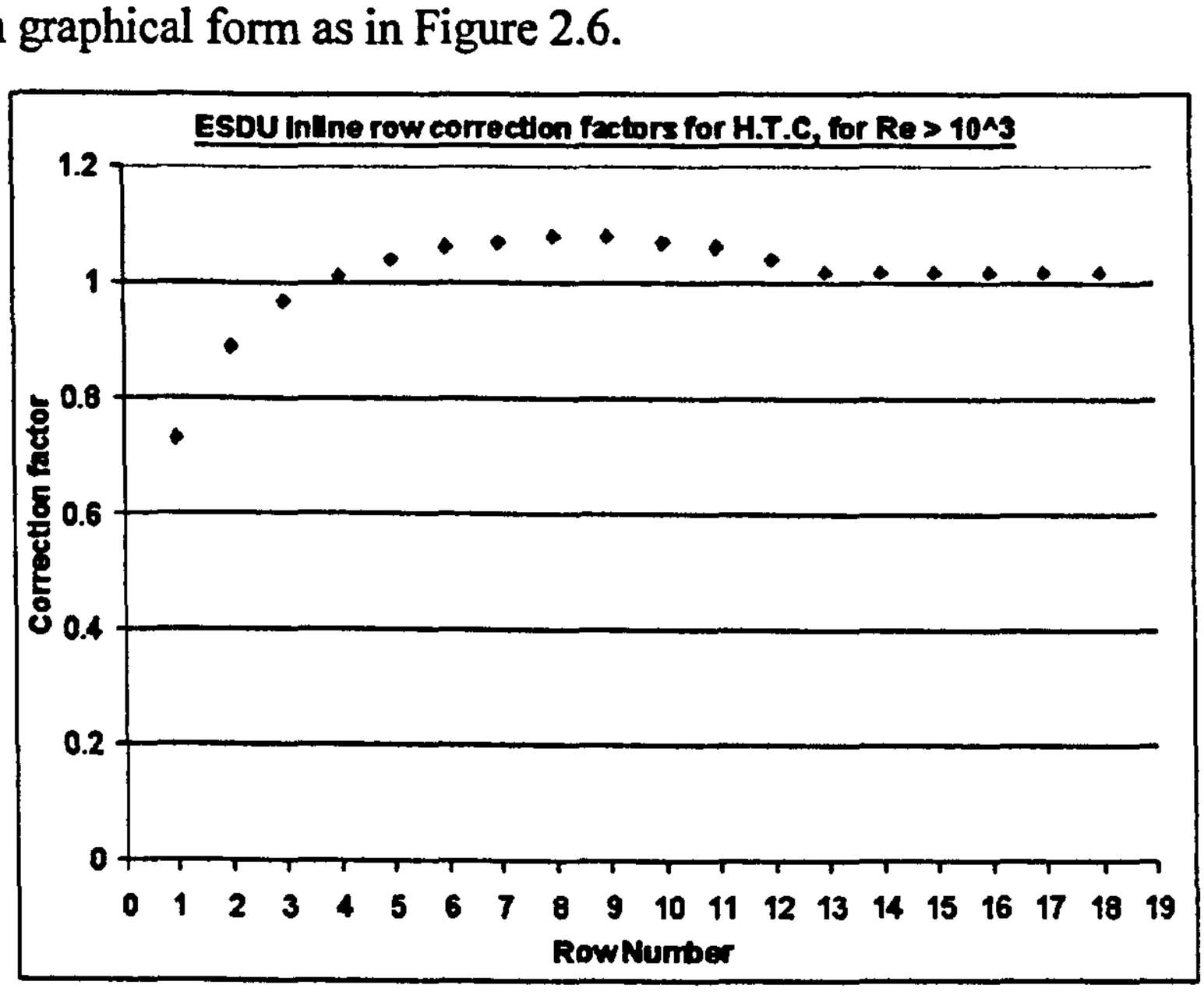

Figure 2.6: ESDU correction factors for inline banks of plain tubes

It can be seen from Figure 2.6 that the correction from the overall HTC for the first tube row is quite low (0.73) and this increases to a maximum of 1.08 by the eighth tube row.

The correction then decreases to become asymptotic at 1.02 for thirteen and above tube rows. What this shows is that the row coefficient will be lowest on the first tube row, and highest between the 7^{th} and 9^{th} rows. The coefficient will stabilise after the 13^{th} row. It should be pointed out that this applies to tube banks where the crossflow Reynolds number is greater than 10^3. Below this Re value another curve applies, but is not felt relevant to forced/induced draft crossflow heat exchangers.

2.5.3 Results of finned tube inline bundle studies

Brauer [10] showed that for inline tube banks with an extended surface to bare tube area ratio of approximately nine, the heat transfer decreases as the number of tube rows crossed increases. He found that the dependence of the heat transfer on the number of tube rows decreases as the approach velocity increases. Critically, he states that stable heat transfer, whereby the temperature rise of the air in the bundle becomes monotonic with increasing tube row, occurs by the fourth tube row. As the ratio of extended surface to bare tube ratio decreases the heat transfer becomes less dependent on the number of the row, and then finally increases with the number of tube rows, mimicking the behaviour normally found in banks of inline plain tubes. At this condition, the heat transfer then increases, due to turbulence, as the number of rows increases, in a manner noted by the ESDU [43] method above.

Later, Brauer [24] discussed the flow fields for inline finned tube bundles. He showed that there was a large influence on the heat transfer of inline bundles by the gap flow stream between the fin tips in the transverse direction, essentially stating that the flow could be categorised as either tube and fin flow or gap stream flow. The bulk of the heat transfer would be done by the tube and fin flow, and the gap flow would essentially bypass the finned tubes and not contribute to the heat transfer process. He mentioned that there might be some mass interchange between the two streams.

Rabas and Huber [44] studied deep and shallow inline finned tube banks and measured temperature profiles both in the transverse gaps between tubes, and in the longnitudinal gaps between tube rows in a segmented fin bundle. Their study was biased towards comparison of inline tube banks with staggered banks, but they put forward the following conclusions:

1. A number of tube rows are required before fully developed flow patterns exist and heat transfer stabilises. This number of rows depends on the Reynolds number of the flow.
2. The entrance effect, whereby the flow field is not yet established, effects shallow bundles (small number of tube rows) to a greater extent than in deep bundles.
3. The heat transfer performance of deep inline banks 'should increase with, or be almost independent of, the number of tube rows.

The bundle for which their temperature profiles were taken had 15 tube rows and 4 tubes per row, with serrated fins. It is therefore assumed in this instance that the gross flow behaviour is not modified significantly from the plain high fins that are the focus of this thesis. Their process side fluid was condensing steam. They state that they used the forced draft method of passing the air over the exchanger, implying a moderate level of turbulence in the approach to the bundle.

Their results concentrate on considering the overall heat transfer coefficient based on the overall surface area for each row using the classic formula:

$$Q_{Row} = h \cdot A_{Tot} \cdot \Delta T$$

where Q is the calculated duty per row (W), h is the overall HTC based on the total outside surface area per row (W/m^2K), A_{Tot} is the total outside surface area of the row (m^2) and ΔT is the LMTD (K) over the row.

While they did not present their measured heat transfer coefficients, or tube duties, as they clearly state that their data was not of suitable quality to publish, they did state that their row correction factors were largely similar to those of ESDU.

The bundle data described in detail by Rabas and Huber was used by Bell and Yang [45] who developed a model based on two distinct streams; tube/fin and gap flow. They postulate that the row effect in inline bundles is due to the flow mixing, or lack thereof between these two distinct streams.

Figure 2.7 shows their calculated row heat transfer coefficients. The derivation of these are based on their model, the temperature profiles of Rabas and Huber [44], the velocity profiles of Weierman et.al [46] and the heat transfer coefficient prediction method of

Briggs and Young [3] to provide a validation. Using these inputs they calculated an overall bundle HTC, and then overall row HTCs. They then determined that the overall HTC, based on the total outside surface area per row, increased with increasing tube row number. Their results are shown in Figure 2.7.

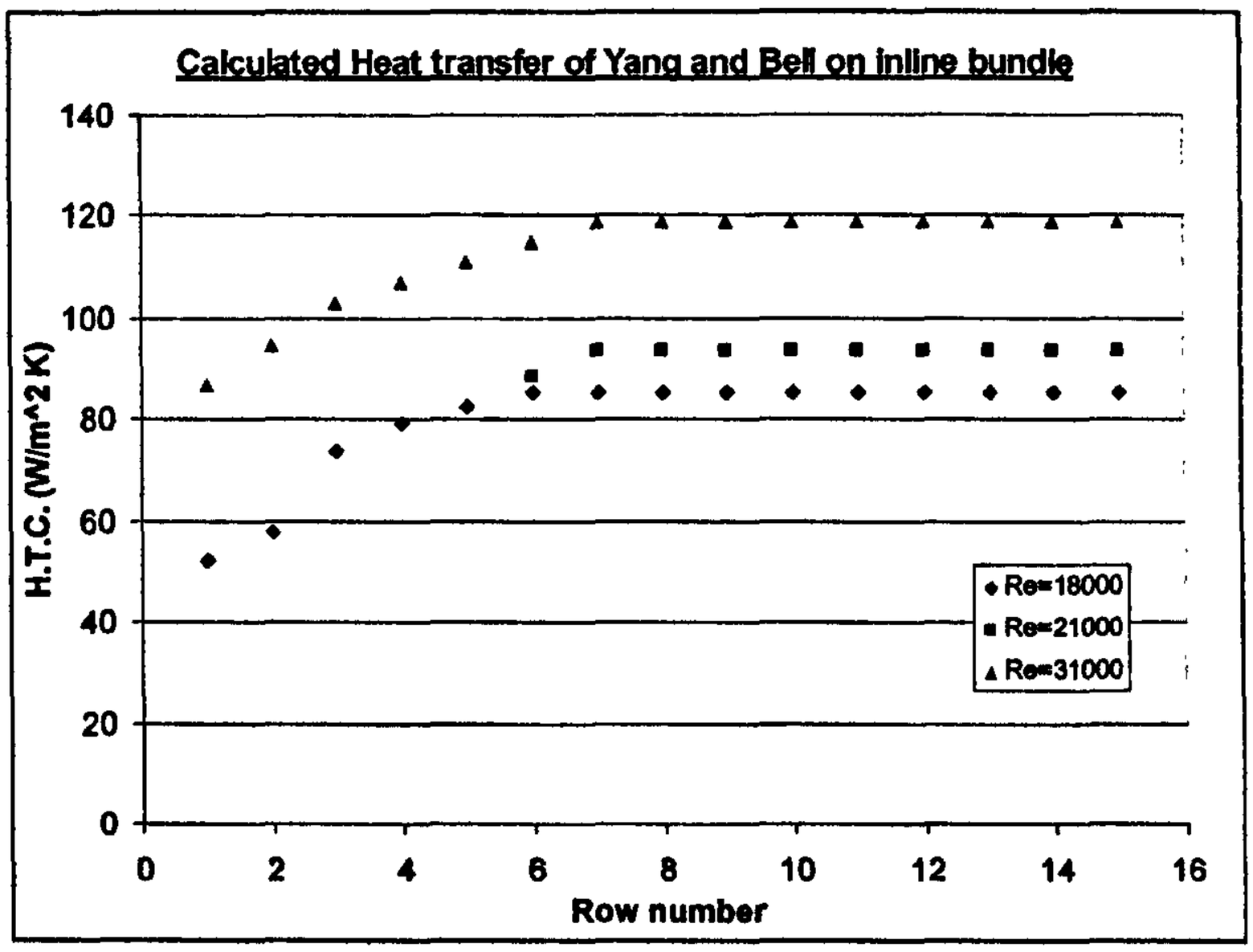

Figure 2.7: Heat Transfer Coefficients of Yang and Bell (1993)

The only suspicious result is that of the Re = 21000, which, as clearly stated, had the first five rows thermally inactive. However it can be seen that the HTC between sixth and seventh rows rises sharply, as by now the flow field and the bypass flow between the tubes in the flow direction would be fully developed. This adds credence to their theory of stream mass interchange.

The model outlined proposed that a portion of mass flow can be considered to surround the first tube (primary stream). The remaining portion flows, unimpeded, through the effective bypass lane between the fin tips (secondary stream). After the first tube there is an element of mass exchange, due to turbulence, whereby heated flow from the primary stream moves in to the secondary stream, and some cool secondary stream moves into the primary stream. This newly combined flow is then considered the approach flow to the following tube row, and the procedure begins again for this next tube row. This is then repeated for all the tube rows. Using this method they estimated their row heat transfer coefficients (h).

Zukauskas and Ulinskas [36] reviewed a number of works on staggered and inline banks thermal performance, with respect to the number of tube rows. They presented a summary of the work of Yudin and Tokhtarova [47] and Kuntiesh and Iokhvedov [48], all of whom found that the overall bundle heat transfer coefficient decreases with an increasing number of rows.

Yudin [49] tested a number of inline tube banks and concluded that the overall heat transfer coefficient decreases with an increasing number of tube rows. He also stated that the heat transfer becomes fully established by the fourth tube row.

2.5.4 Stability of heat transfer

When the effect of rows on heat transfer is addressed it is usually accompanied by a discussion on the row number where the heat transfer stabilises and the temperature rise (or decrease) through the bundle will become monotonic.

Brauer [9] found that that steady heat transfer conditions in inline layout bundles occurred by the fourth row.

Ward and Young [59] measured the heat transfer coefficients in a staggered layout bundle with eight tube rows. They found that the coefficient of the first tube row was 0.65-0.85 that of the last tube row, and the second row was 0.95 that of the last row. Their conclusion was that the heat transfer stabilised by the third tube row.

Mirkovic [61] also tested an eight row staggered bundle. He concluded that the third row was the stabilisation point.

Neal and Hitchcock [41] observed that for their staggered layout bundle the heat transfer stabilised at the sixth row.

Rabas and Huber's [44] presented temperatures measured behind each tube row in their segmented fin inline bundle. They showed that the temperature rise of the air became monotonic with increasing row number after the eighth tube row. However this must be viewed with caution, as segmented fins will propagate both higher and differing levels of turbulence compared with plain high fins.

It is believed that the variation in these results are due to the turbulence of the incoming air. High inlet turbulence would increase the heat transfer in the first few tube rows, and could explain the differing findings from other workers.

2.5.5 Conclusion

It can be seen that there are considerable differences in the reported results. The results of the flow patterns discussed by Brauer [9] are the most satisfactory physical explanations.

It is thought that the differences in the results are due to the levels of turbulence in the approach airflow to the bundles and the turbulence that is generated, or perhaps even cancelled, as this disturbed flow passes through the finned tube bundle. It can therefore be reasoned that a high inlet turbulence level would increase the heat transfer in the first few rows. This would account for the variation seen by the quoted researchers.

2.6 Computational Fluid Dynamics modelling of tube bundles

2.6.1 Necessity of CFD

Experimental studies on heat exchangers are generally carried out to measure the overall heat transfer and pressure drop performance. Local measurement is rarely done due to the difficulty to instrument the confined spaces in the test bundle. Flow visualisation is extremely rare in full bundle testing. Neal and Hitchcock [41] reported local flow and heat transfer measurements in a large-scale staggered tube bank using smoke and tufts for flow visualisation. A single tube heated and instrumented with thermocouples was used for the local heat transfer measurement. The results of using a single heated and instrumented tube is questionable, as there is no incoming heat flux on the measuring tube, so the heat transfer measurements are heavily biased towards overestimation. Lymer and Ridal [67] tested a large-scale bundle using the novel method of water as the crossflow fluid seeded with polystyrene beads to observe the flow patterns. Their heat transfer experiments on the bundle used small heaters installed on the fins of the tubes allowing them to determine the local heat transfer coefficients. Both of these bundles were of the staggered arrangement.

It was demonstrated by these studies, and many that they referenced, that the process of visualising flows in finned tube banks is extremely difficult. This is due to difficult

access to the gaps between the fins, and the close spacing of the fins in practical bundles. To this end it is expedient to use Computational Fluid Dynamics (CFD) for local examination of flow, providing the models can be validated in some way. It is also important, however, that there is a tangible result from the CFD so that the flow can be analysed to provide local data for model development.

2.6.2 Plain tube banks

Stanescu et al. [96] used two-dimensional CFD to develop a prediction for the optimum number of tubes and tube spacing, to maximise heat transfer in a cavity of fixed volume. Using a series of assumptions they developed some dimensionless parameters and developed a theoretical model for the spacing and sizing of tubes in a staggered array. Using the CFD package FIDAP they quickly determined a few characteristic results, and developed an experimental rig to provide validation. Using the CFD results they developed a modified version of their heat transfer correlation which was shown to give very good agreement with the experimental results.

Kondjoyan, and Boisson [76] studied the surface heat transfer of cylinders in turbulent crossflow by comparing predictions made by the STAR-CD CFD code with experimental data. They found that to match their CFD results to those of an experimental depended on wall treatment, and they concluded that the capacity for prediction of surface heat transfer is dependant on having experimental data for validation. They also found that adjusting the constants embedded in the wall heat transfer models also helped to match the predictions to the experimental data.

Many other studies exist using CFD to model plain tube banks and single plain tubes. However most are centred around furthering the modelling that takes place within the CFD codes themselves, rather than producing results to be used in practical applications.

2.6.3 Finned tube banks

A survey of material on the CFD modelling of plain helical finned tube bundles showed that no significant work appears to have yet been published.

FLUENT [97] have shown demonstrations of staggered tube bundle heat exchangers with plate fins. They state that using the RNG k-epsilon turbulence model, the

differential viscosity option and non-equilibrium wall functions that their models could predict the Colburn j factor within ±10% and the Fanning f-factor within ±35%, however it is not clear whether this is to experimental values, or prediction values from correlations. No correlation or other non-CFD prediction method was suggested.

Grady [98] modelled plate fin staggered tube bundle heat exchangers using the FLUENT code. His emphasis was on improving the heat transfer performance by using vortex generator tabs on the fins. He showed very good agreement between pressure drop prediction and experimental values, with a prediction range of 8.3% underprediction to 3.4% overprediction from the measured values. His heat transfer duty results ranged from 18.2 to 33.5% overprediction. He concluded that the predictive potential for the design of these kinds of heat exchanger was promising, but did not develop any design rules or models from his CFD data.

Other similar CFD studies of refrigeration tube-in-plate fin heat exchanger have been conducted, but the majority have been concerned with a specialised aspect of mass transfer such as condensation and frost deposition on fins. Often they do not quote any kind of validation results to indicate whether or not the performance of their model is representative of actual heat exchangers, outside of their special interest area.

2.6.4 Conclusion

The above shows that there is little published on circular finned tube bundles modelled in CFD, likely due to the high computational demands required for three dimensional modelling, and the difficulty of providing good data for development and validation of the models.

It also shows that when CFD is integrated into a development program it can provide insights into flow behaviour that are difficult to otherwise obtain. This information, as shown above, can then be readily used in generalised modelling, and thus, with care, the CFD can be treated as a virtual experiment. It must be noted, however, that CFD is a general tool that, at the time of this review shows great potential providing that validation from experiments can be provided. Then the user can start to use CFD to investigate similar problems with greater confidence.

2.7 Summary and project objectives

From the above reviews it became apparent that a program of work was necessary to address the areas of weakness in the currently available prediction methods. The identified areas were:

- The deficiency of the HTFS method of Ralston and Chu [22] meant that an improved method for the pressure drop and heat transfer performance of staggered bundles is required.
- The available methods for inline layout bundles have been shown to poorly predict the limited experimental data, so new data and a new prediction method is necessary,
- The influence of using corbels at the wall of a finned tube bundle is unclear. A method of predicting the pressure drop performance when corbels are used that are not half finned tubes is necessary, as such a method has not been previously presented.
- The influences of bypassing flow on finned tube bundles with respect to the change in heat transfer and hydraulic performance is not clear. As most, if not all, performance prediction methods do not allow for any flow bypassing, a study of these effects should be made. Therefore a method to predict the influence of bypassing on finned tube bundles should be developed.
- A simple method of predicting the heat transfer coefficient of individual tube rows is required. The methods presented by other workers have either been for plain tube bundles or extremely complicated (Yang and Bell [45]). This method must take into account the key features of heat transfer through finned tube bundles: the temperature difference and the turbulence.
- There is uncertainty about the point at which heat transfer stabilises, especially in inline arrangement bundles. More investigation is required to try and identify the process that lead to the stabilisation of heat transfer.

The programme of work determined to develop the new methods is listed below:

1. Improve an existing method for predicting the heat transfer and pressure drop performance of staggered finned tube heat exchanger bundles using data from the existing HTFS databank.

2. Collect data from testing inline tube bundles with square and rectangular tube layouts with plain high fins.

3. Develop a prediction method for heat transfer and pressure drop performance of inline tube bundles with square and rectangular pitch finned tube heat exchangers.

4. Collect data from a staggered heat recovery and a staggered air cooler bundle with bypassing flow.

5. Develop a prediction method for heat transfer and pressure drop of staggered bundles with bypassing flow.

6. Collect data from staggered arrangement air cooler bundle with various shapes of wall-sealing devices (corbels).

7. Develop a prediction method for pressure drop of staggered bundles with wall sealing devices in place.

8. Develop a method to determine the row heat transfer coefficient using local data derived from Computational Fluid Dynamics (CFD) studies. The test data for the experimental inline bundles will be used to provide validation and comparison with the CFD result, therefore the initial model will treat inline bundles only.

In the course of the work it will be shown that testing and open literature data were used to develop the new models. It will be shown that CFD augmented these studies, to provide insight into local flow behaviours and provide qualitative data for aspects of the method development.

The overall objective could be summarised as 'to create a new suite of prediction methods for HTFS software products (ACOL and FIHR) and handbook sheets for the air/gas side of finned tube crossflow heat exchangers'.

CHAPTER 3

Experimental Equipment

3.0 Introduction

The majority of experiments carried out for this project were conducted in a small-scale wind tunnel designed to test representative sections of air-cooled heat exchangers. The following sections detail the layout and instrumentation of the tunnel. The tunnel was located at the NEL site, firstly in the Rankine building and then in the Reynolds building. As the wind tunnel was used for a variety of test applications it was dubbed the Multi Purpose Wind Tunnel, or MPWT. This abbreviation will be used throughout the remainder of the thesis. Nine Bundles of inline air coolers were tested in this facility, and one staggered air cooler bundle with bypassing and various corbel shapes.

Two heat recovery bundles were tested in a specialised wind tunnel that replicated the conditions of a process fired exhaust. This tunnel was designed to test heat recovery bundles, typically used in fired heater convective banks, and was dubbed the High Temperature Wind Tunnel, or HTWT. This abbreviation will be used throughout the remainder of the thesis.

3.1 Multi Purpose Wind Tunnel (MPWT)

3.1.1 Test facility

The tube bundles described in Section 3.3 and 3.5 below were tested in the Multi-Purpose Wind Tunnel (MPWT) facility at NEL. A schematic diagram of the test facility is shown in Figure 3.1. Air was supplied across the tube bundle, and steam is condensed inside the tubes.

Ambient air was drawn into the MPWT ducting through an inlet flow measurement cone constructed to BS848. The centrifugal fan discharges the air into a conditioning section to supply uniform airflow distribution to the test bundle. Two thermocouple grids, each containing 9 thermocouples, were fitted upstream and downstream of the test bundle to measure the average air inlet and outlet temperatures. The pressure drop across the test bundle was measured using a differential pressure transducer connected to two piezometer rings. Each piezometer ring had four pressure tapings. Sufficient length of tunnel ducting was provided to ensure uniform flow upstream and downstream of the test bundle. The warm air leaving the test bundle was then exhausted safely to the atmosphere.

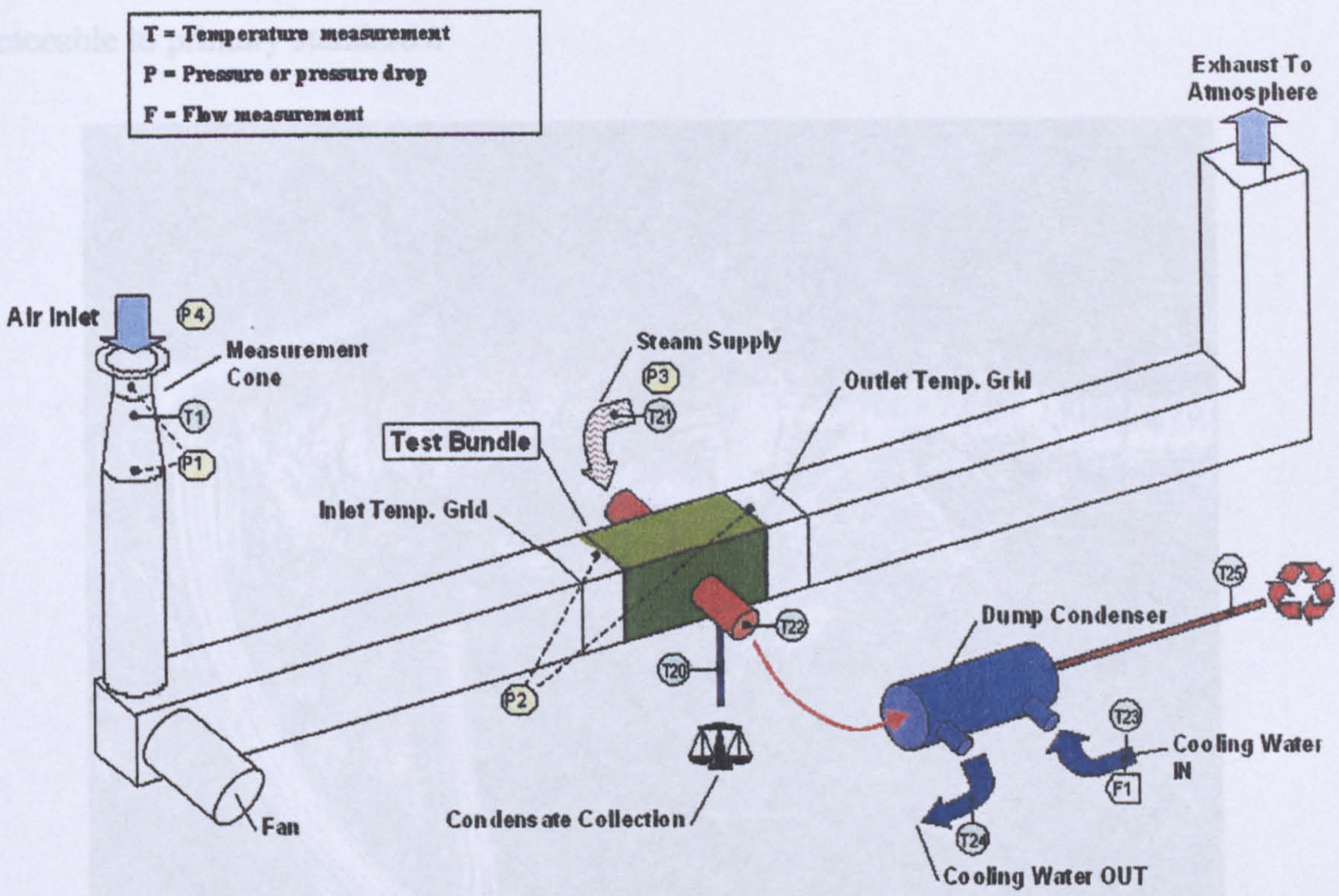

Figure 3.1: Schematic of the NEL Multi Purpose Wind Tunnel (MPWT)

The wind tunnel cross section was $0.25m^2$ with the duct having a 0.5m square section. The bundle approach face was 4.5m from the fan exit. The inlet pressure tappings and thermocouple grid were 1.2m and 1.42m from the working section approach face, respectively. The outlet pressure tappings and thermocouple grid were 0.85m and 1m from the working section exit face, respectively.

On the tubeside, a controlled flow of steam is supplied to the tubes through an inlet nozzle connected to a box type header. Complete condensation was avoided in all of the tests to ensure that the entire tube surface was active in heat transfer. At each measurement point the condensate flowrate was obtained by collecting the condensate over an average period of three minutes and weighing it. The excess steam was condensed in a dump condenser. An energy balance between the cooling water supplied to the dump condenser and the steam side was used to calculate the steam mass flowrate entering the dump condenser. The mass flowrate of the steam supplied to the test bundle was found from the sum of condensate flowrate from the test bundle and the steam flowrate to the dump condenser. A full list of the instrumentation used on the MPWT for

these tests can be found in Tables 3.1–3.4. All instrumentation was fully calibrated and traceable to primary standards.

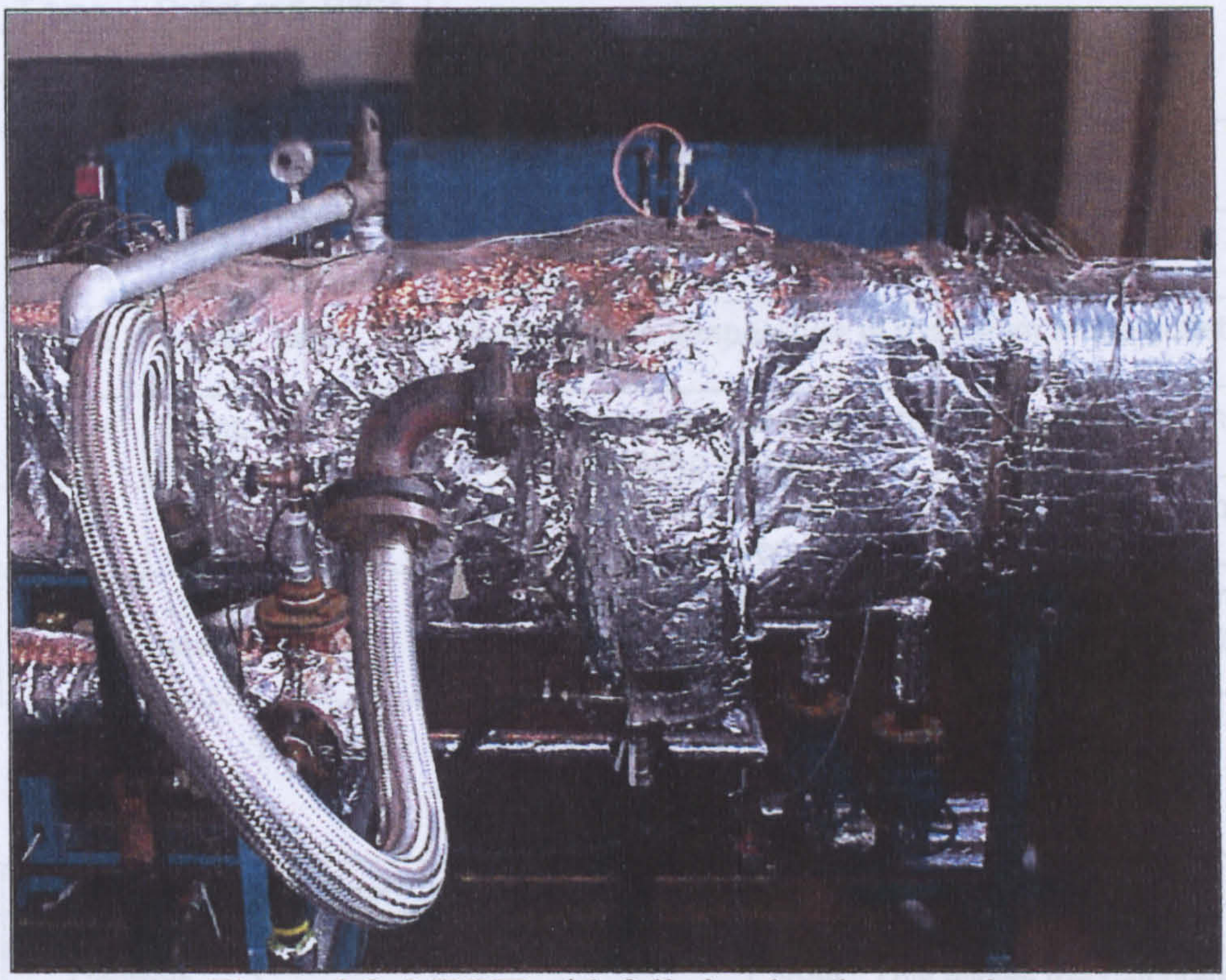

Figure 3.2: MPWT with fully insulated test section

The test bundle and a significant part of the inlet and outlet ducting were insulated as shown in Figure 3.2.

ID	Model	*Location on rig*	Function
T001	T type	Inlet cone	Measures the temperature of the air entering the system
T002	T type	Inlet grid R1C1	These thermocouples are arranged in a 3x3 grid across the ducting upstream of the test piece. These allow the operator to see any temperature variations and are used to calculate a mean temperature at this location.
T003	T type	Inlet grid R1C2	
T004	T type	Inlet grid R1C3	
T005	T type	Inlet grid R2C1	
T006	T type	Inlet grid R2C2	
T007	T type	Inlet grid R2C3	
T008	T type	Inlet grid R3C1	
T009	T type	Inlet grid R3C2	
T010	T type	Inlet grid R3C3	
T011	T type	Outlet grid R1C1	As above but fitted downstream of the test section.
T012	T type	Outlet grid R1C2	
T013	T type	Outlet grid R1C3	

T014	T type	Outlet grid R2C1	
T015	T type	Outlet grid R2C2	
T016	T type	Outlet grid R2C3	
T017	T type	Outlet grid R3C1	
T018	T type	Outlet grid R3C2	
T019	T type	Outlet grid R3C3	
T020	T type	Condensate from header.	Measures the temperature of the condensate at the outlet header
T021	T type	Steam inlet	Measures the temperature of the steam in the inlet header
T022	T type	Steam outlet	Measures the temperature of the steam in the outlet header
T023	T type	Dump cond CW inlet	Measures the temperature of the cooling water at the inlet to the dump condenser
T024	T type	Dump cond CW outlet	Measures the temperature of the cooling water at the outlet of the dump condenser
T025	T type	Dump cond steam return	Measures the condensate temperature from the dump condenser. Allows a check of the degree of cooling taking place.

Table 3.1: Thermocouples used on MPWT

ID	Manufacturer	Model	Location on rig	Function
PT001	Furness Controls	FCO44	Inlet cone	Measure ΔP across the inlet cone. This allows the calculation of the mass flowrate of air entering the system.
PT002	Furness Controls	FCO44	ΔP across bundle	Measures the ΔP across the test section.
PT003	Data Instruments	SA25A	Steam inlet header	Measures the pressure in the test section header
PT004	Sensor Technics	144SCO 811-BARO	Mounted on wall behind rig	Measures local atmospheric pressure at the rig

Table 3.2: Pressure transducers used on MPWT

ID	Manufacturer	Model	Location on rig	Function
WS001	Oertling	MD60	Located in WT control area below MPWT	Timed measurement of the mass of the collected condensate

Table 3.3: Weigh scales used on MPWT

ID	Manufacturer	Model	Location on rig	Function
FM001	UCC	DATAFLOW	CW inlet line to the dump condenser	Measurement of the cooling water mass flow. Used for energy balances

Table 3.4: Flowmeter used on MPWT

3.1.2 Data Acquisition System (DAS)

The data acquisition software was a Microsoft Visual Basic (VB) program designed by NEL staff. The program ran on the Microsoft Windows 95 operating system, on an IBM compatible computer, fitted with a 133MHz Pentium processor and 64Mb of RAM.

The program presented the user with a simple series of forms that required the operator to input some details of the test runs such as the manually input data of condensate collection time, and mass of condensate collected. Other details were operator name and date for NEL quality procedures.

Forms were available that reported the stability of the thermocouple grids during warm up, and the readings from the instruments during running. The other forms in the program were used to select test and instrument scanning options, and instigate data capture for a test run.

The output, once accepted by the operator, was saved as a delimited text file with a predetermined layout of parameters such as steam inlet temperature, and all the other measurements detailed throughout Section 3.1.1 above.

The data capture unit was a Hewlett-Packard 3852A. This was connected to the rig computer by a parallel port interface. All of the output from all of the instrumentation was a voltage, with the exception of the turbine flow meter, which was a frequency signal. The instrumentation was connected to the capture unit by analogue to digital (A/D) converter cards that were grouped by type.

3.1.3 Analysis Software

The DAS output data analyser was a Microsoft Excel spreadsheet based application. It was specially written at the beginning of the project, based on a similar application written by NEL staff for the High Temperature Wind Tunnel, which will be discussed in Section 3.2.

It used Visual Basic for Applications (VBA) modules of calculation code written to execute data reading, processing and carrying out the uncertainty analysis, provided by

NEL staff, which is shown in Appendix A. Performance calculations for the test bundle and fluid physical property modules were incorporated, based on a combination of standard flow and heat transfer theory and proprietary HTFS methods. Performance predictions from HTFS and open literature methods were also programmed into the code.

Using the VBA code modules allowed error checking to be performed in a logical fashion that would not be possible with standard formula based spreadsheet cell functions.

The application was divided using the premise of separate sheets in the spreadsheet to allow a split of standard data, bundle geometry, rig calculations etc. This allowed a flow of data to be passed from one sheet to the next, and simplify the build and debug process. The sheets were as shown in this list:

1. Test information/introduction to the software
2. Version control (for NEL quality procedures)
3. Instrument calibration and measurement uncertainty data
4. Bundle specification geometry input
5. Geometric calculations performed on the geometry (surface areas etc.)
6. A display of the imported raw rig data
7. Performance calculations based on the rig data
8. Performance prediction calculations, using HTFS and open literature methods.
9. Summary results of measured and predicted performance
10. Uncertainty analysis
11. Performance graphs

3.1.4 Operation of the rig

To operate the rig the following steps were required:

1. The rig software was started on the computer
2. The differential pressure transducers were zeroed using the manual adjustment potentiometer on the transducer, based on the reading from the DAS software readout
3. The fan for the wind tunnel was started to the desired speed setting

4. The dump condenser coolant valves (feed and return) were opened to cool the condenser
5. The steam inlet valves were opened, sequentially and progressively, to prevent water hammer from condensation in the lines. The valving system is shown in Figure 3.3

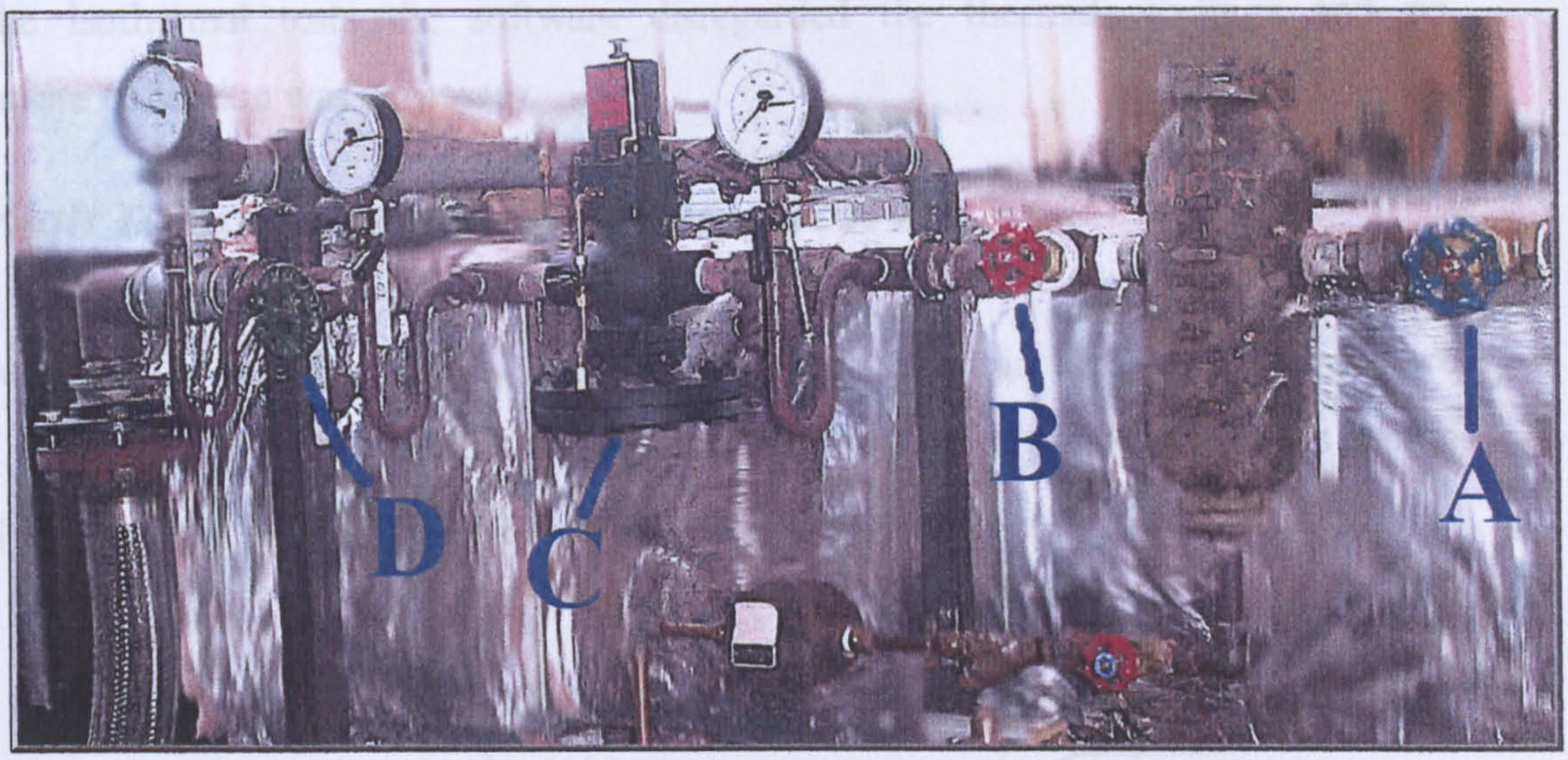

Figure 3.3: Steam inlet valving system

A shows the main flow control valve which was followed by a separator to remove any excess water from the steam. B is the second control valve, opened when the steam separator has had time to warm up and the steam deemed dry enough. C was a pressure reducer, and it was adjusted to ensure near atmospheric pressure of the steam at the bundle inlet. This was done iteratively once the entire system reached equilibrium. D was the final flow control valve used to control the flow once the system reached equilibrium.

6. The computer displays were monitored until thermal equilibrium had been reached
7. The data point collection was started by placing the condensate collection barrel under the collection valve nozzle, activating the data collection procedure on the software and activating the timer to open the condensate valve
8. The timer was stopped after 180 seconds, with the software stopping shortly thereafter, and weighed on the scales
9. The exact collection time and condensate mass were added to the data input form on the software

10. The heat balance of the test run was checked by calculations performed by the software, and if within ±5% the run was accepted and stored. If not the instrument readings were checked, flows adjusted if necessary and the run re-done

For the isothermal tests the software disregarded the thermal readings and no condensate collection was necessary.

3.2 High Temperature Wind Tunnel (HTWT)

3.2.1 Test Facility

The tube bundle described in Section 3.4 below was tested in the High-Temperature Wind Tunnel (HTWT) facility at NEL. A schematic diagram of the test facility is shown in Figure 3.4. The tunnel was dismantled in early 2001.

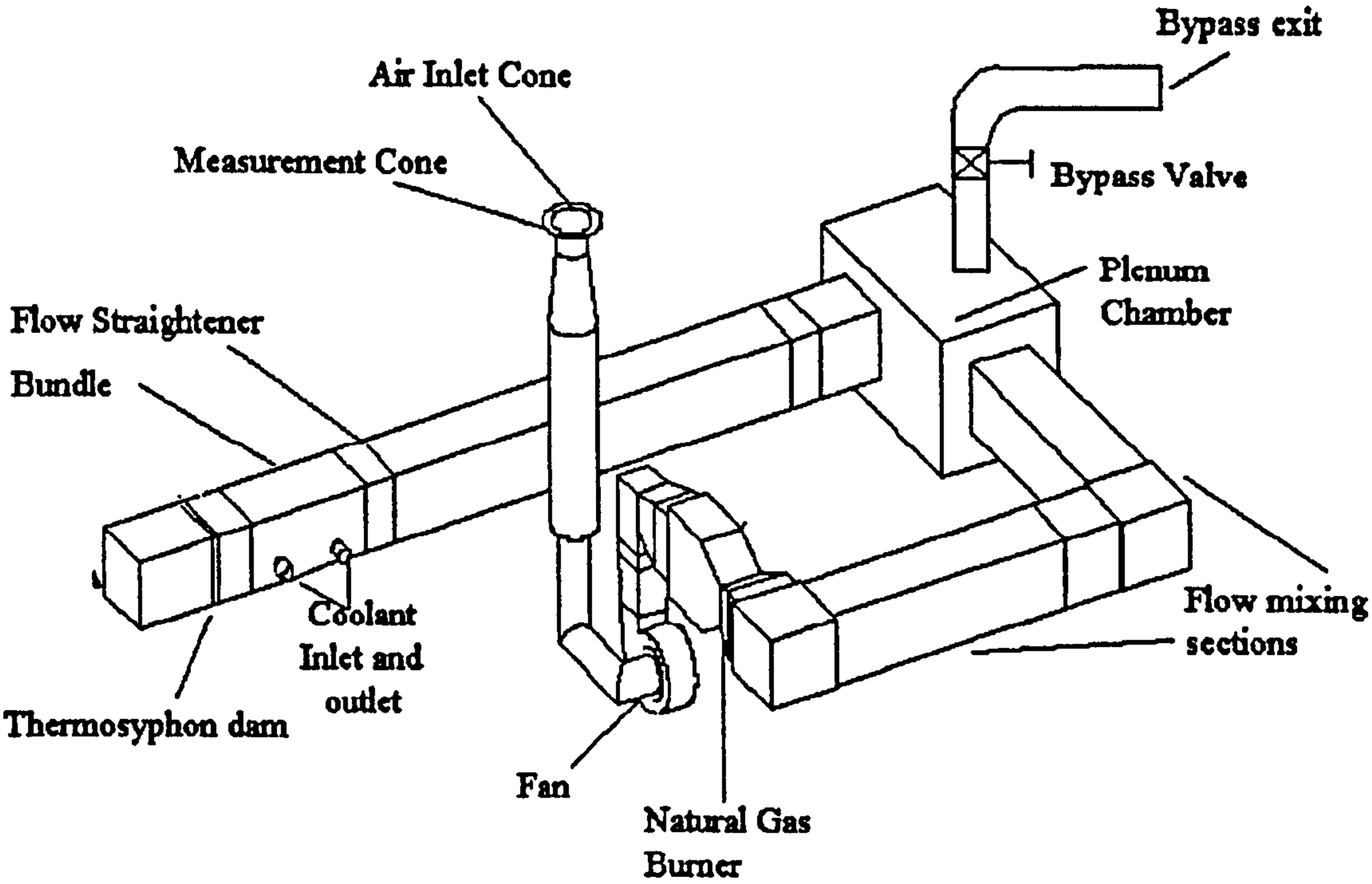

Figure 3.4: Schematic of High Temperature Wind Tunnel

Air was drawn into the inlet cone at which point a measurement of inlet air temperature and mass flow rate can be made, using the method presented in BS EN848. The flow was drawn in by a centrifugal fan, and passed through the burner section. Here fuel was added, which mixed with the airflow, and combustion initiated. The hot gas flow then

passed along the mixing length to a turning vane at the elbow then passesd along a flow mixing section to a plenum chamber. In this plenum chamber some of the flow could be exhausted through a bypass valve, to allow operation at low flow rates. The flow leaving the plenum was passed through a long section with flow straighteners. These straighteners conditioned the flow before it passed through the tube bundle. The bundle and its coolant manifolds were covered in a combination of ceramic-fibre boards and foil coated glass-fibre blankets to minimise heat loss to the atmosphere. The entire tunnel from the burner unit onwards was insulated similarly.

The HTWT tested heat recovery bundles by passing a Water/Glycol mixture through the tube side of the bundle. The coolant flow rate and its temperature rise could be measured, thus a tubeside duty could be calculated. The coolant was fed through the bundle at a maximum of 14 kg/s. Hot gas was passed over the heat exchanger crossflow side, supplied by a natural gas burner, which could produce 3.2MW of heat. The tunnel was made from high-chrome steel so that it could cope with a maximum design temperature of 500°C.

A variable speed centrifugal fan capable of delivering a maximum of 8 kg/s provided the gas-flow. The mass flow rate of this gas was calculated from air measurements and fuel addition. A heat balance was determined from the heat recovered by the coolant and the measured gas side temperature difference and flow rates.

The wind tunnel cross section was 1.27m^2 with the duct being 1.27m tall and 1m wide. The inlet pressure tappings and thermocouple grid were 1m and 1.04m from the working section approach face, respectively. The outlet pressure tappings and thermocouple grid were 1.35m and 1.55m from the working section exit face, respectively

After the flow passed over the bundle it passed though a thermosyphon dam. The dam was in place for two reasons: By measuring the pressure drop across the dam the true mass flow rate passing over the bundle, after any of the flow had escaped through the bypass valve, could be determined and to prevent any backflow of cold air in to the tunnel at particularly low mass flow rates. The dam itself was a plate across the whole area of the duct. One was for low mass flow rates and had 100 25mm diameter, equally

spaced holes drilled into it. The plate used in high mass flow rate tests had 100 40mm holes. These complied with BS EN1042 for the calculation of mass flow rates through orifice plates. The gas was then vented to atmosphere. All of the measurements were recorded by a PC based Acquisition system. The recorded data was then imported into the analysis software, as described for the MPWT.

The wind tunnel was designed, built and modified by NEL staff from 1992 onwards.

3.2.2 Bundles

The bundles themselves were fitted to the tunnel by way of flanges on the wind tunnel and on the bundles. These flanges were bolted together, with a layer of Goretex thread sealant applied to ensure an airtight seal. This should have allowed for any differential expansion of the bundle to the tunnel, and the duct would remain airtight. In practise it was extremely difficult to prevent air from leaking from and into the duct flanges, due to the magnitude of operating temperatures. The bundles used will be described in section 3.4.

3.2.3 Instrumentation and measurements

Table 3.5 –3.8 detail the instrumentation used on the rig.

Location on rig	Function
Fuel supply to burner	Returned volumetric fuel flow rate to be used in the fuel supplied mass flow rate calculation.
Coolant inlet line	Returned volumetric flow rate of coolant for heat balance calculations.

Table 3.5: Flowmeters used on HTWT

Model	*Location on rig*	Function
K type	Inlet cone	Measures the temperature of the air entering the system
K type	Fuel inlet	Measure the temperature of the fuel entering the burner
K type	1st flow mixing section	Measured the gas temperature immediately after the burner
K type	Inlet grid R1C1	These thermocouples are arranged in a 4x4 grid across the ducting upstream of the test piece. These allow the operator to see any temperature variation and are used to calculate a mean temperature at this location.
K type	Inlet grid R1C2	
K type	Inlet grid R1C3	
K type	Inlet grid R1C4	
K type	Inlet grid R2C1	

K type	Inlet grid R2C2	
K type	Inlet grid R2C3	
K type	Inlet grid R2C4	
K type	Inlet grid R3C1	
K type	Inlet grid R3C2	
K type	Inlet grid R3C3	
K type	Inlet grid R3C4	
K type	Inlet grid R4C1	
K type	Inlet grid R4C2	
K type	Inlet grid R4C3	
K type	Inlet grid R4C4	
K type	Outlet grid R1C1	As above but fitted downstream of the test section.
K type	Outlet grid R1C2	
K type	Outlet grid R1C3	
K typ	Outlet grid R1C4	
K type	Outlet grid R2C1	
K type	Outlet grid R2C2	
K type	Outlet grid R2C3	
K type	Outlet grid R2C4	
K type	Outlet grid R3C1	
K type	Outlet grid R3C2	
K type	Outlet grid R3C3	
K type	Outlet grid R3C4	
K type	Outlet grid R4C1	
K type	Outlet grid R4C2	
K type	Outlet grid R4C3	
K type	Outlet grid R4C4	
K type	Coolant inlet manifold	Measures the temperature of the coolant entering the bundle
K type	Coolant outlet manifold	Measures the temperature of the coolant leaving the bundle

Table 3.6: Thermocouples used on HTWT

Location on rig	Function
Inlet cone	Measure ΔP across the inlet cone. This allows the calculation of the mass flowrate of air entering the system.
Fuel inlet	The fuel pressure had a regulator valve to ensure constant pressure, and the transducer related this pressure to the data aquisition system
ΔP across bundle	Measures the ΔP across the test section.
Mounted on wall next to rig	Measures local atmospheric pressure at the rig
Across thermosyphon dam	Measures the ΔP across the thermosyphon dam plate

Table 3.7: Pressure transducers used on HTWT

3.2.4 Data Acquisition System (DAS)

The data aquisition system used for the HTWT was similar to that of the MPWT. The program ran on the Microsoft Windows 95 operating system, on an IBM compatible digital computer, fitted with a 66MHz 86486 processor and 32Mb of RAM. The data capture unit was a Hewlett-Packard 3852A.

3.2.5 Operation of the rig

To operate the rig the following steps were required:

1. The rig software was started on the computer.
2. The differential pressure transducers were zeroed using the manual adjustment potentiometer on the transducer, based on the reading from the DAS software readout.
3. The centrifugal fan was started to the desired flow rate
4. The burner was activated from its control panel.
5. The coolant supply valve was opened.
6. The burner temperature was monitored and adjusted while the tunnel reached thermal equilibrium. This was done by monitoring the thermocouple readings via the stability monitor form on the data acquisition software.
7. The readings were then taken via the software. Multiple readings were taken at the same flow rate.
8. The flowrate was adjusted for the next data point.

3.3 Inline Air Cooler Bundles

The main objective of these test was to gather data from a wide range of inline bundle geometry to help in the development of the new inline tube bundle performance prediction method. Two sets of tests were performed:

- Square pitch inline layouts
- Rectangular pitch inline layouts

The range of geometries for both sets of tests were approved by the HTFS Crossflow Review Panel.

3.3.1 Square Pitch Bundles

The geometry of these bundles is shown in Table 3.8.

bundle Number	1	2	3	4
Tube OD (D_o), m	0.0256	0.0256	0.0256	0.0256
Tube wall thickness (S_w), m	0.0023	0.0023	0.0023	0.0023
Tube ID (D_i), m	0.021	0.021	0.021	0.021
Tube Length (L_t), m	0.465	0.465	0.465	0.465
Fin Type	G-finned	G-finned	G-finned	G-finned
Fin tip diameter (D_f), m	0.0572	0.0572	0.0508	0.0572
Fin Root diameter (D_r), m	0.0256	0.0256	0.0256	0.0256
Mean Fin Thickness (S_f), m	0.000247	0.000247	0.000247	0.000247
Fin Frequency [1/m] (N_f)	433	433	433	236
Clearance between fin tips	0.0028	0.0095	0.0032	0.0028
Transverse Pitch (P_t), m	0.06	0.0667	0.054	0.06
Longitudinal Pitch (P_l), m	0.06	0.0667	0.054	0.06
No. of tubes/ row	8	7	9	8
No of tube rows (N_r)	6	6	6	6
Bundle Height (vertical in rig) (H_b), m	0.480	0.4669	0.486	0.480
Bundle length (in flow direction) (L_b), m	0.3572	0.3907	0.321	0.3572
Tube Material	Carbon Steel	Carbon Steel	Carbon Steel	Carbon Steel
Fin Material	Aluminium	Aluminium	Aluminium	Aluminium
Total gas side surface area (m^2)	41.75	36.53	35.13	23.57

Table 3.8: Geometry of square pitch test bundles.

A general schematic of the bundle layout is shown in Figure 3.5. All of these square pitch bundles consisted of 6 rows of tubes with a nominal bore diameter of 1 inch arranged in an inline layout. The first and the fourth bundles have the same geometry apart from the fin frequency. In addition to the fin frequency the key geometrical parameters that have been varied are tube pitch, number of tubes per row and the fin tip diameter.

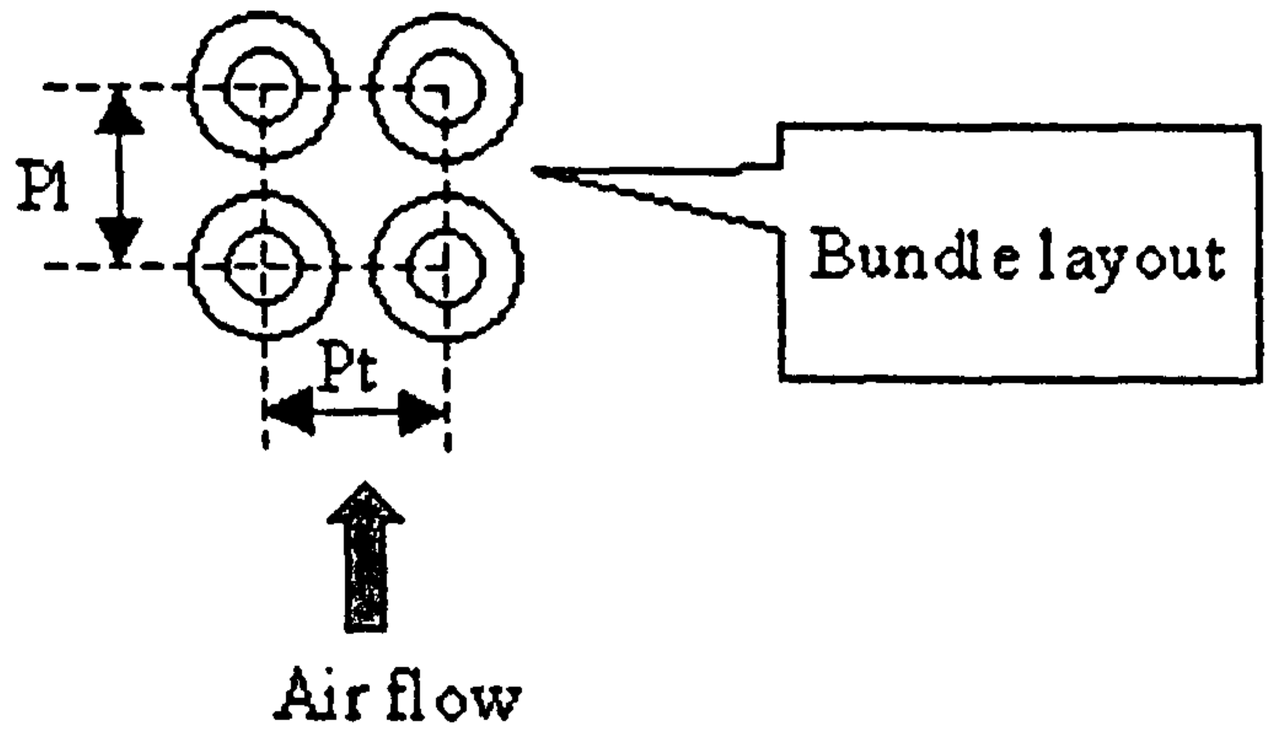

Figure 3.5: Schematic of square pitch inline tube bundle

3.3.2 Rectangular pitch bundles

The second set of bundles comprised of five rectangular pitch air inline air coolers. These are often referred to as irregular pitch bundles. These were all systematic alterations on the original four bundles, with a new bundle being added (Bundle 9) with a grossly extended longitudinal pitch to allow collection of data for a bundle with Pl/Pt of 1.21. A general schematic of the bundle layout is shown in Figure 3.6. The rectangular bundles consisted of both 6 and 5 rows of tubes to maintain a flow length that suited the steam inlet headers.

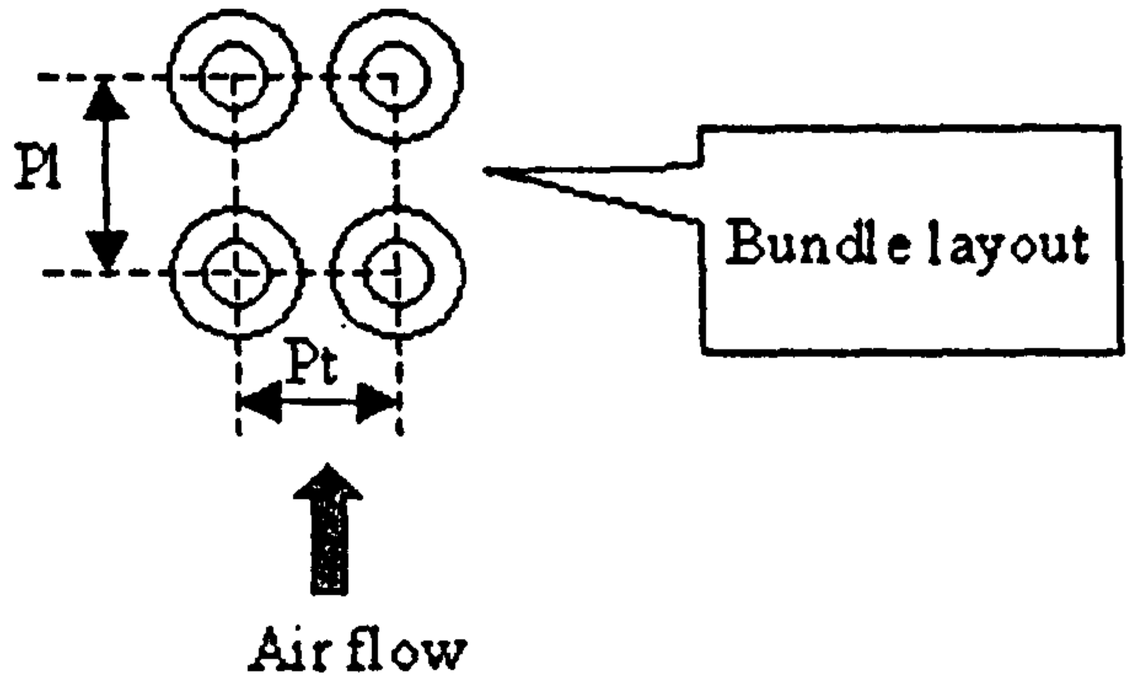

Figure 3.6: Schematic of rectangular pitch inline tube bundle

The geometry of the bundles is given in table 3.9 below.

Bundle Number	5	6	7	8	9
Tube OD (D_o), m	0.0256	0.0256	0.0256	0.0256	0.0256
Tube wall thickness (S_w), m	0.0023	0.0023	0.0023	0.0023	0.0023
Tube ID (D_i), m	0.021	0.021	0.021	0.021	0.021
Tube Length (L_t), m	0.465	0.465	0.465	0.465	0.465
Fin Type	G-finned	G-finned	G-finned	G-finned	G-finned
Fin tip diameter (D_f), m	0.0572	0.0572	0.0508	0.0572	0.0572
Fin Root diameter (D_r), m	0.0256	0.0256	0.0256	0.0256	0.0256
Mean Fin Thickness (S_f), m	0.000247	0.000247	0.000247	0.000247	0.000247
Fin Frequency [1/m] (N_f)	433	433	433	236	433
Clearance between fin tips	0.0028	0.0095	0.0032	0.0028	0.0028
Transverse Pitch (P_t), m	0.06	0.0667	0.054	0.06	0.06
Longitudinal Pitch (P_l), m	0.0667	0.0727	0.060	0.0667	0.0727
No. of tubes/ row	8	7	9	8	8
No of tube rows (N_r)	6	5	6	6	5
Bundle Height (vertical in rig) (H_b), m	0.480	0.4669	0.486	0.480	0.480
Bundle length (in flow direction) (L_b), m	0.3907	0.348	0.3508	0.3907	0.348
Tube Material	Carbon Steel	Carbon Steel	Carbon Steel	Carbon Steel	Carbon Steel
Fin Material	Aluminium	Aluminium	Aluminium	Aluminium	Aluminium
Total gas side surface area (m^2)	41.75	30.445	35.131	23.574	34.794

Table 3.9: Geometry of rectangular pitch test bundles.

3.4 Staggered Heat Recovery Bundle

Chapters 8 and 9 will show test work done to investigate the pressure drop and heat transfer performance of finned tube bundles with and without corbels. This section details the one heat recovery bundle tested in the HTWT specifically for this project.

3.4.1 Geometry of Bundle

Figure 3.7 shows the bundle with the half finned tube corbels at the walls to create a 'perfect' bundle. The details of what a perfect bundle means, and why it is the case, will be explained further in Chapter 8.

Figure 3.7: Heat Recovery Bundle with corbels in place

The photograph shows how the tubes are fixed into the tube sheets. A finned half tube corbel can be seen at the bottom of the tube row nearest bundle inlet, on the left hand side of the photograph.

This bundle geometry is given in Table 3.10.

Bundle Number	Heat Recovery
Tube OD (D_o), m	0.1413
Tube wall thickness (S_w), m	0.00655
Tube ID (D_i), m	0.1282
Tube Length (L_t), m	1
Fin Type	G-finned
Fin tip diameter (D_f), m	0.1794
Fin Root diameter (D_r), m	0.1413
Mean Fin Thickness (S_f), m	0.0015
Fin Frequency [1/m] (N_f)	197
Clearance between fin tips	0.0028
Transverse Pitch (P_t), m	0.254
Longitudinal Pitch (P_l), m	0.22
No. of tubes/ row	5
No of tube rows (N_r)	8
Half tubes per row	1
Total number of active tubes	40
Bundle Height (vertical in rig) (H_b), m	1.3966
Bundle length (in flow direction) (L_b), m	1.0594
Tube Material	Mild Steel (A106B)
Fin Material	Mild Steel (A106B)
Total gas side surface area (m^2)	170.41

Table 3.10: Bypass Study Heat Recovery Bundle Geometry

Figure 3.8 shows the bundle with half tubes at the wall. This is considered as a 'perfect' bundle from the flow point of view, as it prevents flow bypassing the tubes.

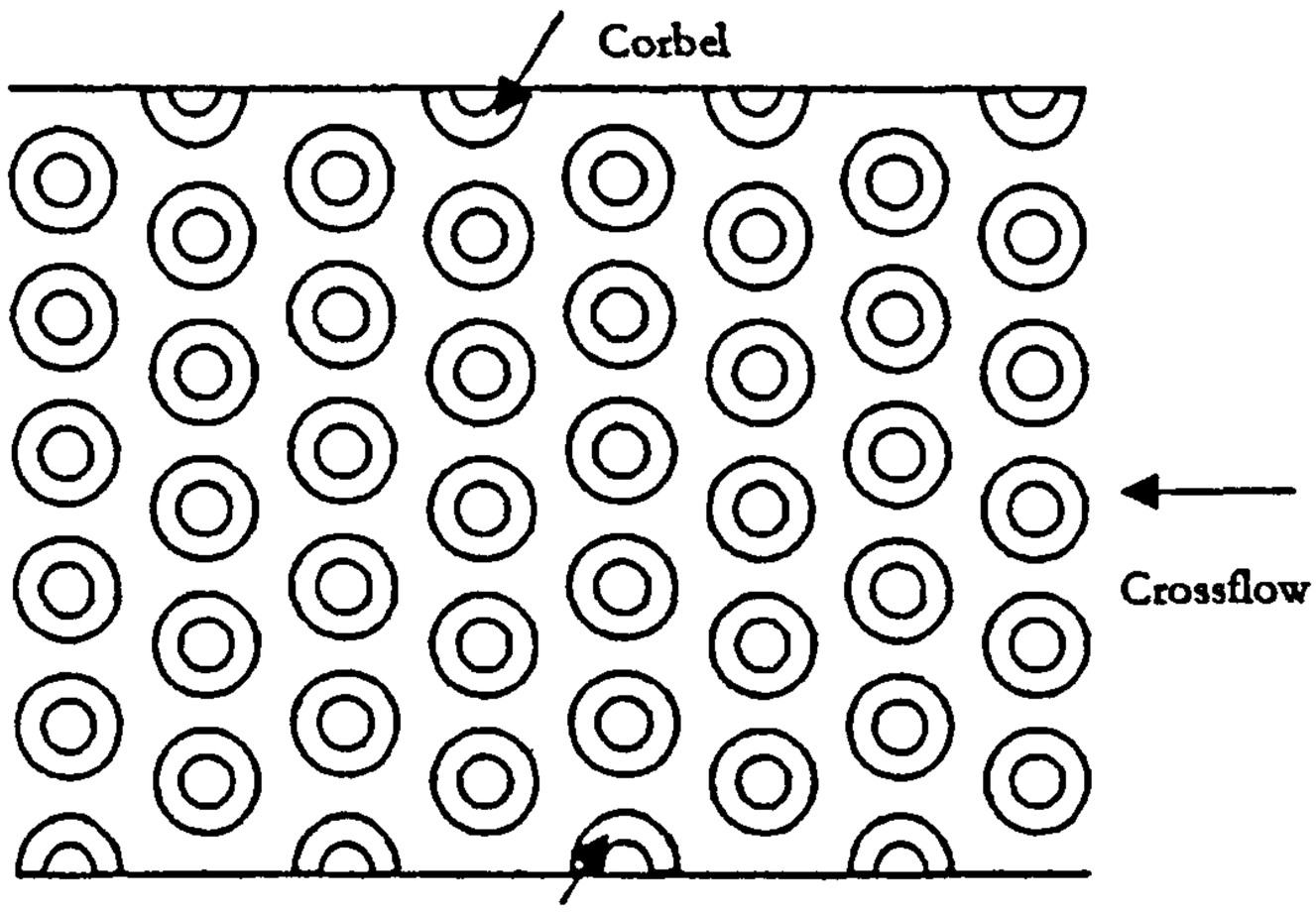

Figure 3.8: Heat Recovery Bundle with corbels

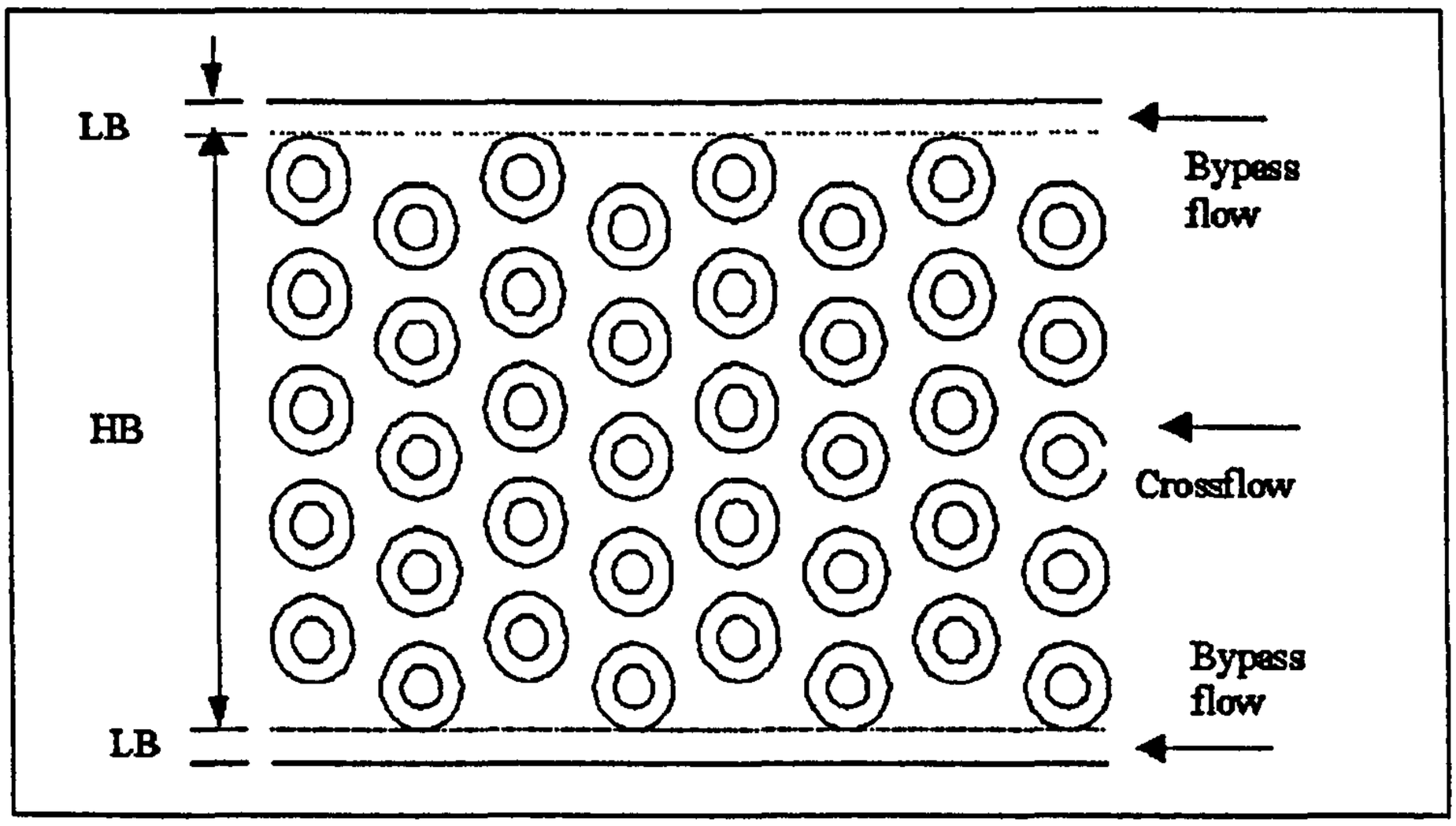

Figure 3.9: Heat Recovery Bundle without corbels (defined bypassing lane)
No Corbels (LB = 0.0373 m and HB = 1.322 m)

When corbels are not installed two bypass lanes are created, at the top and the bottom of the bundle, as shown in Figure 3.9. The geometry specified in Table 3.10 still stands, with the exception that a bypass lane height (H_{gap}) now needs to be quoted. The lane height (at both the top and bottom of the bundle) was 0.0373m.

The corbels were held to the duct floor and roof by means of bolts threaded into inserts fitted into the tubes.

3.4.2 Construction of Bundle

3.4.2.1 Duct construction

The duct was fabricated from steel sections; one floor sheet, one roof sheet, and two tube sheets to support the tubes in the desired pitch arrangement. The tubes were connected by u-shaped pipes to allow the coolant to pass through from tube row to tube row. The bundle was connected in a multi pass arrangement, whereby the coolant is pumped counter to the gas flow, so that the maximum amount of heat is picked up by the coolant. A diagram of this is shown in Figure 3.10.

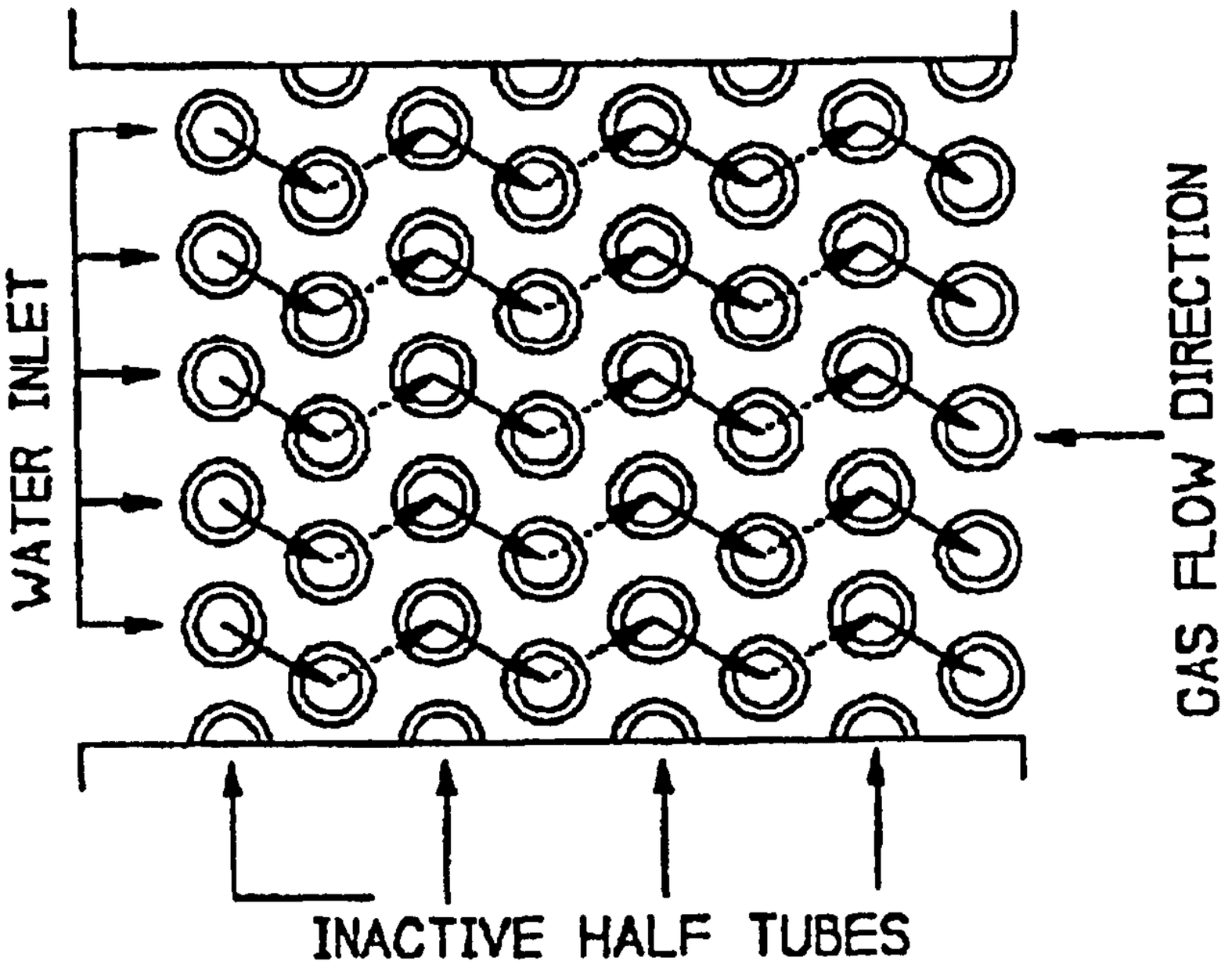

Figure 3.10: Schematic of multi pass coolant flow

3.4.2.2 Finned Tubes

The tubes were manufactured from A106B Mild Steel. The fins were also A106B Mild Steel. They were spiral wound on to the tube and held in place purely by mechanical tension. The tubes were arranged in 8 tube rows in the flow direction with 5 tubes being present in each tube row.

3.4.2.3 Tube side arrangement

The tubes were fitted with concentric cores to reduce the tube inner cross sectional area. These have the effect of increasing the coolant side velocity for a given coolant mass flow rate, and thus increasing the tube side heat transfer coefficient. This helped to achieve a good heat balance, and reduce the error in the calculation of the heat transfer coefficient.

3.4.3 Thermocouple Correction

Henry [50] demonstrated that an uneven temperature profile can be expected downstream of the bundle. This arises because the gas-side stream flowing near the upper and lower walls of the bundle is not heated nor cooled by the half tubes and therefore the temperature change through the bundle edge is less than for the gas-side stream flowing nearer the centre of the bundle. However, the gas-side stream can be expected to mix between tube rows and therefore the tube duct wall effects can be

expected to migrate towards the centre. He demonstrated close agreement between predicted and experimental temperature profiles after the tube bundle.

The practical consequence of this work are that an average gas-side downstream temperature found by averaging the measurements from a grid of thermocouples will be optimistic because a straight average does not take account of the inactive half tubes.

A member of NEL staff devised a correction method based on this work, which approximated the temperature mixing between tube rows and determined the distortion immediately behind the bundle.

The temperature readings from the thermocouple grid used for these tests was found to require a very small correction factor, which was almost unity.

3.5 Staggered air cooler bundle with and without corbels

A bundle was designed for the purpose of conducting flow visualisation tests as well as collecting isothermal pressure drop data for tests with corbels fitted to the walls and also with defined bypassing lanes. The following sections will briefly discuss the bundles and corbel shape designs.

3.5.1 Bundle Design

The bundle tube sheets, floor and roof were constructed from 12mm thick transparent acrylic. This meant that both tube sheets and the floor and roof of the bundle were all available for optical access.

Due to the nature of these tests the design required that the floor and roof of the bundle could be removed to allow the corbels to be replaced/removed without removing the bundles from the MPWT. A design was developed that allowed the tube sheets to be constantly held in place to prevent the tubes from coming loose. This was done by attaching aluminium strips to each end (in the flow direction) of each sheet. Figure 3.11 shows a design drawing of the bundle without the tubes fitted.

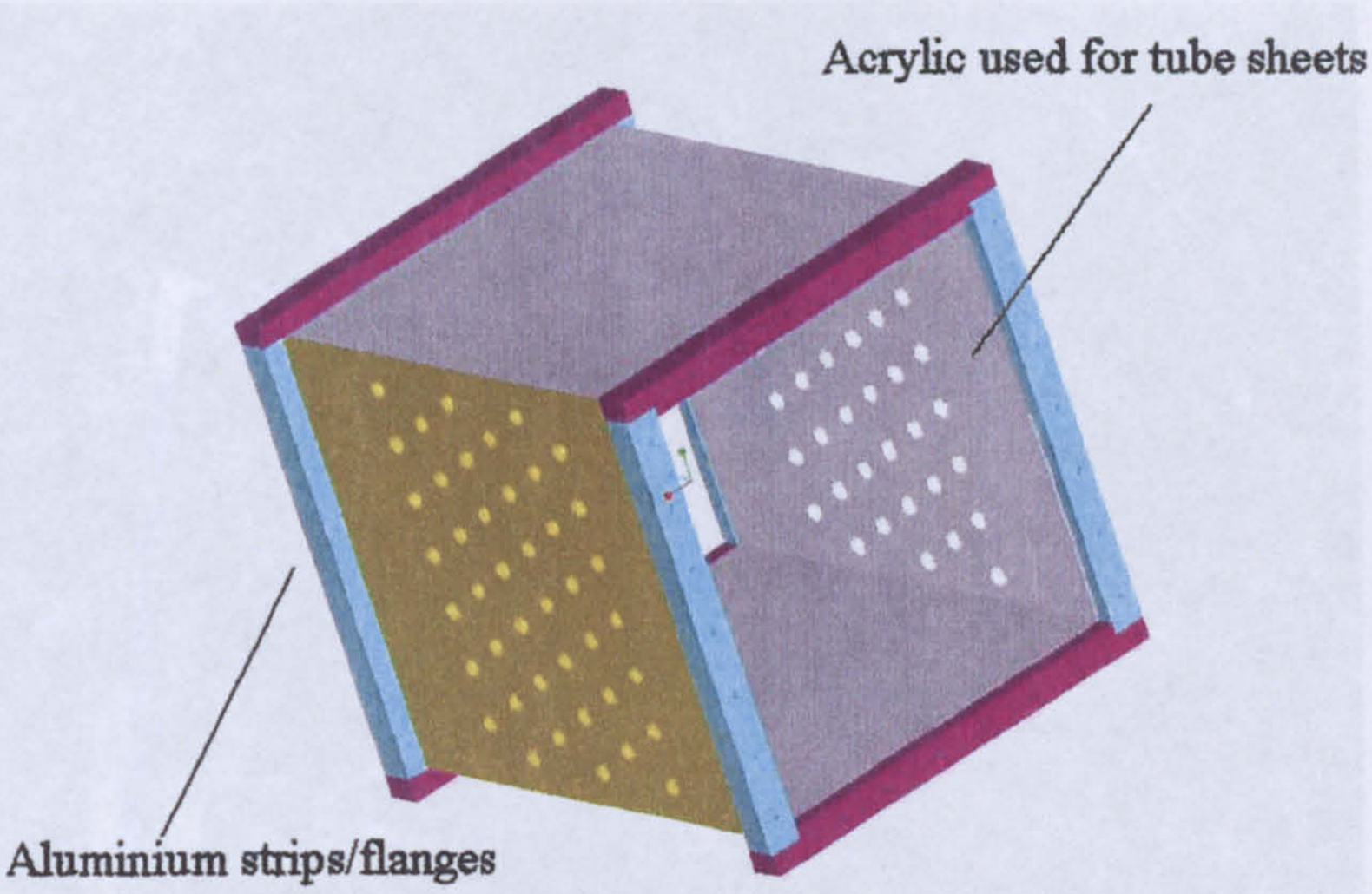

Figure 3.11: 3D representation of duct

The strips also acted as flanges to allow fitment into the MPWT and also to hold the panels to each other. This can be seen in Figure 3.12. To achieve this the panels were designed to lock together to create a seal to prevent air leakage. The edges of the floor and roof panels were notched and screws tapped into the edges to ensure the bundle sealed properly along the seam. The edges of the tube sheets were also notched to create the locking effect, as shown in Figure 3.12 below.

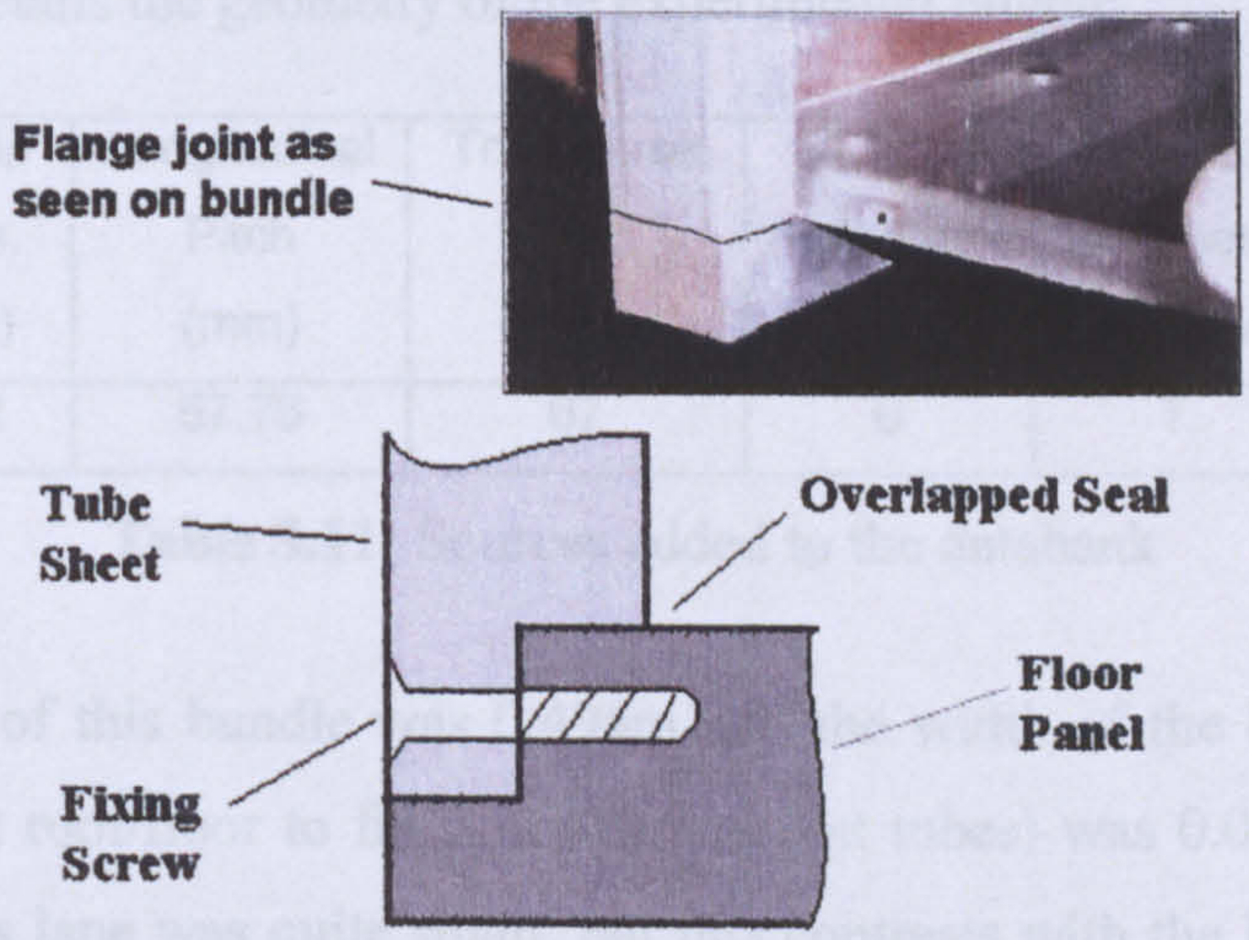

Figure 3.12: Schematic and picture of tube sheets to floor/roof sealed joint

Figure 3.13 shows the bundle before placement in the wind tunnel. The overlapping flanges can be seen on the corners of the bundle where the MPWT transition sections are fitted.

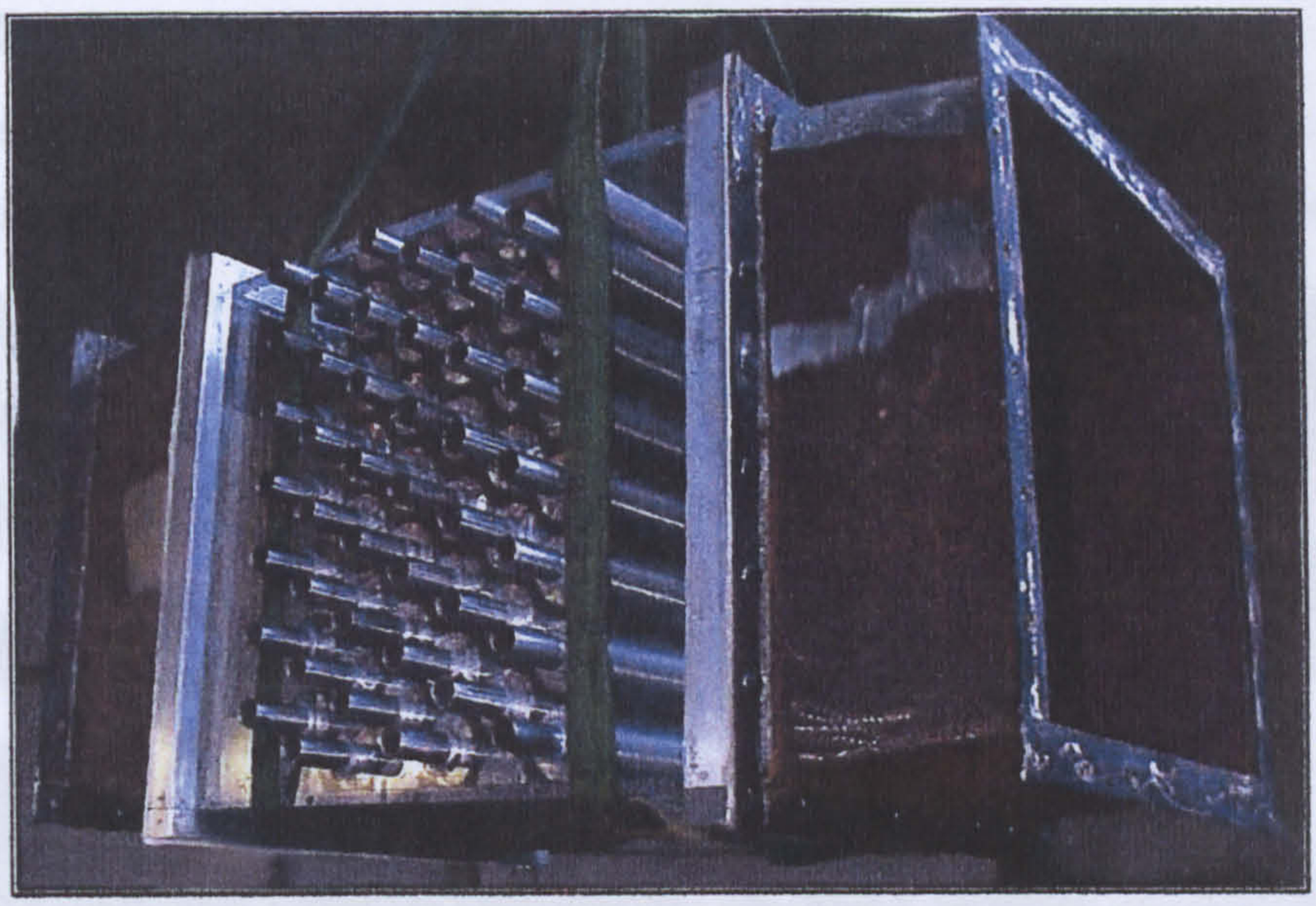

Figure 3.13: The bundle and transition sections being fitted into the wind tunnel

It should be noted that to ensure structural integrity and minimise any torsion on the bundle only one panel (floor or roof) was removed at a time during corbel fitting and removal.

3.5.2 Tube layout

Table 3.11 below details the geometry of the experimental bundle.

Tube Diam. (mm)	Fin Tip Diam. (mm)	Longitudinal Pitch (mm)	Transverse Pitch (mm)	Number of rows	Number of tubes per row	Fin frequency (1/m)
25.4	57.2	57.76	67	6	7	433

Table 3.11: Sources added to the databank

The overall height of this bundle was 0.494m and the width of the bypass lane itself (distance from duct roof/floor to fin tip of the nearest tubes) was 0.00065m. It can be seen that the bypass lane was quite small, but this contrasts with the lane height of the heat recovery bundle whose geometry was given in Table 3.10.

The tubes were sealed into the tube sheets with a silicon sealant to prevent any air loss.

3.5.3 Corbel design

All of the corbels used in the study were made, as would industrial corbels, from standard material sections. Figure 3.14 shows the various corbel shapes in position

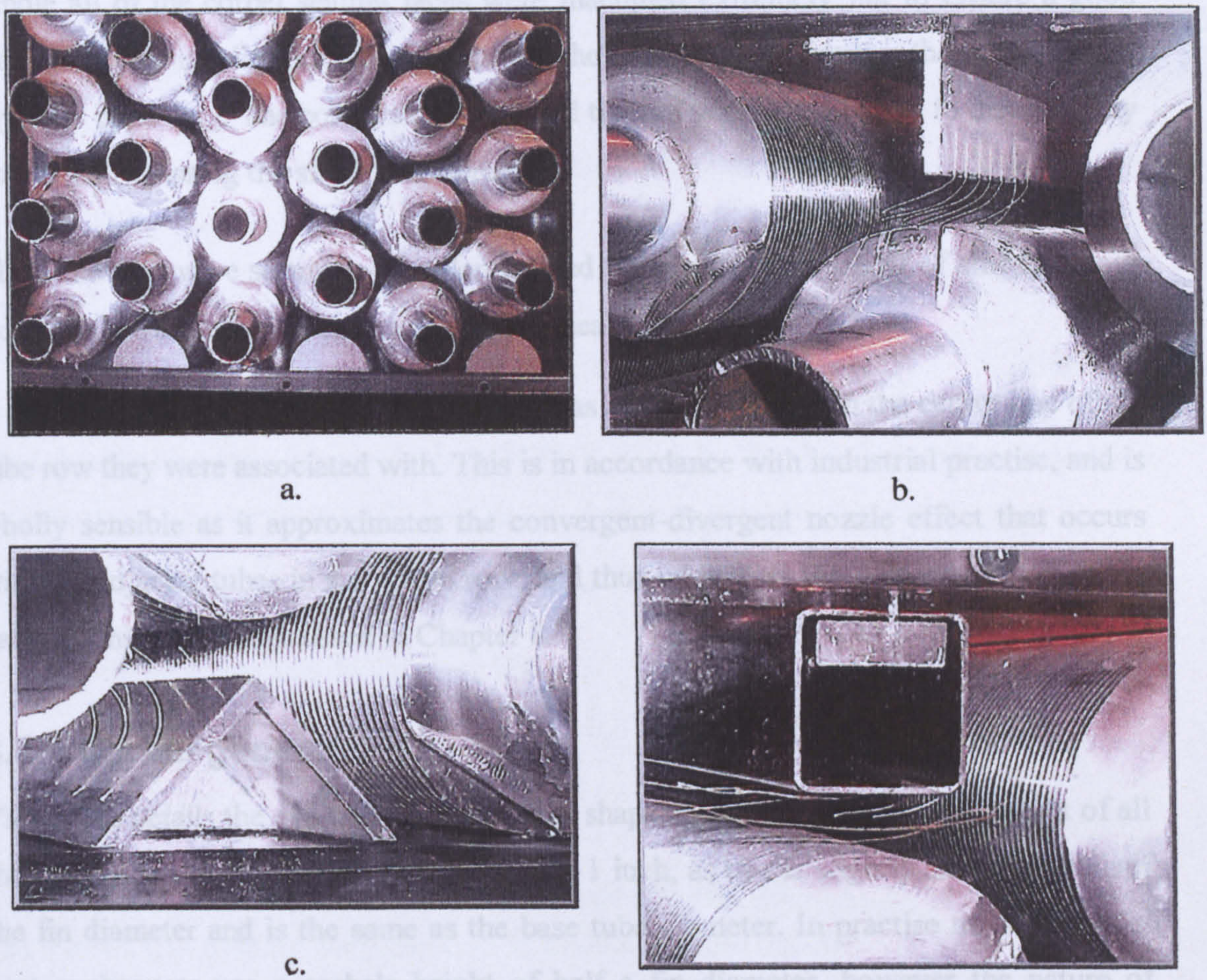

a. b. c. d.

Figure 3.14: The corbels a. Half tubes, b. Sealing strips, c. Inverted V and d. Square block

Figure 3.14a shows the half tubes corbels. These were manufactured from 2-inch diameter aluminium bar. Figure 3.14b shows the sealing strips. These were fabricated from 1-inch (25.4mm) aluminium angle section. The inverted Vs shown in Figure 3.14c were made from 2-inch (50.8mm) angle section rotated to form the shape with blocks placed inside the v to allow a fitting screw to be threaded into them to allow attachment to the floor/roof panels. Figure 3.14d shows the square blocks. These were made from hollow 1 inch square section tubing with reinforcement plates welded inside them to allow the fitting screws to be threaded into them. Both the half tubes and sealing strips

had the screws threaded straight into the material with no additional parts required. Normally the corbels would be welded to the duct floor/roof panels, which would give a seal at the base of the corbel to remove any underpassing of the airflow. In the test bundle all of the corbel sealing faces were machined extremely flat to ensure a good seal against the acrylic roof/floor panels and the tube sheets to remove the possibility of any flow bypassing. The corbel strips spanned the full width of the duct to disallow any flow from bypassing the side of the corbels.

All the corbels were secured with allen headed bolts, and had a smear of silicon grease along the bottom edges to ensure a complete seal

It can be seen that the centre of the corbels was always in line with the centre line of the tube row they were associated with. This is in accordance with industrial practise, and is wholly sensible as it approximates the convergent-divergent nozzle effect that occurs with the adjacent tubes in any given row, and thus minimises the disruption to the flow pattern. This will be discussed in Chapter 8.

3.5.4 Corbel geometries

Table 3.12 details the geometry of the corbel shapes used in the study. The height of all the corbels was fixed at 25.4 mm, nominally 1 inch, as this is slightly smaller than half the fin diameter and is the same as the base tube diameter. In practise most industrial heat exchangers use a corbels height of half a fin diameter, however the nature of corbels is to be a cheap and quick solution to sealing the walls, therefore standard sections (usually multiples of 1 inch) are most often used regardless of the exact fin dimensions.

Corbel Type	Height (mm)	Bottom Width (mm)	Top Width (mm)
Half Tube	25.4	50.8	-
Sealing Strip	25.4	0.2	0.2
Square Block	25.4	25.4	25.4
Inverted V	25.4	50.8	-

Table 3.12: Corbel Geometry

3.6 Method of data reduction/analysis

The following is the method from which the performance characteristics and other information about the performance of the bundles was derived.

3.6.1 Heat Balance

The heat balance was performed to ensure that the calculated airside duty matched (or came within a reasonable tolerance of) the calculated tubeside duty. The definitions can be found in the nomenclature.

The airside heat transfer rate is given by Equ.3.3:

$$Q_x = mfr_x Cp_x \Delta T_x \qquad \text{(Equ.3.3)}$$

The tubeside heat transfer rate in the MPWT is given by Equ.3.4. This will be expanded on in Section 7.1. For the HTWT only the coolant duty need be considered.

$$Q_T = Q_{lat} + Q_{Sup} + Q_{Sub} \qquad \text{(Equ.3.4)}$$

The heat balance was then found from Equ.3.5:

$$Heat\ balance = \frac{(Q_T - Q_x)}{Q_T} 100\% \qquad \text{(Equ.3.5)}$$

6.3.2 Determination of heat transfer coefficients

The overall heat transfer coefficient, *U,* is calculated from Equ.3.6.

$$U = \frac{Q_x}{A_{oT} \Delta T_{lm}} \qquad \text{(Equ.3.6)}$$

where the temperature difference is as given in Equ.3.7

$$\Delta T_{lm} = \frac{(T_{tin} - T_{xout}) - (T_{tout} - T_{xin})}{\ln\left(\frac{T_{tin} - T_{xout}}{T_{tout} - T_{xin}}\right)} \qquad \text{(Equ.3.7)}$$

The tube wall heat transfer coefficient referred to the tube outer diameter, α_{wall} is given by Equ.3.8:

$$\alpha_{Wall} = \frac{2k_t}{D_o \cdot \ln\left(\frac{D_o}{D_i}\right)} \qquad \text{(Equ.3.8)}$$

For the MPWT data the tubeside heat transfer coefficient is evaluated by applying the Nusselt analysis for gravity-controlled condensation, in which the local heat transfer coefficient for condensation outside a circular horizontal tube as given in Equ.3.9:

$$\alpha_{tube} = 1.2\lambda_c \left(\frac{\rho_c(\rho_c - \rho_s)g}{\eta_c^{\,2}\,\mathrm{Re}_c} \right)^{1/3} \qquad \text{(Equ.3.9)}$$

This is applied to condensation inside a horizontal tube by multiplying by a factor of 0.8 to allow for liquid hold-up in the bottom of the tube as recommended in HTFS Handbook Sheet CP4. The tubeside heat transfer coefficient referred to the tube outside diameter is then calculated from Equ.3.10:

$$\alpha_t = 0.8 \frac{D_i}{D_o} \left[1.2\lambda_c \left[\frac{\rho_c(\rho_c - \rho_s)g}{\eta_c^{\,2}\,\mathrm{Re}_c} \right]^{1/3} \right] \qquad \text{(Equ3.10)}$$

From HTFS handbook sheets CP4 and CM12, Re_c is given by Equ.3.11:

$$\mathrm{Re}_c = \frac{2\dot{M}_c}{\eta_c L_T} \cos\theta \qquad \text{(Equ.3.11)}$$

For a horizontal tube ($\theta = 0°$) this can be simplified to give Equ.3.12:

$$\mathrm{Re}_c = \left(\frac{2\dot{M}_c}{\eta_c L_t} \right) \qquad \text{(Equ.3.12)}$$

In the HTWT the tubeside heat transfer coefficient was calculated by Equ.3.13, due to a single phase fluid being used.

$$\alpha_{tube} = \frac{Nu_{wat}\lambda_{wat}}{D_e} \qquad \text{(Equ.3.13)}$$

Where the Nusselt number was calculated iteratively from an HTFS correlation, and D_e is the equivalent diameter of the tube inner diameter minus the tube core diameter.

The measured airside coefficient α_x referred to the tube outside diameter was extracted from the overall heat transfer coefficient using the tubeside heat transfer coefficient and the wall heat transfer coefficient:

$$\alpha_x = \left(\frac{1}{U} - \frac{1}{\alpha_{tube}} - \frac{1}{\alpha_{Wall}} \right)^{-1} \quad \text{(Equ.3.14)}$$

The heat transfer coefficient was then referred to the total surface area from Equ.3.15:

$$\alpha_{ox} = \alpha_x \frac{A_{oT}}{A_{ox}} \quad \text{(Equ.3.15)}$$

The uncorrected value of the airside coefficient, α_{oxu}, referred to the outside surface area is obtained by iteration from:

$$\alpha_{oxu} = \frac{\alpha_{ox}}{\gamma} \quad \text{(Equ.3.16)}$$

where the surface effectiveness, γ, is given by Equ.3.17:

$$\gamma = \left[1 - \frac{A_f}{A_{ox}} (1 - \varepsilon_f) \right] \quad \text{(Equ.3.17)}$$

The fin efficiency, ε_f, is given by Equ.3.18:

$$\varepsilon_f = \frac{\tanh(m_f \phi_f)}{m_f \phi_f} \quad \text{(Equ.3.18)}$$

where the corrected fin height ϕ_f is Equ.3.19:

$$\phi_f = \frac{D_r}{2} \left(\frac{D_f}{D_r} - 1 \right) \left(1 + 0.35 \ln \left(\frac{D_f}{D_r} \right) \right) \quad \text{(Equ.3.19)}$$

and the fin heat transfer number m_f is Equ.3.20:

$$m_f = \sqrt{2 \frac{\alpha_{oxu}}{\lambda_f s_f}} \quad \text{(Equ.3.20)}$$

6.3.3 Heat Transfer Characteristics

The dimensionless heat transfer characteristics were determined from the following equations.

The airside heat transfer characteristics are presented in the form of Colburn *j*-factor, given in Equ.3.21:

$$j = \frac{\alpha_{conv}}{c_p mfr} \mathrm{Pr}^{2/3} \qquad \text{(Equ.3.21)}$$

where the Prandtl number was calculated by Equ.3.22.

$$\mathrm{Pr} = \frac{c_p \eta}{\lambda} \qquad \text{(Equ.3.22)}$$

6.3.4 Pressure loss characteristics

The pressure loss characteristics are presented in the form of the friction factor using the measured pressure drop from Equ.3.23:

$$f = \frac{2\rho \, \Delta P}{N_r mfr^2} \qquad \text{(Equ.3.23)}$$

6.3.5 Airside Reynolds number

The analysis considers the variation of the f and j factors with maximum airside Reynolds number defined by Equ.3.24:

$$\mathrm{Re}_{max} = \frac{mfr \; D_r}{\eta} \qquad \text{(Equ.3.24)}$$

6.3.6 Uncertainty analysis

An uncertainty analysis was conducted to define the uncertainty associated with the derived values of the f and j factors and Re_{max}.

The calculation of the uncertainty associated with the measurements and instruments is fully described in Appendix A.

CHAPTER 4

Experimental Results

4.0 Introduction

This Chapter presents the results of the test programmes undertaken during the period of the project, using the experimental apparatus described in Chapter 3.

4.1 Test programme

Three test programmes were undertaken:

- 9 Inline Air Cooler Bundles
- 1 Heat Recovery Bundle (with/without Corbels)
- 1 Staggered Air Cooler Bundle (isothermally, with 4 types of corbels and with bypassing)

The measured pressure drop and experimentally determined j factor results are shown here along with other pertinent data that will be discussed/used in upcoming chapters. The results of the uncertainty analysis for each bundle, where applicable, are also presented.

4.2 Test conditions

4.2.1 inline air cooler bundles

The measurement of the square pitch bundles was undertaken with the MPWT in its original location, and the measurements of the characterising dimensionless *f* and *j* factors were conducted under the following test conditions:

- The airside Reynolds Number (Re_{Max}) : 4500 to 13,000.
- Air conditions at bundle inlet: Ambient condition (nominally 20°C, and atmospheric pressure)
- Inlet steam: Saturated condition.
- All measurements were taken with a heat balance better than ±5%.

The measurements of the heat transfer and pressure drop performance for the rectangular pitch bundles were conducted in the NEL Reynolds building, and were taken under the following conditions:

- Air side Reynolds Number (Re_{max}) range, 5000 to 21000.
- Inlet air, nominally 20°C and atmospheric pressure.
- Inlet steam at or slightly above saturation condition.

- Measurements taken within a heat balance tolerance of ±5%.

4.2.2 Heat recovery bundle

In each test, measurements of pressure drop and heat transfer were conducted over a reasonable range of test conditions as given below:

- Range of gas side Re_{max}: 5000 to 25,000.
- Upstream average gas temperatures: around 250° C, and 410° C.
- The waterside Reynolds number was maintained above 5000 whilst ensuring a measurable water temperature rise.

The range of Re_{max} given above is typical of the conditions found in process fired heater convection banks.

4.2.3 Staggered air cooler with and without corbels

The measurements of pressure drop performance were taken under the following conditions:

- Air side Reynolds Number (Re_{max}) range, 4000 to 16500.
- Inlet air, nominally 20°C and atmospheric pressure.

The tests were all performed isothermally

4.3 Inline air cooler bundles

The first test programme undertaken was of four square pitch air cooler bundles. Their geometry is shown in Table 3.8. The second programme undertaken was of the five irregular pitch air cooler bundles. Their geometry is shown in Table 3.9.

4.3.1. Results of square pitch bundles

Measurements of pressure loss and heat transfer characteristics are presented in the form of f and j factors in Table 4.1. The associated uncertainties are also presented in this table.

The main objective of these experiments was to collect data for inline bundles with various geometries to help in the development of HTFS correlations. Therefore in these experiments, with the exception of the fin frequency, none of the other geometrical parameters such as fin pitch or fin tip diameter were varied systematically. It is

therefore difficult to see clearly the influence of these parameters on bundle performance.

Bundle No.	Air face velocity (m/s)	Re_{max}	Re_{max} uncertainty (±)	*f*-factor	*f*-factor uncertainty (±)	*j*-factor	*j*-factor uncertainty (±)
Bund. 1	1.57	4630	275.21	1.109	0.1358	0.00383	0.000111
	1.99	5829	218.49	0.955	0.0765	0.00351	0.000093
	2.49	7235	181.96	0.825	0.0454	0.00326	0.000084
	2.87	8385	158.82	0.746	0.0319	0.00308	0.000076
	3.39	9849	147.21	0.678	0.0241	0.00292	0.000032
	3.86	11264	139.06	0.631	0.0183	0.00279	0.000067
	4.3	12540	131.64	0.585	0.0263	0.00255	0.000062
Bund. 2	1.76	4772	255.45	0.857	0.1032	0.0033	0.000072
	2.2	5975	201.91	0.747	0.0589	0.0029	0.000062
	2.65	7170	176.81	0.678	0.0421	0.0026	0.000056
	3.01	8138	152.26	0.625	0.0298	0.0024	0.000051
	4.12	11080	124.71	0.531	0.0177	0.0023	0.000052
	4.54	12545	127.32	0.506	0.0173	0.0022	0.000047
Bund. 3	1.59	5164	291.03	0.933	0.1092	0.003	0.000028
	2.04	6549	233.24	0.77	0.0589	0.0028	0.000048
	2.53	8050	199.96	0.696	0.0376	0.0027	0.000057
	3.04	9673	159.98	0.62	0.0259	0.0026	0.000054
	3.45	10999	153.68	0.58	0.0187	0.0025	0.000054
	3.96	12503	131.06	0.54	0.0172	0.0023	0.000051
	4.4	13929	153.85	0.515	0.0201	0.0022	0.000047
Bund. 4	1.78	4787	248.68	0.58	0.0709	0.0049	0.000108
	2.22	6284	193.32	0.509	0.041	0.0044	0.000059
	2.66	7543	180.77	0.471	0.0295	0.0042	0.000089
	3.06	8690	150.51	0.446	0.0212	0.0041	0.00009
	3.56	10075	140.65	0.423	0.0155	0.0039	0.000053
	4.09	11550	121.28	0.407	0.0129	0.0039	0.000051
	4.55	12764	132.63	0.401	0.0119	0.0038	0.000089

Table 4.1: Summary of Test Results and Associated Uncertainties of square pitch bundles

4.3.2 Characteristics of square pitch bundles

The influence of fin frequency can be shown for bundles 1 and 4 as these two bundles have the same geometry apart from this parameter (433 vs. 236 fins/m, respectively) . Figure 4.1 shows that, as expected, the bundle with higher fin frequency (Bundle 1) has the higher pressure loss.

Table 3.8 shows that Bundle 2 has the largest gap between fin tips (9.5 mm), and consequently the pressure loss is less than that of bundles 1 and 3. For the same reason Bundle 3 has lower pressure drop than Bundle 1.

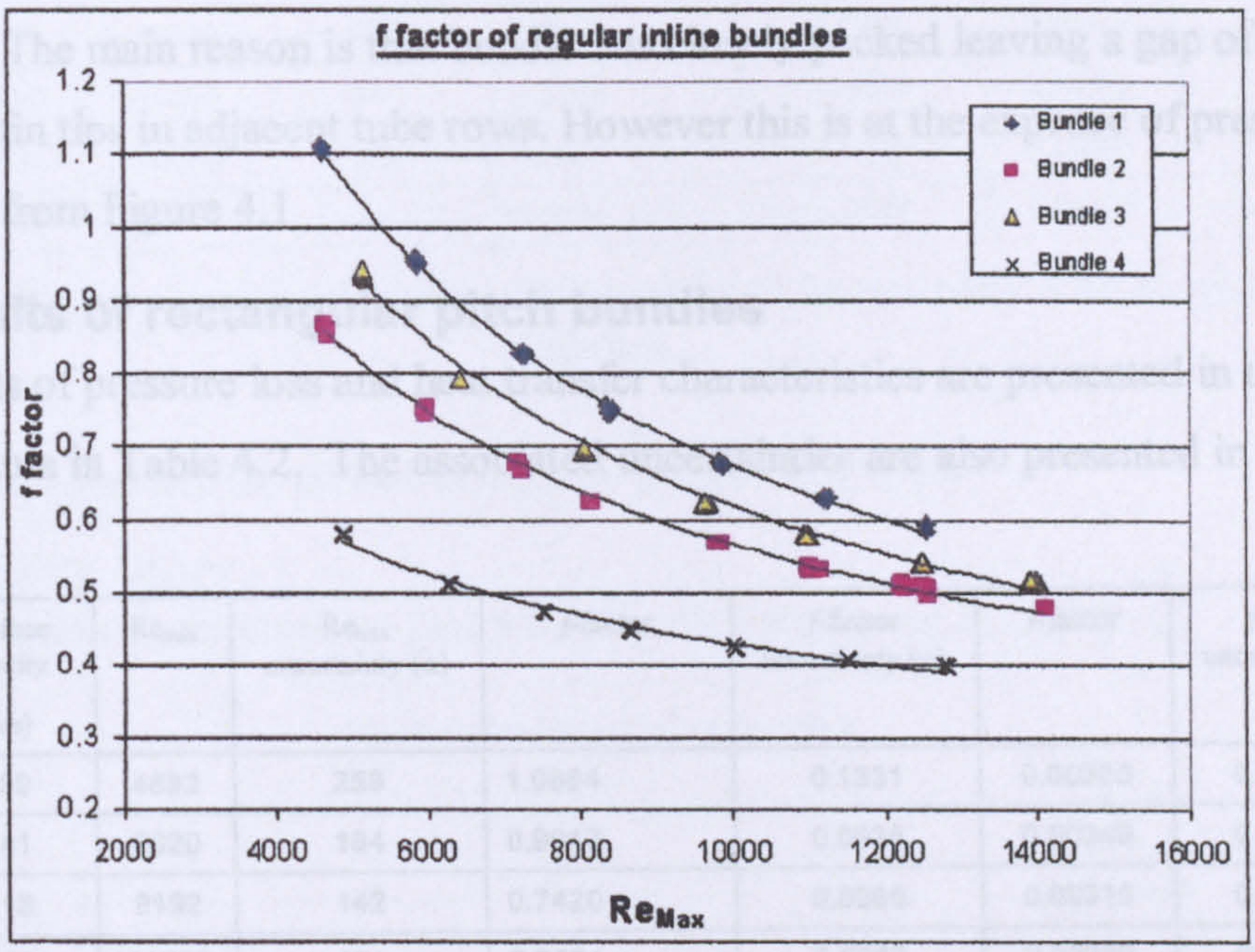

Figure 4.1: *f* factor comparisons of all square pitch bundles

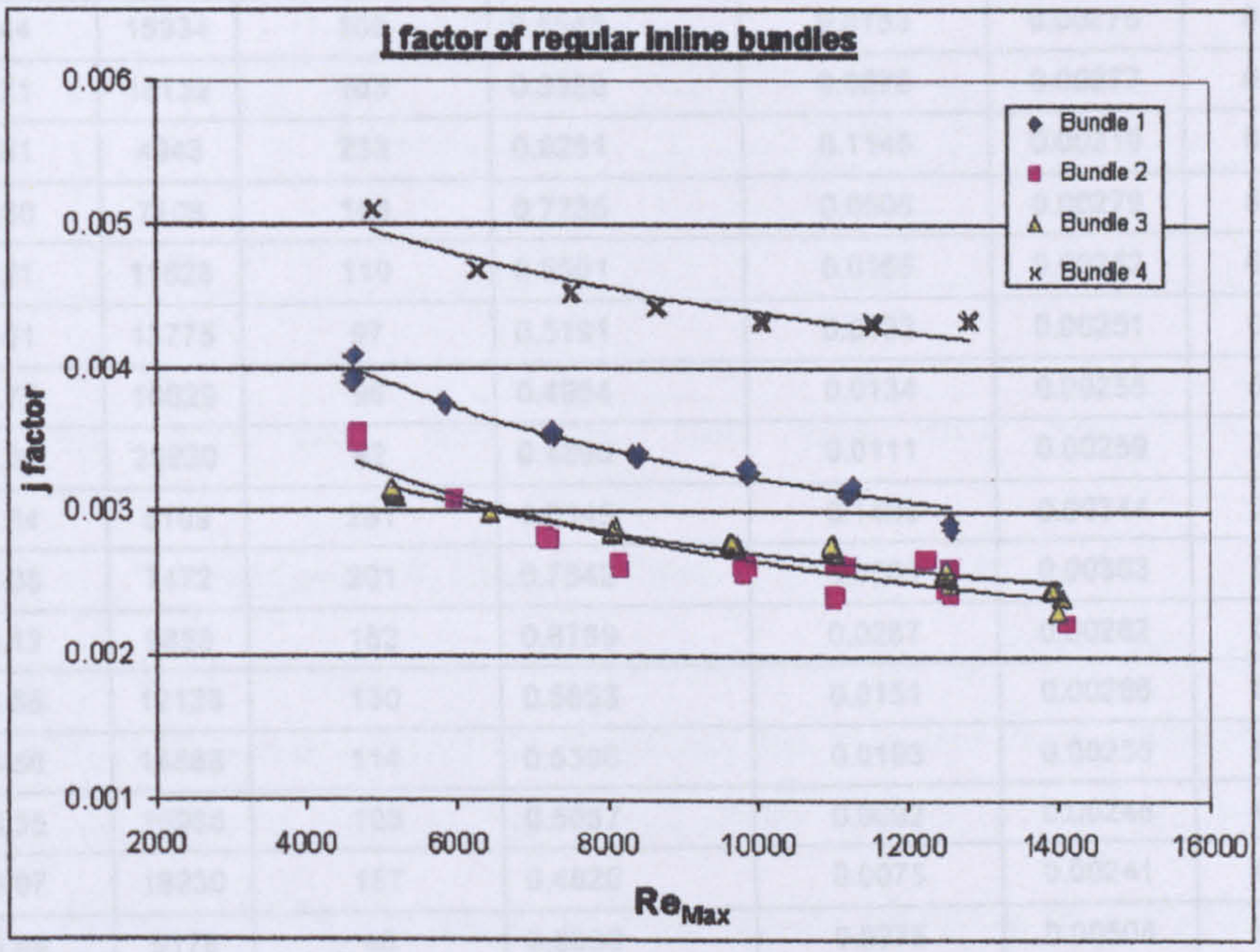

Figure 4.2: j factor comparisons of all square pitch bundles

In the heat transfer calculations the heat transfer coefficient is referred to the total heat transfer area. Consequently when comparing bundles 1 and 4, Figure 4.2 shows that the

j factor decreases as the fin frequency increases for a given duty. For a direct comparison of the heat transfer coefficient, the *j* factor should be multiplied by the ratio of total heat transfer area to the bare tube area. Figure 4.2 also shows that although bundle 3 has slightly less heat transfer area than bundle 2 it gives better heat transfer performance. The main reason is that bundle 3 is closely packed leaving a gap of 3.2 mm between fin tips in adjacent tube rows. However this is at the expense of pressure drop, as seen from Figure 4.1

4.3.3. Results of rectangular pitch bundles

Measurements of pressure loss and heat transfer characteristics are presented in the form of *f* and *j* factors in Table 4.2. The associated uncertainties are also presented in this table.

Bundle No.	Air face velocity (m/s)	Re_{max}	Re_{max} uncertainty (±)	*f*-factor	*f*-factor uncertainty (±)	*j*-factor	*j*-factor uncertainty (±)
Bund. 5	1.69	4882	259	1.0664	0.1331	0.00393	0.000118
	2.41	6920	184	0.9017	0.0635	0.00349	0.000094
	3.18	9192	142	0.7420	0.0265	0.00315	0.000079
	3.93	11369	131	0.6581	0.0286	0.00299	0.000073
	4.65	13533	108	0.6041	0.0119	0.00282	0.000071
	5.44	15934	108	0.5543	0.0133	0.00275	0.000068
	6.21	18132	103	0.5380	0.0078	0.00277	0.000071
Bund. 6	1.81	4943	233	0.9281	0.1145	0.00319	0.000067
	2.60	7108	168	0.7235	0.0506	0.00279	0.000055
	4.21	11628	110	0.5591	0.0166	0.00252	0.000050
	5.01	13775	97	0.5191	0.0133	0.00251	0.000053
	5.79	16029	96	0.4954	0.0134	0.00255	0.000055
	7.35	20230	92	0.4895	0.0111	0.00259	0.000073
Bund. 7	1.64	5109	291	1.0549	0.1409	0.00344	0.000085
	2.38	7472	201	0.7842	0.0509	0.00303	0.000067
	3.12	9853	162	0.6789	0.0287	0.00282	0.000060
	3.85	12138	130	0.5853	0.0151	0.00266	0.000056
	4.60	14568	114	0.5396	0.0193	0.00255	0.000054
	5.35	16986	103	0.5057	0.0092	0.00246	0.000052
	6.07	19230	157	0.4820	0.0075	0.00241	0.000052
Bund. 8	1.84	5178	46	0.6330	0.0275	0.00508	0.000015
	2.60	7302	30	0.5279	0.0209	0.00466	0.000012
	3.38	9525	66	0.4622	0.0030	0.00458	0.000009
	4.04	11395	38	0.4546	0.0050	0.00472	0.000020
	4.83	13583	30	0.4583	0.0024	0.00492	0.000004

	6.38	18010	225	0.4512	0.0030	0.00510	0.000022
	5.61	15845	38	0.4491	0.0066	0.00499	0.000011
Bund. 9	1.72	5025	14	1.0921	0.0080	0.00390	0.000033
	2.50	7320	37	0.8594	0.0105	0.00352	0.000014
	4.05	12039	33	0.6488	0.0008	0.00306	0.000024
	4.81	14240	45	0.6036	0.0089	0.00307	0.000011
	5.55	16588	34	0.5760	0.0066	0.00309	0.000014
	6.31	18629	140	0.5607	0.0086	0.00306	0.000023
	7.09	21091	84	0.5509	0.0017	0.00318	0.000024

Table 4.2: Summary of Test Results and Associated Uncertainties of rectangular pitch bundles

4.3.4. Characteristics of rectangular pitch bundles

4.3.4.1 Pressure Drop

The pressure drop characteristics for all test bundles are shown in Figure 4.3.

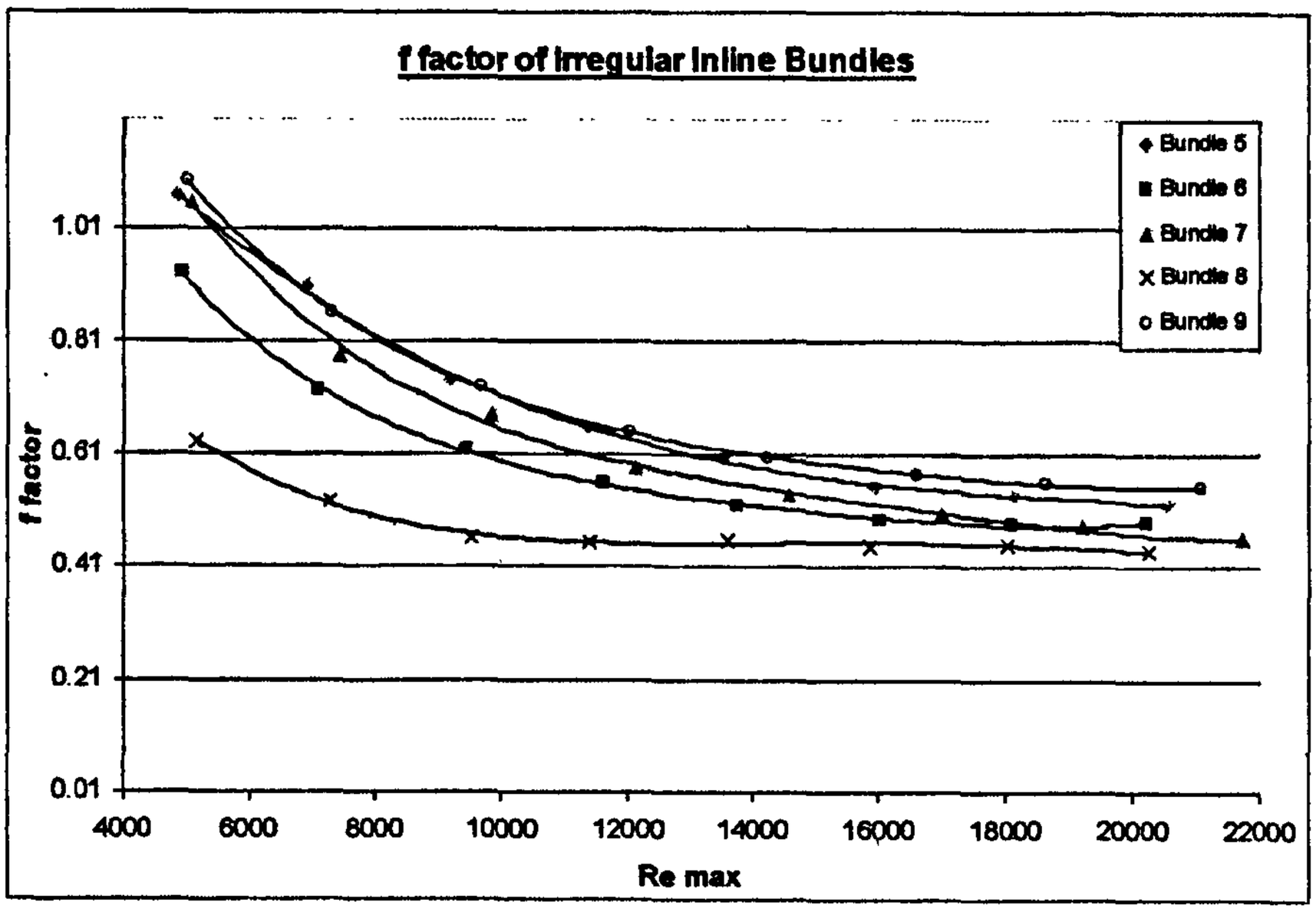

Figure 4.3: Pressure Drop Characteristics

Bundles 5 and 8 have the same tube layout but, as shown in Table 3.9, differ in fin frequency. As Bundle 8 has a lower fin frequency the pressure drop is therefore lower, as there is less face and fin skin area. At values of Re_{max} greater than 14000 the f factor curve is flat indicating that the pressure drop would increase at a lesser rate with increasing air velocity.

Because the friction factor is calculated per tube row, the influence of the longitudinal pitch can be studied by comparing bundles 5 and 9 where the longitudinal pitch varies

most while other geometry parameters are the same. Figure 4.3 shows that the friction factor is not significantly different indicating that, for inline bundles, the change in longitudinal pitch has little influence on pressure drop. Bundle 6 and bundle 9 have geometries that vary only the in gap between the fin tips and the number of tubes per row, so as would be expected; the bundle 6 pressure drop is lower than that of bundle 9. For the same reason the pressure drop for bundle 6 is less than that of bundle 5 and similarly the pressure drop for bundle 7 is less than that of bundles 5 and 9. These results indicate that for inline bundles, within the range of P_L / P_T tested, the influence of transverse pitch on pressure drop is more significant than the longitudinal pitch.

4.3.11.2. Heat Transfer

The results of heat transfer are presented in Figure 4.4. In order to achieve a like with like comparison between the 5 tube bundles the *j*-factor is referred to the bare tube area.

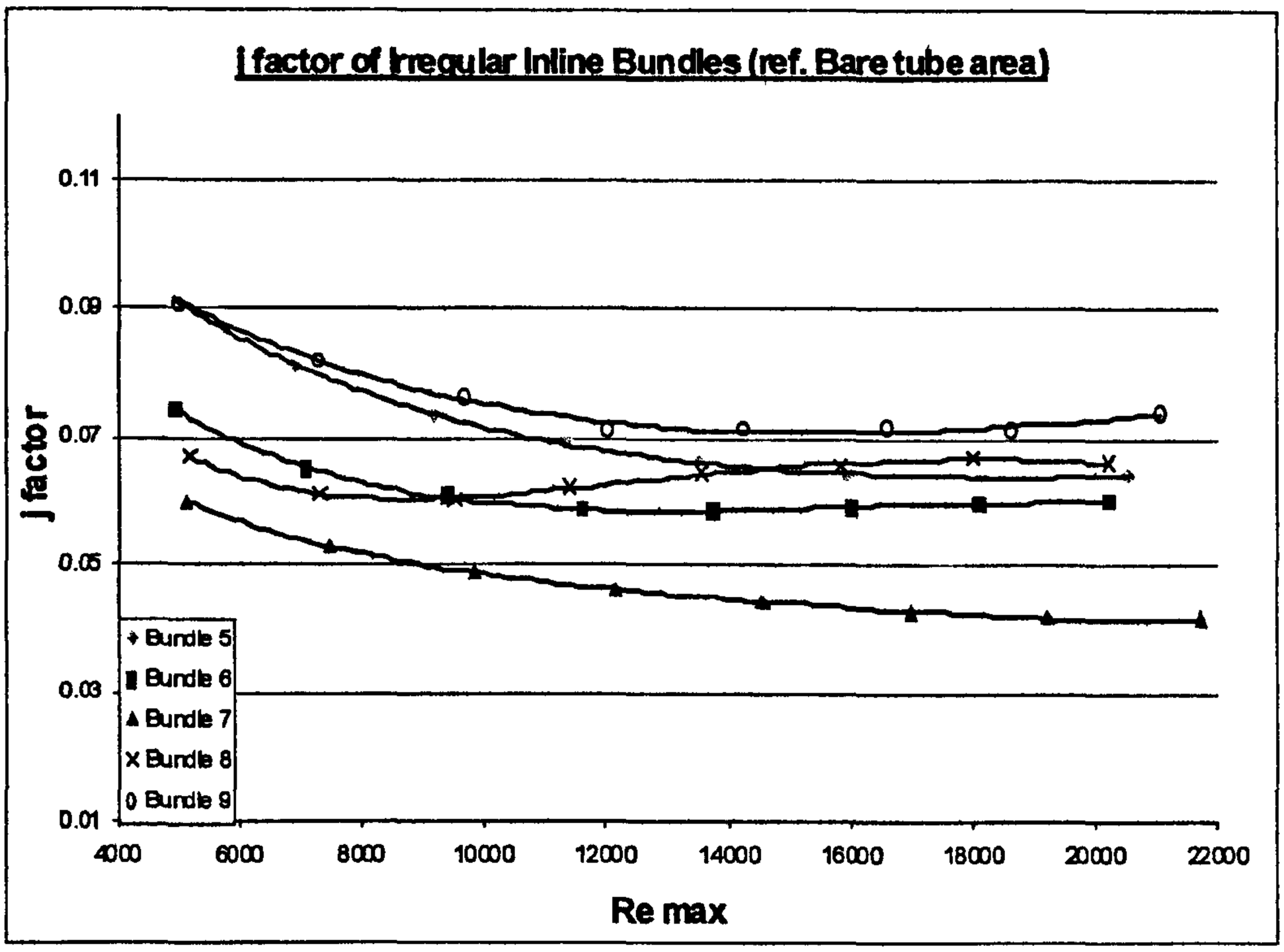

Figure 4.4: j factor of rectangular pitch bundles

As noted in table 3.2.2, Bundles 5 and 9 vary only in P_L. It can be seen in Figure 4.4 that at the lowest flow rate the heat transfer performance is nearly identical, but at higher Re_{max} the *j*-factor for bundle 5 decreases more rapidly than that of bundle 9 although it has smaller P_L.

A brief explanation for this is that in a bundle with a shorter longitudinal pitch the recirculation region is larger, and the following tube is always in the wake of the preceding tube, as explained by Brauer [24], Zukauskas and Ulinskas [36] and systematically examined by Hetz et.al. [56]. As the velocity increases the wake of the preceding tube should increase until the following tube is almost completely submerged in its wake as illustrated in Figure 4.5 for the short P_L diagram. This would lead to reduced heat transfer on the following tube, as it is submerged in the hot wake flow. A stagnant region will form between the two tubes, which tends to become trapped as the faster bypassing flow over the top, and bottom of the tubes carries more momentum and the mixing between the two streams is minimal. The recirculation regimes for inline bare tubes with increasing P_L are discussed by Zdravkovich [39].

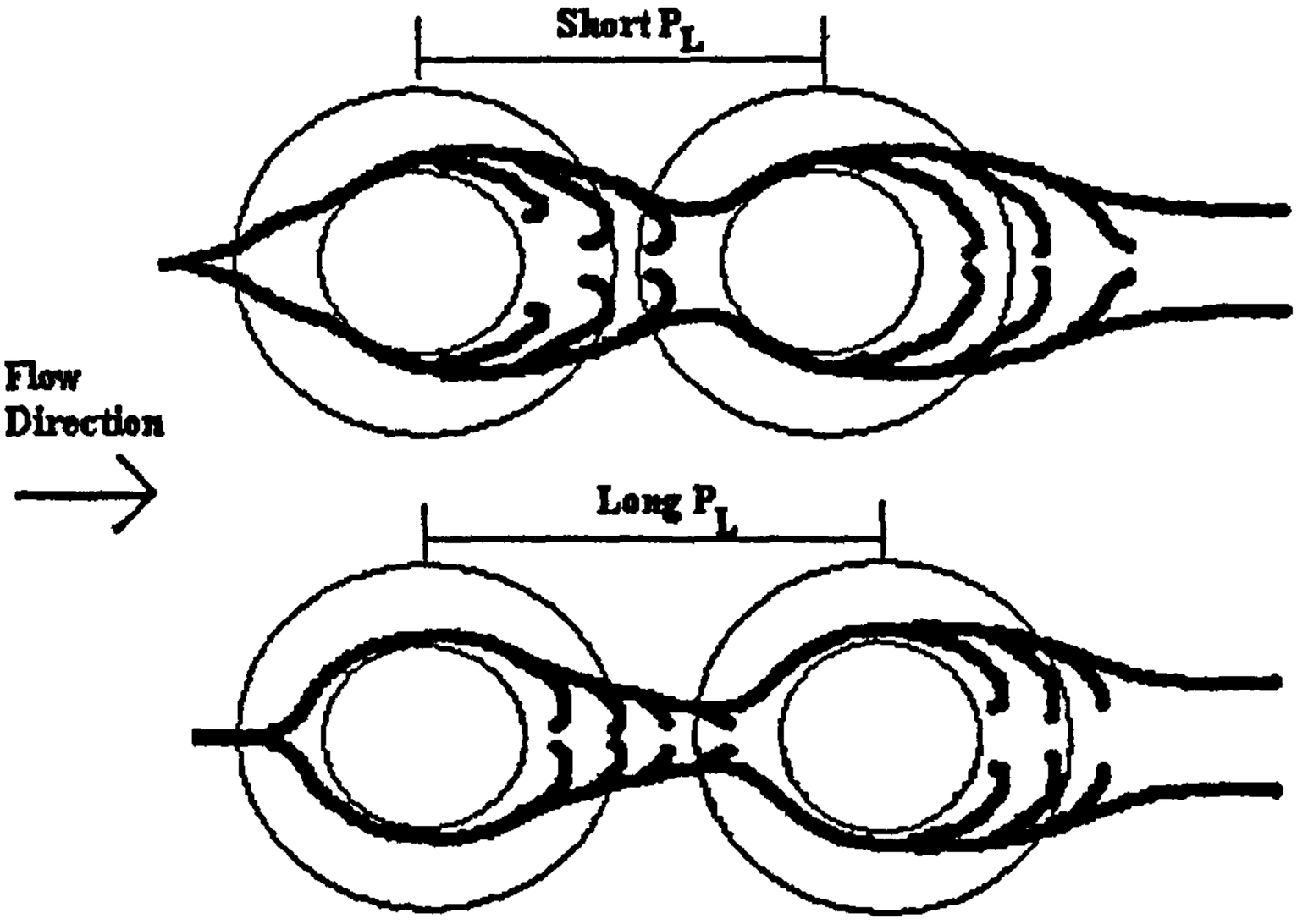

Figure 4.5: Variation of Flow with Variation of P_L

From this it is proposed that the bundle with larger P_L (bundle 9) will tend towards having the leading tube wake partially exhausted by the increased distance, reducing the area of the following tube face that is held in hot wake flow. This also means that there is less of a flow-trapping tendency, and thus the following tube face is exposed to slightly more cooler, mixed flow. The outcome of this is that the overall heat transfer coefficient is improved, and as shown in Figure 4.4 the *j*-factor will be higher. An illustration of this can be seen in Figure 4.5, for the long P_L diagram. A full explanation

of why the heat transfer performance increases in Bundle 9 as the air face velocity increases is not readily apparent. The data was reprocessed and the experimental equipment checked for faults and the same result was found.

Compared to other tube bundles, Bundle 8 shows an unusual trend. The *j*-factor varies little with Re_{max} resulting in a curve which increases, rather than show the typical decreaset. This bundle is the same as the square pitch bundle 4 but was modified to increase the longitudinal pitch from 60mm to 66.7mm. A comparison between the *j*-factors of these two bundles is given in Figure 4.6. It can be seen that the curve exhibits an unusual rise from the mid Re_{max} range before flattening out in the higher Re_{max} range. The square pitch bundle, although not tested over the same flow range, shows the expected decline in performance. It is suggested that the difference in the magnitude of the profiles shown in Figure 4.6 are attributable to the change in P_L, as described above for Bundles 5 and 9.

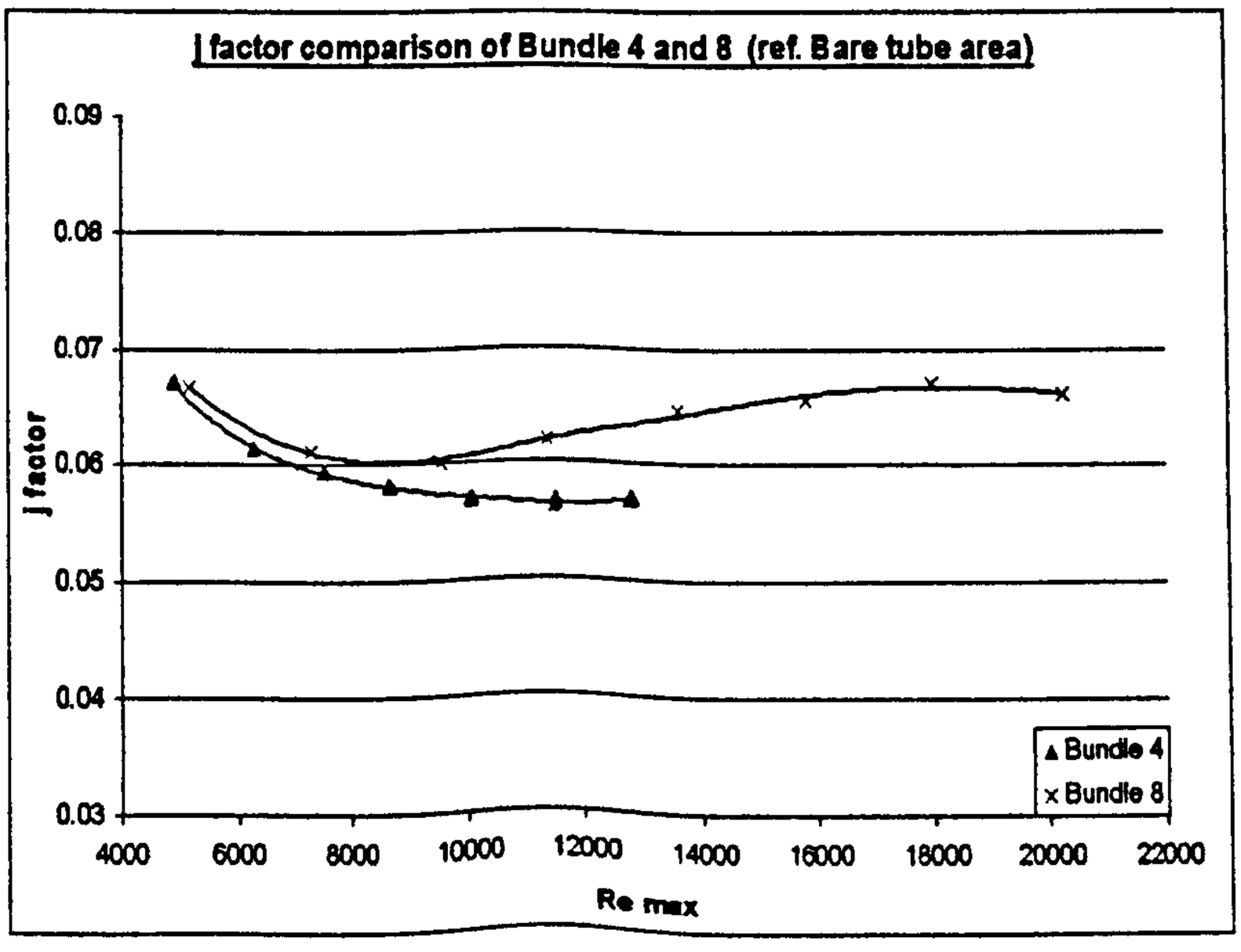

Figure 4.6: Comparison of j factor for Bundle 8 and Bundle 4

As Bundle 8 has a lower fin frequency than the other bundles, it is expected that the flow straightening effect will diminish, therefore damping of turbulence at higher values of Re_{max} will be less than other bundles and a higher heat transfer rate per unit surface area will result. This is an explanation as to why Bundle 8 has a higher j factor than bundles 5, 6 and 7 at high Re_{max} values as shown in Figure 4.4.

As shown in Table 3.9 Bundles 6 and 9 have the same geometry except for the transverse pitch (P_T) and number tubes per row. Bundle 6 has a wider P_T and fewer tubes per row and so as expected it will transfer less heat than bundle 9.

With respect to a bare tube area, Figure 4.4 shows that Bundle 7 has the poorest performance. This is a tightly packed bundle compared to the others and it can be said that as well as the longitudinal spacing effects discussed for Bundles 5 and 9, the slightly bigger fin tip clearance may play a part in the poorer performance

4.3.5 Predicted performance of square pitch bundles

The main objective of this testing was to examine the HTFS initial method reported by Chu and Ralston [23] and determine if the currently available methods were really accurate and if not develop new methods using the newly collected data. For reference, the comparisons also include predictions from open literature methods, PFR [13] and Weierman [14]. Figures 4.7 to 4.14 show the deviation of predicted *f* and *j* factors from measured data over a range of maximum Reynolds number. The deviation of predicted values from measured values is defined as:

$$Deviation = \frac{prediction - measurement}{measurement} x100$$

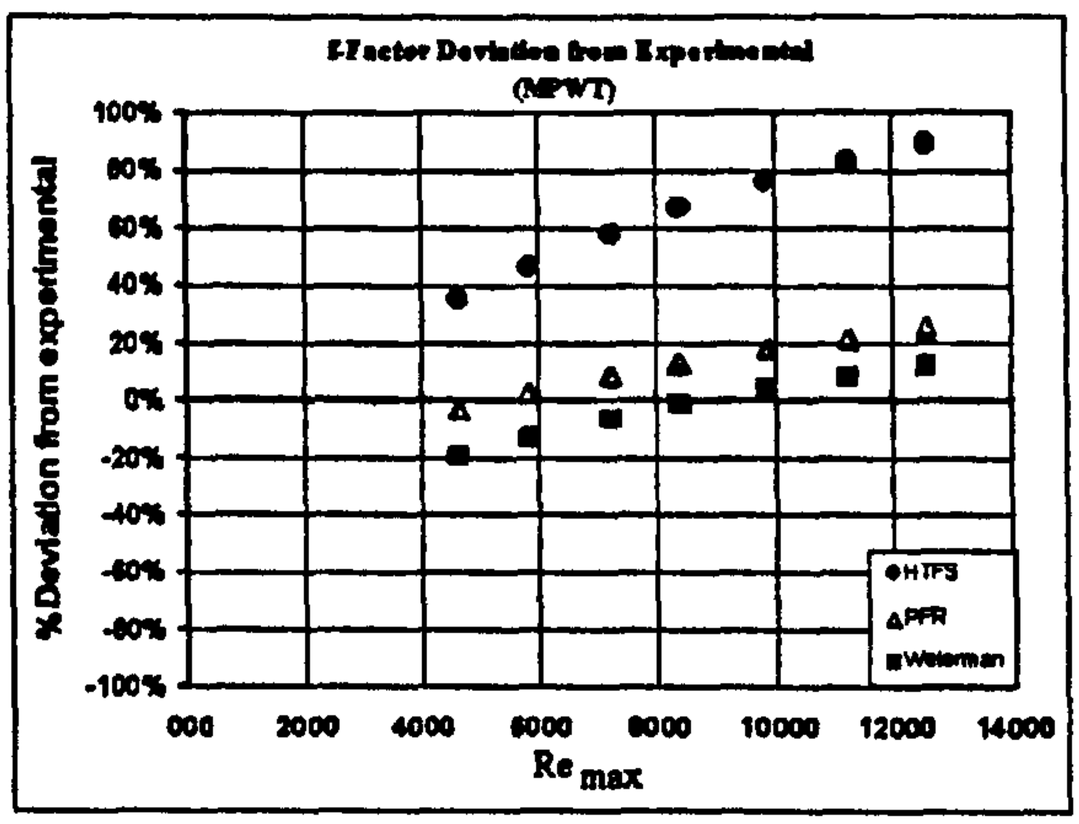

Figure 4.7: *f* factor comparisons, bundle 1

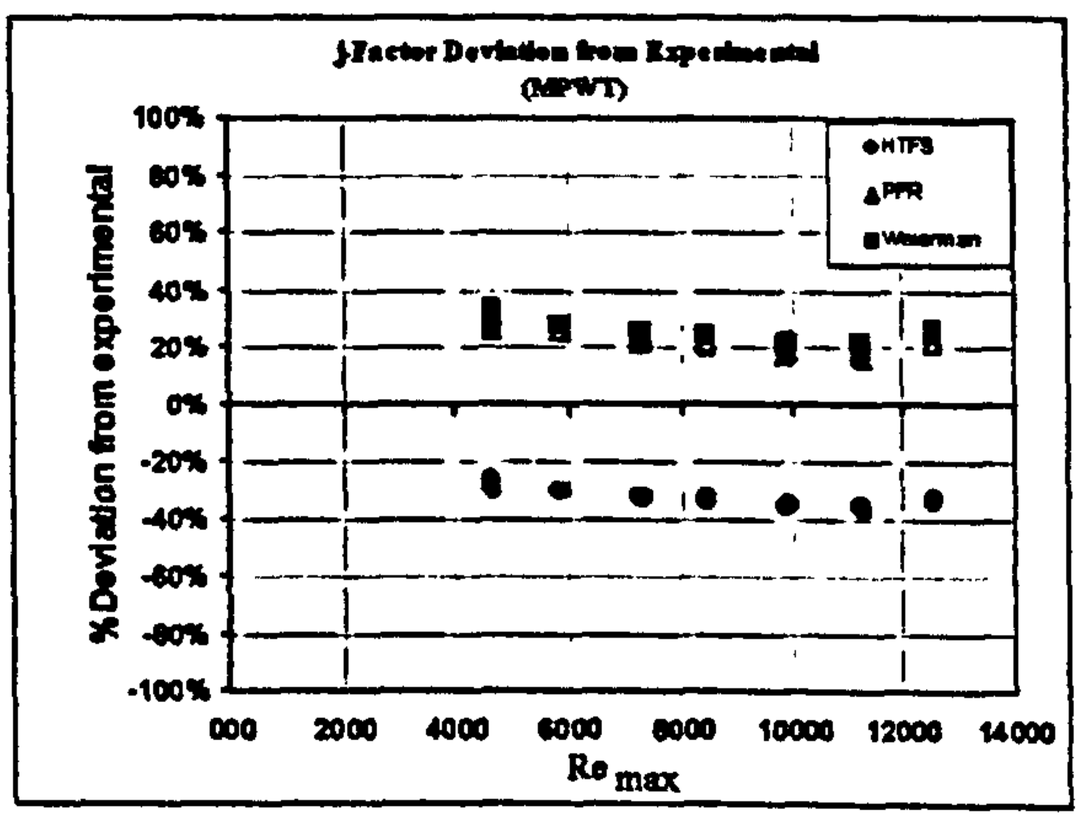

Figure 4.8: *j* factor comparisons, bundle 1

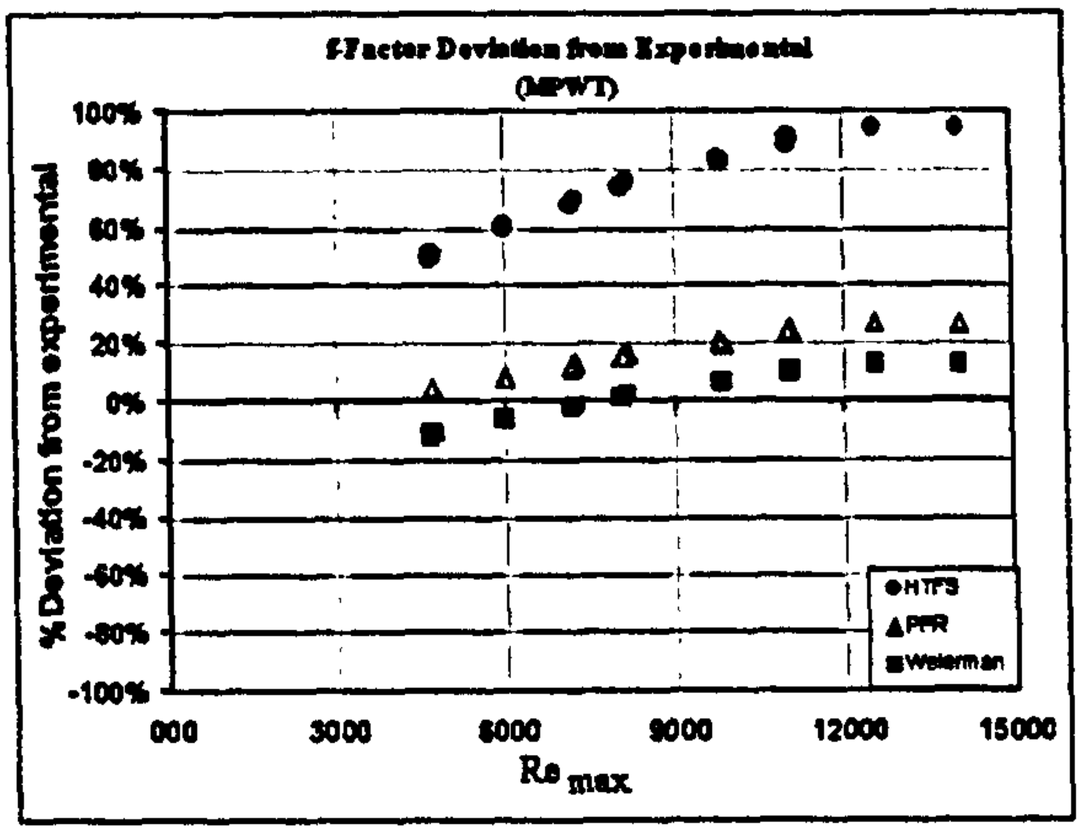

Figure 4.9: f factor comparisons, bundle 2

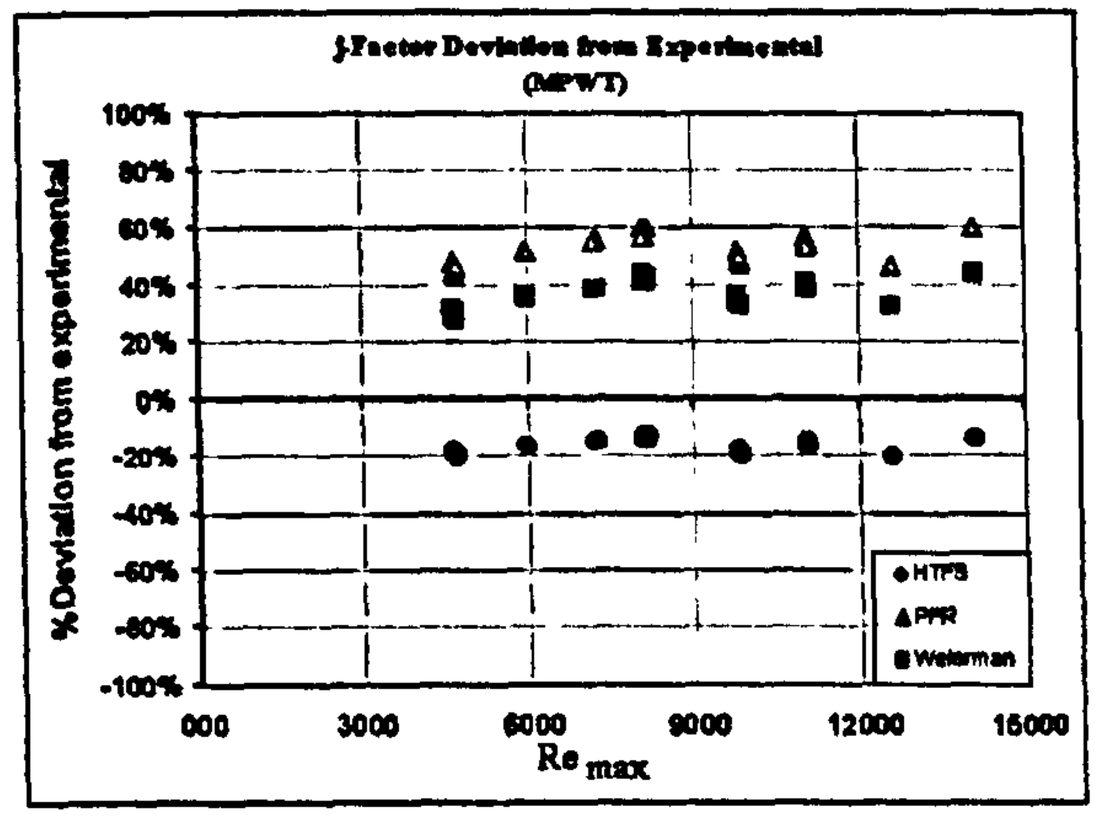

Figure 4.10: *j* factor comparisons, bundle 2

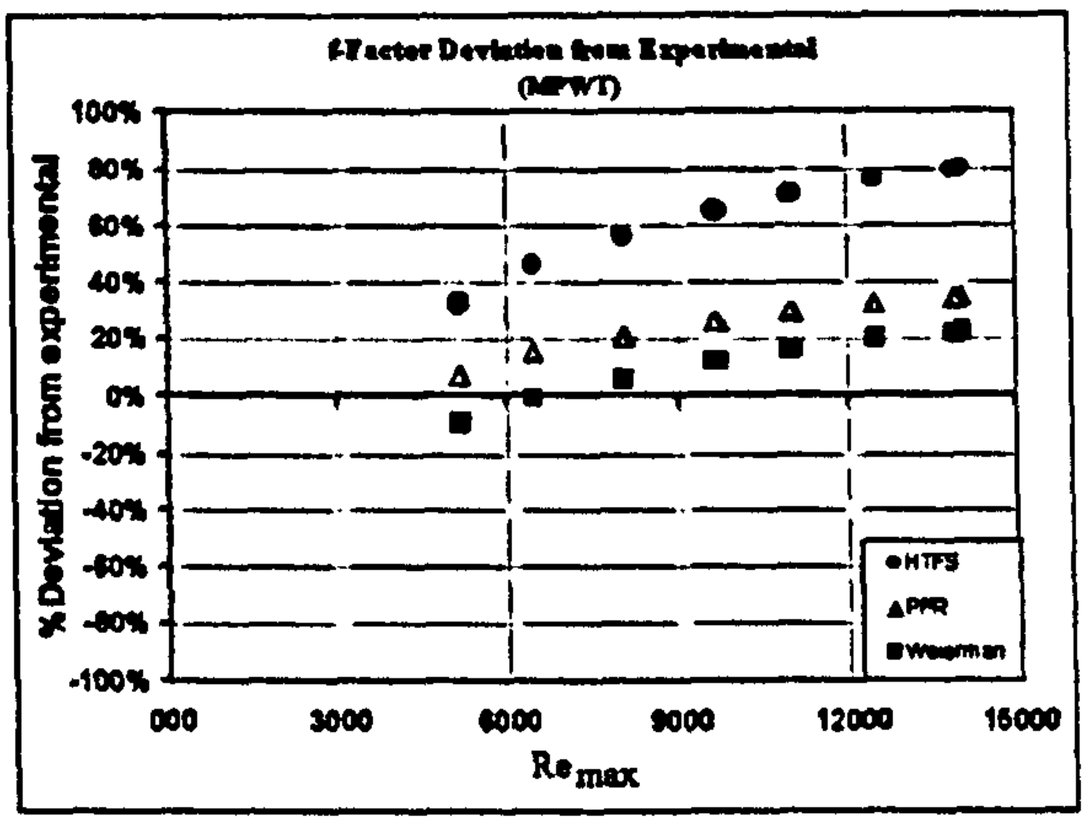

Figure 4.11: *f* factor comparisons bundle 3

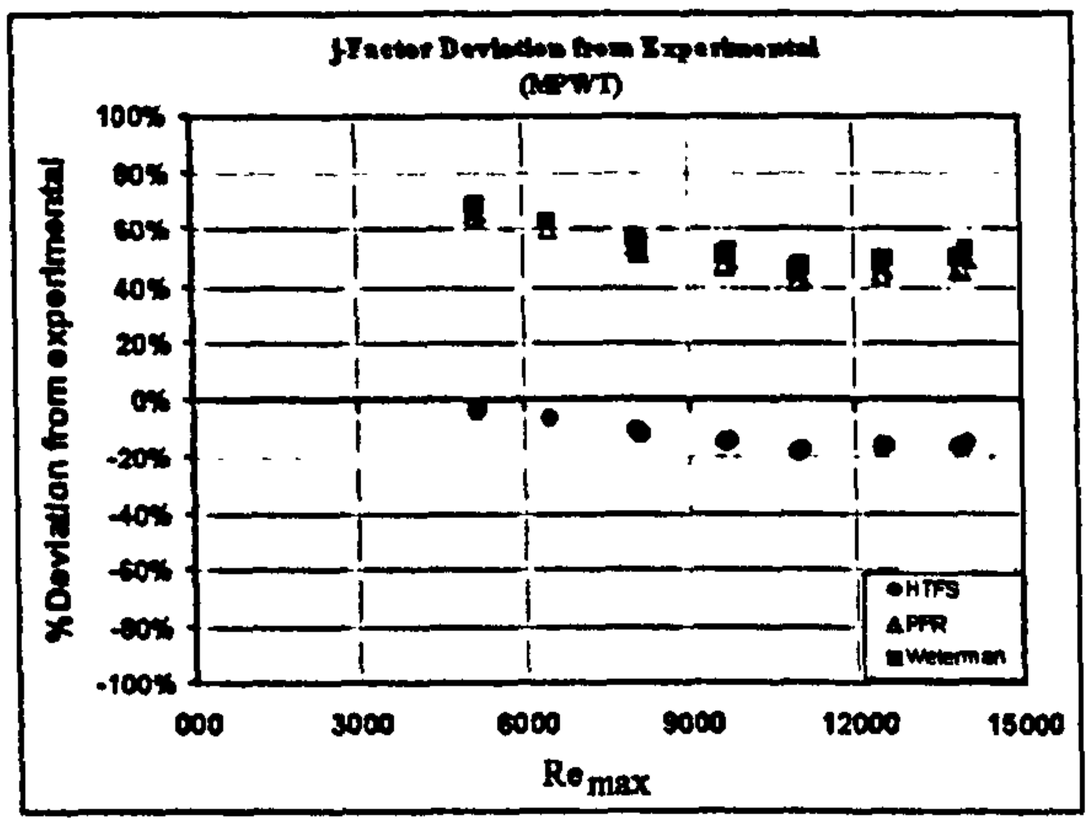

Figure 4.12: *j* factor comparisons, bundle 3

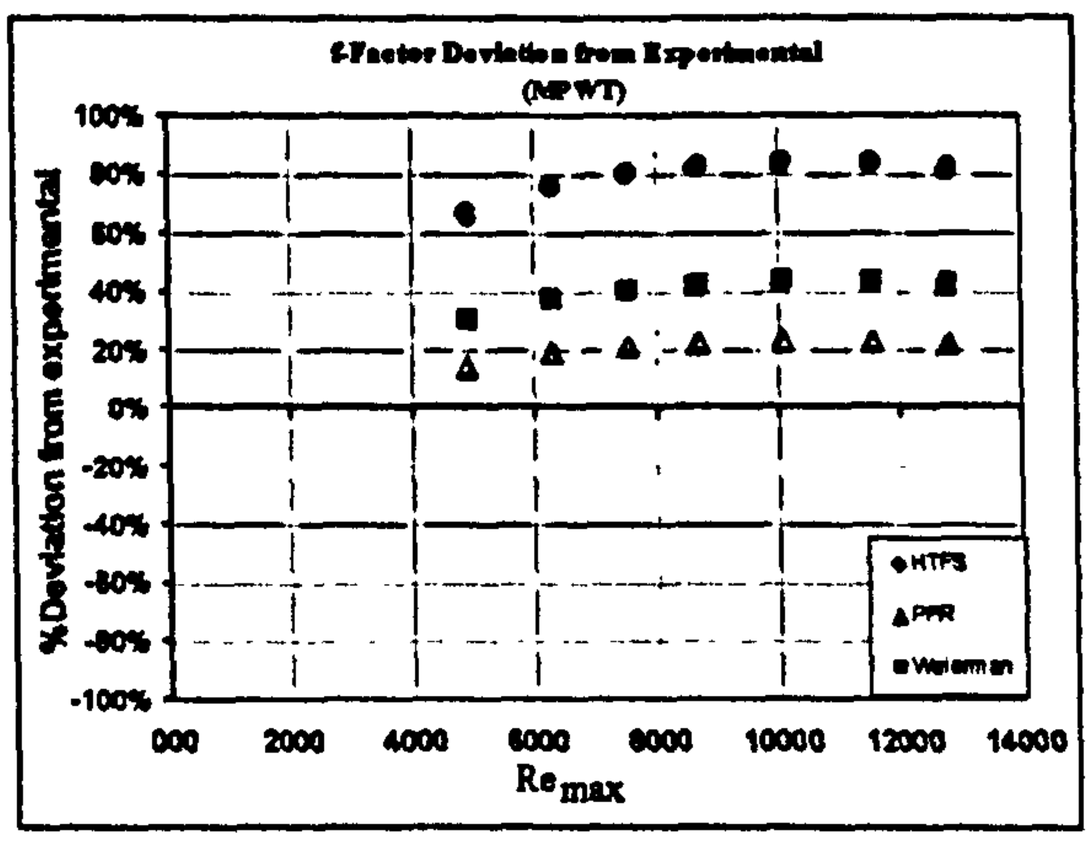

Figure 4.13: *f* factor comparisons, bundle 4

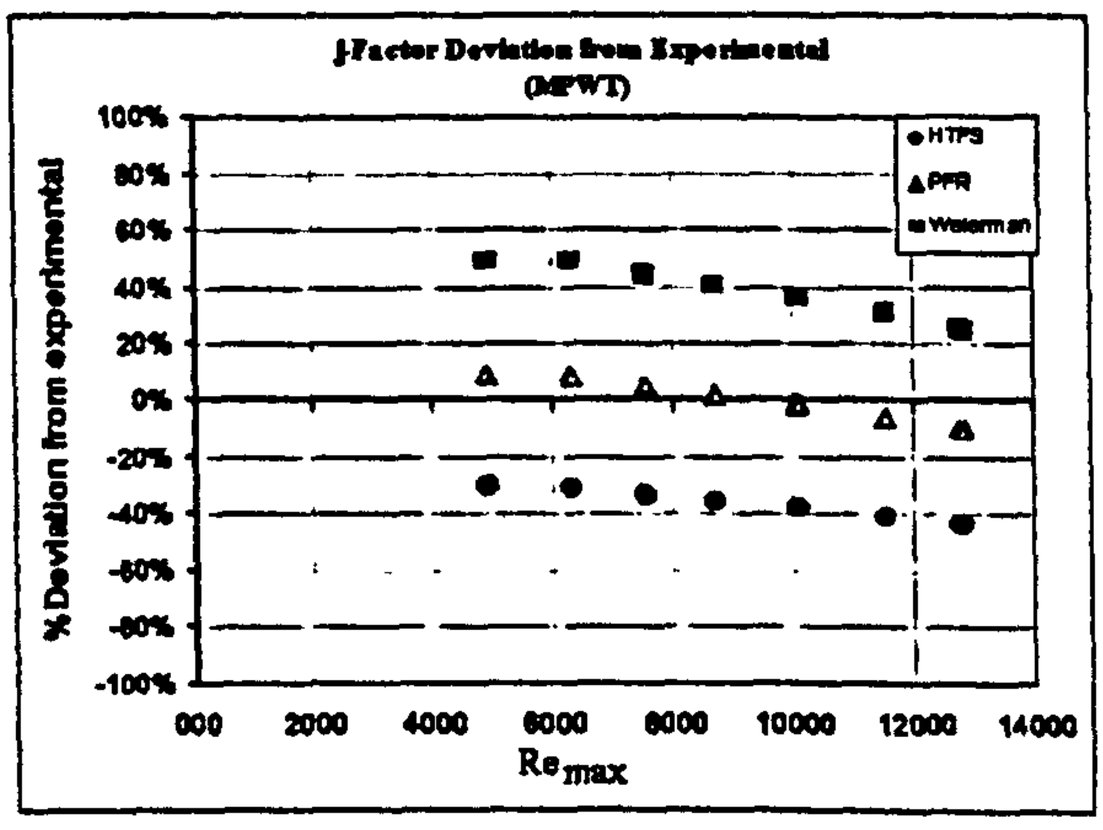

Figure 4.14: *j* factor comparisons, bundle 4

From the comparisons shown in Figures 4.7 to 4.14 it is clear that the Chu and Ralston [23] method overpredicted the pressure drop significantly for all bundles while both

PFR [13] and Weierman [14] gave comparable results, with Weierman being closer to the test data for bundles, 1, 2 and 3. This will be expanded on in Chapter 7.

For heat transfer it seems that the Chu and Ralston [23] method is on the conservative side while the other methods are non-conservative. Their method underpredicts the heat transfer by up to 20% for Bundles 2 and 3 and by up to 40% for Bundles 1 and 4. The other methods give overprediction ranging from 20% to 60% except Bundle 4 where PFR [13] give good agreement with data.

4.3.6 Predictions on rectangular pitch bundles

The comparisons shown in Figures 4.15 to 4.24 are the percentage deviations from experimental values with the method of Chu and Ralston [23], PFR [13] and Weierman [14].

The deviation in the predicted f factors from the above three methods are presented in Figures 4.15,17,19 and 21 for the five test bundles. It can be seen that the Chu and Ralston [23] method generally overpredicts pressure drop by up to 90%. The PFR [13] and the Weierman [14] methods generally show comparable results with better agreement with the data although the trend is not predicted correctly.

It can be seen that the results of the heat transfer predictions given below are not satisfactory. The Chu and Ralston [23] method underpredicts the *j*-factor for all bundles by up to –40%. The PFR [13] and the Weierman [14] methods generally overpredict the heat transfer by up to +55% with PFR being slightly better for most bundles. It is clear that none of the methods predicts the trends correctly.

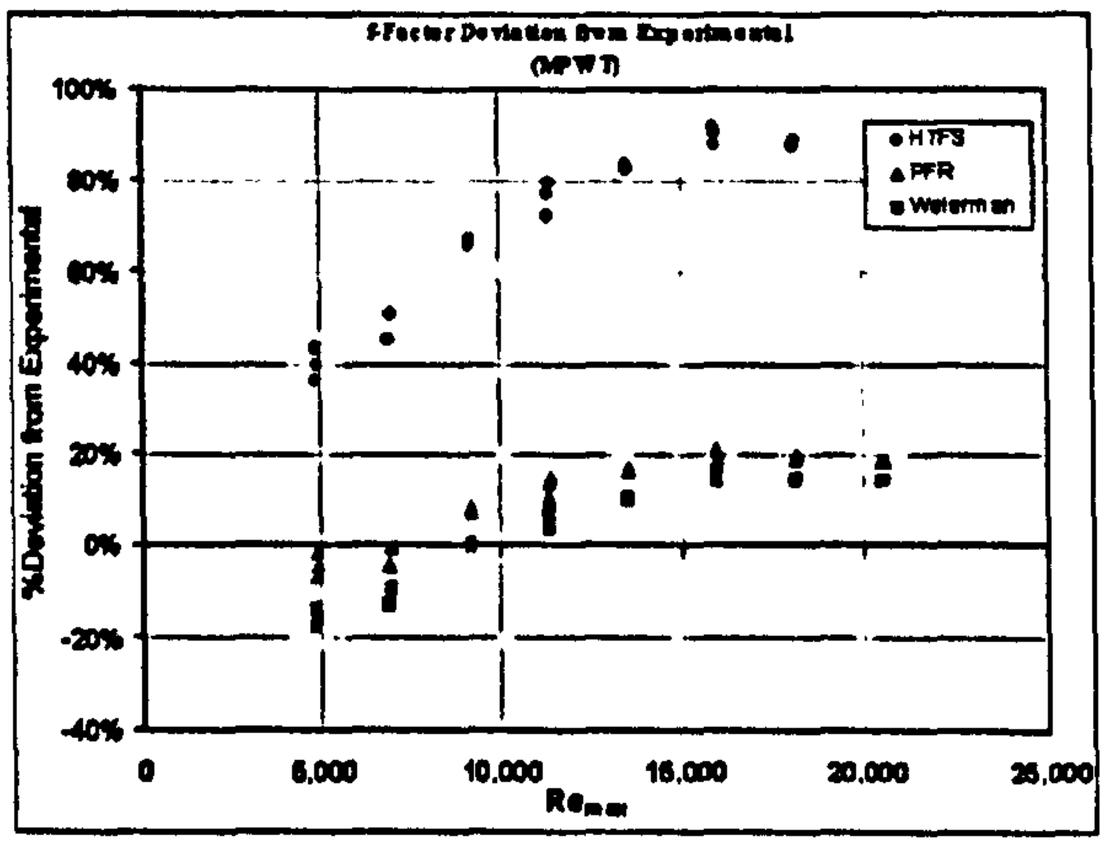

Figure 4.15: *f*-factor Predictions for Bundle 5

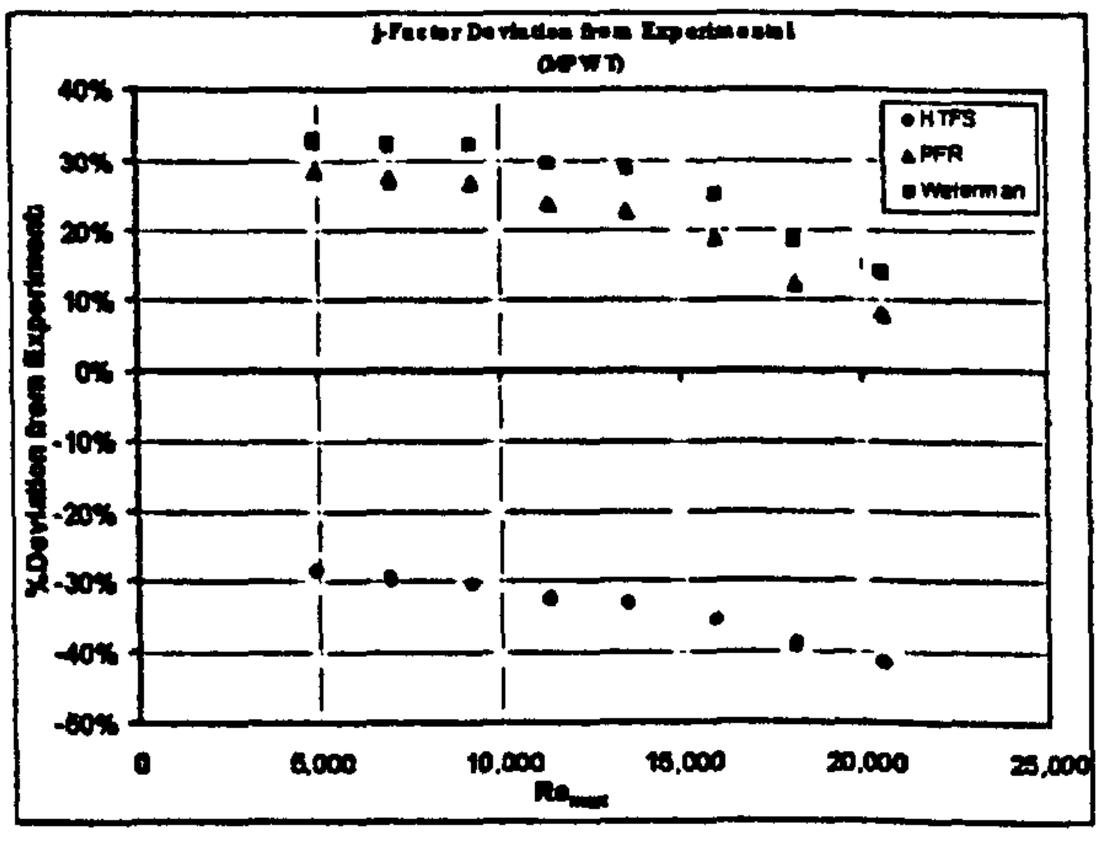

Figure 4.16: *j*-factor Predictions for Bundle 5

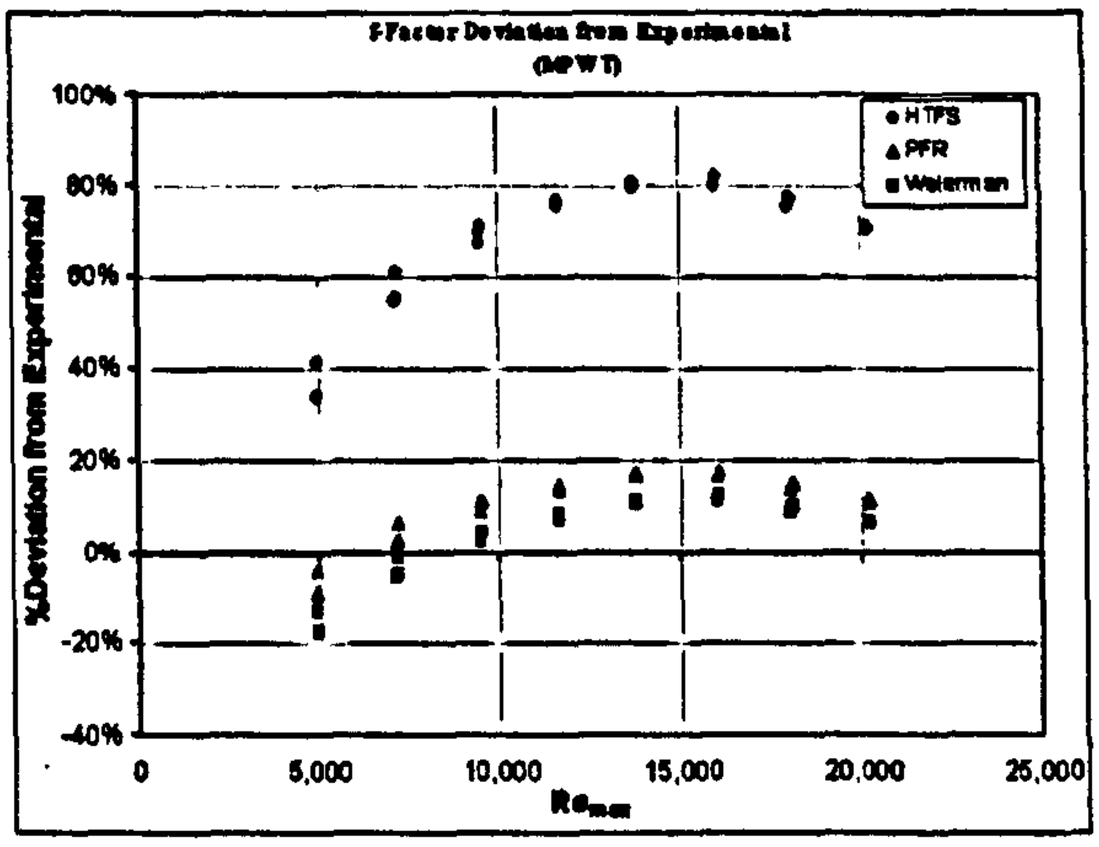

Figure 4.17: *f*-factor Predictions for Bundle 6

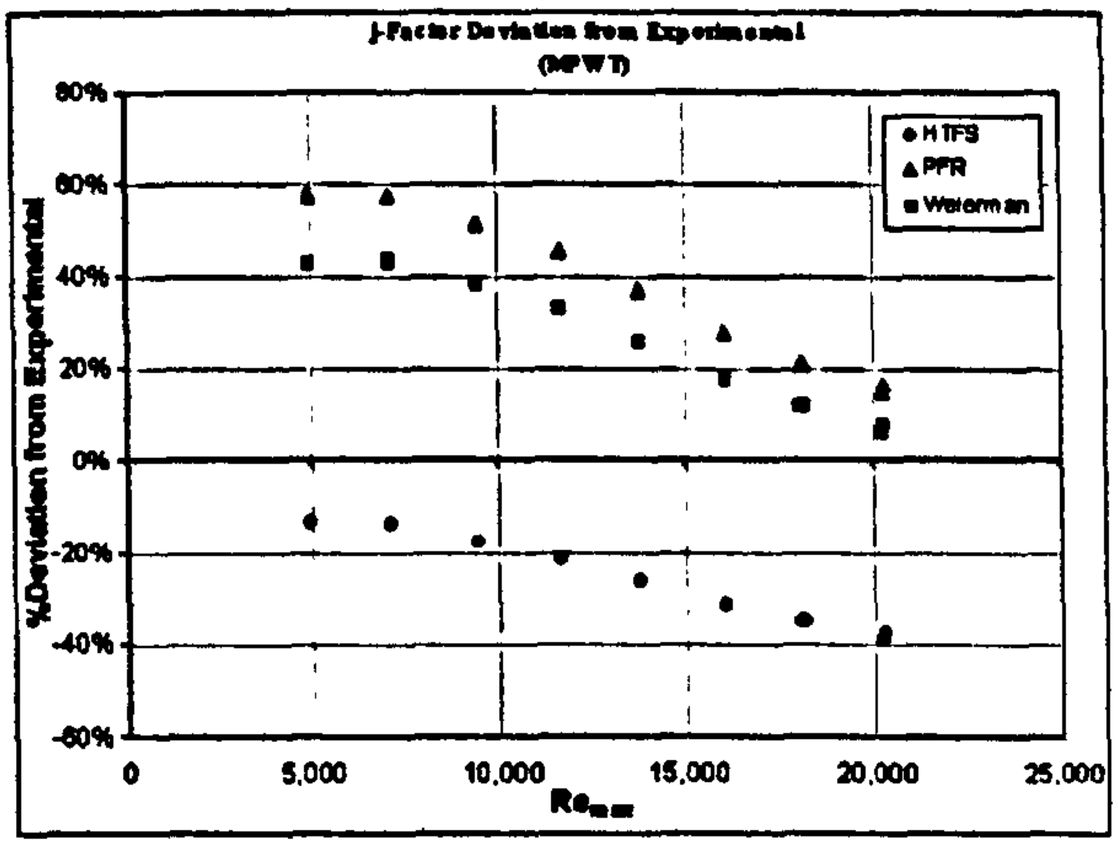

Figure 4.18: *j*-factor Predictions for Bundle 6

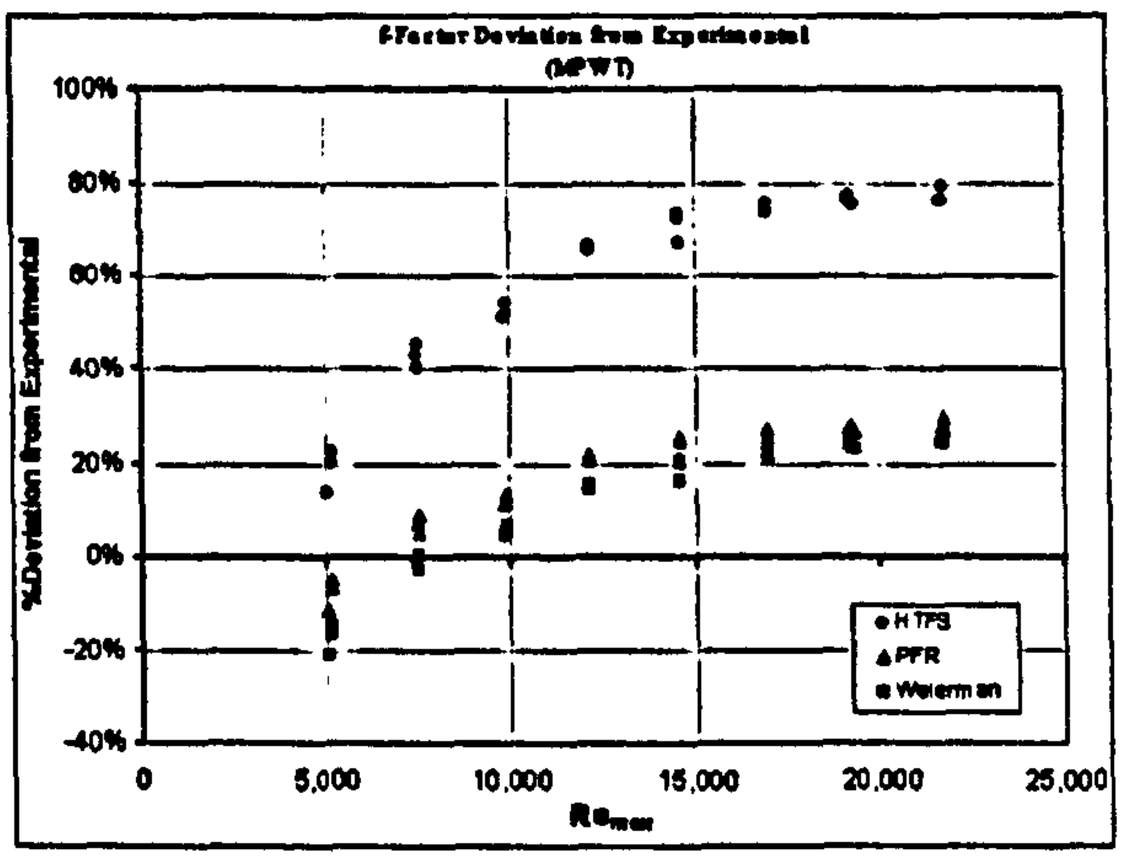

Figure 4.19: *f*-factor Predictions for Bundle 7

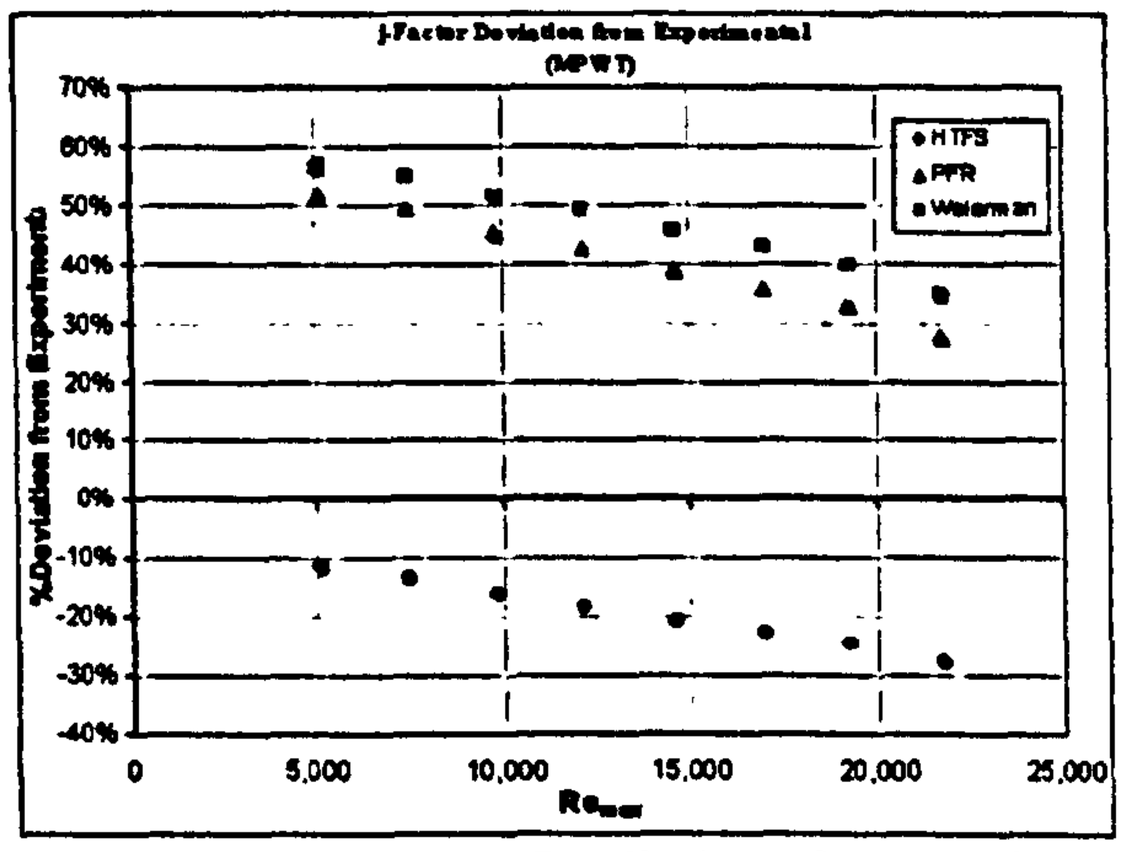

Figure 4.20: *j*-factor Predictions for Bundle 7

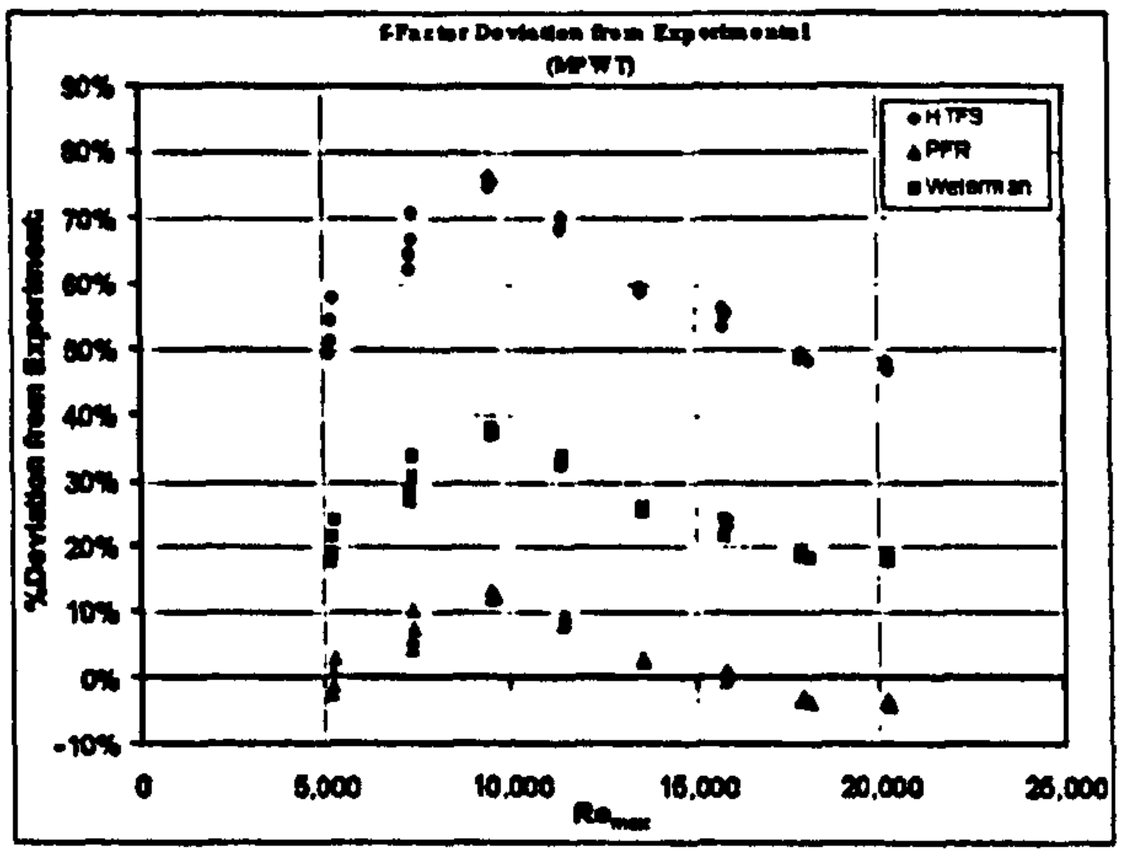

Figure 4.21: *f*-factor Predictions for Bundle 8

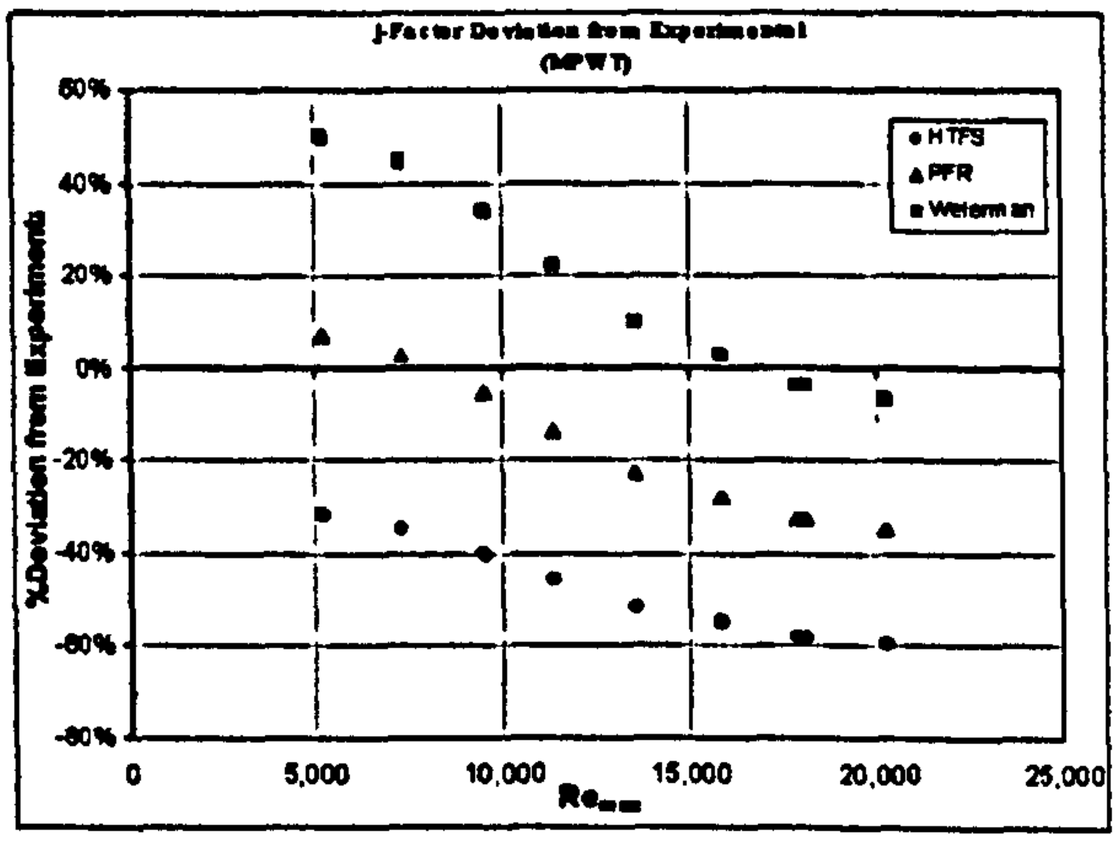

Figure 4.22: *j*-factor Predictions for Bundle 8

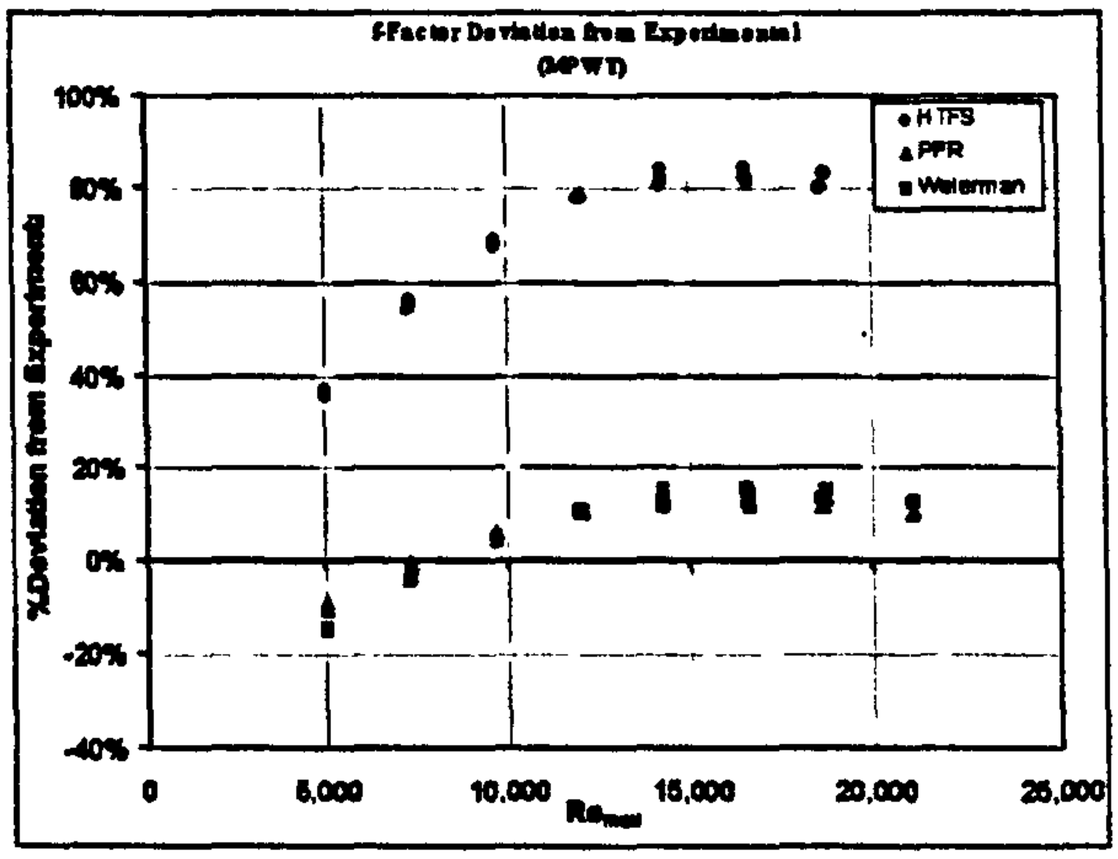

Figure 4.23: *f*-factor Predictions for Bundle 9

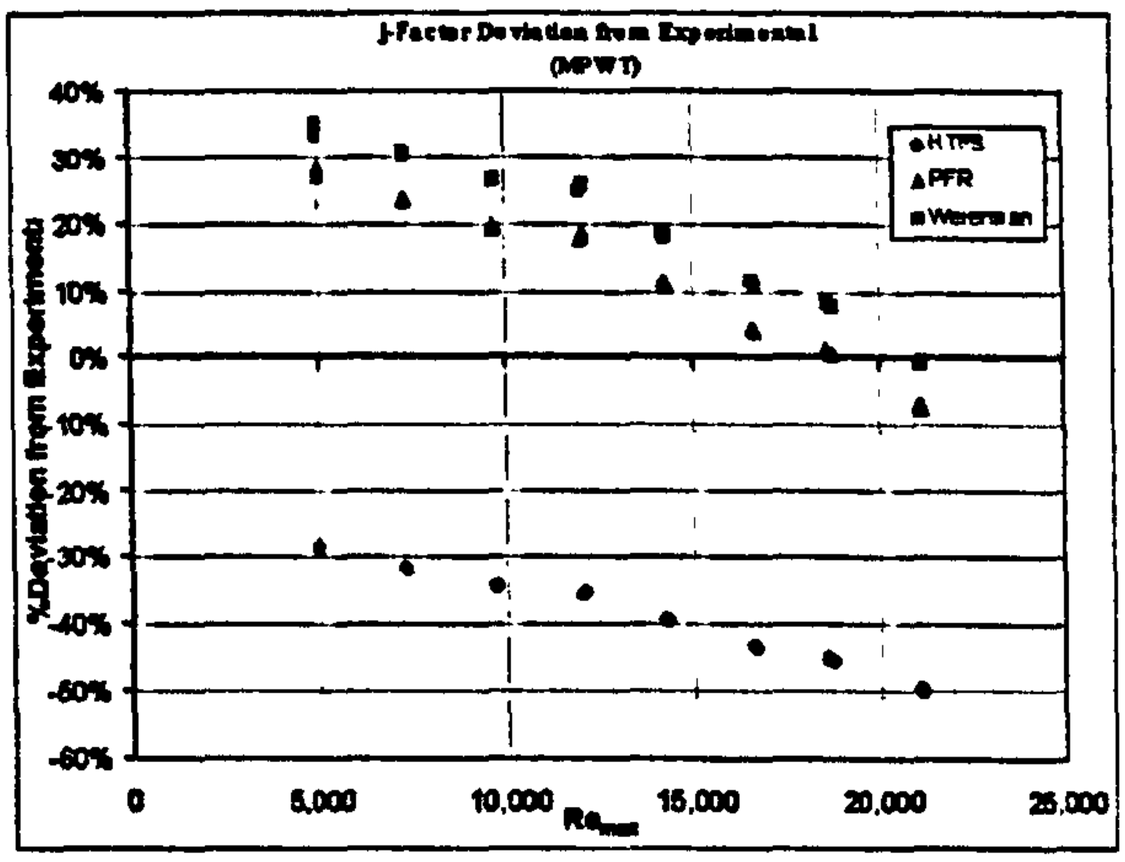

Figure 4.24: *j*-factor Predictions for Bundle 9

4.3.7 Conclusions on square pitch bundles

An analysis of new data for heat transfer and pressure drop of in-line bundles of plain-finned tubes has shown that the initial method reported by Chu and Ralston [23] overpredicts pressure drop and underpredicts heat transfer.

The PFR [13] and Weierman [14] methods gave reasonable and conservative predictions of pressure drop but consistently overpredicted the heat transfer.

4.3.8 Conclusions on rectangular pitch bundles

The predictions of pressure drop and heat transfer indicate that the PFR [13] method gives the best agreement in comparison with other presented methods. However none of the methods gives consistent agreement with data for both heat transfer and pressure drop, nor has the trend of data been correctly predicted. The conclusion from this was that a new method for inline bundles using the square and rectangular pitch data presented here, in addition to any reliable open literature data in the HTFS databank, was required. This will be described in Chapter 7.

4.4 Heat Recovery Bundle with and without corbels

4.4.1 Heat transfer characteristics with and without corbels

The measured j factors with and without corbels for the heat recovery bundle are shown in Figure 4.25.

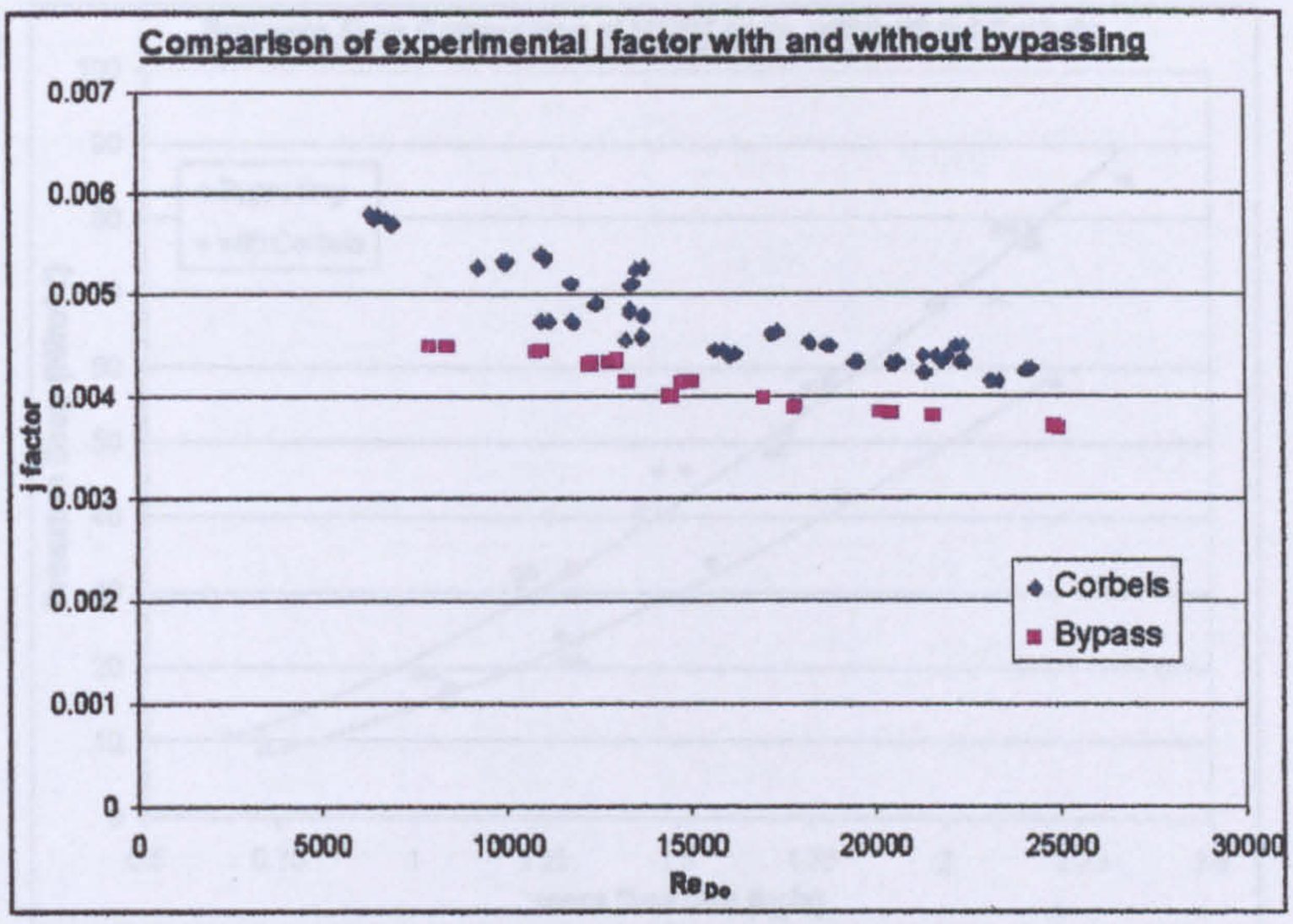

Figure 4.25: Measured j factors with and without corbels

It can be seen that when there is bypassing the heat transfer performance is significantly lower. It can be seen that there is quite a lot of scatter in the data. This was due to unavoidable leaks in the HTWT.

4.4.2 Measured Pressure Drop and Calculated Bypass Flow

When the inactive half tubes were removed from the bundle, two bypass lanes were created, one at the top and one at the bottom of bundle. In this case it was deemed necessary to estimate how much flow will bypass the tubes ($\dot{M}_B$) so that the heat transfer calculation can be based on the crossflow ($\dot{M}_C$) through the tubes.

The pressure drop measurements for the bundle, with and without the corbels were used to estimate the bypass flow rate. The pressure drop data is presented against the total mass flow rate supplied to the bundle in Figure 4.26. From this figure it can be seen that, for a fixed value of pressure drop, the total flow rate supplied to the bundle without corbels is higher than the one with corbels due to the decrease of resistance to flow.

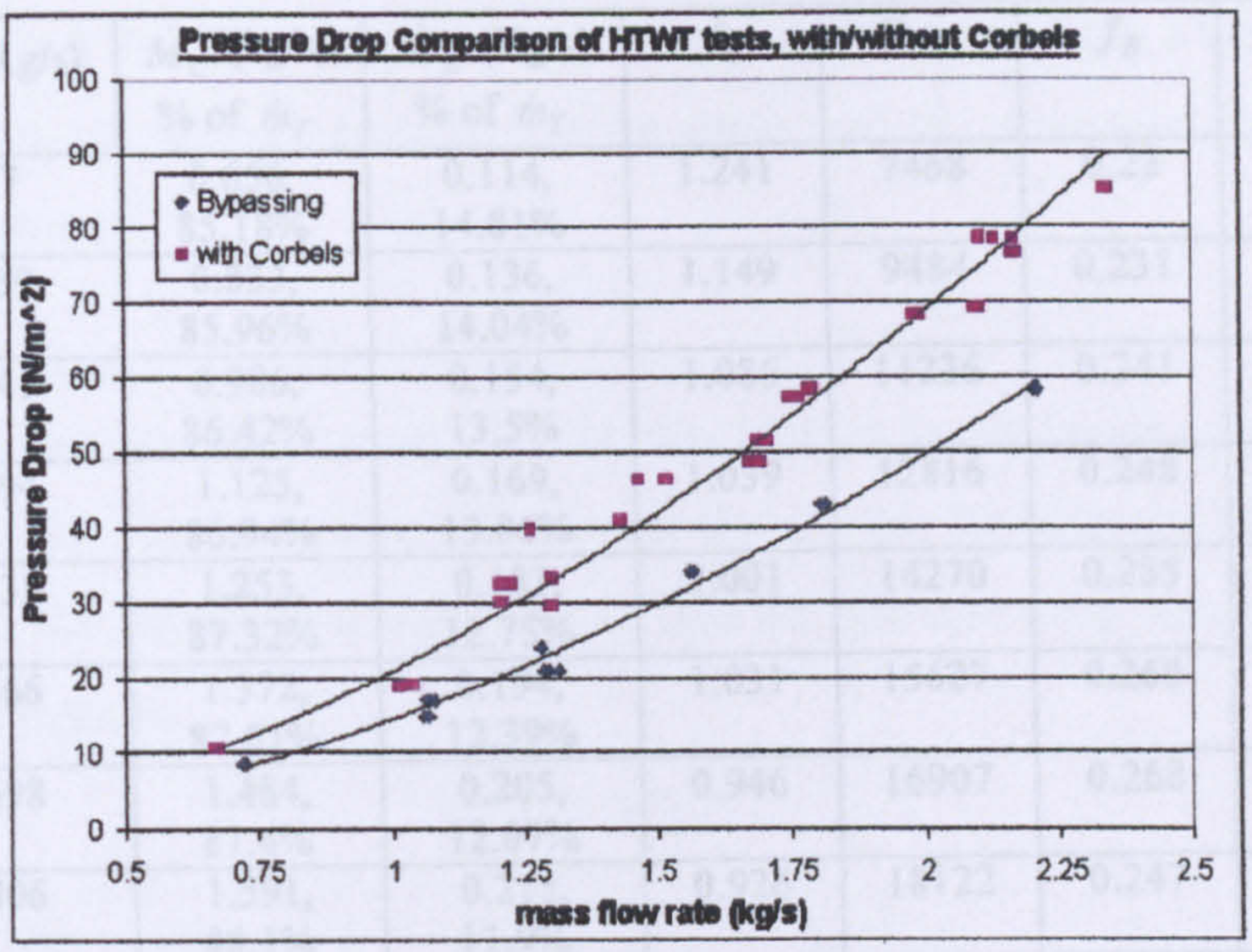

Figure 4.26: Pressure drop of heat recovery bundle with and without corbels

Using a curve fit, the data was processed to give a pair of idealized curves. These are presented in Figure 4.27. It can be seen on this graph, that for a chosen pressure drop there is a difference in mass flow rate.

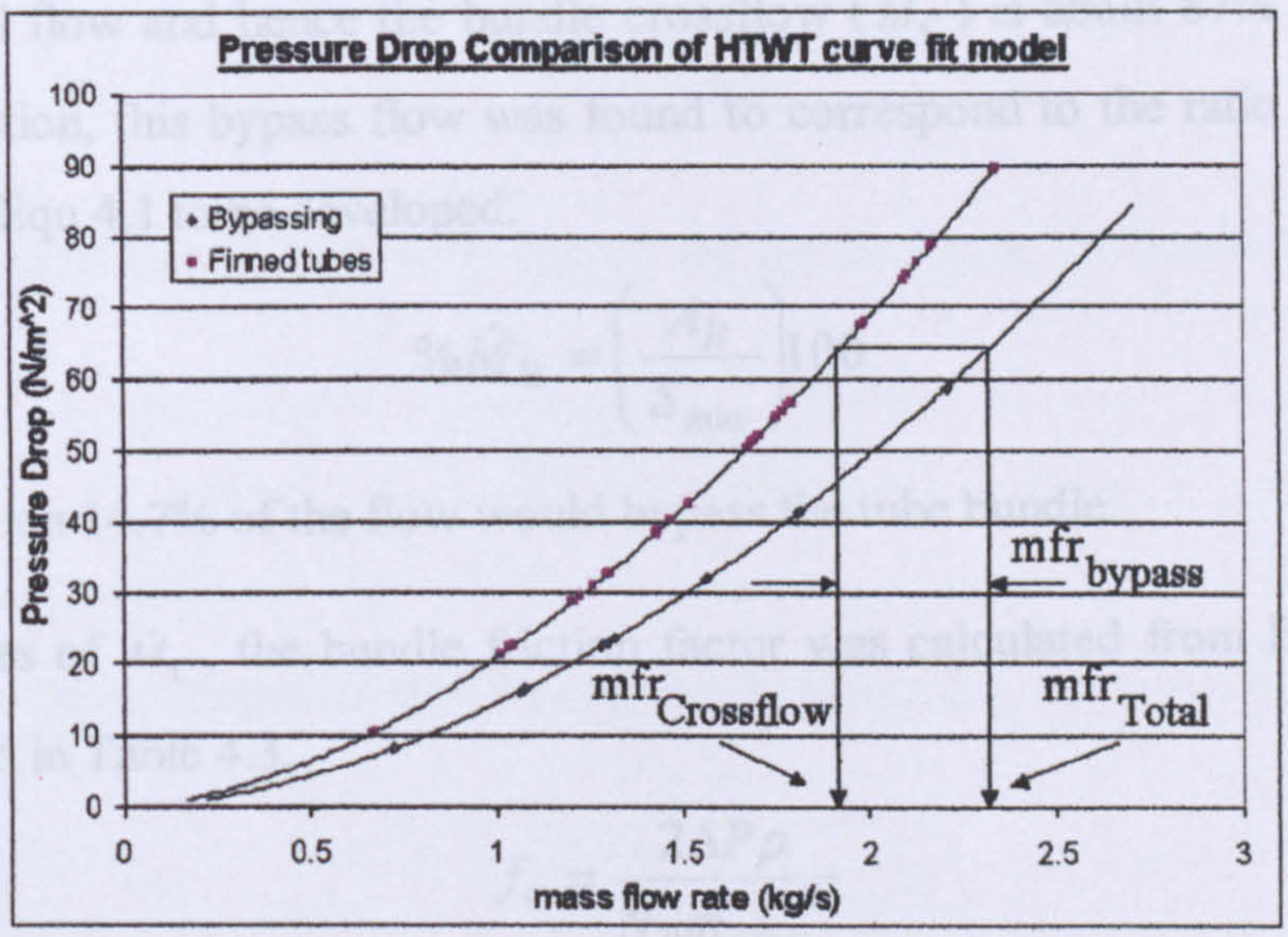

Figure 4.27: Representation of portion of mass flow rate that bypasses

The difference between the two flow rates was attributed to the bypass flow. Using idealized data presented in Figure 4.27, the bypass flow and the crossflow rates were estimated for the measured range of pressure drops. The results of these calculations are shown in Table 4.3.

Measured ΔP, Pa	$\dot{M}_T$ (Kg/s)	$\dot{M}_C$ (kg/s), % of $\dot{m}_T$	$\dot{M}_B$ (Kg/s), % of $\dot{m}_T$	f_C	Re_C	f_B	Re_B
10	0.77	0.656, 85.18%	0.114, 14.81%	1.241	7468	0.22	5228
15	0.969	0.833, 85.96%	0.136, 14.04%	1.149	9484	0.231	6172
20	1.141	0.986, 86.42%	0.154, 13.5%	1.086	11236	0.241	6927
25	1.294	1.125, 86.94%	0.169, 13.06%	1.039	12816	0.248	7567
30	1.435	1.253, 87.32%	0.183, 12.75%	1.001	14270	0.255	8124
35	1.566	1.372, 87.61%	0.194, 12.39%	1.031	15627	0.260	8622
40	1.698	1.484, 87.4%	0.205, 12.07%	0.946	16907	0.268	9072
45	1.806	1.591, 88.1%	0.215, 11.9%	0.926	18122	0.247	9485
50	1.917	1.693, 88.32%	0.224, 11.86%	0.91	19283	0.28	9866
55	2.024	1.791, 88.49%	0.233, 11.51%	0.899	20397	0.288	10220

Table 4.3: Mass flow splits and f factors for Bypassing and corbelled conditions

With reference to Table 4.3, it was deduced that the average bypass flow ($\dot{M}_B$) is about 13% of the total flow and hence the bundle crossflow ($\dot{M}_C$) is about 87% of the total flow. By inspection, this bypass flow was found to correspond to the ratio of the flow areas, allowing Equ.4.1 to be developed.

$$\%\dot{M}_B = \left(\frac{A_B}{S_{\min}}\right)100 \qquad \text{(Equ.4.1)}$$

From this equation 14.7% of the flow would bypass the tube bundle.

Using the values of $\dot{M}_C$, the bundle friction factor was calculated from Equ.4.2. The results are listed in Table 4.3.

$$f_C = \frac{2\Delta P\rho}{N_R \dot{m}_{\max C}{}^2} \qquad \text{(Equ.4.2)}$$

Where Equ.4.3 is the maximum mass flux through the bundle.

$$\dot{m}_{\max C} = \frac{\dot{M}_C}{S_{\min}} \qquad \text{(Equ.4.3)}$$

When the crossflow friction factor data was plotted against the crossflow Reynolds number it was expected that the data would agree with that plotted for the bundle with

corbels. It was shown that this was the case, confirming that the bundle friction factors in both cases (with and without corbels) are the same, and the suggested bypass flow estimation was correct.

4.4.3 Bypass friction factor

The experimental data was used to calculate bypass friction factor, based on the method shown by Wills [29]. For the bundle with bypass flow, it can be assumed that the total flow approaching the bundle will distribute so that the pressure drop across the tubes equals that of the bypass.

$$\Delta P_B = \Delta P_C$$

As the bypass flow is defined and the bundle pressure drop is known, it was possible to calculate the bypass friction factor from the equations given by Wills [29].

$$f_B = \frac{\Delta P_B}{2 N_R \rho U_B^{\,2}} \qquad \text{(Equ.4.4)}$$

where

$$U_B = \frac{\dot{M}_B}{\rho A_B} \qquad \text{(Equ.4.5)}$$

The data was then plotted (Figure 4.28) against the bypass Reynolds number, calculated from Equ.4.6.

$$\mathrm{Re}_B = \frac{\dot{M}_B D_e}{\eta A_B} \qquad \text{(Equ.4.6)}$$

Where the bypass equivalent diameter D_e is given by Wills [29], as shown in Equ.4.7.

$$D_e = \frac{4 A_B}{2\left(\sum_{i=1}^{i=n} L_B + n L_t\right)} \qquad \text{(Equ.4.7)}$$

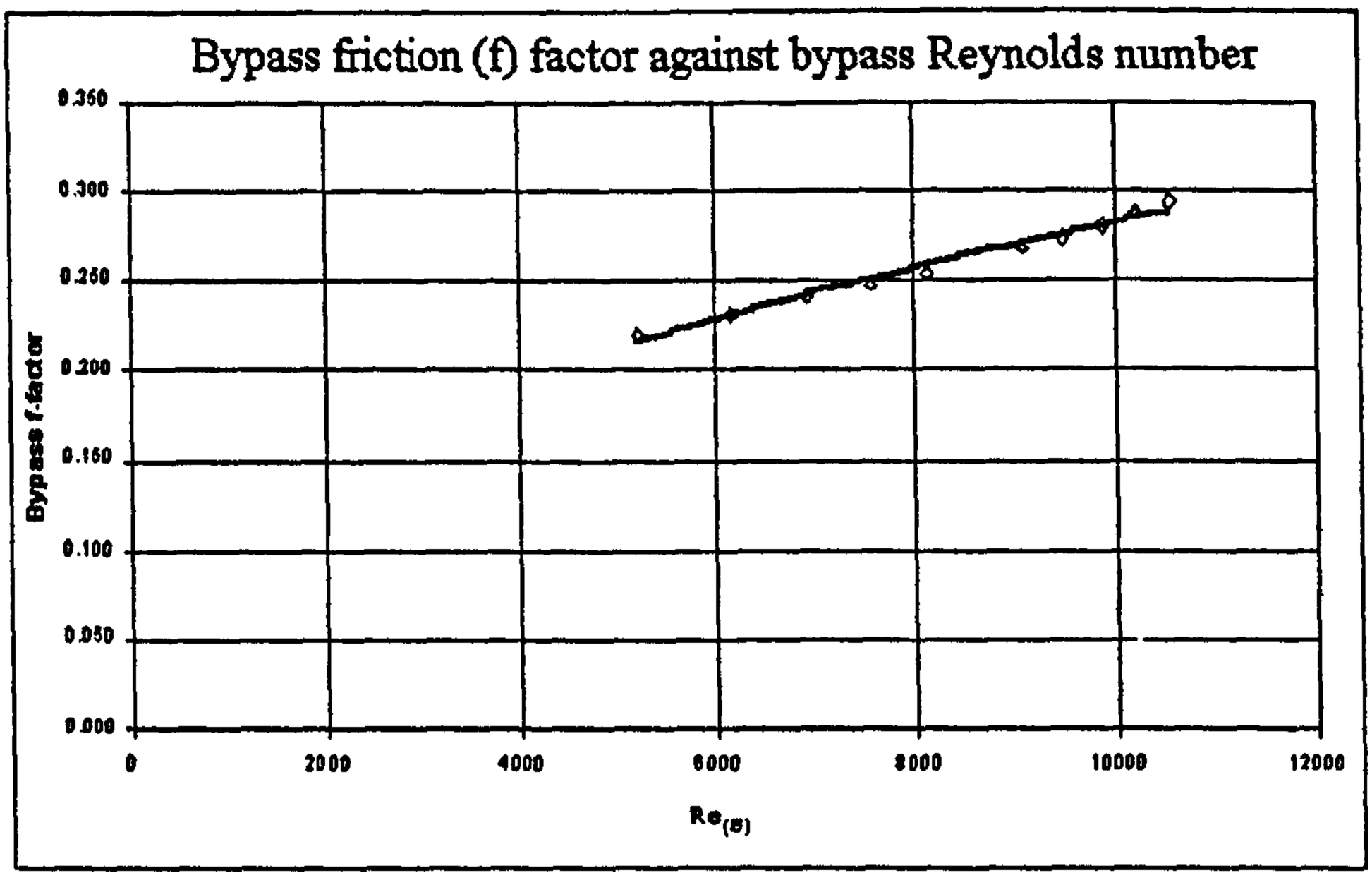

Figure 4.28: Bypass friction factor

From Figure 4.28 the bypass friction factor can be represented by the following correlation (Equ.4.8):

$$f_B = 0.0064 \mathrm{Re}_B^{0.4119} \qquad \text{(Equ.4.8)}$$

4.4.4 Differences in heat transfer

The analysis given in the previous section suggests that when corbels are removed the bundle heat transfer performance will drop due to the bypass flow not contributing to the heat transfer. This means, for a given duty, the bundle performance can only be the same as that of the corbelled bundle if the total flow supplied to the bundle is increased by the amount equivalent to the bypass flow. When this was done the performance of the bundle with and without corbels was found to be nearly identical as demonstrated in Figure 4.29.

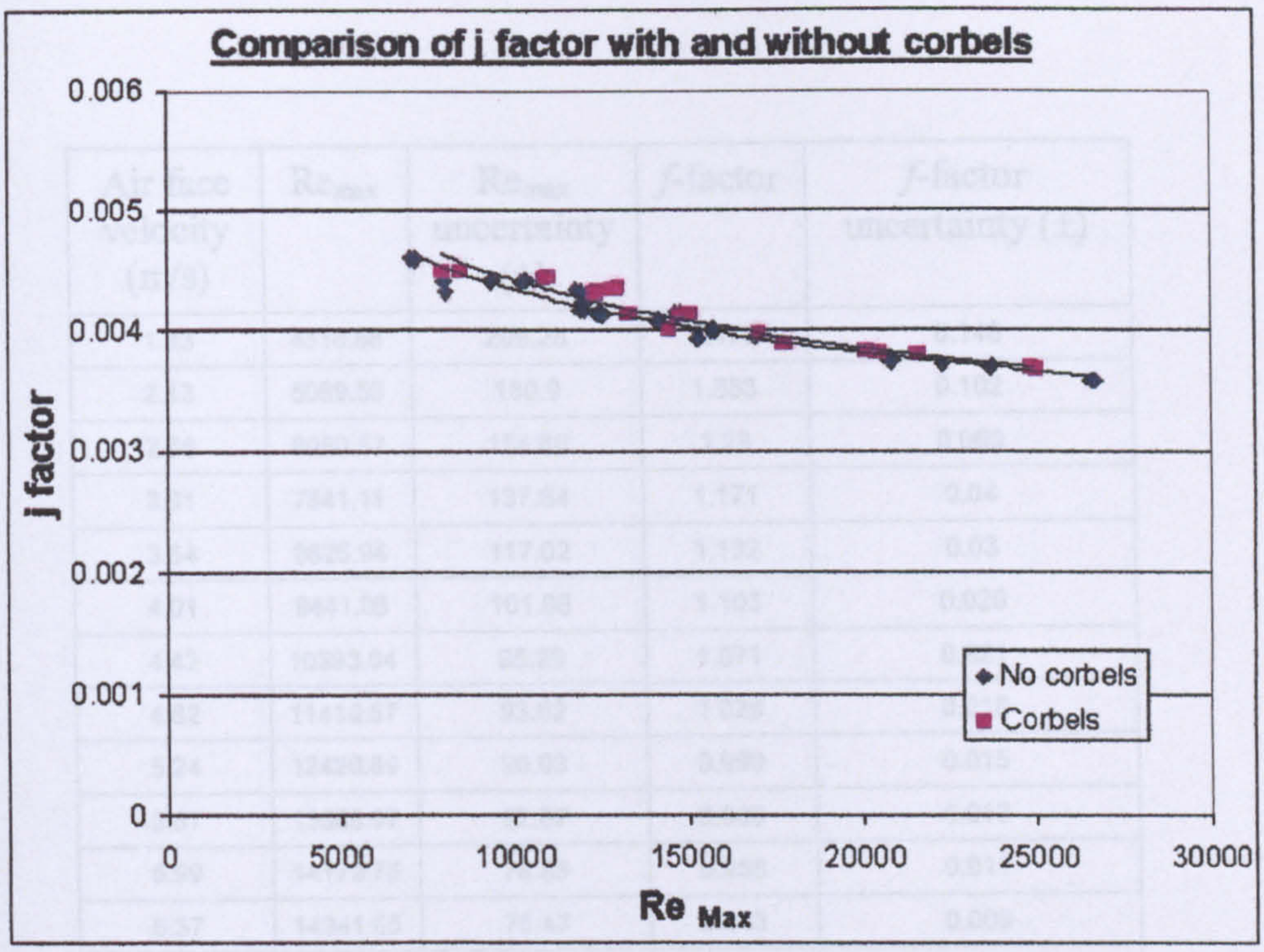

Figure 4.29: j factor of corbelled bundle and bypassing bundle

For this test bundle the consequence of not using corbels was a drop of about 7% in heat transfer performance.

4.5 Staggered air cooler with varying corbel shapes and flow bypassing

The geometry of the test bundle is shown in Table 3.11, only the corbel types varied during the tests.

4.5.1 Results of bundles with varying corbels

Measurements of pressure loss characteristics are presented in the form of *f* factors in Tables 4.4-4.8. These are the grouped values. The associated uncertainties are also presented in the following tables. It can be seen that the low values of uncertainty associated with the measurements indicate that the measurements are reliable.

Air face velocity (m/s)	Re_{max}	Re_{max} uncertainty (±)	*f*-factor	*f*-factor uncertainty (±)
1.83	4316.68	209.25	1.477	0.148
2.13	5089.59	180.9	1.353	0.102
2.56	6080.57	154.66	1.28	0.069
3.31	7841.11	137.64	1.171	0.04
3.64	8626.94	117.02	1.132	0.03
4.01	9441.06	101.66	1.103	0.026
4.42	10393.04	95.29	1.071	0.021
4.82	11410.67	93.62	1.029	0.018
5.24	12420.69	90.03	0.999	0.015
5.57	13065.97	82.67	0.988	0.013
5.99	14179.75	78.85	0.956	0.011
6.37	14941.65	76.47	0.943	0.009
7.07	16542.94	76.35	0.908	0.008

Table 4.4: Summary of grouped test results and associated uncertainties of bundle with half tubes

Air face velocity (m/s)	Re_{max}	Re_{max} uncertainty (±)	*f*-factor	*f*-factor uncertainty (±)
1.69	4025.28	226.41	1.638	0.188
2.04	4853.84	190.11	1.509	0.123
2.37	5628.77	165.08	1.421	0.087
2.73	6487.57	145.39	1.344	0.065
3.07	7281.88	132.42	1.28	0.051
3.36	7988.5	121.95	1.248	0.043
3.76	8912.74	110.93	1.187	0.032
4.1	9734.82	102.77	1.164	0.029
4.44	10515.19	106.53	1.131	0.024
5.17	12221.47	87.74	1.077	0.016
5.55	13118.07	87.26	1.054	0.017
5.92	13995.27	87.197	1.03	0.013
6.28	14855.73	89.02	1	0.012

Table 4.5: Summary of grouped test results and associated uncertainties of bundle with sealing strips

Air face velocity (m/s)	Re_{max}	Re_{max} uncertainty (±)	*f*-factor	*f*-factor uncertainty (±)
1.71	4069.17	223.57	1.631	0.183
2.06	4901.47	191.14	1.485	0.12
2.39	5676.78	163.37	1.393	0.09
2.72	6467.68	148.48	1.318	0.063
3.07	7286.97	129.37	1.258	0.049
3.41	8073.23	119.96	1.219	0.039
3.77	8947.08	111.3	1.164	0.034
4.11	9750.67	104.09	1.139	0.029
4.43	10489.33	104.92	1.109	0.026
4.81	11390.71	101.09	1.073	0.021
5.19	12278.99	92.63	1.046	0.017
5.53	13086.54	93.73	1.024	0.016
5.87	13867.32	91.32	1	0.014
6.24	14768.13	91.45	0.987	0.012
6.64	15686.53	81.44	0.965	0.01

Table 4.6: Summary of grouped test results and associated uncertainties of bundle with inverted v

Air face velocity (m/s)	Re_{max}	Re_{max} uncertainty (±)	*f*-factor	*f*-factor uncertainty (±)
1.76	4117.52	219.53	1.614	0.179
2.12	4982.07	187.67	1.473	0.115
2.46	5774.97	157.57	1.373	0.08
2.84	6677.29	139.07	1.287	0.058
3.16	7401.3	125.6	1.243	0.046
3.52	8251.28	116.34	1.198	0.035
3.9	9152.04	104.3	1.164	0.03
4.11	9629.55	101.74	1.135	0.029
4.62	10837.67	92.97	1.085	0.021
4.98	11666.52	89.34	1.058	0.018
5.36	12552.38	84.51	1.032	0.014
5.84	12809.39	88.59	1.031	0.015
6.09	14224.29	80.25	0.992	0.011
6.49	15185.82	97.515	0.965	0.012

Table 4.7: Summary of grouped test results and associated uncertainties of bundle with square blocks

Air face velocity (m/s)	Re_{max}	Re_{max} uncertainty (±)	*f*-factor	*f*-factor uncertainty (±)
1.78	4143.55	214.4	1.334	0.145
2.14	4979.87	180.5	1.223	0.098
2.49	5802.86	157.41	1.133	0.07
2.85	6635.68	138.24	1.075	0.051
3.2	7452.79	127.1	1.023	0.042
3.53	8219.88	121.38	0.983	0.036
3.92	9131.95	106.9	0.948	0.026
4.29	9979.84	97.55	0.914	0.02
4.66	10846.45	92.61	0.882	0.017
5.01	11645.37	93.95	0.866	0.014
5.4	12556.07	83.63	0.843	0.014
5.77	13397.69	91.34	0.823	0.011
6.16	14290.67	81.94	0.807	0.01
6.55	15194.12	80.54	0.791	0.009
6.84	15867.14	83.99	0.78	0.008

Table 4.8: Summary of grouped test results and associated uncertainties of bundle with bypassing

4.5.2 Pressure drop results and pressure loss characteristics

The measured pressure drop of each bundle is shown in Figure 4.30.

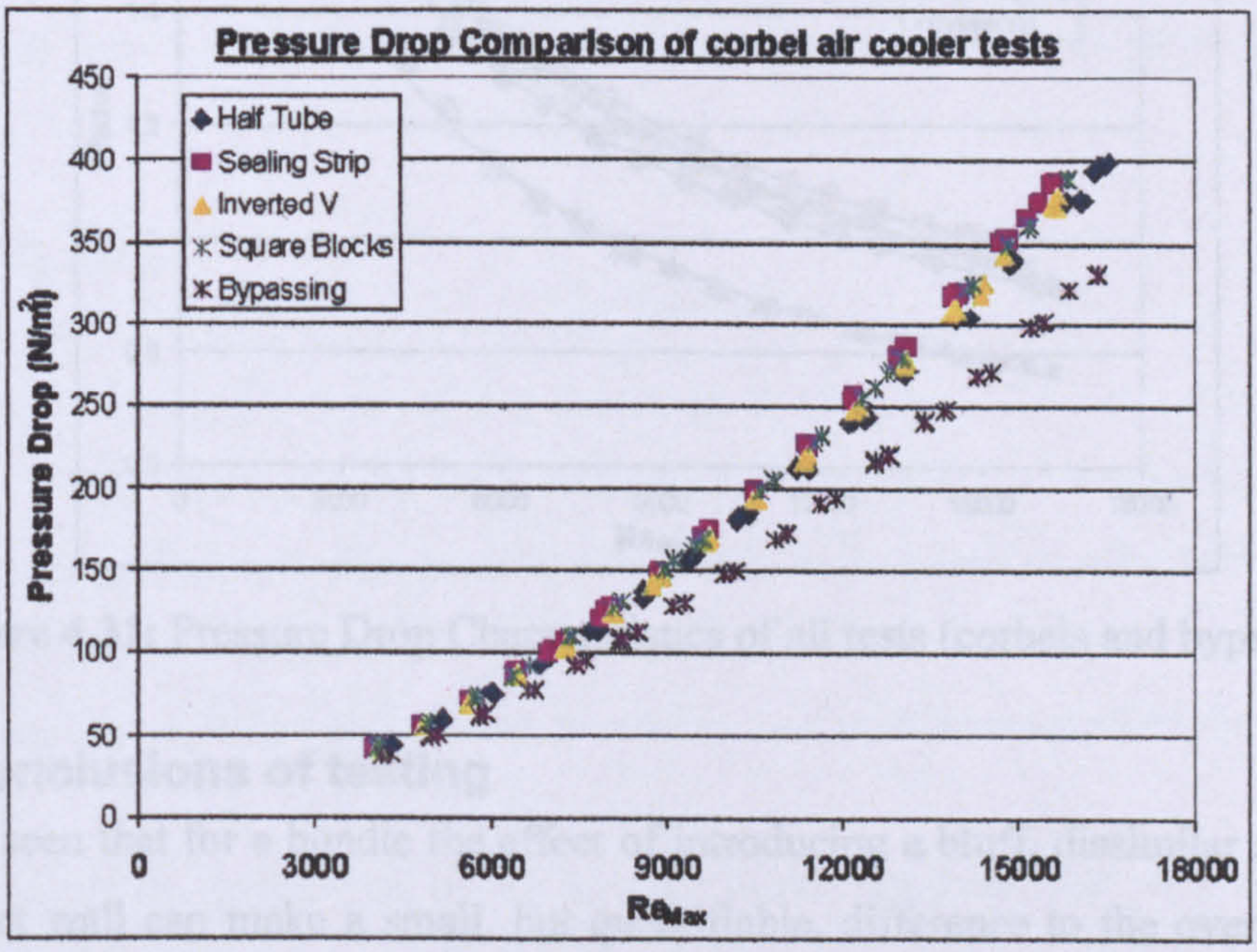

Figure 4.30: Pressure drop results of all tests (corbels and bypassing)

It can be seen that pressure drop increases in the order of:

- No corbels (bypass)
- Corbels
- Inverted V
- Square Blocks
- Sealing strips

Figure 4.30 shows that the difference between the pressure drops is reasonably small but it can be clearly seen in Figure 4.31, when reduced to the friction factor, that the sealing strip produces a noticeably higher result than either of the other shapes. It can therefore be reasoned that in a deeper bundle with an increasing number of rows (N_R) or at higher mass flow rates this difference would become more apparent. These two figures show why a study of this nature is important.

A review of the literature, as shown in Chapter 2, reveals that very little work of this type has been published, or perhaps even undertaken.

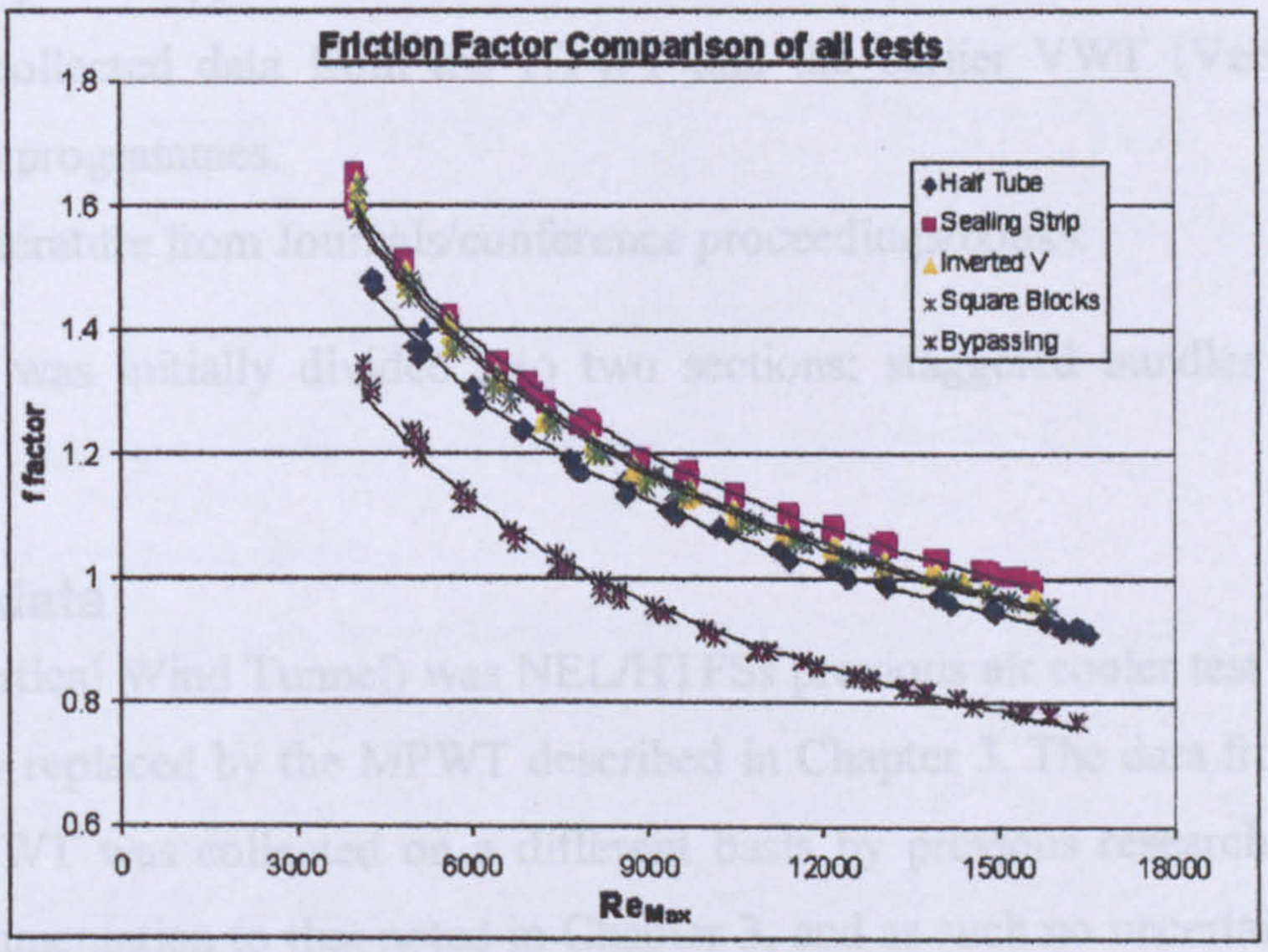

Figure 4.31: Pressure Drop Characteristics of all tests (corbels and bypassing)

4.5.3 Conclusions of testing

It can be seen that for a bundle the effect of introducing a bluff, dissimilar shape, body at the duct wall can make a small, but quantifiable, difference to the overall pressure drop. However it can be imagined that in a bundle with a large number of tubes per row

(N_T) these effects will diminish. Therefore an understanding of what effect the individual corbels have on the flow patterns in the duct wall region of an exchanger bundle, and how best to model this is required. These points will be addressed in Chapter 8.

As seen on the heat recovery bundle described in section 4.2, removing the corbels showed a significant reduction in pressure drop. A preliminary study similar to that described in sections 4.4.2 and 4.4.3 was conducted on this bypass data, and a distinctly different trend of mass flow splits (bypassing and crossflow) was found. It was also apparent that an estimation method based on a simple friction factor model would not be sufficient to correlate data from both sources. Theses points will be addressed in Chapter 9.

4.6 Data from the HTFS Databank

4.6.1 Data Source Types

It must be stressed that a large databank collected by numerous research programs was used in this study. Two types of data existed in this databank:

1. HTFS collected data from the HTWT and the earlier VWT (Vertical Wind Tunnel) programmes.
2. Open literature from Journals/conference proceedings/books.

This databank was initially divided into two sections: staggered bundles and inline bundles.

4.6.2 HTFS data

The VWT (Vertical Wind Tunnel) was NEL/HTFSs previous air cooler test tunnel, and was essentially replaced by the MPWT described in Chapter 3. The data from both the HTWT and VWT was collected on a different basis by previous researchers, and by differing instrumentation to that noted in Chapter 3, and as such no uncertainty data, as shown in previous sections, exists. The assumption was that the HTFS collected test data was carefully recorded and as such is reliable, and within reasonable tolerances.

Table 4.9 shows the geometries of the bundles in this databank that were used in the staggered bundle method development. The HTFS source code numbers are also on the

tables to allow reference to their original sources. Source 15 refers to air-coolers tested in the VWT, source 17 refers to heat recovery bundles tested in the HTWT.

Source Code	Tube diameter (m)	Fin diameter (m)	Fin Thickness (m)	Fin Frequency (1/m)	Trans. Pitch (m)	Long. Pitch (m)	No. of tube rows
15.1	0.0254	0.0572	0.0004	433	0.0667	0.05776	6
15.2	0.0254	0.0572	0.0004	433	0.0667	0.05776	4
15.3	0.0254	0.0572	0.0004	316	0.0667	0.05776	6
15.4	0.0254	0.0572	0.0004	236	0.0667	0.05776	6
15.5	0.0254	0.0445	0.0004	433	0.0667	0.05776	6
15.6	0.0254	0.0508	0.0004	433	0.0667	0.05776	6
15.7	0.0254	0.0508	0.0004	433	0.0603	0.05222	6
17.1	0.1413	0.1794	0.0015	197	0.254	0.22	8
17.2	0.1413	0.1794	0.0015	98	0.254	0.22	8
17.4	0.0603	0.0984	0.0015	197	0.154	0.132	8
17.5	0.0603	0.0984	0.0015	98	0.154	0.132	8
17.6*	0.1413	0.1794	0.0015	197	0.1794	0.1554	8
17.7	0.0603	0.0984	0.0015	98	0.1524	0.132	8
17.8	0.0603	0.0984	0.0015	197	0.1524	0.132	8
17.10	0.1413	0.1794	0.0015	197	0.254	0.22	8

Table 4.9: Geometries of staggered bundles in HTFS databank

*17.6 was an isothermal test

The only HTFS inline data was that already presented in Section 4.1.

4.6.3 Open literature data

The open literature data was derived from published results of finned tube crossflow heat exchanger tests. Often the values of the crossflow fluid properties were unknown, certainly throughout the test range. This is a limitation, however this data was 'weighted' accordingly so that in the method development any extreme, unreliable data was excluded. This was done by Henry [58] who determined that the pressure drop, f factor, j factor or heat transfer coefficient data would subscribe to being characterised by a power law curve. Therefore if the data had a reasonable fit to a power law curve (determined by its R^2 value) it was accepted for the databank.

As this data was gathered from various papers that had different emphasis there are few that are complete pressure drop and heat transfer sources. Tables 4.10 and 4.11 show the geometries of the bundles tested for heat transfer and pressure drop, respectively, in the databank that were used in the staggered bundle method development. The HTFS source code numbers are also on the tables to allow reference to their original sources.

Source Code	Tube diameter (m)	Fin diameter (m)	Fin Thickness (m)	Fin Frequency (1/m)	Trans. Pitch (m)	Long. Pitch (m)	No. of tube rows
2.2	0.016	0.0365	0.00048	354	0.0397	0.0444	8
3.9	0.0097	0.0234	0.00046	288	0.0248	0.0203	5
3.10	0.0097	0.0234	0.00046	343	0.0248	0.0203	5
3.11	0.0107	0.0219	0.00048	343	0.0248	0.0203	5
4.10	0.0139	0.0226	0.00106	314	0.0274	0.0238	6
4.11	0.0136	0.0227	0.00202	246	0.0274	0.0238	6
4.12	0.0291	0.0585	0.00043	314	0.0623	0.054	6
4.13	0.0236	0.0499	0.00052	386	0.0571	0.0495	6
4.14	0.02451	0.0573	0.00055	379	0.0623	0.054	6
4.15	0.0409	0.0698	0.00046	311	0.0715	0.0619	6
4.16	0.0278	0.0513	0.00043	355	0.0557	0.0482	6
4.17	0.0262	0.0507	0.00033	397	0.0557	0.0482	6
5.8	0.0159	0.0187	0.00041	767	0.0238	0.0206	6
5.9	0.0139	0.0193	0.00043	446	0.0238	0.0206	6
5.10	0.0141	0.0227	0.00046	441	0.027	0.0234	6
5.11	0.0111	0.0227	0.00056	284	0.027	0.0234	6
5.12	0.029	0.0498	0.00056	201	0.0556	0.0481	4
5.13	0.0285	0.0497	0.00053	407	0.0556	0.0481	4
5.14	0.0291	0.0585	0.00043	314	0.0619	0.0536	8
6.4	0.0216	0.0489	0.000445	420	0.0521	0.0451	3
6.5	0.0318	0.0762	0.000445	433	0.0794	0.0688	2
6.6	0.0254	0.0572	0.000318	4333	0.0603	0.0522	3
7.3	0.016	0.0365	0.00048	354	0.0397	0.0444	8
9.20	0.028	0.032	0.0015	181	0.0505	0.0505	4
9.21	0.028	0.038	0.0015	181	0.0535	0.0535	4
9.22	0.028	0.058	0.0015	181	0.059	0.059	4
10.10	0.02	0.039	0.0008	250	0.039	0.039	3
10.11	0.02	0.048	0.001	250	0.049	0.049	3
10.12	0.029	0.0486	0.0004	312	0.05	0.056	4

11.2	0.038	0.056	0.001	222	0.065	0.065	8
12.4	0.0316	0.051	0.001	276	0.0052	0.052	-
13.14	0.0254	0.0444	0.00127	236	0.1	0.06	8
13.15	0.0254	0.0444	0.00127	236	0.12	0.07	8
13.16	0.0254	0.0444	0.00127	236	0.1	0.08	8
13.17	0.0254	0.0444	0.0127	236	0.1	0.07	8
13.18	0.0254	0.0444	0.00127	236	0.109	0.07	8
13.19	0.0508	0.0698	0.00127	236	0.1	0.08	8
13.20	0.0381	0.0571	0.00127	236	0.1	0.08	8
13.21	0.0508	0.0762	0.00127	236	0.1	0.08	8
13.22	0.0508	0.0825	0.001524	236	0.1	0.08	8
13.23	0.0508	0.0762	0.00127	118	0.1	0.08	8
13.24	0.0508	0.0762	0.00127	157	0.1	0.08	8
13.25	0.0508	0.0762	0.001575	157	0.1	0.08	8
13.26	0.0508	0.0762	0.002032	157	0.1	0.08	8
16.8	0.0483	0.07366	0.0009	238	0.0757	0.1612	2
16.9	0.073	0.0984	0.0016	157	0.1004	0.0985	2
16.10	0.0382	0.0584	0.0016	236	0.0663	0.0572	2
16.11	0.0483	0.0737	0.0009	98	0.0757	0.0875	2
16.12	0.0483	0.0737	0.0009	238	0.0757	0.0875	2
16.13	0.0483	0.0805	0.0009	197	0.098	0.0875	2
16.14	0.0483	0.0737	0.0009	118	0.0757	0.0875	2

Table 4.10: Geometries of staggered bundles in Open Literature databank

(Heat Transfer)

Source Code	Tube diameter (m)	Fin diameter (m)	Fin Thickness (m)	Fin Frequency (1/m)	Trans. Pitch (m)	Long. Pitch (m)	No. of tube rows
1.1	0.0186	0.0397	0.00047	430	0.049	0.0424	6
1.2	0.0186	0.0397	0.00047	430	0.0428	0.0371	6
1.5	0.0409	0.0698	0.00046	311	0.0857	0.0742	6
1.7	0.0409	0.0698	0.00046	311	0.076	0.0658	6
1.8	0.0278	0.0577	0.0006	352	0.0686	0.0594	6
1.11	0.0266	0.0512	0.0004	364	0.1143	0.099	6
1.13	0.0266	0.0512	0.0004	364	0.0857	0.0742	6
1.14	0.0266	0.0512	0.0004	364	0.0686	0.0594	6
1.15	0.0266	0.0512	0.0004	364	0.0566	0.049	6

2.1	0.016	0.0365	0.00048	354	0.0397	0.0444	8
4.7	0.0186	0.0396	0.00047	430	0.0428	0.0371	6
5.1	0.0159	0.0187	0.00041	767	0.0238	0.0206	6
5.2	0.0139	0.0193	0.00043	446	0.0238	0.0206	6
7.1	0.016	0.0365	0.00048	354	0.0397	0.0444	8
7.2	0.016	0.0365	0.00048	354	0.0397	0.0444	8
9.11	0.028	0.058	0.0015	181	0.059	0.059	4
11.1	0.038	0.056	0.001	222	0.065	0.065	8
13.1	0.0254	0.0444	0.00127	236	0.1	0.06	8
13.2	0.0254	0.0444	0.00127	236	0.12	0.07	8
13.3	0.0254	0.0444	0.00127	236	0.1	0.08	8
13.4	0.0254	0.0444	0.00127	236	0.1	0.07	8
13.5	0.0254	0.0444	0.00127	236	0.109	0.07	8
13.6	0.0508	0.0698	0.00127	236	0.1	0.08	8
13.7	0.0381	0.0571	0.00127	236	0.1	0.08	8
13.8	0.0508	0.0762	0.00127	236	0.1	0.08	8
13.9	0.0508	0.0825	0.001524	236	0.1	0.08	8
13.10	0.0508	0.0762	0.00127	118	0.1	0.08	8
13.11	0.0508	0.0762	0.00127	157	0.1	0.08	8
13.12	0.0508	0.0762	0.001575	157	0.1	0.08	8
13.13	0.0508	0.0762	0.002032	157	0.1	0.08	8
16.4	0.0483	0.0737	0.0009	98	0.0757	0.0875	2
18.1	0.0254	0.0571	0.0003	236	0.0571	0.05	6
18.2	0.0524	0.0571	0.0003	236	0.0671	0.05	6
18.3	0.0524	0.0571	0.0003	236	0.075	0.05	6
18.6	0.0524	0.0571	0.0003	433	0.0571	0.05	6
18.7	0.0524	0.0571	0.0003	433	0.075	0.05	6
18.8	0.0524	0.0571	0.0003	433	0.062	0.05	6
18.9	0.0254	0.0445	0.0003	433	0.0445	0.05	6

Table 4.11: Geometries of staggered bundles in Open Literature databank

(Pressure Drop)

Tables' 4.12 and 4.13 show the geometries of the bundles in the databank that were used in the inline bundle method development. Only two sources were found to be of suitable quality.

Source Code	Tube diameter (m)	Fin diameter (m)	Fin Thickness (m)	Fin Frequency (1/m)	Trans. Pitch (m)	Long. Pitch (m)	No.of tube rows
9.12	0.028	0.038	0.0015	285	0.0505	0.0505	4
9.13	0.028	0.048	0.0015	285	0.0545	0.0545	4
9.14	0.028	0.058	0.0015	285	0.059	0.059	4
9.15	0.028	0.032	0.0015	181	0.0505	0.0505	4
9.16	0.028	0.038	0.0015	181	0.0535	0.0535	4
9.17	0.028	0.048	0.0015	181	0.0549	0.0549	4
9.18	0.028	0.053	0.0015	181	0.057	0.057	4
9.19	0.028	0.058	0.0015	181	0.059	0.059	4
10.7	0.02	0.039	0.0008	250	0.039	0.039	3
10.8	0.02	0.048	0.001	250	0.049	0.049	3
10.9	0.029	0.0486	0.0004	312	0.05	0.056	4

Table 4.12: Geometries of inline bundles in Open Literature databank (Pressure Drop)

Source Code	Tube diameter (m)	Fin diameter (m)	Fin Thickness (m)	Fin Frequency (1/m)	Trans. Pitch (m)	Long. Pitch (m)	No. of tube rows
9.2	0.028	0.048	0.0015	285	0.0545	0.0545	4
9.3	0.028	0.058	0.0015	285	0.059	0.059	4
10.2	0.02	0.048	0.001	250	0.049	0.049	3
10.3	0.029	0.0486	0.0004	312	0.05	0.056	4

Table 4.13: Geometries of inline bundles in Open Literature databank (Pressure Drop)

4.6.4 Data sources

Table 4.14 shows the original references from which the HTFS and open literature databank contents were derived.

Source No.	Reference
1	Robinson, K.K, and Briggs, D.E, 1966 [12]
2	Cox and Jallouk [58]
3	*Unrecorded by HTFS documentation*
4	Briggs and Young [3]
5	Ward and Young [59]
6	*Unrecorded by HTFS documentation*
7	Cox [60]
8	*Unused*
9	Brauer [6]
10	Schmidt [4]
11	Brauer [10]
12	*Unused*
13	Mikovic [61]
14	*Unused*
15	McLean, and Spence [62] and McLean, Ralston and Henry [63]
16	Chu, Farrant, Spence, McLean [64]
17	McLean, Barrie and Henry [65]
18	Stasiulivicus and Skrinska [66]

Table 4.14: Databank references

CHAPTER 5

Computational Fluid Dynamics (CFD); general considerations for models of finned tube crossflow heat exchangers

5.0 Introduction

With the limitations associated with local flow measurements indicated in Section 2.6.1, another technique for determining what is occurring inside a bundle is necessary. It is widely accepted that using Computational Fluid Dynamics (CFD) as a tool to study the local flow behaviour is feasible. However little work is available in the open literature for modelling multi-row finned tube bundles, and most of the related work is restricted to plain tube (cylinders) bundles, as shown in Section 2.6.

Building on from the limited literature available, this chapter presents the 'best practice' developed during a lengthy examination of various options available to the user in the CFD package. The geometries of the bundles used for all of the development were those of the inline bundles described in Section 3.3 and will be shown in Chapter 7, along with the results of the study. The other bundles modelled using the experience gained on the inline bundle CFD modelling will be shown in Chapters 6 (staggered finned tubes) and 8 (staggered simplified bundle with bypassing/corbels)

The CFD package used was FLUENT v.5.3. The models were run on a variety of PC Workstations, for time reasons. The principal machines were an 800MHz single processor workstation with 512Mb of RAM, and a Dual processor Workstation with two 1.7GHz Intel Xeon processors and 2Gb of RAM. The average run time of an individual model was approximately 5 days, using one processor.

5.1 Theory of CFD modelling

5.1.1 The governing equations

Instead of having to analytically solve the equations by inputting mathematical functions of the geometry under examination, the shape of the geometry is expressed in terms of coordinates of, and around, the body under consideration. From these coordinate points, or nodes, discrete solutions can be determined and are held representative of the flow in that immediate vicinity.

The way a flow region around a body becomes discretised is to divide it into cells. The cells are either areas (for two dimensional solutions) or volumes (for three dimensional

solutions). These cells will then have x, y and, if three dimensional, z coordinates in space, with each cell having its own unique set. This is shown in Figure 5.1.

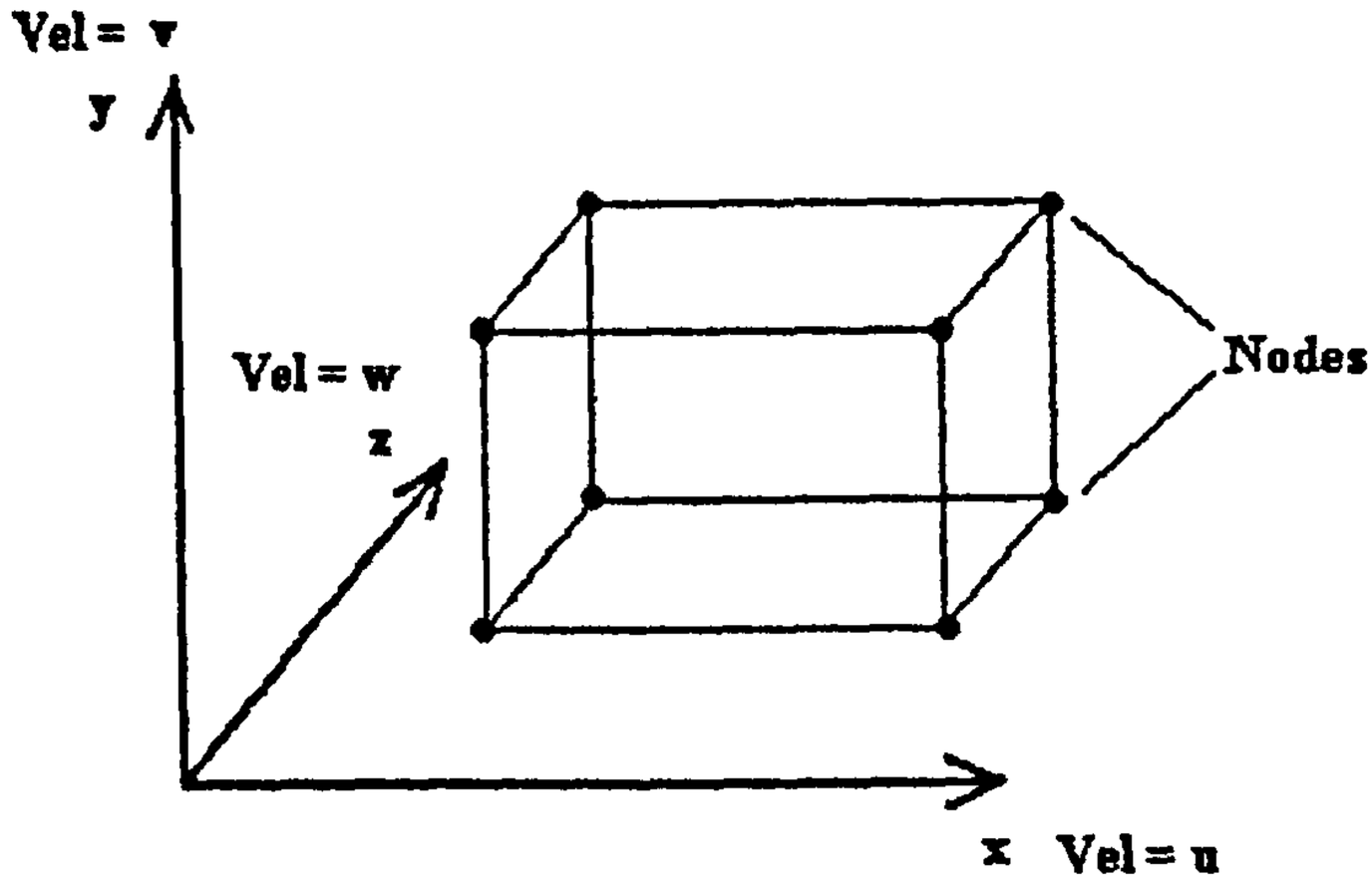

Figure 5.1: Representation of a cell with nodes at the corners

The governing equations in FLUENT are combined forms of the Navier-Stokes equations (e.g. momentum; the product of mass and velocity) rather than primitive forms (e.g. pressure, velocity). There are three key sets of equations are:

1. The conservation of mass equation
2. The conservation of momentum equations
3. The conservation of energy

1. relates the mass leaving a cell is equal to the mass entering it. This ensures that the mass flow rate through the cell is constant. This is a tenet of steady flow (unsteady flow is not considered here), and implies incompressibility of the flow.
2. is described by a set of three partial differential equations (or two for two dimensional models) equations that consider the momentum of the fluid in a cell in all three (two for two dimensional domains) directions, and ensure that the incoming momentum is equal to the outgoing.
3. is a term that considers the energy of the fluid in a cell. The equations relate the viscous and heat energy to the overall kinetic and internal energies in the cell.

A presentation and full derivation of the Navier-Stokes equations is given in Schlichting [68], and can also be found in most advanced fluid mechanics textbooks, such as Raudkivi and Callander [69].

5.1.2 Solving the equations

A straightforward algebraic solution of the equations discussed above would be difficult, so the methods employed to solve these equations are a combination of simplifications, approximated empirical values and sub models.

Although these equations are all defined in terms of differential quantities, the initial inputs, and the solutions of interest, will be based on simple engineering values (pressure, velocity, temperatures etc). The numerical method of solution involves letting these quantities be predicted and corrected by iteration. The end of the calculation will come when there are no residual values between one iteration and the next. However this will never occur with a numerical method as it is only an approximation, thus normally the calculation is halted once the differences between the initial and predicted values become extremely small, and do not significantly alter. This is termed solution convergence.

5.2 Model inlet section

It is known that the pressure field/profile downstream affects the field upstream, therefore the inlet section of the domain must be of sufficient length to avoid any adverse effects from the stagnant region on the front of the tubes in the first tube row, which could affect the inflow. The method employed to determine the necessary length was made by a simple trial and error using the maximum mass flow rate as it was presumed this would create the largest perturbations in the inflow. The results of these tests showed that a reliable format was to make the inlet section equal to 2 longitudinal pitches.

5.3 Model outlet section

To allow an easier convergence for the solver there must be an exit section as part of the domain to allow the wakes and turbulence from the back of the tubes and fins to dissipate and renormalise with the bulk flow. When the flow is normalised, the bulk exit conditions can be determined as they would be in experimental heat exchanger.

To this end a parametric approach was again used, using the maximum experimental mass flow rate that was tested. The exit required a section of about 10 longitudinal pitches for the wakes to fully dissipate within the bulk flow.

5.4 Tubes and fins

The arrangement chosen for all of the models reported here is to have half a fin at the edge of the domain with the fins of parallel tubes inline with each other. This approach maximises the use of symmetry planes, and reduces the size of the model. A sample picture of the symmetry plane model is given in Figure 5.2.

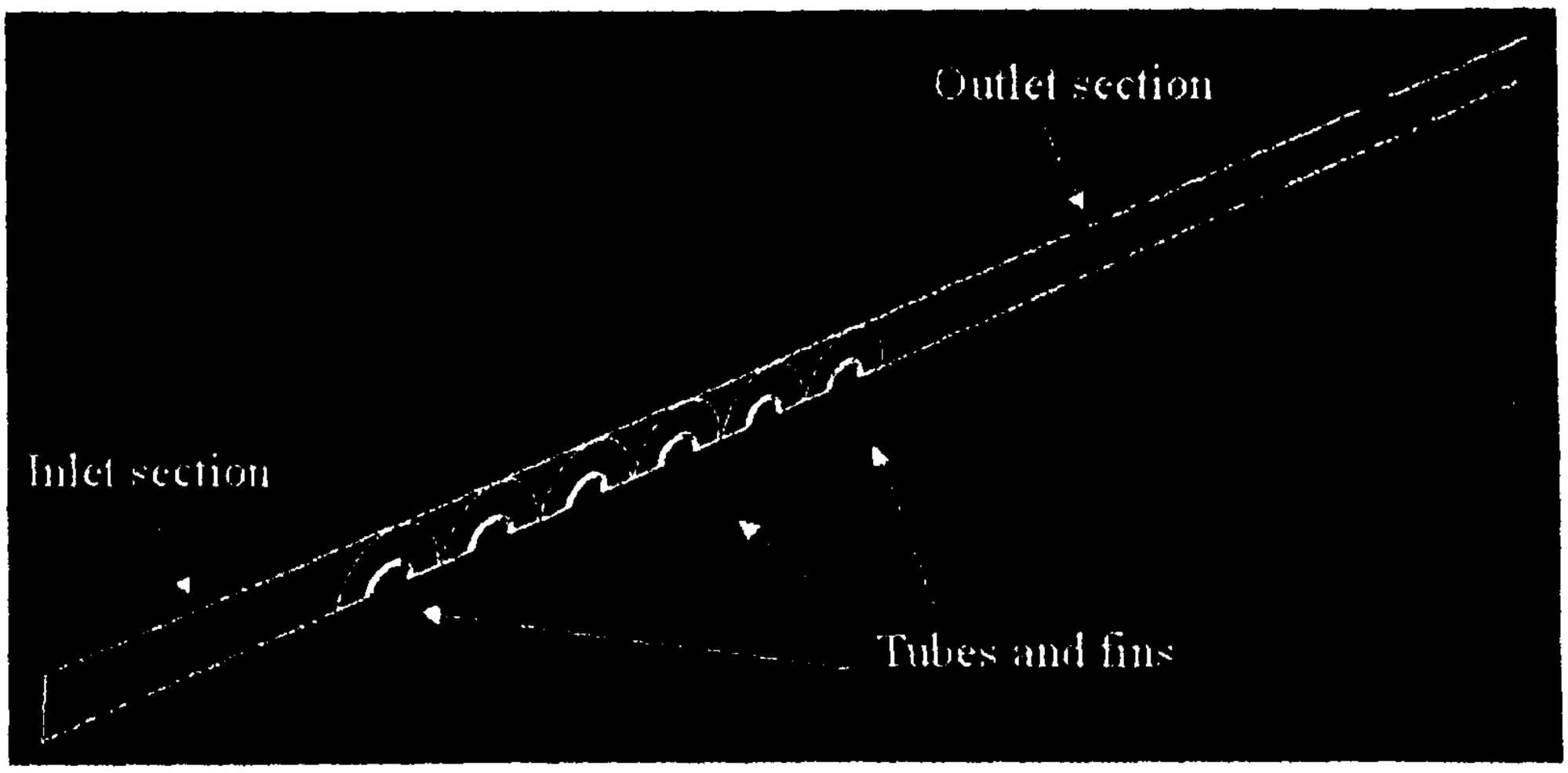

Figure 5.2: CFD model domain of and inline bundle

In the mesh generation package these regions, tube and fin, are specified as materials (continuum entities). Once inside the CFD processor these material regions are defined with the material properties of the metals that were used in inline air cooler tests. The fins were specified as being aluminium with a thermal conductivity of 179.48 W/mK, and the tubes were specified as a carbon steel with a thermal conductivity of 50.97 W/mK.

5.5 Mesh of three dimensional models

The mesh generation was performed in the GAMBIT package that is recommended and supplied with FLUENT. The meshing used for the two dimensional models will be discussed in Chapter 8.

The volume element type chosen for all regions of the three dimensional models was a Hexahedron. The Hexahedron cells in their pure form are cubes with nodes at each corner, known as an 8-node hexahedron. With its adjoining cells, this shape was found to be the best choice for the finned tube bundle. This was because inherently the

hexahedron tends to have aligned faces that make calculations easier and more stable for the solver, and because the cells could be aligned with the local flow direction, which also aids the solution process. The choice of a simple 8-node variant was used to help decrease the running time of the model.

5.5.1 Finned tubes

The flow around the tubes and fins is the most important aspect of these models. Therefore a meshing scheme that allowed close inspection over the tubes was important. Figure 5.3 shows the aligned radial pattern created for the fin and tube meshes.

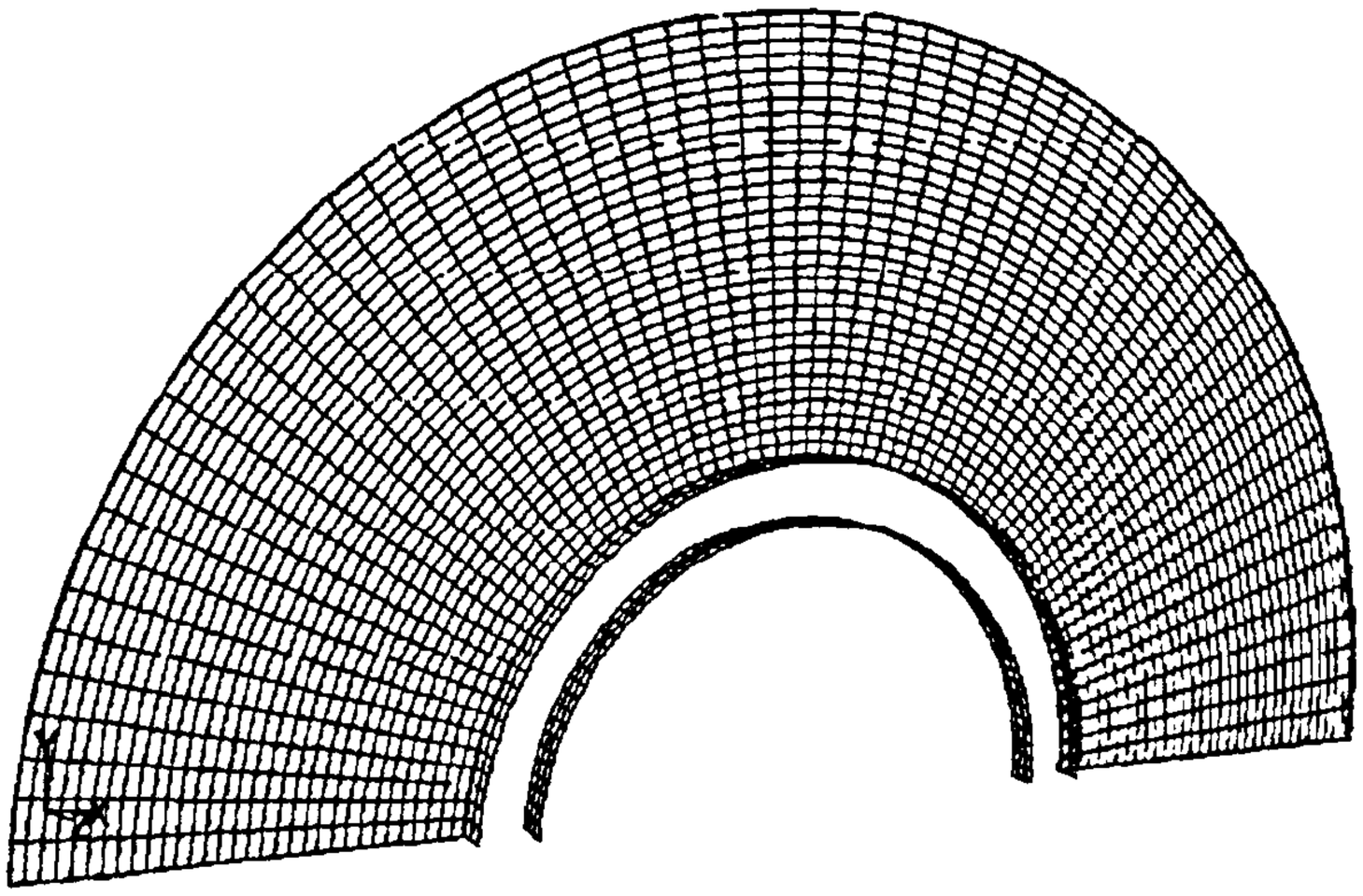

Figure 5.3: Fin and inner and outer tube faces mesh

To get a good mesh density in this region a hexahedral mesh was applied using the tube outer surface and a 'virtual' face set at the same diameter as the fins to create a volume. This allowed a radial mesh to be generated outward from the tubes, with evenly spaced cells that had very low skew. The 8-node hexahedral cells were used with a spacing of 0.8. To mesh the area in question the 'Map' meshing scheme was used, as the semi-circular region could be well discretised with the relatively small cells, with exceptionally low skew, and near 1:1 aspect ratios.

5.5.2 Tube domain

The region immediately around the tubes is the most complex as it varies between the flat boundary faces between the fins, on the symmetry planes, and the curved surfaces of the fin tips. To mesh this region, the Cooper Tool presented by Blacker [70] was

used. The Cooper tool identifies the faces and submaps them to act as a base for projection using a face tool such as the Pave scheme discussed by Blacker and Stephenson [71]. It then builds a mesh between these mapped faces and the bulk unmeshed areas in the region, using the Cooper specific mathematics to fill these bulk areas with a 'barrel' strategy outlined by Blacker [70]. To achieve an easy match with the existing fin and tube region, meshes with a cell spacing of 1.2 was used. This small cell size is justified by the practical concern that the wake regions between the tubes are of interest, so a well discretised mesh will aid in the further detailed analysis of these models. An example of the mesh used on the staggered bundle, that will be shown in Chapter 6, can be seen in Figure 5.4.

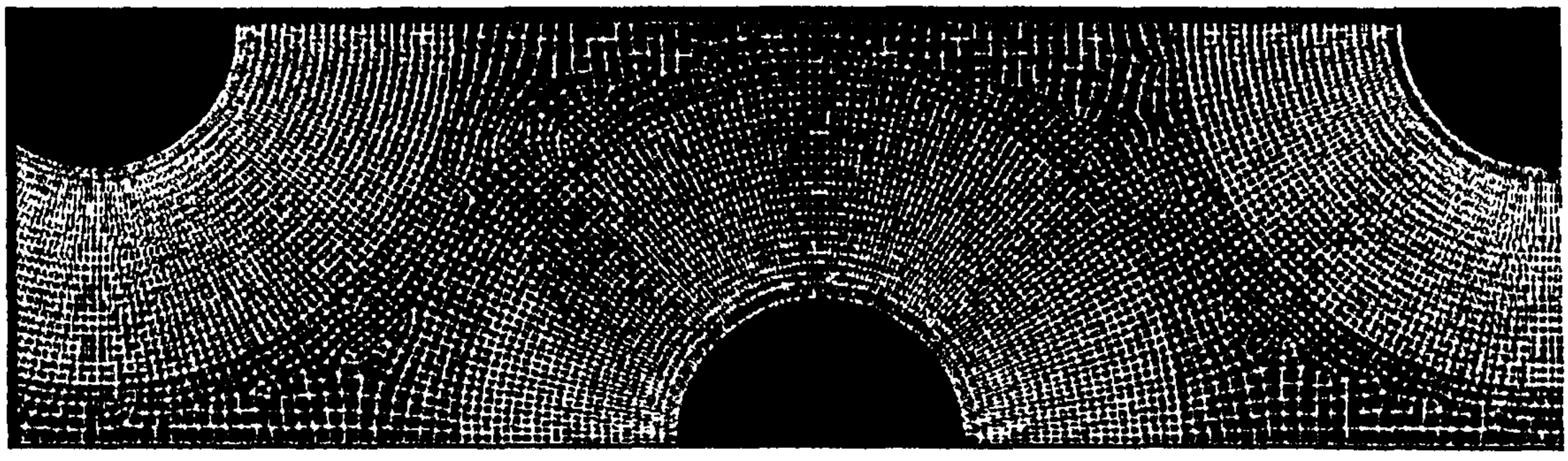

Figure 5.4: Mesh between fin/tube regions (Staggered bundle shown)

The well-aligned tube and fin mesh can be seen surrounded with the more irregular Cooper generated mesh.

5.5.3 Bundle inlet sections

To minimise the number of cells in this area, an inlet zone was defined. The Map meshing tool created the mesh, as the region was simply a cuboid and had no unusual features.

5.5.4 Bundle outlet sections

To minimise the computation time, the outlet section was divided into 3 zones with an increasingly coarser mesh from the back of the bundle. This was to grade the regions according to importance, and distance from the tubes and fins. The logic to this was that the region nearest to the tubes required good resolution, with higher cell density, and the following two sections ensure homogenous mixing, both of which contribute to an

easier to converge solution. The map scheme was used again as the tail sections are cuboids, devoid of sharp flow features.

5.5.5 Mesh independence

The mesh sizing was developed through many trials of balancing the running time of the model with the results gained. Eventually a point was reached whereby greater mesh densities did not yield significantly better results, and often did not produce any significant difference at all. Therefore it is believed that the meshes used and described are optimum for these problems.

5.6 Airside boundary conditions

In the CFD model shown in Figure 5.2 all the external boundaries with the exception of the inlet and outlet faces are set as symmetry planes, as discussed. The inlet face was set as a velocity inlet where air approach velocity, temperature, and operating pressure are defined. As the domain represented a slice in the middle of the bundle no inlet velocity profile was defined, as the incoming flow was assumed to be of a uniform distribution. The outlet face was set as a mass flow outlet, which allowed the solver to determine the conditions at outlet.

5.7 Turbulence models

5.7.1 Turbulence Model Selection

The following is a comparison of the turbulence models considered for the solution, drawn from FLUENT [72], Barnard [73], Shaw [74] and Versteeg and Malalasekera [75]. Turbulence models are sub models that deal with the fluctuations in the flow that occur either naturally from random particle excitement in otherwise undisturbed flow, or due to separation, vorteices or other strong shearing effects caused by interference from a body.

Despite numerous studies identifying turbulence behaviour and generation over bodies there is no exact mathematical treatment currently available, possibly because the true nature of the generation is not understood. Because of this the available models are all a combination of fluid mechanics and empirical relationships. This means that the models will be based on data sets either biased toward certain problems (e.g. backwards facing

step) or generalised (e.g. backwards facing step, flat plate, cylinder in crossflow, turbine blades), and the result is that no one model can (currently) be relied on to produce accurate results for every flow problem.

It also follows that any constants embedded in these models are an amalgam of the results of these data sets, and may not be suitable for some cases (e.g. high mach number flows, flows with strong recirculation).

Hence to find the model that suited the finned tube heat exchanger applications the following models were reviewed and tested.

5.7.2 Spalart-Allmaras model

This is a relatively simple one-equation model that solves a modelled transport equation for the kinematic eddy (turbulent) viscosity. The Spalart-Allmaras model was designed for applications involving wall-bounded flows, and gives good results for boundary layers subjected to adverse pressure gradients, which would imply the tubes used on heat exchangers. The model is effectively a low-Reynolds-number model, requiring the viscous-affected region of the boundary layer to be properly resolved. An advantage to it is that the near-wall gradients of the transported variable in the model are much smaller than the gradients of the transported variables in the *k*-epsilon models. This can make the model less sensitive to numerical error when non-layered meshes are used near walls, as is the case in these heat exchanger models. A drawback of this model is that it does not easily accommodate changes in turbulence length scale, and a known limitation of this is that the model may not provide a good prediction of turbulence decay in homogenous, isotropic turbulent regions, such as in the wake of the heat exchanger bundle.

This model was found to generally overpredict pressure drop, and grossly underpredict air outlet temperature.

5.7.3 k-epsilon

The simplest two-equation turbulence model is the k-epsilon model in which the solutions of two separate transport equations are made. These are a prediction of the turbulent kinetic energy (k), and the rate of dissipation of turbulent kinetic energy.

It can be seen upon examination of the formulations of these equations given by FLUENT [75] that the dissipation terms then relies heavily on experimentally derived data.

This model was found to produce quite good pressure drop results but it generally overestimated the heat transfer by up to 60%.

5.7.4 RNG k-epsilon

The RNG *k*-epsilon model was derived using a statistical technique (called renormalization group theory). It is similar in form to the standard *k*-epsilon model, but is changed by having an additional term that improves the accuracy for flows with large shear rates and gives better appreciation of the effects of swirl on turbulence, but the biggest change was that the RNG theory meant that it introduced a formula to calculate the local turbulent Prandtl number whereas the standard *k*- model uses user-specified, constant values. This should have improved the heat transfer prediction.

It is shown by FLUENT [75] that the inclusion of this R_ε term allows the RNG model to behave similarly in the wall region to the standard model for flows with weak strain. If the flow is more highly strained, such as flows with large streamline curvatures, then RNG will perform better than the standard model as it provides a slightly lower turbulent viscosity. The result is that the RNG model should be more accurate and reliable for a wider variety of flows than the standard *k*-epsilon model.

It was found that this model produced very good pressure drop prediction, but overestimated air outlet temperature by 15-38%.

5.7.5 Realizable k-epsilon

The realizable *k*- model is a newer development of the standard k-epsilon model. It differs by using a different method to calculate turbulent viscosity (part of the epsilon term) and has an improved equation for the turbulence dissipation based on an exact equation that expresses the fluctuation caused by any vorticity in the flow.

An immediate benefit of the realizable model is that it is said to be better at predicting the spreading rate of jets flows, such as may occur in tightly spaced tube banks. It also shows better performance for flows involving boundary layers under strong adverse

pressure gradients, separation, and recirculation, all of which are all salient features of flow around tubes and bundle gaps.

The Realizable transport equations are given in Equ.5.1 and 5.2.

$$\frac{\partial}{\partial t}(\rho k)+\frac{\partial}{\partial x}(\rho k u_j)=\frac{\partial}{\partial x_i}\left[\left(\mu+\frac{\mu_t}{\sigma_k}\right)\frac{\partial k}{\partial x_j}\right]+G_k+G_b-\rho\varepsilon-Y_M \quad \text{(Equ.5.1)}$$

where k is the turbulent kinetic energy, μ_t is the turbulent viscosity, σ_k is the turbulent Prandtl number for kinetic energy, G_k is the generation of mean turbulent kinetic energy, G_b is the generation of turbulent kinetic energy due to buoyancy, ε is the turbulence dissipation rate and Y_M is the 'contribution of the fluctuating dilation in compressible turbulence to the overall dissipation rate'.

$$\frac{\partial}{\partial t}(\rho\varepsilon)+\frac{\partial}{\partial x}(\rho\varepsilon u_j)=\frac{\partial}{\partial x_j}\left[\left(\mu+\frac{\mu_t}{\sigma_\varepsilon}\right)\frac{\partial\varepsilon}{\partial x_j}\right]+\rho C_1 S_\varepsilon-\rho C_2\frac{\varepsilon^2}{k+\sqrt{\nu\varepsilon}}+C_{1\varepsilon}\frac{\varepsilon}{k}C_3 G_b$$

(Equ.5.2)

where ν is the ratio of turbulent to effective viscosity, $C_{1\varepsilon}$, and $C_{2\varepsilon}$ are constants.

C_1 is either a constant or a function of the ratio the turbulent energy to dissipation, depending on which is higher.

Apart from the formulation of the turbulent dissipation term the other major change from the standard model is that C_μ is not a constant, but is a function of the mean strain and rotation rates, the angular velocity of the system rotation and the turbulence fields (k and ε).

This model was found to predict the pressure drop as well as the RNG model, but the heat transfer was much improved.

N.B.: The term ``realizable" means that the model satisfies certain mathematical constraints on the Reynolds stresses, regarded as the most realistic model consistent with the physics of turbulent flows. Neither the standard *k*-epsilon model nor the RNG *k*- model is realizable.

5.7.6 Models in practice

Kondjoyan and Boisson [76] studied the mass transfer around a cylinder in turbulent flow. They tested a number of turbulence models to assess their comparability to

experimental results. Their first assertion is that Large Eddy Simulation (L.E.S) is the most complete model but due to vast computational times this was not a practical proposition. Their conclusion was the use of a k-epsilon model was a good choice for the bulk flow, but a near wall zone at the fluid-solid interface was wasted as the near-wall cell sizes had to be fitted from experimental data for each mass flow rate, thus rendering the predictive capability very low. They make no reference to any modification to the k-epsilon model such as the RNG or realizable, so it is assumed that the only changes they made were on boundary layer /wall treatments.

The models developed for this study, after trial with standard wall functions, used a two zonal model. The two-zone model is a model that resolves the near-wall region all the way down to the wall by splitting the mesh, so it resolves all the way down to the viscous sublayer. This was chosen as a wall function approach does not resolve this region and can be considered a bridge between the 'no slip' conditions at the wall and the near-wall region and turbulence model being used. Although slightly more expensive in terms of CPU time it does go some way to replicate the laminar regions that may be encountered over the front of the leading tubes.

It was anticipated from this that to match the models with experimental data the grid refinement would be an important aspect of the modelling process.

5.7.7 Conclusion of turbulence model selection

Both the realizable and RNG *k*-epsilon models showed substantial improvements over the standard *k*-epsilon model, where the flow features include strong streamline curvature and vortex shedding (a feature towards the rear of tube banks). The result of testing showed that the realizable model predicted the experimental data better than the others and so was chosen for study.

The more involved Reynolds Stress model (RSM) was also investigated but found to take an extremely long time to converge, when the energy term is added to the calculation scheme. Other models such as the Large Eddy Simulation model (LES) was considered to be unsuitable for the steady state cases explored in this study and would have required immense computer resources and time.

5.8 Inlet turbulence approaching the tube bundle

No measurements have been made of the freestream turbulence on the approach to the test bundles in the NEL MPWT. It was deemed necessary to estimate the levels of turbulence in the incoming flow to better replicate the experimental conditions. Thus it was decided to use CFD to estimate the turbulence in the freestream entering the bundle. It will be shown in Chapter 10 why this is important.

As the MPWT used a perforated screen type flow straightener a representative section of this was modelled using symmetry planes in CFD. The mesh was 2mm thick and was perforated with 6mm diameter holes. The CFD representation can be seen in Figure 5.5

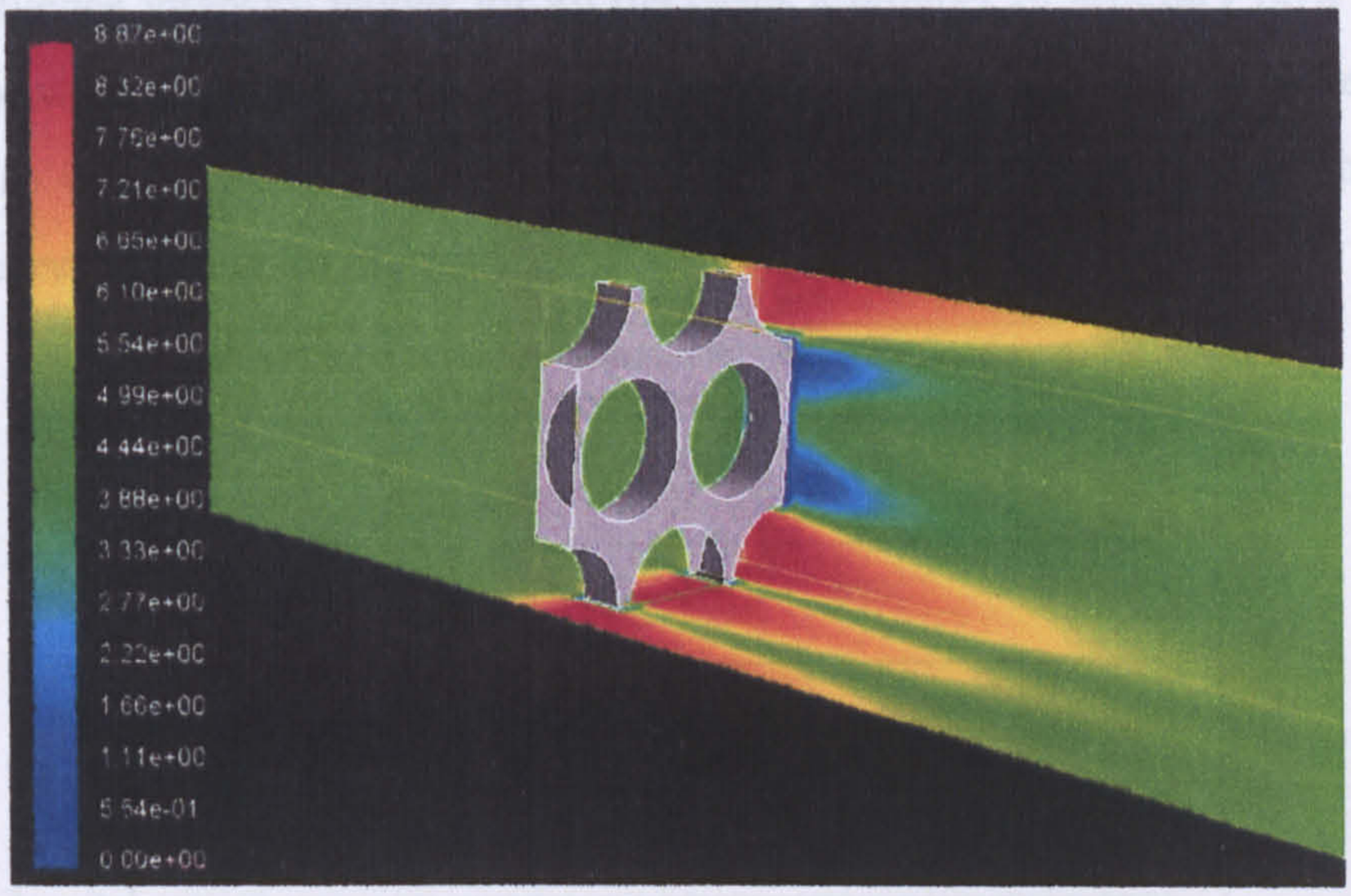

Figure 5.5: CFD model of MPWT straightening mesh, with velocity contours (5m/s air velocity shown, flow direction left to right)

The percentage turbulence intensity was the chosen parameter for the investigation. This was due to the formulation used in the FLUENT software, as shown below, being a measure of intensity with respect to the flow magnitude:

$$I = \frac{\sqrt{\frac{2}{3}k}}{U_{ref}}$$

Where k is the turbulent kinetic energy (m^2/s^2), as calculated by FLUENT, and U_{ref} the mean velocity magnitude of the flow (m/s).

The turbulence at inlet to the flow straightener was arbitrarily set at 30% intensity for all cases, with the length scale being the height of the MPWT duct (0.457m). This intensity

value was derived from a discussion with a NEL staff member who operated a hot wire anemometry wind jet tunnel, which used a centrifugal fan. The model domain had an outlet section that was the measured length from the back of the screen to the fin tips of the inline Bundle1. The inlet section was 250mm long to remove any solution distortions caused by stagnation on the front of the screen.

The screen was treated as an orifice plate and the standard k-epsilon turbulence model was chosen for the solution after discussion with NEL CFD users who had experience in this field.

To gain turbulence intensity values for all the cases a number of arbitrary flow rates in the test range were modelled, the outlet intensity values were collected, and the results plotted. These intensities were used to develop a curve fit to cater for all the cases tested. The curve is shown in Figure 5.6.

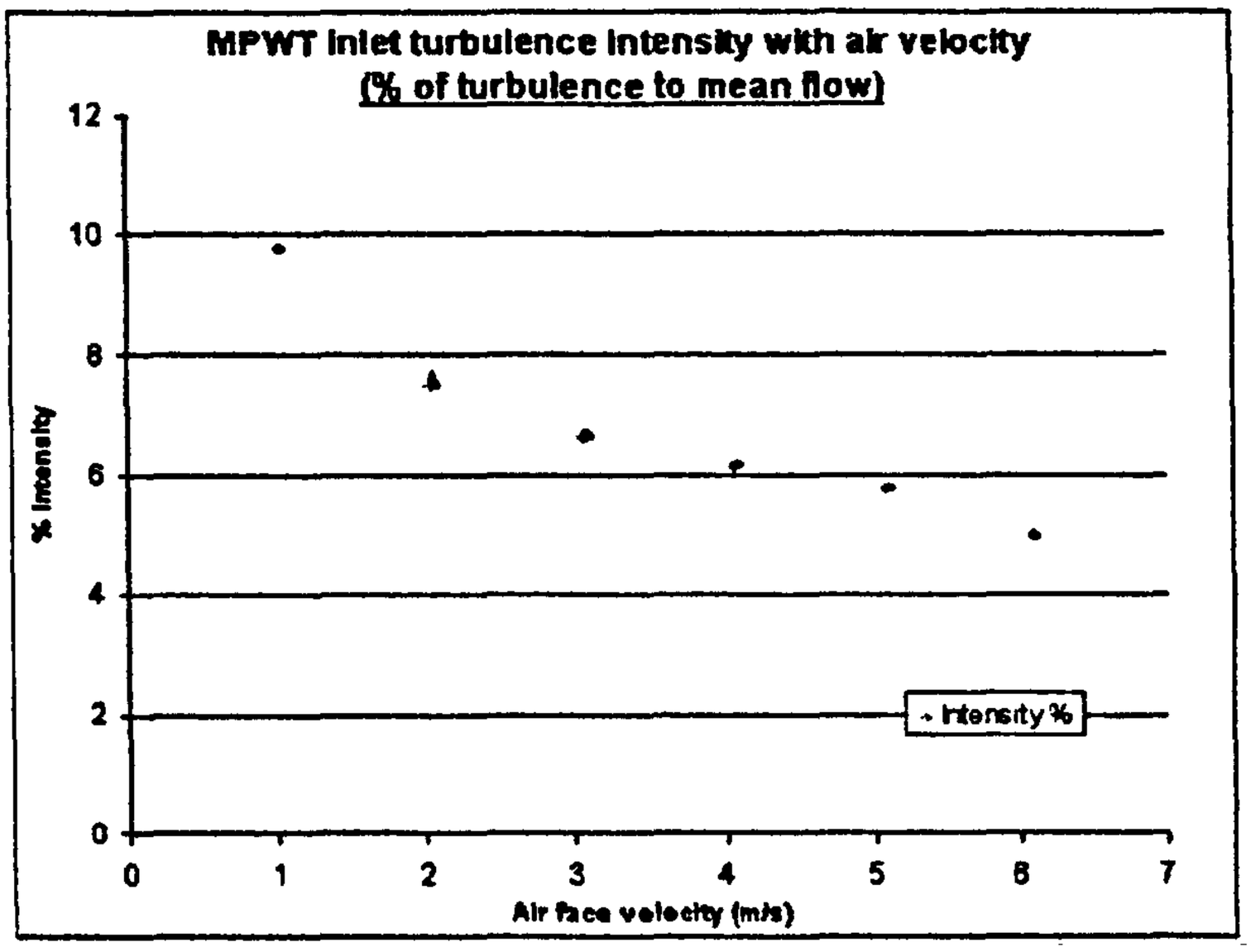

Figure 5.6: Turbulent intensity at screen model outlet

5.9 Wall treatment

5.9.1 Different wall treatments

After experimentation with standard wall functions it was found that a two-layer zonal near-wall model approach provided the best way to tailor the modelling process and develop a 'one mesh fits all' approach. This meant that for the first row at low flow rates, where there was likelihood of large regions of laminar flow over the tube front

and the fins, the near wall functions resolve boundary layer down to a turbulent core, using the turbulence model, and the sublayers, which behave in a completely different manner. Similarly for the following tubes, and for the cases where turbulence was more pronounced, the refinement at the walls provides better modelling of the wall effects. This is because the turbulence model is effective only from a solution-defined height from the wall and another model is used at the wall, which is non-turbulent. A third, interim, buffering layer model is used in the gap between these two known regions.

5.9.2 Resolution at wall

The resolution that takes place with the near wall model is shown in Figure 5.7.

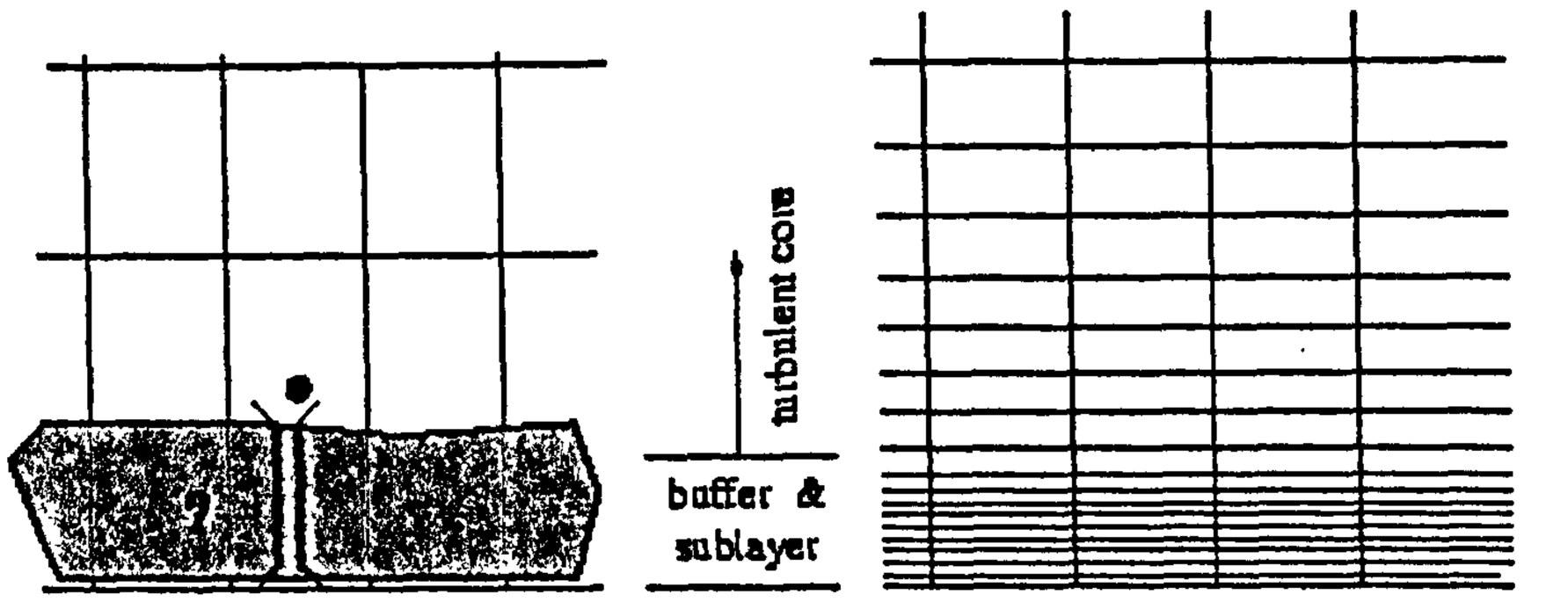

Figure 5.7: Wall treatments. Standard wall model showing std. mesh, Near wall model showing improved resolution near wall. (Taken from FLUENT [72])

The critical height from the wall is in a unit called y^+. The method for calculating this is shown in Equ.5.3, taken from FLUENT [72].

$$Y^+ = \frac{\rho u_T (yp)}{\mu} \qquad \text{(Equ.5.3)}$$

where u_T is the friction velocity, derived from the local shear stress and density, yp is the distance from the wall to a point of interest, P, and μ is the fluid viscosity at point P.

5.9.3 Refining the wall region

FLUENT showed that the critical value of y^+ that bounded the viscous sublayer was approximately 5, and the upper boundary of the buffer layer was approximately 60. Above this the fully turbulent model was used. This indicated that the critical y^+ value for specifying a refining of the mesh had a broad tolerance. After many trials it was found that the y^+ needed for refinement in each model varied between 11 and 17 to achieve good pressure drop and heat transfer performance. Occasionally it was found that two adaptions were required, although no pattern as to geometry or bulk flow velocity was found. The 'physical' manifestation of the resolution is that the CFD software moves the nodes of the cells near the wall to create a finer near wall mesh.

The adaption was performed on the basis of correcting an under or overpredicting solution, as the initial goal of the studies was to produce CFD simulations that were validated against experimental data and would allow inspection of flow and heat transfer, not to predict performance.

The benefit of using this adaption process was that if there was little adaption necessary after the solution residuals have settled to a reasonably stable level (as reported by the software), then it indicated that the mesh used was well suited to the problem.

5.10 Solution scheme

5.10.1 Solution Accuracy

The default method of solving the differential transport equations of the CFD solver are of first order accuracy where calculations are made over a cell. It is recommended by FLUENT [72] that if there areas of the mesh that are not aligned with the local flow direction then it may be more satisfactory to use the second order scheme. Due to the use of the Cooper tool to create the mesh in the region between and around the tubes and fins there are cells that are definitely not aligned, so the selection of the second order solution seemed prudent. In tests this scheme produced notably better heat transfer results. This is thought to be due to the method of interpolating the values through the individual cell based on the incoming quantity gradients taken from previous cells, and the more discrete calculations that can be performed over the exchanger surface. This method is called Second-Order-Upwinding.

The Momentum, Energy, Turbulent kinetic energy and Turbulence dissipation rate were all set to perform second order calculations.

5.10.2 Pressure–Velocity Relation

The SIMPLE scheme was used for all of these models. It was chosen on the basis that it was recommended by FLUENT [72] as being a strong all-purpose coupling to be used with a segregated solver. Initial trials showed that the competing algorithm, SIMPLEC, led to slower more problematic convergence. The other optional algorithm, PISO, was recommended for transient calculations and non-hexahedral meshes. This scheme did not produce very good results.

5.10.3 Pressure Interpolation Scheme

The pressure interpolation scheme is the method by which the solver passes continuity information from one cell to the next for computation. The Standard, default scheme was used. Although it is said to show reduced accuracy for flows exhibiting large pressure gradients this is in terms of high Re flows, and as such this method was found to produce good results, and was significantly quicker than the other available methods.

5.11 Non-standard functions

5.11.1 Air Physical Properties

The standard assumptions built into the FLUENT code are that the physical properties of air are constant. There are options to allow users to specify their desired changes, and for this study it was assumed the density, thermal conductivity, dynamic viscosity and specific heat at constant pressure could all be represented as functions of temperature. These were input to the user-defined module in FLUENT in the form of a fourth order polynomial taken from the dry air at low pressure data given by Rodgers and Mayhew [77].

Equs.5.4, 5.5, 5.6, and 5.7 show the density, thermal conductivity, dynamic viscosity and specific heat equations, respectively. The results of these equations are all used locally in the solution; hence T is the air temperature in any given cell.

$$\rho_{air} = 1\cdot10^{-11}T^4 - 3\cdot10^{-8}T^3 + 3\cdot10^{-5}T^2 - 0.0173T + 4.0272 \qquad \text{(Equ.5.4)}$$

$$k_{air} = -7 \cdot 10^{-15} T^4 + 3 \cdot 10^{-11} T^3 - 6 \cdot 10^{-8} T^2 + 0.0001T - 0.001 \quad \text{(Equ.5.5)}$$

$$\mu_{air} = -2 \cdot 10^{-17} T^4 + 6 \cdot 10^{-14} T^3 - 8 \cdot 10^{-11} T^2 + 8 \cdot 10^{-8} T - 2 \cdot 10^{-7} \quad \text{(Equ.5.6)}$$

$$Cp_{air} = -2 \cdot 10^{-10} T^4 - 3 \cdot 10^{-8} T^3 + 0.0005T^2 - 0.2392T + 1031 \quad \text{(Equ.5.7)}$$

5.11.2 Turbulent Prandtl number

Upon initial comparison with the experimental data, and after initial turbulence model and wall treatment studies, the predicted air outlet temperatures were significantly higher than that of the experimental results. As the segregated solver was being used, whereby the flow and energy calculations are performed sequentially, investigation was made as to whether the aggressive heat transfer could be relaxed.

The thermal transport equation of the Realizable k-epsilon model is shown in Equ.5.8.

$$\frac{\partial}{\partial E}(\rho E) + \frac{\partial}{\partial x_i}[u_i(\rho E + p)] = \frac{\partial}{\partial x_i}\left(k_{eff} \frac{\partial T}{\partial x_i} + u_j (\tau_{ij})_{eff} \right) \quad \text{(Equ.5.8)}$$

where E is the total energy, k_{eff} is the effective thermal conductivity and $(\tau_{ij})_{eff}$ is the deviatoric stress tensor.

It was realised that as a correct value of the local airflow thermal conductivity was being calculated then perhaps the problem lay in a part of the default mathematical model.

As the Realizable k-ε model was being used the option to alter the turbulent Prandtl number, set by default at 0.85, was available. Pr_t is the effective Prandtl number for transport of the turbulent kinetic energy. It is related to the overall thermal conductivity used in the k-ε turbulent heat transfer model by Equ.5.9, given by FLUENT [72].

$$k_{eff} = k_{air} + \frac{c_{p\,air} \mu_t}{\mathrm{Pr}_t} \quad \text{(Equ.5.9)}$$

Where k_{air} is the flow thermal conductivity (Calculated from Equ.5.5), Cp_{air} is the specific heat (Calculated from Equ.5.7), and μ_t is the turbulent viscosity, which is calculated as part of the Realizable k-ε model in FLUENT.

As the other three variables are calculated by known functions it was deemed prudent to review the source material used by FLUENT. It appeared that the default value of 0.85 was derived from very early studies of flat plate and pipe flow and is perhaps an amalgam of many results. Given that from Equ.5.9 it shows that an increase in this constant would lead to a decrease in the overall thermal conductivity used in the turbulent energy model, trials to find a more suitable constant were undertaken. After experimentation it was found that $Pr_t = 2.5$ was a better fit to the experimental data.

5.12 Conclusions

- It should be clear that there were many variables available in the CFD package to allow closer modelling to better replicate and extrapolate on test conditions. The details of model creation, settings and inputs detailed above were a developed 'best practise' procedure for modelling finned tube bundles from many months of trials.

- No one turbulence model is readily applicable to all geometries, and selection must be based on previous usage and theoretical merits.

- The constants embedded in the CFD models must be reviewed carefully when a new problem is being modelled. As the constants are derived from measurements or published experimental data they must be treated with caution, but the effect of changing a constant must be fully reviewed where possible as to its knock-on effect throughout the rest of the model.

CHAPTER 6

Improved performance prediction method for staggered finned tube bundles

6.0 Introduction

Until the introduction of the work presented in this chapter, the best prediction method for the heat transfer and pressure drop of staggered tube bundles was believed to be the method of Chu and Ralston [22] This model was referred to as HTFS2, and this name will be used throughout this chapter. This had been shown to predict more data in the HTFS databank than other methods, as described in Chapter 2. It was found, however, that the HTFS2 method underpredicts the pressure drop for deep bundles with 10 tube rows or more. The underprediction becomes worse as the number of tube rows increases above 10. Using the fin tip clearance parameter (β) in both the fin loss coefficient and gap loss coefficients shown in Section 2.1.3 resulted in an inconsistent trend of pressure drop with fin gap for cases with 10 tube rows or more particularly when the fin gap is very small.

This chapter demonstrates how this problem was addressed, and how the HTFS2 method was improved in general. It shows how CFD models were developed and used to investigate local behaviour and provide insight in to the flow processes, and how this influenced the development of the resulting prediction method.

6.1 Demonstrating HTFS2's deficiency

In order to understand the problem in predicting the pressure drop for deep bundles, a parametric study was conducted to compare predictions from the method of Ralston et.al. [21], referred to as HTFS1, the HTFS2 method and the PFR [13] method. This comparison will show the trend of predicting bundle pressure drop for various tube geometries and highlight inconsistencies in these predictions. The three methods were assembled in a MathCad worksheet, all running from the same input geometry and flow conditions to ensure comparability of results. Elements of the geometry, namely fin gap and number of rows, were then changed to vary between 'normal' (where normal is defined as being a typical application) and 'extreme' (where extreme is defined as a larger or smaller element value that is not typical, but could possibly be used).

A typical tube bundle was selected from the HTFS databank. It was the air-cooler bundle from the VWT source, 15.2, as shown in Table 4.9. This geometry formed the

basis for exploring the dependence of pressure drop on the gap between the fin tips and the number of tube rows up to 24.

Figures 6.1-6.3 show the characteristics of pressure drop for an increasing fin gap (gap between fins in the same row of tubes) for the three tested methods over 4, 6, 12, 18 and 24 rows in the flow direction.

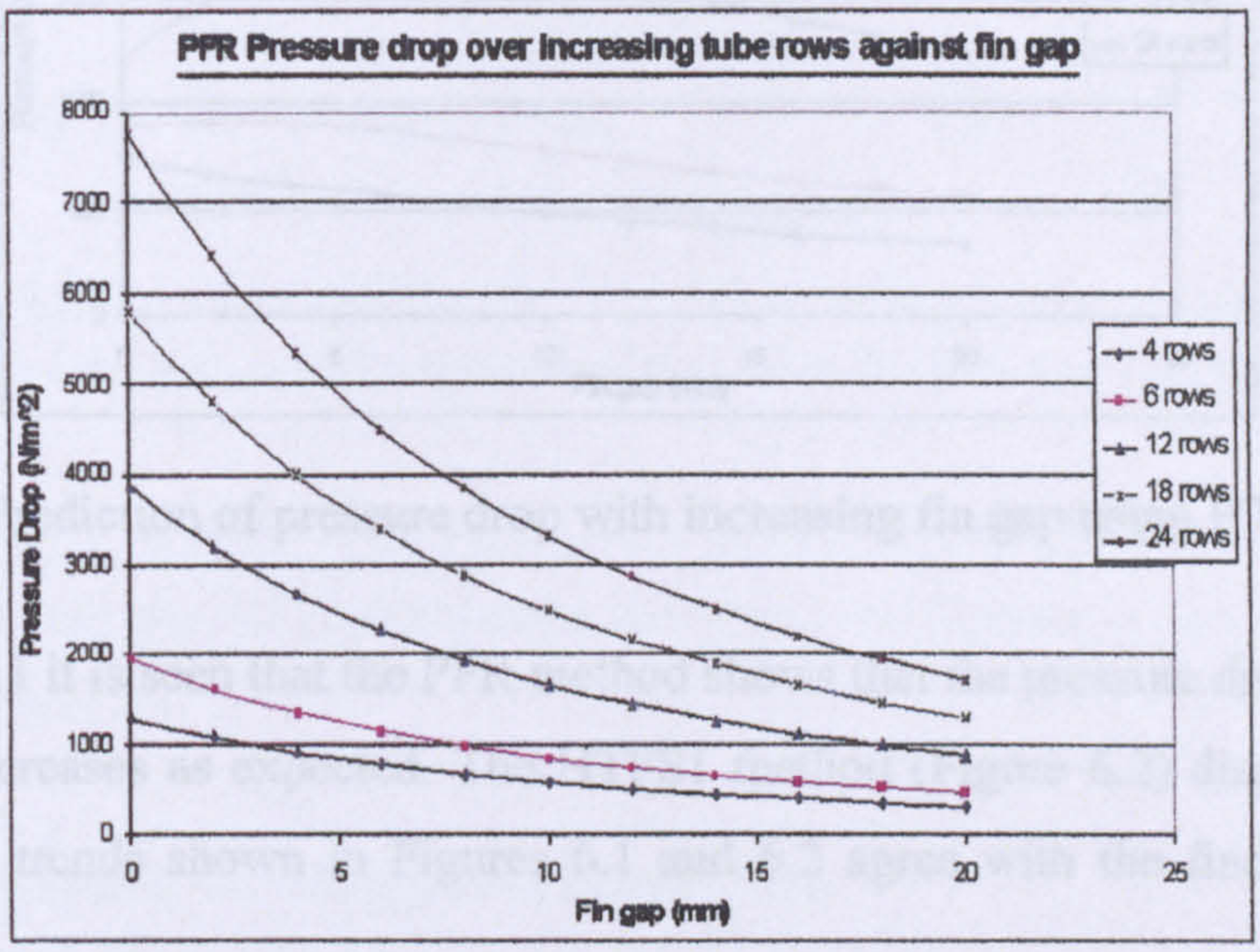

Figure 6.1: Prediction of pressure drop with increasing fin gap using PFR

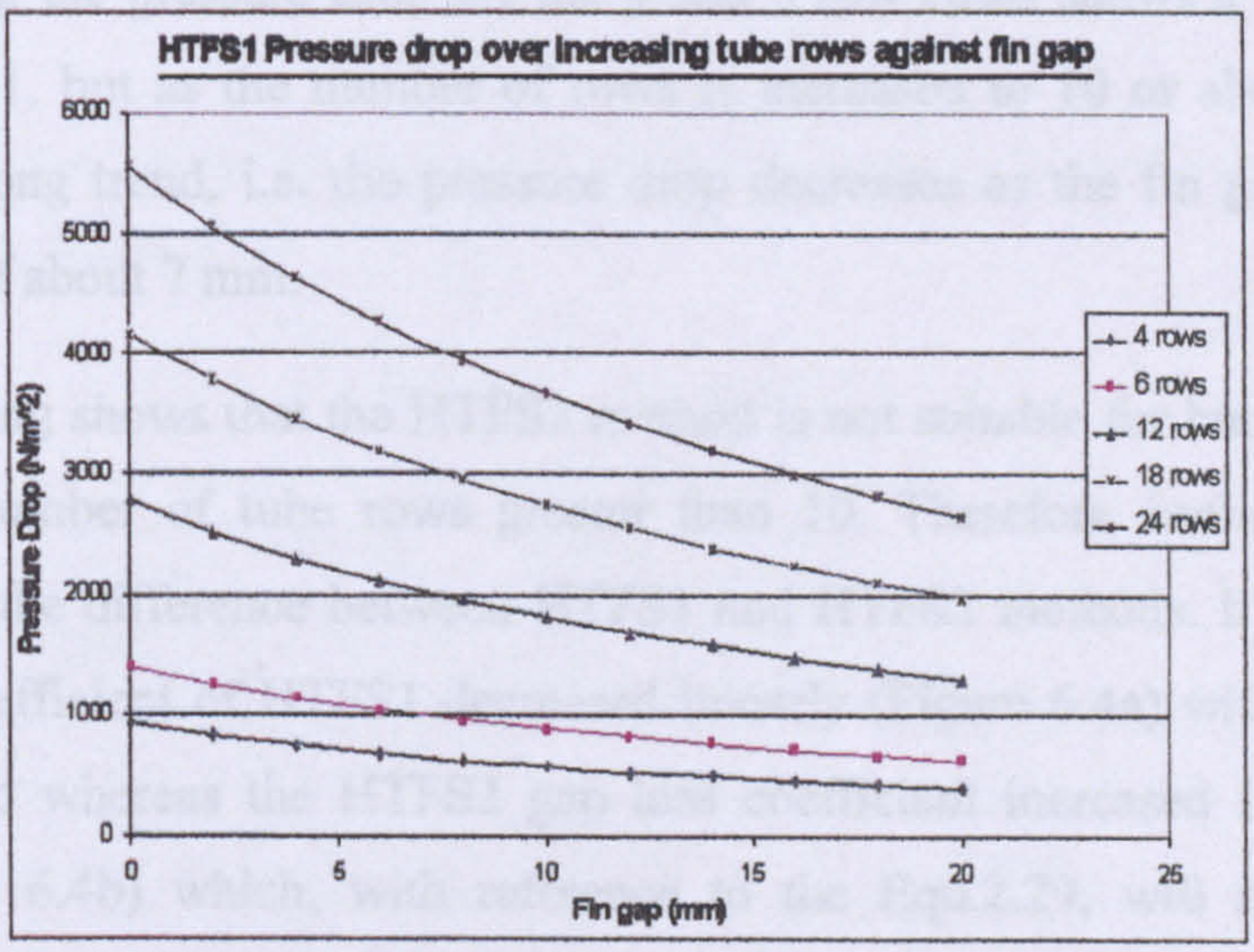

Figure 6.2: Prediction of pressure drop with increasing fin gap using HTFS1 method

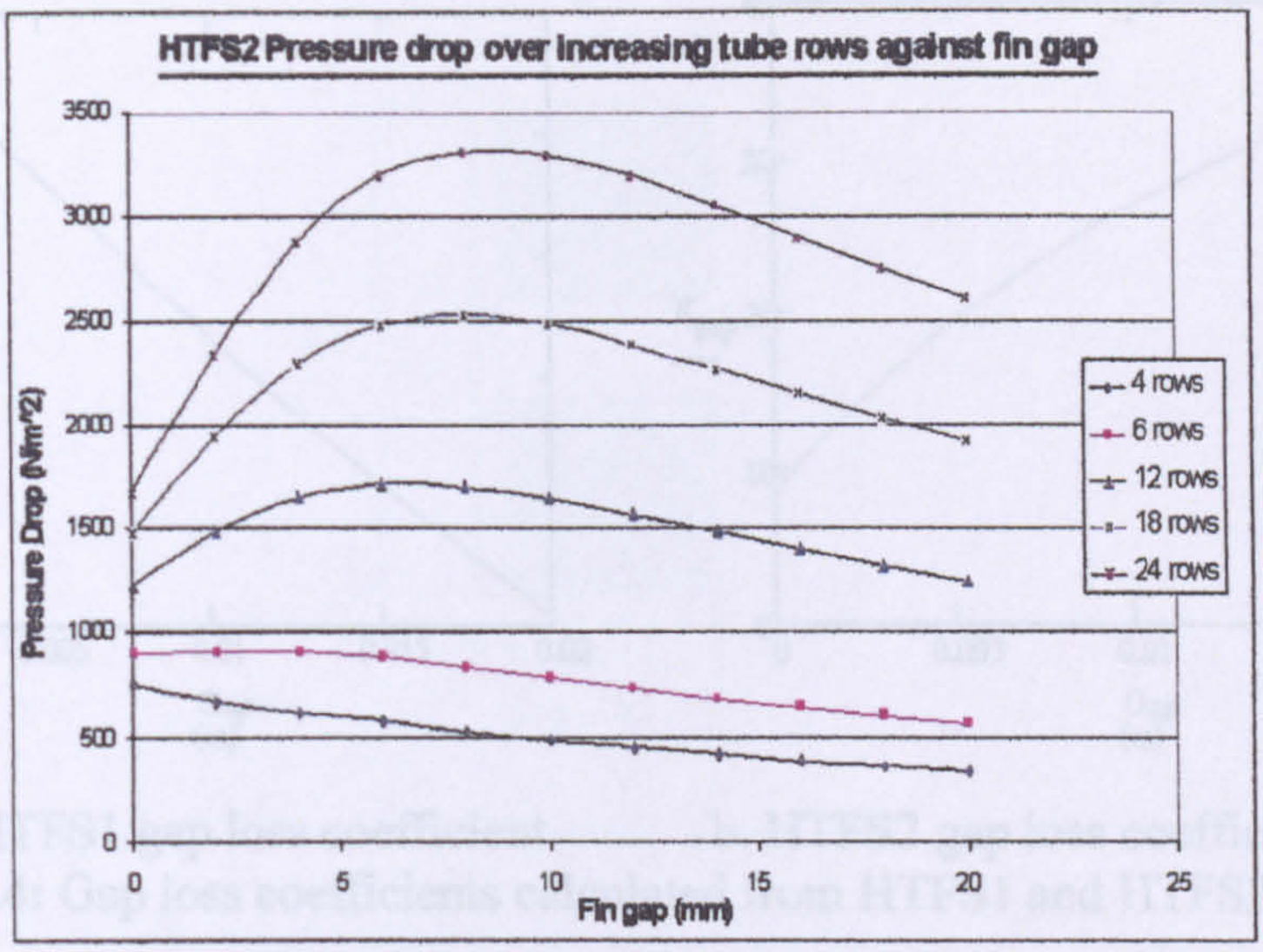

Figure 6.3: Prediction of pressure drop with increasing fin gap using HTFS2 method

From Figure 6.1 it is seen that the PFR method shows that the pressure drop increases as the fin gap decreases as expected. The HTFS1 method (Figure 6.2) displays the same tendency. The trends shown in Figures 6.1 and 6.2 agree with the findings of Henry [19].

However, the HTFS2 method (Figure 6.3) displays a much different trend. When the fin tips are touching the pressure drop for the 4 and 6 row cases shows a similar trend to PFR and HTFS1, but as the number of rows is increased to 10 or above the method predicts the wrong trend, i.e. the pressure drop decreases as the fin gap was reduced below a value of about 7 mm.

The above finding shows that the HTFS2 method is not suitable for bundles with small fin gaps and number of tube rows greater than 10. Therefore further analysis was conducted into the difference between HTFS1 and HTFS2 methods. It was found that the gap loss coefficient of HTFS1 decreased linearly (Figure 6.4a) with increasing fin gap as expected whereas the HTFS2 gap loss coefficient increased in a logarithmic fashion (Figure 6.4b) which, with reference to the Equ.2.29, will not produce the desired behaviour from the model.

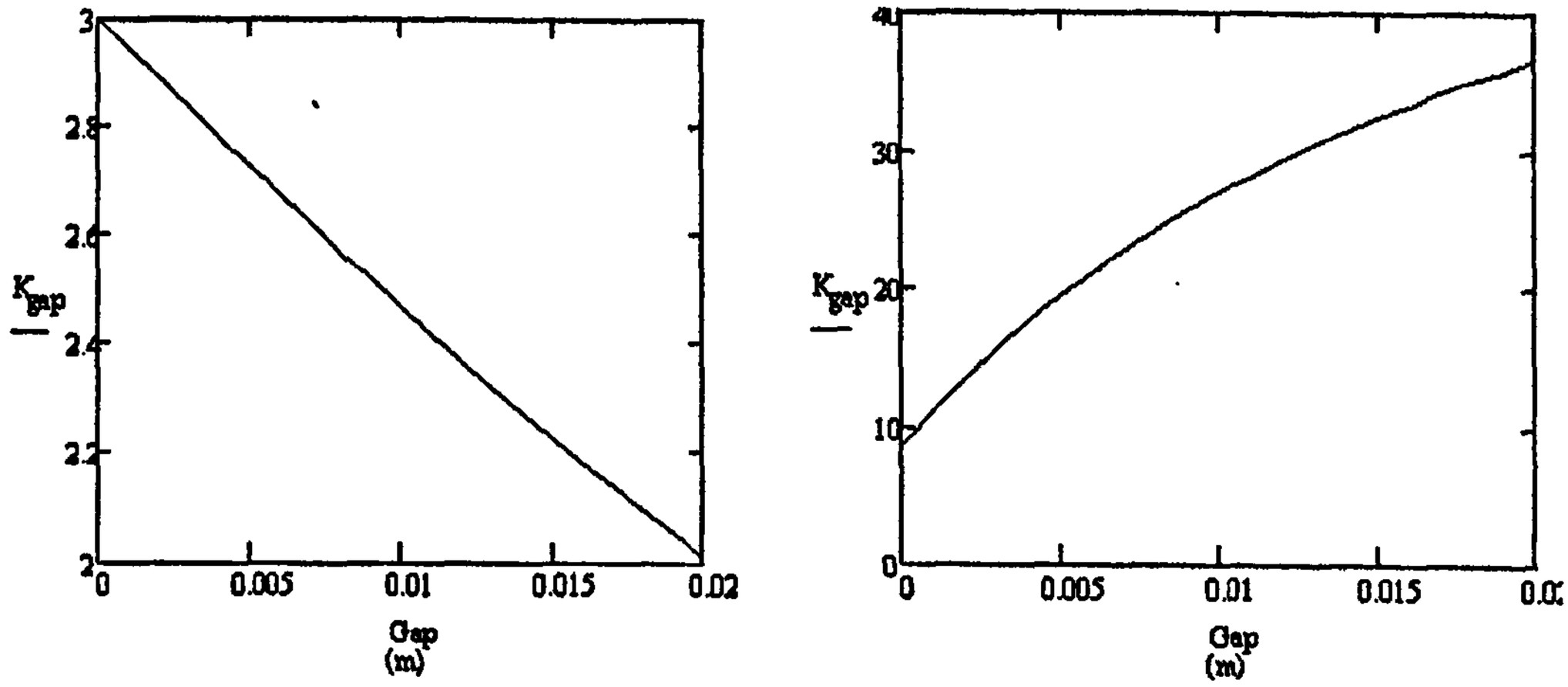

a. HTFS1 gap loss coefficient b. HTFS2 gap loss coefficient

Figure 6.4: Gap loss coefficients calculated from HTFS1 and HTFS2 methods

To develop a better understanding of the flow through staggered finned tube bundles it was decided to use the CFD experience developed in Chapter 5 to model a typical staggered air cooler.

6.2 CFD analysis of staggered bundles

One bundle based on Source 15.1 of the HTFS databank was modelled in CFD. The modelling, meshing and solution strategy was that described in Chapter 5.

6.2.1 Model

6.2.1.1 Domain

Figures 6.5 and 6.6 show the staggered model's domain. It was designed from the geometry given in Table 4.9.

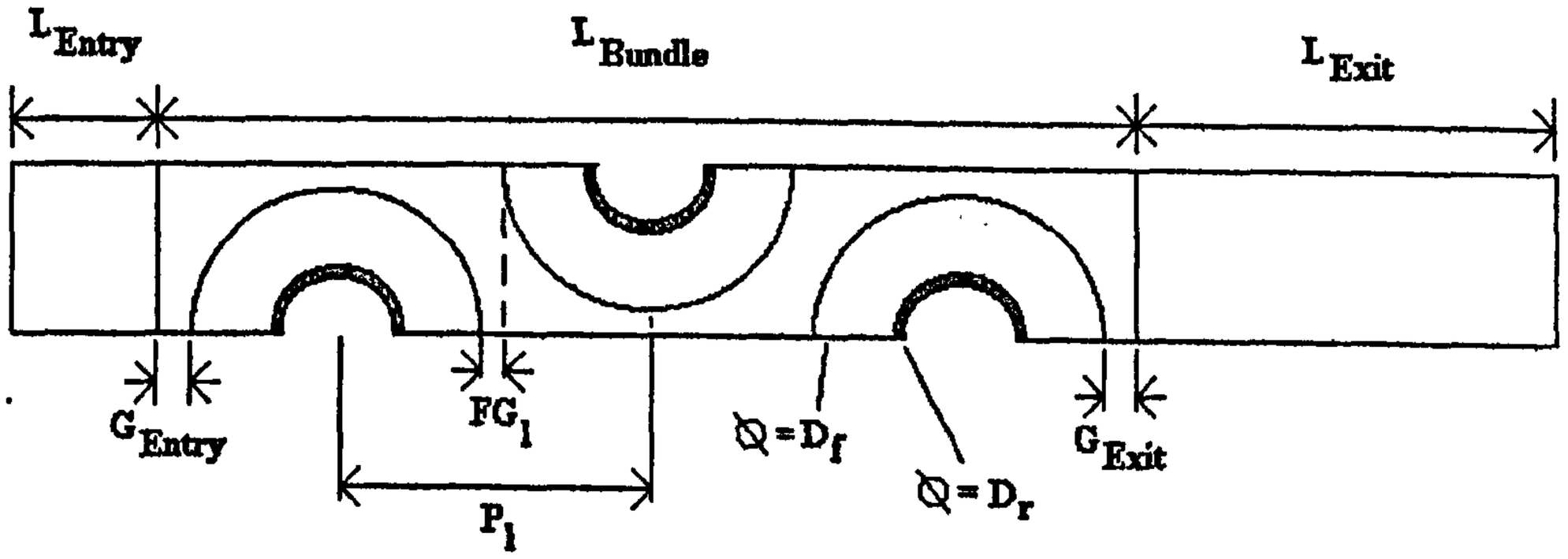

Figure 6.5: CFD domain of bundle Source 15.1 (only three rows shown)

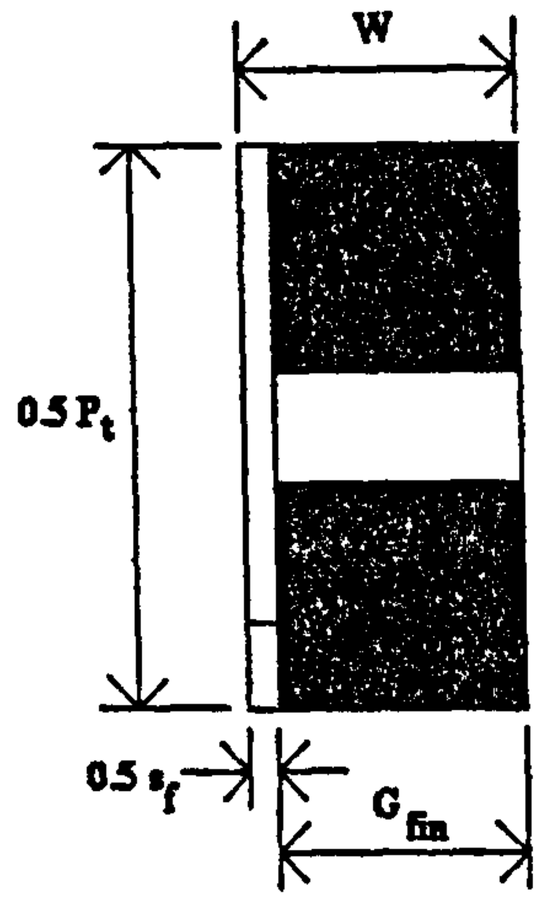

Figure 6.6: CFD domain of bundle Source 15.1 (End elevation)

Bundle:	15.1
P_t	66.7
P_L	57.76
D_o	25.4
D_f	57.2
s_f	0.231
L_{entry}	115.52
L_{bundle}	1039.68
L_{exit}	577.6
G_{entry}	0.5
G_{exit}	0.5
FG_l	0.28
W	1.155
G_{fin}	1

Table 6.1: Geometry of CFD domain (dimensions in mm)

6.2.1.2 Tube side conditions

This bundle was originally tested in the VWT, and as such the tubeside process fluid was a viscous oil, Dowtherm-J, described by McLean and Spence [62] as 'a viscous thermal fluid'. They state that tube inserts were used to ensure a high tubeside heat transfer coefficient, and that on average the temperature drop of this fluid across the bundle was 2°C. Therefore the assumption was made that a fixed tube temperature of 99 °C was acceptable to represent an ideal section in the middle of the bundle for the model, for a nominal 100 °C fluid inlet temperature, and the heat rejection was sensible.

6.2.2 Validation

Table 6.2 shows the CFD results compared to the experimental results. The air outlet temperatures were absent from the contents of the databank, which meant that a comparison between the experimental values and CFD was not possible.

Air Face Velocity (m/s)	Exp. Pressure Drop (N/m^2)	CFD Pressure Drop (N/m^2)	Exp. Air outlet Temperature (°C)	CFD Air outlet Temperature (°C)
1.48	45	48.79	-	98.92
2.68	111.6	108.53	-	95.29
3.82	194.6	202.46	-	90.05
4.88	288.7	314.36	-	88.68
6.02	386.8	401.08	-	83.41

Table 6.2: Results of Source 15.1 CFD model against experimental

6.2.2.1 Pressure drop

It can be seen that the pressure drop was predicted within -2 to +8 % deviation from the experimental results. This is an extremely good result, as minimal wall adaptions (y^+) were used to match the results, indicating that the meshing and solution strategy shown for the inline bundles in Chapter 5 is applicable for staggered bundles.

6.3.2.2 Air outlet temperature

Staggered bundles transfer significantly more heat for a given number of rows and tube/fin dimensions than inline bundles, so an air temperature at low flow rates is expected to approach that of the tube side temperature would be expected. However the result for the lowest flow rate is believed to be overpredicted, as it is only fractions of a degree below the inner tube temperature. These models used the turbulent Prandtl number described in Chapter 5, and even with that modification it would appear that the heat transfer in the CFD is too aggressive. However without the experimental data it is difficult to make a clear statement on the predictions. The behaviour of the trend, however, is as expected.

6.2.3 Results of CFD validation

With only the pressure drop data available to provide reassurance that the models predictions are accurate it was decided to examine the trends shown by the CFD data to provide insights into the flow patterns in staggered bundles. Figures 6.7 and 6.8 show the velocity and temperature contour plots, respectively, of Bundle 15.1. The usage of these will be detailed in the following sections.

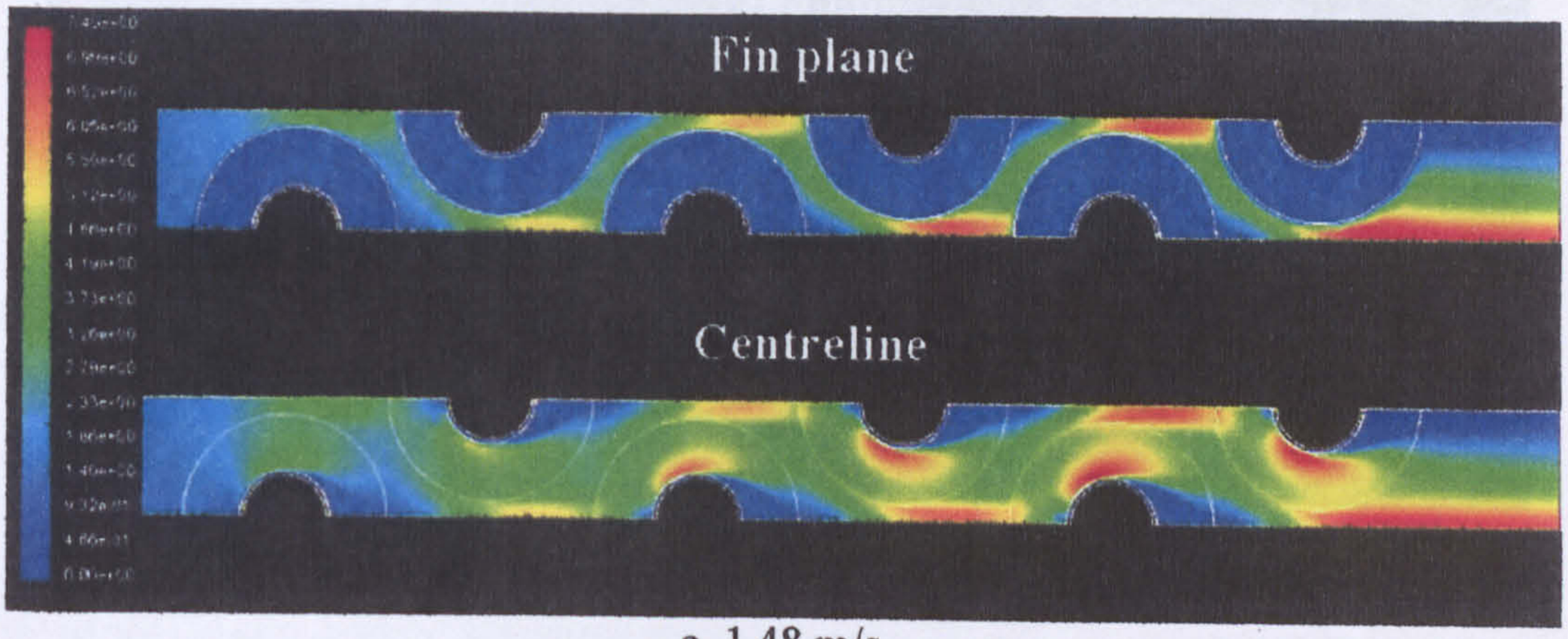

a. 1.48 m/s

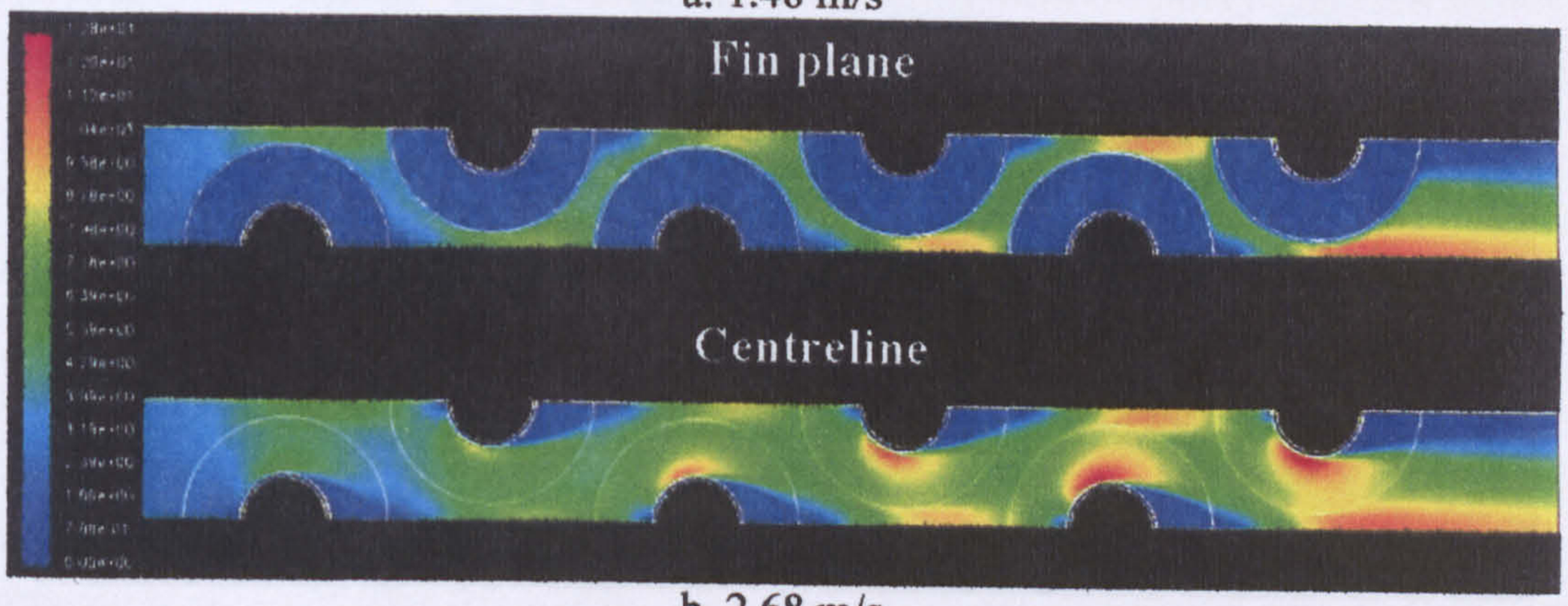

b. 2.68 m/s

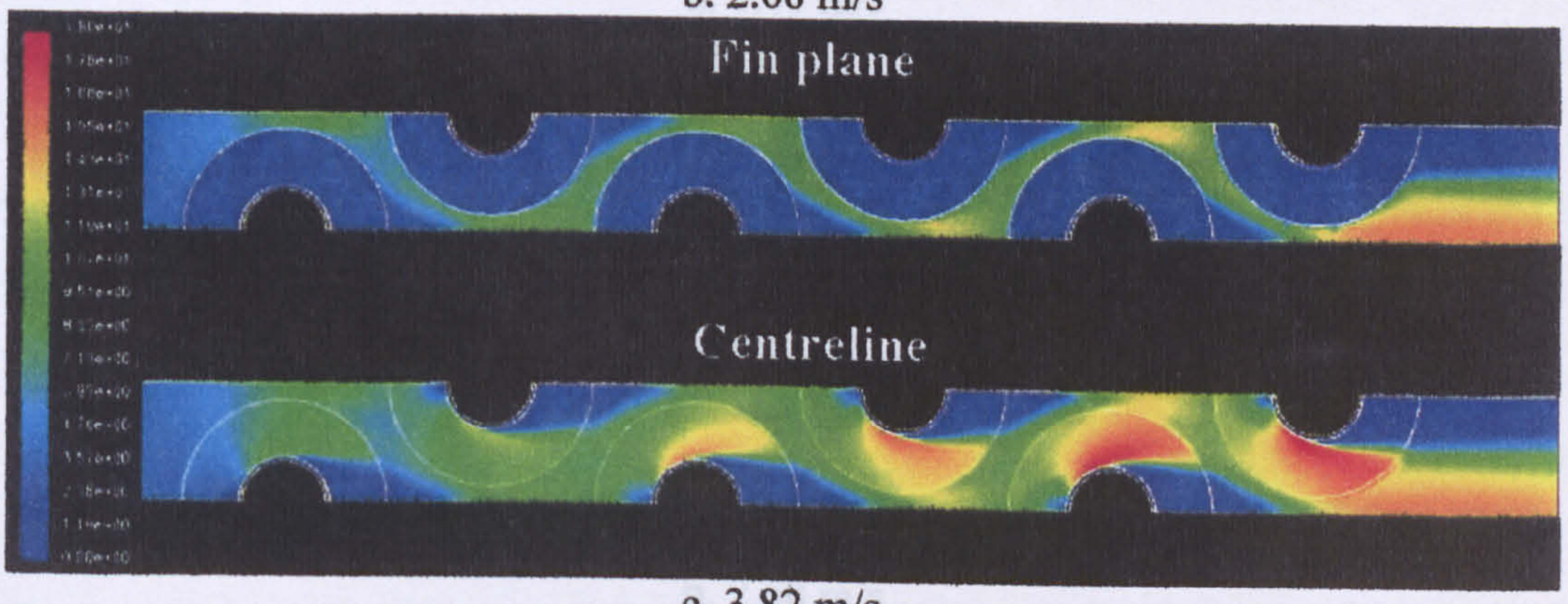

c. 3.82 m/s

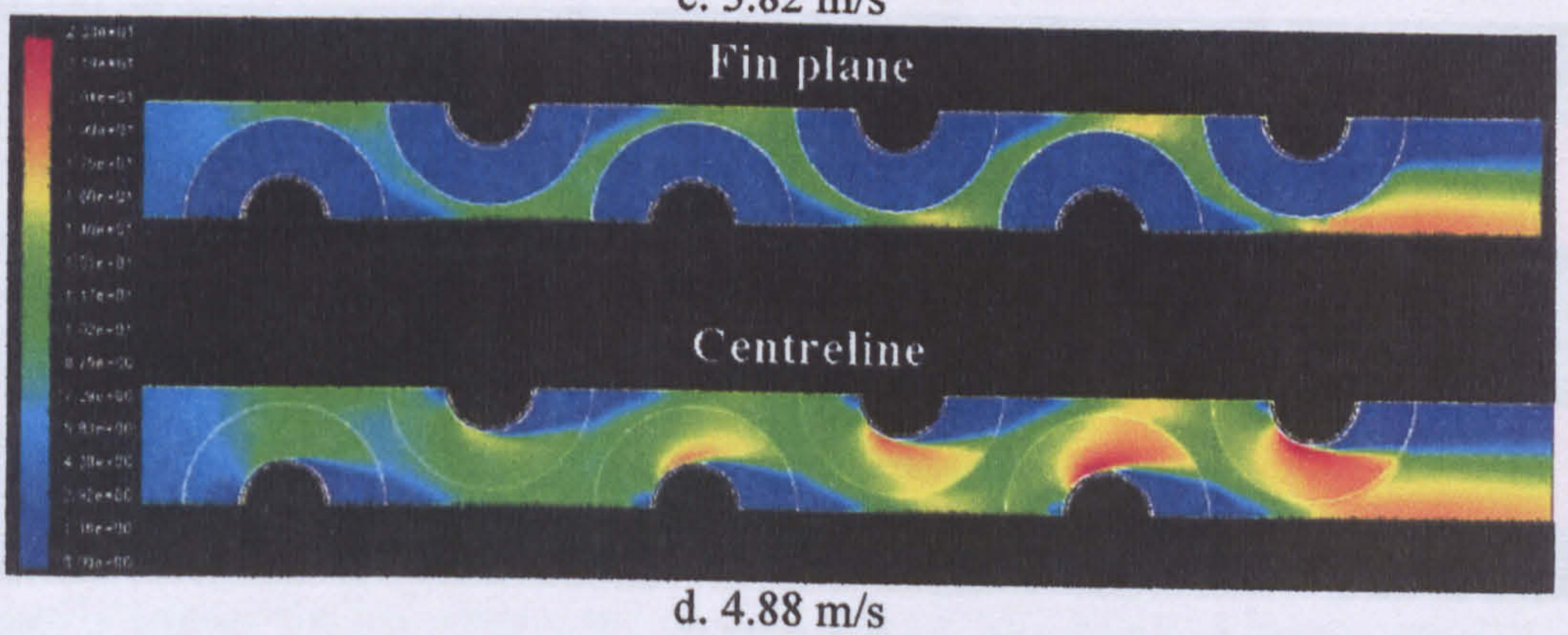

d. 4.88 m/s

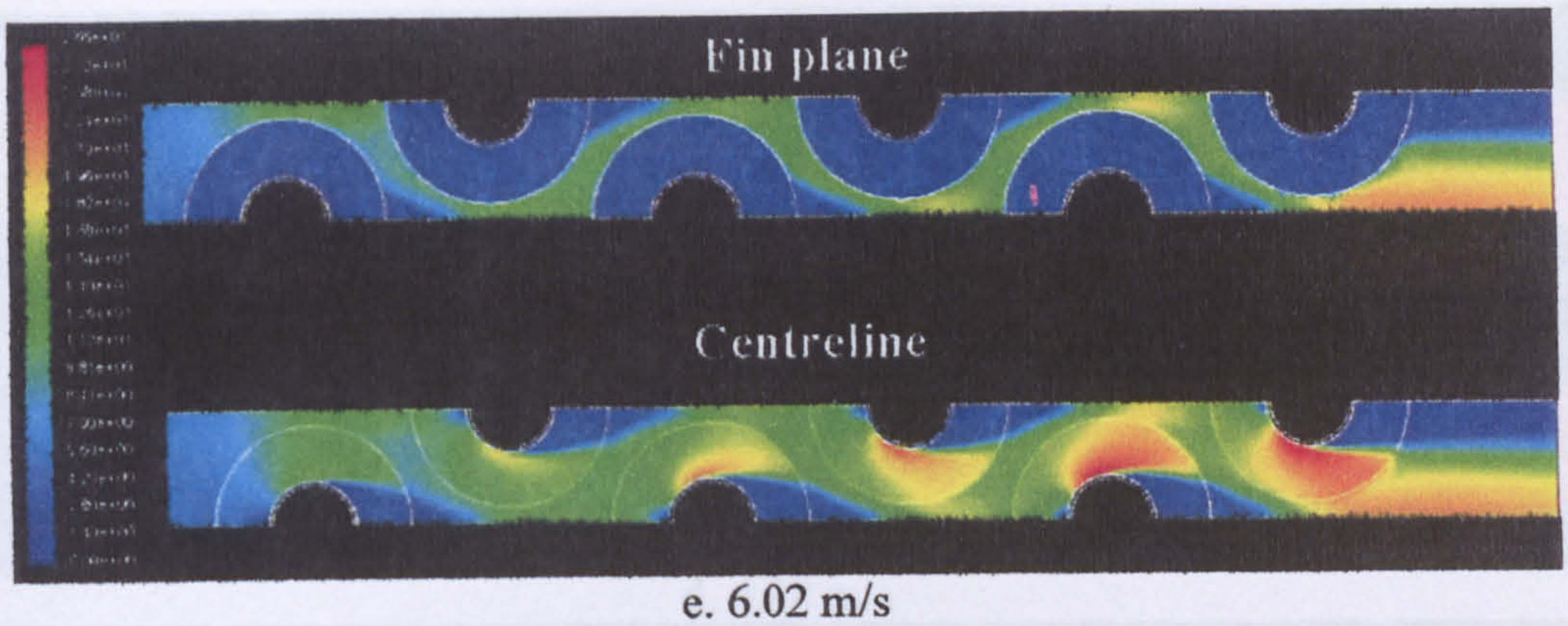

e. 6.02 m/s

Figure 6.7: Contour plots of velocity through bundle with varying face velocities

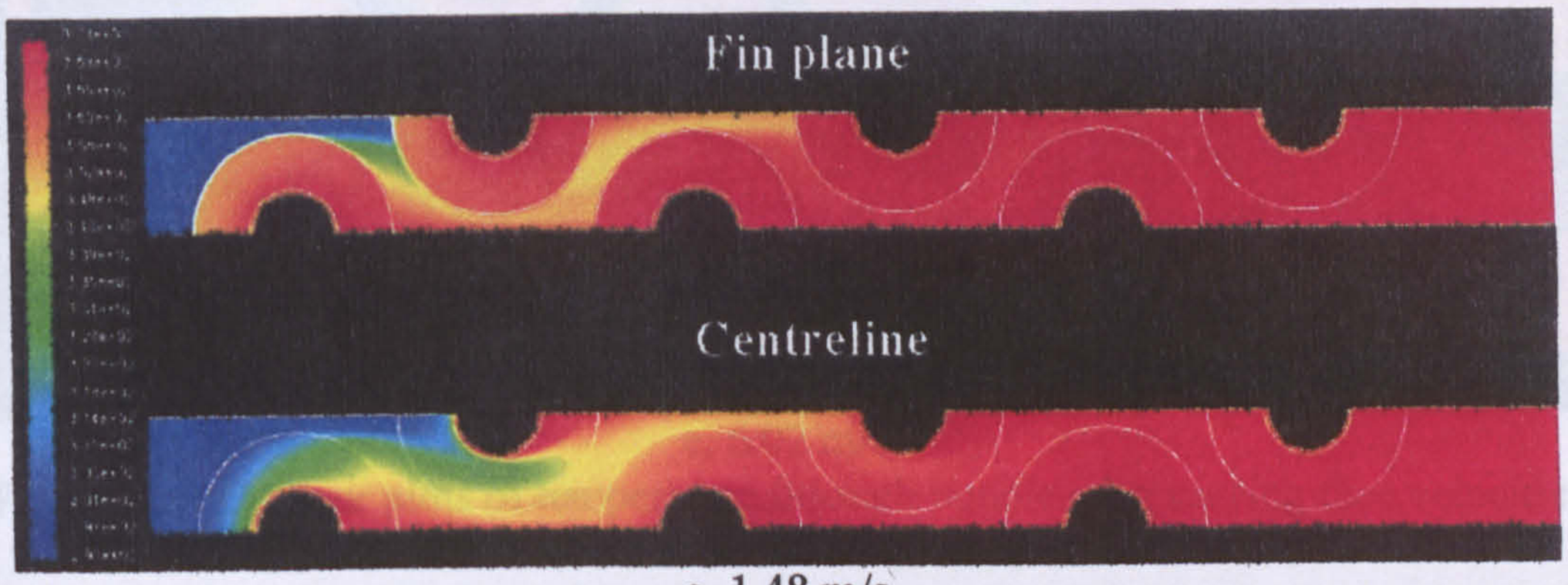

a. 1.48 m/s

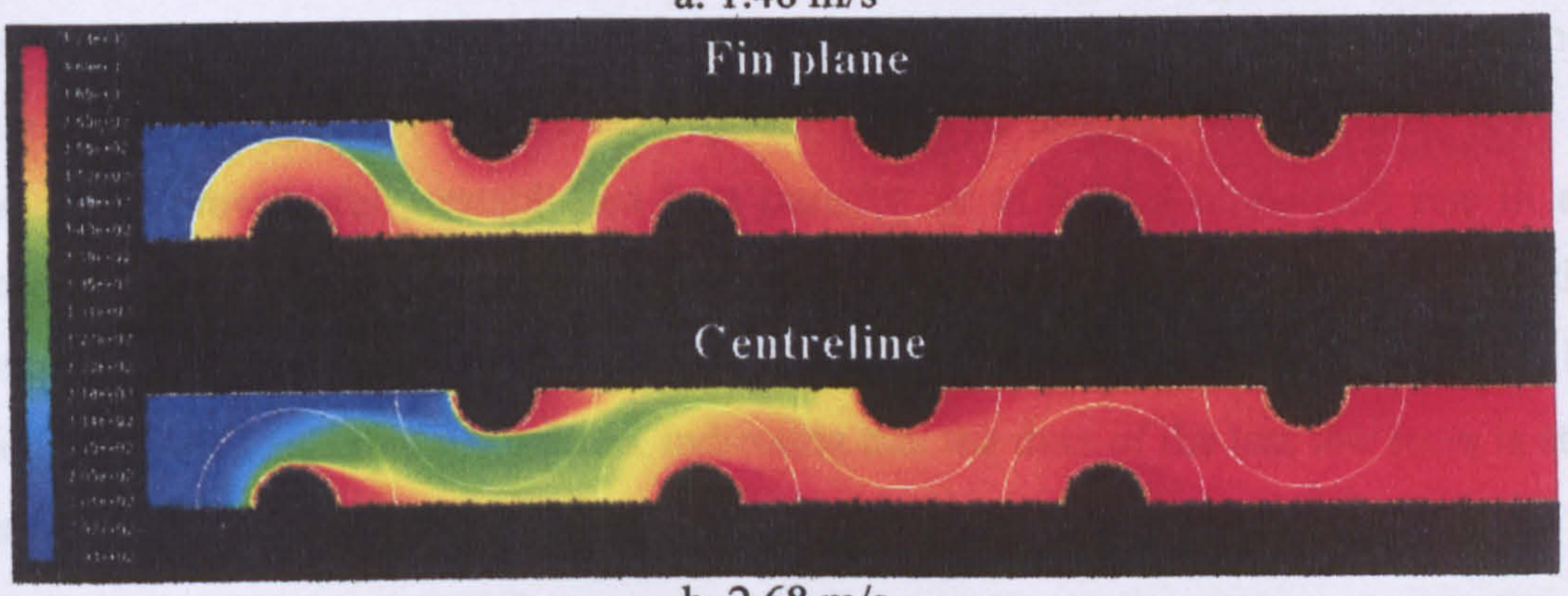

b. 2.68 m/s

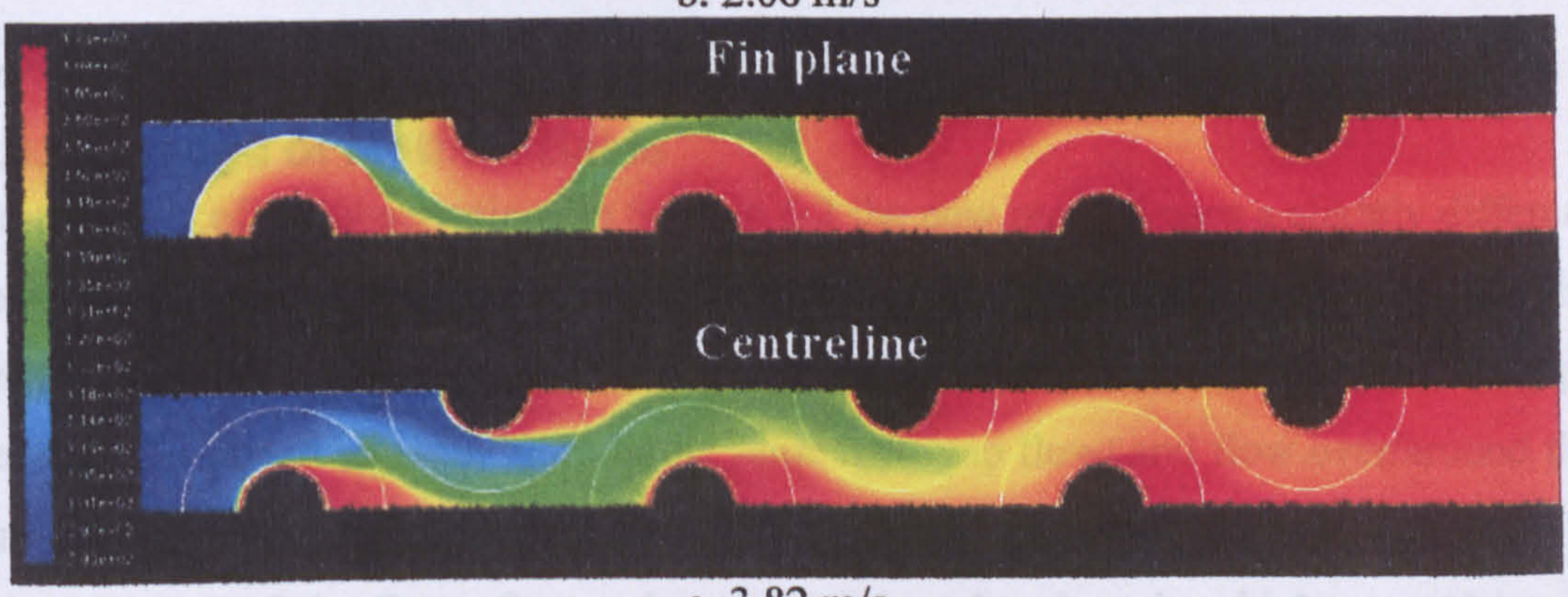

c. 3.82 m/s

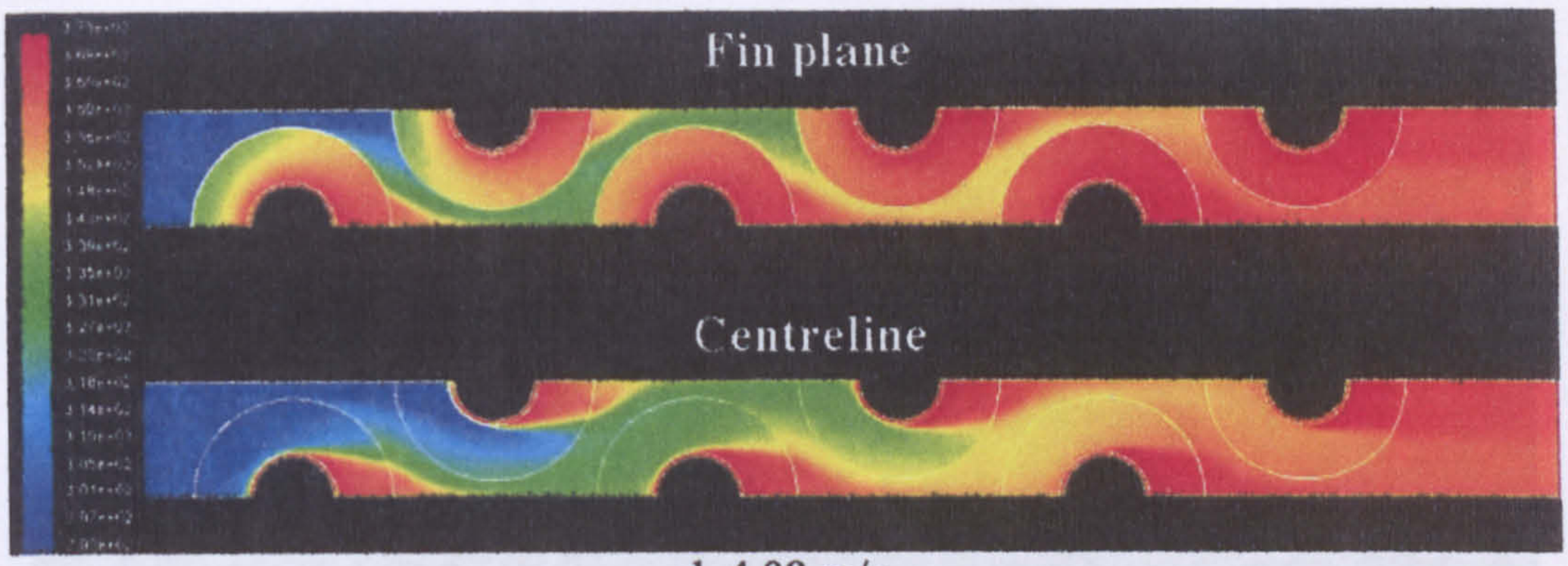

d. 4.88 m/s

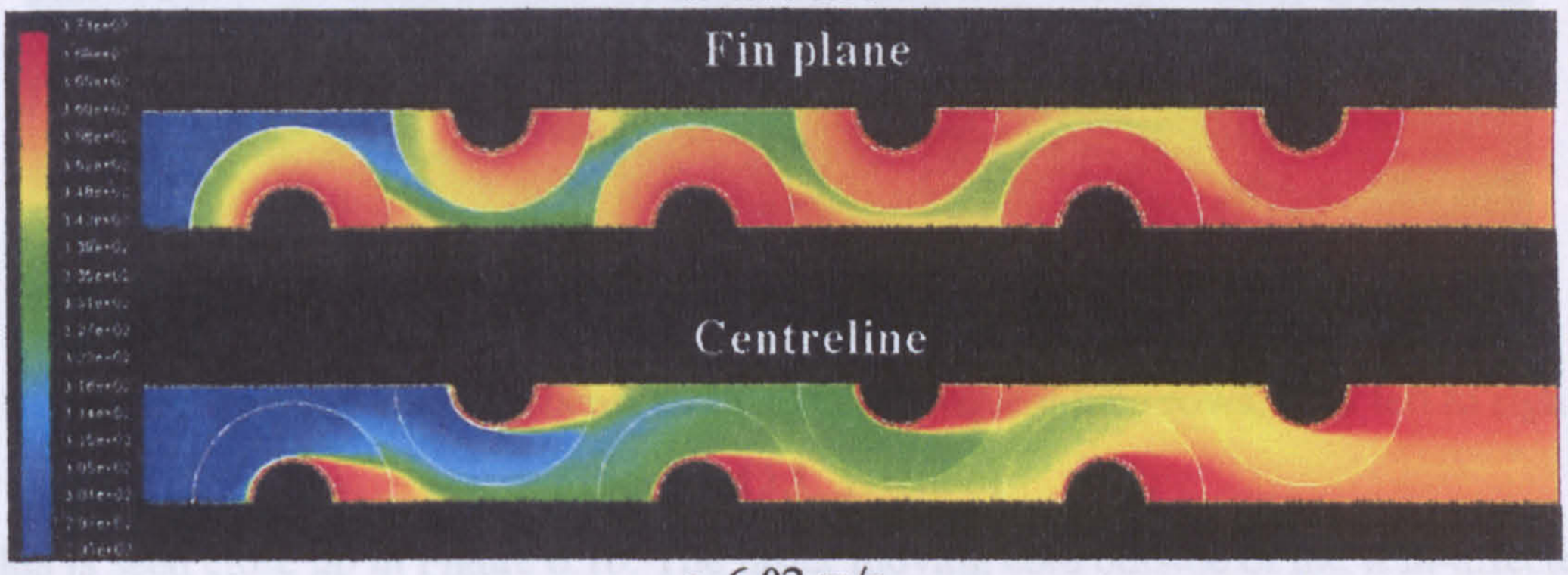

e. 6.02 m/s

Figure 6.8: Contour plots of temperature through bundle with varying face velocities (on fin and centre planes)

It can be seen that the velocity patterns do not alter with increasing face velocity, other than in local magnitude, but the heat transfer does. At low flow rates 4 tube rows is enough to provide fully established heat transfer, or at least a monotonic rise in air temperature for each subsequent row. This is denoted by the constant temperature on the contours for both fin and centre planes. At higher mass flow rates the fin surfaces can be seen to have a temperature variation, indicating that the duty of the last few rows is still varying.

6.3 New method

6.3.1 Change of Method Basis

On the basis of the observations in Section 6.2 the new method uses a slightly different basis from the previous HTFS models. Previously the model had been based on the premise that the flow could be split distinctly into two regions; flow through the gaps between the fins in adjacent tubes in the same row (gap flow) and flow over/around the fins. It can be seen in Figure 6.9 that while the boundary layer (shown in dark blue) is primarily around the fin surface and on top of the tube, there is a higher speed 'core' between the fins (green region).

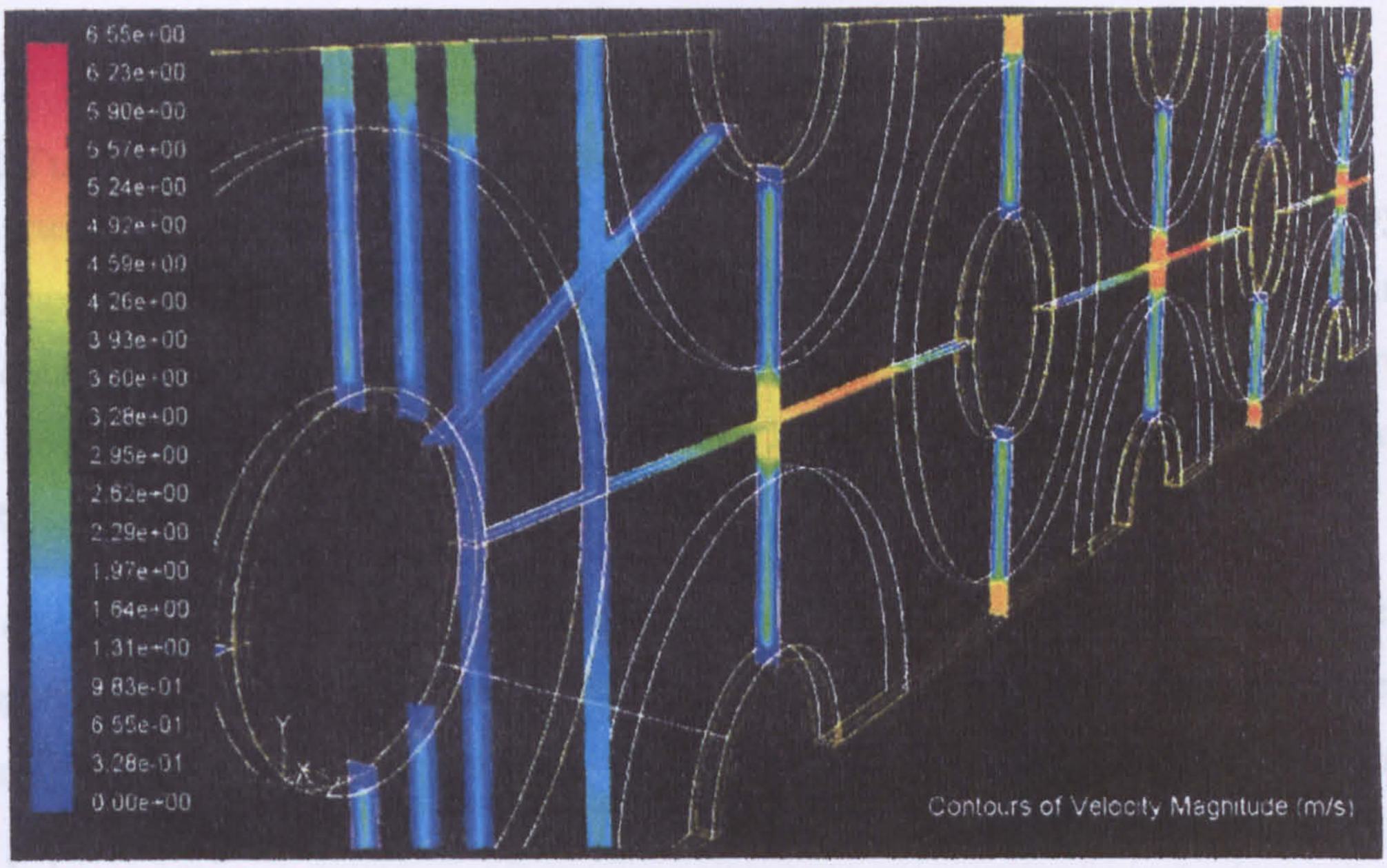

Figure 6.9: Velocity contours between fins, on subsequent tube rows, flow left to right. (Source 15.1, 1.48m/s)

This is seen close up in Figure 6.10. The faster moving core outside of the wall-affected region, which has approximately the same velocity as the flow in the defined gap, is clearly visible. This indicates that a portion of the gap flow passes between the fins. Therefore the new model must reflect these newly identified regions; extended gap and fin flow.

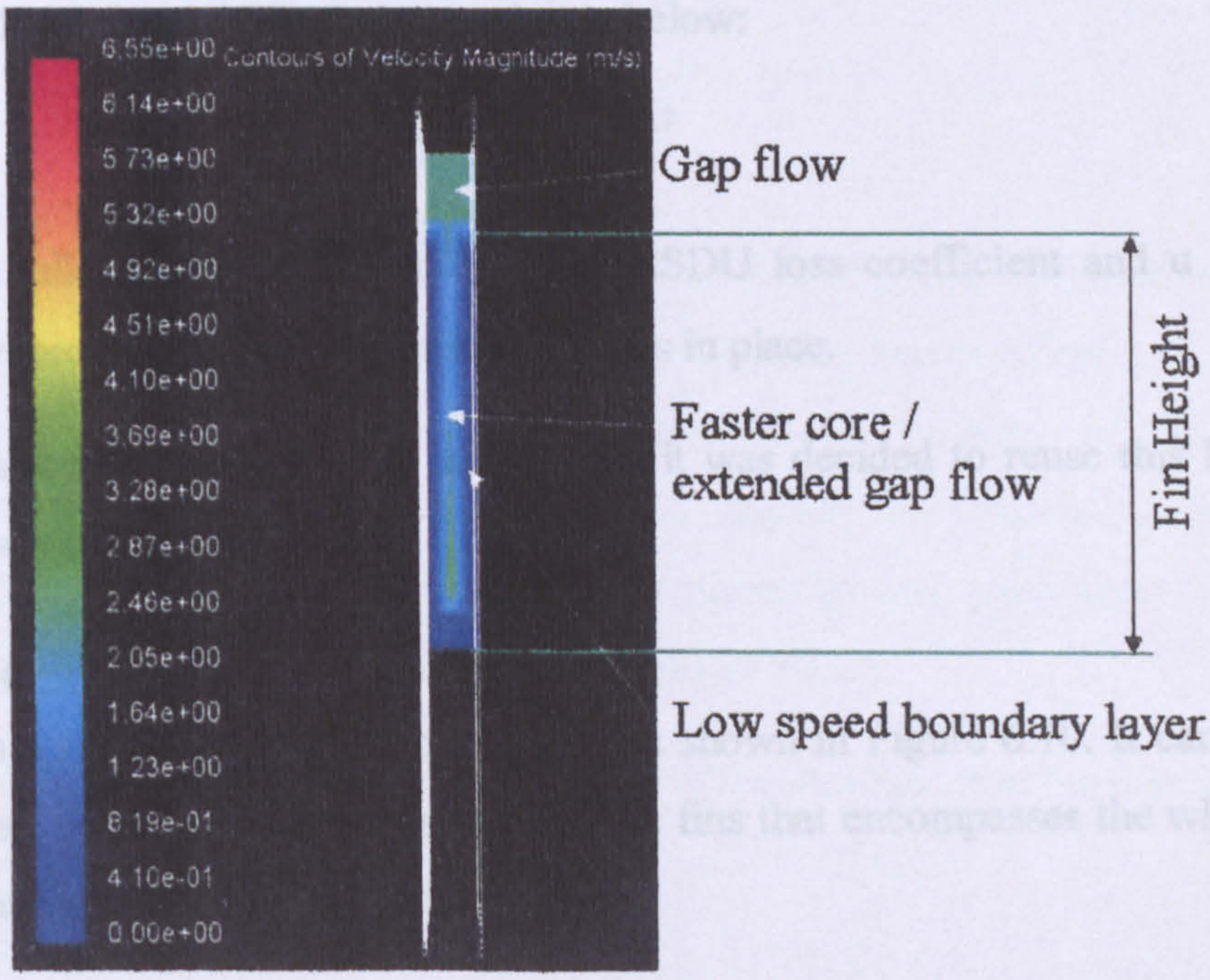

Figure 6.10: Velocity contours on first tube row centreline, shown from flow direction (Source 15.1, 1.48m/s)

6.3.2 Tube loss coefficient

As discussed in Chapter 2, Henry [19] envisaged that a model could be produced by superimposing a fin drag component onto a base tube layout to model a bundle with fin tips touching, then accounting for gap flow to provide relief from this high pressure drop idealised case. This model was first realised by Ralston et al. [21], and later Chu and Ralston [22].

Ralston et al. [21] examined a series of loss coefficients for different bundle pitch arrangements presented in the data of ESDU [20]. From this research they developed the bare tube bank loss coefficient (Equ.6.1) in terms of key geometrical parameters and flow physical properties.

$$K_{tube} = \frac{4.75}{\left(\frac{P_T}{D_r} - 1\right)^{1.7}} \frac{N_R P_L}{D_r^{1.3}} \left(\frac{\eta}{\rho}\right)^{0.3} \qquad \text{(Equ.6.1)}$$

No record of how this model was created exists, so the data of ESDU [20] was examined, and an earlier reference, also from ESDU [28], was referred to. It appears that Equ.6.1 was developed by using the pressure drop method of ESDU [20] and equating it with a HTFS developed relation as shown below:

$$-C\frac{0.5\rho U^2}{D_o} = K_{tube}\rho u^{1.7}$$

Where ρ was the bulk density of the fluid, C the ESDU loss coefficient and u the superficial velocity through the duct, assuming no tubes in place.

As this model was derived from reliable source data it was decided to reuse this loss coefficient in the new model.

6.3.3 Fin Loss Coefficient

Figure 6.11 shows a simplified diagram of the effects shown in Figure 6.10. It can be seen that a zone can be considered to exist around the fins that encompasses the whole fin surface area, thus giving the fin skin friction drag.

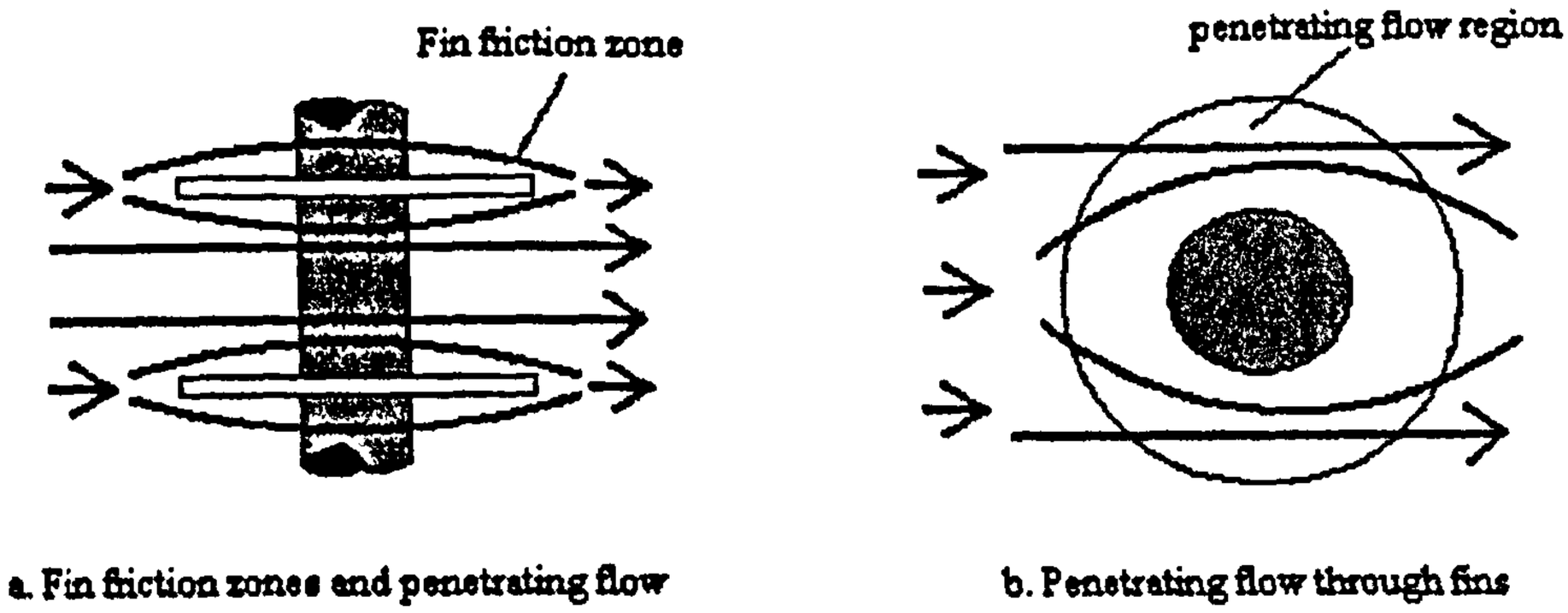

a. Fin friction zones and penetrating flow

b. Penetrating flow through fins

Figure 6.11: Penetration region of flow between and around fins

Henry [19] found that the fin loss coefficient was a function of the product of the ratio of approach area to the minimum flow area (σ) and the total fin surface area per unit approach area (ϕ). On the basis that:

- Henry used data from fin tips touching experiments (bundles with no defined gaps) to provide a baseline.
- The HTFS databank used to derive the new model was not altered since the introduction of the HTFS1 method.

It was decided that the fin loss coefficient should revert to that of HTFS1. This is shown in Equ.6.2.

$$K_{fins} = 2.65 * 10^{-2} \phi \cdot \sigma^{1.7} \qquad \text{(Equ.6.2)}$$

6.3.4 Gap Loss Coefficient

In the HTFS2 method, the formulation of the gap loss coefficient (K_{gap}) was based on an empirically derived hyperbolic tangent function. Given that this loss coefficient caused the pressure drop underprediction problem it was re-examined in terms of the key parameters that could affect gap loss. Henry [79] studied the various standard arrangements used in staggered tube bundles and concluded that the pitch angle has a large influence on the pressure drop and heat transfer performance.

On this basis, it was found by examining the contents of the databank that the following three parameters influence the gap loss term:

- Number of gaps in between tube rows.
- Ratio of effective diagonal gap to transverse gap.
- Pitch Angle between tube centres in adjacent rows.

6.3.4.1 Number of rows

The number of tubes gaps is expressed simply as shown in Equ.6.3:

$$N_G = (N_R - 1) \qquad \text{(Equ.6.3)}$$

This function counts the number of gaps between tube rows and allows the model to scale linearly with an increasing number of tube rows, similarly to the tube and fin loss components. It also has the added benefit of preventing the model being used for single tube rows.

6.3.4.2 Effective gap ratio

The ratio of effective diagonal to transverse gap is addressed by three new terms; the diagonal gap (G_D), the transverse gap (G_T) and a diagonal gap correction term (G_A). These are given in Equs.6.4 - 6.6. The sum of G_D and G_A represents the effective diagonal gap, as shown in Figure 6.12

$$G_D = \sqrt{P_L^{\,2} + (0.5P_T)^2} - D_f \qquad \text{(Equ.6.4)}$$

$$G_T = P_T - D_f \qquad \text{(Equ.6.5)}$$

$$G_A = 0.5(D_f - D_r) \qquad \text{(Equ.6.6)}$$

The sum of G_D and G_A represents the effective diagonal gap, as shown in Figure 6.12.

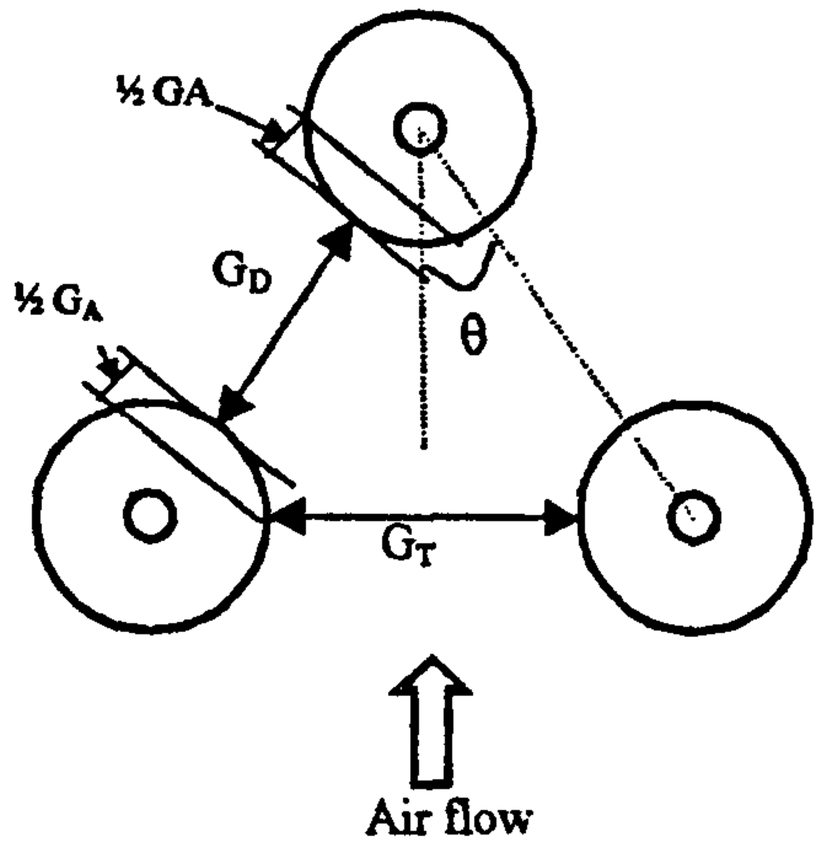

Figure 6.12: Geometric parameters used in the model

By inspection of Figure 6.12 and Equ.6.5 it becomes apparent that the physical gap in the transverse direction is represented by a simple parameter outside of the fin region,

whereas the diagonal gap is the gap between the fins in subsequent rows and an 'allowance'. The allowance was developed by examining the velocity CFD contour plots on the diagonal planes, which can be seen in Figures 6.13.

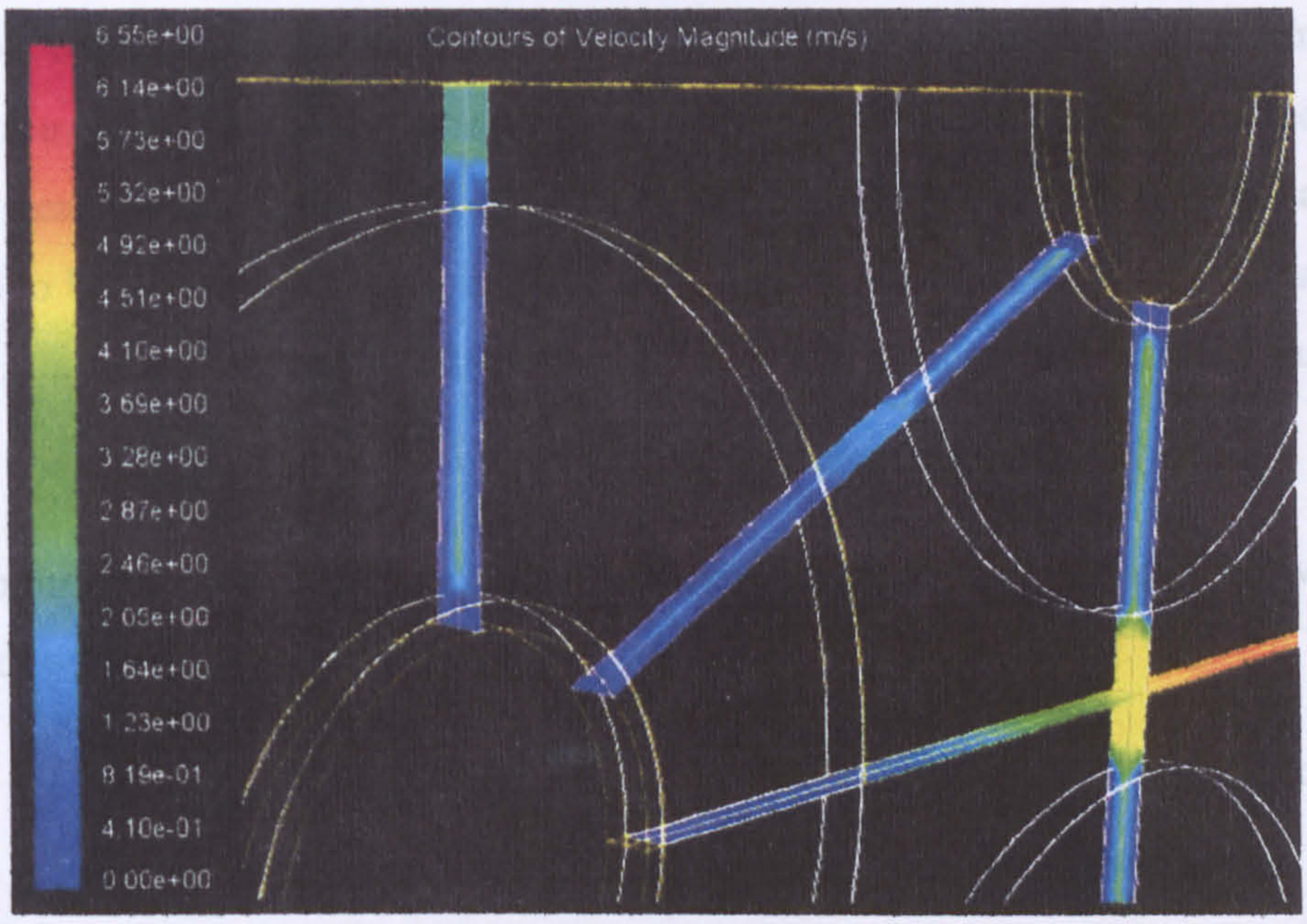

Figure 6.13: Close up of Velocity contours between fins, on subsequent tube rows, flow left to right. (Source 15.1, 1.48m/s)

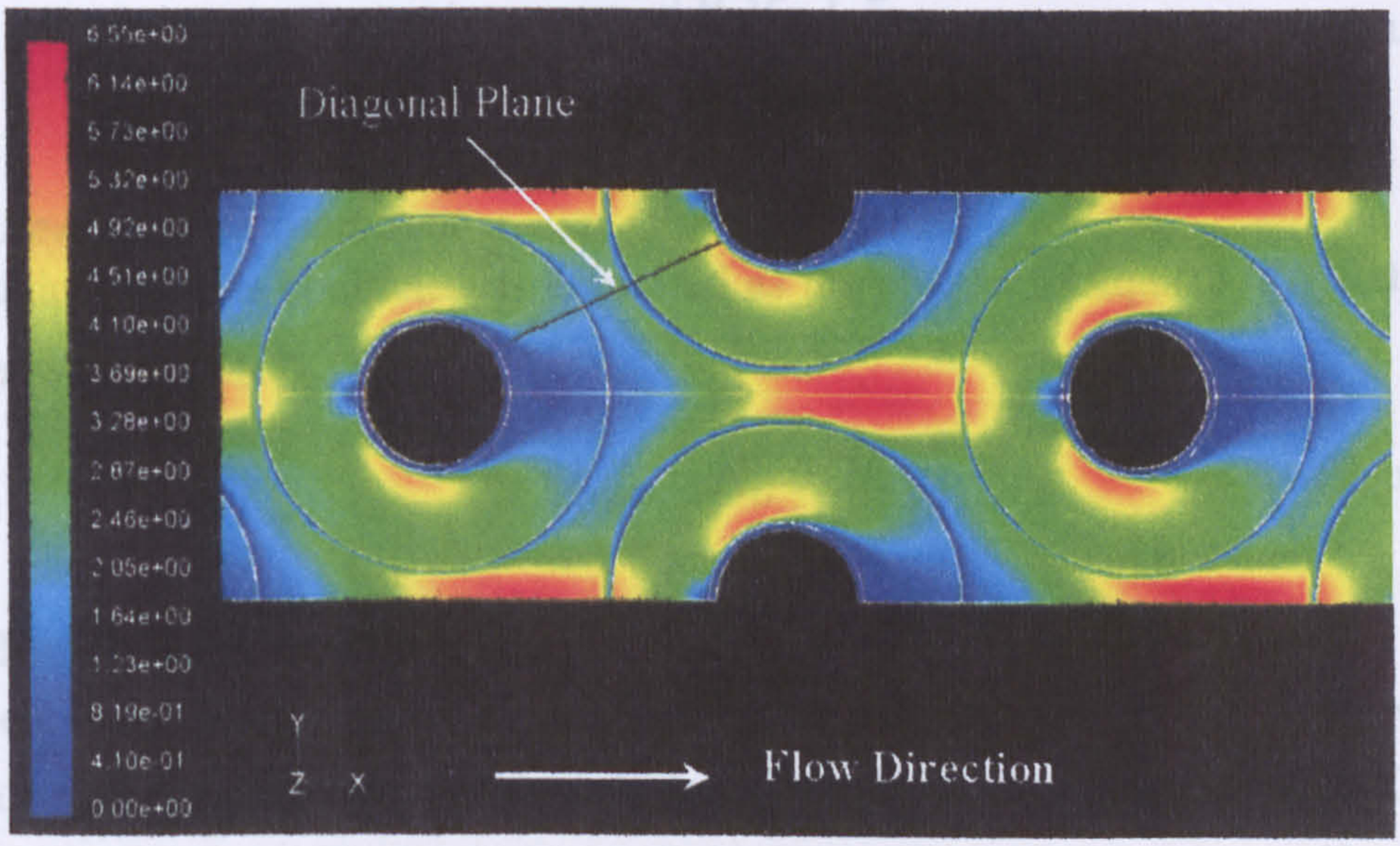

Figure 6.14: Velocity contours on plane between fins
(Source 15.1, 1.48m/s)

Figure 6.14 shows that the low speed wake off the rear of the tube reduces the velocity on the rear portion of the fin and thick boundary layers develop. Figure 6.14 is a centre plane between the fins in the middle of the modelled bundle, where the flow pattern is

fully established. Examining the diagonal plane shows that while the flow on the following tube can be considered as being at approximately mean superficial conditions, the region of the diagonal plane on the rear of the preceding tube lies in a wake region.

As no simple method to directly predict wake width behind a tube exists, an estimation was made to express what part of the diagonal gap might be considered to conduct gap flow in the near tube fin region. The best fit to express this penetration was, for all the data, found to be 0.25, which is applied to the fin height. However as there are two fins to consider, the preceding and the following, this is multiplied by 2 to give 0.5, as seen in Equ.6.6.

By assembling the above terms a dimensionless parameter, called the effective gap ratio, was developed, as given in Equ.6.7:

$$GR_{eff} = \frac{G_D + G_A}{G_T} \qquad \text{(Equ.6.7)}$$

6.3.4.3 Pitch Angle

The pitch angle as given by Henry [79] is shown in Equ.6.8:

$$\theta = \tan^{-1}\left[\frac{0.5P_T}{P_L}\right]\frac{\pi}{180} \qquad \text{(Equ.6.8)}$$

6.3.4.4 New gap loss coefficient

The resulting gap loss coefficient is expressed as the product of Equ.6.3, 6.7 and 6.8, and is shown in Equ.6.9:

$$K_{gap} = N_G \theta GR_{eff} \qquad \text{(Equ.6.9)}$$

6.3.5 Bundle loss coefficient

The model is based on the premise that when there is no gap between the fins and the fins tips are touching the total resistance is due to the fin skin and tube form drag. Given that fin tips touching is rarely, if ever used, in practise the gap loss coefficient is necessary to attenuate the combined fin and tube loss.

The previous formulation of the HTFS models used the overall bundle loss coefficient shown in Equ.6.10. As this contained a mechanism to reduce the denominator to unity if

the transverse fin gap = 0, leaving the fin tips touching condition, it was decided to retain this method of calculating the overall bundle loss.

$$K_B = \frac{K_{ft}}{\left[\frac{D_f}{P_T} + \left(\frac{K_{ft}}{K_{gap}}\right)^{\frac{1}{1.7}} \left(1 - \frac{D_f}{P_T}\right)\right]^{1.7}} \qquad \text{(Equ.6.10)}$$

6.4 Pressure drop model

With the components of the model assembled the model was compared against the data and a correlation constant found. It can be seen in Equ.6.11 that the constant is close to unity, indicating that the model is adequately modelling the processes occurring in bundles.

$$\Delta P = 1.081 K_B \rho u_o^{1.7} \qquad \text{(Equ.6.11)}$$

Using the above equation, the results of the new method, are shown in Figure 6.7. In comparison with the HTFS2 method shown in Figure 6.3, it is clear that the pressure drop calculated by the new method now shows the correct trend against the fin gap.

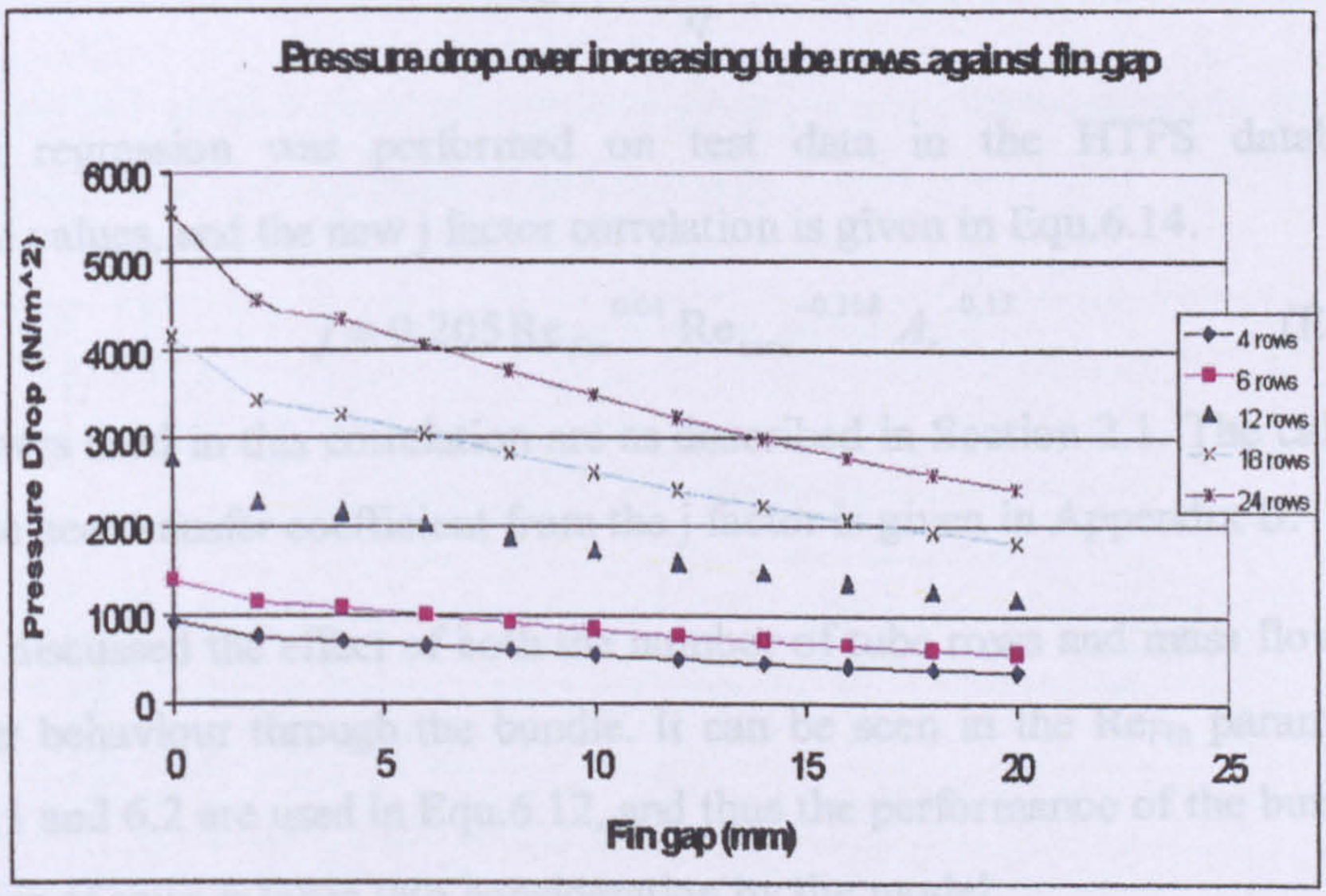

Figure 6.7: Prediction of pressure drop with increasing fin gap using the new method

6.5 Heat transfer

With the new model for gap loss coefficient, to resolve the pressure drop prediction problem, the j factor correlation was re-evaluated. Use was made of an ANOVA

(Analysis Of Variance) technique to determine which parameters were best suited to develop an updated correlation.

The previous parameters were considered, as was the Reynolds number of the gap flow, however it was determined that the format of the previous HTFS models produced the best results.

As noted by Henry [19] the overall velocity was related to the fin velocity via the bundle and fin loss coefficients. This equality was valid for the new model and is shown below (Equ.6.11)

$$K_B u_0^{1.7} = K_{fi} u_{fin}^{1.7} \qquad \text{(Equ.6.11)}$$

From this the fin velocity can be calculated from Equ.6.12:

$$u_{fin} = u_o \left(\frac{K_B}{K_{fi}} \right)^{\frac{1}{1.7}} \qquad \text{(Equ.6.12)}$$

And the definition of the Fin Reynolds number is found from Equ.6.13, as used by Ralston et.al [21]:

$$\mathrm{Re}_{Fin} = \frac{\rho u_{fin} D_r}{\eta} \qquad \text{(Equ.6.13)}$$

Multivariate regression was performed on test data in the HTFS databank of experimental values, and the new j factor correlation is given in Equ.6.14.

$$j = 0.205 \mathrm{Re}_{Fin}^{0.04} \mathrm{Re}_{\max}^{-0.368} A_r^{-0.15} \qquad \text{(Equ.6.14)}$$

The parameters used in this correlation are as described in Section 2.1. The calculation of the airside heat transfer coefficient from the j factor is given in Appendix B.

Section 6.3 discussed the effect of both the number of tube rows and mass flow rate on heat transfer behaviour through the bundle. It can be seen in the Re_{Fin} parameter that both Equ.6.1 and 6.2 are used in Equ.6.12, and thus the performance of the bundle for a given number of rows is taken into consideration by the model.

6.6 Deep tube bundles

To demonstrate that the method suggested above resolves the problem of underpredicting the pressure drop for deep bundles (i.e. with >10 tube rows) it was

compared with HTFS1, HTFS2 and PFR for source 15.2 given in Table 4.4.1, and the number of rows was increased to up 36.

Figure 6.8 and Table 6.3 show the results of this comparison by giving the pressure drop per row, in addition to the total pressure drop given in the Table. The results show that PFR and HTFS1 are scalable with an increasing number of rows while HTFS2 cumulatively underpredicts for deep bundles.

No. of rows	HTFS1 (Pa)	HTFS2 (Pa)	New method (Pa)	PFR (Pa)
4	193.62	157.11	180.21	214.40
8	196.59	137.26	181.56	213.61
12	197.77	123.65	181.95	213.35
16	198.22	114.07	182.14	213.23
20	198.48	106.84	182.24	213.15
24	198.65	101.12	182.31	213.09
28	198.77	96.44	182.36	213.06
32	198.86	92.49	182.40	213.03
36	198.93	89.11	182.43	213.01
Total for 36 rows	7161.34	3207.96	6567.42	7668.2

Table 6.3: Prediction of pressure drop per row for a bundle with 36 rows

The new method gives a constant pressure drop per row, demonstrating that it can be now used reliably for a large number of tube rows.

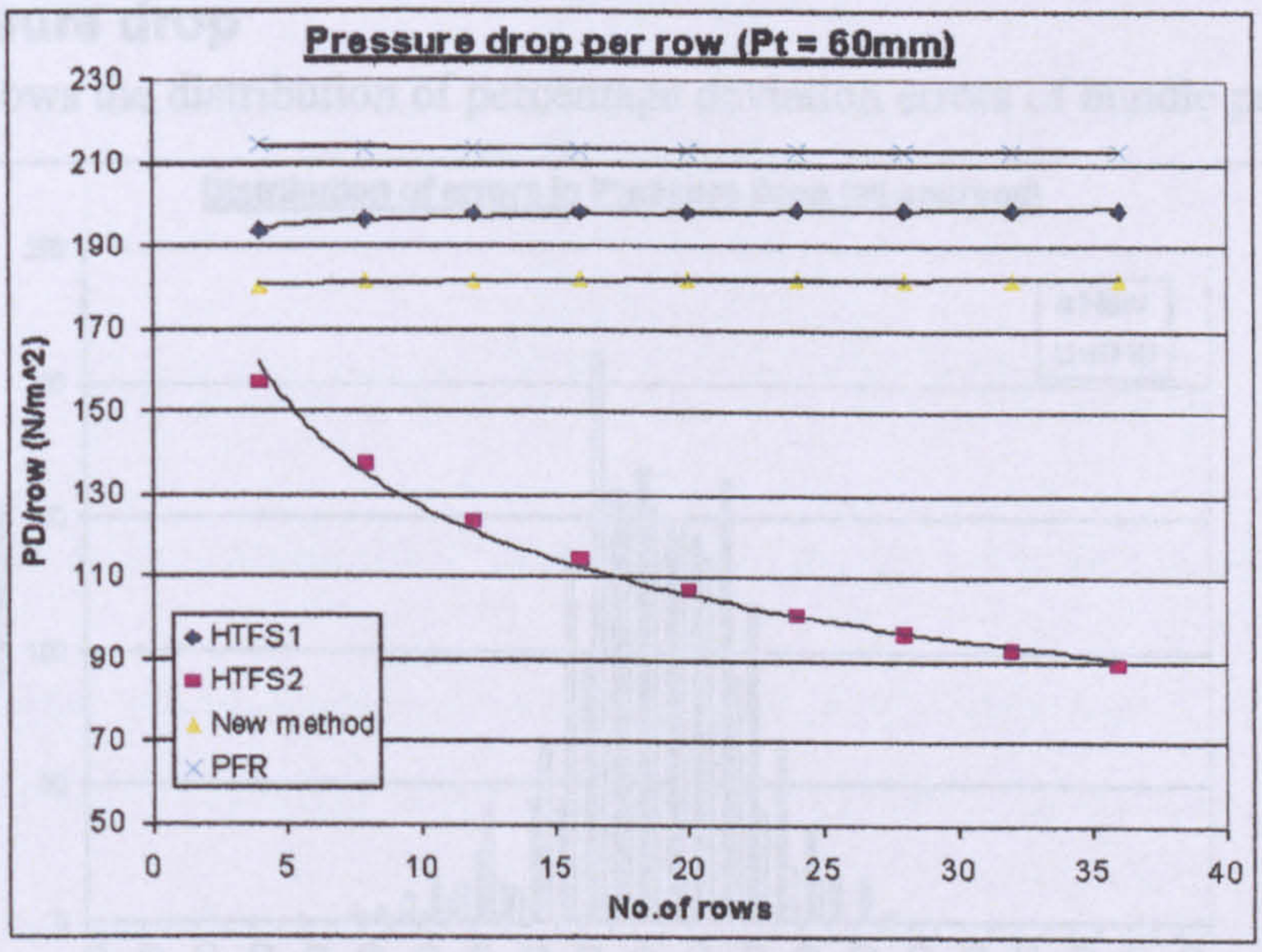

Figure 6.8: Comparison of pressure drop per row

6.7 Comparison With Data

In this section the new method is compared with the HTFS2 method using all the available data in the HTFS databank including the benchmark sources from the VWT, and the HTWT. The results of these comparisons are given in Table 6.4. For reference Table 6.4 also shows comparisons with the PFR and HTFS1 method.

Pressure Drop	PFR		HTFS1		HTFS2		New method	
	Average deviation (%)	RMS deviation (%)	Average deviation (%)	RMS deviation (%)	Average deviation (%)	RMS deviation (%)	Average deviation (%)	RMS deviation (%)
Open lit.	15.62	22.8	10.14	1976	-4.17	17.69	2.24	17.71
VWT	4.53	12.47	5.74	12.57	-6.4	13.33	-1.51	10.94
HTWT	14.67	21.43	-13.97	20.11	-6.87	15.91	4.82	15.88
All sources	12.05	19.71	-2.34	18.19	-6.06	15.7	2.39	15.17
Heat Transfer	PFR		HTFS1		HTFS2		New method	
	Average deviation (%)	RMS deviation (%)	Average deviation (%)	RMS deviation (%)	Average deviation (%)	RMS deviation (%)	Average deviation (%)	RMS deviation (%)
Open lit.	9.46	31.27	5.76	30.69	13.93	37.01	11.52	33.65
VWT	-0.67	14.99	-6.51	18.04	3.43	14.86	1.9	15.07
HTWT	-3.39	15.92	19.37	42.37	-5.99	15.01	-1.67	15.44
All sources	1.9	22.52	8.23	33.65	3.47	25.29	3.95	23.36

Table 6.4: Summary of predictions compared with experimental data

6.7.1 Pressure drop

Figure 6.9 shows the distribution of percentage deviation errors of bundle pressure drop.

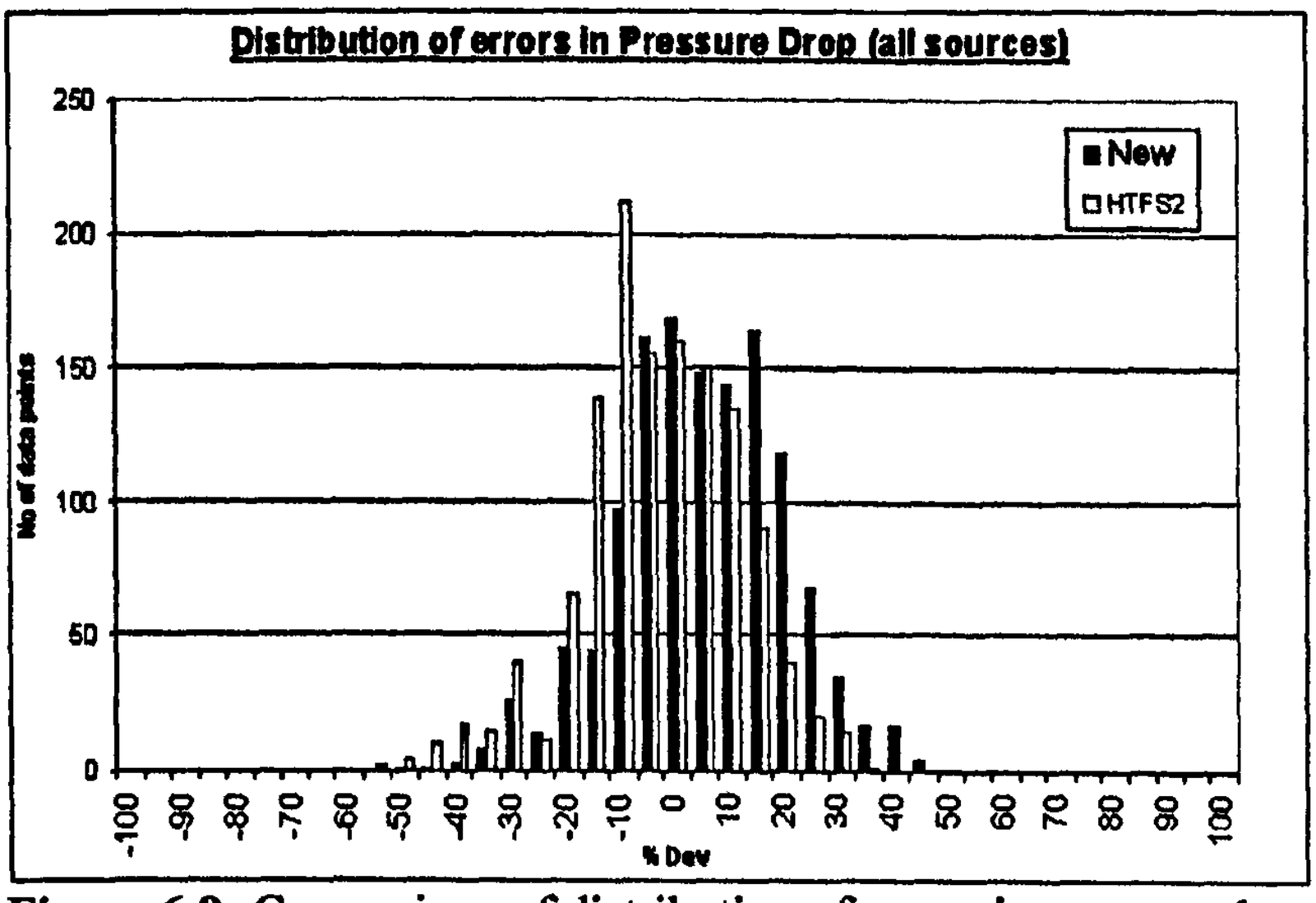

Figure 6.9: Comparison of distribution of errors in pressure drop

It can be seen that the new method displays a more even distribution about the zero line than HTFS2. This is reflected in the lower average and RMS deviations shown in Table 6.4. Approximately 85% of all data is now predicted within ±20% using the new method. This is slightly behind the 89% of HTFS2.

The tendency of the new method is towards slight overprediction, reflected in the positive average deviation value of 2.39%. HTFS2 tends towards underprediction, displaying an average deviation of -6.06%. This means that the new method is slightly on the safe side.

6.7.2 Heat transfer

Figure 6.10 shows the distribution of percentage deviation errors for heat transfer (*j* factor). In this figure it is shown that the new method displays a very similar trend to the HTFS2 method but with the advantage of having slightly better normal distribution. This is demonstrated by the slightly smaller RMS deviation of 23.63% compared to 25.29% for HTFS2.

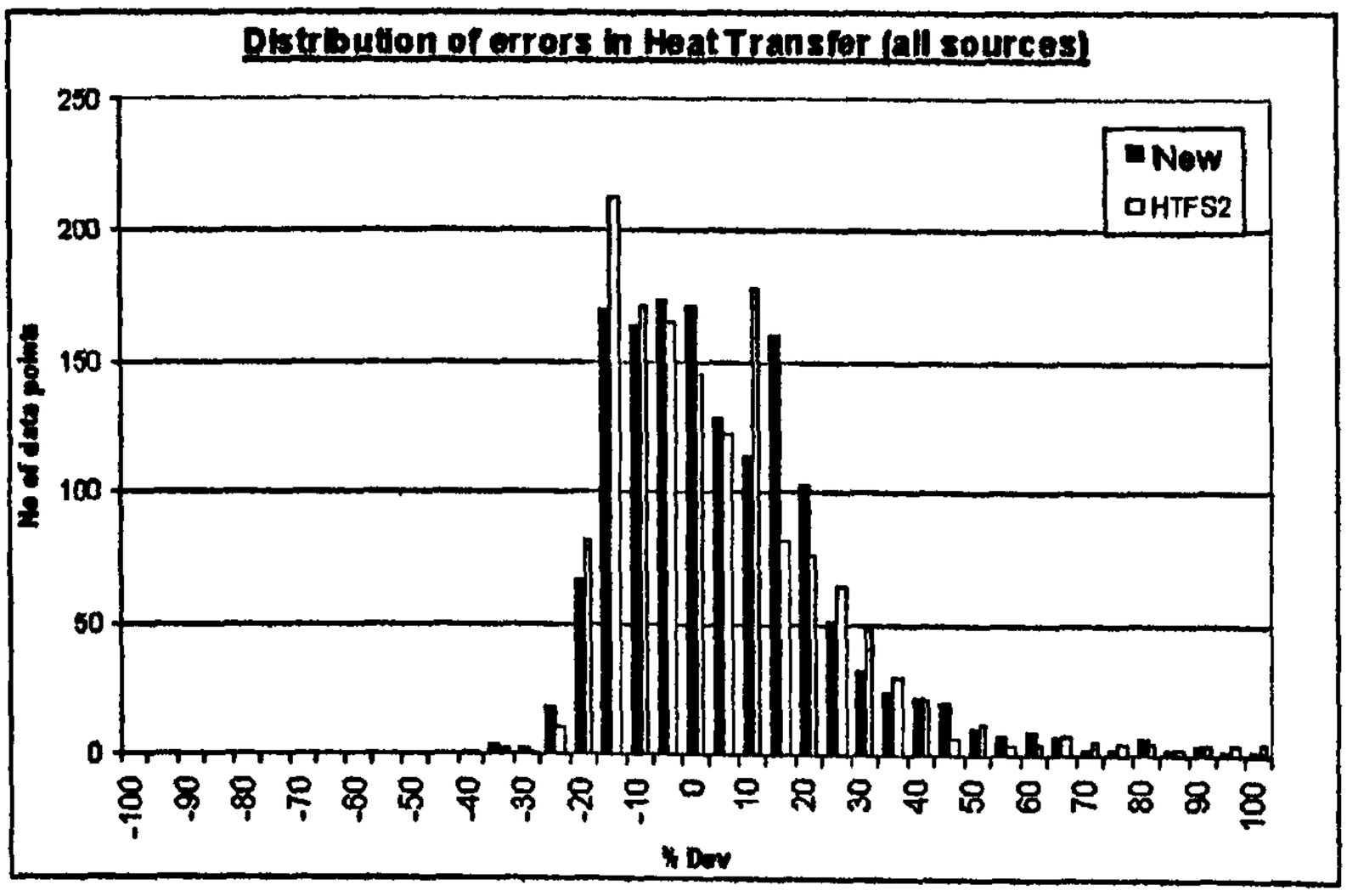

Figure 6.10: Comparison of distribution of errors in heat transfer (j-factor)

The new method predicts approximately 84% of all the data within ±20% of zero deviation showing a very slight improvement over the HTFS2 figure of 83%.

6.8 Comparison with air cooler data

6.8.1 Pressure drop

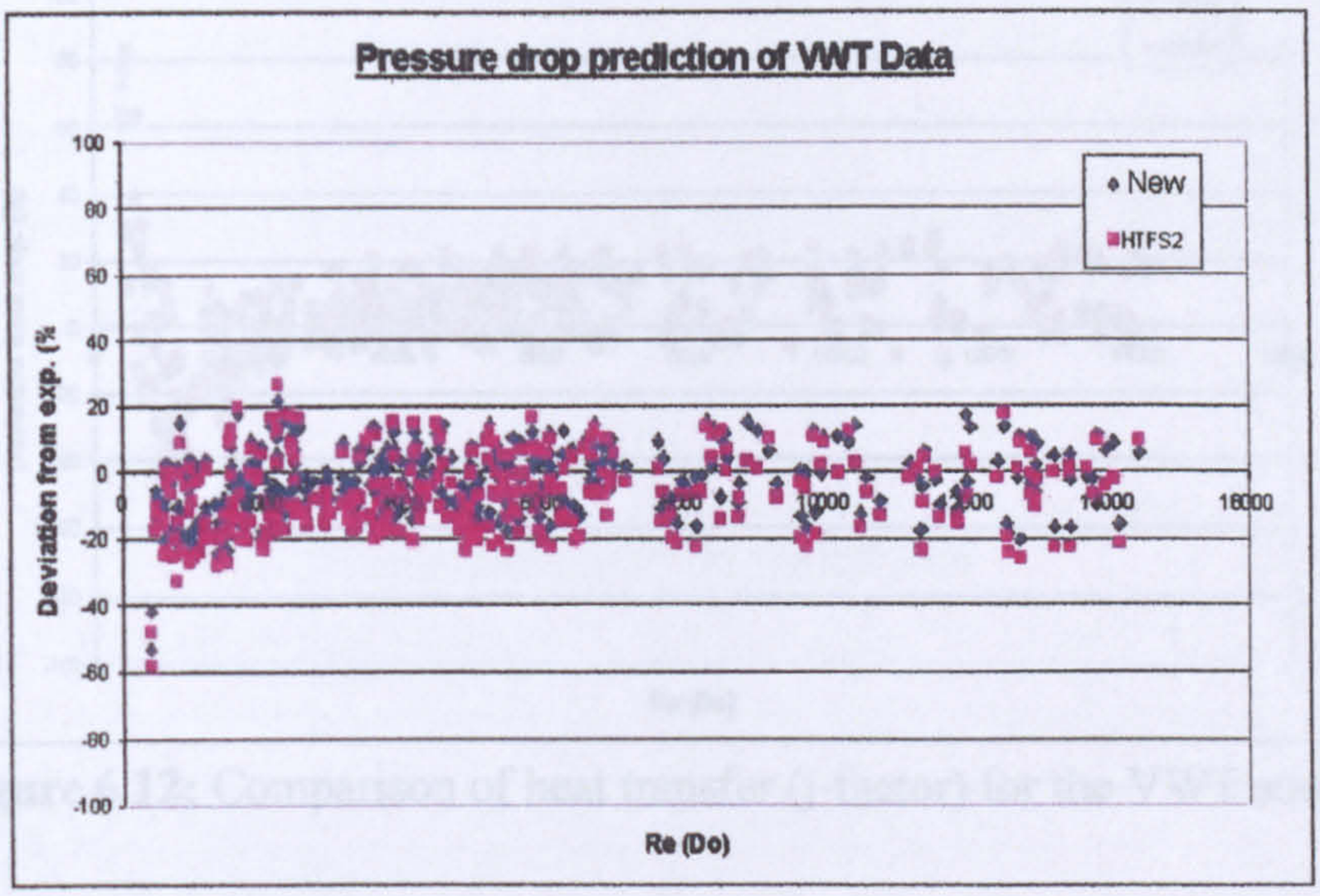

Figure 6.11: Comparison of pressure drop for the VWT source

Figure 6.11 compares the new method with HTFS2 for the air cooler data from the VWT source. It can be seen that both predictions are very well distributed about the zero deviation line. The HTFS2 method gives an average deviation of –6.4% and RMS deviation of 13.33% while the new method is slightly better giving an average deviation of –1.51% and a RMS deviation of 10.94%

HTFS2 shows slightly more prediction scatter, ranging from +26% to –58%, whereas the new method shows scatter with a range of +25% to –52%. The new method also performs generally better at higher Reynolds numbers. The new method predicts 98% of the data within ±20%, whereas the HTFS2 method predicts 96% of the data within the same band.

6.8.2 Heat transfer

Figure 6.12 presents deviation of predicted heat transfer (*j* factor) from the measured data using data from the VWT source. It can be seen that both methods perform poorly for extremely low Reynolds numbers, but very well over the rest of the range. The new method slightly outperforms HTFS2 by giving maximum and minimum deviations of 76% and –42% while HTFS2 gives maximum and minimum deviations of 82% and –40% respectively

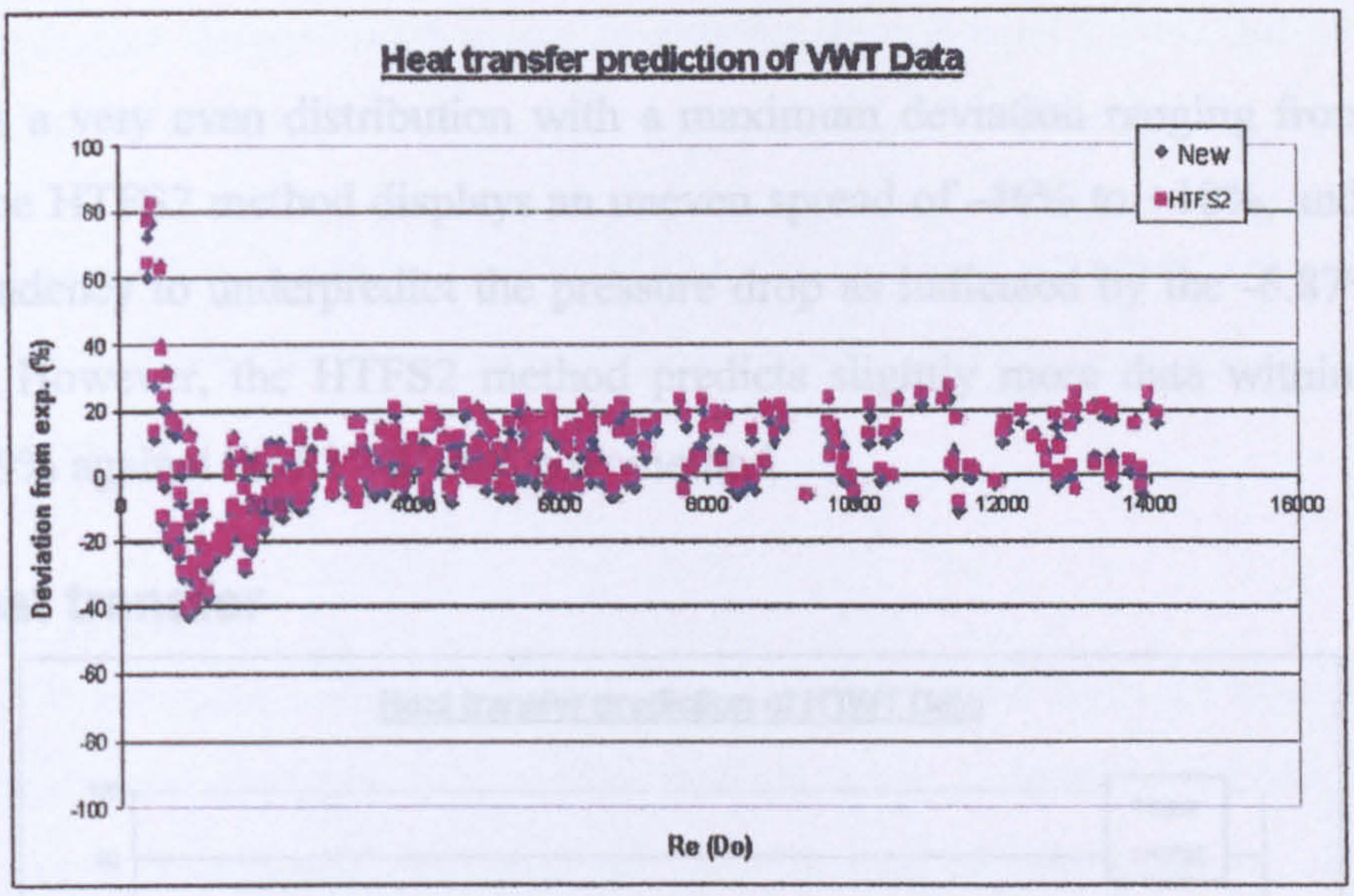

Figure 6.12: Comparison of heat transfer (j-factor) for the VWT source

The new method exhibits a lower average deviation of only 1.9% against an average deviation of 3.43% for HTFS2. 91% of all the data is now predicted within ±20% while HTFS2 predicts 88%.

6.9 Comparison with heat recovery bundles

6.9.1 Pressure drop

Figure 6.13 compares the new method with HTFS2 for the heat recovery test data from the HTWT source. The tendency is for slight overprediction with the new method as shown in the average deviation of 4.82% given in Table 6.4. This makes it safer to use.

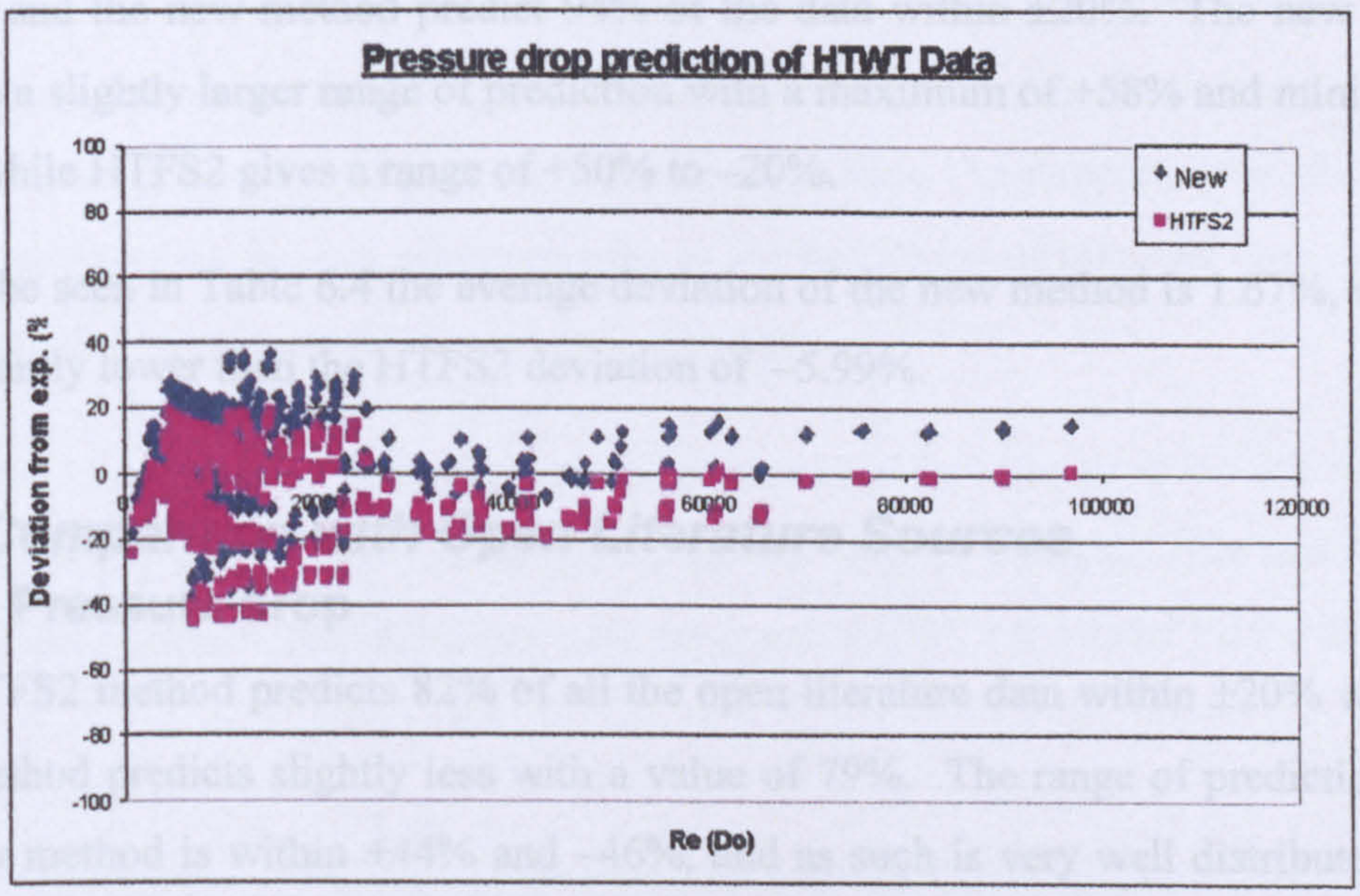

Figure 6.1: Comparison of pressure drop for the HTWT source

It also has a very even distribution with a maximum deviation ranging from -37% to +36%. The HTFS2 method displays an uneven spread of -46% to +18%, and therefore has the tendency to underpredict the pressure drop as indicated by the -6.87% average deviation. However, the HTFS2 method predicts slightly more data within ±20%. It predicts 89% against the 81% by the new method.

6.9.2 Heat transfer

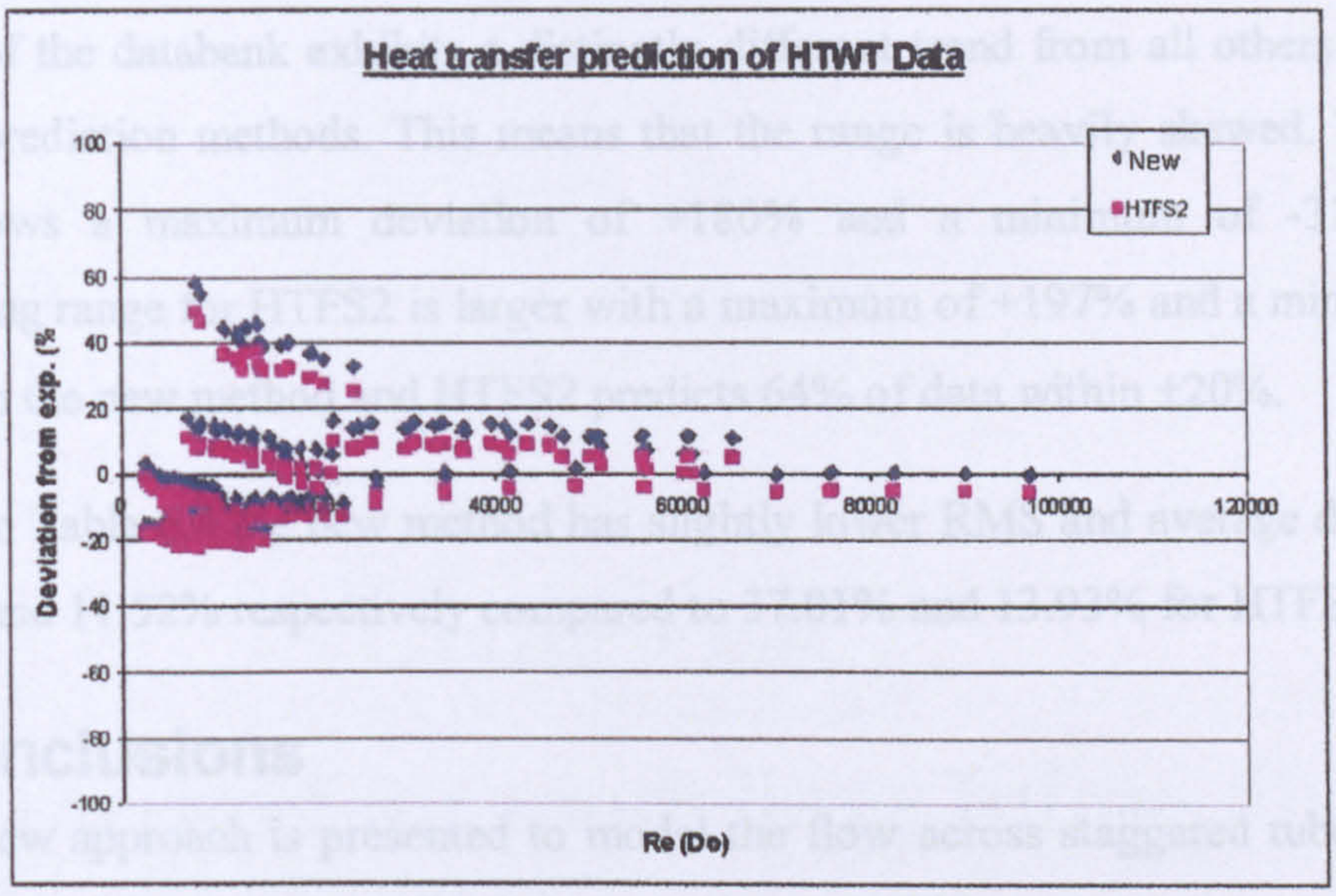

Figure 6.14: Comparison of heat transfer (j-factor) for the HTWT source

Predictions of heat transfer for the HTWT source are shown in Figure 6.14. Both HTFS2 and the new method predict 94% of the data within ±20%. The new method exhibits a slightly larger range of prediction with a maximum of +58% and minimum of –20% while HTFS2 gives a range of +50% to –20%.

As can be seen in Table 6.4 the average deviation of the new method is 1.67%, which is significantly lower than the HTFS2 deviation of –5.99%.

6.10 Comparison with Open Literature Sources

6.10.1 Pressure drop

The HTFS2 method predicts 82% of all the open literature data within ±20% while the new method predicts slightly less with a value of 79%. The range of predictions with the new method is within +44% and –46%, and as such is very well distributed about the zero. This is compared to +34% and -58% for the HTFS2 method.

Table 6.4 shows that the new method has an average deviation of 2.24%, better than the value of –4.17% for HTFS2.

From these comparisons it can be concluded that the new method tends towards a slight over prediction, whereas HTFS2 tends towards underprediction. This indicates that the new method is slightly on the safe side.

6.10.2 Heat transfer

Source 10 of the databank exhibits a distinctly different trend from all others sources, for all the prediction methods. This means that the range is heavily skewed. The new method shows a maximum deviation of +180% and a minimum of -31%. The corresponding range for HTFS2 is larger with a maximum of +197% and a minimum of –29%. Both the new method and HTFS2 predicts 64% of data within ±20%.

As shown in Table 6.4 the new method has slightly lower RMS and average deviations of 33.65% and 11.52% respectively compared to 37.01% and 13.93% for HTFS2.

6.11 Conclusions

- A new approach is presented to model the flow across staggered tube bundles through the use of an effective gap ratio term. This term seems to accurately represent the change in pressure drop due to change in tube layout arrangement over a wide range of flow Reynolds number.

- The new method, resolves the problem of under-predicting the pressure drop for tube bundles with 10 tube rows or more, solving the deficiency of HTFS2. It also provides general improvements to the prediction of pressure drop and heat transfer for staggered tube bundles with plain high fins.

- The new method presents generally improved prediction over the previous methods, and is released by HTFS as the HTFS3 method. This method was implemented in the HTFS software programs ACOL v.6.30 and FIHR v2.10.

CHAPTER 7

New method for modelling Inline finned tube bundles

7.0 Introduction

The original HTFS inline prediction method of Chu and Ralston [23], known as HTFS1α, had been developed from limited data sources, and was acknowledged by them to be an initial attempt rather than a fully developed prediction method. PFR [13] had been shown by Chu and Ralston to overpredict the heat transfer of their databank, although until the work presented in this chapter, it was the method recommended and used by HTFS in its software products, ACOL and FIHR.

The prediction methods of PFR [13] and Chu and Ralston [23] were tested against the newly expanded HTFS databank. Another inline method, that of Weierman [14], was also used. The Weierman method was developed for the ESCOA Corporation and was generally well regarded for the performance prediction of heat recovery bundles. The results of this testing, as will be shown, showed that each of these methods had a deficiency, PFR and Weierman both tending to extreme overprediction of heat transfer performance. This showed that there was a need for a new prediction method.

This Chapter shows the development of a new method for the performance prediction of inline finned tube bundles based on the new inline bundle air-cooler data shown in Chapter 4, the contents of the HTFS inline bundle databank and observations made on CFD models of some of the tested bundles. The use of CFD allowed an insight into the flow behaviour in the bundles and will be shown to have contributed directly to the development of a key part of the model.

7.1 CFD study of inline bundles

7.1.1. Model geometry

The inline tube bundle's domain was a section as shown in Figures.7.1 and 7.2 below.

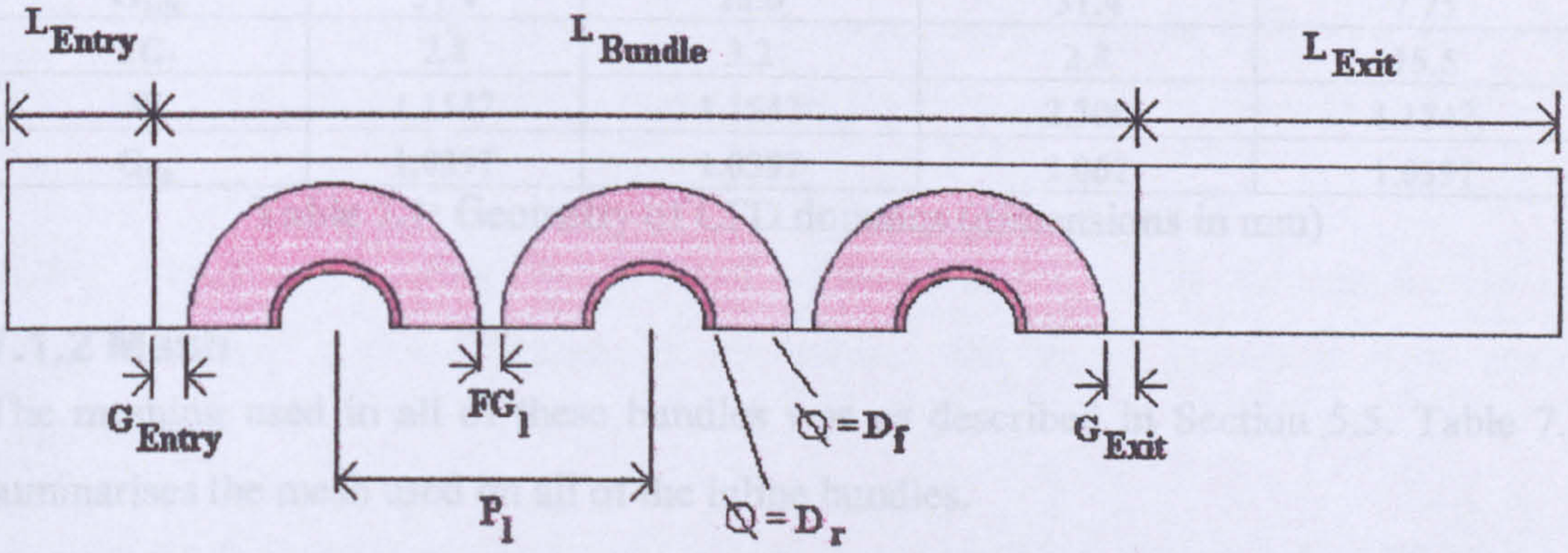

Figure 7.1: Elevation of test section geometry (only three rows shown)

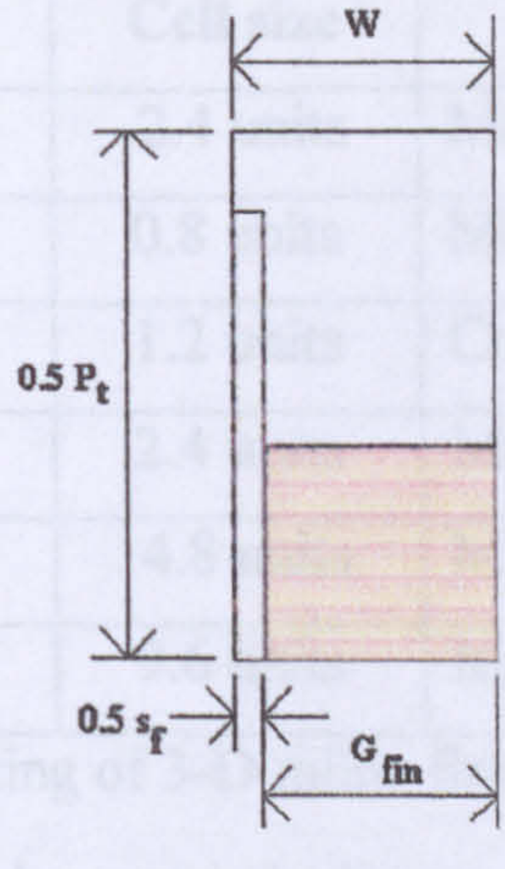

Figure 7.2: End elevation of test geometry

The height of the domain is simply half the transverse pitch of the bundle being modelled, as shown in Figure 7.2.

The inline tube bundles used in the study were Bundles 1, 3, 4 and 9 reported in Section 4.3. The refined geometry used for these bundles is shown in Table 7.1.

Bundle:	1	3	4	9
P_t	60	54	60	60
P_L	60	54	60	72.7
D_r	25.4	25.4	25.4	25.4
D_f	57.2	50.8	57.2	50.8
s_f	0.231	0.231	0.231	0.231
L_{entry}	120	108	120	145.4
L_{bundle}	420	378	420	363.5
L_{exit}	600	540	600	727
G_{entry}	31.4	28.6	31.4	7.75
G_{exit}	31.4	28.6	31.4	7.75
FG_l	2.8	3.2	2.8	15.5
W	1.1547	1.1547	2.309	1.1547
G_{fin}	1.0397	1.0397	2.062	1.0397

Table 7.1: Geometry of CFD domains (dimensions in mm)

7.1.2 Mesh

The meshing used in all of these bundles was as described in Section 5.5. Table 7.2 summarises the mesh used on all of the inline bundles.

Region	Cell type	Cell size	Meshing scheme
Inlet	Hexahedron	2.4 units	Map
Tubes and fins	Hexahedron	0.8 units	Map
Bundle	Hexahedron	1.2 units	Cooper
Exit 1	Hexahedron	2.4 units	Map
Exit 2	Hexahedron	4.8 units	Map
Exit 3	Hexahedron	9.6 units	Map

Table 7.2: Meshing of 3-D inline finned tube bundles

The cell size is proportional to a characteristic dimension of the model geometry and as such has no units, as the mesh is designed in non-dimensional units. SI units are only applied when the model is loaded into the CFD solver.

7.1.3 Tubeside boundary conditions

Given that the models were representing the bundles described in Section 3.3 the following assumptions were made: Only part of the steam entering the tubes was reduced to condensate during the tests, and therefore the energy removed from the process fluid was the latent heat of the steam. Therefore it was believed that an isothermal condensation was taking place, and this led to the assumption that the inner surface of the tubes was maintained at approximately 100°C. For the individual CFD models this temperature was set as the average of the experimentally measured average inner tube steam temperatures. By making this assumption, essentially the heat removed in the CFD models is sensible heat, and the extra duty due to the change in enthalpy is not taken into consideration.

In the MPWT the overall tubeside duty was calculated from the following series of equations. The latent heat removed from the saturated steam was as given in Equ.7.1.

$$Q_{lat} = mfr_{Cond} h_{ev} \qquad \text{(Equ.7.1)}$$

where mfr_{Cond} is the mass flow rate of condensate and h_{ev} is the latent heat of evaporation, and is the difference in the vapour and liquid phases at bulk steam temperature.

The duty performed to remove superheat from the steam was as given in Equ.7.2.

$$Q_{Sup} = mfr_{Steam} h_{Sup} \qquad \text{(Equ.7.2)}$$

where mfr_{Steam} was the mass flow rate of steam, h_{Sup} was the enthalpy of the superheated steam above saturation conditions. Usually there was no superheat present in the steam.

The Subcooling duty of the condensate was calculated from Equ.7.3

$$Q_{Sub} = mfr_{Cond}(Cp_{Sat}T_{Sat} - Cp_{Cond}T_{Cond}) \qquad \text{(Equ.7.3)}$$

where mfr_{Cond} was the mass flow rate of condensate, Cp_{Sat} was the specific heat at constant pressure of the steam at saturation conditions, T_{Sat} was the saturation temperature of the steam, Cp_{Cond} was the specific heat at constant pressure of the condensate, T_{Cond} was the saturation temperature of the condensate at outlet.

The total tubeside duty was calculated from Equ.7.4

$$Q_T = Q_{lat} + Q_{Sup} + Q_{Sub} \qquad \text{(Equ.7.4)}$$

When these calculations were performed with experimental values it was found that the duty attributable to superheat removal and condensate subcooling was a maximum of 1.19% of the total tubeside duty, so could be considered negligible.

The alternative to accepting the constant tubeside temperature solution was to either make a model that replicated the width of the experimental exchanger duct, which was wholly impractical, or set the CFD solver to iterate on steam tubeside conditions. This would have involved using the model geometry sequentially from the steam inlet to the steam outlet, with the solver updating the vapour and liquid condition across each step. Again this was impractical, due to time considerations.

7.1.4 Validation Results

Figures 7.3 to 7.6 show the comparisons of CFD prediction and experimental measurements of pressure drop for the inline air coolers described in Section 3.3.

It can be seen in Figure 7.3 that there is very good agreement, especially for the first and last points. It is unclear why there is scatter in the prediction, rather than a constant over or underprediction tendency. Figure 7.4 shows the predicted pressure drop for Bundle 3. As with Bundle 1 the prediction is generally very good, but shows variations between over and underprediction.

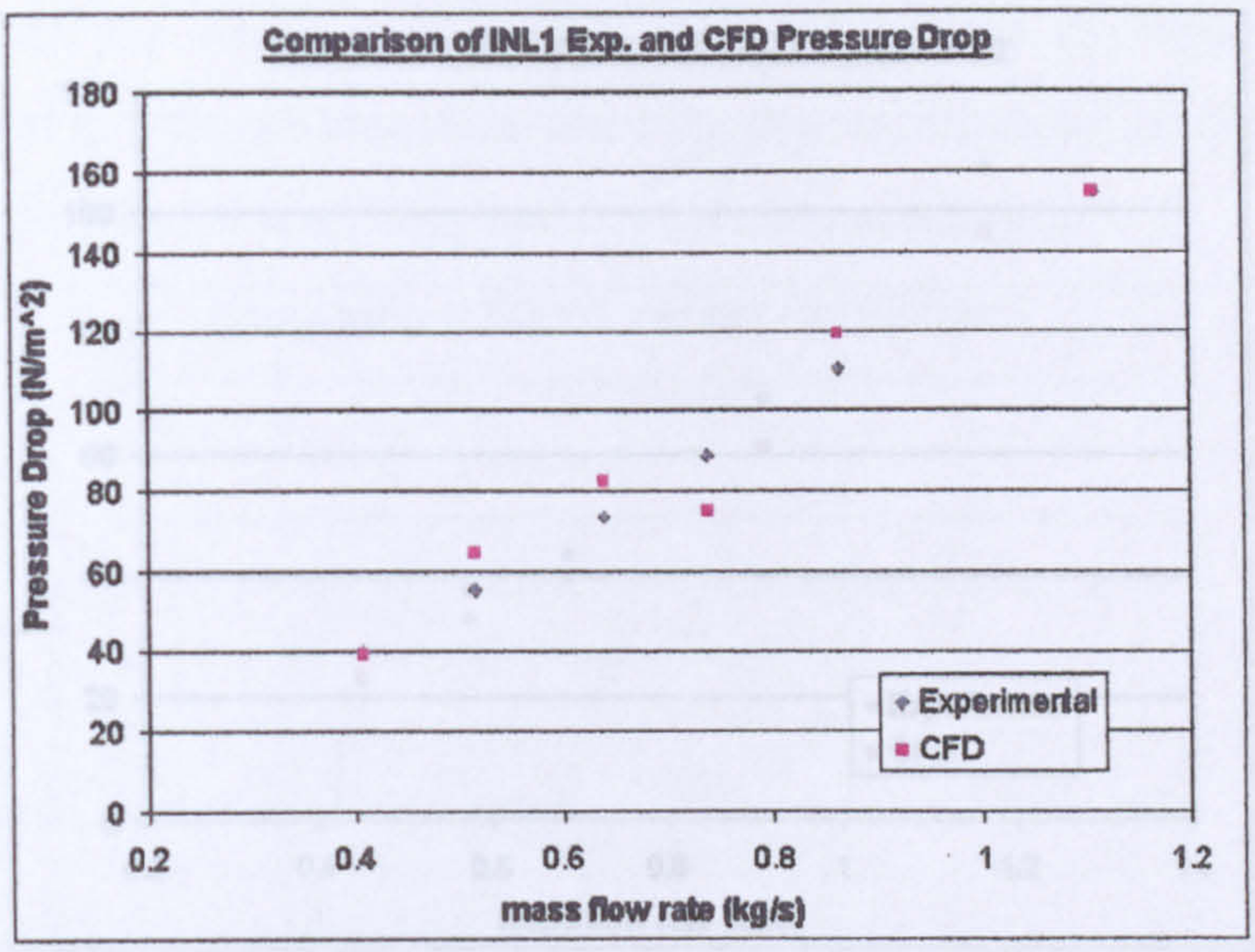

Figure 7.3: Pressure Drop Measurement and Prediction of Bundle 1

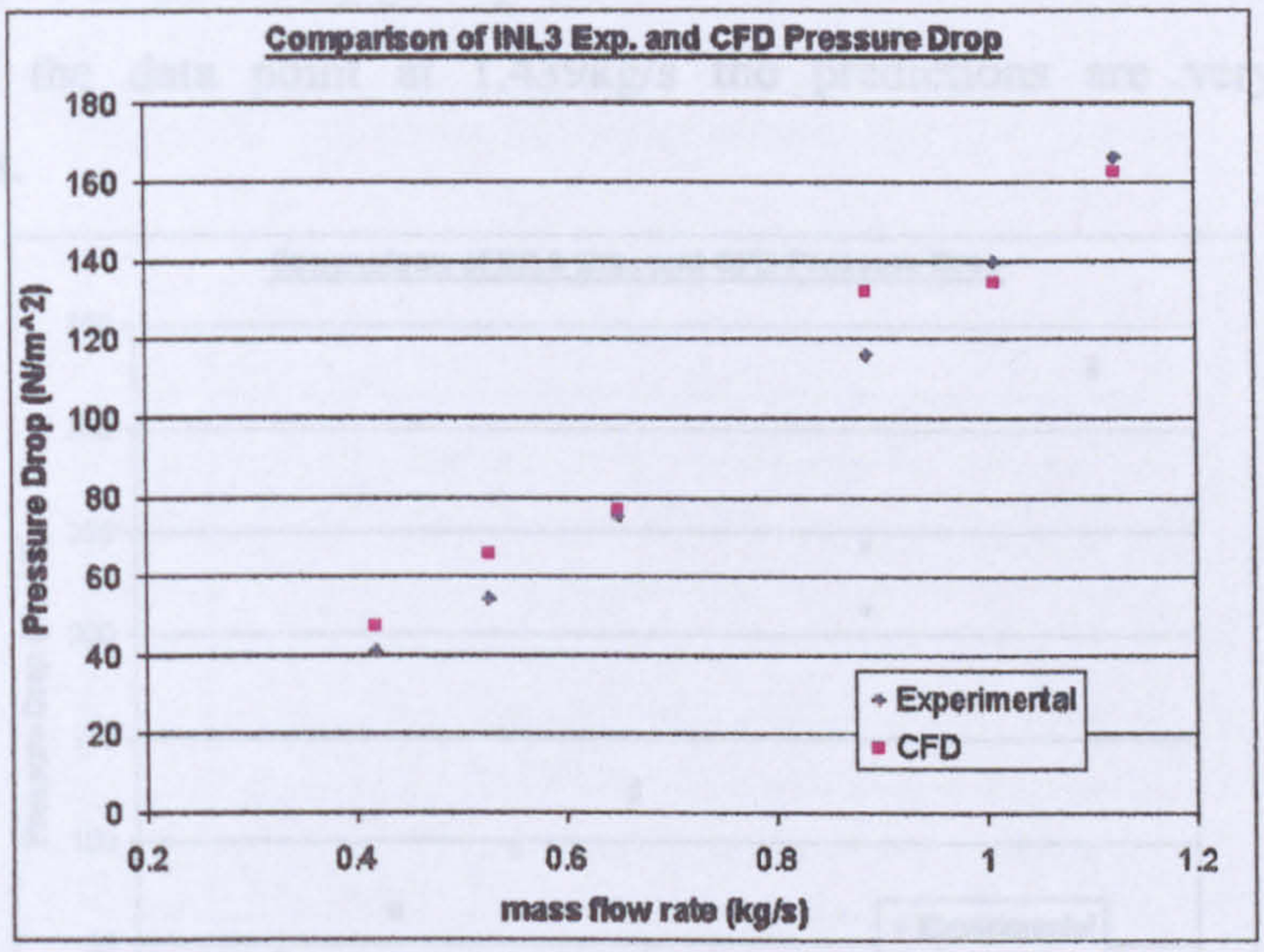

Figure 7.4: Pressure Drop Measurement and Prediction of Bundle 3

Figure 7.5 shows a close prediction for the pressure drop of the bundle with low fin frequency. There is a tendency for underprediction at higher flow rates. This may be due to difficulty for the CFD resolving the relatively high shear in the gap flow between the fins, although it would be expected that the resolved wall model described in Section 5.9.2 would allow for this.

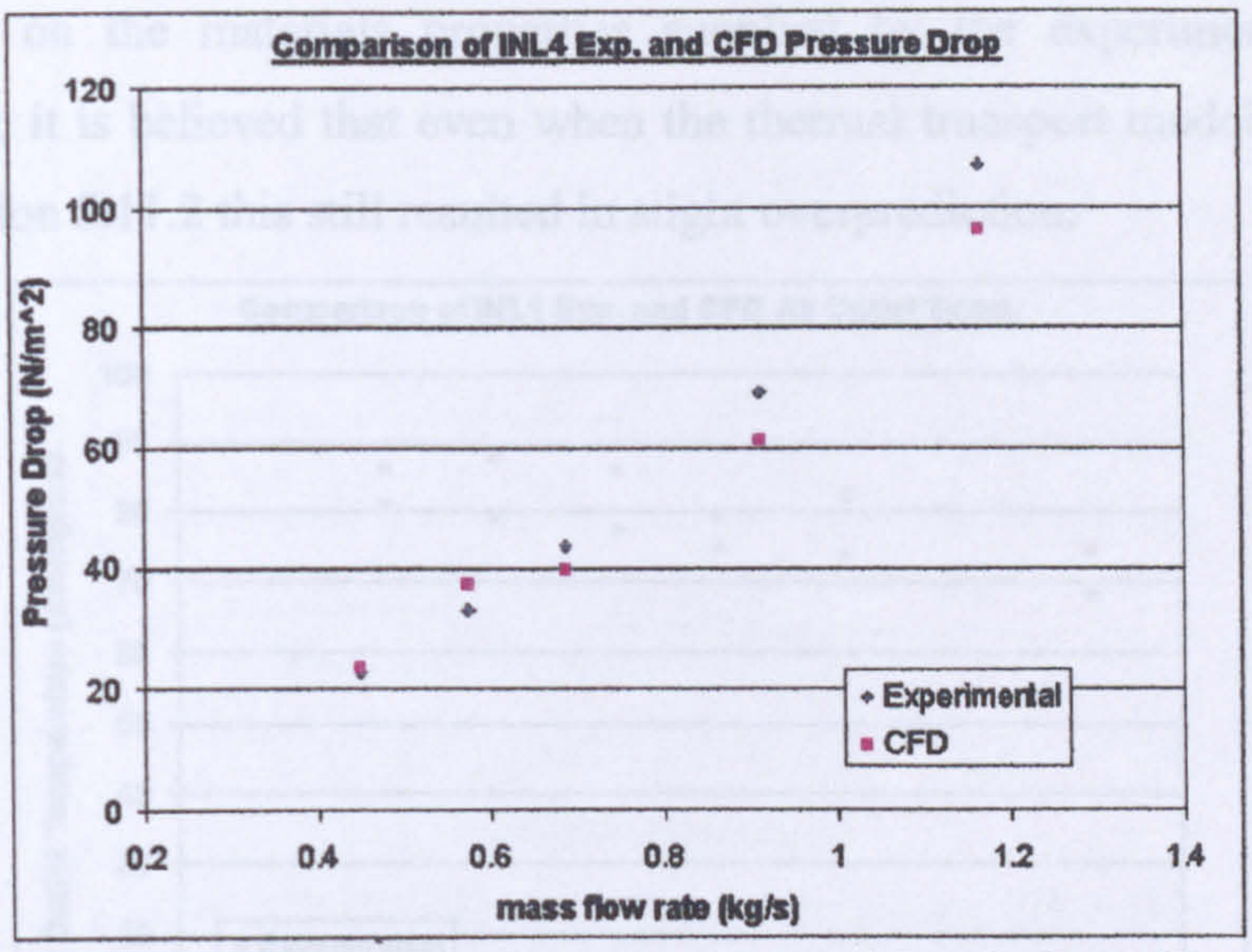

Figure 7.5: Pressure Drop Measurement and Prediction of Bundle 4

Figure 7.6 shows an extremely good prediction for Bundle 9. It can be seen that with the exception of the data point at 1.439kg/s the predictions are very close to the measurements.

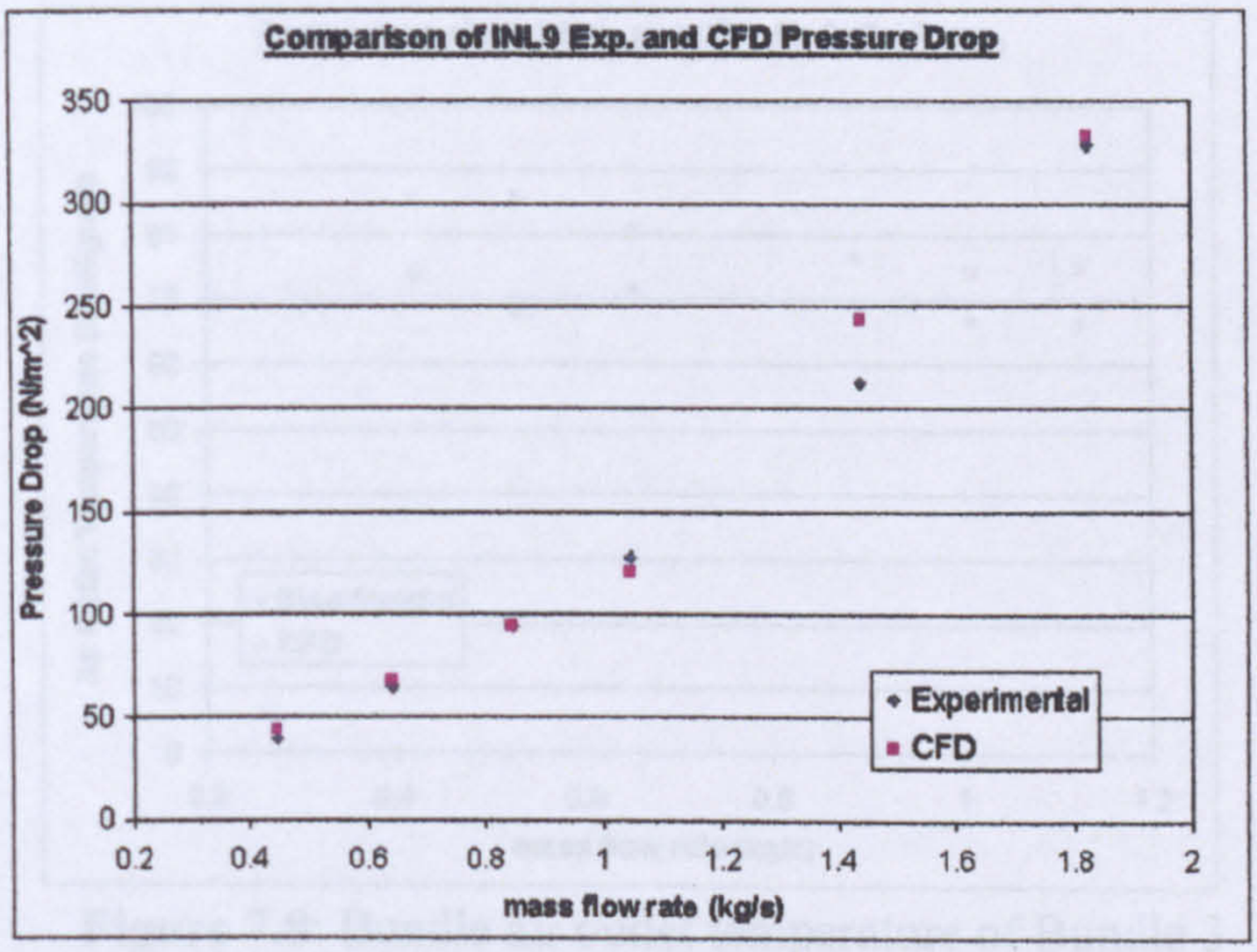

Figure 7.6 Pressure Drop Measurement and Prediction of Bundle 9

7.1.5 Heat Transfer results

It can be seen in Figures 7.7 to 7.10 that even with very careful modelling, the CFD overpredicted the heat transfer. By exhibiting a higher air outlet temperature this indicates that the surface heat transfer coefficients are likely to be over predicted. Given that the thermal conductivity of the fins and tubes were explicitly stated in the CFD

input, based on the materials properties supplied by the experimental equipment manufacturer, it is believed that even when the thermal transport model was altered as noted in Section 5.11.2 this still resulted in slight overprediction.

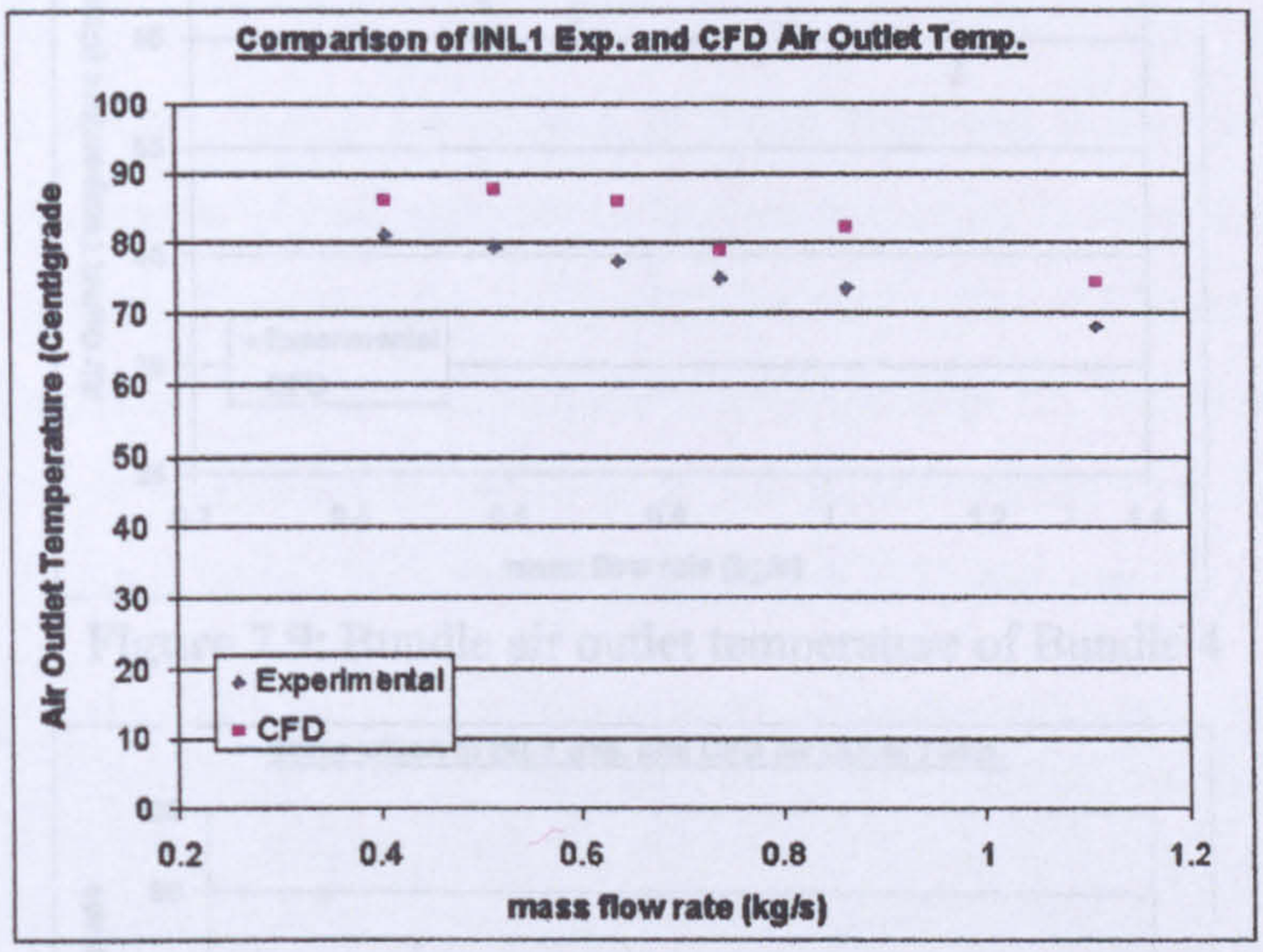

Figure 7.7: Bundle air outlet temperature of Bundle 1

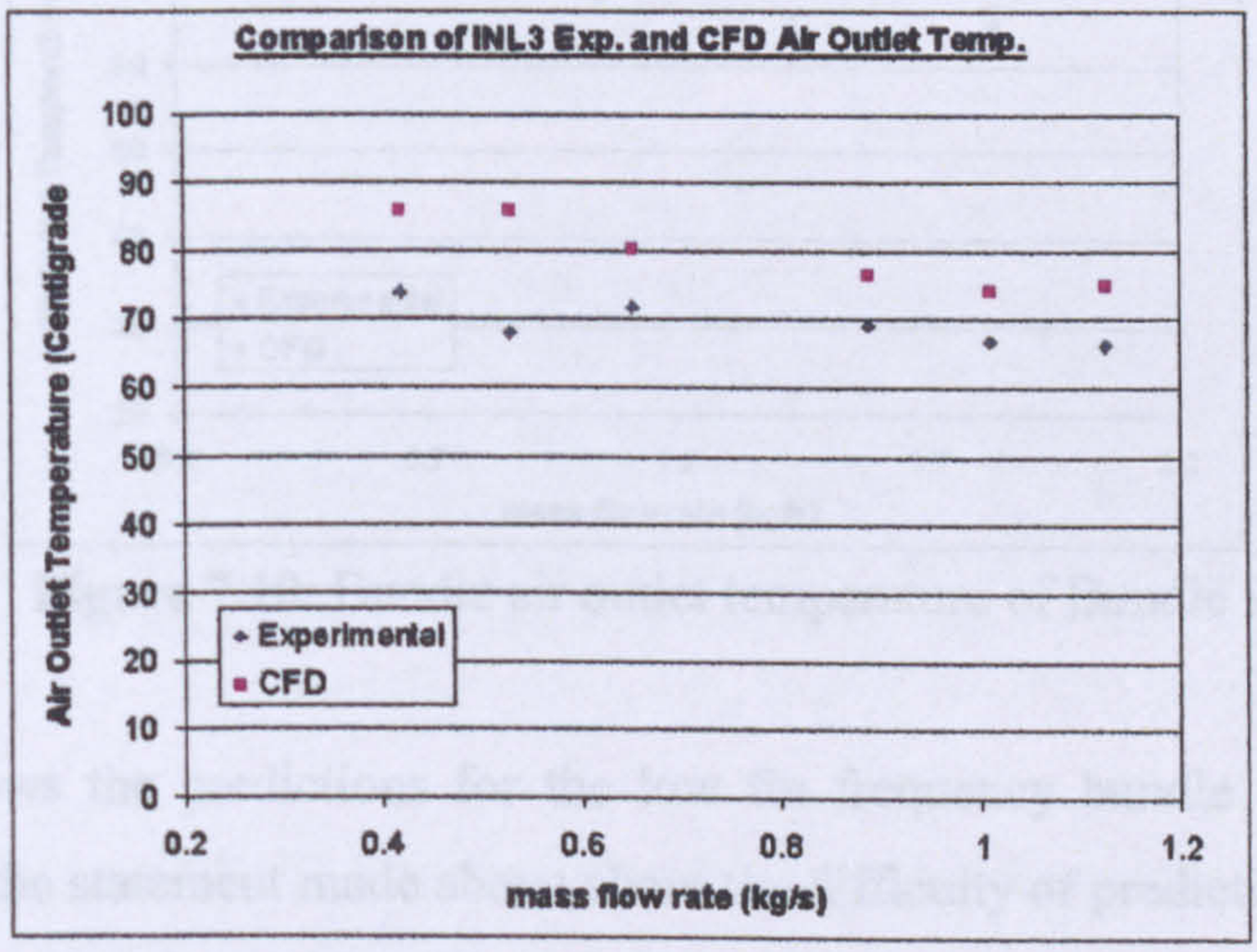

Figure 7.8: Bundle air outlet temperature of Bundle 3

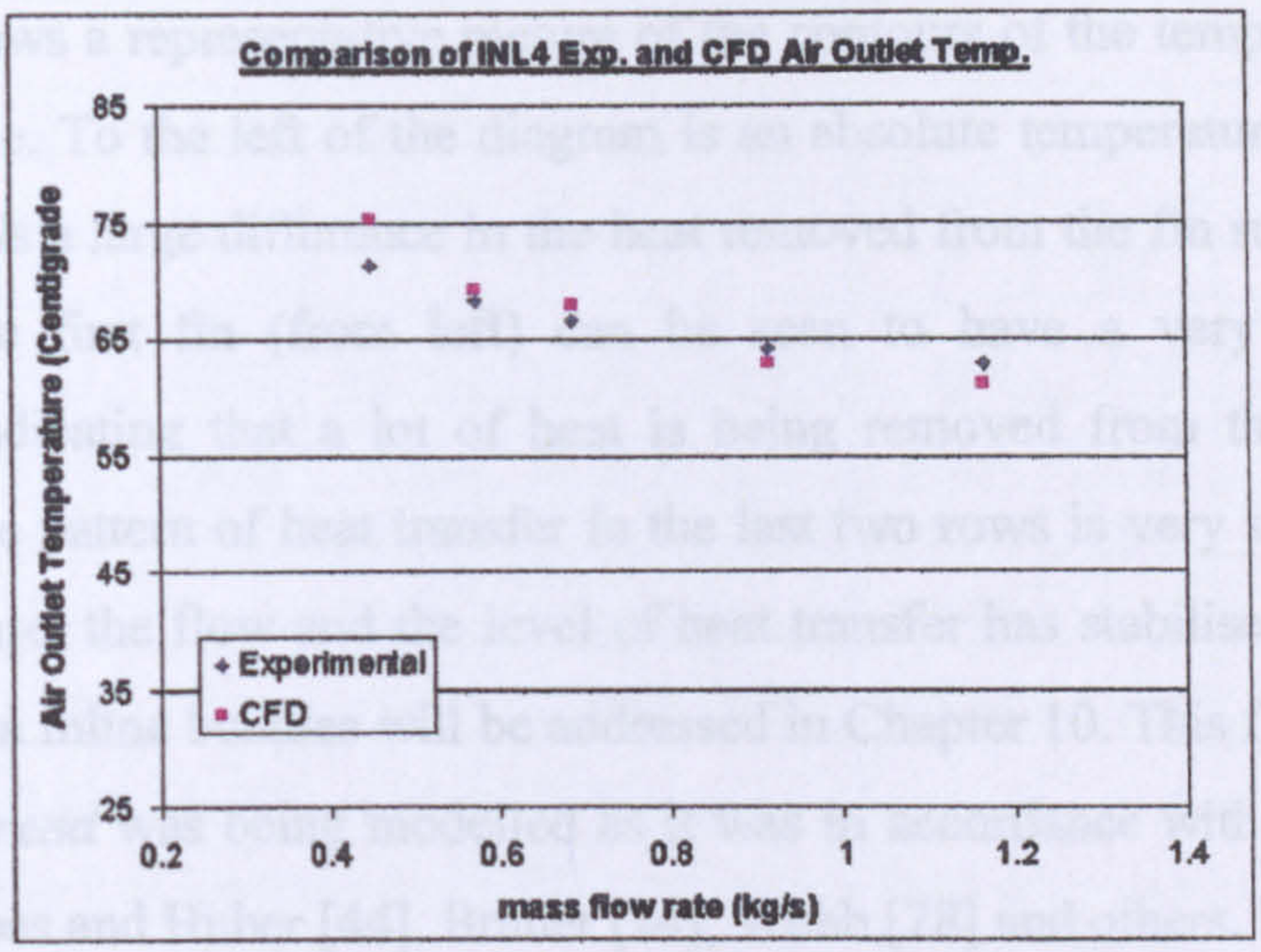

Figure 7.9: Bundle air outlet temperature of Bundle 4

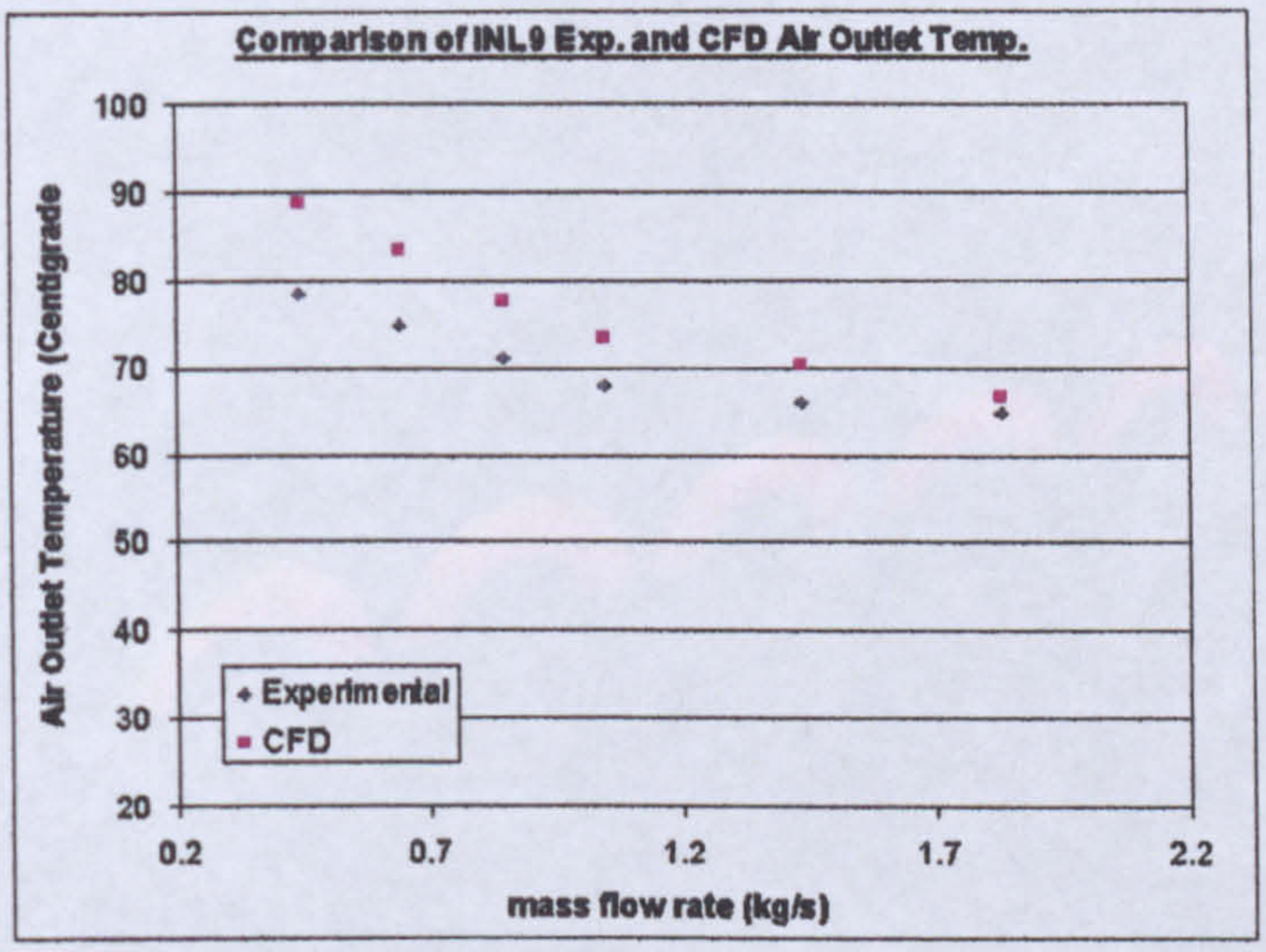

Figure 7.10: Bundle air outlet temperature of Bundle 9

Figure 7.9 shows the predictions for the low fin frequency bundle were particularly good. Despite the statement made above about the difficulty of predicting the high shear region between the fins with such relatively large velocity gradients, the thermal transport model appeared to have less difficulty in resolving the free flow bounded surface heat transfer. The channel between the fins is very narrow and it is likely that the turbulent flow models are in the poorly resolved zone between what would be free turbulent flow and the wall model. Therefore the solver is varying between turbulent and viscous sub-layer heat transfer.

Figure 7.11 shows a representative picture of the contours of the temperature of the fin and tube surface. To the left of the diagram is an absolute temperature scale. It can be seen that there is a large difference in the heat removed from the fin surface as the flow progresses. The first fin (from left) can be seen to have a very reduced surface temperature, indicating that a lot of heat is being removed from the first tube row. Interestingly the pattern of heat transfer in the last two rows is very similar; indicating that, for this case, the flow and the level of heat transfer has stabilised. This point and the row effect in inline bundles will be addressed in Chapter 10. This figure reassures us that a correct *trend* was being modelled as it was in accordance with the experimental findings of Rabas and Huber [44], Brauer [24], Webb [78] and others.

Figure 7.11: Temperature contours over fins and tubes for Bundle 3 at 0.79kg/s
(Flow direction left to right, temperature scale (K) on left)

7.1.6 Deviations of CFD predictions from experimental data

Table 7.4 shows the % deviations of the CFD pressure drop (PD) and air outlet temperature (HT) results.

Bundle 1			Bundle 3			Bundle 4			Bundle 9		
mfr (kg/s)	% Dev PD	% Dev HT	mfr (kg/s)	% Dev PD	% Dev HT	mfr (kg/s)	% Dev PD	% Dev HT	mfr (kg/s)	% Dev PD	% Dev HT
0.406	-1.50	6.34	0.417	14.10	16.15	0.448	2.58	5.65	0.443	14.34	13.44
0.516	16.20	10.64	0.528	21.47	26.36	0.574	12.34	1.60	0.641	5.35	11.46
0.637	12.38	10.99	0.651	1.85	11.83	0.686	-9.12	1.91	0.848	-0.22	9.34
0.739	-15.78	5.41	0.888	13.78	10.28	0.914	-11.53	-1.70	1.049	-5.25	8.20
0.865	7.96	11.88	1.01	-3.62	10.86	1.166	-9.86	-2.83	1.439	14.20	6.54
1.109	0.00	9.43	1.125	-1.98	13.40	-	-	-	1.829	1.28	2.87

Table 7.4: Deviation of CFD predictions from experimental data

Overall the predictions are very good, with the predictions of the low fin frequency bundle, Bundle 4, showing exceptionally good heat transfer results

7.2 Pressure loss characteristics of inline bundles

Henry [19] found that when pressure drop characteristics were plotted against velocity on logarithmic scales all could be said to be parallel and of constant slope. This could be expressed as the pressure drop increasing in proportion to the gas side velocity raised to the power of 1.7. This was repeated for the inline bundles, and the results shown in Figure 7.12. The source numbers of the bundles used are given in the legend, and relate to the source numbers given in Table 4.14.

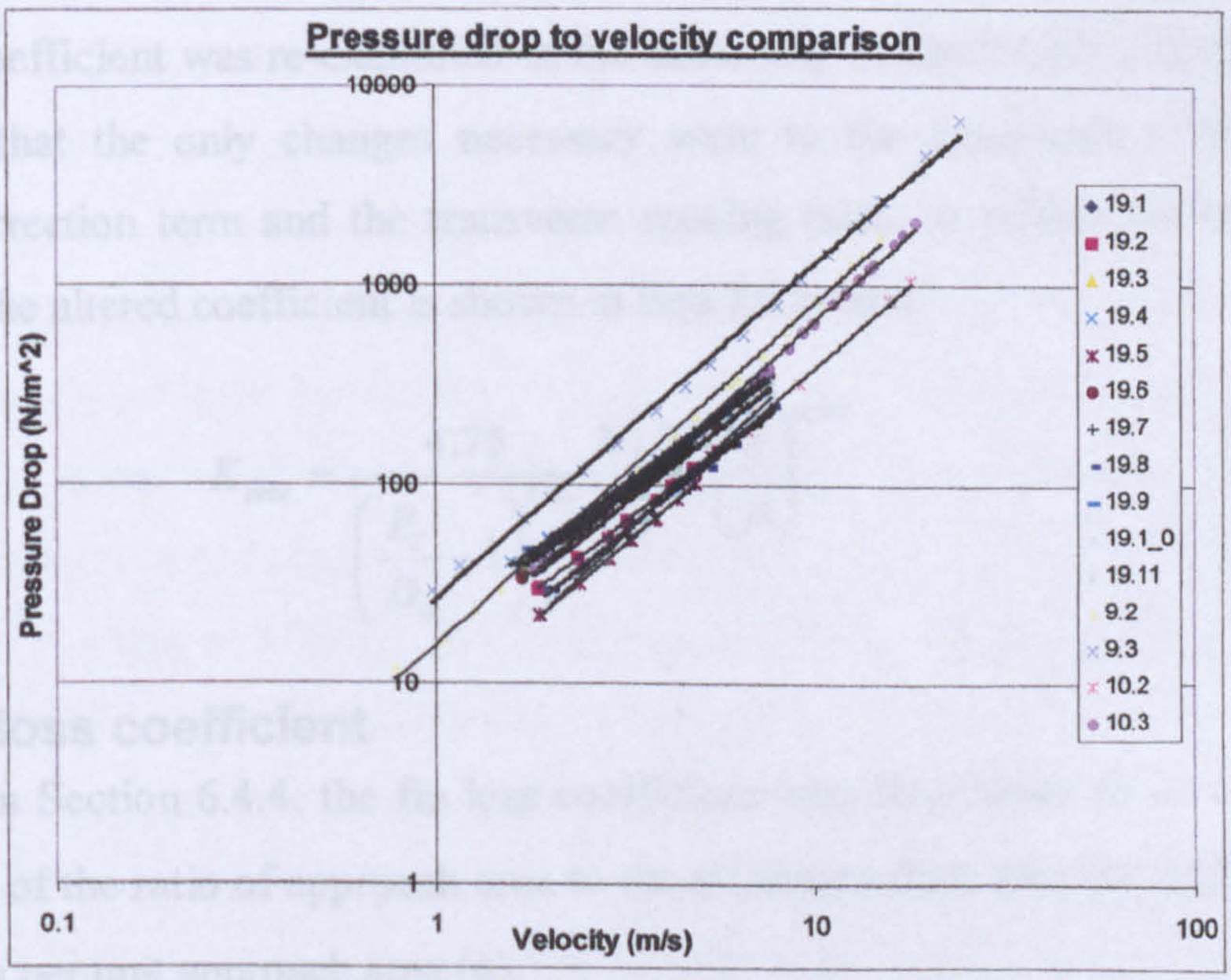

Figure 7.12: Effect of air velocity on pressure loss

It was found that the pressure drop of inline bundles varied in proportion to 1.56. This new exponent would be used in place of the 1.7 velocity exponent shown by Henry [19], but is specific to inline bundles.

7.3 New tube and fin loss model

The new models are based on the premise that the base case is that of fin tips touching, which for a given geometry would result in the maximum possible pressure drop. The more common case where there is a gap between the fin tips will be shown later.

7.3.1 Tube loss coefficient

With a new velocity exponent being found, it was apparent that the importance of the tube contribution to loss was re-evaluated by re-examining the data of ESDU [20], as previously explained in Chapter 6. ESDU [20] did not account for all inline arrangements such as rectangular pitches, but the formulation of the tube loss coefficient (K_{tube}) presented by Ralston et.al. [21] for staggered bundles was found to behave correctly. This was determined by examination of the pressure drop data shown for the three inline air cooler bundles, described in Chapter 4. This data shows that for a given Reynolds number the pressure drop will increase with increasing longitudinal pitch (P_L).

When the coefficient was re-examined in the same way as described in Section 6.4.3 it was found that the only changes necessary were to the exponents of the physical property correction term and the transverse spacing ratio, to reflect the new velocity exponent. The altered coefficient is shown in Equ.7.5 below.

$$K_{tube} = \frac{4.75}{\left(\frac{P_T}{D_o} - 1\right)^{1.56}} \frac{N_R P_L}{D_o^{1.3}} \left(\frac{\eta}{\rho}\right)^{0.44} \qquad \text{(Equ.7.5)}$$

7.3.2 Fin loss coefficient

As shown in Section 6.4.4, the fin loss coefficient was determined to be a function of the product of the ratio of approach area to the minimum flow area (σ) and the total fin surface area per unit approach area (ϕ).

The fin loss coefficient constant was determined by employing a binary search algorithm to determine a value of the leading constant that produced the highest level of data prediction within the ±20% deviation points. A binary search was employed as the 489 data points in the databank, plus associated calculation time and data checking, would have led to an exhaustive search routine estimated to require a minimum of 30 years to complete!

The constant was determined to be 0.029, and the final fin loss equation is shown in Equ.7.6.

$$K_{fins} = 0.029\phi\sigma^{1.56} \qquad \text{(Equ.7.6)}$$

7.3.3 Fin tips touching coefficient

If the fins of adjacent tubes touch (no gaps) then the bundle pressure drop coefficient can be described by Equ.7.7

$$K_{ft} = K_{fins} + K_{tube} \qquad \text{(Equ.7.7)}$$

7.4 Augmented mass transfer coefficient

7.4.1 Horseshoe vortex generation

Previous HTFS models consider only the effects of the fin skin drag in the fin loss coefficient. A high-speed phenomenon not catered for is the formation of horseshoe vortices. These arise from the flow along the fin surface encountering an adverse pressure gradient at the junction of the fin and tube. The shear in the fin boundary layer is deflected by this pressure gradient. The deflected boundary layer is then wrapped around the tube, in the flow direction, by the momentum of the bulk flow through the fins, bounded on one side by the fin surface, and by the bulk flow on the other side, albeit loosely. Horseshoe vortices have been reported in many structures of engineering interest, especially in turbomachinery vanes and blades. Fox and West [81] showed the formation by a series of visualisation tests over a cylinder with end plates, Fisher and Eibeck [87] (1990) used a heated surface and heat sensitive liquid crystal paint to study the downstream effects on heat transfer, but of most relevance is the study of Sung et.al [80] who used a sublimated napthalene technique to quantify the mass transfer aspects that are of interest here. Figure 7.13 shows a diagram of this formation in finned tubes.

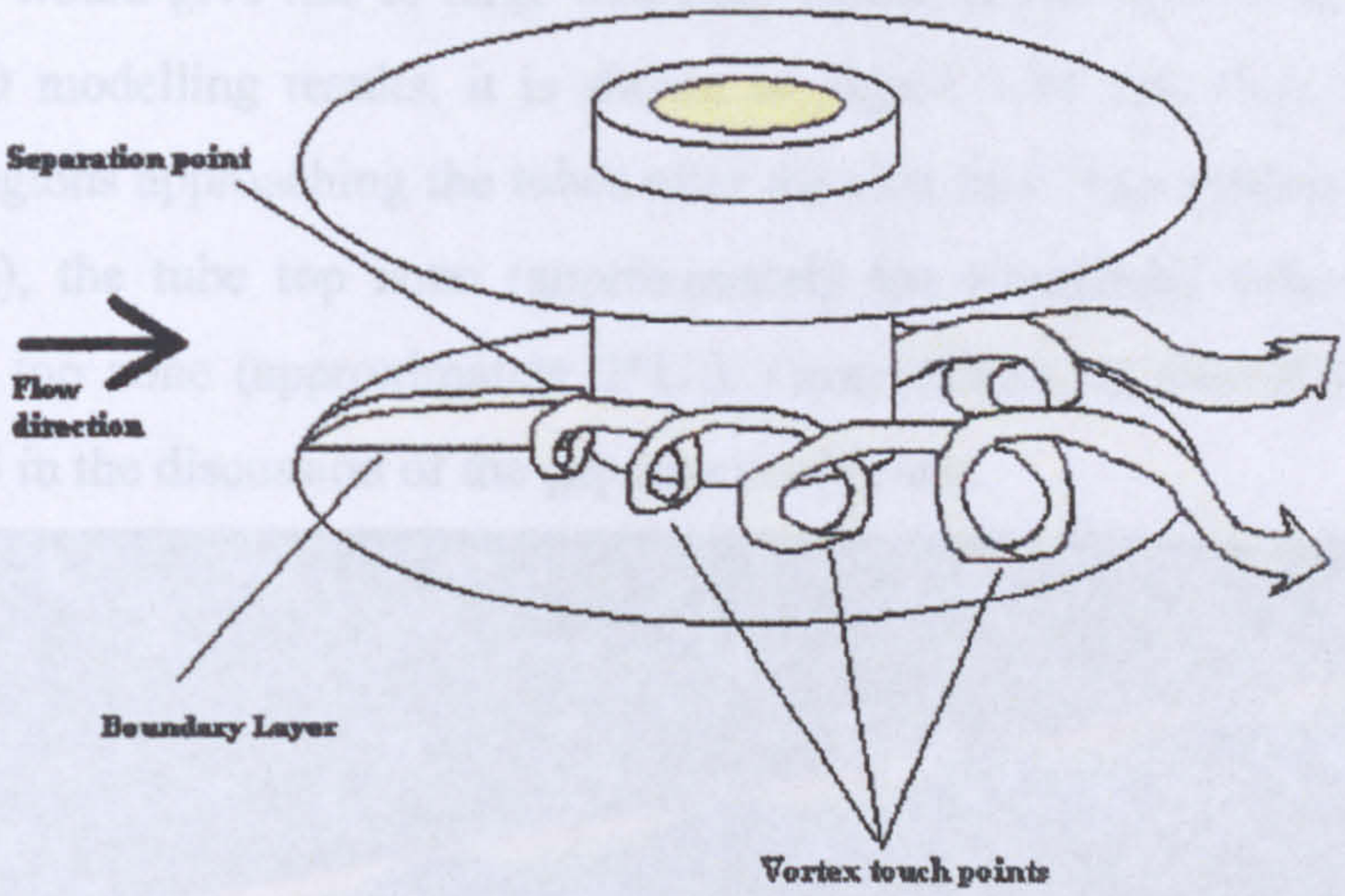

Figure 7.13: Schematic of a horseshoe vortex
(lower fin vortices shown only for clarity)

It was shown by Sung et.al. [80] that as the flow velocity increases for narrow fin gaps (Fin Height to Gap ratio of 0.11 to 0.15) the mass transfer in the fin/tube junction region, Figure 7.2, is improved by the formation of vortices. Fox and West [81] showed agreement with their study on splitter plates used in wind tunnel experiments on cylinders. They showed this in a series of pressure coefficient plots taken in the upper sub-critical Re range, with the splitter plates being progressively brought closer, analogous to finned tube. It can be seen in their results that the pressure coefficient for small plate spacings shows a substantial increase at the plate/cylinder junction. The definition of pressure coefficient is as given in Equ.7.8.

$$C_p = \frac{P_{Base} - P_\infty}{\frac{1}{2}\rho u_\infty^{\,2}} \qquad \text{(Equ.7.8)}$$

Where P_{Base} is the static pressure at any given point on the cylinder, P_∞ is the freestream static pressure, ρ is the freestream density and u_∞ is the freestream velocity.

It can therefore be seen that an increase in pressure coefficient relates to a decrease in local static pressure, which is directly proportional to a decrease in local flow velocity. This is consistent with the notion of the vorticity improving the local mass transfer.

7.4.2 Application to inline bundles

Given the 'shadow' effect discussed by Zukauskas and Ulinskas [36] and Zdravkovich [39], whereby the following tube lies in a low velocity region due to the preceding tubes

wake, this would give rise to large boundary layers on the fins of the following tubes. From CFD modelling results, it is shown in Figure 7.14 that there are three distinct velocity regions approaching the tubes after the first row. The shadow zone (low speed wake area), the tube top zone (approximately the superficial velocity, U_o) and the bypass/fin top zone (approximately $2*U_o$). Other effects of this will be addressed in section 4.5 in the discussion of the gap loss coefficient.

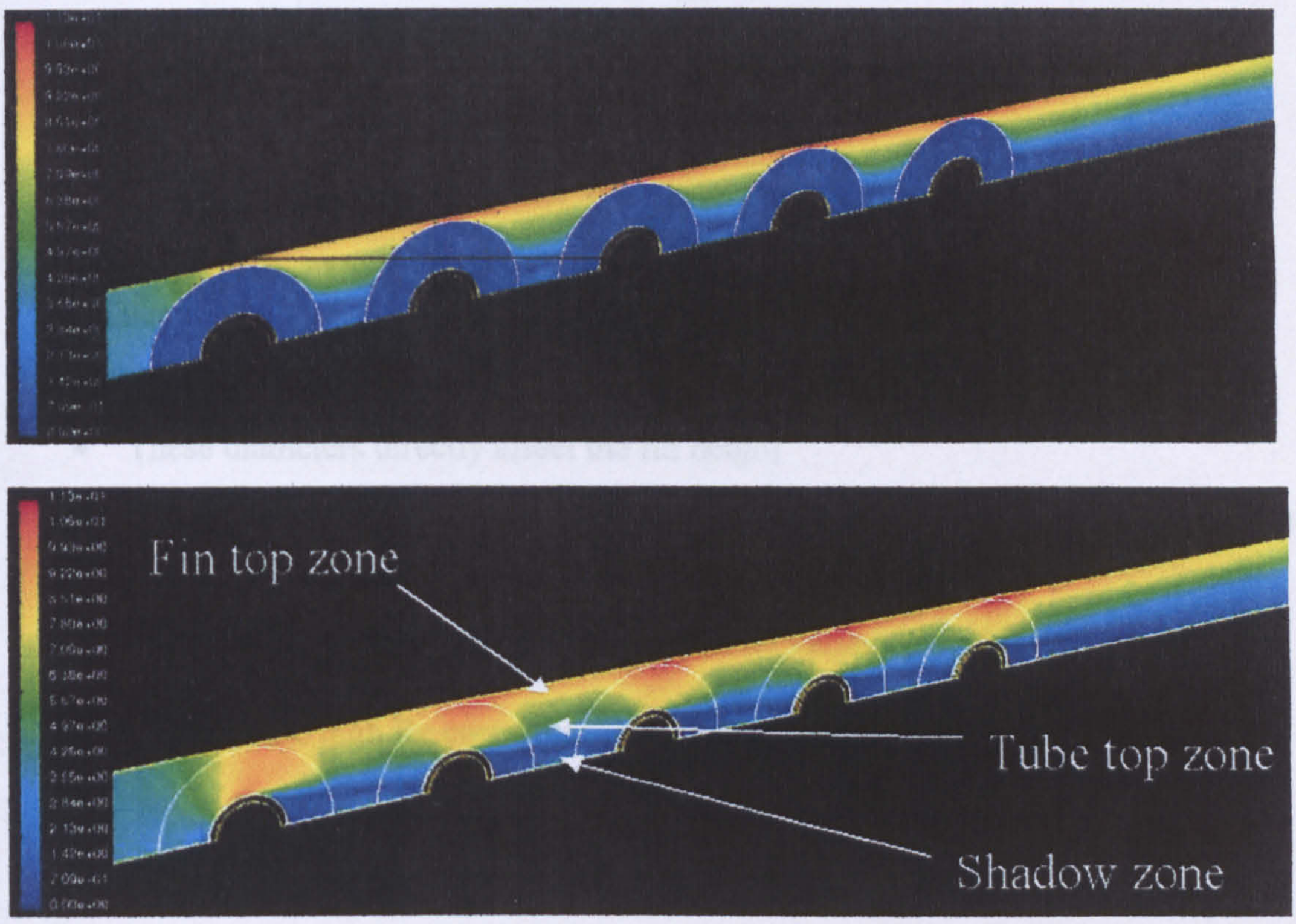

Figure 7.14: CFD velocity contour plots of Bundle 9
(Top: Fin plane, Bottom: midplane)

It is therefore reasonable to say that in inline finned tube bundles the shadow zone will create a thick low speed laminar/transitional boundary layer on the fins. The higher velocity flow will entrain the skewed boundary layers allowing the formation of the horseshoes, and the previously discussed local effects.

7.4.3.Augmented mass transfer model

The data of Sung et.al [80] is shown below. Figure 7.15 shows the averaged measured Sherwood number around a tube with fin gap/height ratios of 0.1-0.125.

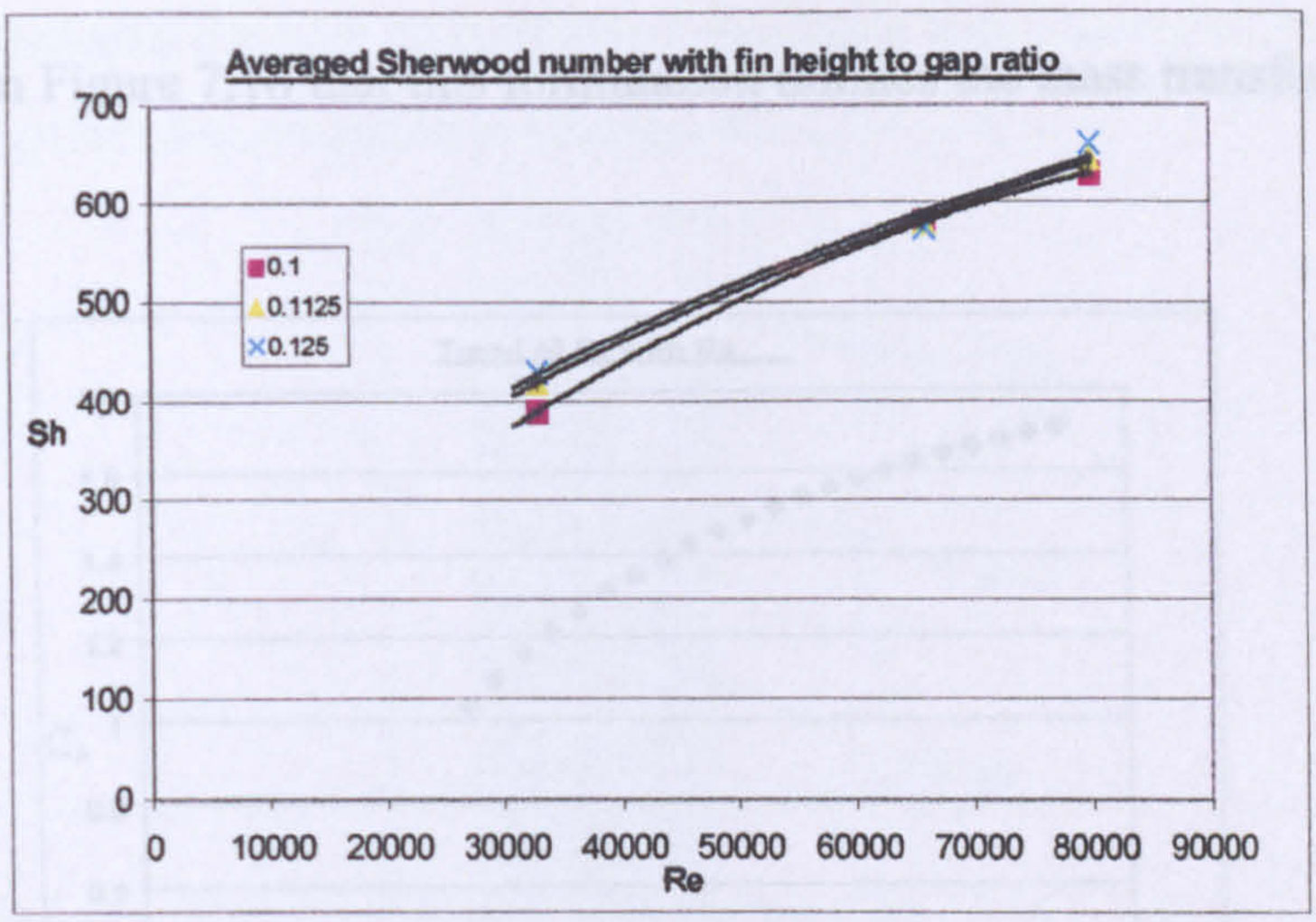

Figure 7.15: Sung et. al. (1996) averaged Sh for varying fin gap

Given that:

- The scale of a heat exchanger is found from its fin and tube diameters.
- These diameters directly affect the fin height
- It can be shown that the fin gap to height ratio varies little in practical exchanger designs (as can be seen in the HTFS databank)
- For these ratios the augmented mass transfer varies only slightly.

The formation of the high Re correction is approximated in Equ.7.9.

$$C_A = \left(\frac{D_f}{D_O}\right)^{\frac{\mathrm{Re}_{Do}-22000}{\mathrm{Re}_{Do}}} \qquad \text{(Equ.7.9)}$$

The caveat on this correction, however is that below a Re_{Do} value of 22000 the correction term is assumed to be unity, as it is unlikely that significant augmented mass transfer will take place below that value. This value is decided by:

- The statements of Sung et.al [80] is that the influence of horseshoe vortices is substantial at higher values of Reynolds number and dissipates quickly as the Re decreases.
- The momentum of the surrounding flow must be high to 'wrap' the vortices around the tube.
- The momentum in the boundary layer must be high for the full layer to be diverted by the pressure gradient, rather than simply dissipate, and flow over the tube as a boundary layer.
- That this value was the best fit for the databank contents.

It can be seen in Figure 7.16 that this formulation mimics the mass transfer trend shown in Figure 7.15.

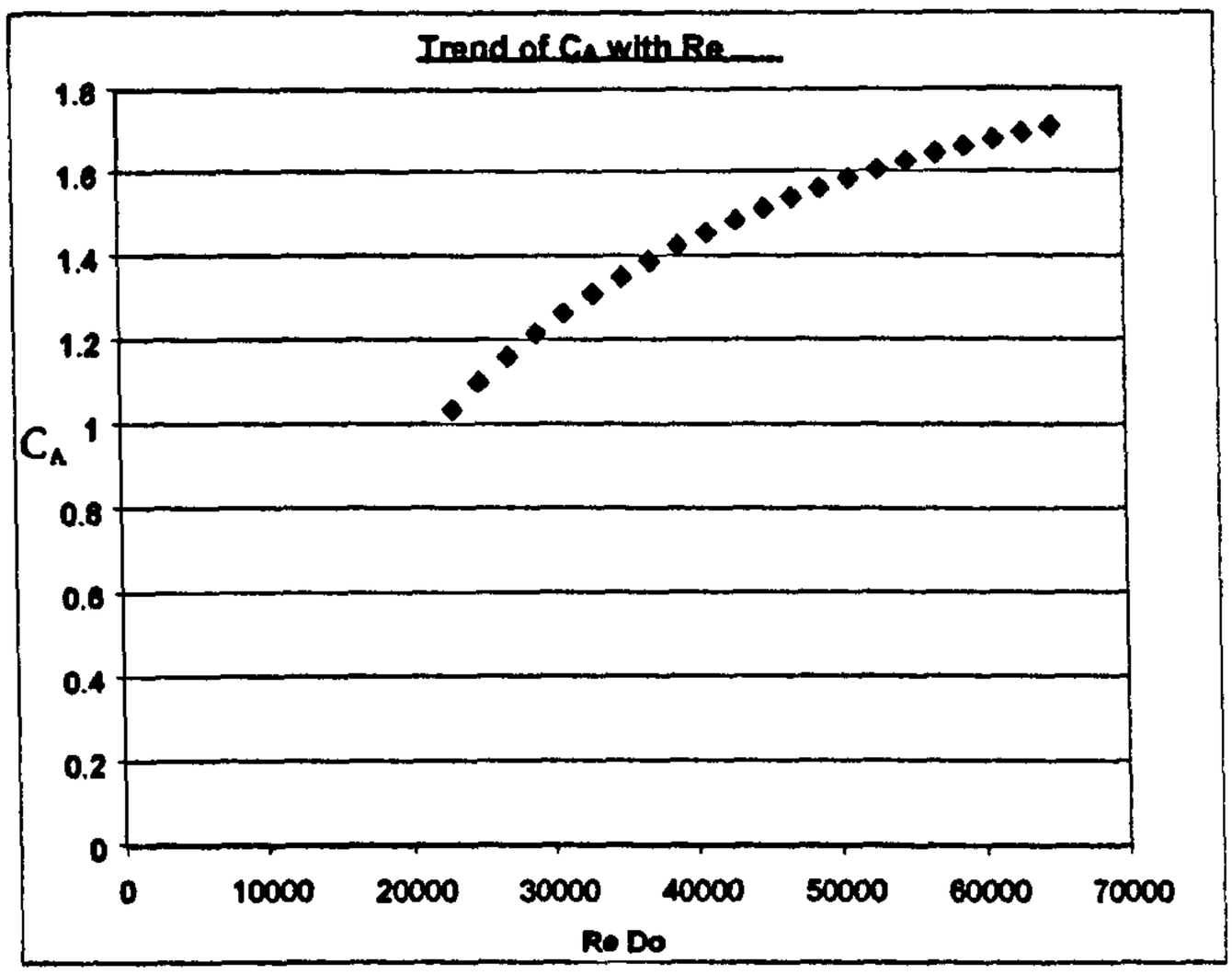

Figure 7.16: Trend of C_A (57.2mm fin, 25.4mm tube)

As indicated in Section 7.4.3 the Augmented Mass transfer Coefficient is therefore used to correct the combined tube and fin loss coefficient as given below in Equ.7.10.

$$K_{fA} = K_f C_A \qquad \text{(Equ.7.10)}$$

7.5 Gap loss coefficient

The gap loss coefficient was the most difficult parameter to determine, as it must reflect the distinct attributes of pure gap flow that is encountered in inline bundles.

The elements considered to characterise the bypass lane between the fin tips, and its development through the bundle were:

- The geometric free flow area.
- Number of rows crossed.
- Pitch arrangement (square, rectangular, rotated rectangular).
- The frictional boundary layer effects on the fin surface.

7.5.1 Flow area relation

As the transverse pitch of an inline bundle is increased, the potential for distinct gap flow increases. This means that the pressure drop will be reduced due to the flow

always going towards the path of least resistance. This was established by the results of the inline air cooler tests described in Chapter 4.

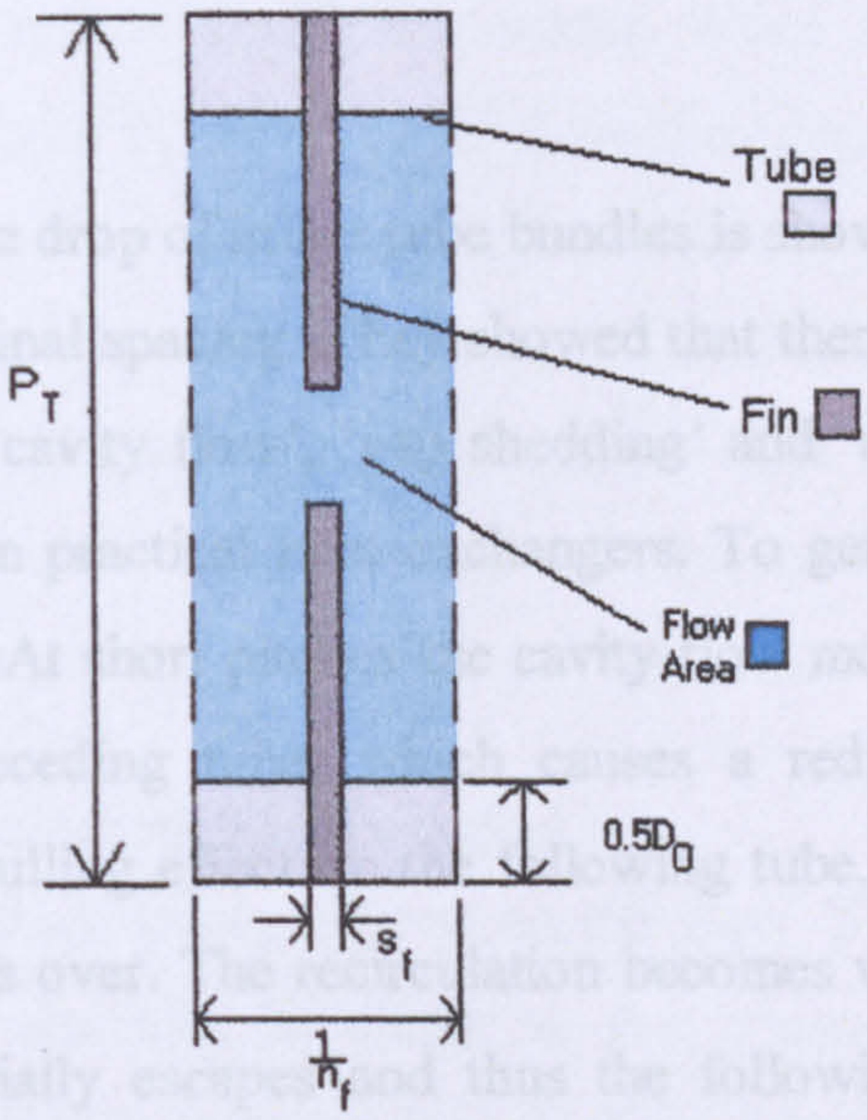

Figure 7.17: Blockage area in a representative section of finned tube

It was found that the free flow area per unit of finned tube, as shown in Figure 7.17, is a convenient factor in characterising this available flow path with increasing or decreasing transverse pitch. A dimensionless ratio of the material unit area to free flow unit area, as defined by Figure 7.17, is presented in Equ.7.11.

$$GR_T = \frac{(D_f s_f) + D_o\left(\frac{1}{n_f} - s_f\right)}{P_T\left(\frac{1}{n_f}\right) - \left[(D_f s_f) + D_o\left(\frac{1}{n_f} - s_f\right)\right]} \qquad \text{(Equ.7.11)}$$

Given a fixed tube and fin geometry it can be seen that an increase in P_T will give a lower ratio. This lower ratio equates to a lower loss attributable to the unit, and it will be shown, reduce to the overall bypass and overall bundle loss coefficients.

7.5.2 Number of rows effect on pressure drop

7.5.2.1 Number of rows

The number of tube row gaps has been shown to be a good scaling parameter in previous HTFS and some open literature, methods. It was found however that due to the new nature of how bypass is perceived the number of tube rows crossed is a more

suitable parameter. The new method treats the gap flow as a feature local to each tube. Therefore the number of tube rows crossed has a direct scale effect.

7.5.2.2 Tube spacing

The row effect on the pressure drop of inline tube bundles is shown by Hetz et.al [56] to be dependant on the longitudinal spacing. They showed that there are various modes of flow over inline tubes. The 'cavity flow', 'gap shedding' and 'unobstructed shedding' modes are of most interest in practical heat exchangers. To generate these modes the longitudinal pitch is critical. At short pitches the cavity flow model will exhibit strong recirculation behind the preceding tube, which causes a reduction in drag on the following tubes due to the pulling effect on the following tube. As the pitch increases the gap shedding effect takes over. The recirculation becomes weaker as wake flow is no longer trapped, but partially escapes and thus the following tube is exposed to effectively fresh flow over its top and bottom sections and hence a mild pushing effect is created, which gives slightly increased drag. With very large longitudinal pitch the unobstructed shedding mode takes over. In this mode the following tube is only exposed to a small amount of recirculating flow and as such the pulling effect is almost gone, and only the drag-inducing element is left. These results are affirmed by the drag coefficient plots of Lam and Fang [83].

These results are for plain banks of tubes, however in the absence of any studies on finned tube bundles, and conclusions drawn from the pressure drop results in Chapter 4 they are believed to be applicable here.

7.5.2.3 Tube row model

As the spacing effect has been shown to have a strong influence on the pressure drop the proposed model for row scaling is given in Equ.7.12 below:

$$K_{row} = N_R^{\,IAP} \qquad \text{(Equ.7.12)}$$

The new indice presented in Equ.7.12 is the Inline Arrangement Parameter. This is found simply from Equ.7.13 shown below.

$$IAP = \frac{P_L}{P_T} \qquad \text{(Equ.7.13)}$$

It can be seen that this is simply the ratio of the longitudinal and transverse pitches, however, it has special significance in that it introduces the longitudinal and gap length element in to the overall gap loss coefficient model. When the ratio is >1 then the bundle will be rectangular, with $P_L > P_T$, in the flow direction. This indicates that the gap between the rows (in the flow direction) will be relatively large. This will have the effect of increasing the row loss scaling parameter, and hence, as will be shown, the gap loss coefficient. Similarly when the ratio <1 the bundle will be rectangular with $P_L < P_T$, and the proportionally shortened tube row gap will be modelled by the row effect parameter decreasing. This accounts for the various flow modes discussed above.

7.5.3 Virtual blockage and mass transfer

Section 7.5.1 details the geometric impositions on the flow. This section considers the friction region around the fins and its effect on the bypass flow. The two-stream philosophy of fins and gap flow is extended here with a method to determine how much effect the gap has in the overall free flow area.

This proposed method uses the principal of assigning boundary layers on the fin surface and assessing what frictional 'blockage' of the free stream flow is incurred. The result is a parameter that can be used to assess how much penetration the gap flow has between the fins. The approach used is to determine the thickness of the boundary layers at three key points on the fin surface from which an average will be found. These zones and their calculation are detailed below. Three points were chosen as inspection of CFD velocity contour plots (such as Figure 7.3) showed that after the first tube row the velocity could be broken down into three regions: Tube centreline zone, tube top zone and fin top zone.

7.5.3.1 CFD velocity results

Figure 7.18 shows an example of the CFD velocity profiles through Bundle 1 from the air-cooler tests. It shows the three distinct regions, and that they are well spaced in terms of their average velocity.

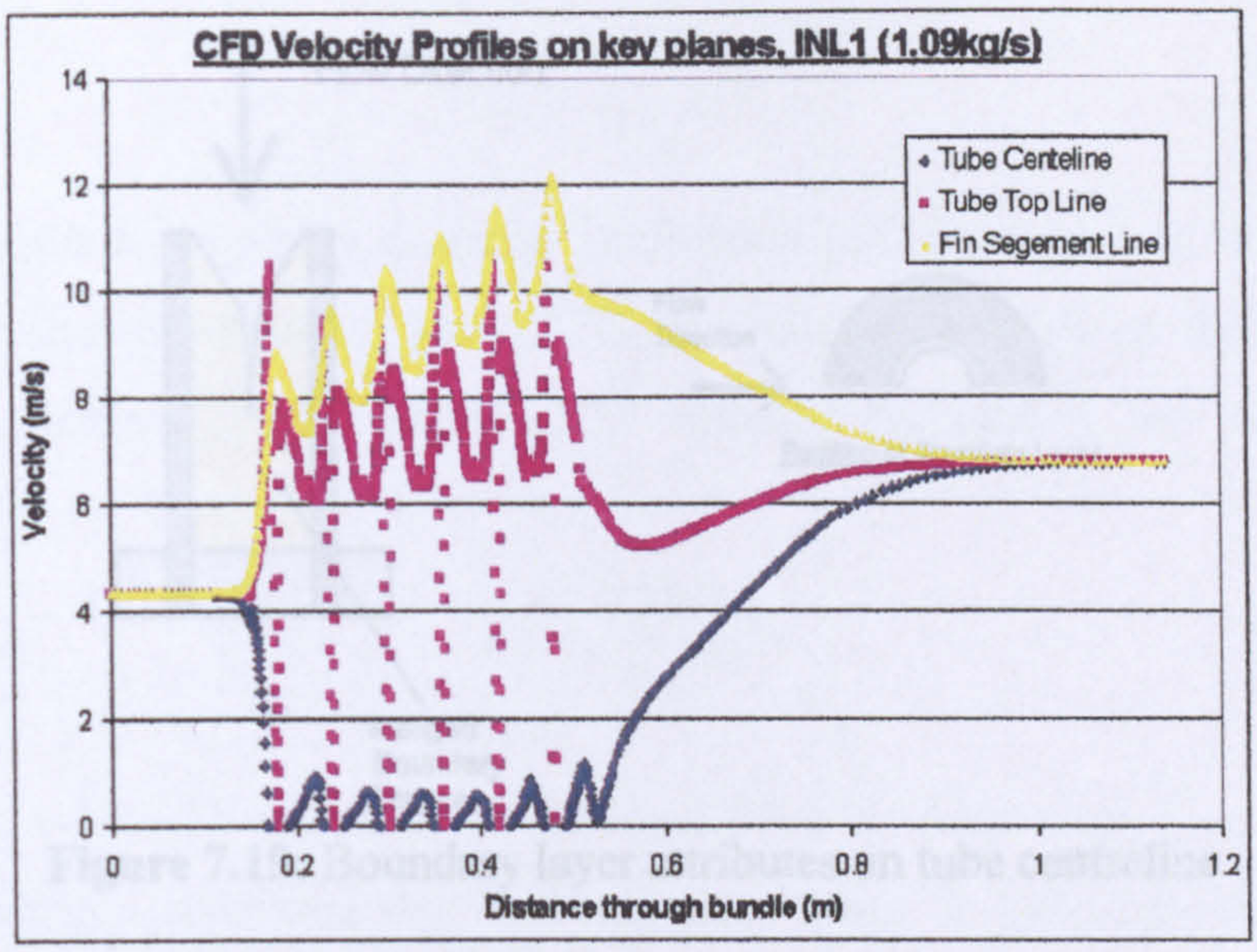

Figure 7.18: Velocity profile through Bundle 1 at 1.09 kg/s (Face velocity 4.44m/s)

By averaging the individual profiles for each bundle at each flow rate it was found that the velocity in each region could be expressed as a proportion of the mean superficial velocity (u_o) through the bundle. The face velocity (u_F) was discarded for the mean superficial velocity, as this allowed for the effects of heat transfer as it is calculated at the bulk density condition.

It was found that the regions could be expressed approximately as:

- Tube centreline: $U_{Local} = 1/3\ u_o$
- Tube top line: $U_{Local} = u_o$
- Fin top line: $U_{Local} = 2u_o$

7.5.3.2 Tube Centreline Level Zone

The incoming flow to a following tube in an inline bundle will generally be slow, as discussed in section 7.4.3, and shown in Figure 7.14. This low speed flow will generally be of lower momentum, thus it will be expected that there will be a relatively thick boundary layer on the fin surface. These layers are shown in Figure 7.19.

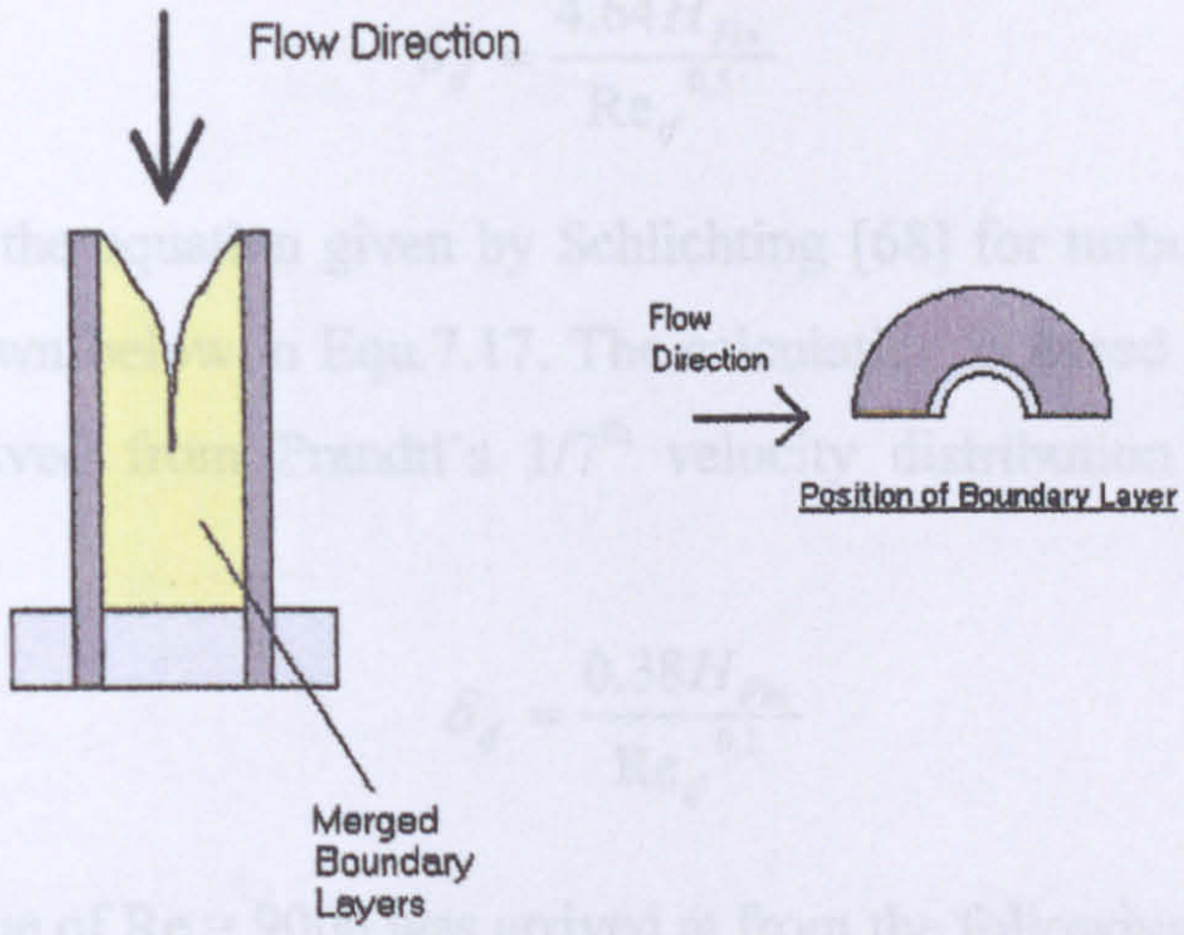

Figure 7.19: Boundary layer attributes on tube centreline

These thick boundary layers will merge, and this removes the possibility of higher speed flow penetrating, and thus the path of least resistance moves out of this region.

Before discussing the calculations a statement of assumptions must be made:

- The incoming flow has moderate turbulence, thus a very short laminar Re range is defined.
- The surface can be regarded as a smooth flat plate.
- No transitional layer or calculation is defined, as this phenomenon is not very well understood, at this time.

Equ.7.14 shows the calculation of the Reynolds number used in the determination of the boundary layer thickness. It will be noted that the velocity used in this calculation is 1/3 of the superficial mean velocity. This is based on the observations of the CFD velocity profiles discussed above in section 7.5.3.1. The characteristic length is that of the fin height, as this is the maximum flow length on this plane.

$$\mathrm{Re}_{if} = \frac{\rho(0.333u_o)H_{Fin}}{\eta} \qquad \text{(Equ.7.14)}$$

Where the fin height is expressed as Equ.7.15:

$$H_{Fin} = 0.5D_f - 0.5D_o \qquad \text{(Equ.7.15)}$$

The fully laminar boundary layer thickness on the fin surface is then predicted by Equ.7.16, given by Schlichting [68].

$$\delta_{if} = \frac{4.64 H_{Fin}}{\mathrm{Re}_{if}^{0.5}} \qquad \text{(Equ.7.16)}$$

If $Re_{if} > 9000$ then the equation given by Schlichting [68] for turbulent flow on a flat plate is used as shown below in Equ.7.17. The calculation is based on those presented by Schlichting derived from Prandtl's $1/7^{th}$ velocity distribution law for turbulent boundary layers.

$$\delta_{if} = \frac{0.38 H_{Fin}}{\mathrm{Re}_{if}^{0.2}} \qquad \text{(Equ.7.17)}$$

The transitional value of Re = 9000 was arrived at from the following:

- Schlichting's statement that "the boundary layer is turbulent already at the leading edge"
- Rodgers and Mayhew's [86] statement "the critical distance [for transition] may be considerably less than this if the free stream approaching the plate is turbulent, as there is always at least a short distance at the nose of the plate over which there is a laminar boundary layer"
- The value was found to be the best fit for the data.

Thus it can be shown that the laminar value will almost always be used, but the facility for extremely high air face velocities is in place.

7.5.3.3 Tube Top Zone

It has been shown that the flow velocity in the tube top region is approximate to the superficial mean velocity (u_o). This region, as shown in Figure 7.20, allows a large layer evolution due to it having a long flow length. Its higher velocity means that a turbulent layer is more likely to form, due mostly to the higher flow momentum, but also due to inherited turbulence from the fast flow region of the preceding tube and fins and fin tip separation turbulence generation.

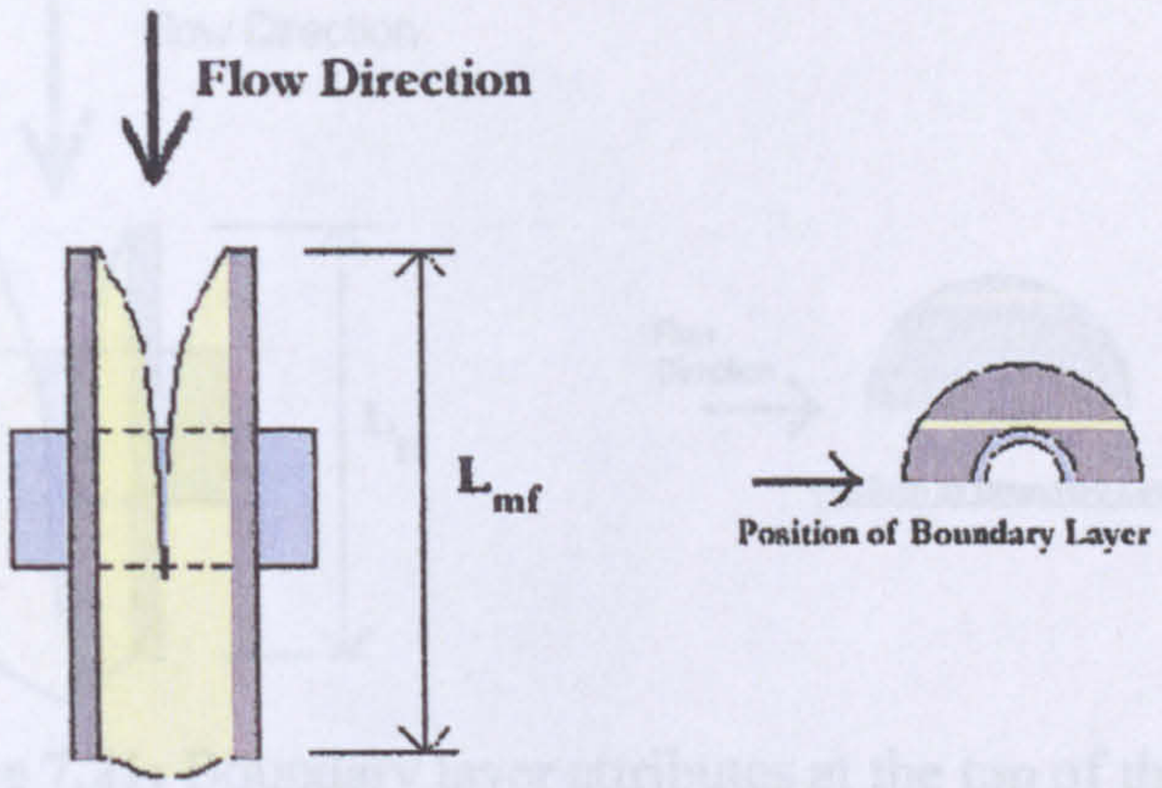

Figure 7.20: Boundary layer attributes at mid-fin point

The same assumptions as noted in section 7.5.3.2 are made in this calculation sequence. The Reynolds number over this region is calculated from Equ.7.18. The characteristic dimension is the distance across the fin at this radius, and is calculated from Equ.7.19.

$$\mathrm{Re}_{mf} = \frac{\rho u_o L_{mf}}{\eta} \qquad \text{(Equ.7.18)}$$

$$L_{mf} = 2\sqrt{(0.5D_f)^2 - (0.5D_r)^2} \qquad \text{(Equ.7.19)}$$

The layer thickness is calculated from Equ.7.20 or if $\mathrm{Re}_{mf} > 9000$, Equ.7.21.

$$\delta_{mf} = \frac{4.64 L_{mf}}{\mathrm{Re}_{mf}^{\ 0.5}} \qquad \text{(Equ.7.20)}$$

$$\delta_{mf} = \frac{0.38 L_{mf}}{\mathrm{Re}_{mf}^{\ 0.2}} \qquad \text{(Equ.7.21)}$$

This layer will usually be transitional to turbulent, and as such will be modelled as turbulent.

7.5.3.4 Fin Top Zone

The fin top zone is exposed to the fastest flow. This is due to the fin top zone being closest to the fin gap lane. The flow length in this zone is quite short as it is at the outer edge of the fin radius, as shown Figure 7.21. The approach velocity at this point can be approximated as being twice the superficial mean velocity, and as such allows a straightforward calculation set.

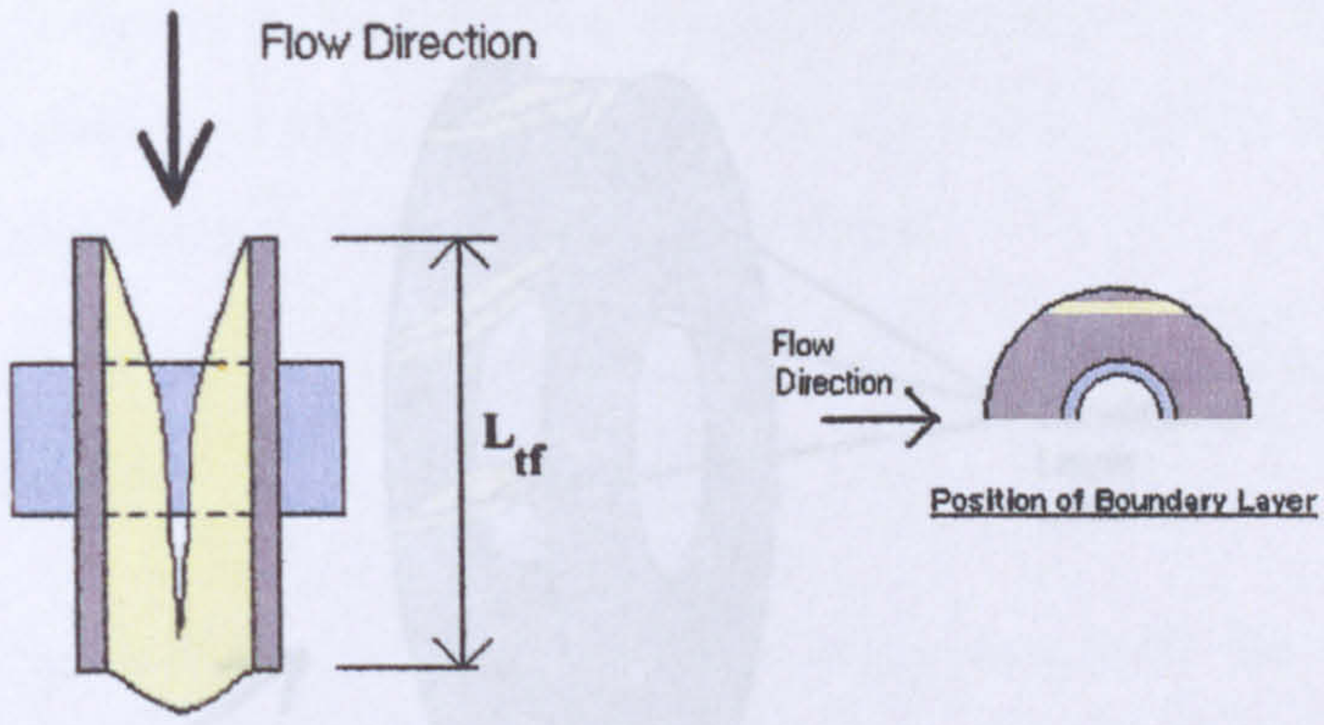

Figure 7.21: Boundary layer attributes at the top of the fin

The assumptions of Section 7.5.3.2 are again made in the following section.

The Reynolds number over this region is calculated from Equ.7.22. The characteristic dimension is the distance across the fin at this radius, and is calculated from Equ.7.23, where the Radius point on the fin is determined from Equ.7.24

$$\mathrm{Re}_{tf} = \frac{\rho(2u_o)L_{tf}}{\eta} \qquad \text{(Equ.7.22)}$$

$$L_{tf} = 2\sqrt{\left(0.5D_f\right)^2 - D_{point}{}^2} \qquad \text{(Equ.7.23)}$$

$$D_{point} = 0.5D_r + 0.75\left(0.5D_f - 0.5D_r\right) \qquad \text{(Equ.7.24)}$$

The layer thickness is calculated from Equ.7.25 or if $\mathrm{Re}_{tf} > 9000$ then Equ.7.26 is used.

$$\delta_{tf} = \frac{4.64L_{tf}}{\mathrm{Re}_{tf}{}^{0.5}} \qquad \text{(Equ.7.25)}$$

$$\delta_{tf} = \frac{0.38L_{tf}}{\mathrm{Re}_{tf}{}^{0.2}} \qquad \text{(Equ.7.26)}$$

7.5.4 The average boundary layer

It can be seen in Figure 7.22, and with reference to Figure 7.14, that different velocities generate all these boundary layers over the fin surface. It can also be seen that the distance over which the layer has to develop varies.

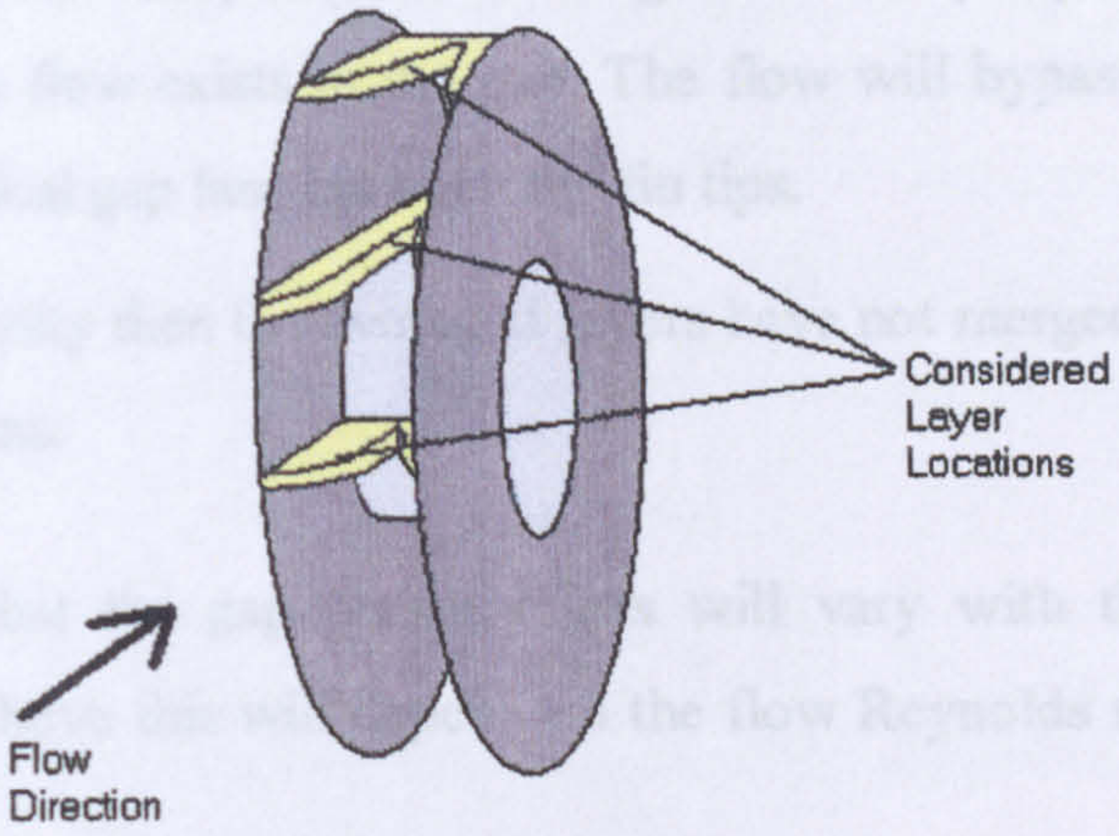

Figure 7.22: Positions of considered boundary layer locations on fins
(Upper section tube/fin layers only shown, for clarity)

As there is no clear data available on the formation of boundary layers on circular plates it is felt that the approach noted above should be considered as a first step, and that further research should be conducted to develop a fully 3 dimensional fin surface boundary layer calculation or routine. In light of this an arithmetic mean is taken of the three boundary layers in the positions described above to determine an average of boundary layer friction zone that is encountered by the incoming flow (Equ.7.27).

$$\delta_{Mean} = \frac{\delta_{if} + \delta_{mf} + \delta_{tf}}{3} \qquad \text{(Equ.7.27)}$$

The ratio of the fin gap to the thickness of boundary layer on the fins can then be used as a parameter to express the strength of bypass flow in the fin gap, and form part of the gap loss coefficient. The ratio is shown in Equ.7.28.

$$R_{BL} = \frac{\left(\frac{1}{n_f} - s_f\right)}{2\delta_{Mean}} \qquad \text{(Equ.7.28)}$$

Where the 2 on the denominator represents the fact that there are two forming boundary layers in the fin gap.

The ratio can then be seen to be working in one of three ways:

1. When the denominator equals the numerator the ratio will become unity. This indicates that the boundary layers have just touched.

2. If the ratio drops below unity then the averaged boundary layer has merged, and virtually no free stream flow exists in the gap. The flow will bypass the finned tubes, and move into the physical gap lane between the fin tips.

3. If the ratio exceeds unity then the averaged layers have not merged and there exists a gap flow between the fins.

The above indicates that the gap pressure loss will vary with the boundary layer formation. As shown above this will depend on the flow Reynolds number and bundle geometry.

7.5.5 Building the gap loss coefficient

The Transverse Gap Ratio described in section 7.5.1 can be regarded as the fixed aspect of the gap loss and this is attenuated by the fin frictional effect detailed above in section 7.5.4. The K_{row} is a scaling geometric parameter, and expresses the tube row gap effects discussed in section 7.5.2. The gap loss coefficient is therefore expressed as the product of the above terms as given in Equ.7.29 below:

$$K_{gap} = K_{row}(GR_T R_{BL}) \qquad \text{(Equ.7.29)}$$

7.6 Overall bundle loss coefficient

The layout of the bundle loss coefficient is similar to the previous HTFS methods. The alterations that were made were:

- The substitution of the newly determined velocity exponent to balance the units of the model.
- The addition of the augmented mass transfer coefficient (C_A) being used to increase the fin and tube loss components (K_{ft}), when necessary.

The new bundle loss coefficient is given in Equ.7.30

$$K_B = \frac{K_{ftA}}{\left[\frac{D_f}{P_T} + \left(\frac{K_{ftA}}{K_{gap}}\right)^{\frac{1}{1.56}}\left(1 - \frac{D_f}{P_T}\right)\right]^{1.56}} \qquad \text{(Equ.7.30)}$$

7.7 Overall bundle pressure drop

To recount, the new models dynamic loss term sees the velocity raised to the power of 1.56, derived in Section 7.2 and the loss coefficient has been derived from a combination of flow features and bundle geometry. The new pressure drop prediction equation is expressed as the product of these factors, and is shown in Equ.7.31 below:

$$\Delta P = K_B \rho u_o^{1.56} \qquad \text{(Equ.7.31)}$$

Where ρ is the mean bulk density of the crossflow fluid.

When the new model was tested using the contents of the inline bundle databank it was found that there was no need for a leading constant, unlike most models, which would imply that the geometric parameters and the physics of the flow are adequately modelled.

7.8 Heat transfer

7.8.1 Previous model basis

The first HTFS heat transfer correlation of Ralston et.al [21] used a formulation whereby the Colburn j factor was predicted by a function of the fin Reynolds number and extended surface to base tube area. This model took account of the 'drag' velocity around the fins predicted by the relation of the bundle loss coefficient (K_B) and the fin and tube portion of this loss (K_{ft}) originally postulated by Henry [19]. Chu and Ralston [23] found better agreement when they used a formulation based on two Reynolds number: the fin velocity based Re attenuated by the maximum Re. The models were all derived from multi-variate linear regression.

7.8.2 New model basis

Upon inspection of CFD data and contour plots for the bundles tested in Chapter 5, it was apparent that although most of the heat transfer is carried out on the finned surfaces, the gap flow has an effect in drawing the hotter fin flow out. This means that there is an element of mass exchange between the fin and gap flows. This also has the effect of transferring the heat from the fin tips. Figure 7.23 shows the temperature contours on the fins, and the plane between the fins, and these effects.

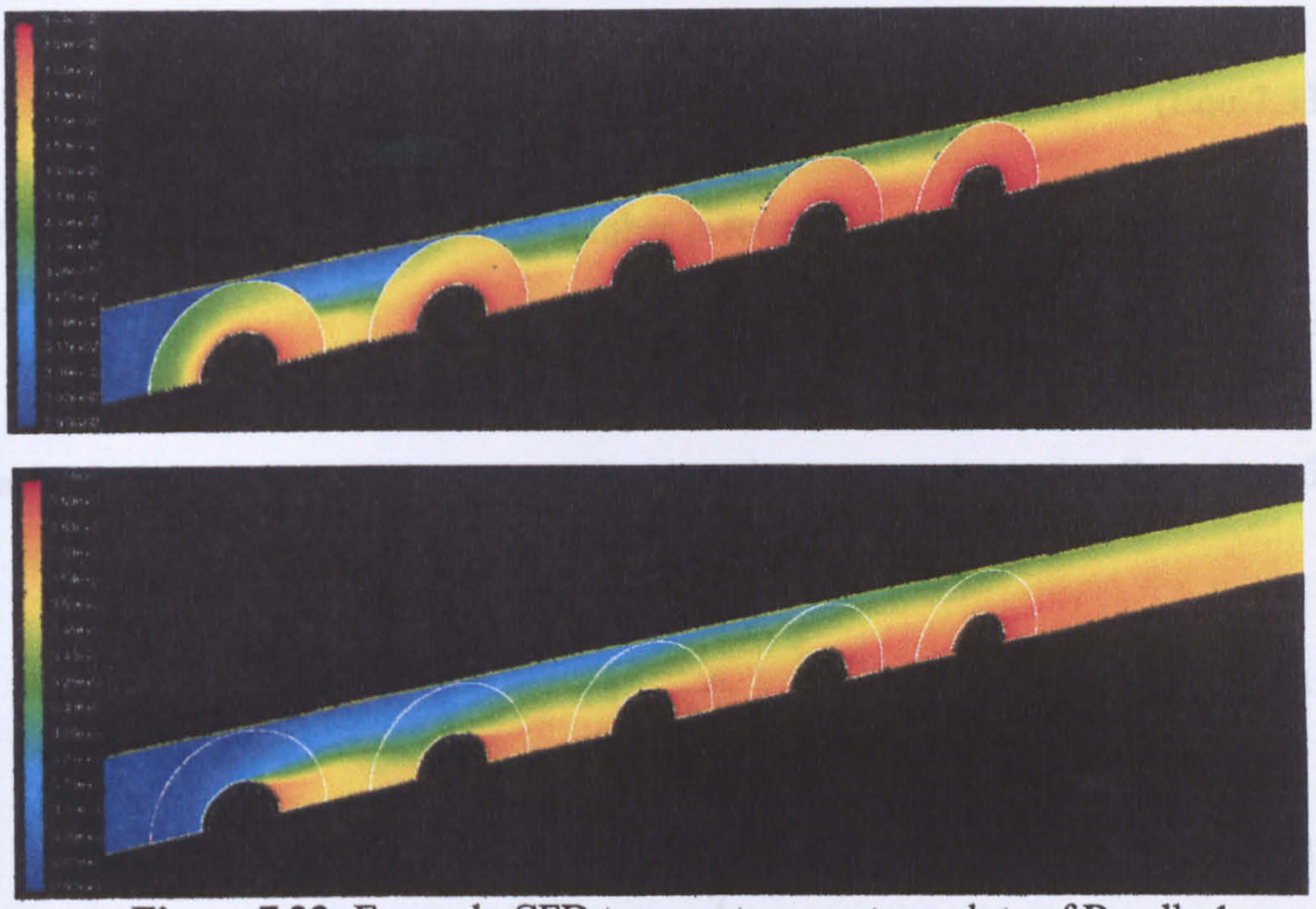

Figure 7.23: Example CFD temperature contour plots of Bundle 1
(Top: Fin plane, Bottom: centre plane)

The overall CFD contours and local area examinations on fin tip temperature and fin tip heat flux show that the gap flow influences the development of the bypass lane temperature uptake in line with the findings of Yang and Bell [45]. They showed a model that used a two-stream philosophy; fin flow and gap flow, which is coherent with the way that the pressure drop model was approached. This led to the conclusion that both the gap velocity and the fin velocity would be important factors in the new heat transfer correlation.

7.8.3 Implementation of gap flow effects

In Section 7.5 the gap loss effects on pressure drop were described. A balance of the pressure loss over the bundle in terms of the loss coefficients was presented by Henry [19]. He stated that the superficial velocity was related to the fin velocity via the bundle and fin loss coefficients. It followed from this that the gap flow must also be related to the superficial velocity by the same equality. This was readdressed in terms of the new velocity exponent shown below (Equ7.32).

$$K_B u_0^{1.56} = K_{fA} u_{fin}^{1.56} = K_{Gap} u_{gap}^{1.56} \qquad \text{(Equ.7.32)}$$

From this the new fin velocity is calculated from Equ.7.33:

$$u_{fin} = u_o \left(\frac{K_B}{K_{fin}} \right)^{\frac{1}{1.56}} \qquad \text{(Equ.7.33)}$$

And the definition of the Fin Reynolds number is found from Equ.7.34:

$$\mathrm{Re}_{Fin} = \frac{\rho u_{fin} D_o}{\eta} \qquad \text{(Equ.7.34)}$$

Similarly the gap characteristics can be found in the same way to give Equations 7.35 and 7.36.

$$u_{gap} = u_o \left(\frac{K_B}{K_{gap}} \right)^{\frac{1}{1.56}} \qquad \text{(Equ.7.35)}$$

$$\mathrm{Re}_{gap} = \frac{\rho u_{gap} D_f}{\eta} \qquad \text{(Equ.7.36)}$$

It will be noted that the characteristic dimension used in Equ.7.36 is not the base tube diameter (D_o), but the fin tip diameter (D_f). This is due to the fact that the gap flow stream crosses the fin flow length with little influence on the tube or inner fin region heat transfer, therefore it was felt that this was a more characteristic dimension.

7.8.4 New j factor Correlation

Multi-variate linear regression based on a combination of the following elements:

- The maximum Reynolds number, (Re_{max})
- The area ratio of the bundle (A_r), which has been used in almost every finned tube bundles heat transfer prediction method to describe the amount of extended surface to bare tube surface.
- The fin Reynolds number (Re_{fin})
- The gap flow Reynolds number (Re_{gap})

Using an ANOVA technique to determine the usefulness of each parameter, using different treatments, it was found that the best fitting correlation was a combination of all of the listed parameters.

The new j factor correlation is now expressed as shown below in Equ.7.37:

$$j = 0.2855 \frac{\mathrm{Re}_{fin}^{1.322} \mathrm{Re}_{gap}^{0.00365}}{\mathrm{Re}_{max}^{1.633}} Ar^{-0.213} \qquad \text{(Equ.7.37)}$$

The leading constant was determined from an average correlation coefficient of all the data points in the inline databank. It can be seen that the gap flow Reynolds number has only small significance, but that was expected as the magnitude of flow interchange and fin tip heat transfer are quite small in relation to the fin and tube heat transfer characterised by the fin Reynolds number.

7.8.5 Horseshoe effect on heat transfer model

Fischer and Eibeck [87] explain that the increased vorticity touching the fin surface behind the tube (in the flow direction) will aggressively mix the flow and could lead to an improvement in heat transfer. This can be visualised in Figure 7.13 from the 'vortex touch points', whereby cooler fluid is swept towards the hot fin surface, and the hot fluid at the wall is drawn away into the cooler stream. In terms of fluid and fin temperature the reverse would be true for heat recovery applications.

However their results and conclusions showed that any noticeable improvement might not be possible on typical finned tubes for the following reasons:

- Augmented heat transfer was only visible at Re > 77000 (cylinder diameter of 83mm).
- Augmentation was only noted from x/D = 3.5 onwards, where x was the stream wise distance from the rear of the cylinder, and D was the diameter of the cylinder.
- "The wake of the obstacle should tend to augment convection...except possibly in a stagnant recirculating region" which is likely to develop between tubes in inline tube bundles.

On this basis no clear statement as to the effect horseshoe vortex formation would have in inline finned tube bundles can be made. The effect is embedded in the heat transfer model as the overall bundle loss and the fin loss coefficients could use it. However it can be seen by tracing Equs.7.33, 7.34 and 7.37 that the magnitude of this effect becomes increasingly diminished, and would not significantly affect the result of the j factor calculation. It must also be remembered that final correlation accounted for these effects as its inputs had a few values that used the augmentation coefficient.

A parametric test on various bundles from the databank indicated that the j factor, when given a theoretical face velocity of 17 m/s (maximum Reynolds number of 45400), would undercut a non-augmented solution by a maximum 4.2%. As this velocity figure is well beyond the design condition this is deemed a reasonable figure.

7.9 Influence of geometric parameters

To ensure the new method scales correctly to geometries outside of the range of the database used in its development it was necessary to trial cases with exaggerated parameters. The charts and discussion below show experimental evidence of systematic variation, that is comparison where only one parameter is differing. Also included are charts of the variation predicted by the method using a known geometry and increasing and reducing the parameter under investigation. The results show that the method is scalable for geometries outside of it database, although it must be noted that use of the model outside of the range of its database should be treated with caution.

7.9.1 Effects of varying longitudinal pitch

7.9.1.1 Pressure Drop

Figure 7.24 show the experimental friction factor from Bundles 1, 5 and 9. As can be seen in Tables 3.8 and 3.9 these bundles had increasing longitudinal pitch (P_L) while the other geometric parameters are the same. It must be noted that the friction factor parameter is shown in this chart as Bundles 9 had 5 rows in the flow direction, whereas Bundles 1 and 5 had 6, therefore a directly measured pressure drop comparison was not applicable.

The friction factor is directly proportional to the pressure drop across a bundle, so it can be concluded from Figure 7.24 that with increasing longitudinal pitch the pressure drop will increase.

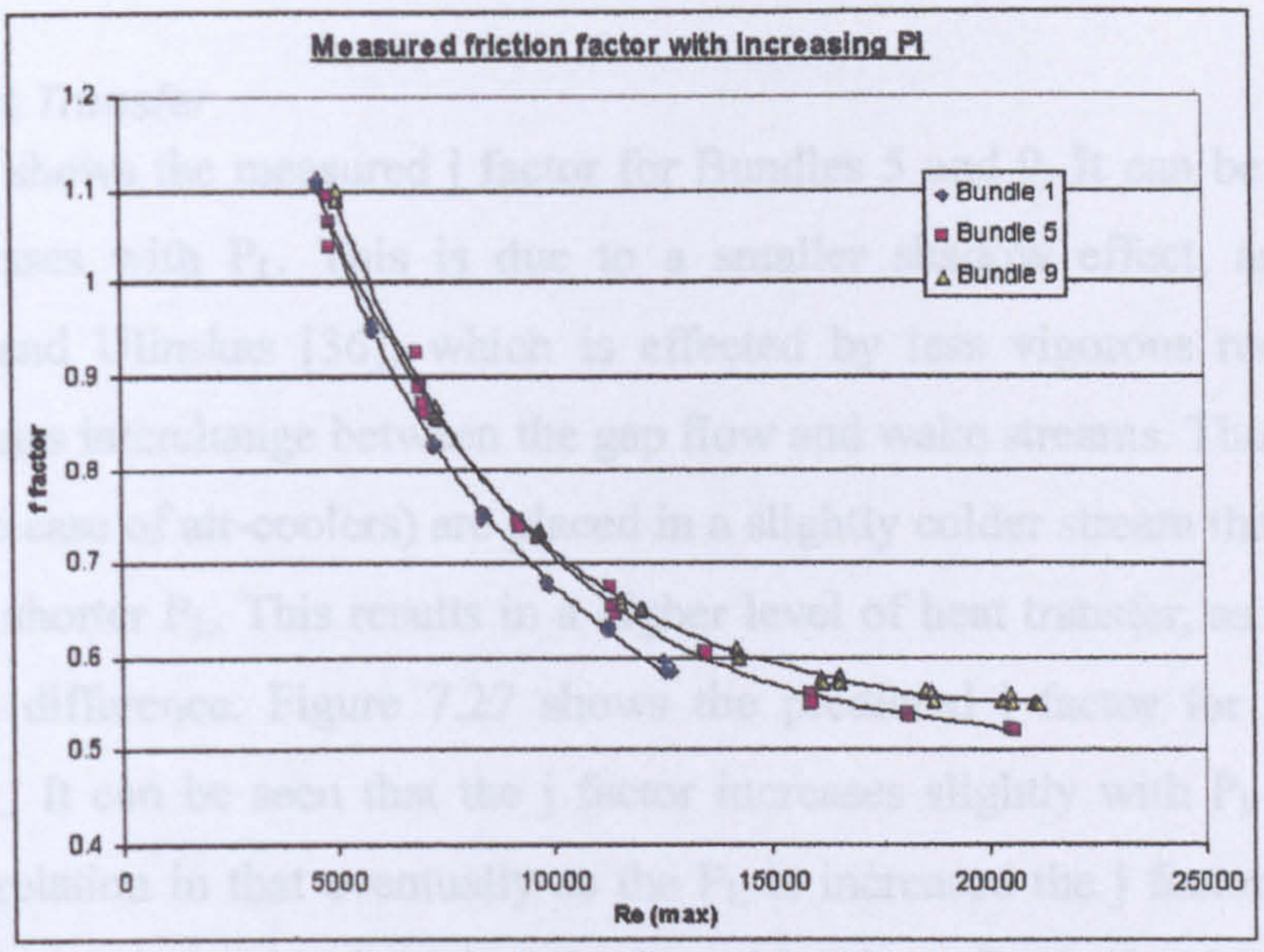

Figure 7.24: Friction factor of bundles with differing longitudinal pitches

In Figure 7.25 it can be seen that the predicted pressure drop increases as per experimental findings.

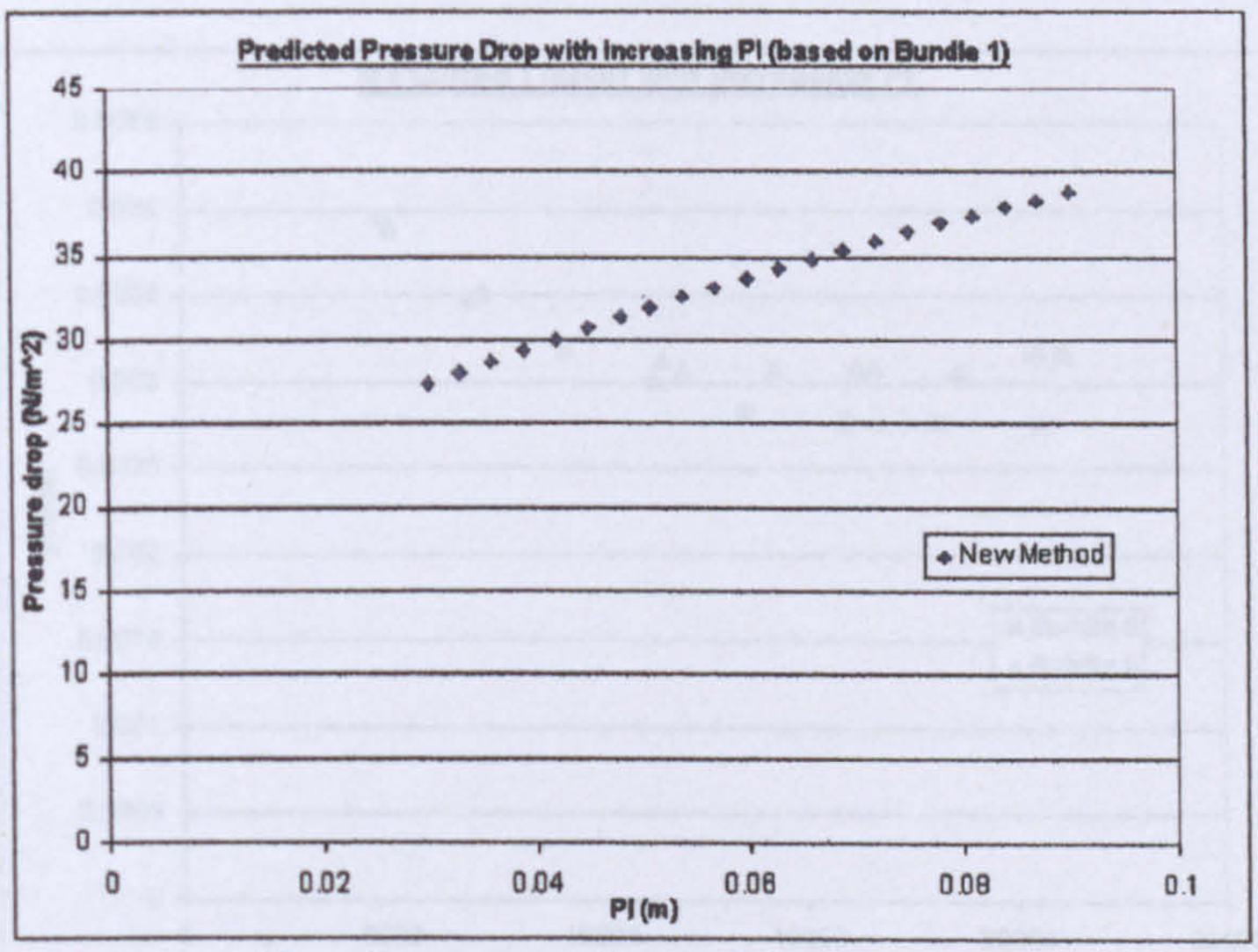

Figure 7.25: Predicted pressure drop with increasing longitudinal pitch (Bundle 1 used as basis)

It can be shown that the trend can be said to follow a power law relation, meaning that the pressure drop will almost level out once the P_L exceeds a certain value. This feature is in accordance with the findings of Lam and Fang [83], Zdravkovich [39], Pearce [38], and Hetz et.al [56] for banks of inline plain tubes, who all note that once a critical longitudinal spacing ratio is reached the tubes will behave as single rows of tubes.

7.9.1.2 Heat Transfer

Figure 7.26 shows the measured j factor for Bundles 5 and 9. It can be seen that the j factor increases with P_L. This is due to a smaller shadow effect, as described by Zukauskas and Ulinskas [36], which is effected by less vigorous recirculation and improved mass interchange between the gap flow and wake streams. Thus the following tubes (in the case of air-coolers) are placed in a slightly colder stream than would be the case with a shorter P_L. This results in a higher level of heat transfer, as there is a large temperature difference. Figure 7.27 shows the predicted j factor for Bundle 1 with extended P_L. It can be seen that the j factor increases slightly with P_L and it obeys a power law relation in that eventually as the P_L is increased the j factor will vary very little. This is coherent with the principle that with a large P_L the local wake behind the preceding tube will have mixed with the high temperature fin stream and the slightly heated bypass stream to give a near constant approach flow temperature to the following tube.

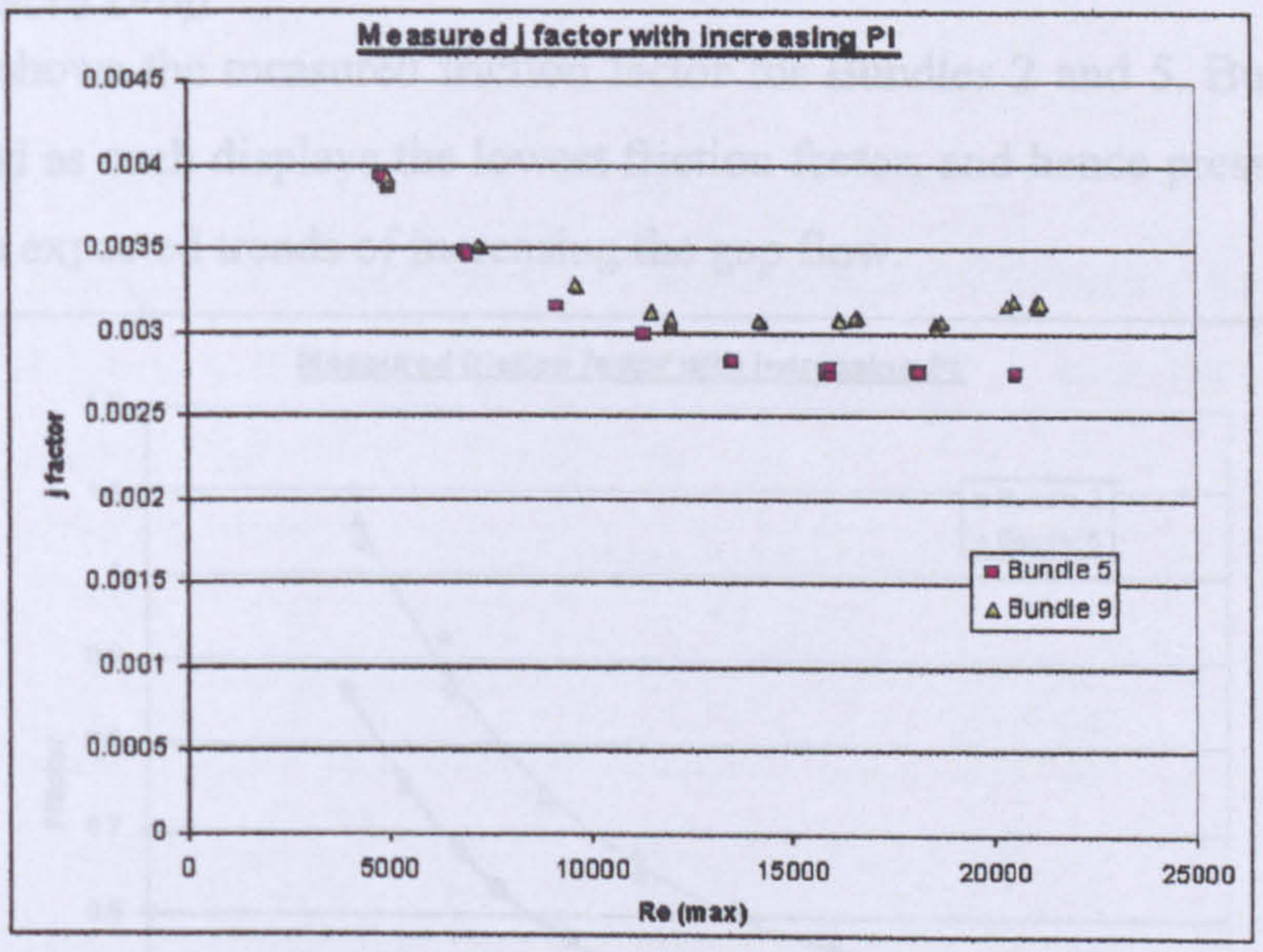

Figure 7.26: j factor of bundles 5 and 9

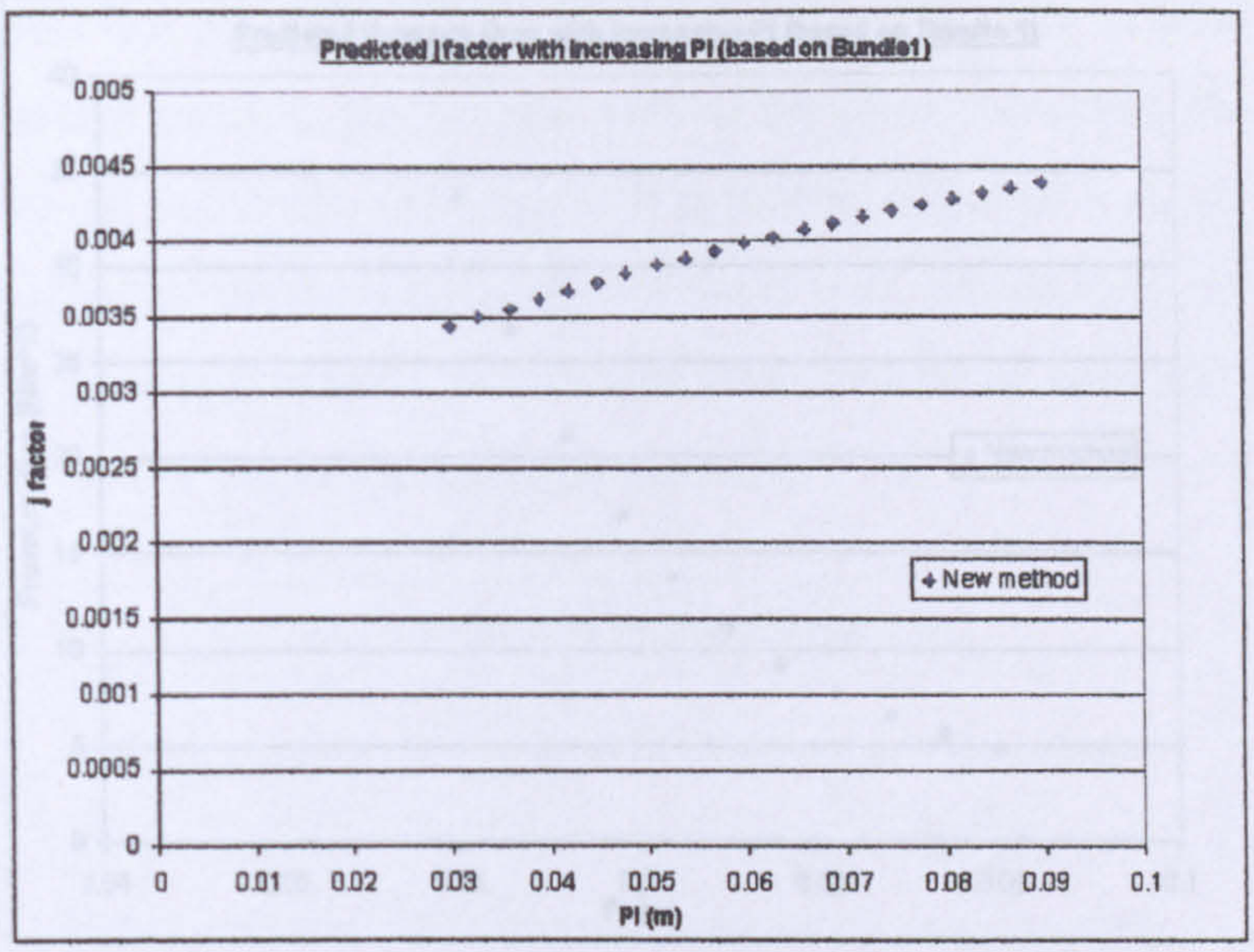

Figure 7.27: predicted j factor with differing longitudinal pitch

(Bundle 1 used as basis)

7.9.2 Effects of varying transverse pitch

7.9.2.1 Pressure Drop

Figure 7.28 shows the measured friction factor for Bundles 2 and 5. Bundle 2 has the largest P_T and as such displays the lowest friction factor, and hence pressure drop. This is inline with expected trends of increasing the gap flow.

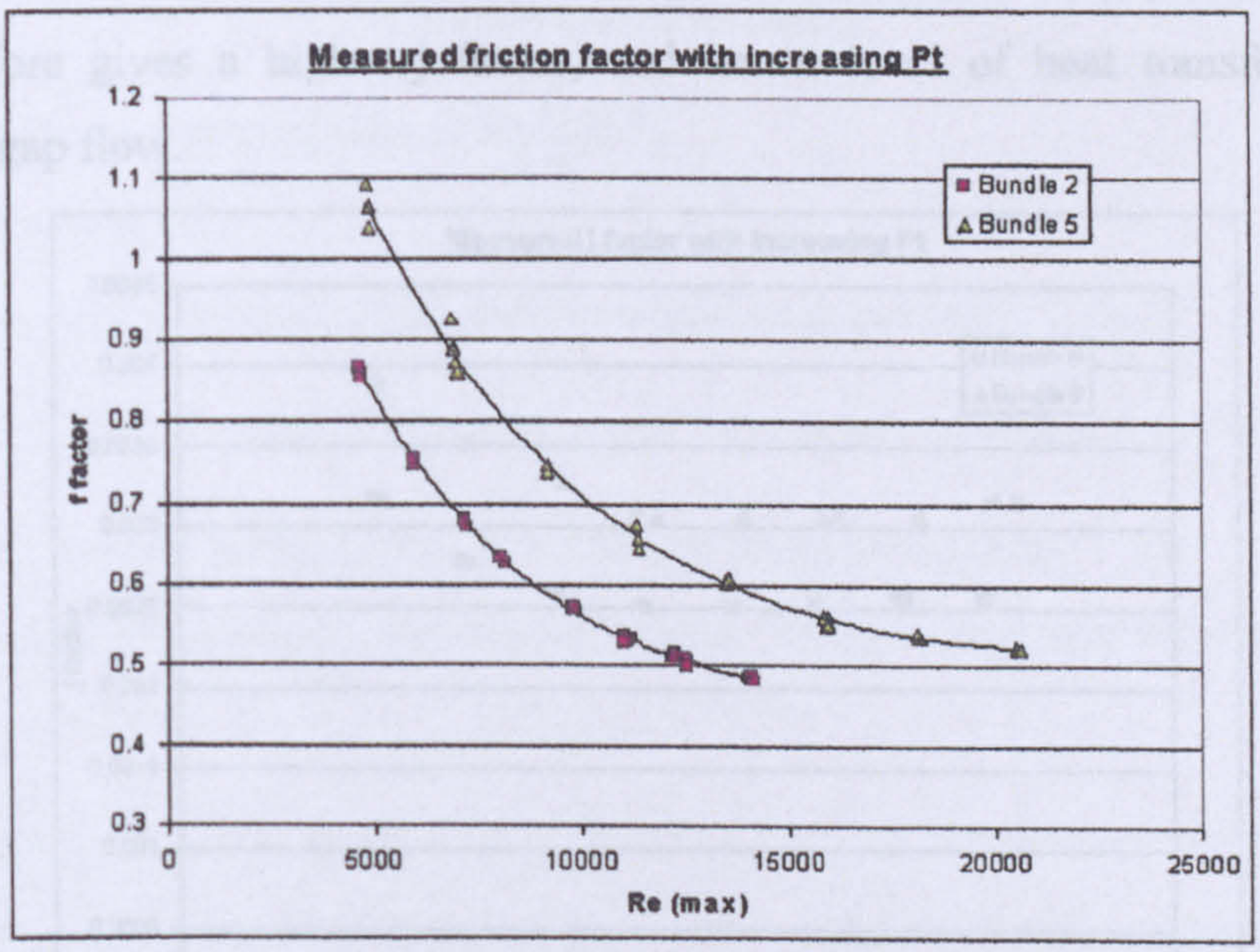

Figure 7.28: Friction factor of bundles 2 and 5 with differing transverse pitch

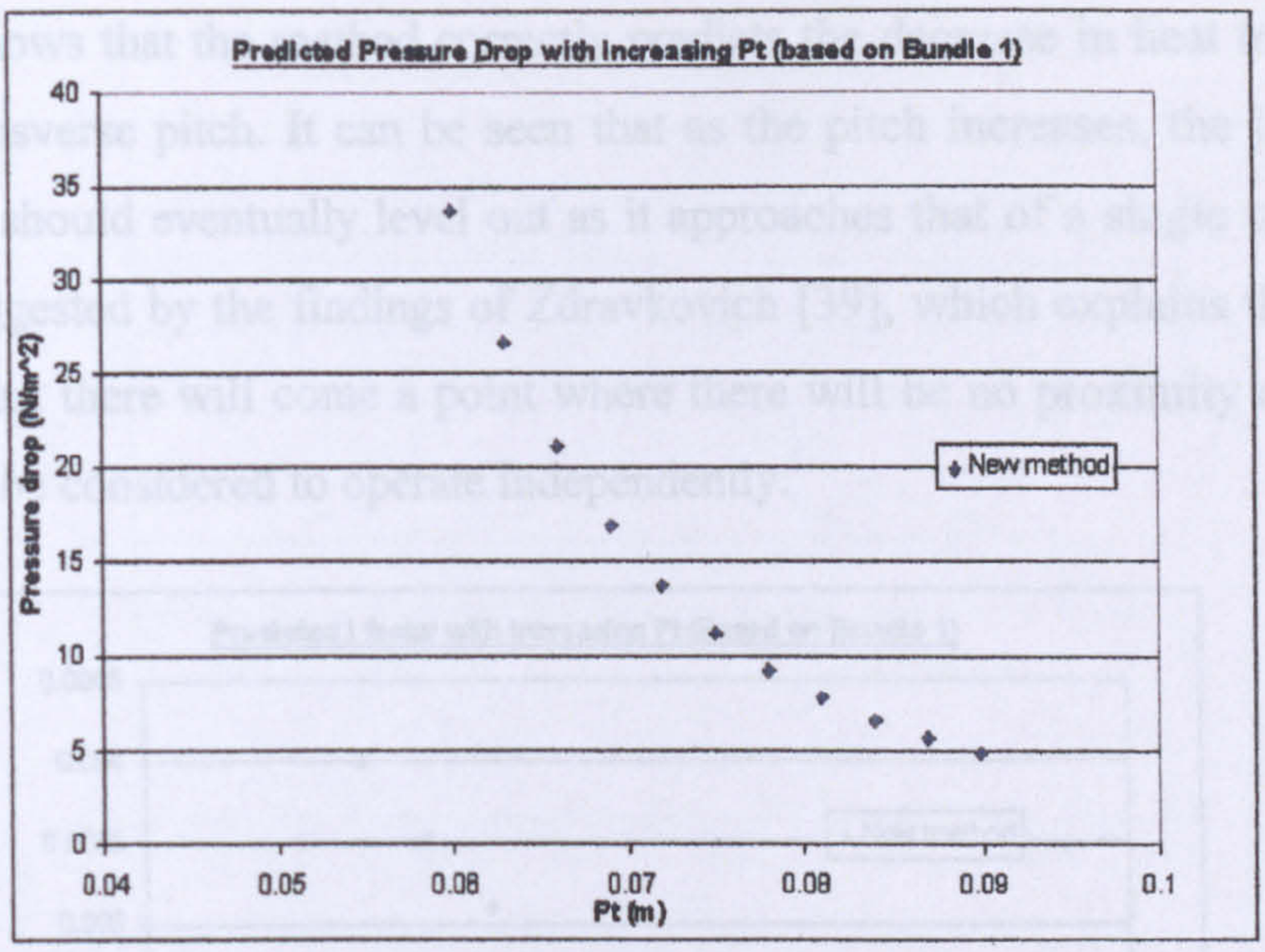

Figure 7.29: Predicted pressure drop with increasing transverse pitch (Bundle 1 used as basis)

Figure 7.29 shows the predicted pressure drop with an increasing P_T. It shows that the model predicts the decreases in pressure drop, as would be expected, as the pitch is increased.

7.9.2.2 Heat Transfer

Figure 7.30 shows the measured j factor of Bundles 6 and 9. Bundle 9 has the smaller P_T and therefore gives a higher j factor, and hence level of heat transfer due to the decreased gap flow.

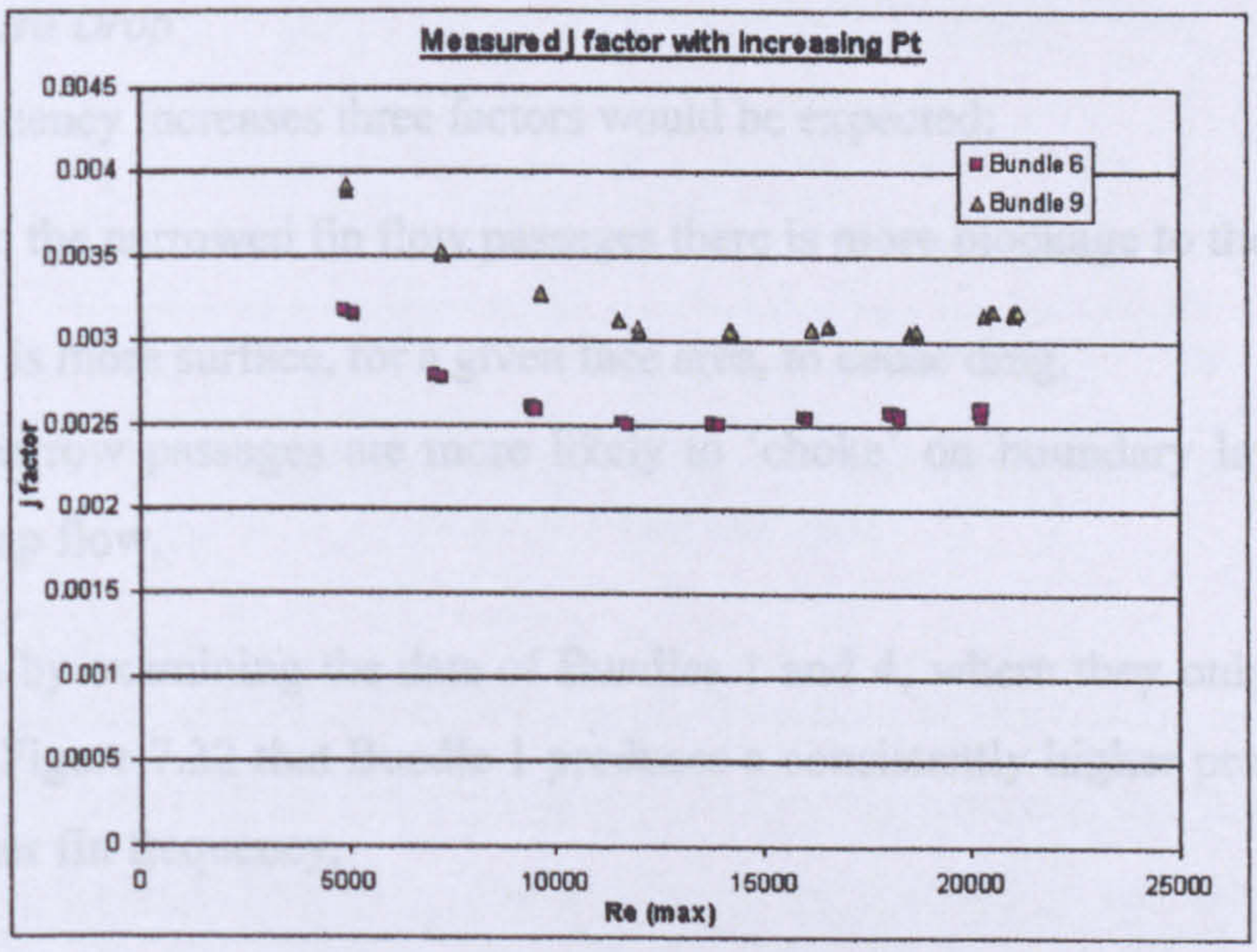

Figure 7.30: Measured j factor of bundles 6 and 9 with increasing transverse pitch

Figure 7.31 shows that the method correctly predicts the decrease in heat transfer with increasing transverse pitch. It can be seen that as the pitch increases, the j factor will decrease, and should eventually level out as it approaches that of a single tube. This is confirmed suggested by the findings of Zdravkovich [39], which explains that as tubes are moved apart there will come a point where there will be no proximity effects, thus each tube can be considered to operate independently.

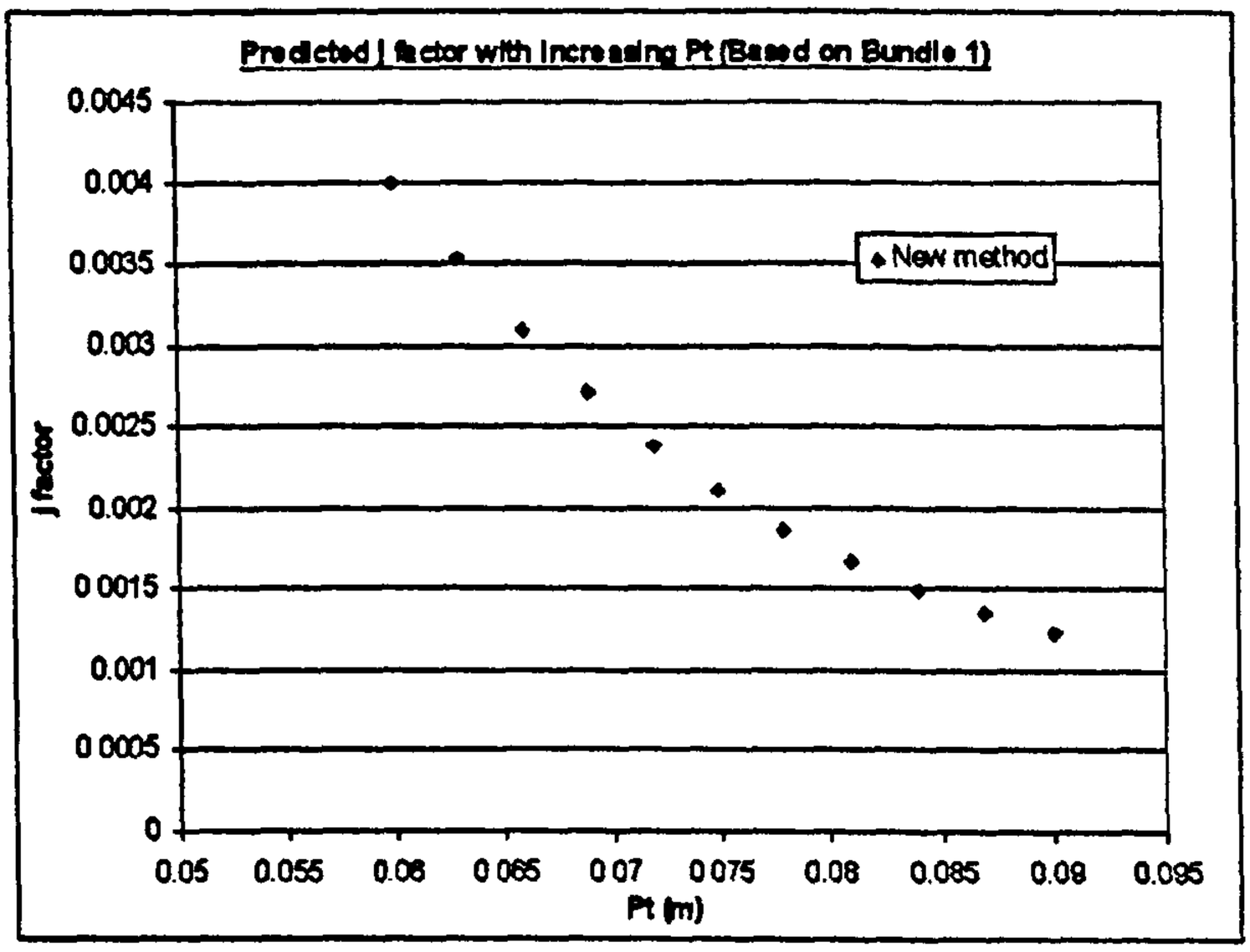

Figure 7.31: Predicted j factor with increasing transverse pitch
(Bundle 1 used as basis)

7.9.3 Effects of varying fin frequency

7.9.3.1 Pressure Drop

As the fin frequency increases three factors would be expected:

- Due to the narrowed fin flow passages there is more blockage to the flow.
- There is more surface, for a given face area, to cause drag.
- The narrow passages are more likely to 'choke' on boundary layer, allowing less gap flow.

It can be seen by examining the data of Bundles 1 and 4, where they only differ in fin frequency, in Figure 7.32 that Bundle 1 produces a consistently higher pressure drop as it has the higher fin frequency.

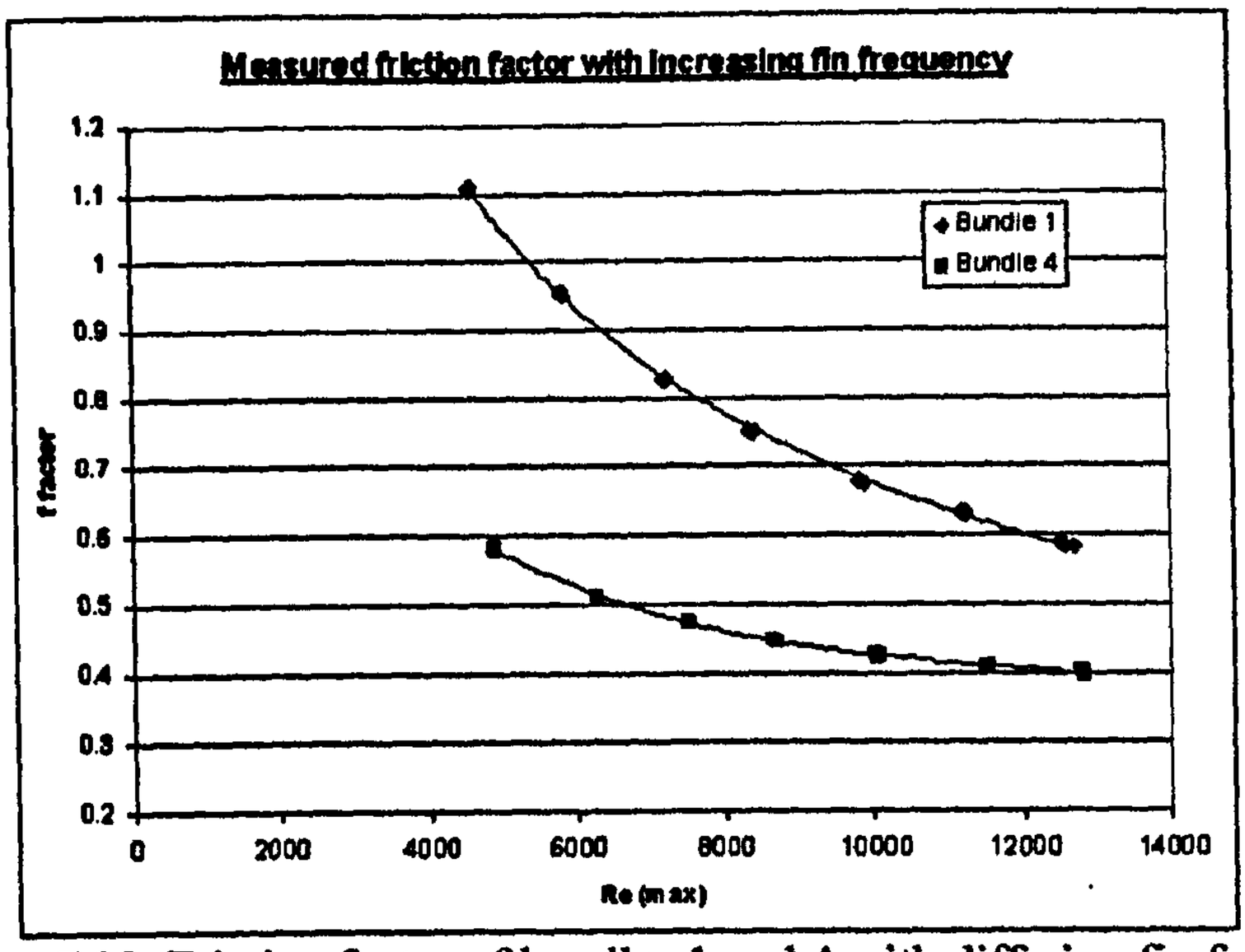

Figure 7.32: Friction factor of bundles 1 and 4 with differing fin frequency

Figure 7.33 shows that the model predicts the correct trend, by increasing the pressure drop with increasing fin frequency.

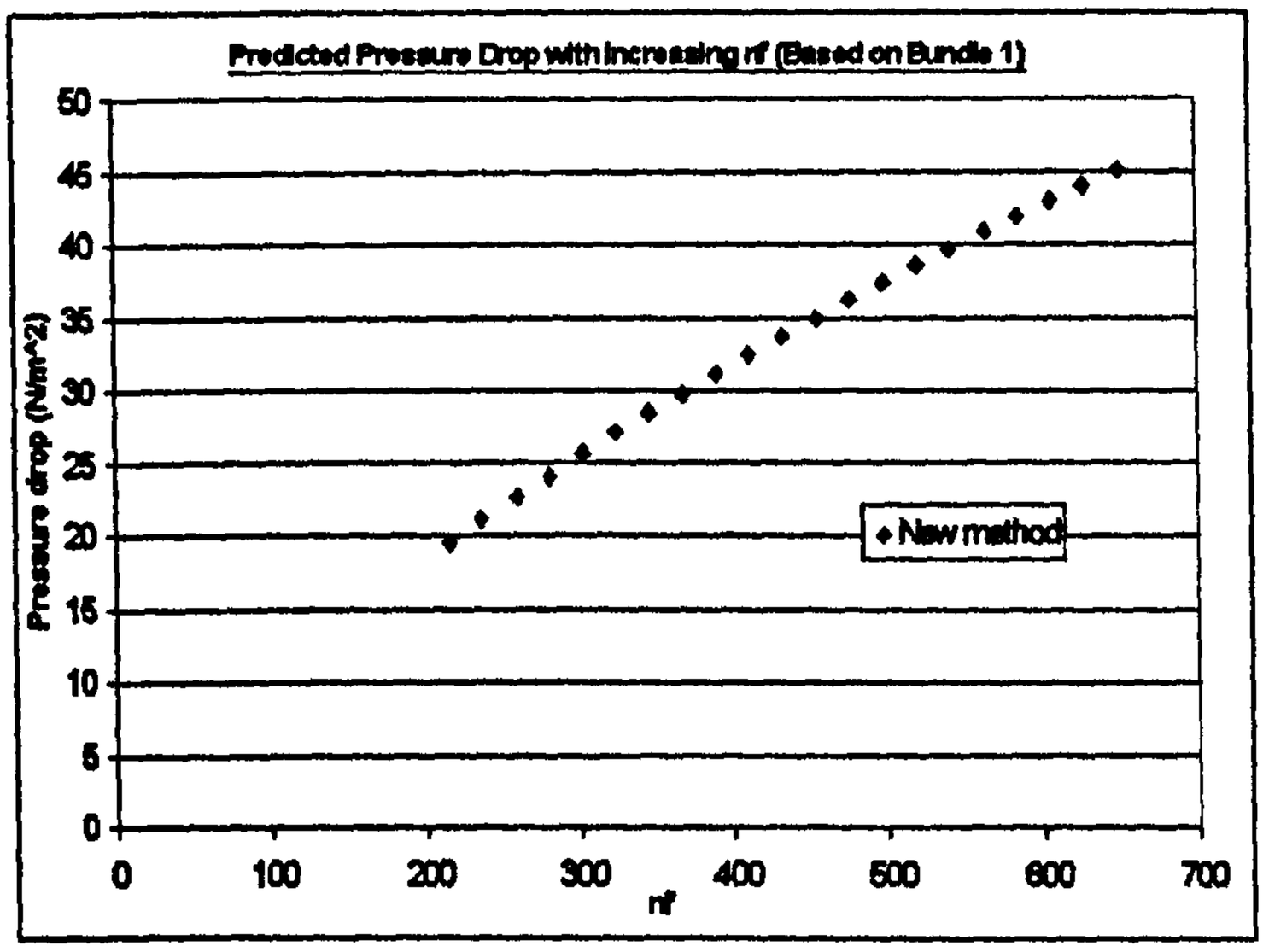

Figure 7.33: Predicted pressure drop with increasing fin frequency (Bundle 1 used as basis)

7.9.3.2 Heat Transfer

As the fin frequency increases the thermal performance of the bundle will increase, but this is not obviously reflected in the j factor. To directly compare the j factor of bundles with differing fin densities both bundles should be referred to the bare tube area by multiplying by A_r. It can then be seen that the higher fin frequency bundle, 1, will give

better heat transfer performance. Figure 7.34 shows the experimental j factors for Bundles 1 and 4, which differed by having 433 fins/m and 236 fins/m, respectively.

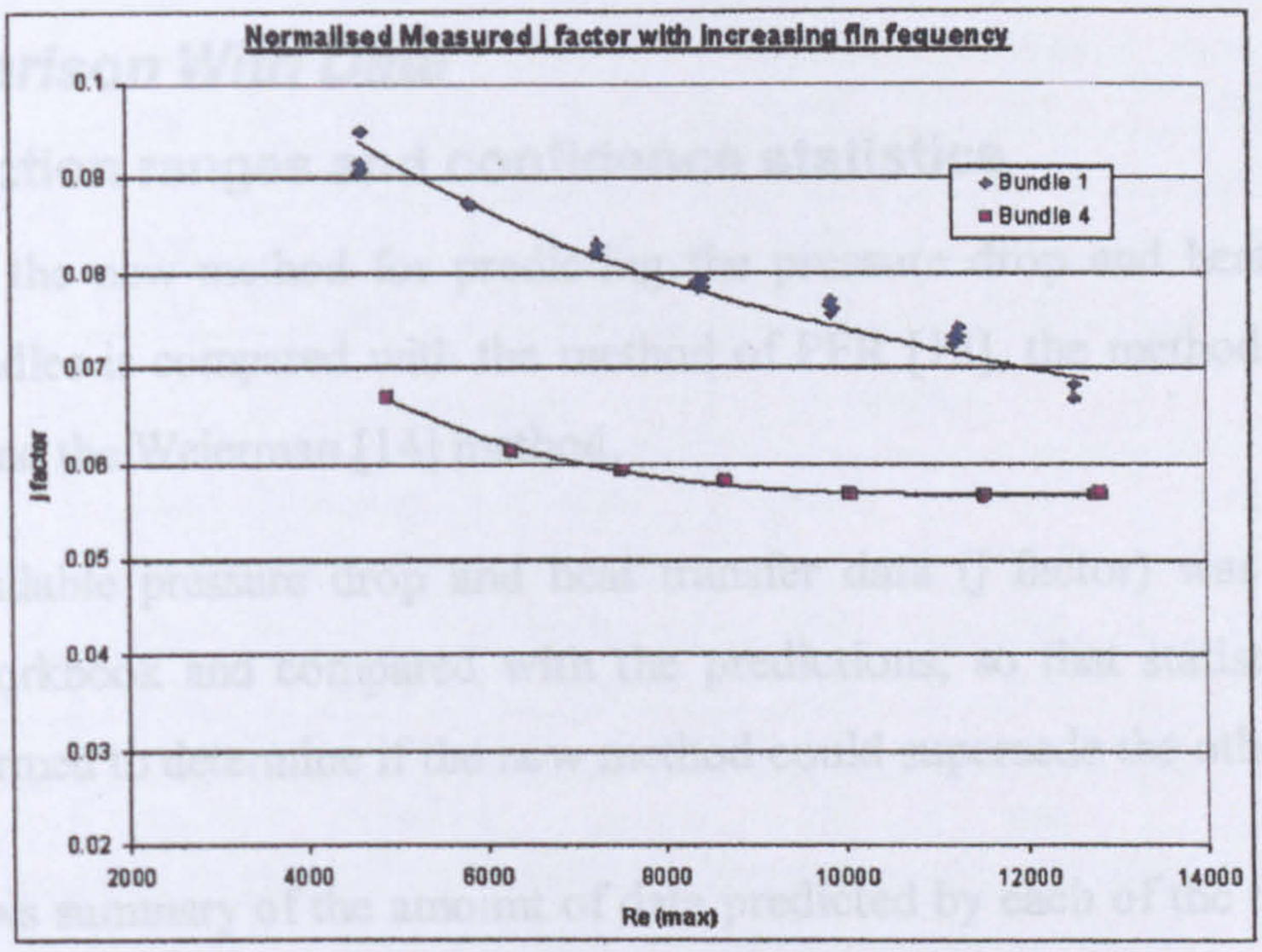

Figure 7.34: Measured j factor of bundles with differing fin frequency (based in bare tube area)

Figure 7.35 shows the predicted j factor for Bundle 4. It can be seen that an increase in fin frequency produces an increase in performance.

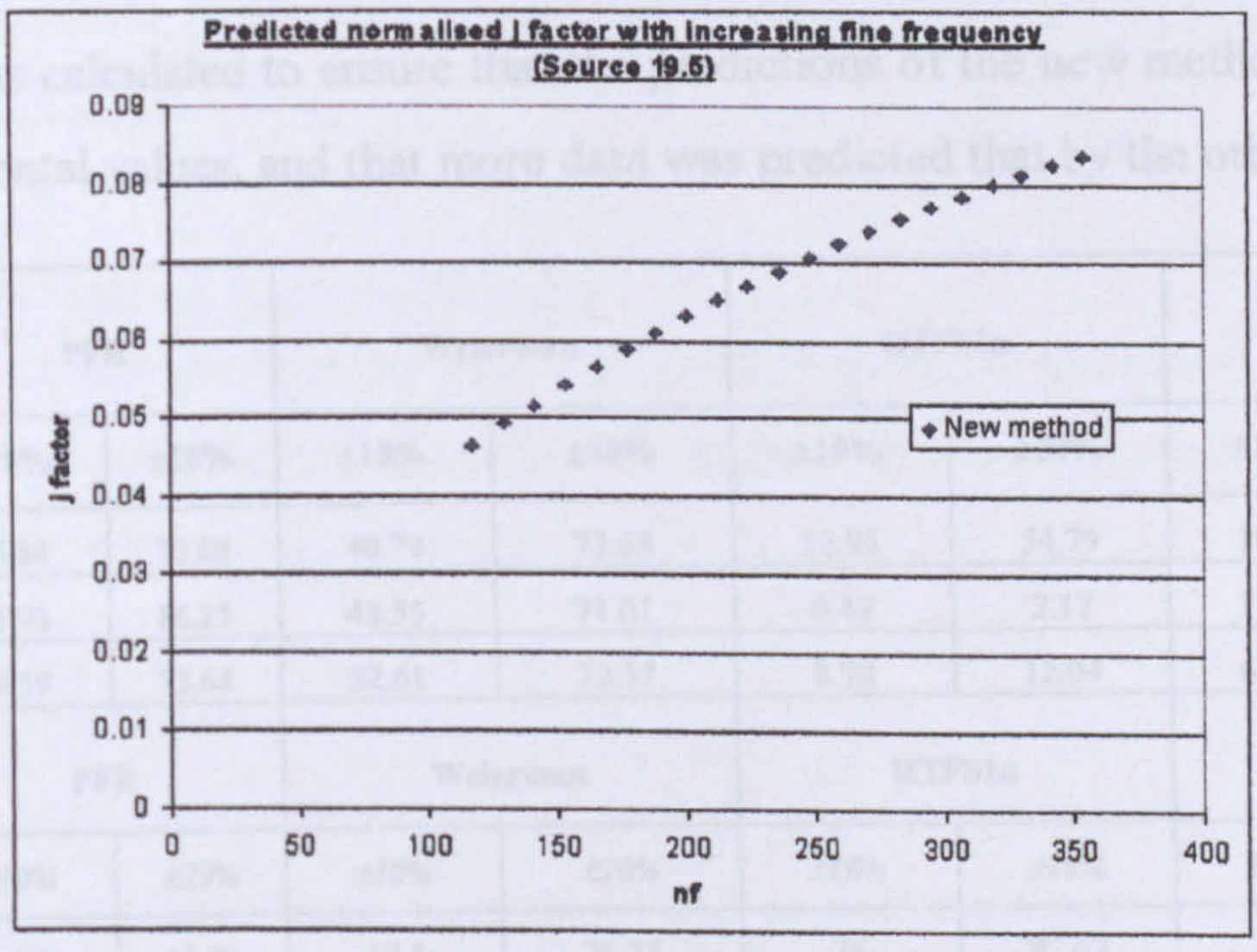

Figure 7.35: Predicted j factor with increasing fin frequency (Bundle 4 used as basis)

It will be seen that the trend is for the performance to level out as the fin frequency increases. This is due to the small fin spacings not allowing penetration from the bypassing flow, and thus minimal interchange occurring between the fin and bypass

streams, leading ultimately to a pinch point forming, whereby increased finning will not show any improvement on performance

7.10 Comparison With Data

7.10.1 Prediction ranges and confidence statistics

In this section the new method for predicting the pressure drop and heat transfer of inline tube bundles is compared with the method of PFR [13], the method of Chu and Ralston [23], and the Weierman [14] method.

All of the available pressure drop and heat transfer data (j factor) was placed in a spreadsheet workbook and compared with the predictions, so that statistical analysis could be performed to determine if the new method could supersede the other methods.

Table 7.4 shows summary of the amount of data predicted by each of the methods. The deviation of the predictions from the experimental data conducted using Equ.7.38.

$$Deviation = \frac{\Pr ediction - Measurement}{Measurement} * 100 \qquad \text{(Equ.7.38)}$$

This gives an indication of how much under or overprediction is given by the method in comparison to the measurement. The amount of data predicted within the ±10% and ±20% band was calculated to ensure that the predictions of the new method were close to the experimental values, and that more data was predicted that by the other methods.

Pressure Drop	**PFR**		**Weierman**		**HTFS1α**		**New Method**	
	±10%	**±20%**	**±10%**	**±20%**	**±10%**	**±20%**	**±10%**	**±20%**
Open lit.	36.84	73.68	40.79	73.68	53.95	54.79	10.53	38.16
MPWT	51.93	86.23	48.55	71.01	0.48	2.17	78.74	99.28
All sources	49.59	73.68	52.61	79.37	8.78	12.04	68.19	89.9
Heat Transfer	**PFR**		**Weierman**		**HTFS1α**		**New Method**	
	±10%	***±20%***	***±10%***	***±20%***	***±10%***	***±20%***	***±10%***	***±20%***
Open lit.	4.2	13.99	17.5	26.25	76	92.67	40	79.33
MPWT	21.19	31.52	15.25	28.42	20.93	41.34	70.54	95.87
All sources	16.6	26.79	15.63	28.05	36.31	55.68	62.01	91.25

Table 7.4: Summary of pressure drop and heat transfer deviations from predicted

Pressure Drop	PFR		Weierman		HTFS1α		New Method	
	Average deviation (%)	RMS deviation (%)	Average deviation (%)	RMS deviation (%)	Average deviation (%)	RMS deviation (%)	Average deviation (%)	RMS deviation (%)
Open lit.	11.73	14.85	9.52	15.34	12.58	22.17	-28.75	30.85
MPWT	9.29	14.26	117.27	331.44	63.71	66.42	-0.99	9.69
All sources	9.67	14.33	100.56	304.65	55.78	61.66	-5.3	15
Heat Transfer	**PFR**		**Weierman**		**HTFS1α**		**New Method**	
	Average deviation (%)	RMS deviation (%)	Average deviation (%)	RMS deviation (%)	Average deviation (%)	RMS deviation (%)	Average deviation (%)	RMS deviation (%)
Open lit.	52.67	7.28	85.43	9.27	-0.2	0.29	3.93	1.99
MPWT	26.81	5.18	32.78	5.73	-27.79	5.28	1.35	1.16
All sources	34.03	5.84	47.79	6.9	-20	4.48	2.07	1.44

Table 7.5: Summary of prediction statistics when compared with experimental data

Table 7.5 shows the statistical results of all the methods over the updated databank. As it was recognised that the open literature databank sources are less reliable than the newly collected data, comparison were conducted on the different elements of the databank. It can be seen that for both heat transfer and pressure drop elements and over the entire databank the new method performs extremely well, and significantly better than the other methods.

7.10.2 Evaluation of new method

The results above indicate that the PFR [13] method currently used by HTFS, was the closest in terms of data prediction to the new method, therefore the following sections only contrast PFR with the new method.

7.10.3 Pressure drop

It can be seen in Table 7.4 that the new method predicts significantly more data over both the ±10% and ±20% bands than the PFR [13] method. The new method predicts 90% of all the data is predicted within the key ±20% band, while PFR predicts 74%. This is even more marked in the ±10% range, with new inline method predicting 68% to PFR's 50%. Figure 7.36 shows deviations of predicted data from measurements, against Re_{max}.

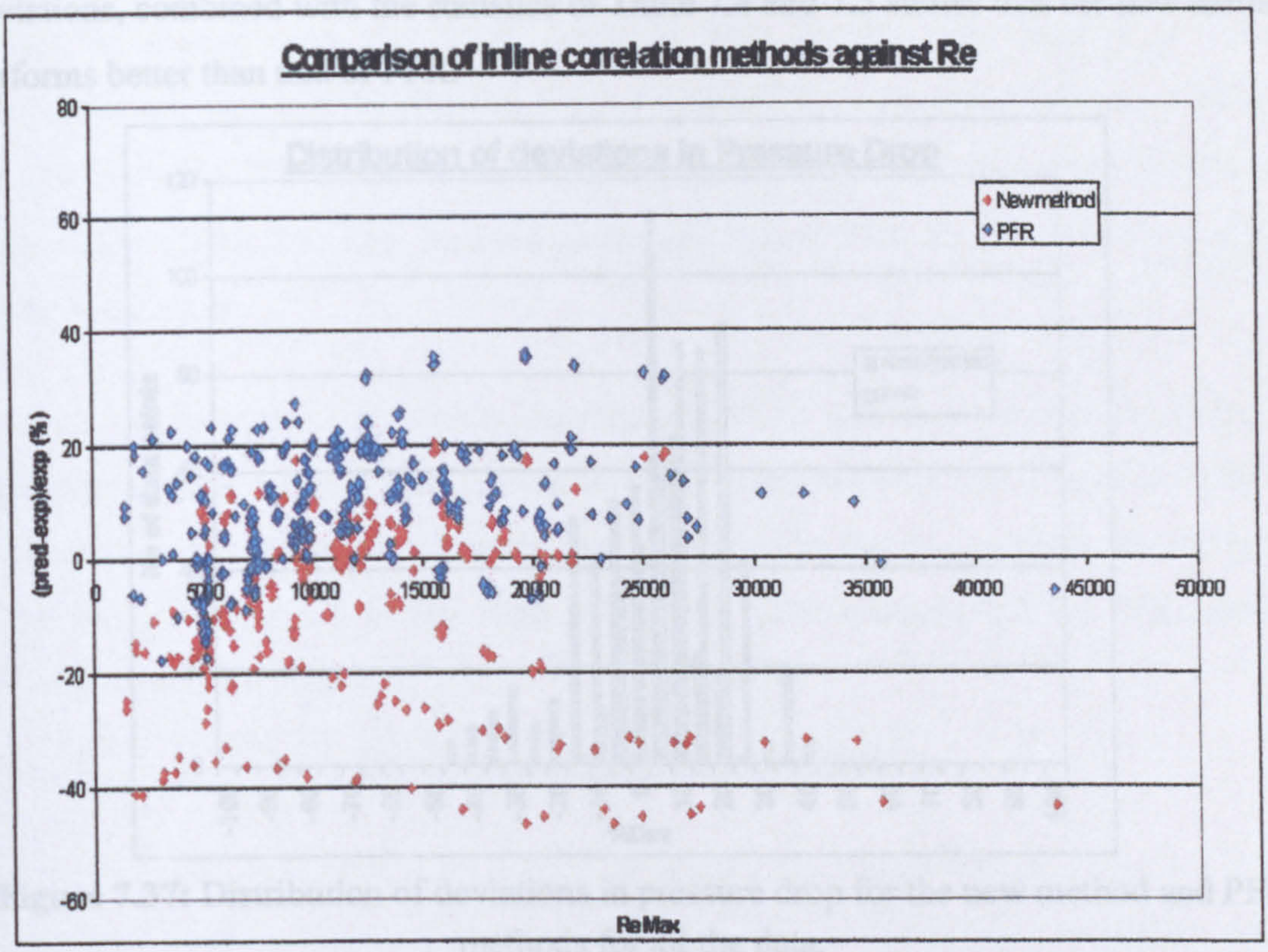

Figure 7.36: Deviations of pressure drop prediction from measured data for the entire databank

It can be seen in Figure 7.36 that the new method appears to underpredict two sources quite noticeably. Inspection of the databank showed that these were sources 9 and 10, of the open literature data. This Figure also shows that there are no strong prediction tendencies (under/overprediction) with increasing flow rate.

The reason for this was found to relate directly to the fact that the physical properties of the x-side fluid for the open literature data is constant, whereas the collected test data has properly varying values. As the new method relies in multiple instances on physical properties for tube loss and bypass loss coefficients it follows that an incorrect prediction will follow if this data is not correct. The open literature prediction methods have less reliance on this as they use a series of correction factors with strong influence on the final result, and do not resolve the subtleties of processes occurring within finned tube bundles.

Figure 7.37 shows a histogram of the number of data points predicted by the two methods for the range of percentage deviations. This visual representation of the

deviations, combined with the statistics of Table 7.4 and 7.5 shows that the new method performs better than that of PFR.

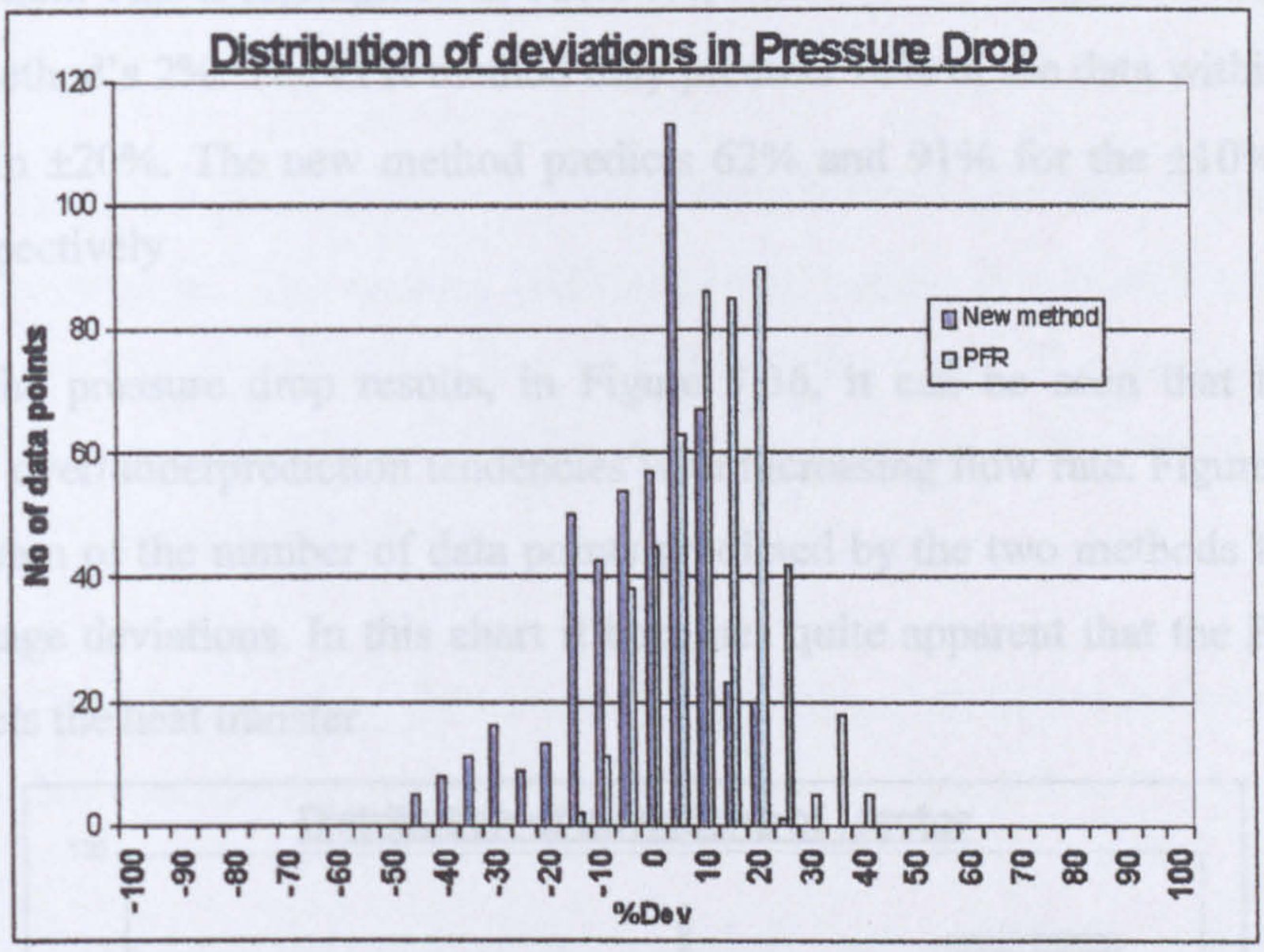

Figure 7.37: Distribution of deviations in pressure drop for the new method and PFR methods for all the data.

7.10.4 Heat transfer

Figure 7.38 compares the deviations in predictions of j factor for the new method and PFR [13].

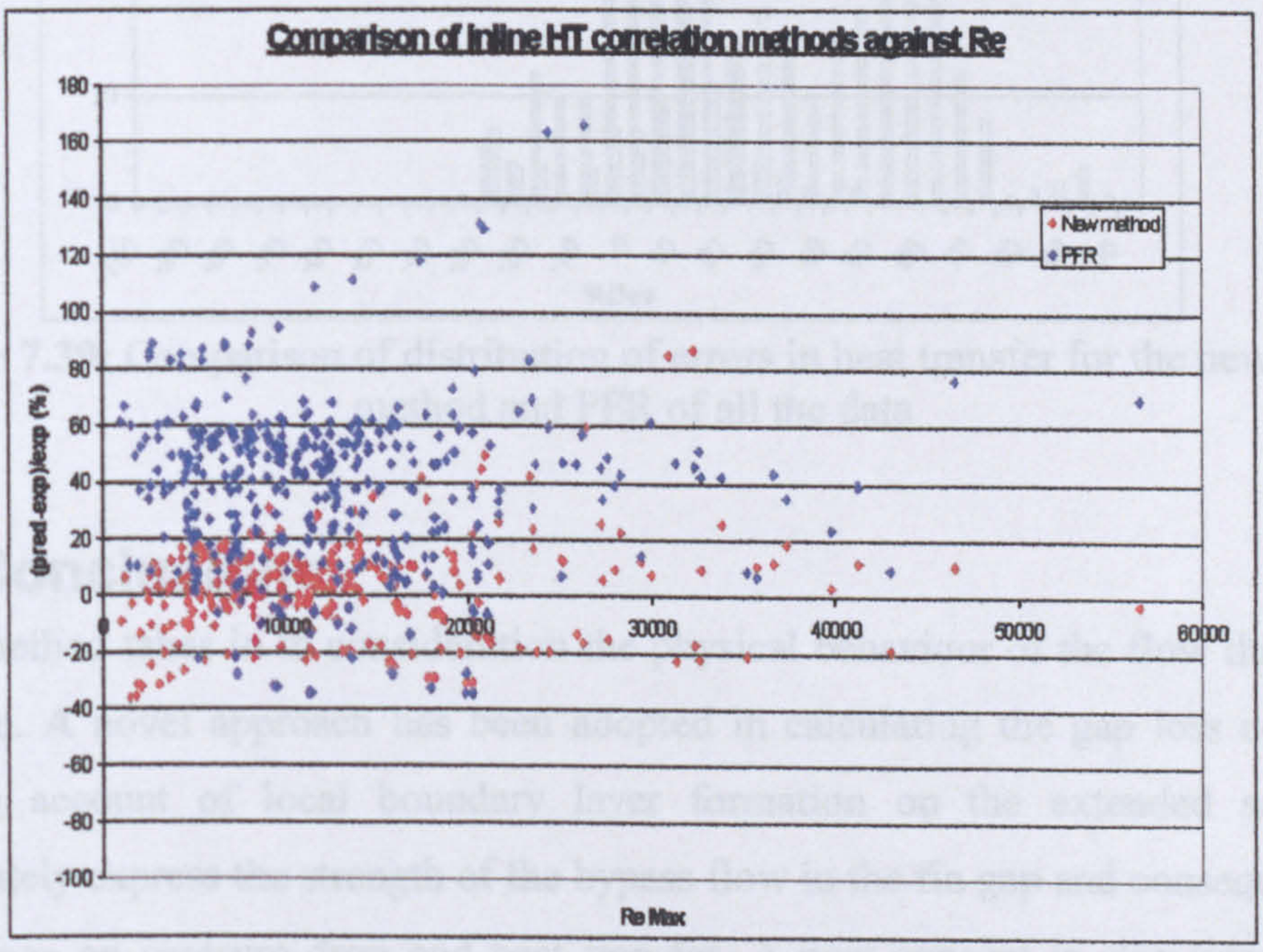

Figure 7.38: Deviations of j factor prediction from measured data, for the entire databank

It can be clearly seen that PFR performs very poorly, with serious levels of overprediction. This is highlighted in Table 7.4, with PFR's average deviation of 34% to the new method's 2%. The PFR method only predicts 16% of the data within ±10% and 27% within ±20%. The new method predicts 62% and 91% for the ±10% and ±20% bands, respectively

As with the pressure drop results, in Figure 7.36, it can be seen that there are no noticeable over/underprediction tendencies with increasing flow rate. Figure 7.39 shows the histogram of the number of data points predicted by the two methods for the range of percentage deviations. In this chart it becomes quite apparent that the PFR method, overpredicts the heat transfer.

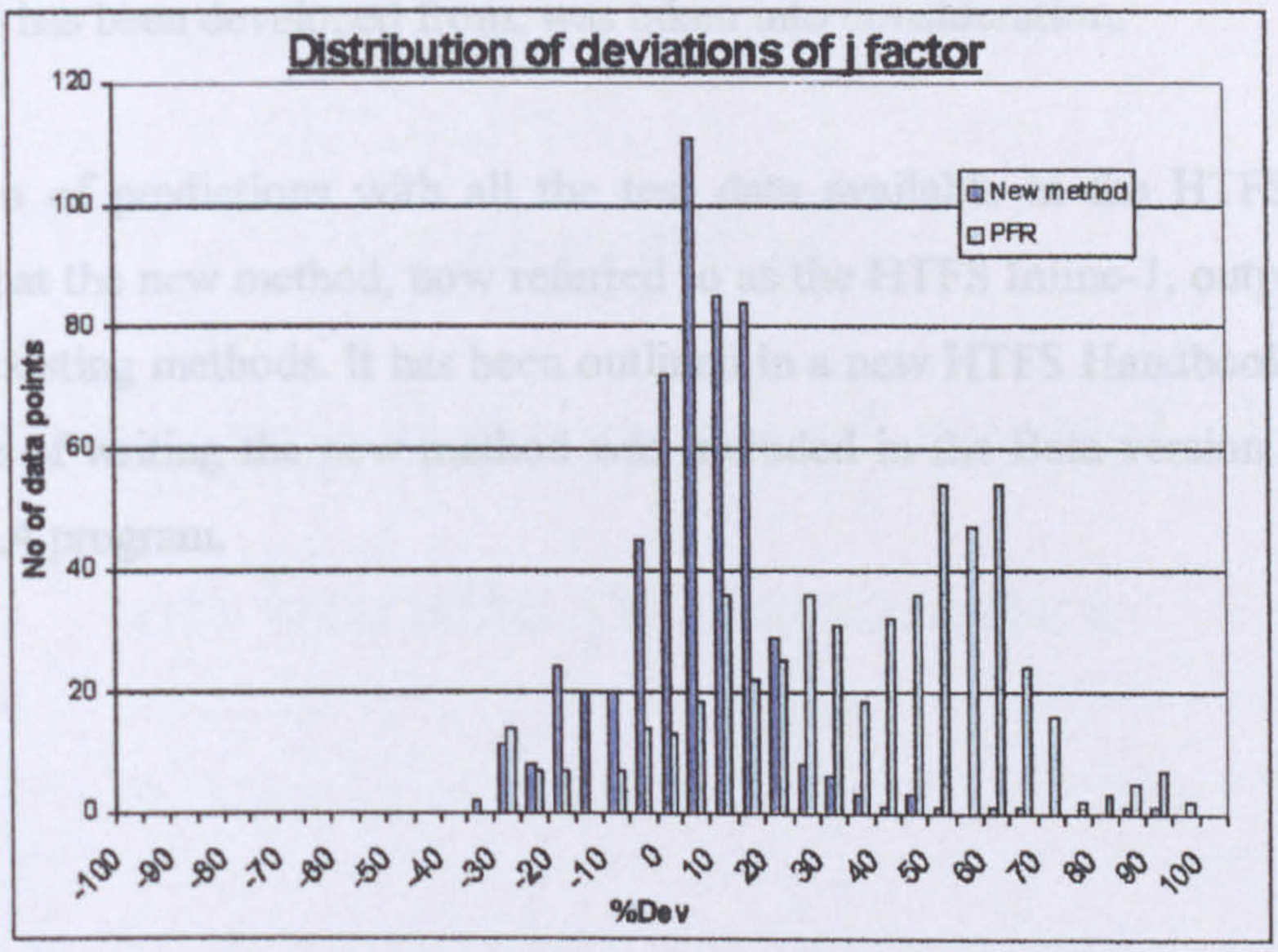

Figure 7.39: Comparison of distribution of errors in heat transfer for the new inline method and PFR of all the data

7.11 Conclusions

- The method takes in to consideration the physical behaviour of the flow through the bundle. A novel approach has been adopted in calculating the gap loss coefficient taking account of local boundary layer formation on the extended surface to accurately express the strength of the bypass flow in the fin gap and consequently the influence on pressure drop and heat transfer. A new concept is also introduced to correct the combined pressure loss coefficient for the fins and tubes by including an

augmented mass transfer coefficient. This coefficient has been developed from review of open literature and CFD analysis of data from the NEL Multi-Purpose Wind Tunnel.

- It is important to note that a correlation coefficient is no longer used on the pressure head loss formulation. This implies that the overall bundle loss coefficient accounts accurately for the geometry and the physics of the flow. The inclusion of the influence of the gap flow stream on heat transfer on the extended surface resulted in improved predictions of the j factor.

- The scalability of the method for unusual geometries, outside the data range which the method has been developed from, was taken into consideration.

- Comparison of predictions with all the test data available in the HTFS databank indicates that the new method, now referred to as the HTFS Inline-1, outperforms all available existing methods. It has been outlined in a new HTFS Handbook Sheet and at the time of writing the new method was included in the Beta version of HTFS's ACOL v.6.4 program.

CHAPTER 8

Modelling the influence of corbel shapes on bundle performance

8.0 Introduction

The staggered bundle models presented in Chapter 6, as with most open literature methods, were all developed from data with finned half tubes at the walls. This ensured that the flow through the bundle was 'perfect', that is the flow pattern at the walls was the same as through the middle of the bundle, hence the statement can be made that the test bundle gives the same behaviour as a bundle of infinite width ($N_T \rightarrow \infty$). Corbels also ensure that there is no bypassing of the flow at the walls, which would affect heat transfer and pressure drop. Bypassing will be dealt with in Chapter 9.

A finned half tube is expensive and difficult to produce so in practise other shapes, that will be detailed below, are used instead. This means that an aerodynamically dissimilar shape is introduced into the bundle, and will have ramifications on pressure drop. The new staggered bundle method (Chapter 6) takes no account of bypass flow, as the heat transfer and pressure drop model was developed from data for bundles with no bypassing flow (i.e with ideal corbels). The work in this chapter aims to show the effects of these shapes on the air-cooler bundle introduced in Chapter 3, to discuss the implications of using each corbel, and to show a prediction method that can be used to extend the new staggered pressure drop model.

The work was performed in two stages. The first stage was a two-dimensional CFD study using all the corbel shapes shown in Figure 2.4. After this initial study the corbel shapes that were considered for study were selected, and the test bundle and test program described in Sections 3.5 and 4.3 were initiated to provide experimental validation of the CFD results, and provide data for prediction method development.

8.1 Initial CFD study

It was found that modelling the test bundle in three dimensions was computationally impractical. A number of approaches were tried based on the work presented in Chapter 5, but the models had too many cells and the simulations would exhibit unusual behaviour, and would rarely even initialise to a first iteration. Increasing the cell size to create a larger, less dense, mesh resulted in highly skewed cells that, even though not recommended to start with, also caused problems in the initialisation stages. Therefore it was decided to conduct a shorter study using a simpler two-dimensional model.

8.1.1 Model Domain

As the majority of crossflow heat exchangers are staggered bundle arrangements the design had alternating rows fitted with corbels, as shown in Figure 8.1

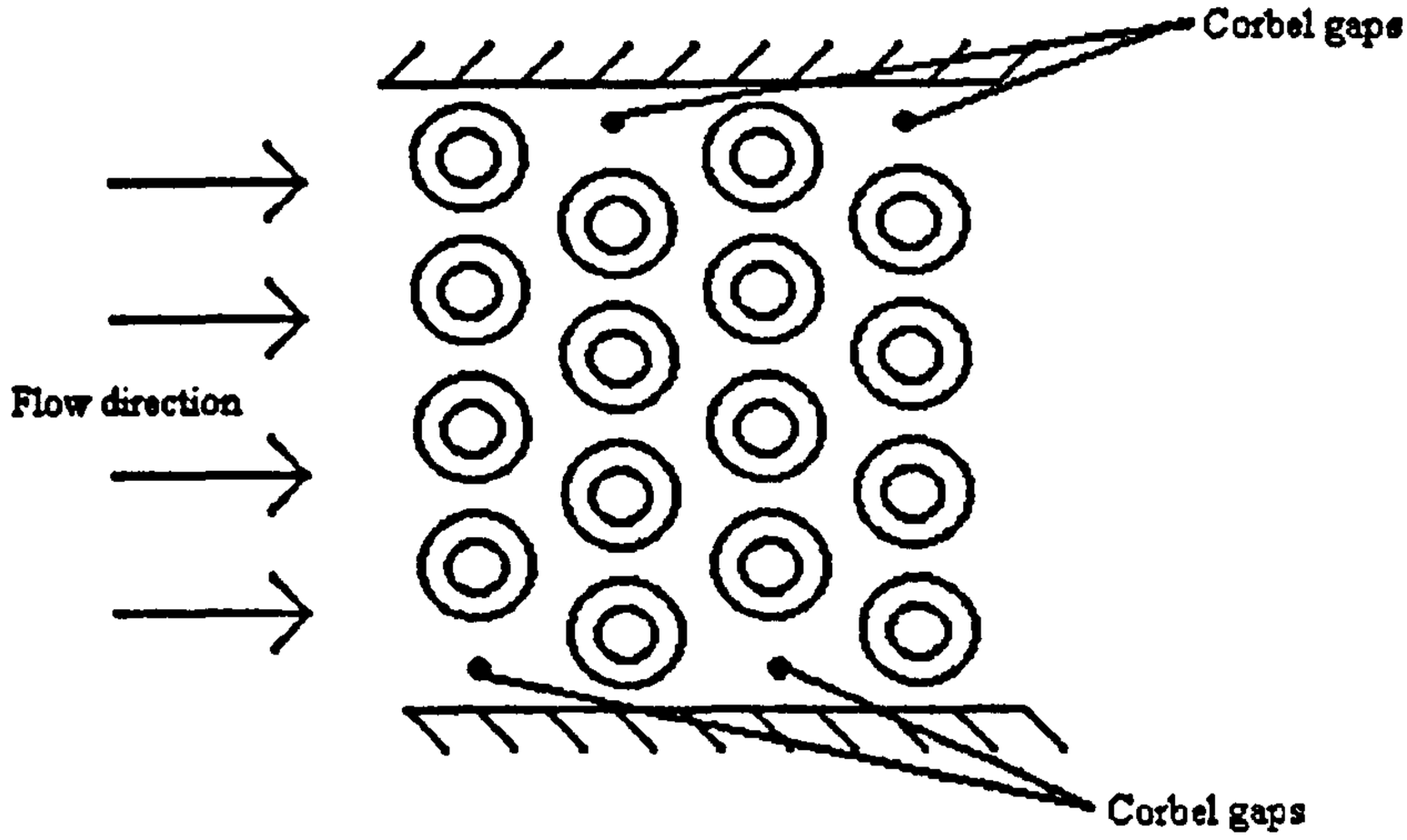

Figure 8.1: Corbel placement

With the use of a two-dimensional isothermal model, it is possible to consider the finned tubes as blockages in the flow direction. To achieve this, the concept of an equivalent diameter was devised based on the blockage incurred in a duct by the finned tubes. By calculating the approach area to the bundle, from Equ.8.1,

$$A_d = H_{Duct} \cdot L_T \qquad \text{(Equ.8.1)}$$

and subtracting the minimum flow area (S_{min}), as defined by PFR [13]; the area that would be blocked by finned tubes is calculated from Equ.8.2

$$A_{bl} = A_d - S_{\min} \qquad \text{(Equ.8.2)}$$

This blockage area was then divided by the tube length and the number of tubes in the first row to give the equivalent diameter of tubes that creates the same blockage:

$$D_{eq} = \frac{A_{bl}}{N_T L_T} \qquad \text{(Equ.8.3)}$$

This equivalent diameter was used as the diameter of the tubes in the 2-D domain. The bundle geometry that was modelled was the (later manufactured) experimental bundle shown in Table 3.5. The tube equivalent diameter was calculated to be 33.61mm. The corbels were all of a constant height of 25.4 mm.

In this modelling work, the bundle was assumed to sit inside a duct as shown in Figure 8.2. As the wake at the rear of the bundle would be of interest, the model was given a large exit region. The other geometry of the tube bundle was as given in Table 3.11.

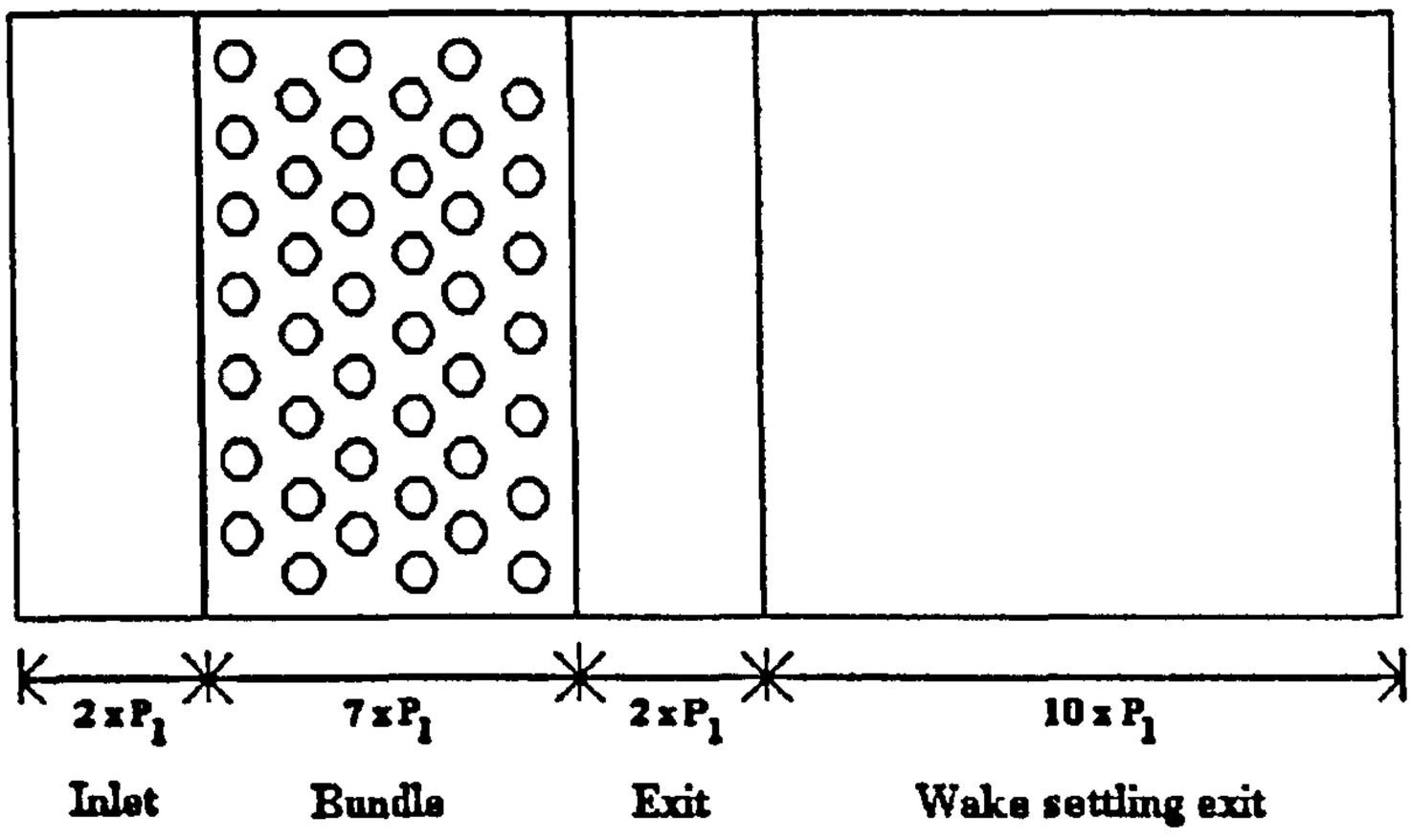

Figure 8.2: CFD Domain for bundle (shown with no corbels)

8.1.2 Mesh

To avoid generating a large mesh, the domain was split into 4 regions with graded sizes of cells. These are the duct inlet region, the bundle and two regions for the exit duct, as seen in Figure 8.2. The bundle meshing is given in Table 8.1. The mesh units are discussed in Section 7.1.2.

Region	Cell type	Cell size	Meshing scheme
Inlet	Quadrilateral	3 units	Map
Bundle	Quadrilateral	1 unit	Pave (with Laplacian smoothing)
Exit	Quadrilateral	2 units	Map
Wake settling exit	Quadrilateral	4 units	Map

Table 8.1: Meshing in 2-D bundle

8.1.3 Boundary Conditions

A constant mass flowrate (flat inlet velocity profile) was specified at the duct inlet.The duct top and bottom walls were set as walls. This is simply a rigid boundary which is not flow permeable. The corbels were set as non-permeable walls. The tubes were also set as walls as they act as a boundary to the flow. The outlet was specified as a fully developed outflow.

8.1.4 Numerical Solution

Once the mesh and boundary conditions have been specified a solution was obtained by selecting a suitable turbulence model and discretization scheme.

8.1.4.1 Turbulence model

As indicated in Chapter 5, the realisable model was chosen as it uses improved method for the calculating the turbulent viscosity and shows better performance for flows under strong adverse pressure gradients and recirculations which are common features of flows in tube bundles.

8.1.4.2 Solution scheme

A quick survey of discretization schemes available in FLUENT resulted in selecting the following schemes for each solved property: -

- Pressure – Standard
- Momentum – First Order Upwind
- Pressure-Velocity coupling – SIMPLE
- Turbulent kinetic energy (k) – First Order Upwind
- Turbulence dissipation rate (epsilon) – First Order Upwind

As there was no experimental data at this time, the initial guess of inlet pressure values was deduced from the air-cooler studies of McLean and Spence [65] who tested similar geometries with corbels in place. Table 8.2 shows the mass flow rates, corresponding air face velocities and initial gauge pressures.

Mass flow rate (kg/s)	Inlet Gauge Pressure (N/m^2)	Face Velocity (m/s)
0.5	37.5	0.826
1	110	1.652
1.5	240	2.478
2	380	3.304
2.5	540	4.131
3	720	4.957
3.5	880	5.783
4	1040	6.609

Table 8.2: Model operating conditions

8.2 CFD Results

The results of flow patterns for each corbel shape are shown in Figures 8.3, 8.4, 8.5 and 8.6. The simulations were conducted at a range of air mass flow rate values as given in Table 8.2. For brevity only the 1 and 4kg/s results of the flow patterns will be shown, however, the results of pressure drop will be given for all cases.

8.2.1 Flow patterns

Figure 8.3 shows velocity contours for the bundle with no corbels. The common trend of these contours is that the red-orange areas (those with the highest velocity) are the bypass regions between the duct walls and the nearest tube column parallel to the wall, see Figure 8.2. As expected the flow will escape through the least resistance path. It can be seen that in the transverse gaps, between tubes in the same row, an air jet with high velocity, shown as light orange regions, develops and then expands around the tube in the next tube row. The flow then diverts around either side of the tube and expands through the diagonal gap, shown by the light green regions, and reforms as another near jet flow entering the subsequent tube row. This pattern continues throughout the bundle.

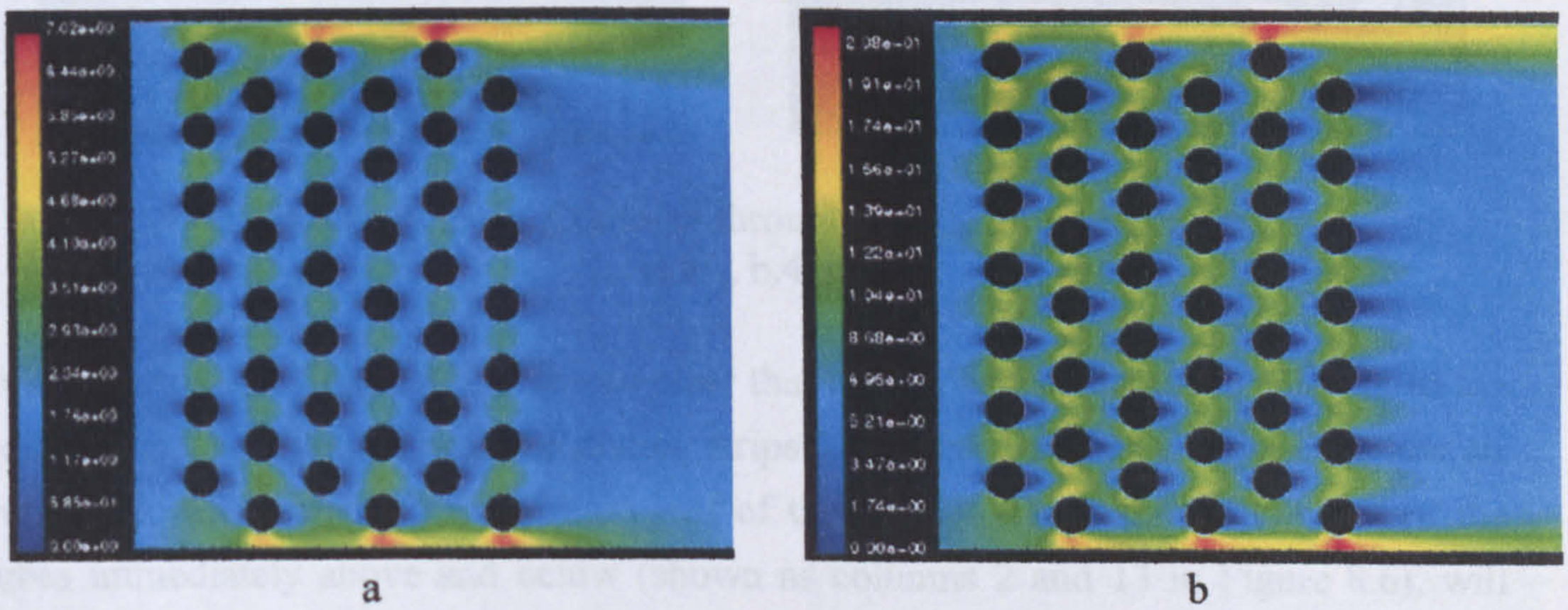

a b

Figure 8.3: Velocity Contours through bundle with bypassing

[a.1kg/s, b.4kg/s]

The corresponding velocity contours for the bundle with sealing strip, half tube, square block, tapered block and inverted V corbels are shown in Figure 8.4, 8.6, 8.7, 8.8 and 8.9 respectively. In general the presence of the corbels resulted in flow diversion toward the bundle, causing increased flow in the bundle but at various degrees depending on

the corbel shape and face velocity. The shape of the corbel has a significant effect on the local flow behaviour, which in turn would likely have influence on heat transfer and is demonstrated to have an effect on pressure drop.

8.2.1.1 Sealing strips

From Figure 8.4, for the sealing strips, it is clear that the impingement of the airflow on the face of the strip causes the air to separate in towards the middle of the bundle. This can be seen quite clearly for the highest mass flow rate in the velocity vectors of the top corbels in Figure 8.5. However the geometry of the strip dictates a low pressure region behind it with a high level of recirculation resulting in large wakes that increase in length with increased air face velocity.

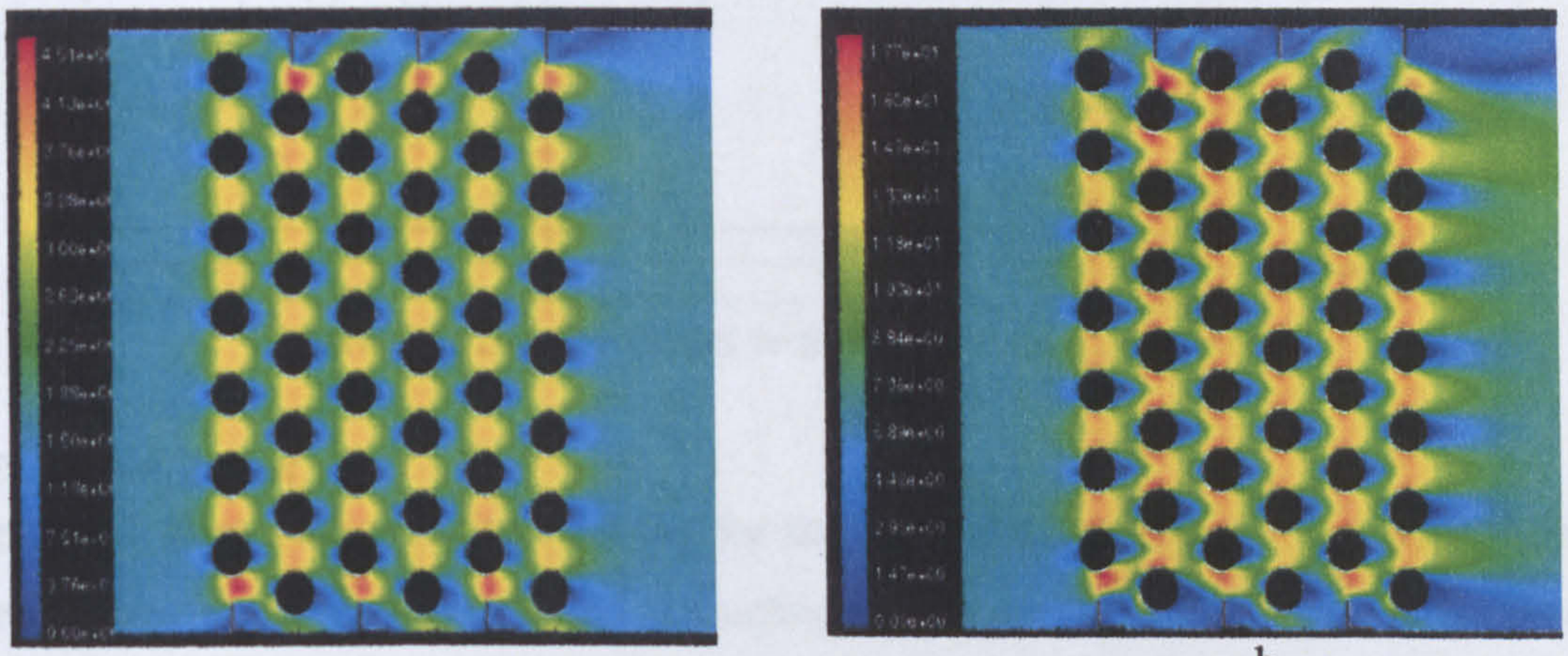

a b

Figure 8.4: Velocity Contours through bundle with sealing strips
[a.1kg/s, b.4kg/s]

With reference to Figure 8.6, it is also clear that the top half of the tubes adjacent to the corbels, in tube columns near the sealing strips (Columns 1 and 14), experience low air velocity in comparison to the bottom half of these tubes. However the top half of the tubes immediately above and below (shown as columns 2 and 13 in Figure 8.6), will experience faster flow due to the flow separation in this region especially at the early tube rows. In a practical case, the latter may compensate for the lower local heat transfer experienced in the former.

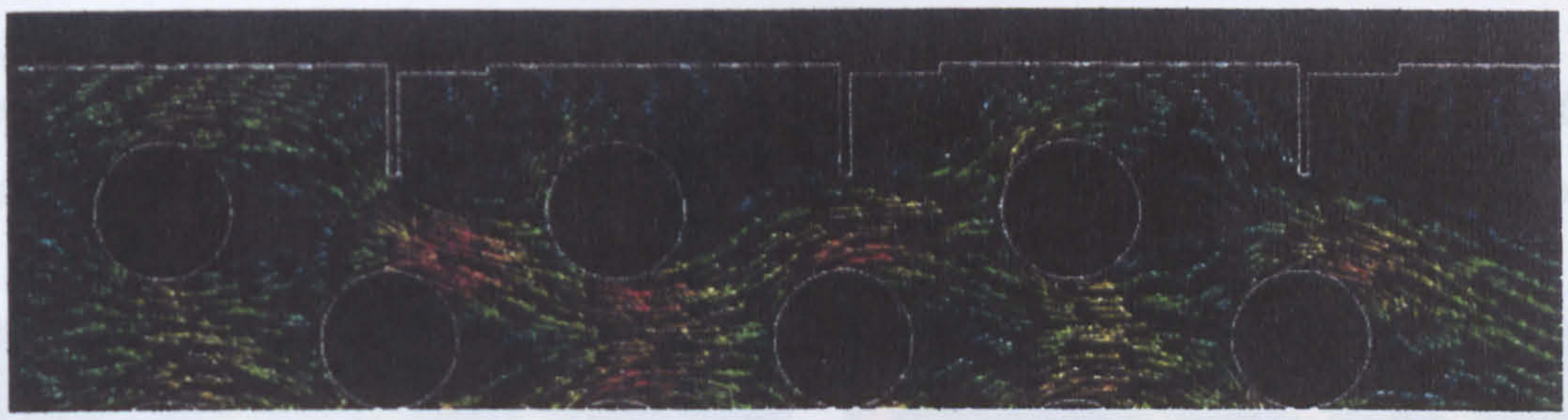

Figure 8.5: Close up of velocity vectors of sealing strip corbels at 4 kg/s

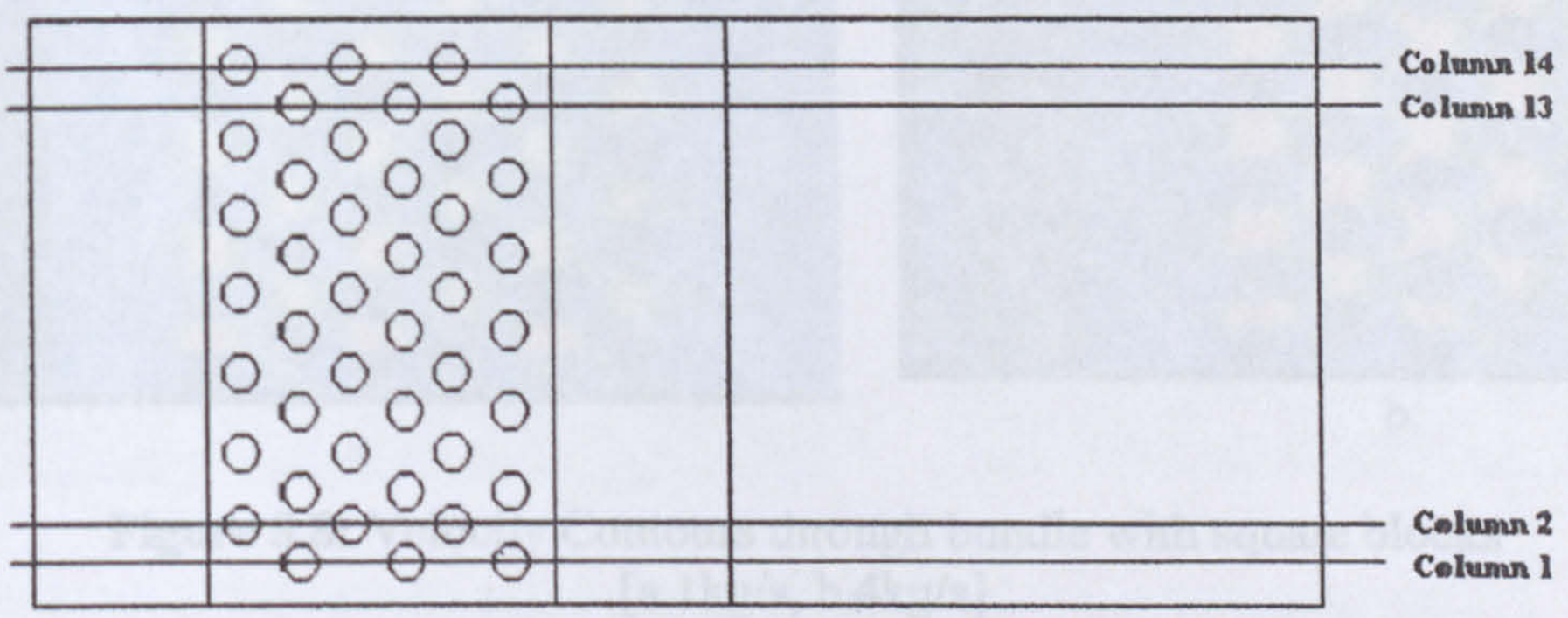

Figure 8.6: Bundle model with tube columns numbered

8.2.1.2 Half tubes

Figure 8.7 shows the velocity contours for the half tube corbel case. The flow shows itself to be more evenly distributed throughout the bundles, than for any of the other corbel shapes.

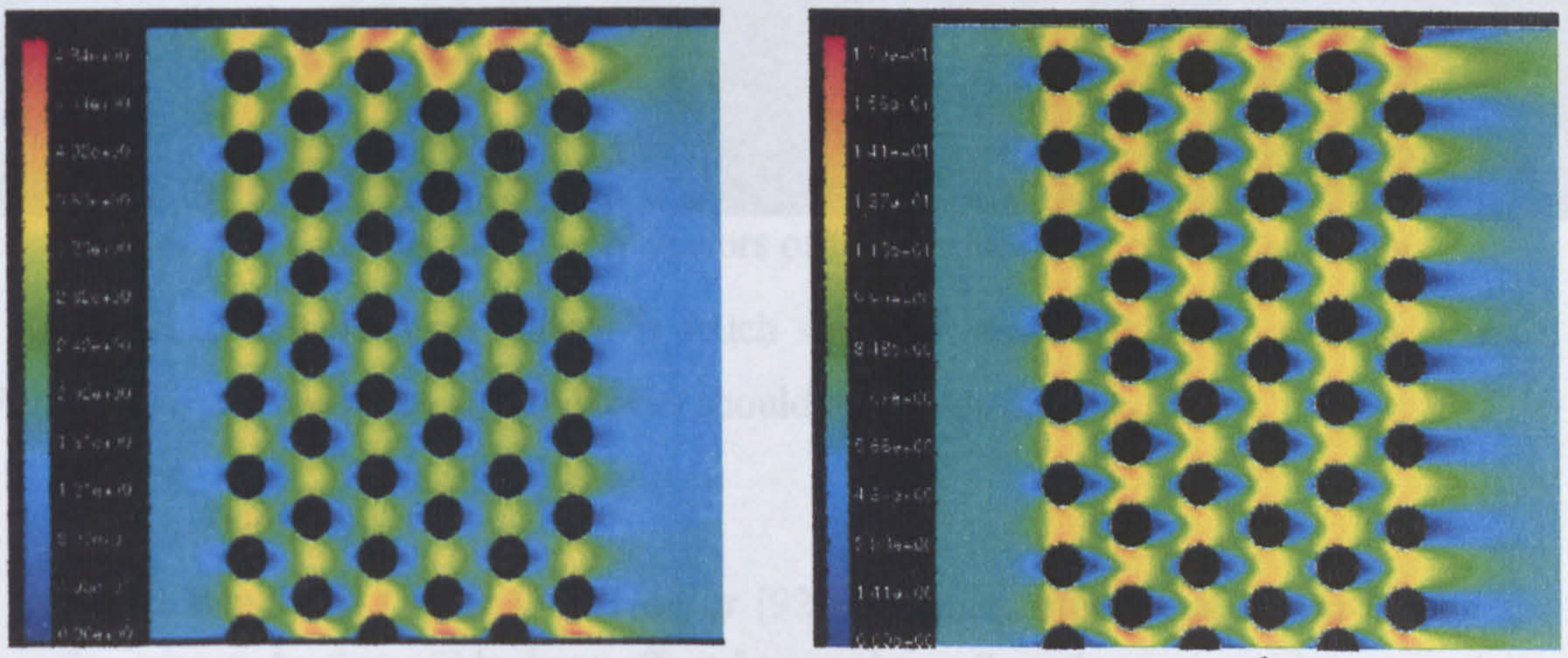

a b

Figure 8.7: Velocity Contours through bundle with half tubes

[a.1kg/s, b.4kg/s]

8.2.1.3 Square Blocks

The drag incurred by the square block corbels is due to a high degree of fore and aft separation. This can be seen in Figure 8.8 as the velocity rise on the forward edges of the corbels and the large wake region over the trailing edges.

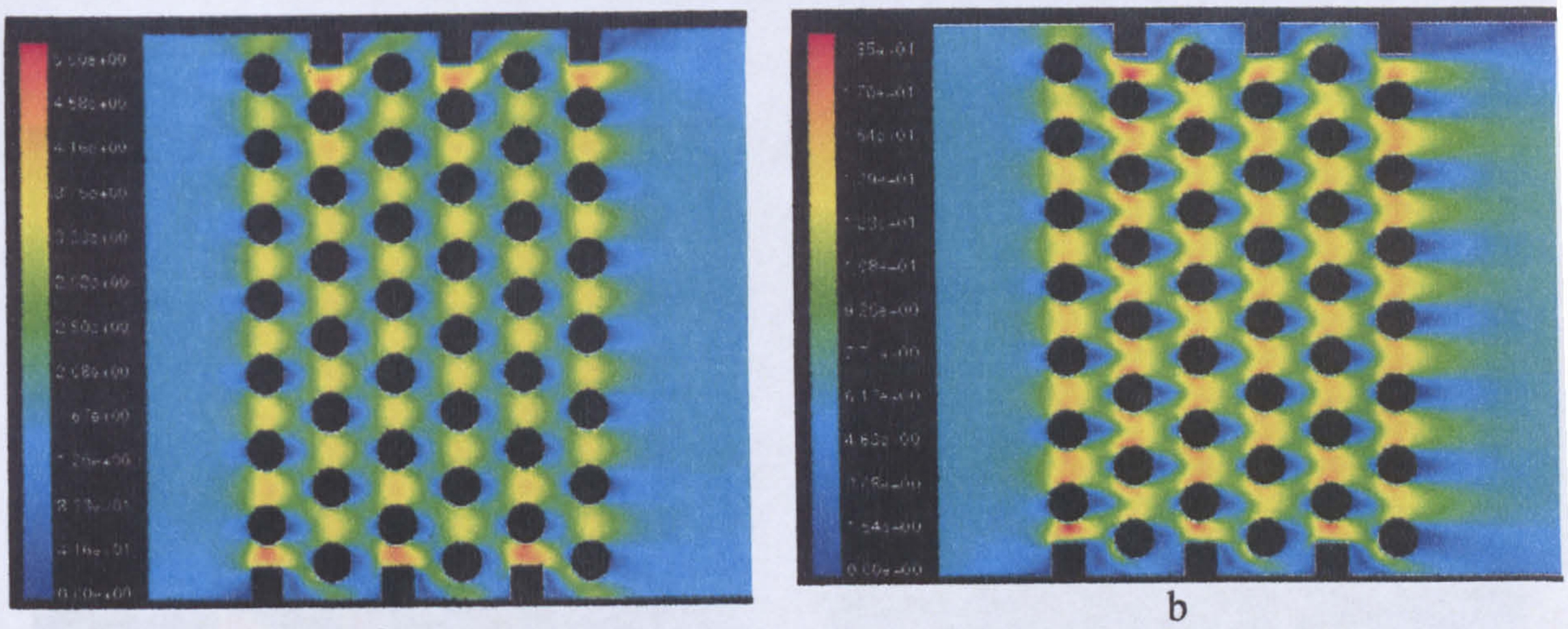

a b

Figure 8.8: Velocity Contours through bundle with square blocks [a.1kg/s, b.4kg/s]

This is shown in close up in Figure 8.9, where the velocity vectors indicate both magnitude and direction of flow

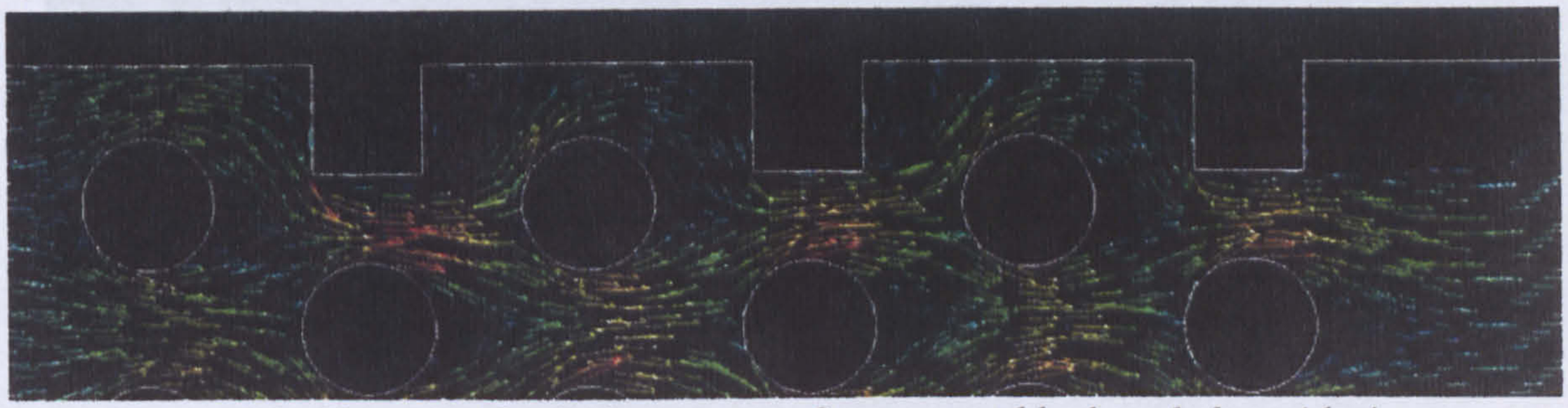

Figure 8.9: Close up of velocity vectors of top square block corbels at 4 kg/s

It can be seen that the flow pattern is much smoother than that of the sealing strips (Figure 8.5), and hence the square blocks should incur less drag.

8.2.1.4 Tapered Blocks

It has been shown by Tanner [91], Hoener [92] and many others that if you incline a face (ignoring reduction of blockage effects) normal to a flow the pressure drop over the body decreases.

Examining Figure 8.10, and the velocity vectors in Figure 8.11, show that the approach face incurs a smaller region of stagnant flow at its root compared to the square block.

Immediately it can be visualised how this reduces drag. The angle between the approach face and the top of the block is reduced and thus it can be reasoned, and seen, that separation effects will be smaller due to the smaller change in approach flow direction. The result of this is the tapered block should show a lower drag than the square blocks and the sealing strips.

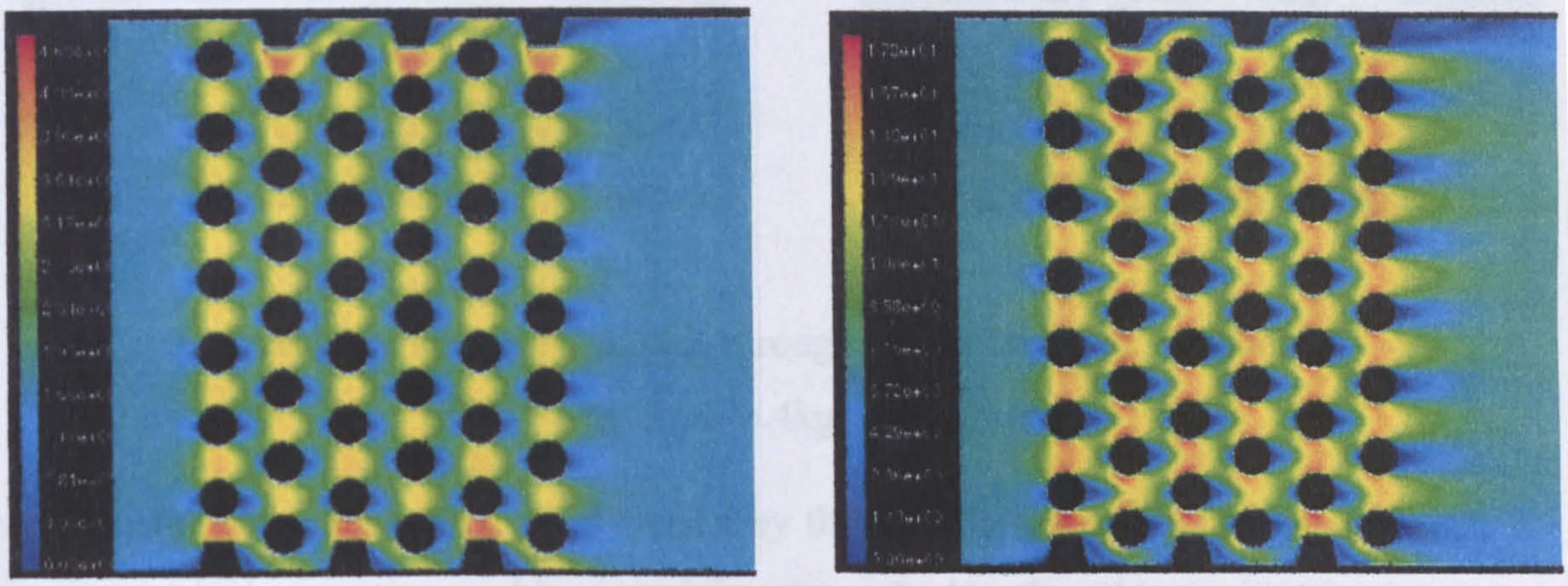

a b

Figure 8.10: Velocity Contours through bundle with tapered blocks [a.1kg/s, b.4kg/s]

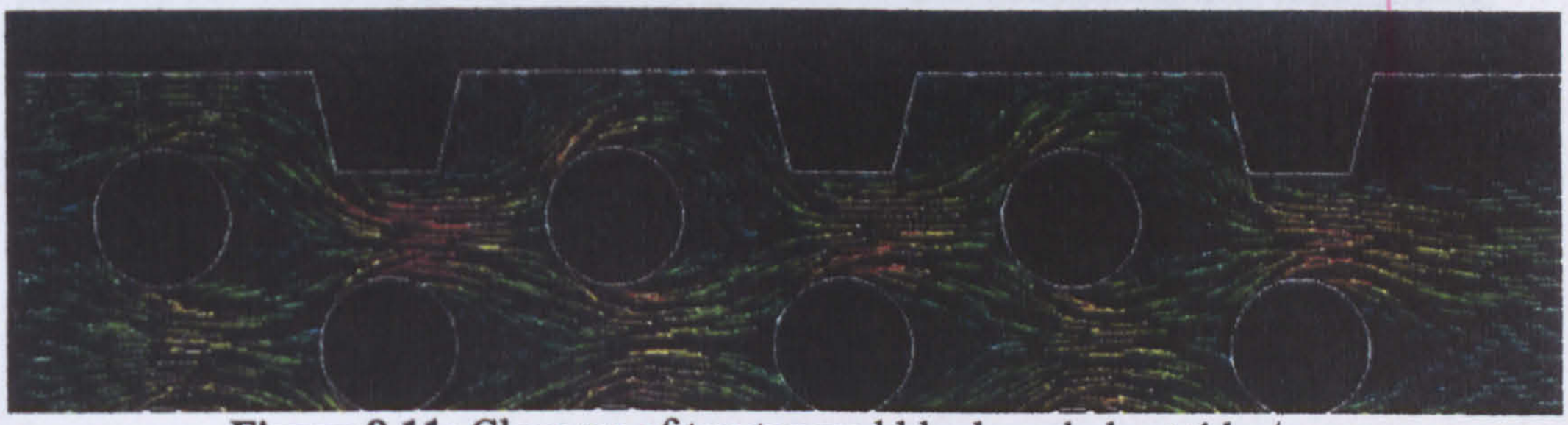

Figure 8.11: Close up of top tapered block corbels at 4 kg/s

8.2.1.5 Inverted V

Figure 8.12 shows that the more inclined approach face of the Inverted V corbel almost completely eradicates all forward recirculation zones, which should reduce form drag.

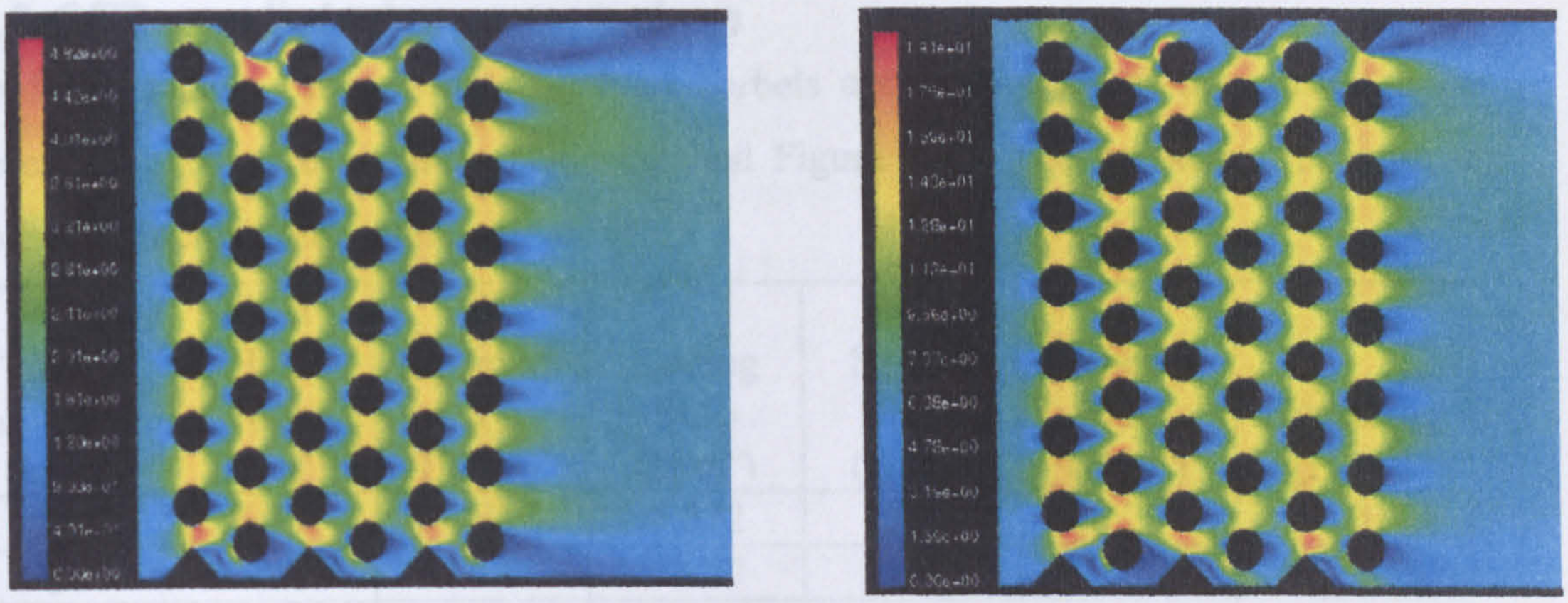

a b

Figure 8.12: Velocity Contours through bundle inverted V corbel

[a.1kg/s, b.4kg/s]

However the sharp separation point caused by the equally steep rear face is shown to create a marked separation, and by examining the wake length and intensity (the deeper blue region) it can be surmised that drag of this corbel shape is quite high.

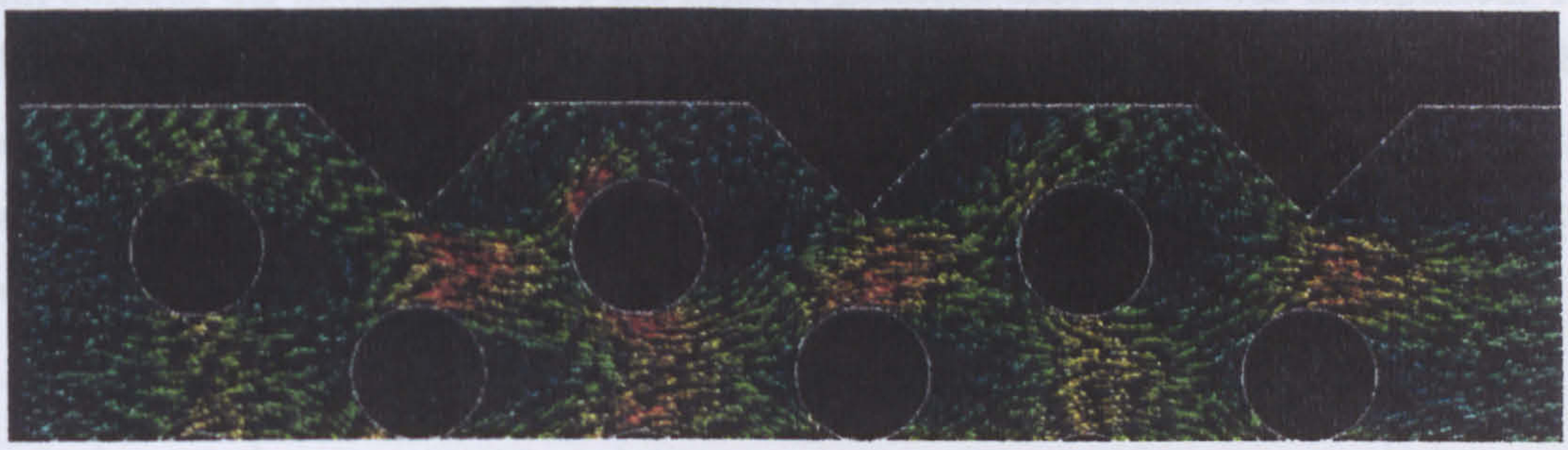

Figure 8.13: Close up of velocity vectors of top Inverted V corbels at 4 kg/s

Figure 8.13 shows the velocity magnitude and direction vectors close up at a flow rate of 4 kg/s, where the separation and recirculation is more apparent.

8.2.2 Heat transfer

With respect to thermal performance it is believed that although the corbel shape has an influence on the local flow behaviour and thus local heat transfer, the bulk effect on the bundle heat transfer performance may not be significantly different.

8.3 CFD predicted pressure drop

Predicted bundle pressure drop without corbels and with each of the corbel shapes described above are given in Table 8.3 and Figure 8.15. The pressure drop with no corbels is included for reference.

Mass flow Rate (kg/s)	Plain Half Tube (N/m^2)	Inverted V (N/m^2)	Sealing Strip (N/m^2)	Square Block (N/m^2)	Tapered Block (N/m^2)	Bypassing (N/m^2)
0.5	6.55	7.31	8.572	12.54	8.20	6.01
1	N/A	N/A	73.27	73.47	70.61	52.34
1.5	95.89	114.25	124.37	125.59	119.59	87.97
2	166.23	177.94	172.98	170.69	166.09	128.78
2.5	220.99	237.40	212.39	210.27	205.27	163.32
3	280.44	304.26	259.03	258.3	249.37	195.15
3.5	N/A	386.02	322.64	322.73	300.45	232.31
4	430.8	477.46	398.45	399.57	380.11	279.57

Table 8.3: Pressure drop across CFD bundle with varying corbel shapes, and bypassing

With corbels, the inverted V gave the highest-pressure drop. This was unexpected. The half tube corbel gives the next highest value due to the small gaps between the corbel and adjacent tubes as shown in Figure 8.1. This is followed by both the square block and the sealing strip, which appear to give the same pressure drop. The tapered block gives the lowest pressure drop in comparison with other corbels.

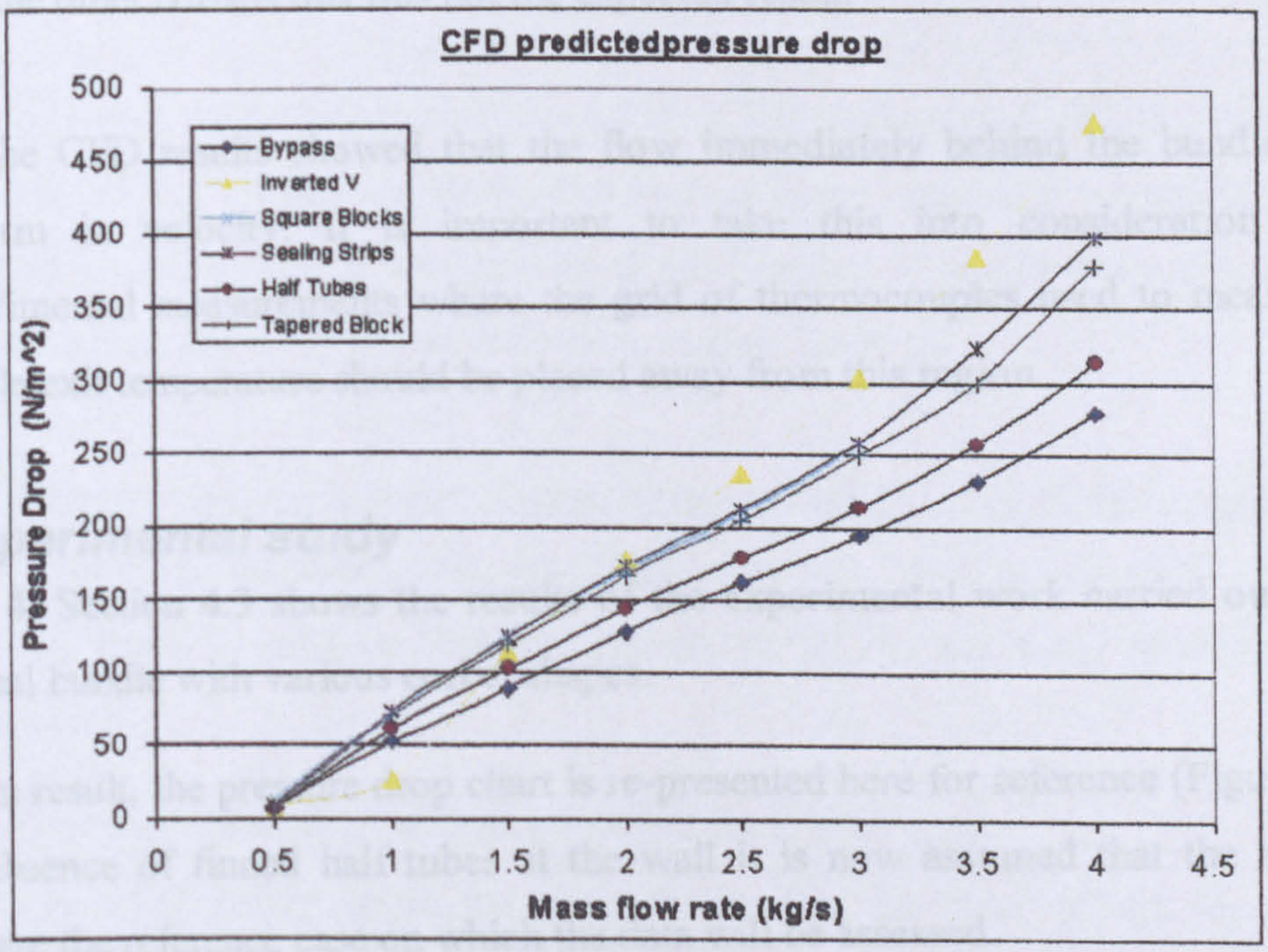

Figure 8.14: Predicted bundle pressure drop without and with various corbels

At an air face velocity of 6.6 m/s (4 kg/s), Figure 8.14 shows that the pressure drop will increase by about 20% if inverted V corbels are used instead of tapered blocks. In practice the choice of corbel shape will be dictated by the cost of manufacture. It is anticipated that the corbels made from readily available sections, such as sealing strips or square blocks, are normally used. If it is assumed that the corbel shape will not affect the heat transfer, the design engineer then needs to balance the cost of manufacture against the pressure drop penalty and reach a decision. In the simulations, the results clearly indicate that tapered blocks are the recommended choice. The effects of bypassing will be discussed in Chapter 9.

8.4 Conclusions of CFD work

- The CFD analysis demonstrates that the corbel shape has an influence on the local flow behaviour. However the variation of flow in different parts of the bundle suggests that the bulk effect on the bundle heat transfer may not be as significant. This conclusion should be verified by experimental measurements.

- The inverted V corbels give the highest pressure drop while the tapered blocks give the lowest pressure drop. Given the slightly more streamlined shape when compared with the other corbels this was not the expected result.

- The CFD results showed that the flow immediately behind the bundle is not uniform in velocity. It is important to take this into consideration during experimental measurements where the grid of thermocouples used to measure the bundle exit temperature should be placed away from this region.

8.6 Experimental study

Chapter 4, Section 4.3 shows the results of the experimental work carried out on the isothermal bundle with various corbel shapes.

The main result, the pressure drop chart is re-presented here for reference (Figure 8.15). In the absence of finned half tubes at the wall it is now assumed that the half tube corbels are the reference case on which the data will be assessed.

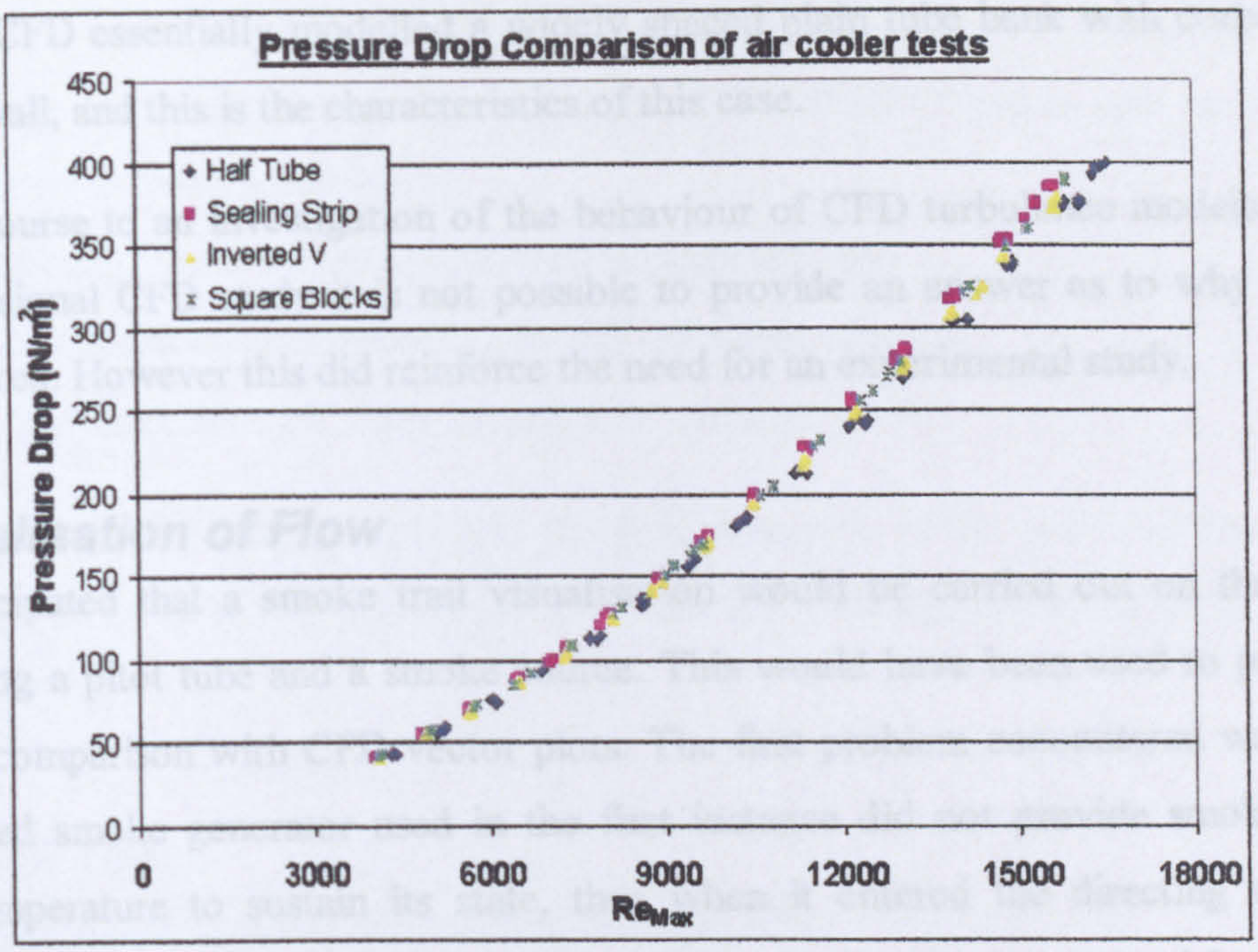

Figure 8.15: Pressure drop against flow rate for experimental corbel bundle

It can be seen that pressure drop increases in the order of:

- Half Tube
- Inverted V
- Square Blocks
- Sealing strips

This is different from the observations of the CFD study above. While it would have been expected that the Sealing strips, due to their fierce separation regime, would incur the largest pressure drop it was unclear if the Inverted V would cause more pressure drop over the square block, given their distinct flow features.

8.7 Differences between experimental data and CFD predictions

The experimental measurements are direct readings from a calibrated differential pressure transducer, and as such are not in doubt, so the CFD models must be questioned.

There were two explanations that may account for this difference:

- The CFD solver could not properly resolve the local effects for the sharp separation that occurred over the inverted V.

- The CFD essentially modelled a widely spaced plain tube bank with corbels at the wall, and this is the characteristics of this case.

Without recourse to an investigation of the behaviour of CFD turbulence models, or a three-dimensional CFD study it is not possible to provide an answer as to why these results differed. However this did reinforce the need for an experimental study.

8.8 Visualisation of Flow

It was anticipated that a smoke trail visualisation would be carried out on the tube bundle, using a pitot tube and a smoke source. This would have been used to provide local flow comparison with CFD vector plots. The first problem encountered was that the oil based smoke generator used in the first instance did not provide smoke at a suitable temperature to sustain its state, thus when it entered the directing tube it recondensed into oil. A second aerosol oil based smoke generator was used but it did not generate either the required volume or density of smoke needed.

A third method was developed, involving a smoke cartridge used in industrial HVAC ducting leak testing. This involved using a plastic barrel to hold the burning cartridge while a centrifugal pump drew the smoke out to a flexible tube with the pitot tube attached. When tested the system appeared to let the heavy smoke particles sink in the pump and the result was that only air was drawn through the pitot. This system had to be discarded.

With the difficulties of using a smoke method it was decided to use a more prosaic method of visualisation. White cotton thread tufts were used, as suggested by Sindo [93]. These tufts were placed on the leading and trailing faces of the corbels.

On the square block corbels tufts were added to the top faces as well to look for the separation indicated by the CFD, as shown in figure 8.18. Streamers were attached to the tubes in the last row. To record the visualisation a 26 frames per second digital video camera was used mounted on a tripod to record the movement of the tufts throughout the flow rate range. The individual results are discussed below.

During the visualisation photographs were taken, but it was found that direct comparisons between the tuft angles and the CFD velocity vectors was not possible. This was due to a combination of

- Lighting issues in the experimental rig (MPWT) bay.
- Limitations of light balancing of still and video cameras.
- Light reflections off shiny fin and tube surfaces.

The following photographs represent the best examples of the collected photos, and discuss results seen at the time of the tests. The tufts are highlighted in green to allow easier viewing.

8.8.1 Half Tubes

No usable visualisation was conducted on the half tubes.

8.8.2 Sealing Strips

Figure 8.16 shows the position of the visualisation tufts at air face velocities of 1.7m/s and 5.7m/s.

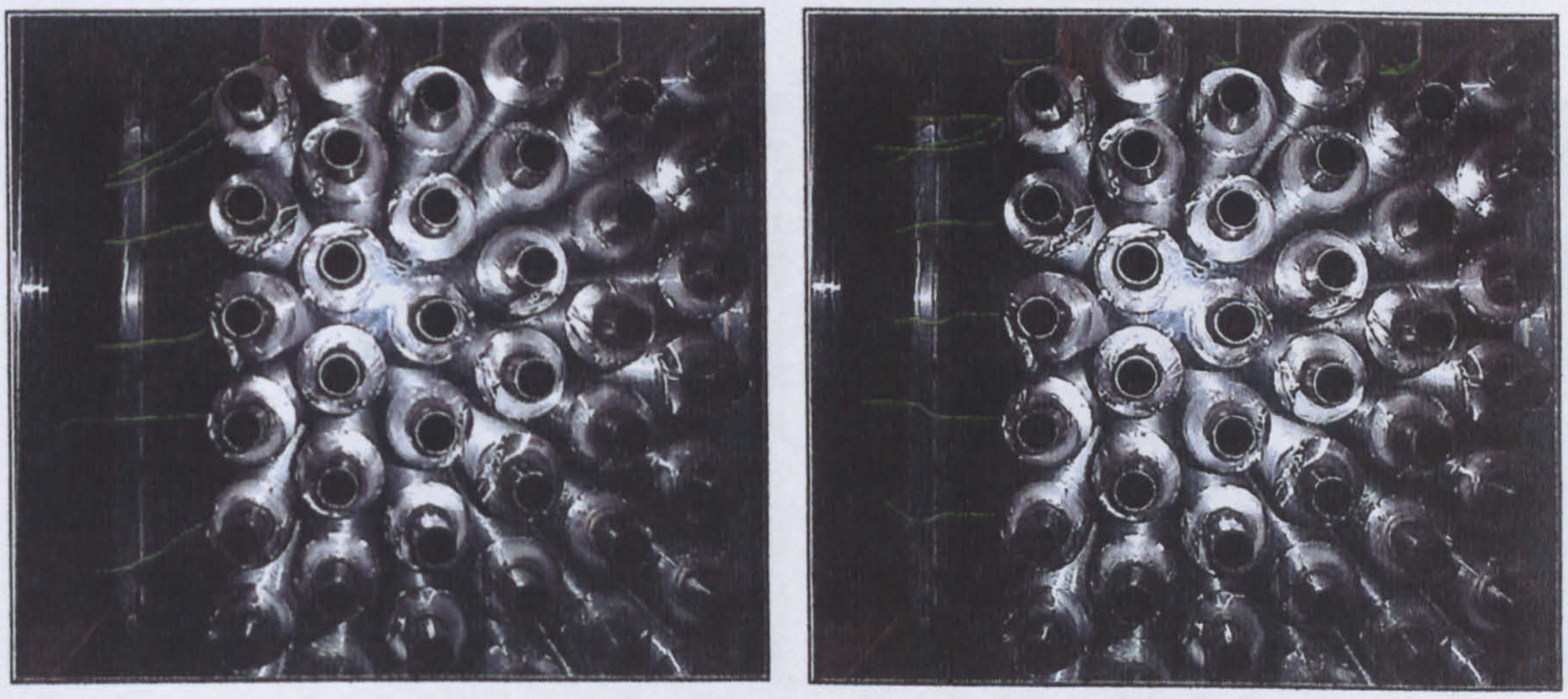

a. b.

Figure 8.16: Tufts and streamers on the bundle with sealing strips

a. 30% flow rate (1.7m/s), b. 80% flow rate (5.7 m/s)

Figure 8.16a shows that the streamers on the tubes at the rear of the bundle sag towards the floor. This is due to the gravity effect on the tufts. It can be seen that the tufts on the corbels also sag, although there was a tendency for the end of the tuft to move into the recirculation region behind the corbels.

At the higher flow rate (Figure 8.16b) the gravity effect was apparently overcome, and the tufts on the corbels show a distinct tendency to lift into the recirculation region immediately behind the corbel. The tuft on the rearmost corbel in particular can be seen to lift into the wake region. This is due to the low dynamic pressure in the wake of the corbel compared to the higher dynamic pressure in the biased jet; the tuft moves to with the pressure gradient: high to low. This compares very favourably with the dynamic pressure plots from the CFD result, and indicates that the tufts were well positioned to determine such flow details. The streamers on the tubes were also found to be better aligned with the flow direction at the higher flow rates, but simply due to the higher momentum of the flow and the lift generated overcoming the gravity effect. It does confirm the assumption that the flow through, and at the rear of the middle of the bundle, is fairly uniform and that it is only the tubes near the wall that are affected by the introduction of corbels.

8.8.3 Inverted V

Figure 8.17 shows the tufts and streamers with inverted v corbels in place with a face velocity of 1.65 m/s and 5.7m/s.

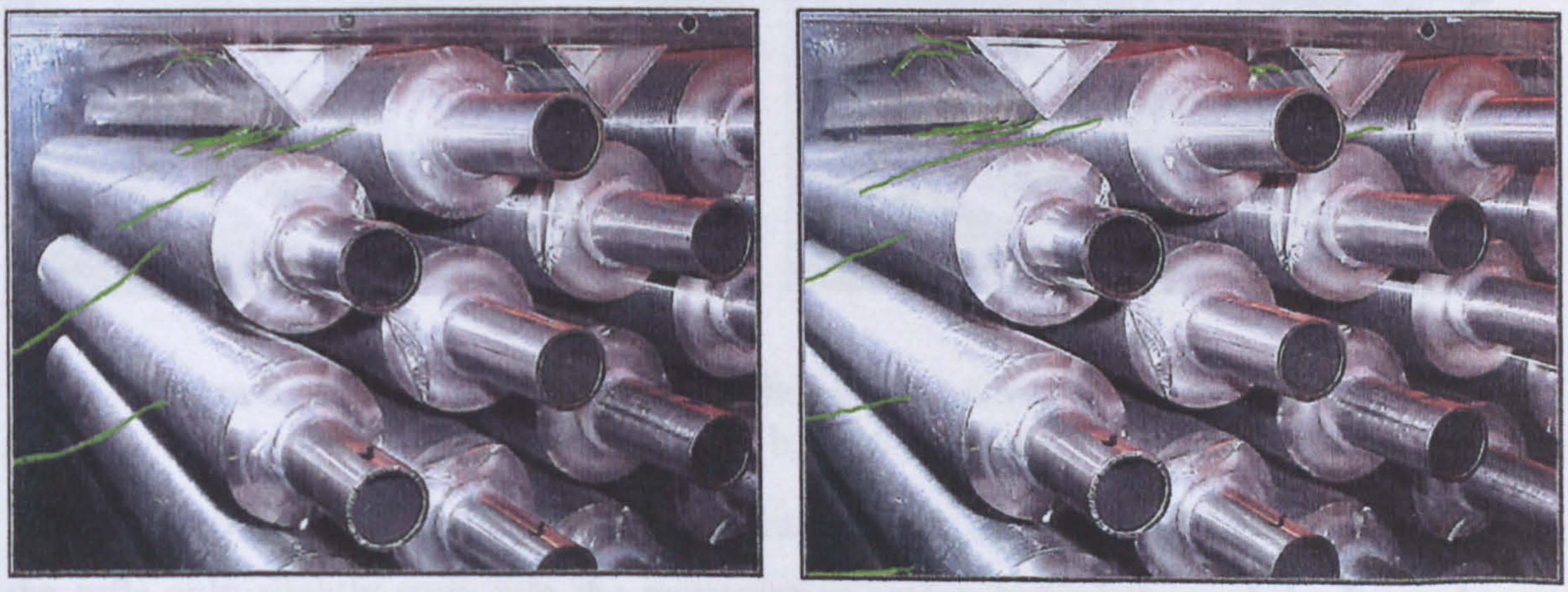

a. b.

Figure 8.17: Tufts and streamers on the bundle with inverted v corbels
a. 30% flow rate (1.65 m/s) b. 80% flow rate (5.7 m/s)

Figure 8.17a shows the same gravity effect noted in Section 8.8.2. The tufts over the top of the corbel are slightly lifted due to the small pressure gradient and the lift on the tuft itself.

Figure 8.17b shows that the higher momentum flow has straightened out the streamers behind the tubes in the middle region of the bundle (the lower tubes in the photograph) and this flow is developed throughout the middle section of the bundle. The top tube in the photograph adjacent to the corbel shows its streamer angled slightly downward. This is due to the wake and jet effect described for the corbel tufts of the sealing strips. Similarly the tufts on the corbels can be seen to have a distinct curve that follows the expected recirculation pattern that the CFD indicted, and was seen in Figure 8.14. This again indicates broad correlation between the CFD and experimental results.

8.8.4 Square Block

Figure 8.22 shows the square block corbels being tested with an air face velocity of 1.65m/s. Figure 8.23 shows the bundle with an air face velocity of 5.7m/s. The tufts and streamers can be clearly seen in the photographs.

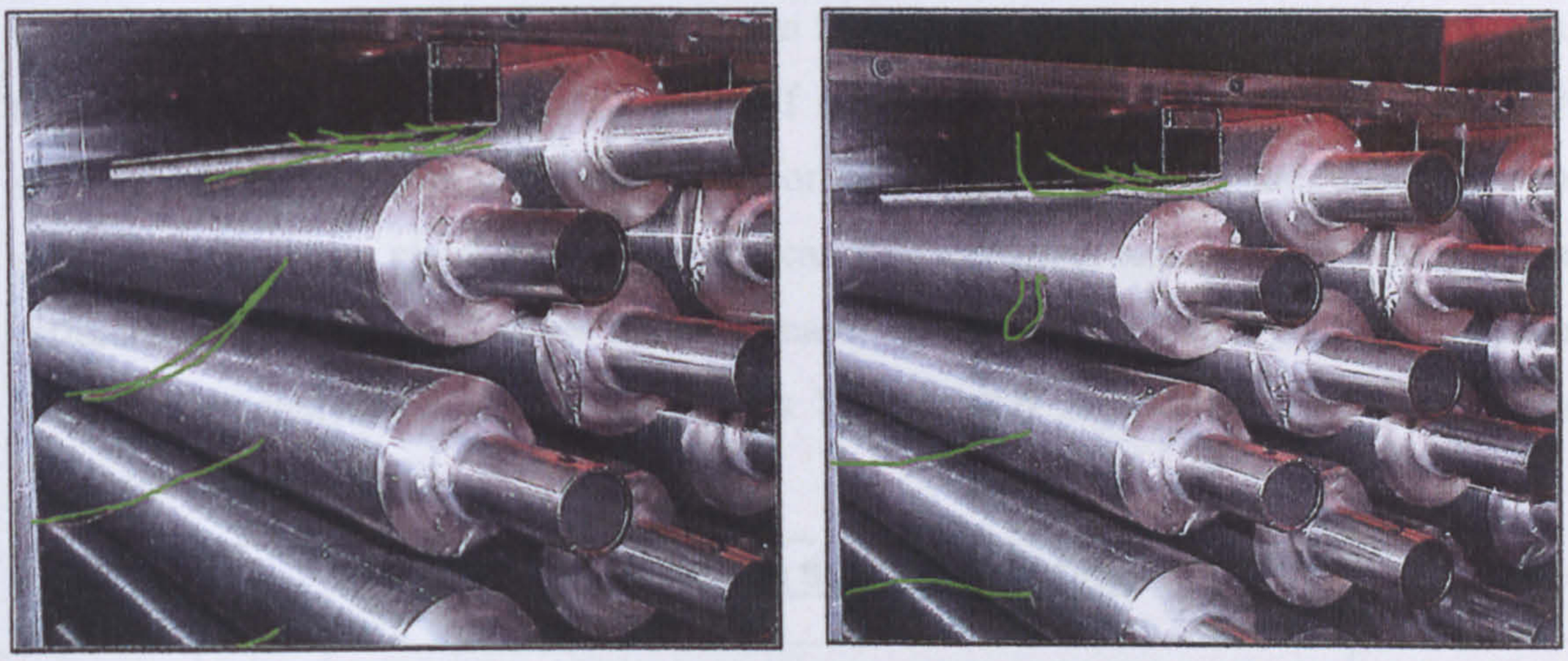

a. b.

Figure 8.18: Tufts and streamers on the bundle with square block corbels
a. 30% flow rate (1.65 m/s), b. 80% flow rate (5.7 m/s)

At 1.65m/s (Figure 8.18a) the flow has a relatively low momentum. This explains why the tufts only slightly stray into the recirculation region behind the corbels. It can be seen that the shorter tufts, which have less of a gravity effect due to their lower mass, do attempt to follow the recirculating flow indicating it is quite strong even in this low momentum approach flow.

For the higher speed flow (Figure 8.18b) it can be seen that the streamers for the lower tubes in the photograph are reasonably straight, indicating a well established flow through the middle of the bundle. The tufts over the corbels show strong direction

change and follow the expected recirculation pattern. The long tuft especially shows the strength of the recirculation behind this last corbel in the flow direction.

8.9 Corbel model developed from experimental data

If the ideal corbel shape is that made of half finned tubes then a model should be developed to determine the increase in bundle pressure drop when the corbel shape deviates from the ideal shape. Due to cost consideration, a half-finned tube corbels was not explored, and it was assumed that the half-tube corbel would best approximate that of the ideal case. It was envisaged that the method would be a correction factor that could be applied to the to the pressure drop predicted by the new staggered bundle method presented in Chapter 6. The product of the prediction and the corbel correction term would become the bundles overall predicted pressure drop.

To analyse the data and derive the correction factors, the variation in pressure drop with the various corbels against that of the half tube corbel was determined. Figure 8.19 shows a random result for the sealing strip corbels. From this data the difference in pressure drop at any given mass flow rate can be calculated, and a table of percentage differences can be drawn for the range of mass flow rate tested. This is given in Table 8.4. Similar analyses are given in Tables 8.5 and 8.6 for the other corbel shapes indicated above.

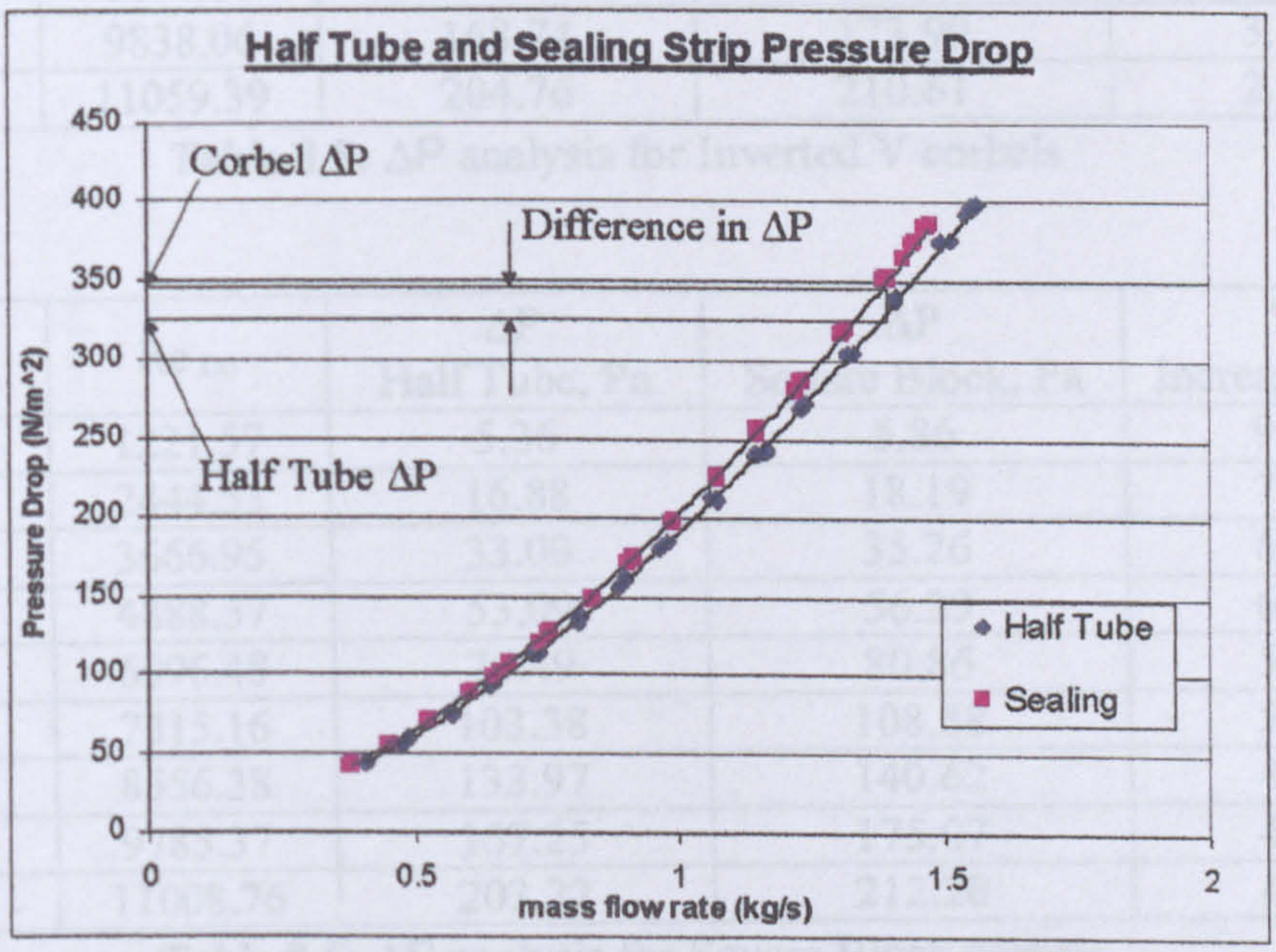

Figure 8.19: Bundle Pressure drop analysis for sealing strip against half tube corbels

The increase in bundle pressure drop when sealing strips, inverted V and square block corbels are used instead of half tube corbels could be used as a criterion for the increase in bundle pressure drop due to the additional resistance imposed on the flow.

Mass flow rate, (kg/s)	Re_{Do}	ΔP Half Tube, Pa	ΔP Sealing Strip, Pa	% Increase in ΔP
0.2	1227.70	5.41	5.76	6.52
0.4	2454.69	17.00	18.06	6.23
0.6	3681.78	33.22	35.24	6.07
0.8	4919.72	53.65	56.85	5.95
1	6149.62	77.59	82.14	5.86
1.2	7380.35	104.91	110.98	5.79
1.4	8616.97	135.54	143.29	5.72
1.6	9848.53	169.04	178.62	5.67
1.8	11080.15	205.40	216.94	5.62

Table 8.4: ΔP analysis for Sealing Strip corbels

Mass flow rate, (kg/s)	Re_{Do}	ΔP Half Tube, Pa	ΔP Inverted V, Pa	% Increase in ΔP
0.2	1226.09	5.39	5.81	7.68
0.4	2452.28	16.97	18.01	6.13
0.6	3683.63	33.25	34.99	5.24
0.8	4911.98	53.51	55.98	4.61
1	6140.59	77.41	80.60	4.12
1.2	7378.17	104.86	108.77	3.73
1.4	8608.60	135.32	139.91	3.39
1.6	9838.06	168.74	173.99	3.11
1.8	11059.39	204.76	210.61	2.86

Table 8.5: ΔP analysis for Inverted V corbels

Mass flow rate, (kg/s)	Re_{Do}	ΔP Half Tube, Pa	ΔP Square Block, Pa	% Increase in ΔP
0.2	1221.57	5.36	5.86	9.32
0.4	2444.53	16.88	18.19	7.75
0.6	3666.95	33.00	35.26	6.84
0.8	4888.57	53.09	56.39	6.20
1	6096.48	76.49	80.86	5.72
1.2	7315.16	103.38	108.88	5.31
1.4	8556.38	133.97	140.62	4.97
1.6	9785.37	167.25	175.07	4.68
1.8	11008.76	203.22	212.20	4.42

Table 8.6: ΔP analysis for Square Block corbels

It can be seen from the "% increase in ΔP" columns in tables 8.4 to 8.6 that there is a trend of this value with Reynolds number. It decreases with increasing Reynolds number. The results of these "% increase in ΔP" are plotted against the Reynolds number and shown below in Figures 8.20 to 8.22.

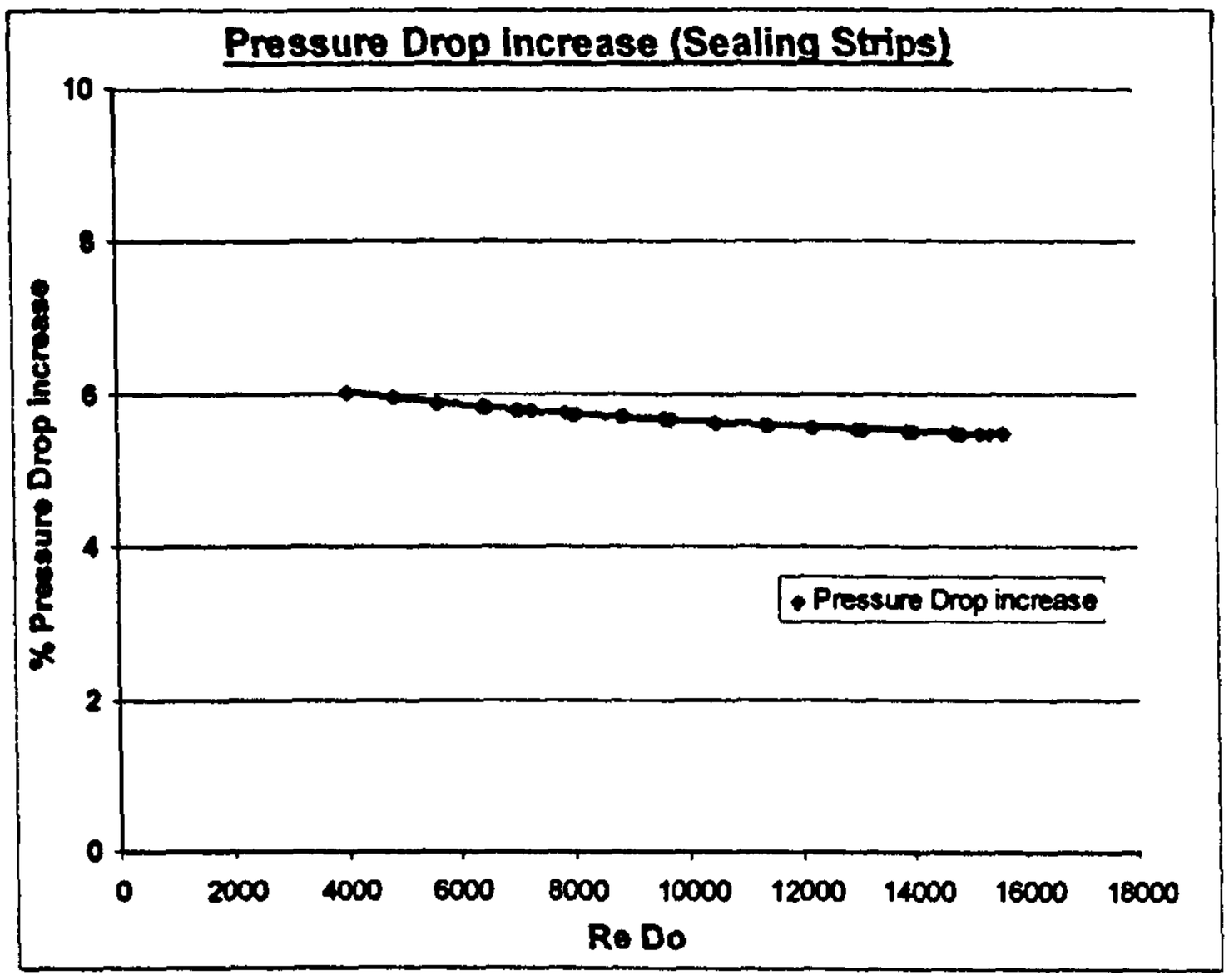

Figure 8.20: % increase in bundle pressure drop for Sealing Strip corbel

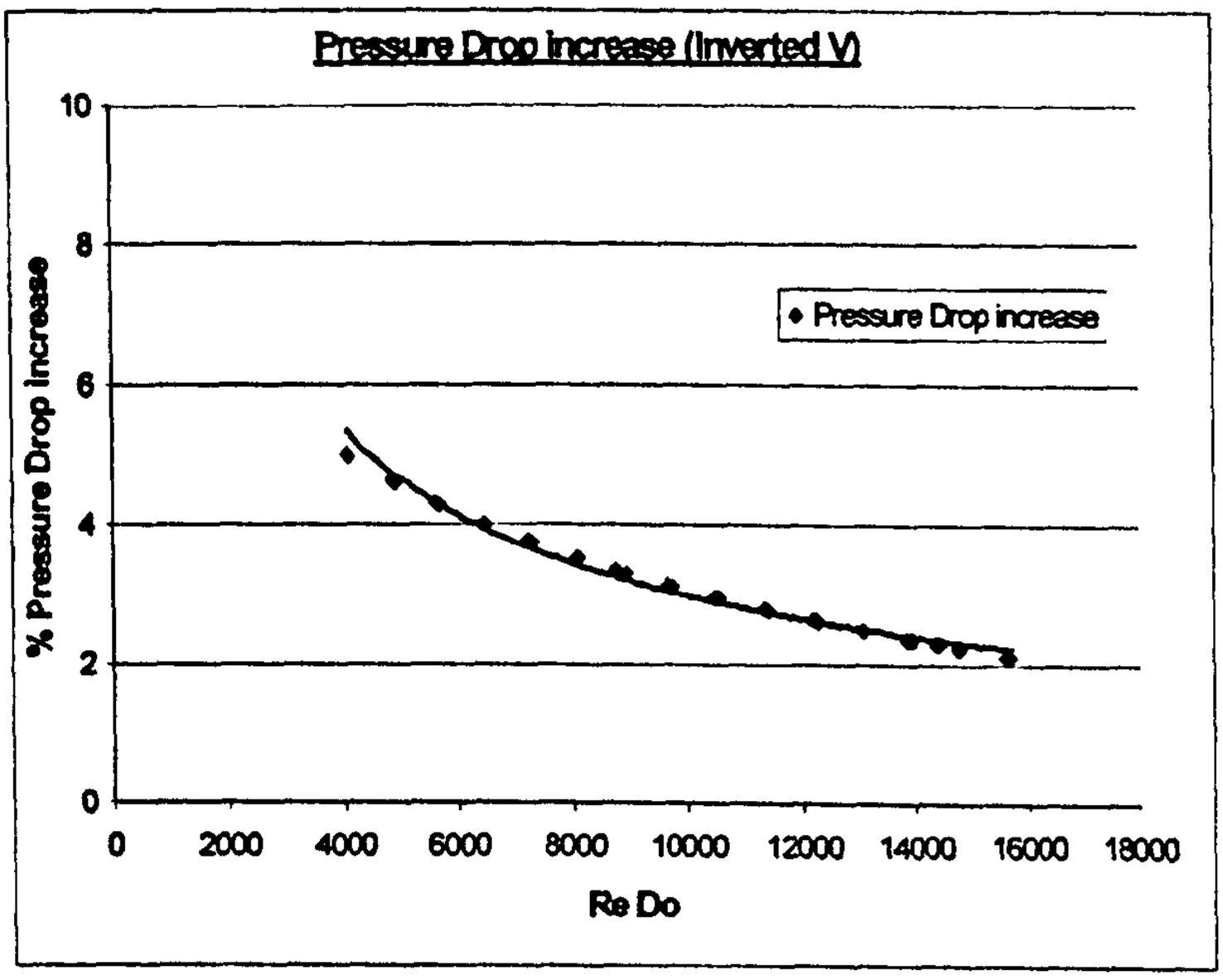

Figure 8.21: % increase in bundle pressure drop for Inverted V corbel

It can be seen that the "% increase in ΔP" with Re_{Do} is apparent in the cases of inverted V and square block corbels, however this variation is generally small (i.e. within about 2.5%).

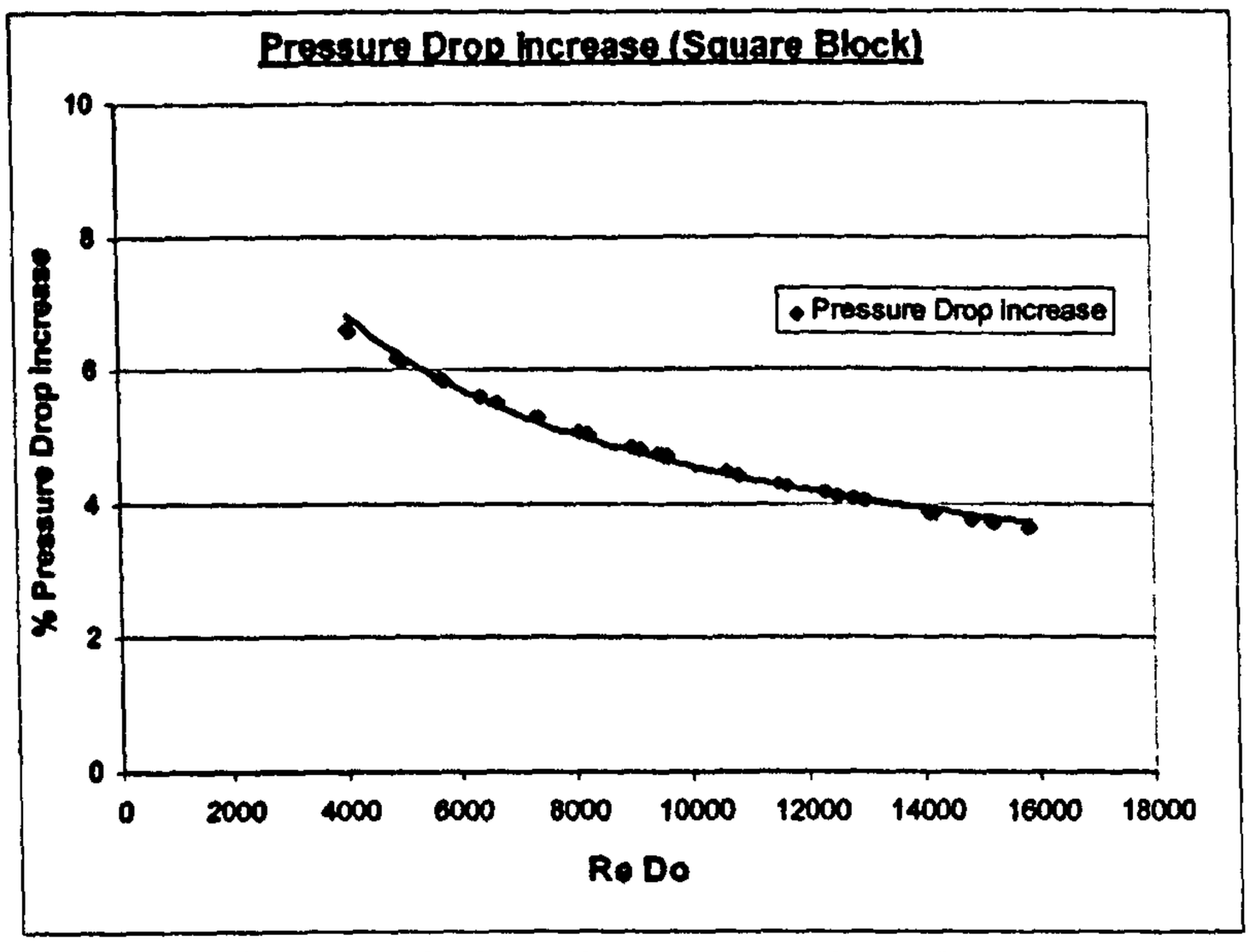

Figure 8.22: % increase in bundle pressure drop for square block corbel

Given that the variation indicated above appeared small, an initial attempt was made to apply an averaged constant from the data above to correct the pressure drop when any corbel shape, other than the half tube corbel, is used but it was found that this approach is not accurate. It was decided to investigate developing a correction as a function of the Reynolds number.

The correction necessary for each shape was determined simply by transforming the percentage increase in pressure drop to a decimal e.g. 9.52% = 1.0952

8.10 Scalability concerns

It is believed that as the number of tubes per row (N_T) increase; the influence of corbel shape on the overall bundle performance will diminish, as the resistance imposed by the corbels on the incoming flow becomes less significant.

After discussion with a number of heat exchangers manufacturers, via the HTFS Crossflow review panel, it was assumed that by $N_T = 60$ the effect would be negligible. Therefore the correction needed for such a high duct height would be unity.

Therefore the ratio of the corbel height to the height of the duct was considered as a factor in the model formulation. The duct height is directly proportional to the number of tubes per row and was determined as Equ.8.4 below.

$$H_{Duct} = P_T(N_T - 0.5) + 2H_{CC} \qquad \text{(Equ.8.4)}$$

Where H_{CC} is the height from the duct wall to the centre of the tube nearest the wall.

By relating the height of the corbel to the height of the duct a direct scaling parameter is provided. It will be shown in the following section that this geometric parameter seems to address the influence of the corbel geometry satisfactorily when the duct height changed. Other geometric parameters such as the pitch angle and fin frequency were not explored for time considerations, but are expected to have much less influence than the previous parameter.

8.11 Corbel correction models

As indicated above it is assumed that the pressure drop calculated from the new staggered method (ΔP) will approximate the case for the half tube corbel. If the corbel shape deviates from that of the half tube then a correction factor is used as shown in the following formulation (Equ.8.5):

$$\Delta P_{Total} = Cf_{Corbel} \cdot \Delta P \qquad \text{(Equ.8.5)}$$

This correction factor (Cf_{Corbel}) is assumed to be unity for the half tube corbels and greater than unity for the other corbel shapes.

A different model was developed for each corbel shape using a multi-variate linear regression on the experimentally derived correction factor, the values of Re_{Do} and the ratio of corbel to duct heights using a logarithmic transform. On the premise that when $N_T = 60$, $Cf = 1$ a few cases were added to the database based on the experimental conditions, but with the forced condition $N_T = 60$. This allowed for the ratio of corbel height to duct height to be regressed.

A correlation constant was then determined by averaging the differences from the experimentally derived coefficients for each corbel shape.

Equ.8.6 shows the correction factor for the sealing strip corbels.

$$Cf_{SealingStrip} = 1.179 \cdot \left(\frac{H_{Co}}{H_{Duct}}\right)^{0.0263} \cdot \mathrm{Re}_{Do}^{-0.00346} \qquad \text{(Equ.8.6)}$$

The model for the inverted V corbels is as shown in Equ.8.7.

$$Cf_{InvertedV} = 1.277 \cdot \left(\frac{H_{Co}}{H_{Duct}}\right)^{0.0151} \cdot \mathrm{Re}_{Do}^{-0.01846} \qquad \text{(Equ.8.7)}$$

The model for the square block corbels is given by Equ.8.8.

$$Cf_{SquareBlock} = 1.326 \cdot \left(\frac{H_{Co}}{H_{Duct}}\right)^{0.0223} \cdot \mathrm{Re}_{Do}^{-0.01855} \qquad \text{(Equ.8.8)}$$

The models presented were all derived from data with a Re_{Do} between 4000 and 16500. However it is believed that the Reynolds number based function will extrapolate beyond these values better than a constant model.

8.12 Comparing the model with measurements

It is important to stress that performance of the suggested model (Equ.8.5) will depend on the accuracy of the new staggered bundle method. The results of Chapter 6 indicate that the new staggered model predicts 85% of the HTFS databank within ±20%. Therefore, for a particular bundle there is a chance of overpredicting or underpredicting the pressure drop within the 20% band. In the results presented in Figure 8.23 below it can be seen that the new method slightly overpredicts the pressure drop (4% to 13%) for the base case (i.e. with half tube corbel) of this test bundle. If we assume that this prediction is the base line, then when the comparison is made with test data for other corbel shapes, it is clear from Figures 8.24, 8.25 and 8.26 that the new staggered bundle method is underpredicting the results by the differences discussed in section 5 for each corbel shape. When the corbel correction is applied these figures show that the model corrects the results for each corbel shape.

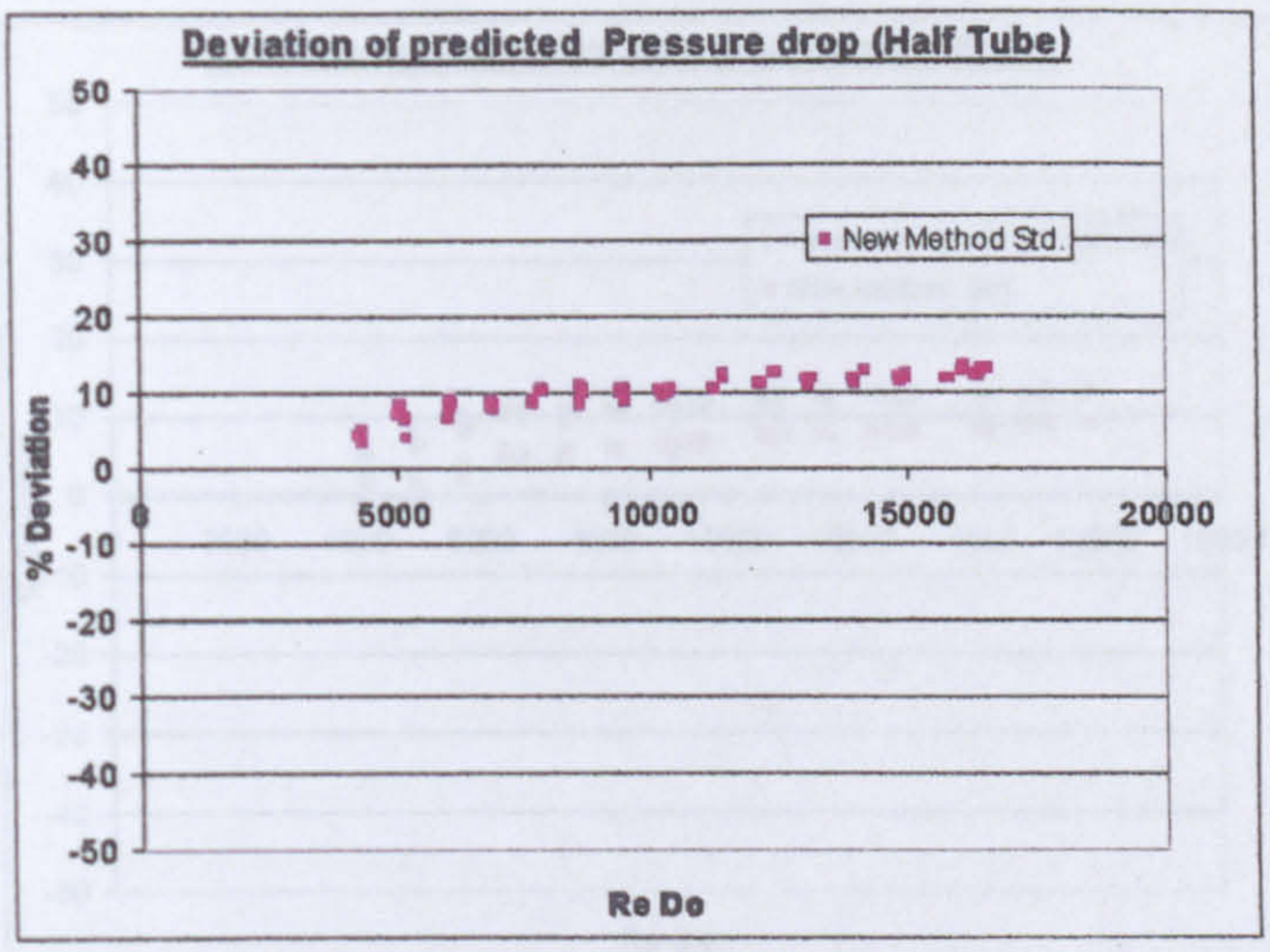

Figure 8.23: Pressure drop prediction for Half Tube corbel (Base case)

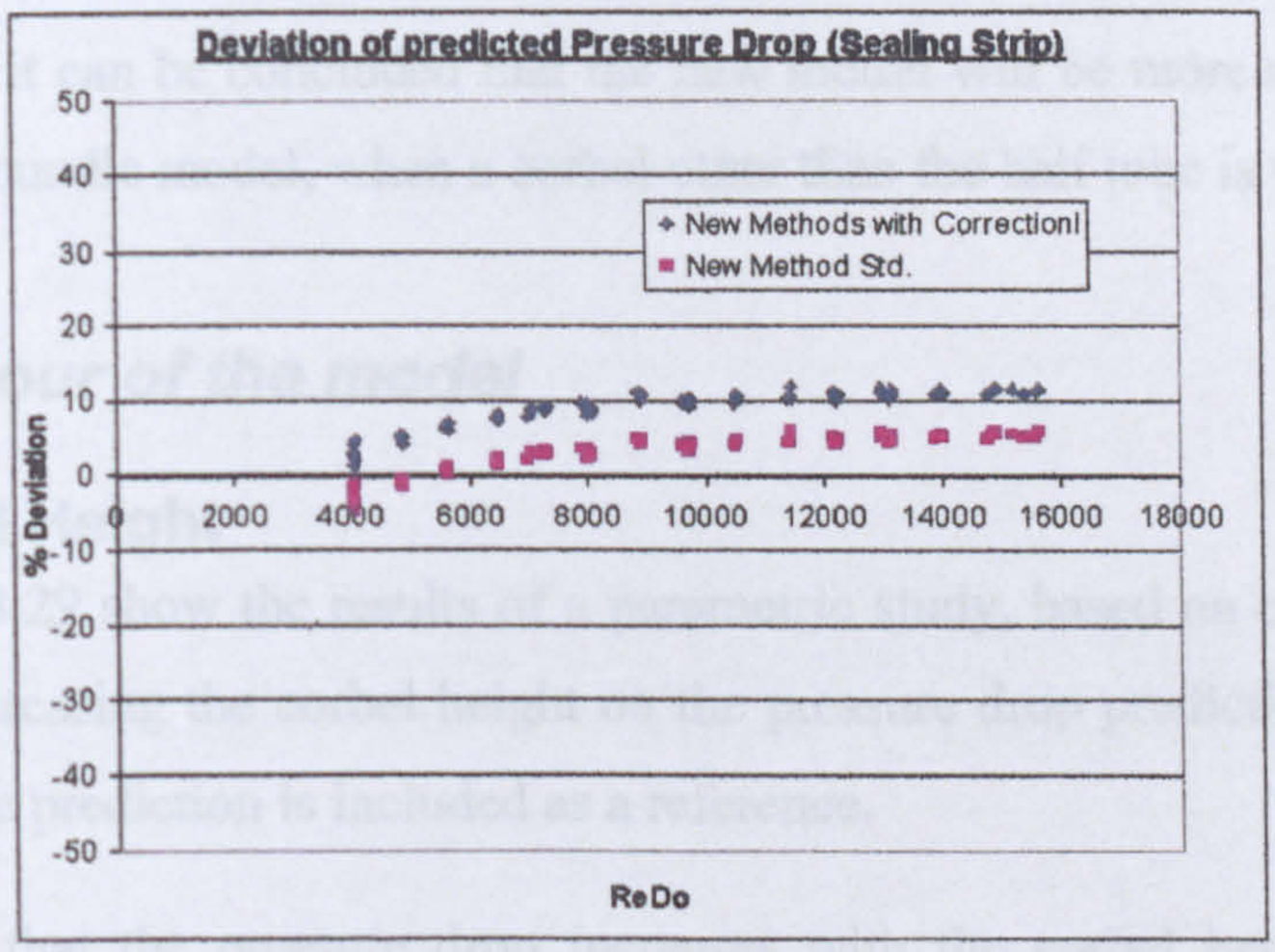

Figure 8.24: Pressure drop prediction for Sealing Strip corbel

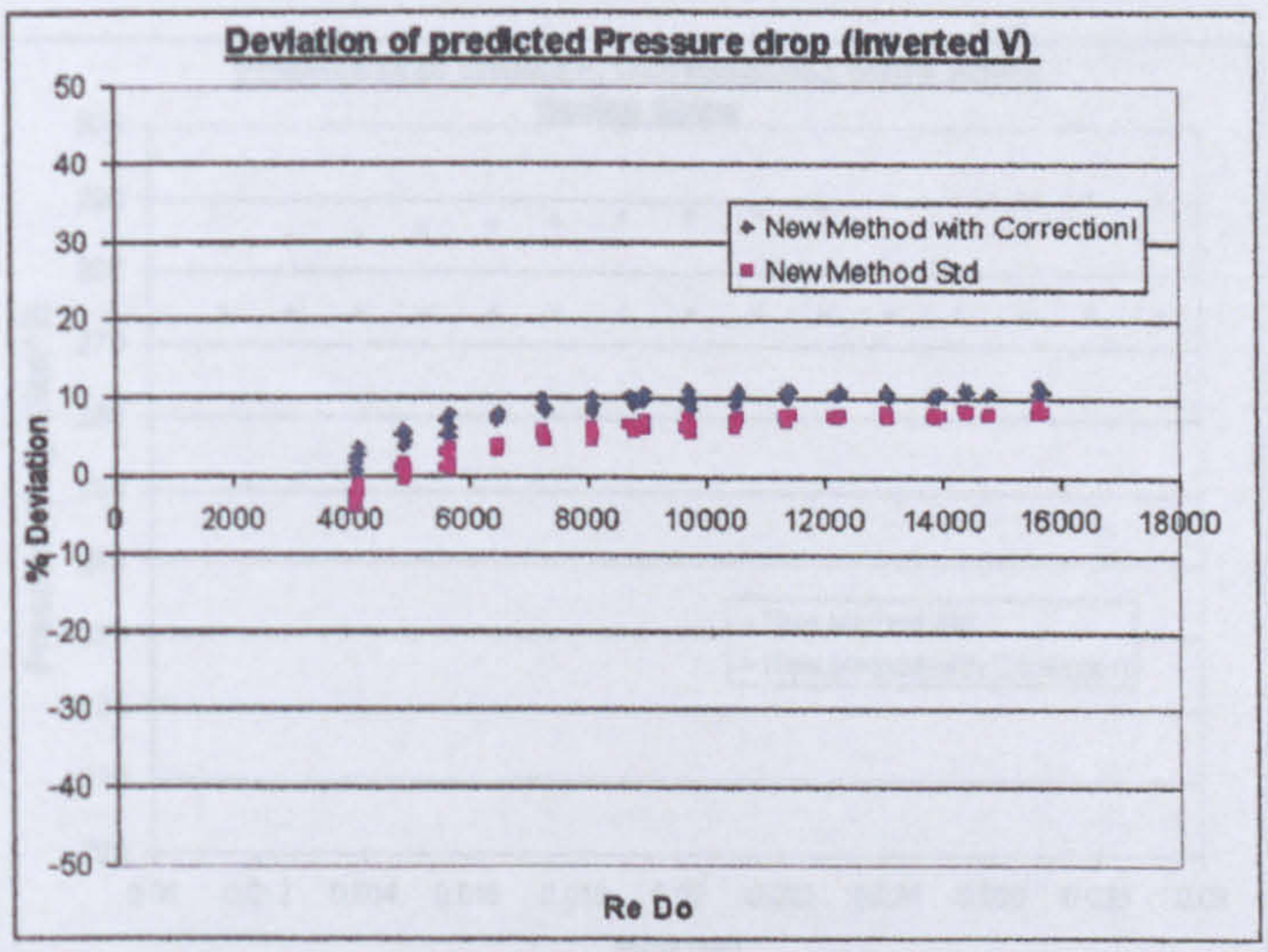

Figure 8.25: Pressure drop prediction for Inverted V corbel

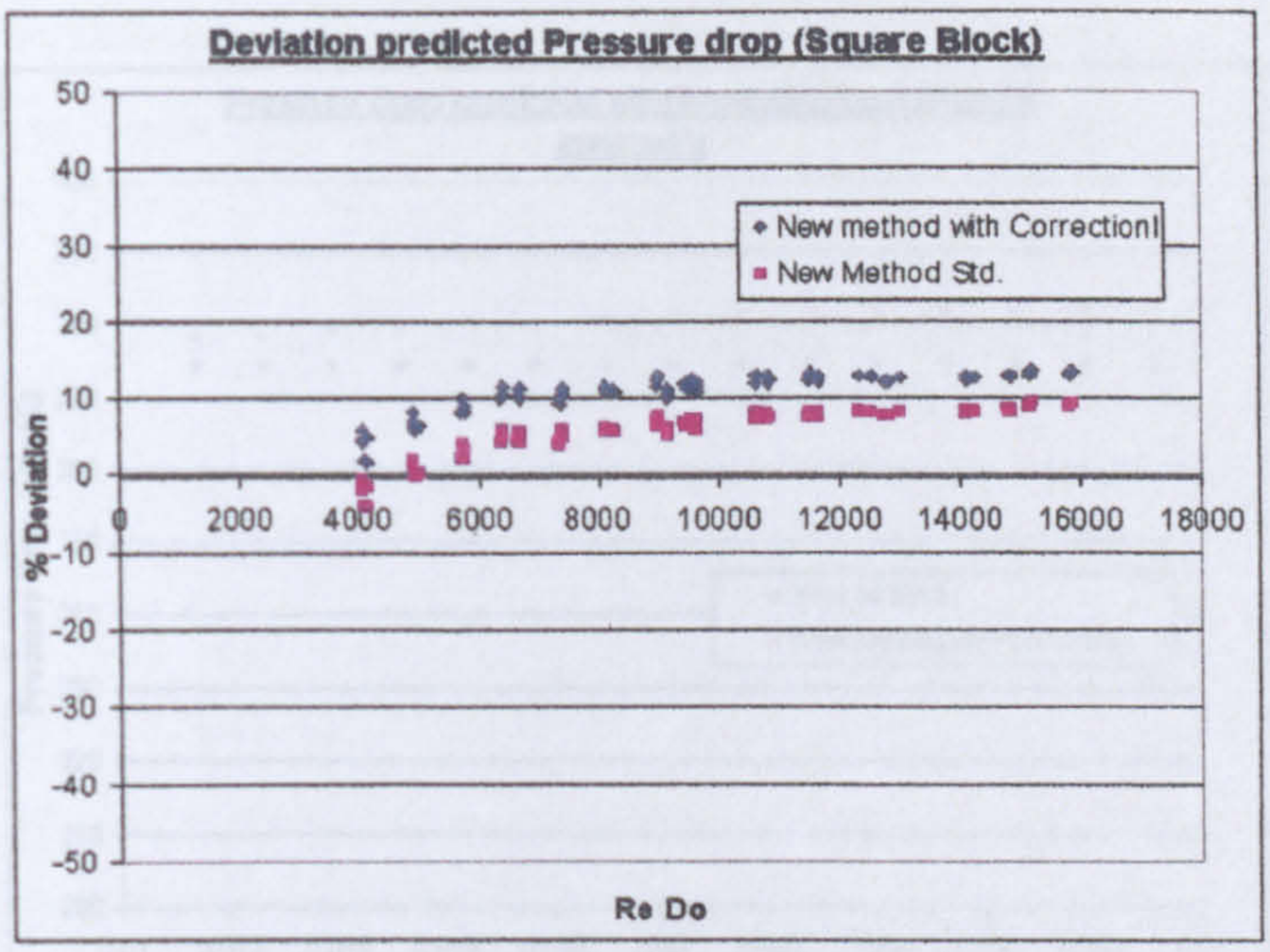

Figure 8.26: Pressure drop prediction for Square Block corbel

From the above it can be concluded that the new model will be more accurate than the basic staggered bundle model, when a corbel other than the half tube is used.

8.13 Behaviour of the model

8.13.1 Corbel Height

Figures 8.27 – 8.29 show the results of a parametric study, based on one data point, of the effect of increasing the corbel height on the pressure drop prediction. The standard staggered bundle prediction is included as a reference.

It can be seen that the pressure drop increases with the corbel height as would be expected.

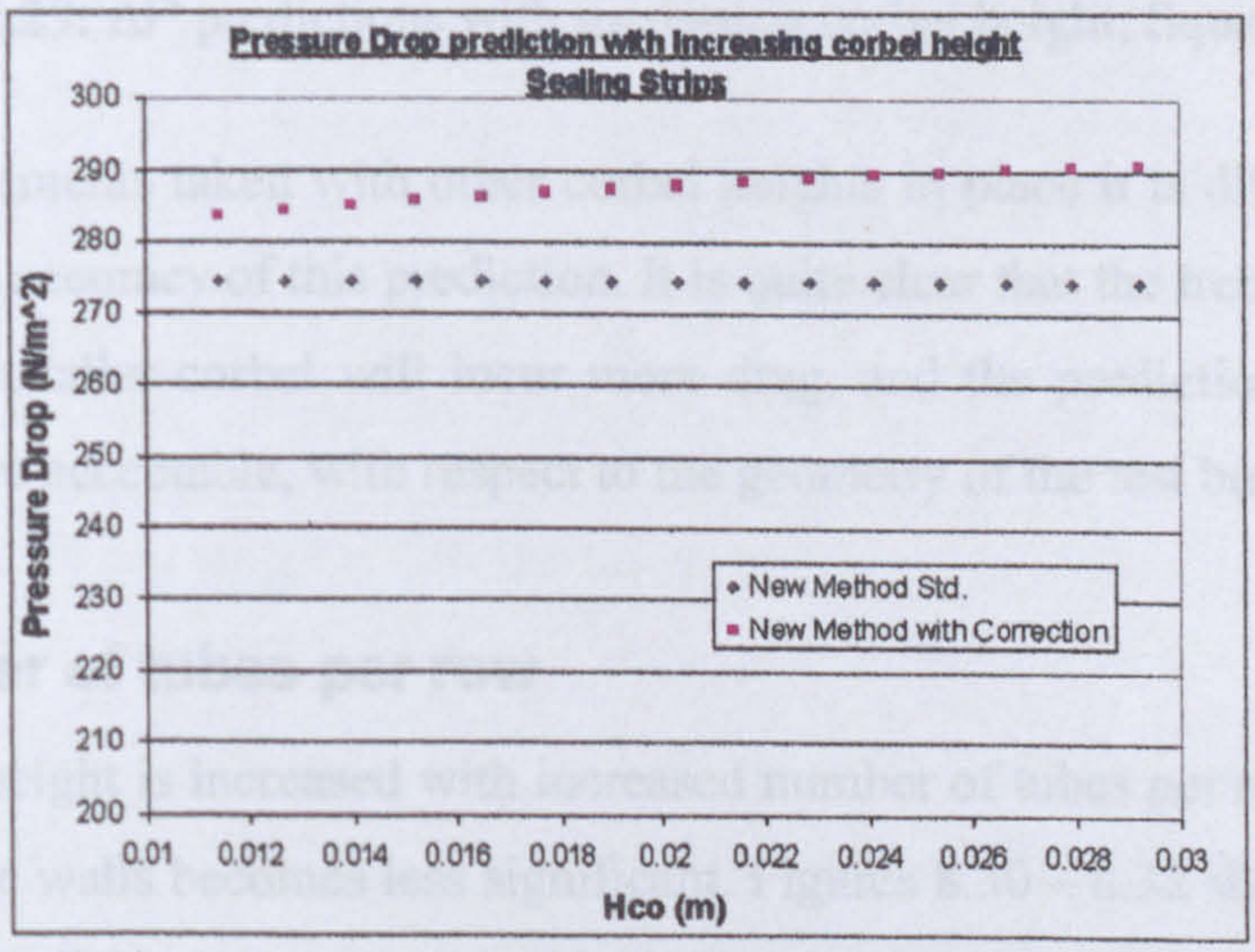

Figure 8.27: ΔP predictions with increasing corbel height; Sealing Strip

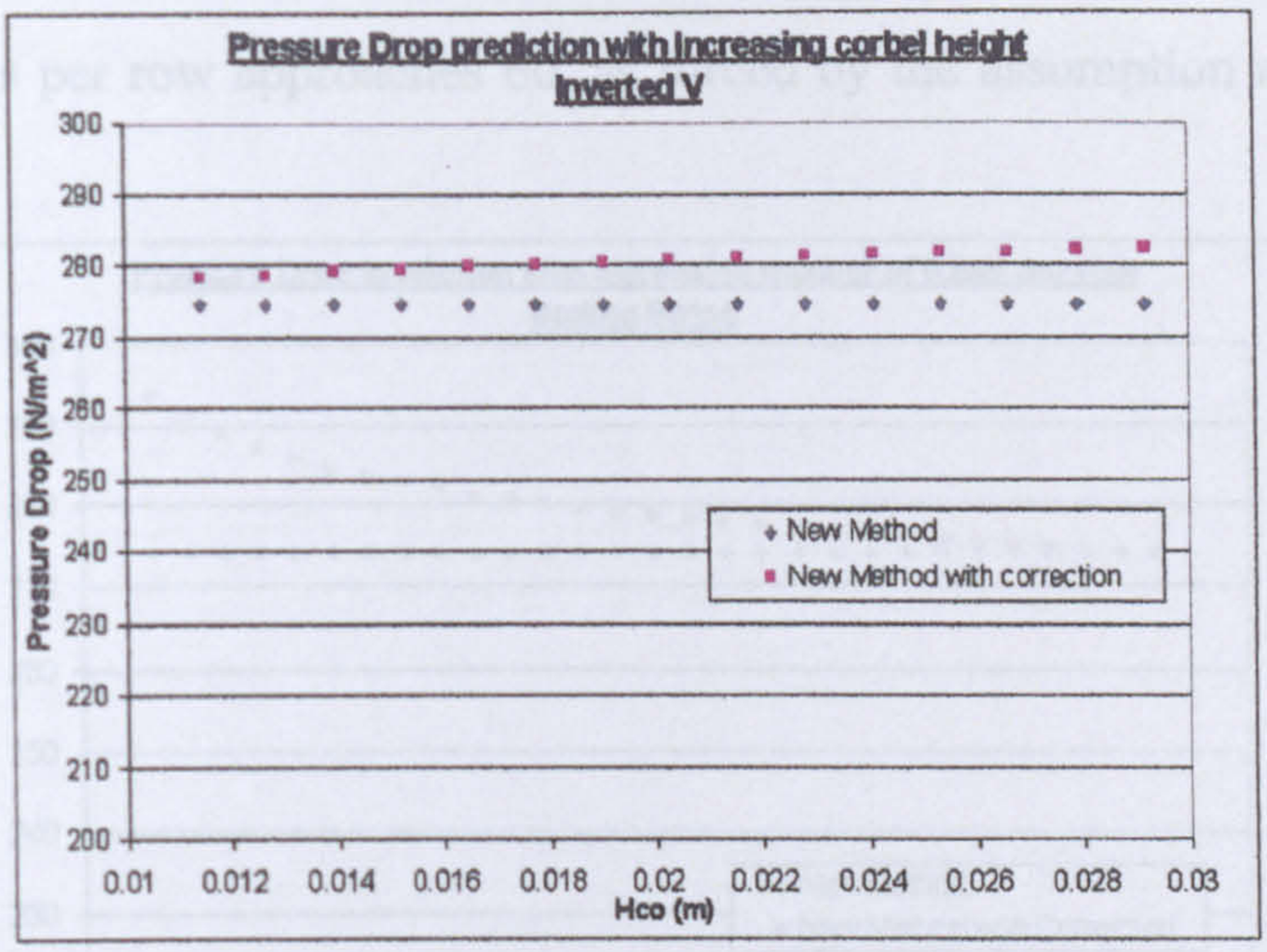

Figure 8.28: ΔP predictions with increasing corbel height; Inverted V

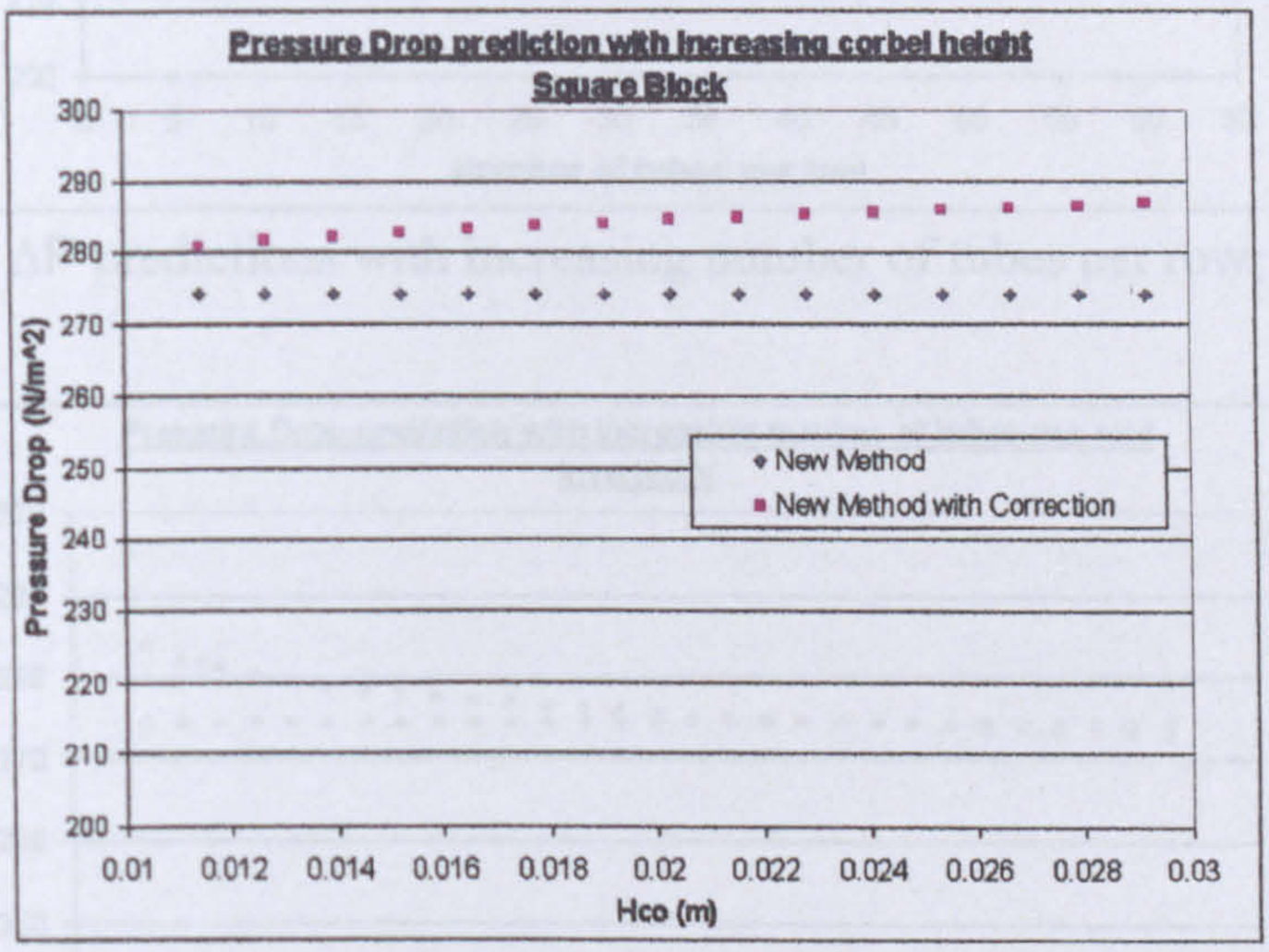

Figure 8.29: ΔP predictions with increasing corbel height; Square Block

Without measurements taken with other corbel heights in place it is difficult to make a statement on the accuracy of this prediction. It is quite clear that the trend is correct with the notion that a taller corbel will incur more drag, and the predictions shown in the above Figures are acceptable, with respect to the geometry of the test bundle.

8.13.2 Number of tubes per row

When the duct height is increased with increased number of tubes per row the effects of the corbels at the walls becomes less significant. Figures 8.30 – 8.32 show the results of a parametric study of the pressure drop prediction with all the corbels when the number

of tubes per row is increased. It can be seen that the correction term tends to unity as the number of tubes per row approaches 60, as forced by the assumption made in Section 8.12.

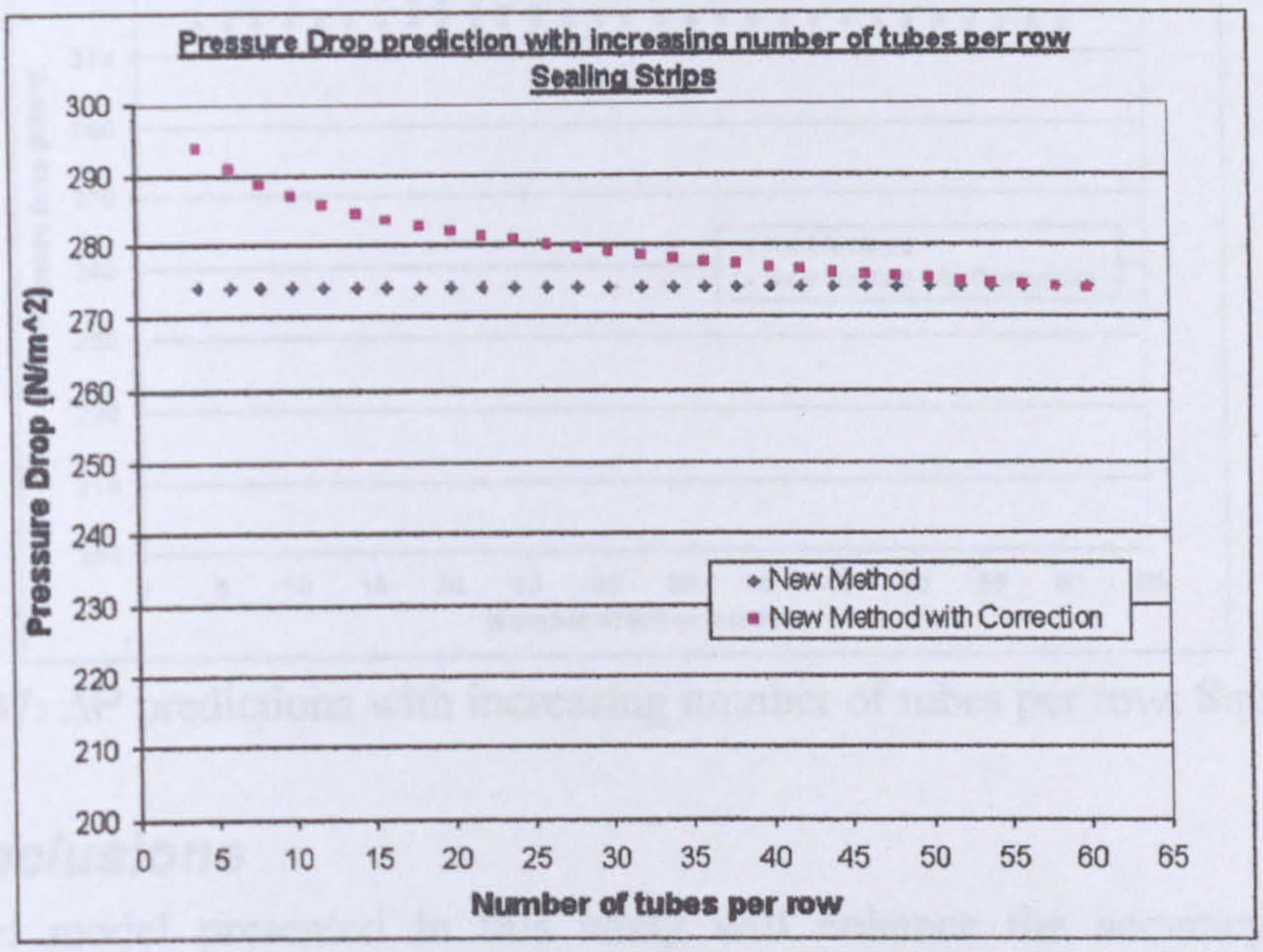

Figure 8.30: ΔP predictions with increasing number of tubes per row; Sealing Strip

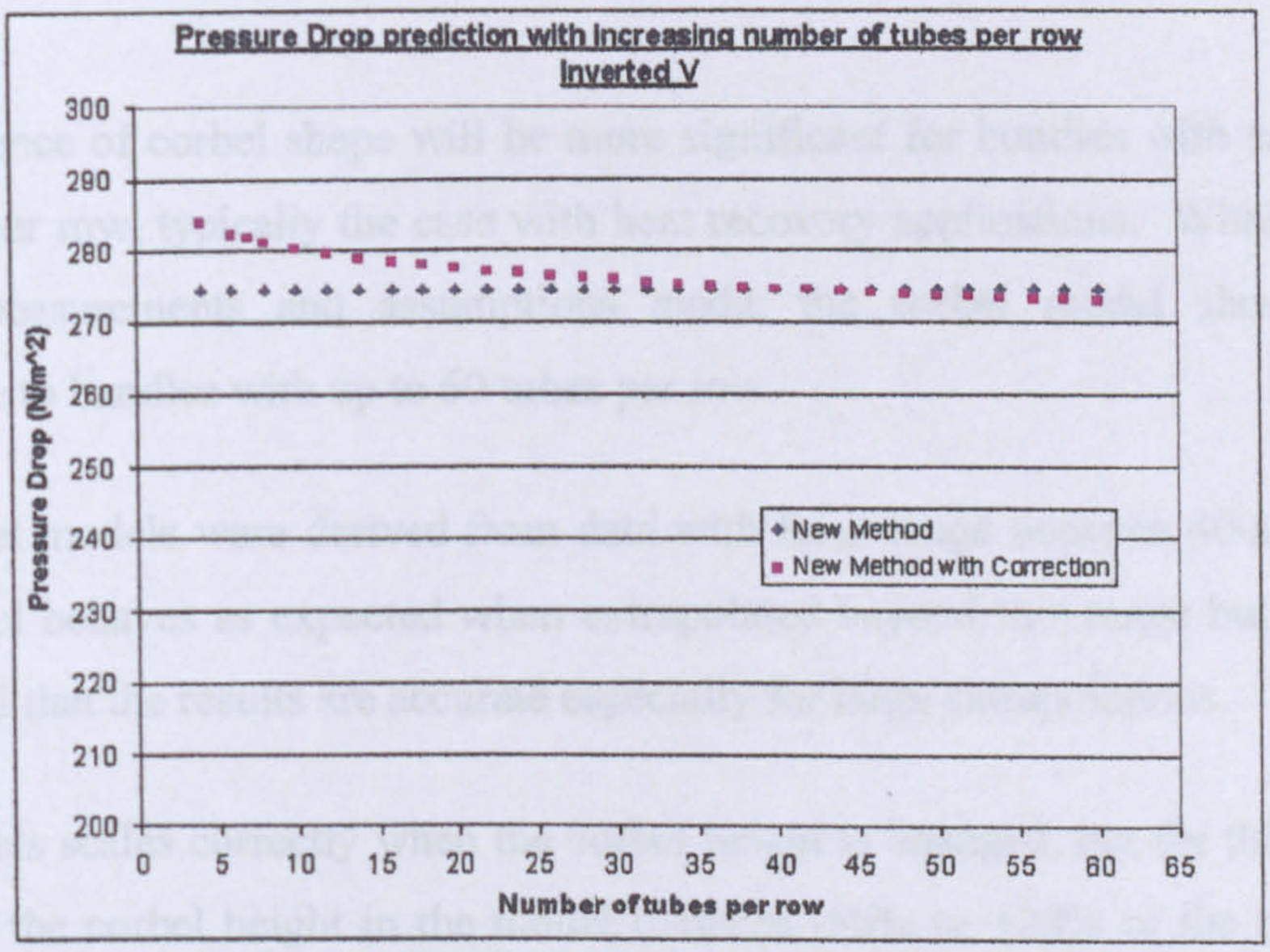

Figure 8.31: ΔP predictions with increasing number of tubes per row; Inverted V

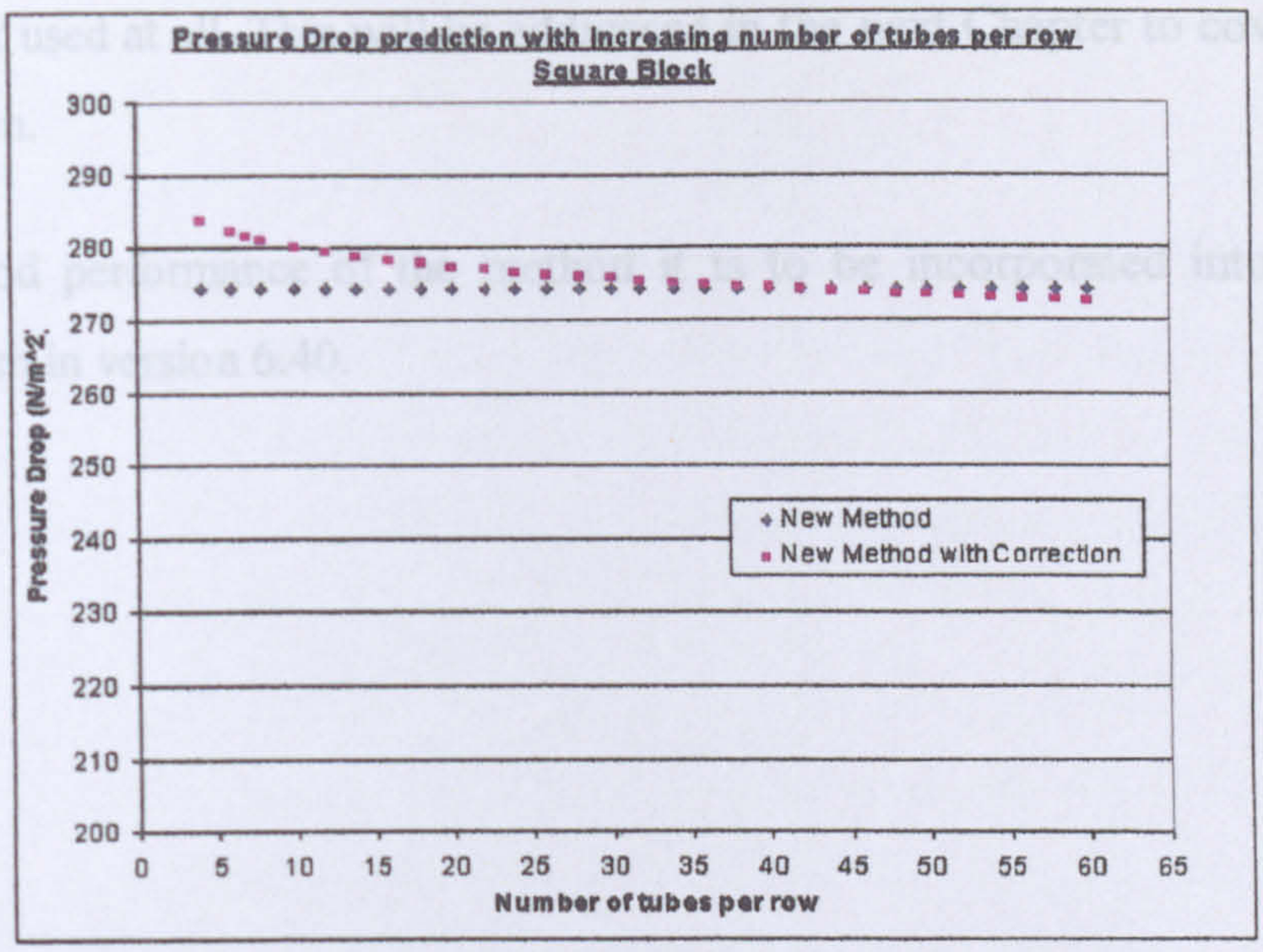

Figure 8.37: ΔP predictions with increasing number of tubes per row; Square Block

8.14 Conclusions

- The corbel model presented in this study will enhance the accuracy of the new staggered bundle method (Chapter 6) when corbel shapes other than the half tube corbel are used.

- The influence of corbel shape will be more significant for bundles with small number of tubes per row, typically the case with heat recovery applications. Within constrains of the measurements and assumptions made, the corbel model should only be applicable to bundles with up to 60 tubes per row.

- The corbel models were derived from data with Re_{Do} range between 4000 and 16500. The model behaves as expected when extrapolated beyond this range but it cannot be confirmed that the results are accurate especially for large extrapolations.

- The models scales correctly when the corbel height is changed, but for this test bundle changing the corbel height in the model between -50% to +20% of the typical height seems to influence the pressure drop little (i.e. within 2%).

- No attempt was made to quantify the influence of corbel shape on heat transfer as these measurements were performed isothermally. It is anticipated that this influence will be small. The more important question to explore is the influence on heat transfer when

corbels are not used at all. This will be addressed in the next Chapter to cover the flow bypass question.

- Given the good performance of the method it is to be incorporated into the HTFS ACOL program in version 6.40.

CHAPTER 9

A method to evaluate the influence of flow bypassing on staggered finned tube bundles

9.0 Introduction

It was indicated in Chapter 8 that finned tube bundle heat exchangers are usually equipped with inactive finned half tubes at the duct walls to ensure that the flow pattern remains intact at the edges of the bundle. This is done so that the reasonable assumption can be made that the bundle is behaving as if it is of infinite width. A finned half tube, however, is very expensive to construct, as it cannot be created by conventional fin winding techniques or even by pushing the fins onto the tube. If a finned tube bundle does not have these half tubes at the wall then two problems can occur; 1.The edge flow (flow around the outermost tubes) will differ from the flow in the bulk of the bundle. 2. Bypassing of the bundle can occur, as the mass flow will divert towards this path of lesser resistance. This last point is particularly the case in heat recovery applications, where bypass lane size, and heat transferring mass loss could be significant. Traditionally two approaches have been taken to this problem;

1. To ignore it if the designer feels the gap is sufficiently small.
2. Use standard sections of material that fit in the gaps created by the absence of half tubes (Corbels).

The previous Chapter covered point 2. This Chapter examines the behaviour and effects of the bypass flow when corbels are not used. It examines the experimental data presented in Sections 4.3, and presents a new method for calculating a flow split between the tube bundle and the bypass lanes. It shows how this can be used in the overall pressure drop prediction, and discusses the effects of bypassing on heat transfer.

9.1 Initial method

The determination of a friction factor for the bypass of the heat recovery bundle was described in Section 4.2

With this correlation and the predicted cross flow friction factor from the method of Chu and Ralston [22], it was possible to develop a method to calculate the bypass flow for tube bundles. However it became apparent that this friction factor model was not behaving in the correct manner. This will be demonstrated in Section 9.6.3.

9.2 Air cooler experimental bundle

Figure 9.1 shows the air cooler bundle previously shown in Section 3.5 with the corbels removed to create small bypassing lanes. Air-coolers tend to be designed with the fin tips nearly touching the duct wall, and as such the designers will often not consider the bypass flow as an issue, when corbels are not used.

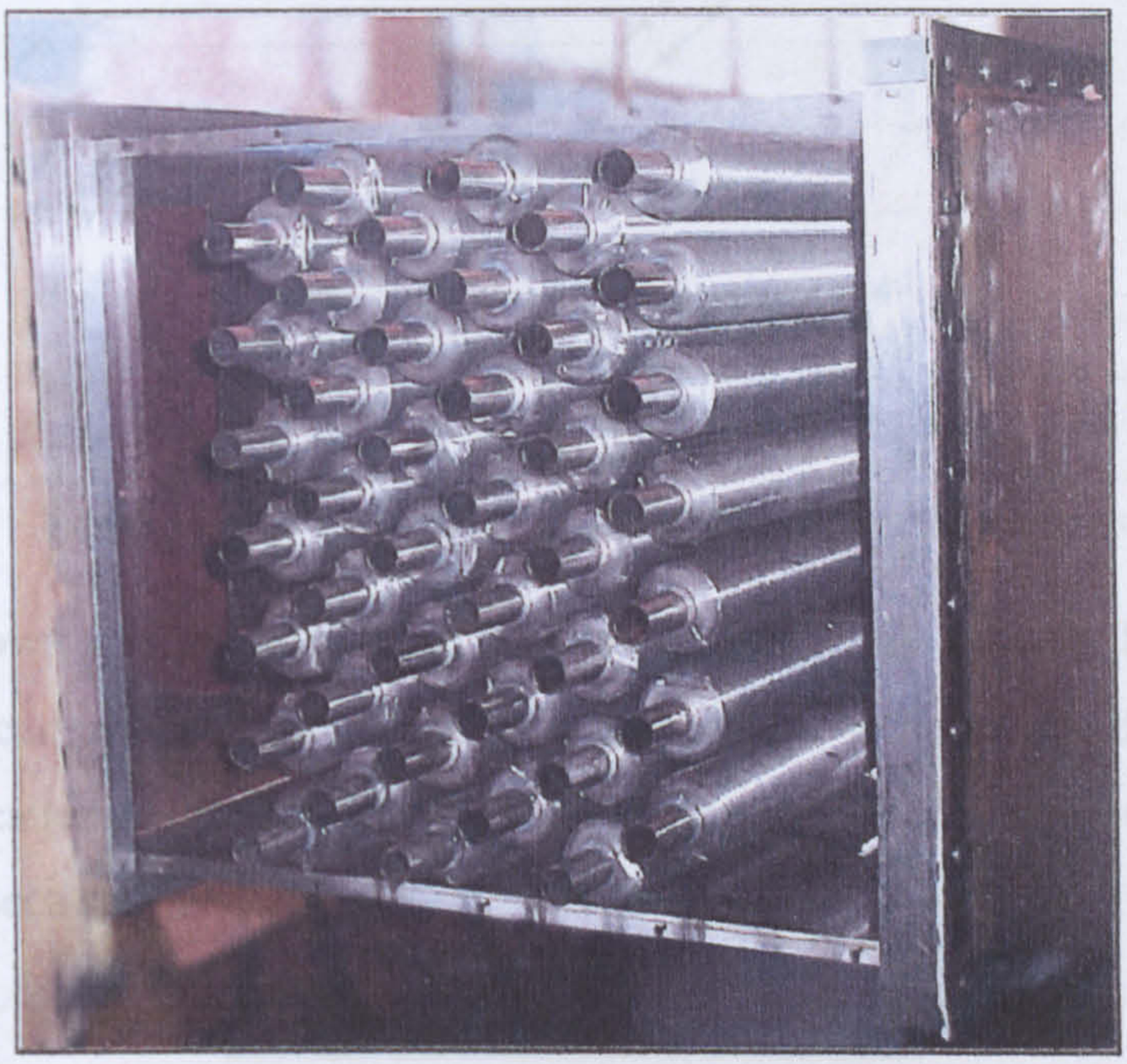

Figure 9.1: The bypassing air-cooler bundle in place in the MPWT

In contrast heat recovery bundles tend to have a noticeable gap at the walls. This is to allow soot blowing or other cleaning equipment access to the finned tubes to remove any deposits caused by the 'dirty' process streams that heat recovery bundles encounter. This means that generally heat recovery bundles are more likely to experience adverse effects from bypassing. However, as will be shown the effects of bypassing on air cooler bundles with a small numbers of tubes per row could be significant.

9.3 Experimental air cooler results

9.3.1 Results

Figure 9.2 shows the measured pressure drop against the mass flow rate the test air cooler bundle. It can be seen that where a bypass lane exists the pressure drop for a given mass flow rate is significantly lower than when there is a half tube corbel at the wall. This is simply due to the lower overall resistance caused by the absence of corbels.

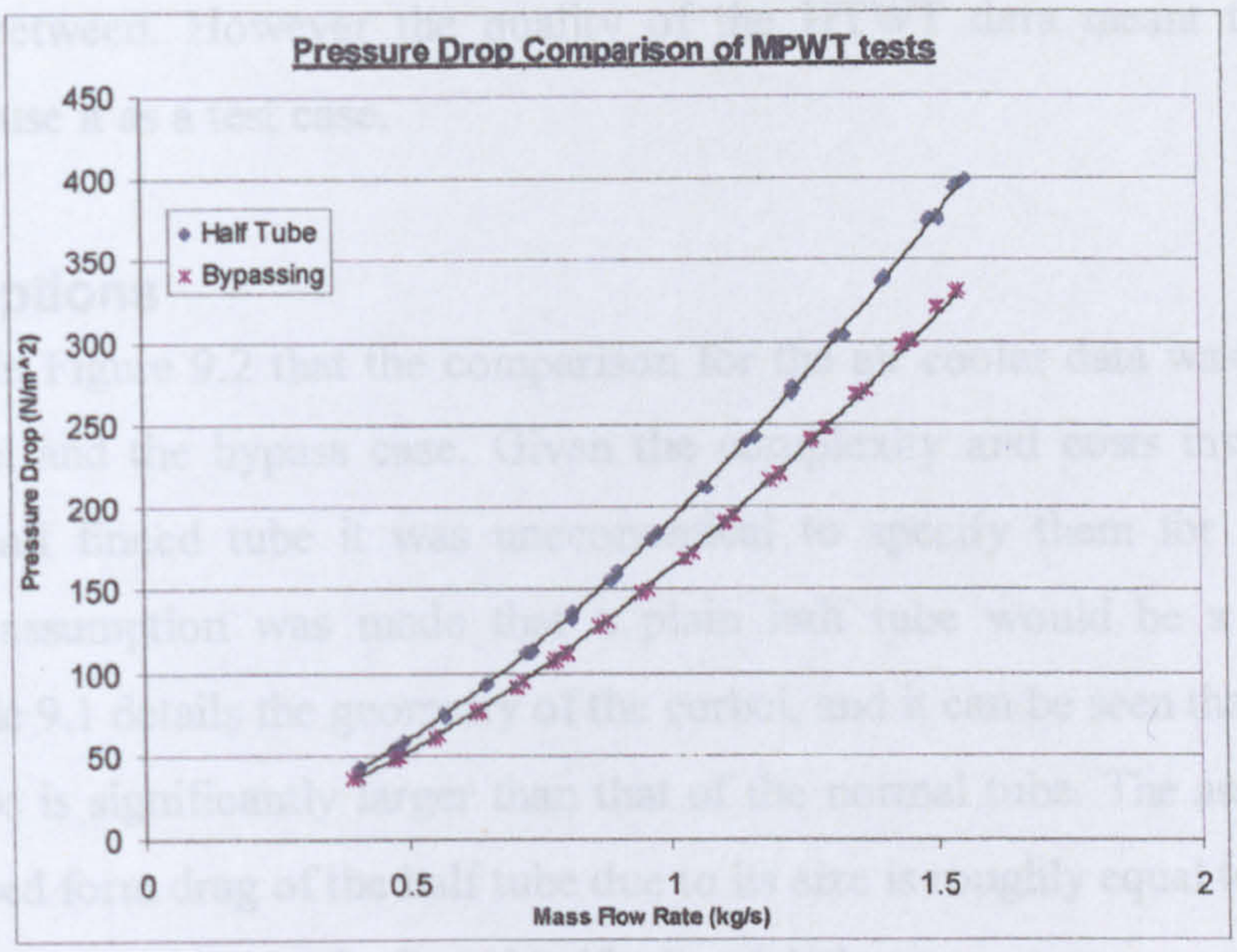

Figure 9.2: Pressure drop results of all air cooler tests

Figure 9.3 shows the pressure drop results for the heat recovery bundle shown in Section 4.2. It can be seen that the scatter of this data is much greater than that of the air cooler. The scatter is attributable to leakage through the flanges of the bundle as mentioned in Sections 4.2.1.

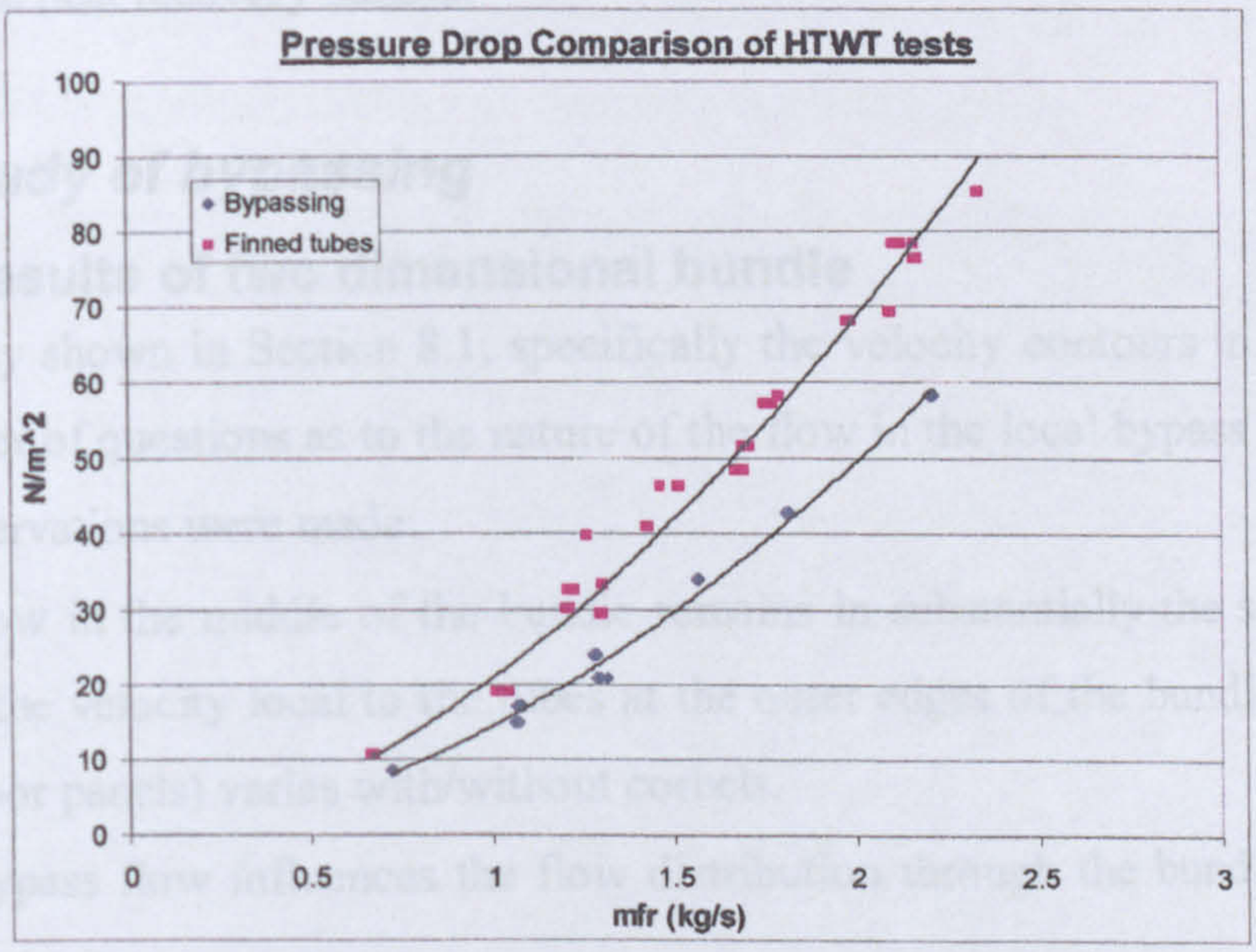

Figure 9.3: Pressure drop results of heat recovery tests

It was anticipated that both of these bundles would be used in the development of a model, to ensure that it is applicable to air cooler and heat recovery bundles and

geometries in between. However the quality of the HTWT data meant that it was decided to only use it as a test case.

9.3.2 Assumptions

It can be seen in Figure 9.2 that the comparison for the air cooler data was between a half tube corbel and the bypass case. Given the complexity and costs involved with fabricating a half finned tube it was uneconomical to specify them for these tests. Therefore the assumption was made that a plain half tube would be a reasonable substitute. Table 9.1 details the geometry of the corbel, and it can be seen that the radius of this half tube is significantly larger than that of the normal tube. The assumption is that the increased form drag of the half tube due to its size is roughly equal to that of the combined form and skin drag of a finned half tube corbel.

Corbel Type	Height (mm)	Bottom Width (mm)	Top Width (mm)
Half Tube	25.4	50.8	-

Table 9.1: Sources added to the databank

Due to the larger scale and the resultant easier manufacture of the finned half tube, they were used in the heat recovery bundle.

9.4 CFD study of bypassing

9.4.1 CFD results of two dimensional bundle

The CFD study shown in Section 8.1, specifically the velocity contours in Figure 8.3, raised a number of questions as to the nature of the flow in the local bypass region. The following observations were made:

- The flow in the middle of the bundle remains in substantially the same pattern while the velocity local to the tubes at the outer edges of the bundle (near roof and floor panels) varies with/without corbels.
- The bypass flow influences the flow distribution through the bundle due to its high velocity.

Figure 9.4 shows CFD path lines through the bypassing model. These are coloured by the local velocity. It can be seen, by reference to the velocity scale, that by the fifth tube row, with the tube nearest the wall, the local velocity is extremely high.

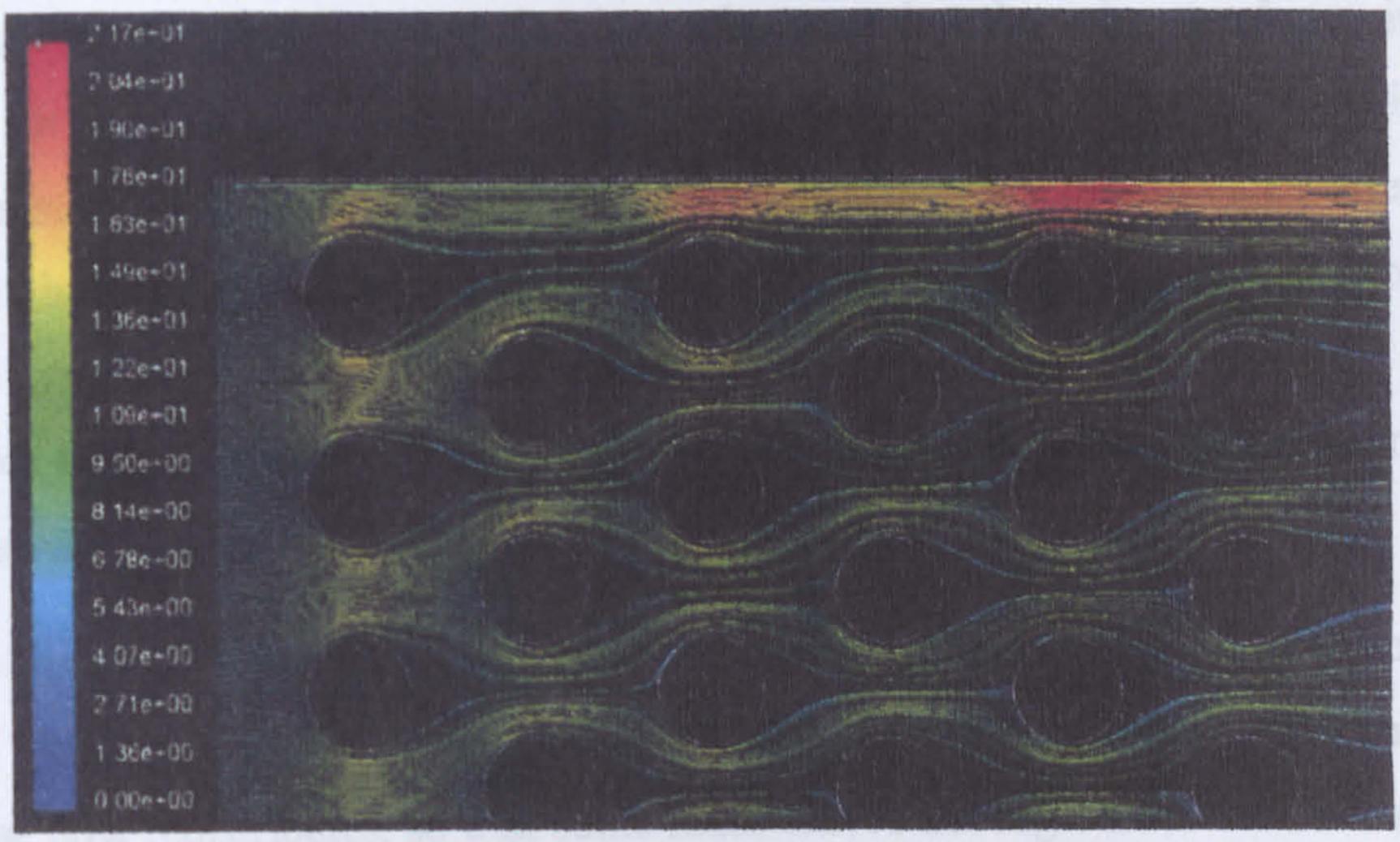

Figure 9.4: Pathlines through bundle, coloured by Velocity in the bypass region (mfr: 4 kg/s, Face Velocity: 6.58m/s)

Figure 9.5 shows same flow conditions, but with half tubes at the wall. It can be seen that the peak velocity through the bundle is experienced in the transverse gas between the tubes, notably between the tubes adjacent to the corbels in the same row. The obvious dissimilarity of the tubes in the bundle and the half tubes at the wall is due to the tube being representative blockages, as described previously in Section 8.1.1, and that half tubes being representative of actual physical half tubes.

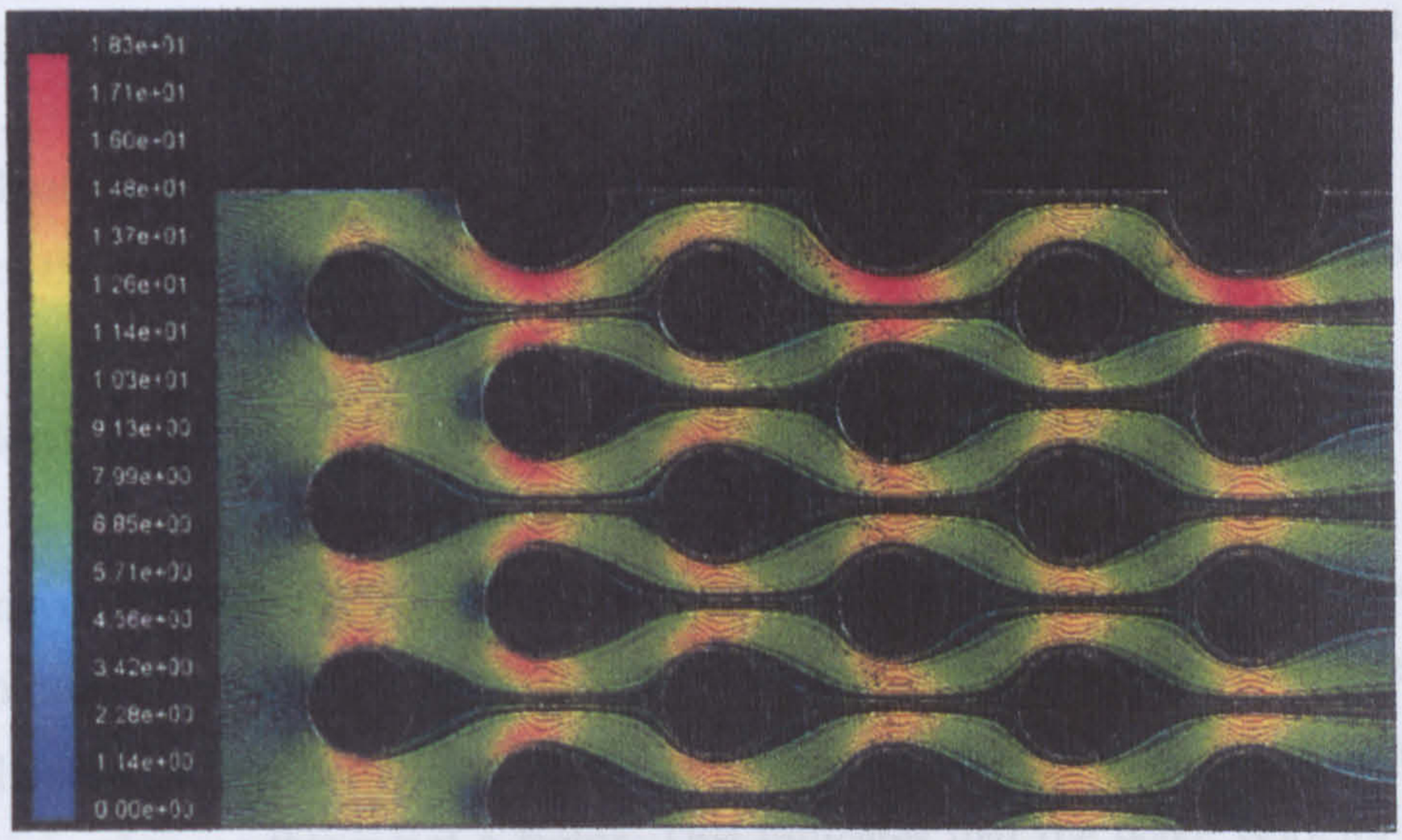

Figure 9.5: Pathlines through bundle with half tube corbels, coloured by Velocity (mfr: 4 kg/s, Face Velocity: 6.58m/s)

By following the path lines in Figure 9.4 it can be seen that there is a tendency in the bypass case for the flow to move towards the bypass lane. Inspection of the tubes in the column nearest the wall shows that the wakes are biased, with a less obvious effect on the wakes of the second column tubes. This indicates that the mass flow is redistributing towards the bypass lane, simply because there are no obstructions. Examining the tubes in the column nearest the wall it can be seen that the velocity between the tubes and the wall increases with the number of rows.

The theory developed from this is that, assuming the approach flow is of a uniform profile; the bypass lane flow behaves similarly to the transverse gap flow. After the first tube row the flow redistributes, so that some mass leaves the region around the tubes in the first and second columns. Flow from the middle of the bundle then redistributes accordingly, the net effect being that mass has moved out from the bundle and into the bypass lane. This will then continue with each subsequent tube row.

9.4.2 Application to actual finned tubes

In a finned tube bundle it is therefore believed that this same process will take place, although it is likely that the effects may be exacerbated due to the higher resistance of finned tubes compared to blockage equivalent plain tubes.

9.5 Visualisation of Flow

The visualisation technique used for the bypass tests was as described in Section 8.9.

The visualisation results on the air cooler bundle are very limited. This is by the nature of the fact that there is nothing in the bypass lane to visualise with. Therefore the interest is in the streamers on the tubes. These have been highlighted in green for clarity in the following photographs. It was seen, as shown in Figure 9.6, that the trend of the streamers on the tubes nearest the bypass lanes is to lift, overcoming the gravity effect. When compared with the streamers on the tubes in the last tube row it can be seen that they are noticeably parallel to the flow direction, whereas the streamers on the rear row tubes still sag slightly with the gravity effect. It will be noticed that all the streamers are in the tubes wakes, so this is not a factor. This indicates that the wake velocity behind these outer tubes is higher; hence the surrounding and approach velocities must be higher.

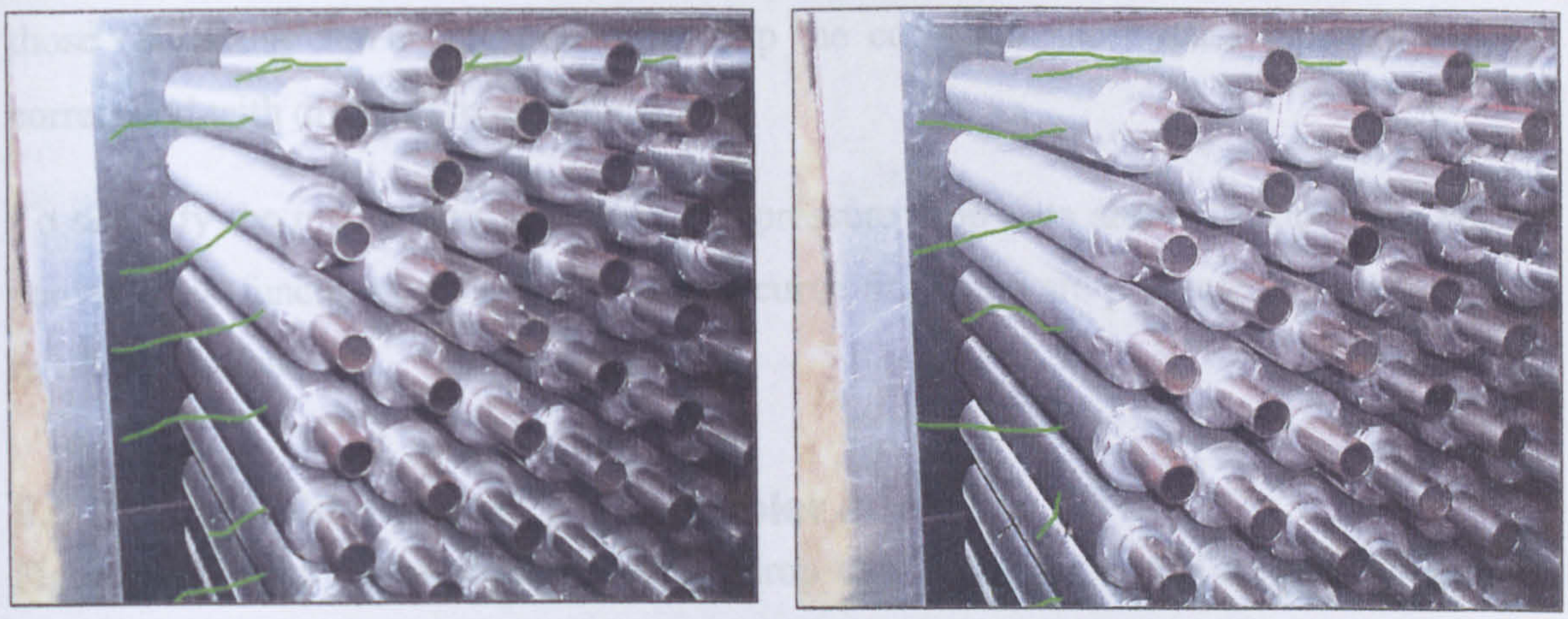

a. b.

Figure 9.6: Rear corbels and streamers at a.2.4 m/s and b.6.5m/s

It can be seen in Figure 9.6b that the trend of the streamers on the tubes nearest the bypass lanes is to lift noticeably from being parallel with the flow direction. The streamers on the tubes in the last tube row were observed to be now parallel with the flow direction, although partially this is due to the higher velocity lift.

It was also observed that the streamers on the tubes at the bottom of the duct lay downwards, whereas the nearby rear row streamers maintained a parallel path. This indicated that the flow through the bulk of the bundle was reasonably uniform, but the bypass lane does exert an influence.

These results reinforce the hypothesis developed, by examining the CFD pathlines, that the bypass lane represents a path of least resistance. Therefore there will be a migration of mass flow from the bundle into the bypass lane. The visualised results showed this, especially at higher flow rates when the tufts at the top of the bundle, as shown in Figure 9.6a, are so obviously raised.

9.6 Determining the bypass flow

9.6.1 Contribution of bypass flow

The initial analysis shown Section 4.4.2 showed that the amount of mass flow that bypassed the tubes could be determined by analysing the pressure drop against mass flow rate data, such as those presented in Figures 9.2 and 9.3. It can be seen in both of

those charts that for a given pressure drop the corbelled and bypass pressure drops correspond with different mass flow rates.

To simplify the mathematical analysis the pressure drop data and mass flow rate were converted to functions, using a power law curve fit. These are presented and discussed in the sections below.

9.6.2 Flow split analysis for air cooler bundle

Figure 9.7 shows the re-plotted pressure drop curves for the corbelled and bypassing results, based on the experimental mass flow rates. It can be seen that the curves are virtually identical to those of the recorded experimental results shown in Figure 9.2. This is due to the extremely good grouping and repeatability of the MPWT data.

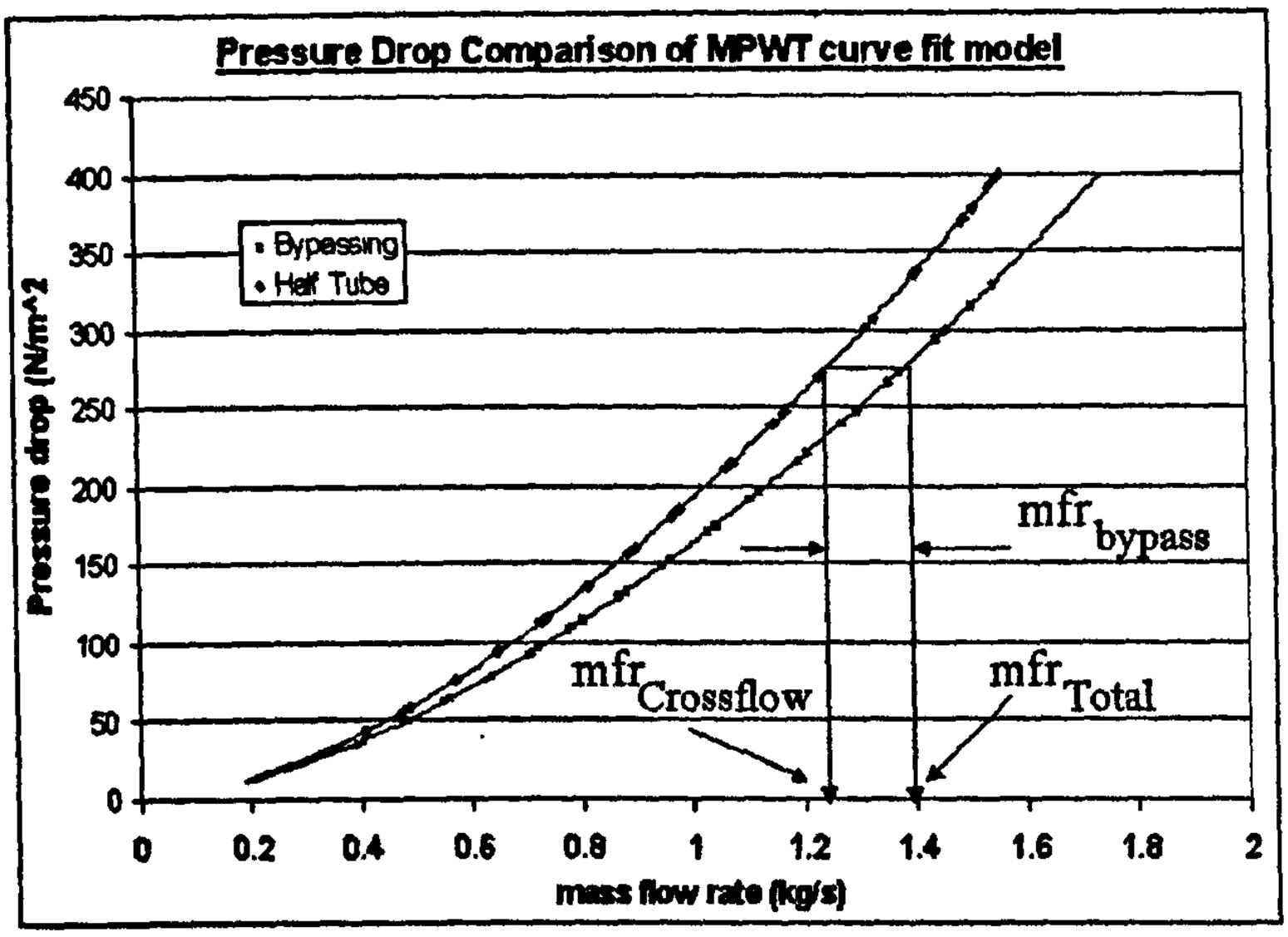

Figure 9.7: Flow split analysis for air cooler bundle

Table 9.2 shows the mass flow splits from these idealised curves. It can be seen that as the approach flow rate increases the amount of flow that bypasses the bundle increases. Figure 9.8 reinforces this, where it can be clearly seen that the amount of mass flow rate through the bundle decreases. This is an important point as it directly relates to the effective mass flow rate that will be used in the heat transfer calculations. Figure 9.8 shows the mass flow rates against the Bypass Reynolds number. The method for calculating this will be given in Section 9.8.2.

Pressure Drop (N/m^2)	mfr Crossflow (kg/s)	mfr Total (kg/s)	mfr Bypassing (kg/s)	% of flow in crossflow	% of flow in bypassing
40	0.3875	0.4181	0.0306	92.68	7.32
80	0.5898	0.6429	0.0531	91.73	8.27
120	0.7540	0.8269	0.0729	91.18	8.82
160	0.8976	0.9886	0.0910	90.80	9.20
200	1.0275	1.1354	0.1079	90.50	9.50
240	1.1476	1.2715	0.1239	90.25	9.75
280	1.2599	1.3992	0.1393	90.05	9.95
320	1.3661	1.5201	0.1540	89.87	10.13
360	1.4672	1.6354	0.1683	89.71	10.29
400	1.5639	1.7460	0.1821	89.57	10.43

Table 9.2: Flow split in air cooler bundle from curve fits

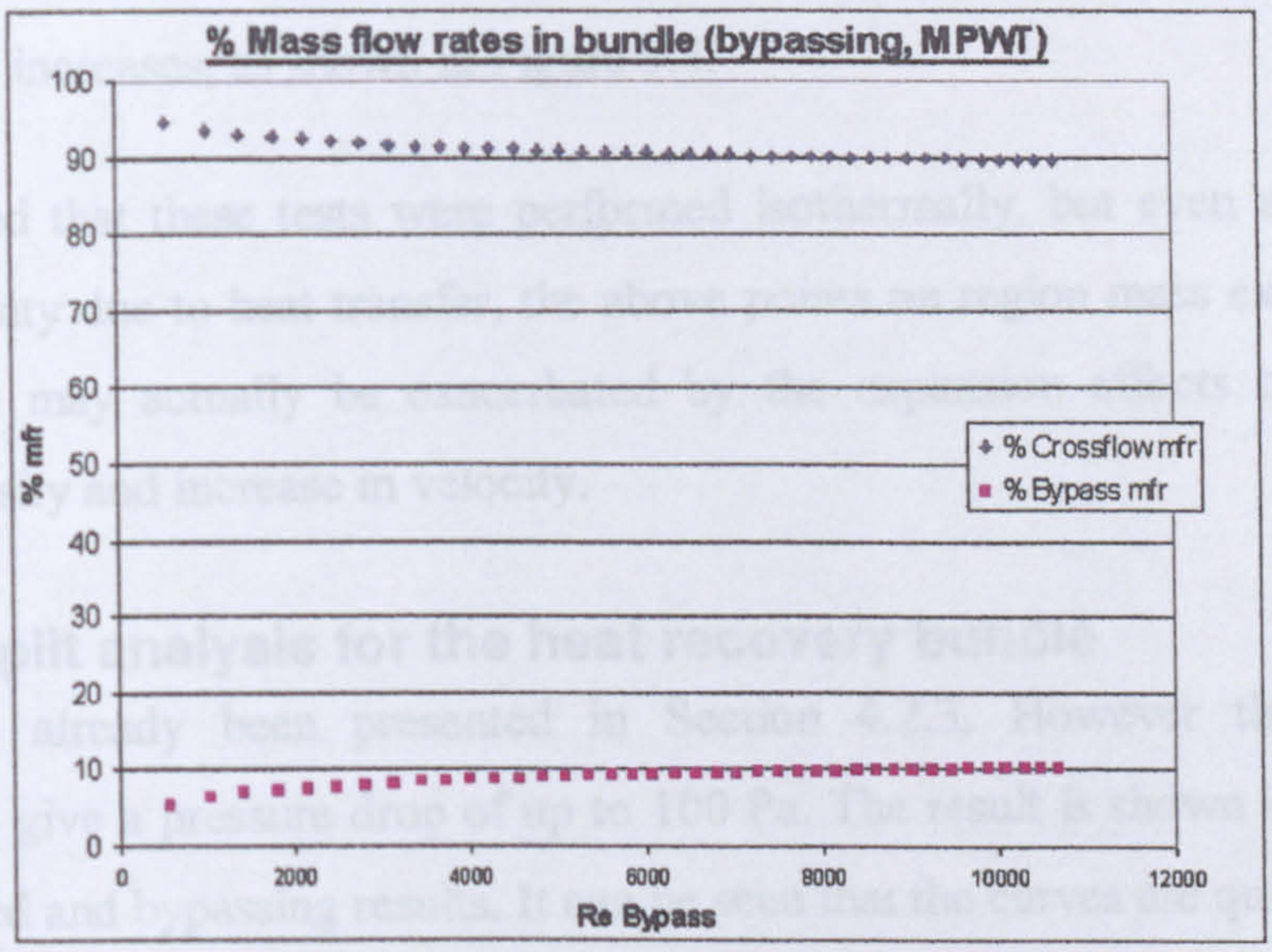

Figure 9.8: % Mass flow splits in crossflow and bypass regions

It is assumed that the approach flow to a bundle is of a uniform distribution. In the MPWT experiments this assumption is reasonable, and the CFD study had a uniform profile specified.

At low mass flow rates the momentum within the approach flow means that the flow will pass into the tube bundle, and will try to escape to the lower resistance lanes. The low momentum means that the flow in the middle of the bundle will redistribute slightly. The low momentum flow on the outer edges of the bundle nearest the lanes will successfully escape and be entrained with the flow originally distributed into the lanes at the entrance to the bundle. Thus a slightly larger proportion of bypass flow than can be initially predicted from the geometric approach areas will exit the bypass lane at

the rear of the bundle. The geometric approach was described in Section 4.2.3, and is now proved invalid.

At higher flow rates the high momentum means that the flow in the middle of the bundle will move significantly to redistribute through the tube bundle towards the edges. The high momentum flow on the outer edges of the bundle nearest the lanes will redistribute into the bypass lane and become entrained with the flow originally distributed into the lanes at the entrance to the bundle. Thus a larger proportion of bypass flow than can be initially predicted from the geometric approach areas will exit at the rear of the bundle. This results in the increases of bypass mass flow rate when the air face velocity increases, as shown in Figure 9.8.

It must be noted that these tests were performed isothermally, but even allowing for changes in density due to heat transfer, the above points on region mass exchange will still stand, and may actually be exacerbated by the expansion effects caused by a decrease in density and increase in velocity.

9.6.3 Flow split analysis for the heat recovery bundle

This data has already been presented in Section 4.2.3. However the data was extrapolated to give a pressure drop of up to 100 Pa. The result is shown in Figure 9.9 for the corbelled and bypassing results. It can be seen that the curves are quite dissimilar to those of the recorded experimental results shown in Figure 9.3. This is due to a higher level of scatter in the data, notably in the corbelled results. This means that the resultant curve fits do not match the trends of divergence shown in both the idealised and actual data of the air cooler bundle shown above.

It will therefore be seen in Table 9.3 that the indications are that the mass exchange process explained for the air cooler above are reversed.

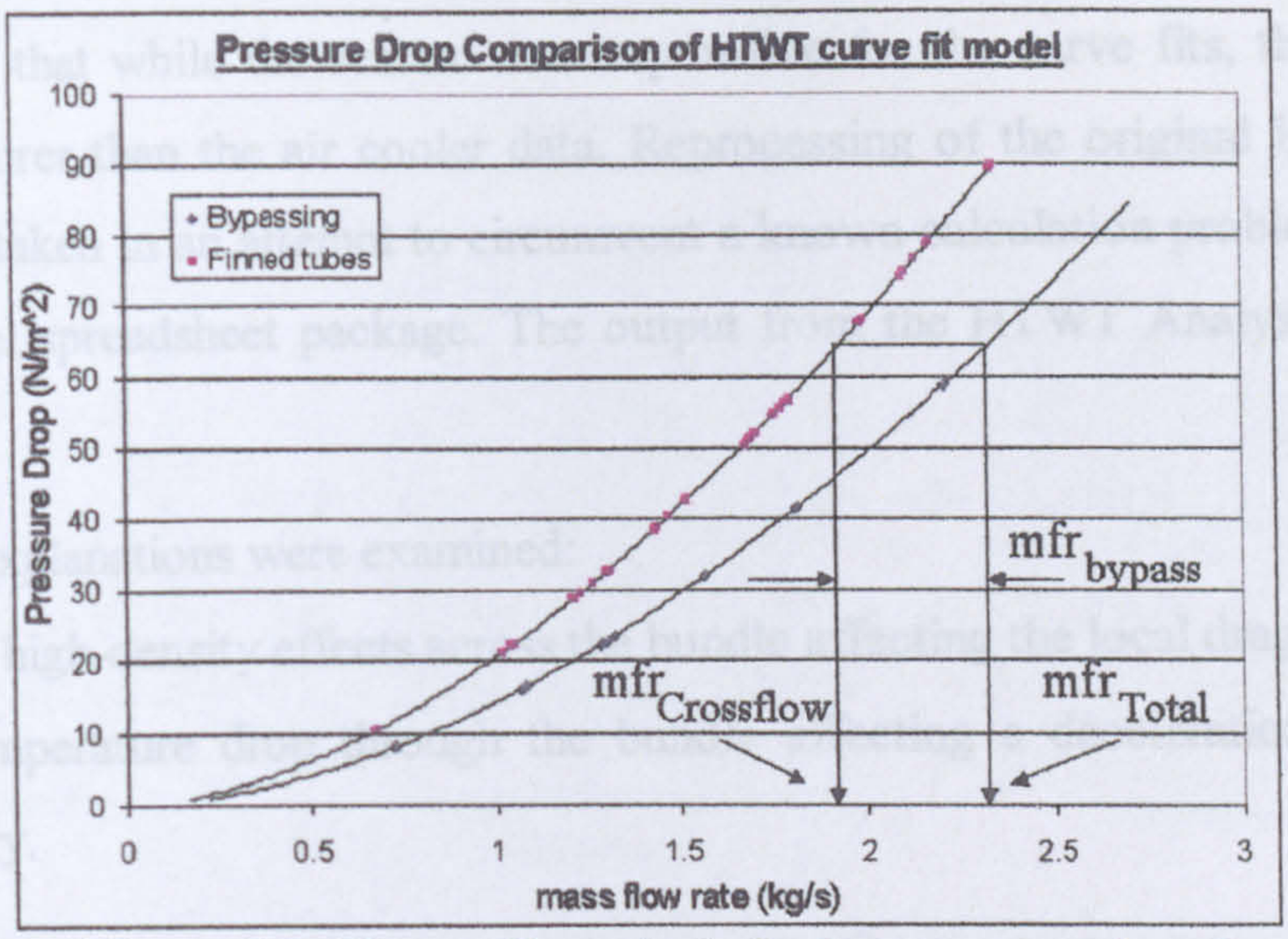

Figure 9.9: Flow split analysis for heat recovery bundle

Pressure Drop (N/m^2)	mfr Crossflow (kg/s)	mfr Total (kg/s)	mfr Bypassing (kg/s)	% of flow in crossflow	% of flow in bypassing
10	0.6520	0.7701	0.1181	84.66	15.34
20	0.9761	1.1406	0.1644	85.58	14.42
30	1.2360	1.4351	0.1991	86.13	13.87
40	1.4613	1.6892	0.2278	86.51	13.49
50	1.6641	1.9168	0.2527	86.81	13.19
60	1.8504	2.1254	0.2750	87.06	12.94
70	2.0242	2.3194	0.2952	87.27	12.73
80	2.1878	2.5016	0.3139	87.45	12.55
90	2.3431	2.6743	0.3312	87.61	12.39
100	2.4913	2.8388	0.3475	87.76	12.24

Table 9.3: Flow split in HTWT bundle from curve fits

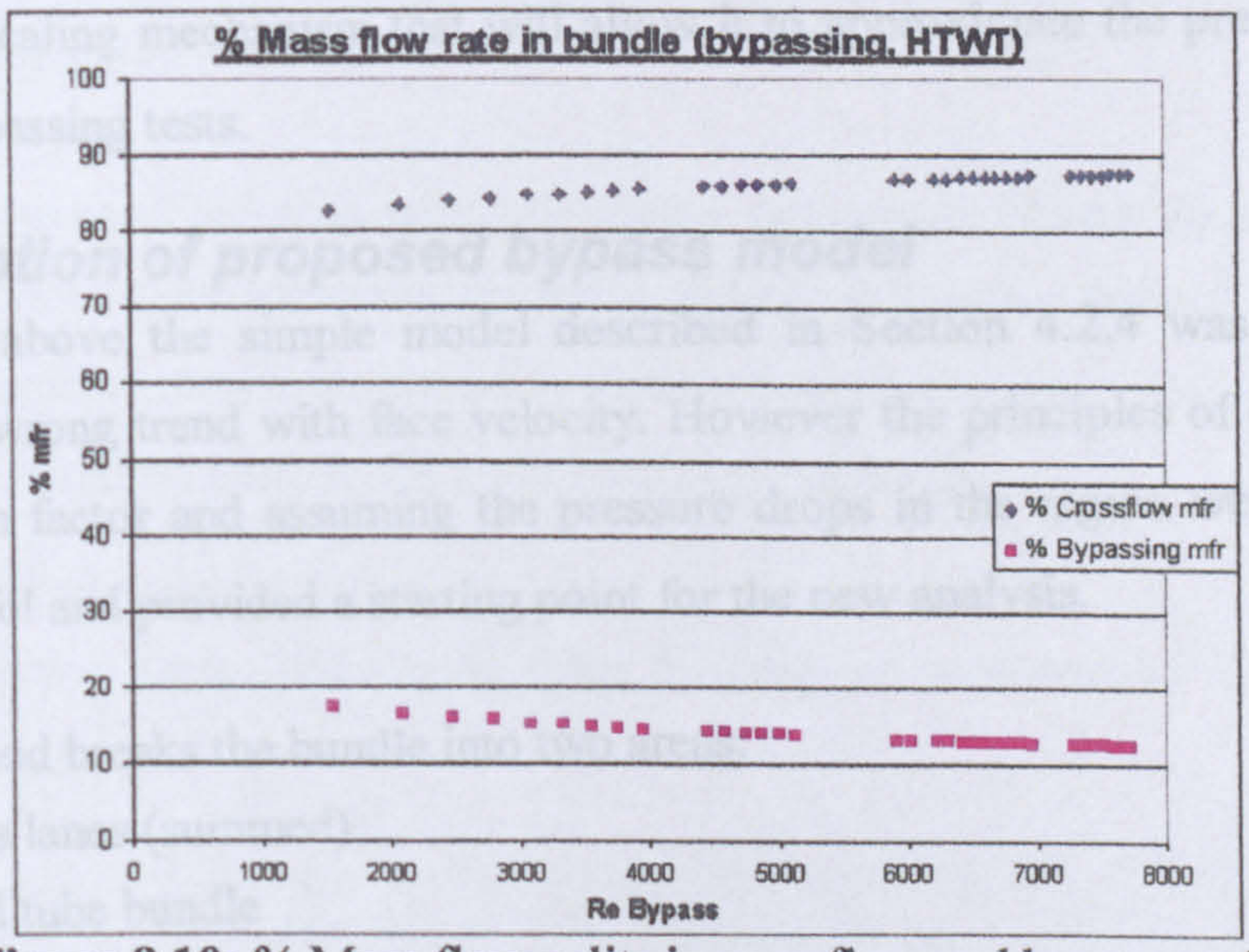

Figure 9.10: % Mass flow splits in crossflow and bypass regions

It was believed that while the scatter was responsible for the curve fits, the data was intrinsically poorer than the air cooler data. Reprocessing of the original HTWT data files was undertaken in an attempt to circumvent a known calculation problem with the Microsoft Excel spreadsheet package. The output from the HTWT Analyser software was the same.

Two possible explanations were examined:

- Low to high-density effects across the bundle affecting the local drag.
- Gas temperature drop through the bundle affecting a decelerational pressure recovery.

Neither of these explanations could be correct, as the change in density means that the change to higher gas density towards the back of the bundle would lead to higher friction, so a higher resistance would actually help to expel more mass into the bypass lane. Also, at these mass flow rates the decelerational pressure recovery component could be shown to be very small compared to the frictional component.

It is concluded that the trend exhibited from this data is incorrect, and must be excluded from the method development. However the scatter of the bypassing data is less severe than that of the corbels and the range of the pressure drop measurements is assumed to still be valid, as no fault could be found in the pressure transducer recordings. Therefore, as will be seen in the following sections the developed model will incorporate a scaling mechanism that will allow it to approximate the pressure drop of the HTWT bypassing tests.

9.7 Description of proposed bypass model

As explained above the simple model described in Section 4.2.4 was flawed as it predicted the wrong trend with face velocity. However the principles of determining a bypass friction factor and assuming the pressure drops in the region were equal were both very useful and provided a starting point for the new analysis.

The new method breaks the bundle into two areas:

- Bypass lanes (summed)
- Finned tube bundle

This is shown in figure 9.11

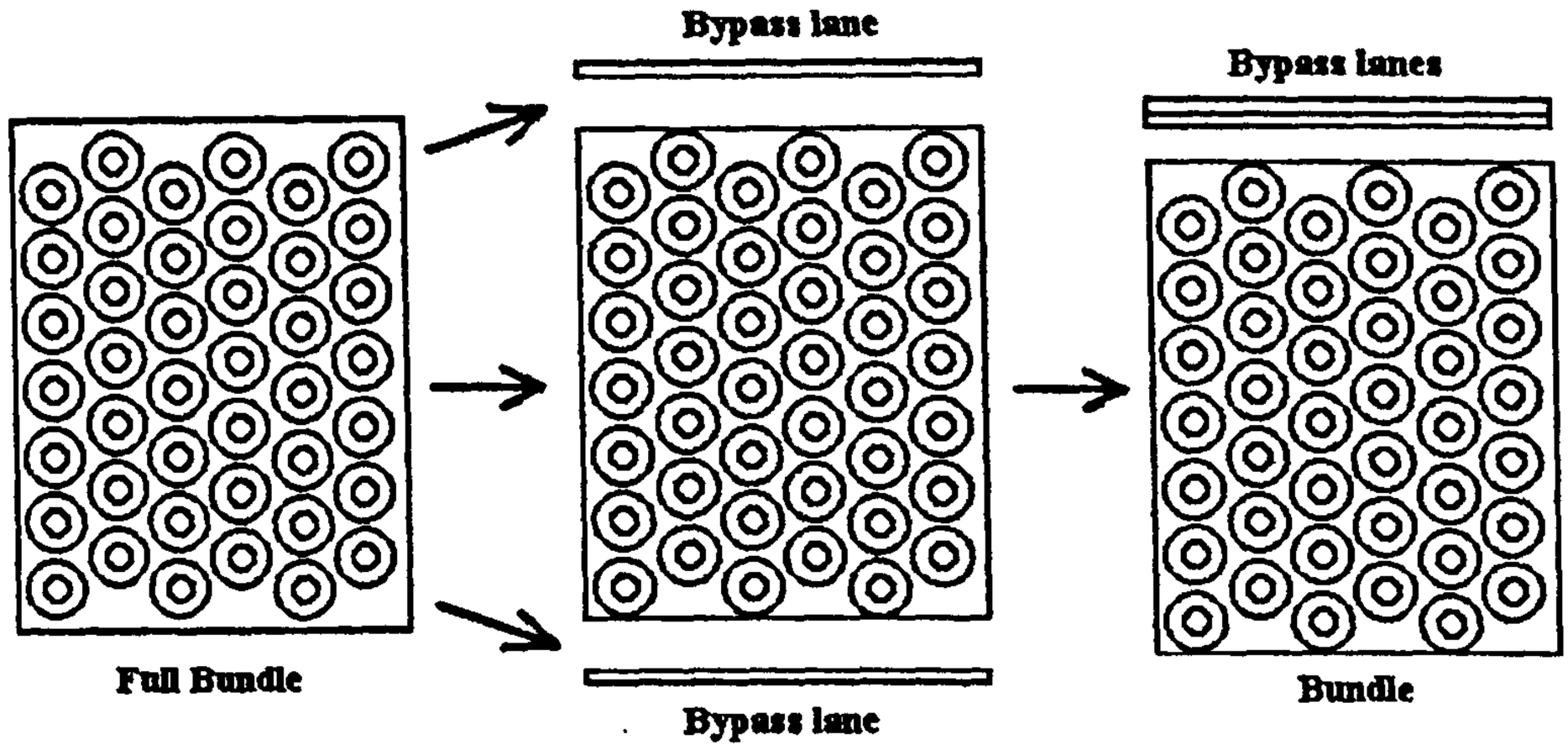

Figure 9.11: Conceptual model of bundle and bypass regions

It is assumed that each of these regions has the same pressure drop therefore it can be said that Equ.9.1 applies.

$$\Delta P_{Bundle} = \Delta P_{Bypass} \qquad \text{(Equ.9.1)}$$

Using this principle a flow split can be worked out to calculate the bypass flow and the crossflow through the bundle that satisfies Equ.9.1. The bundle pressure drop is simply calculated from the new staggered method presented in Chapter 6, while the bypass pressure drop will be calculated using a new method proposed in the following sections. It will be noted that this development is based on the air cooler data due to the problems noted above in the HTWT data. Despite this, it will be shown that the new model is scalable to larger geometries.

9.8 Development of the new bypass pressure loss model

When the air cooler data was analysed using the curve fit based analysis shown above the bypass mass flow rates were found in a method similar to those shown in Table 9.2. The actual measured pressure drops were used in the analysis.

9.8.1 Friction factor of bypass

The bypass friction factor rearranged from the original presented by Wills [29] is as shown in Equ.9.2.

$$f_B = \frac{\Delta P_B}{2N_R \rho u_B^{\,2}} \qquad \text{(Equ.9.2)}$$

Where the bypass velocity is found from Equ.9.3

$$u_B = \frac{mfr_B}{\rho A_{Bypass}} \qquad \text{(Equ.9.3)}$$

When this formula was tested against the experimental data the friction factor was found to be a power law function of the bypass velocity. To generalise this the bypass velocity was transformed in to a bypass Reynolds number.

As the characteristic scaling parameter of the bypass lane is the lane height (H_{bypass}) the Bypass Reynolds number calculation is performed using Equ.9.4

$$\mathrm{Re}_B = \frac{H_{bypass}\rho u_B}{\eta} \qquad \text{(Equ.9.4)}$$

The friction factor was replotted against the bypass Reynolds number and the resultant friction factor was realised as shown in Figure 9.12.

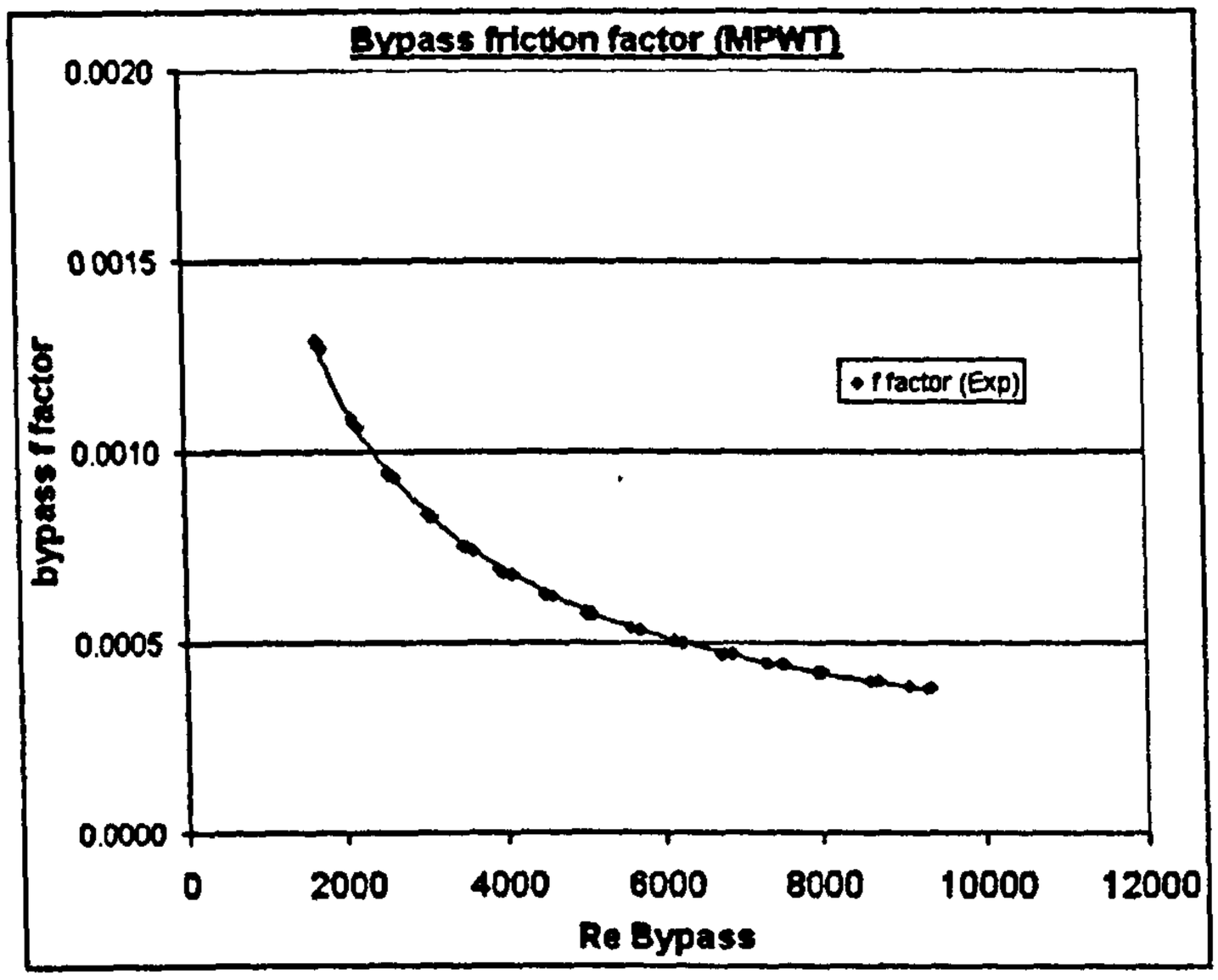

Figure 9.12: Bypass friction factor against bypass Reynolds number

From this the friction factor was determined to be as shown in Equ.9.5.

$$f_B = 0.2568\,\mathrm{Re}_B^{-0.714} \qquad \text{(Equ.9.5)}$$

9.8.2 Expanded range bypass model

To make the f factor model more functional, to give an answer in terms of pressure drop, a substitution of the derived Reynolds number function (Equ.9.5) was made into

the rearrangement of Equ.9.2 to give a pressure drop expression. The substitution of Equ.9.5 into this new expression was made.

The resulting function had repeating terms and was not found to be scalable for the HTWT data. It is shown in Equ.9.6.

$$\Delta P_B = 0.2568 \cdot \left(\frac{\rho_{Bulk} u_B H_{bypass}}{\eta} \right)^{-0.714} 2 N_R \rho \, u_B{}^2 \qquad \text{(Equ.9.6)}$$

The standard aerodynamic relation for drag forces contains a dynamic term, the density of the fluid the body is submerged in and a shape factor based on the body in question. In this case the area is disregarded as the pressure loss is of importance.

By simplifying Equ.9.6, and examining various parameters that characterise the bypass lane and the scale of the bundles, a model was found that met the scalability criteria. The model includes three terms and is similar in layout to the previous bundle pressure drop models discussed in Chapters 6.and 7. The expression developed for the pressure drop in the bypass lane is shown in Equ.9.7.

$$\Delta P_B = K_{Bypass} \cdot \rho^{0.286} u_B{}^{1.286} \qquad \text{(Equ.9.7)}$$

K_{Bypass} is the geometric term that scales Equ.9.7 to account for varying geometries. This is shown in Equ.9.8. This term is the combination of dimensionless ratios of immediate relevance to the bypass lane dimensions and parameters that characterise the physical size of the bundle. The constants were found using a binary search routine to find a best fit for all the data.

$$K_{Bypass} = \frac{6824.015 \cdot D_o \cdot D_f \cdot N_R \cdot H_{bypass}{}^{0.286}}{0.0254 \cdot H_{Duct}} \eta^{0.714} \qquad \text{(Equ.9.8)}$$

Where H_{Duct} is the total height of the duct including the bypass lanes.

9.9 Bypass pressure drop calculation procedure

9.9.1 Flow chart

Figure 9.13 shows a flow chart of the steps needed to calculate the bundle and bypass lane pressure drop.

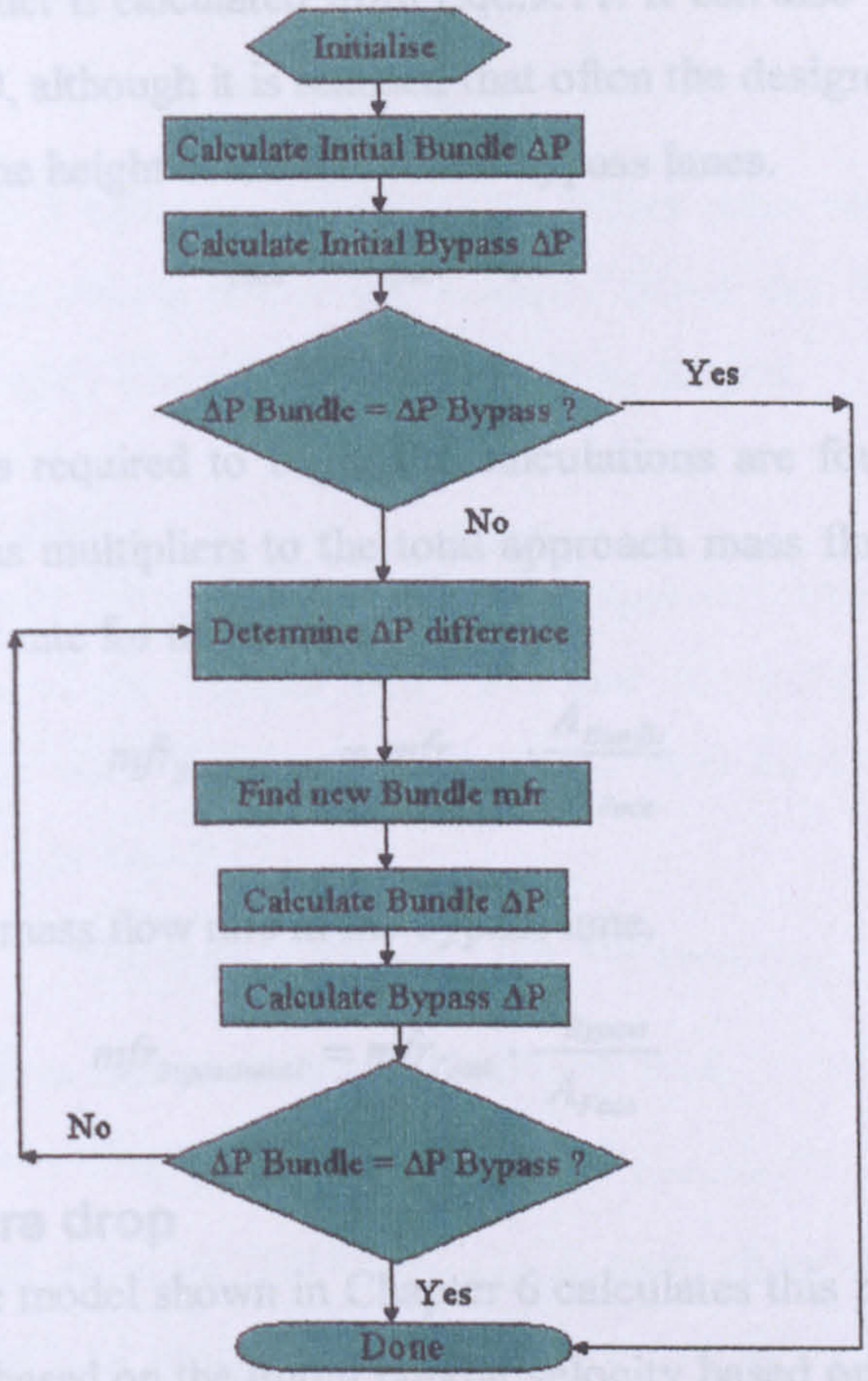

Figure 9.13: Flow chart of calculation procedure

9.9.2 Iteration Method

The following sections are the actual calculation steps necessary to complete the iteration procedure as laid out in Figure 9.13.

Initialise

Geometry

The routine is begun by calculating the initial guess mass flow rates. These are effectively the mass flow rates based on the geometric face areas of the two regions. Equ.9.9 shows the face area of the bypass lane.

Note: The total bypass area is considered, hence the multiplier of 2.

$$A_{Bypass} = 2 \cdot H_{bypass} \cdot L_T \qquad \text{(Equ.9.9)}$$

The face area of the bundle is calculated from Equ.9.10

$$A._{Bundle} = ((N_R - 0.5) \cdot P_T + D_f) L_T \qquad \text{(Equ.9.10)}$$

The total face area of the duct is calculated from Equ.9.11. It can also be calculated by summing Equs.9.9 and 9.10, although it is realised that often the designer will know the overall duct height before the height of the individual bypass lanes.

$$A_{Face} = H_{Duct} \cdot L_T \qquad \text{(Equ.9.11)}$$

Mass flow rates

The initial mass flow rates required to begin the calculations are found by using the proportions of face areas as multipliers to the total approach mass flow rate. Equ.9.12 shows the initial mass flow rate for the bundle.

$$mfr_{BundleInitial} = mfr_{Total} \cdot \frac{A_{Bundle}}{A_{Face}} \qquad \text{(Equ.9.12)}$$

Equ.9.13 shows the initial mass flow rate in the bypass lane.

$$mfr_{BypassInitial} = mfr_{Total} \cdot \frac{A_{Bypass}}{A_{Face}} \qquad \text{(Equ.9.13)}$$

Initial bundle pressure drop

The new staggered bundle model shown in Chapter 6 calculates this pressure drop. The initial calculation will be based on the initial bundle velocity based on the initial bundle mass flow rate calculated above using Equ.9.14.

$$u_{BundleInitial} = \frac{mfr_{BundleInitial}}{\rho A_{Bundle}} \qquad \text{(Equ.9.14)}$$

Initial bypass pressure drop

The initial pressure drop in the bypass lane is calculated by the new bypass pressure drop equation (Equ.9.7). This initial calculation will be based on the initial bypass velocity based, as shown in Equ.9.15, on the initial bypass mass flow rate that was calculated above.

$$u_{BypassInitial} = \frac{mfr_{BypassInitial}}{\rho \cdot A_{Bypass}} \qquad \text{(Equ.9.15)}$$

Pressure Drop equality

Once these two pressure drops have been calculated a simple convergence check is to be performed on the initial calculations to determine if further iteration is necessary, to minimise computation time. This is shown in Equ.9.16.

$$DR = \frac{\Delta P_{Bypass}}{\Delta P_{Bundle}} \qquad \text{(Equ.9.16)}$$

If the difference ratio (DR) is equal to unity then no further steps need be performed. Otherwise the further steps shown below are needed. Given the results during the method development it is highly likely that iteration will be needed.

New mass flow rate splits

To determine the new bundle mass flow rate, the total approach mass flow rate the is multiplied by the product of the bypass mass flow rate (or initial if it is the first iteration) and the difference ratio. This is then subtracted from the total approach mass flow rate (mfr_{Total}) as shown in Equ.9.17.

$$mfr_{BundleNew} = mfr_{Total} - DR \cdot mfr_{BypassOld} \qquad \text{(Equ.9.17)}$$

Similarly the new bypass flow rate is calculated from Equ.9.18.

$$mfr_{BypassNew} = mfr_{Total} - mfr_{BundleNew} \qquad \text{(Equ.9.18)}$$

It is however possible that the term ($DR^{*}mfr_{BypassOld}$) from either the initial guess or subsequent iterations could lead to the bypass mass flow rate being higher than that of the total mass flow rate, which is impossible. This would lead to the calculated bundle mass flow rate being a negative value. Therefore if the condition occurs whereby the product of the Difference Ratio and bypass mass flow rate becomes greater than or equal to the total mass flow rate then Equ.9.19 is used.

$$mfr_{BundleNew} = mfr_{Total} - F_{Relax} \cdot \left(DifferenceRatio \cdot mfr_{BypassOld}\right) \qquad \text{(Equ.9.19)}$$

Equ.9.19 introduces a new term, F_{Relax}. This is a convergence relaxation factor used to combat the condition described above. It was found during development of the method that $F_{Relax} = 0.25$ was a suitable value to solve problems when processing the Heat Recovery bundle data. This is a very low value, and could lead to a long iteration procedure, but will ensure eventual solution stability.

New Bundle pressure drop

To calculate the new bundle pressure drop the new staggered bundle method is used. This means that the mean superficial velocity based on the newly found bundle mass flow rate must be found. This is calculated from Equ.9.20.

$$u_{Bundle} = \frac{mfr_{BundleNew}}{A_{Bundle}\rho} \qquad \text{(Equ.9.20)}$$

New Bypass pressure drop

To calculate the new bypass pressure drop the new method (Equ.9.7) is used. This means the mean superficial velocity based on the bypass mass flow rate must be found. This is calculated from Equ.9.21.

$$u_{Bypass} = \frac{mfr_{Total} - mfr_{BundleNew}}{A_{Bypass}\rho} \qquad \text{(Equ.9.21)}$$

New Pressure Drop equality

Once again a check is made to see if Equ.9.1 is satisfied using Equ.9.16. If the pressure drop ratio given by Equ.9.17 is not close to unity then the iteration will continue and all the steps described between Equ.9.17 to Equ.9.21 will be repeated. Convergence is achieved if the pressure drop ratio (Equ.9.17) is close to unity within ±0.1%. A typical convergence chart is shown in Figure 9.14 for the air cooler bundle.

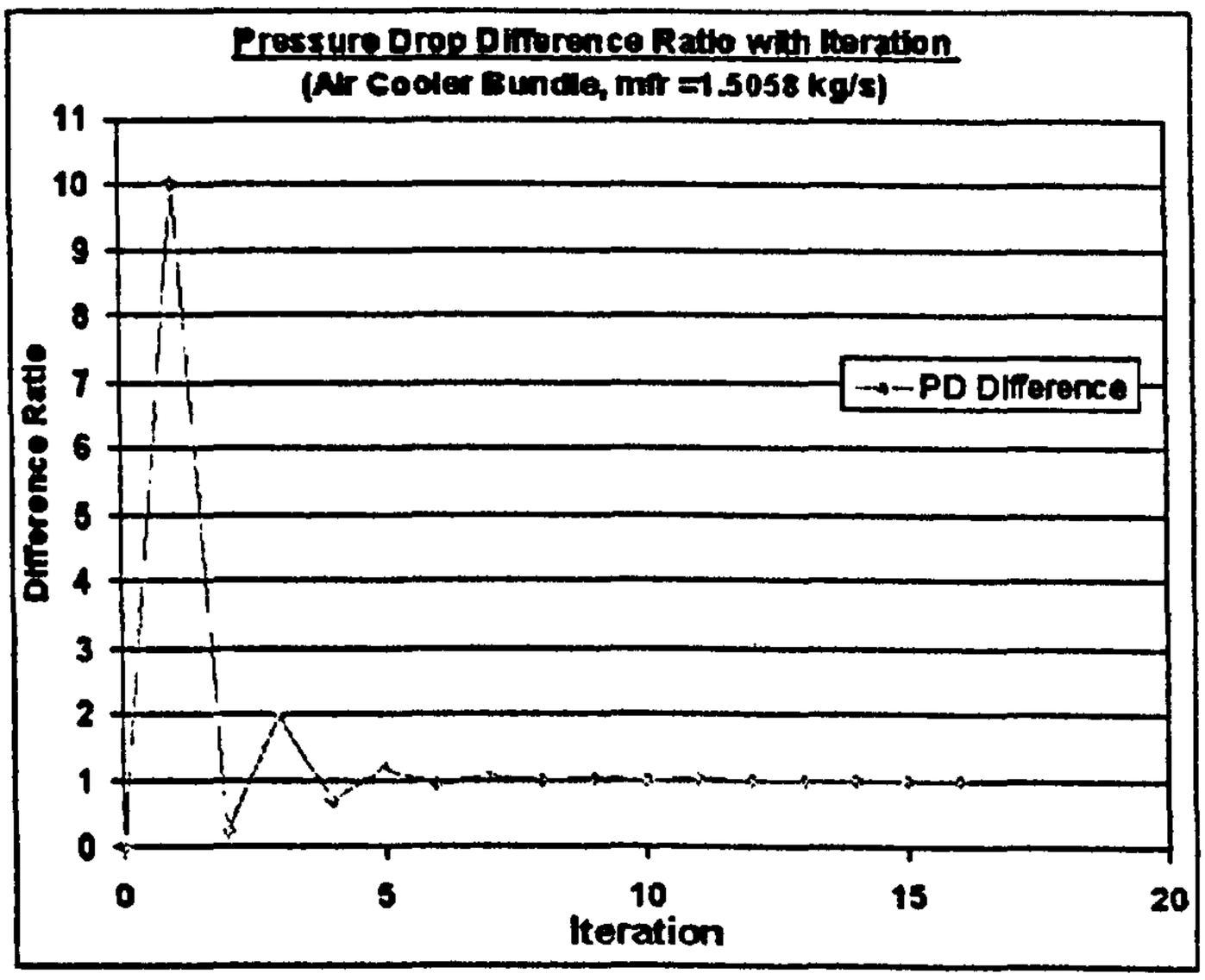

Figure 9.14: Typical convergence history output
(Air cooler bundle with mfr = 1.5058 kg/s)

End of program (Done)

When the criteria above is met, the program is finished and the pressure drops in the two zones will have equalised. This means that a stable pressure drop prediction has now been achieved.

9.10 Heat Transfer in a bypassing bundle

Having identified the flow split, a simple assumption can be made that the bypass flow calculated from the method above will leave the bundle without contributing to the heat transfer, as seen from the lower j factor when the corbels are removed in Figure 4.25, leading to poorer performance. In practice as the bypass flow crosses the bundle some of it will mix with the nearby flow, crossing the tubes, and thus may contribute to heat transfer. The amount of this escaped flow will depend on the balance of resistances between the bundle itself and the bypass lanes. However it is extremely difficult to quantify this escaped flow, therefore using the bypass flow calculated at the bundle bulk conditions is a reasonable simplification as it will lead to heat transfer calculation slightly on the conservative side. However this approach would be more accurate than not accounting for the bypass flow at all.

9.11 Comparison with data

9.11.1 MPWT pressure drop data

Figure 9.15 shows the experimentally derived mass flow splits for the crossflow and bypass regions determined from the MPWT tests. The predictions based on the method presented above are also shown.

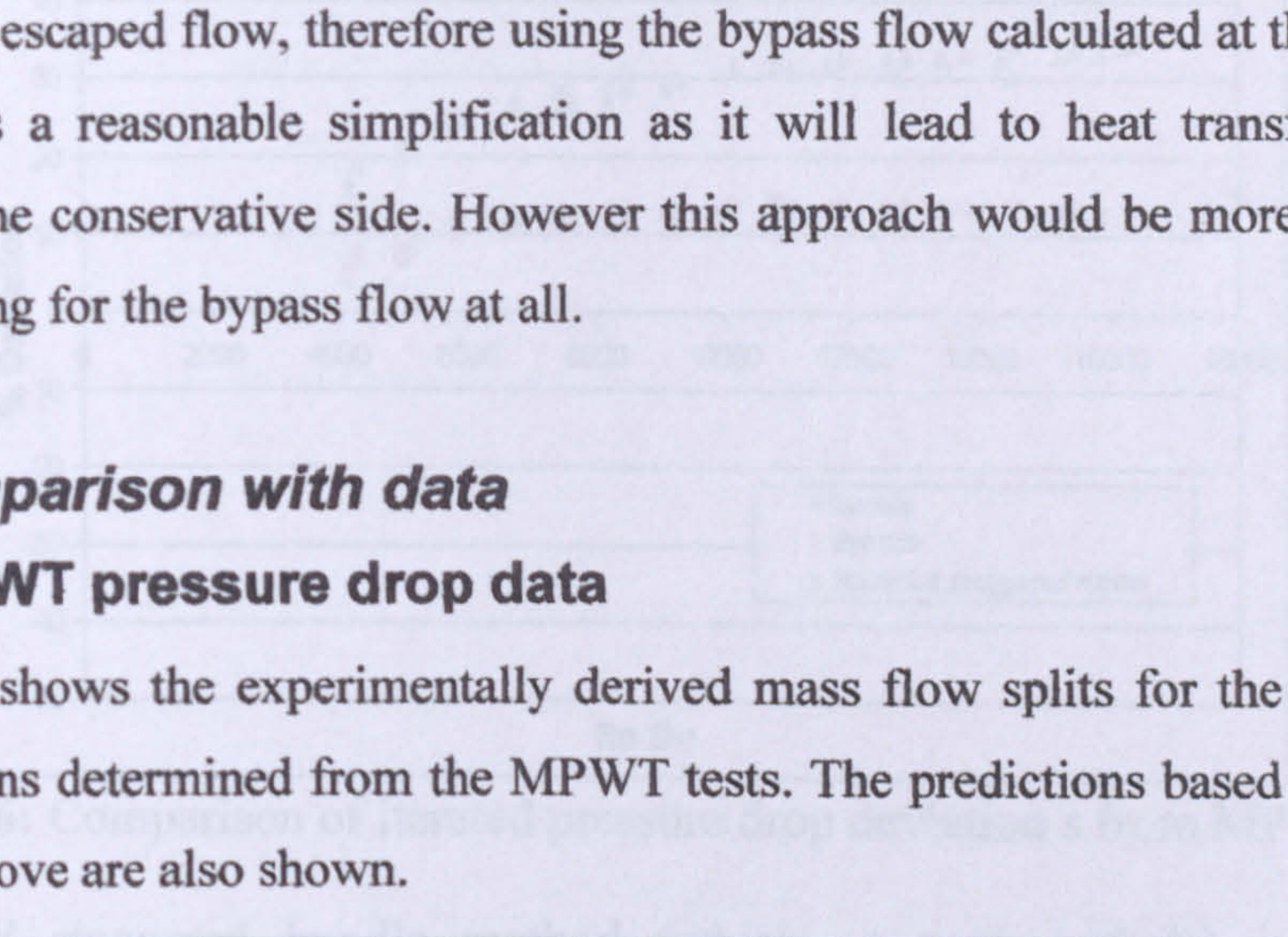

Figure 9.15: Flow split of bundle and bypass flows for air cooler bundle

It can be seen that the difference between the predicted flow splits and the experimental flow splits is minimal. This is due mostly to the fact that the model was developed from

this data. Nonetheless the prediction is excellent, given the optimisation necessary to attempt to match the HTWT bundle performance.

The iterative procedure shown in Section 9.9.2 was tested against the data set from the MPWT tests. Figure 9.16 shows the predicted pressure drop of the bundle. It should be noted that the 'Bundle' and 'Bypass' points overlay, as they are converged, and hence equal.

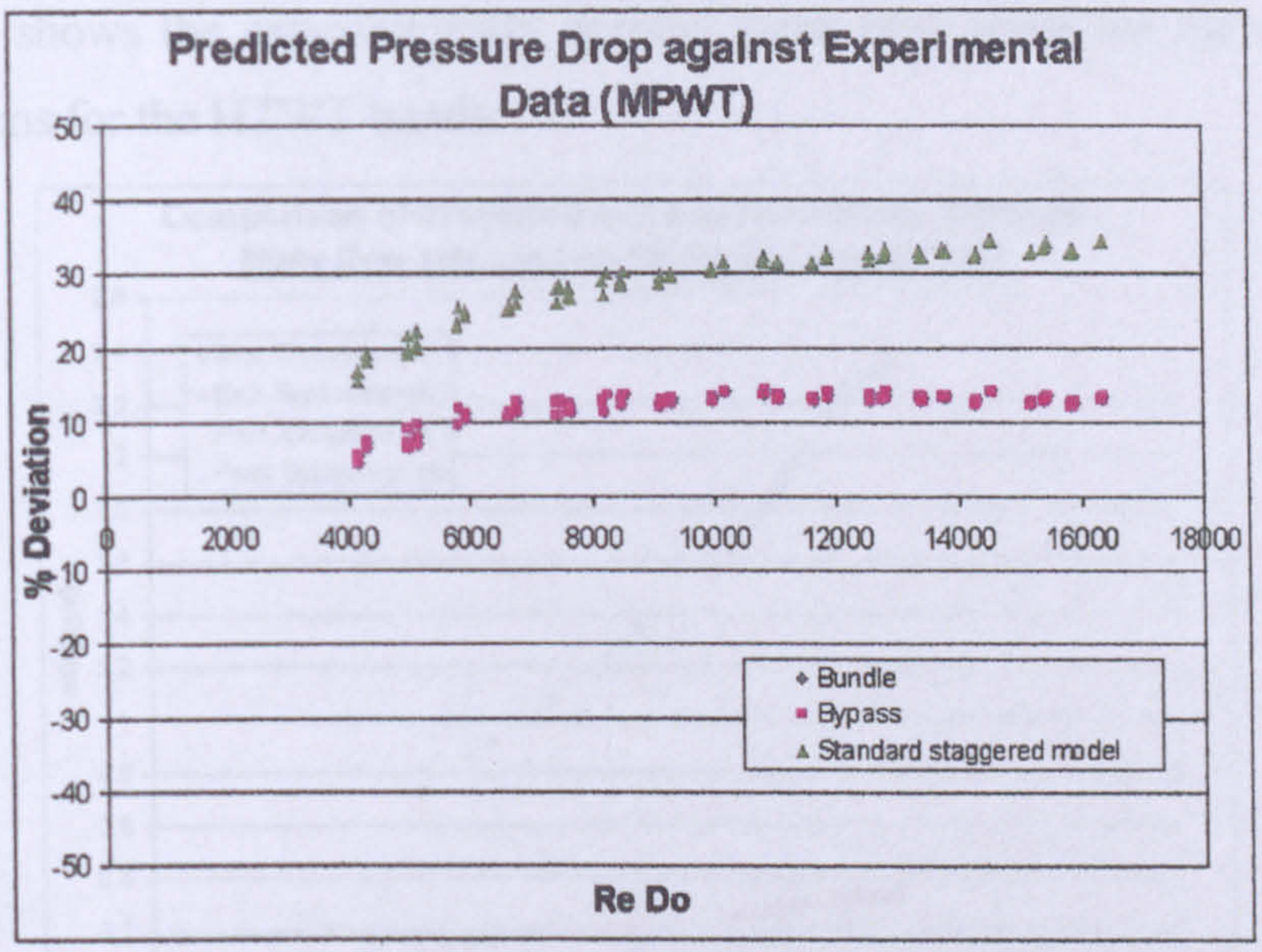

Figure 9.16: Comparison of iterated pressure drop deviation s from MPWT test data

The standard staggered bundle method (which assumes corbels) is included for comparison.

From Figure 9.16 the following can be noted:

- The predicted bundle and bypass pressure drops from the new model are equal as suggested by the model.
- The predicted pressure drops from the new model overpredict the MPWT data between 6% and 14% over the test range. This overprediction is the result of using the new staggered bundle prediction method in the iterative model. But as can be seen the model results are more accurate than the standard staggered bundle method, as it uses the crossflow mass flowrate for the bundle pressure drop calculation instead of the total flowrate, which is used by the standard method. The latter has therefore overestimated the pressure drop by 17% to 31%. Therefore using the new

pressure drop model for bundles with bypass flow has improved the results by 11% to 17% over the test range for this test bundle.

- It must be noted that for cases where the standard method underpredicts the pressure drop, using the new model for bundles with bypass flow may result in an even more conservative results. However this will not be the case for the majority of bundles.

9.11.2 HTWT pressure drop data

Figure 9.17 shows the experimentally derived mass flow splits for the crossflow and bypass regions for the HTWT bundle.

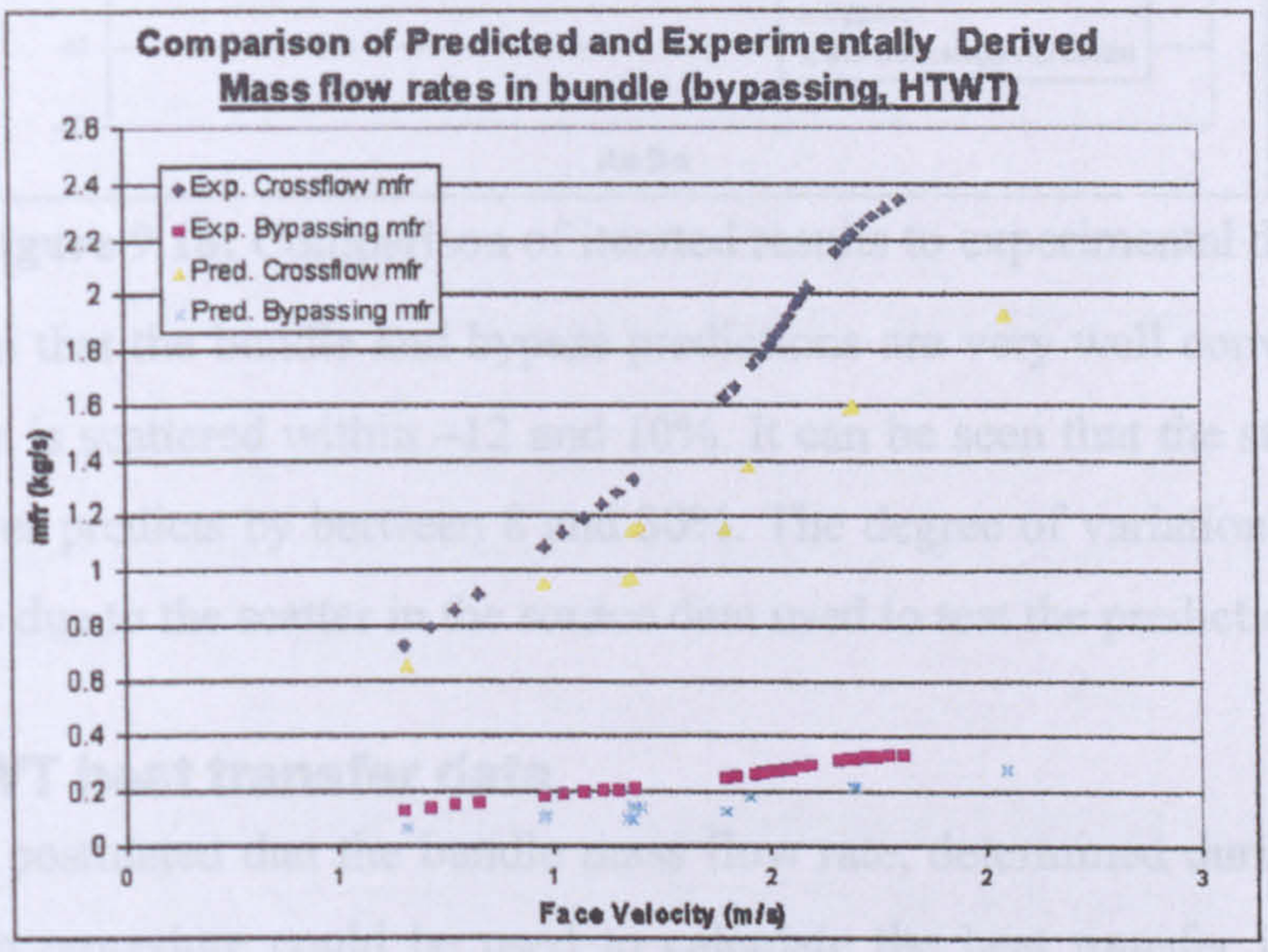

Figure 9.17: Flow split of bundle and bypass flows for air cooler bundle

It can be seen that the there is quite a difference in the predictions to the experimentally gathered data. This is due to two reasons: The standard staggered bundle core model, as will be shown below, generally overpredicts for this particular bundle, and the level of scatter in the experimental data is high causing the convergent trend discussed in Section 9.6.3. These two factors mean that a close tie up between the model and experimental data was not likely. It can be seen, however, that the predictions are most certainly of the correct order of magnitude, and the difference is only readily apparent at higher face velocities.

When the iteration procedure outlined in Section 9.9.2 was tested against the HTWT data the converged results were as shown in Figure 9.18. It should be noted that the 'Bundle' and 'Bypass' points overlay, as they are converged, and hence equal.

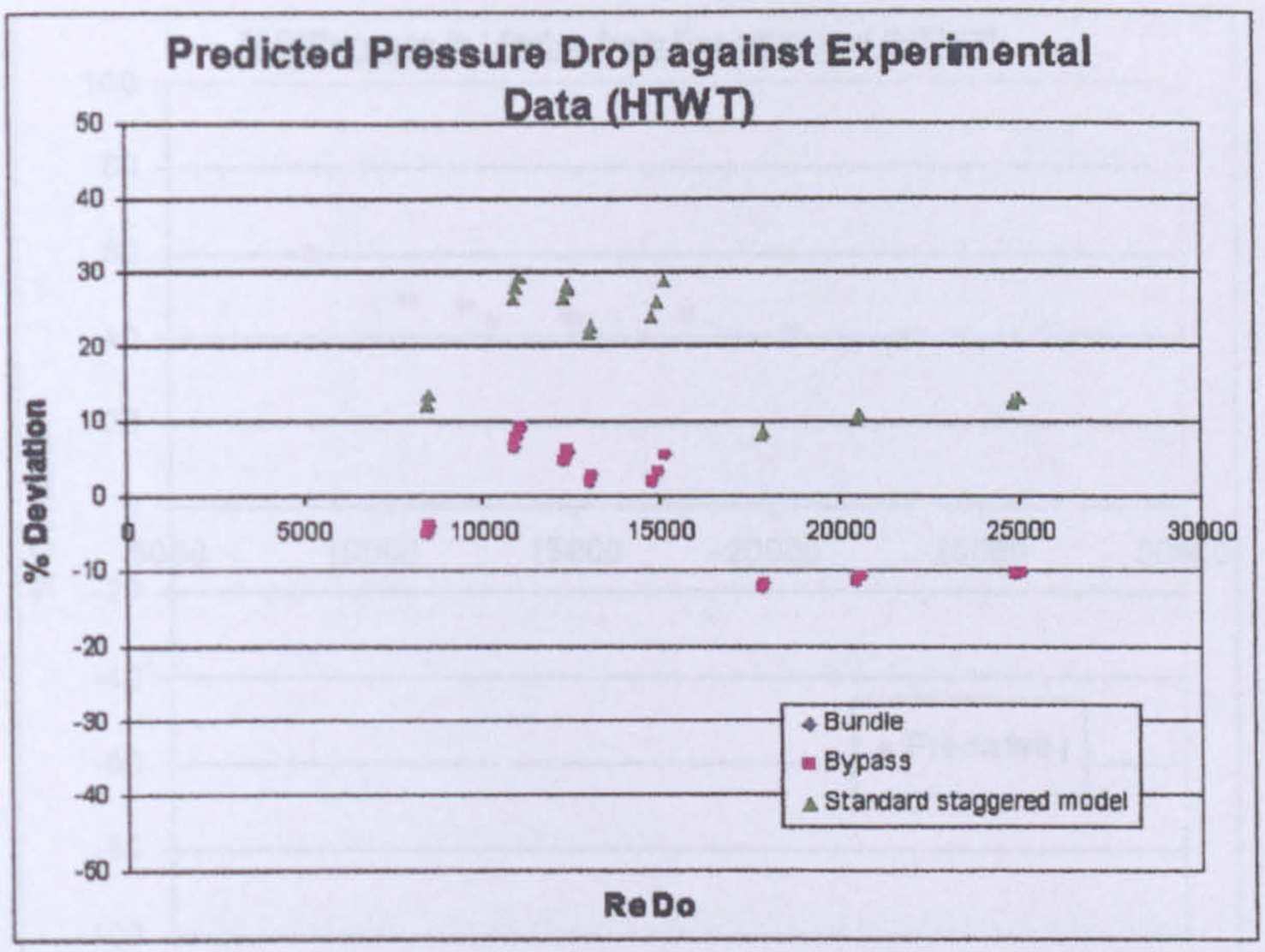

Figure 9.18: Comparison of iterated results to experimental data

It can be seen that the bundle and bypass predictions are very well converged and that the prediction is scattered within –12 and 10%. It can be seen that the standard method prediction over predicts by between 8 and 30%. The degree of variation in both sets of predictions is due to the scatter in the source data used to test the predictions.

9.11.3 HTWT heat transfer data

Section 9.10 postulated that the bundle mass flow rate, determined during the pressure drop iteration procedure could be used to calculate the heat transfer in the bypassed bundle, rather than using the total approach flow. It was demonstrated in Section 4.4.4 that to achieve the same thermal performance as a corbelled bundle the mass flow rate supplied to the tube bundle needs to be increased by the amount of the bypassing flow.

Figure 9.19, of the j factor, shows the deviation from the experimental bypassing data of the prediction using the mass flow rate calculated using the bundle-only mass flow rate. It can be seen that the overprediction is quite high ranging from 38 to 60%. It was shown in Chapter 6 that the deviations of the new staggered bundle model for similar bundles are quite evenly distributed and that no prediction exceeds +/-40%. Accepting that the prediction could then be overpredicting by up to 40% the extra deviation becomes unaccounted for.

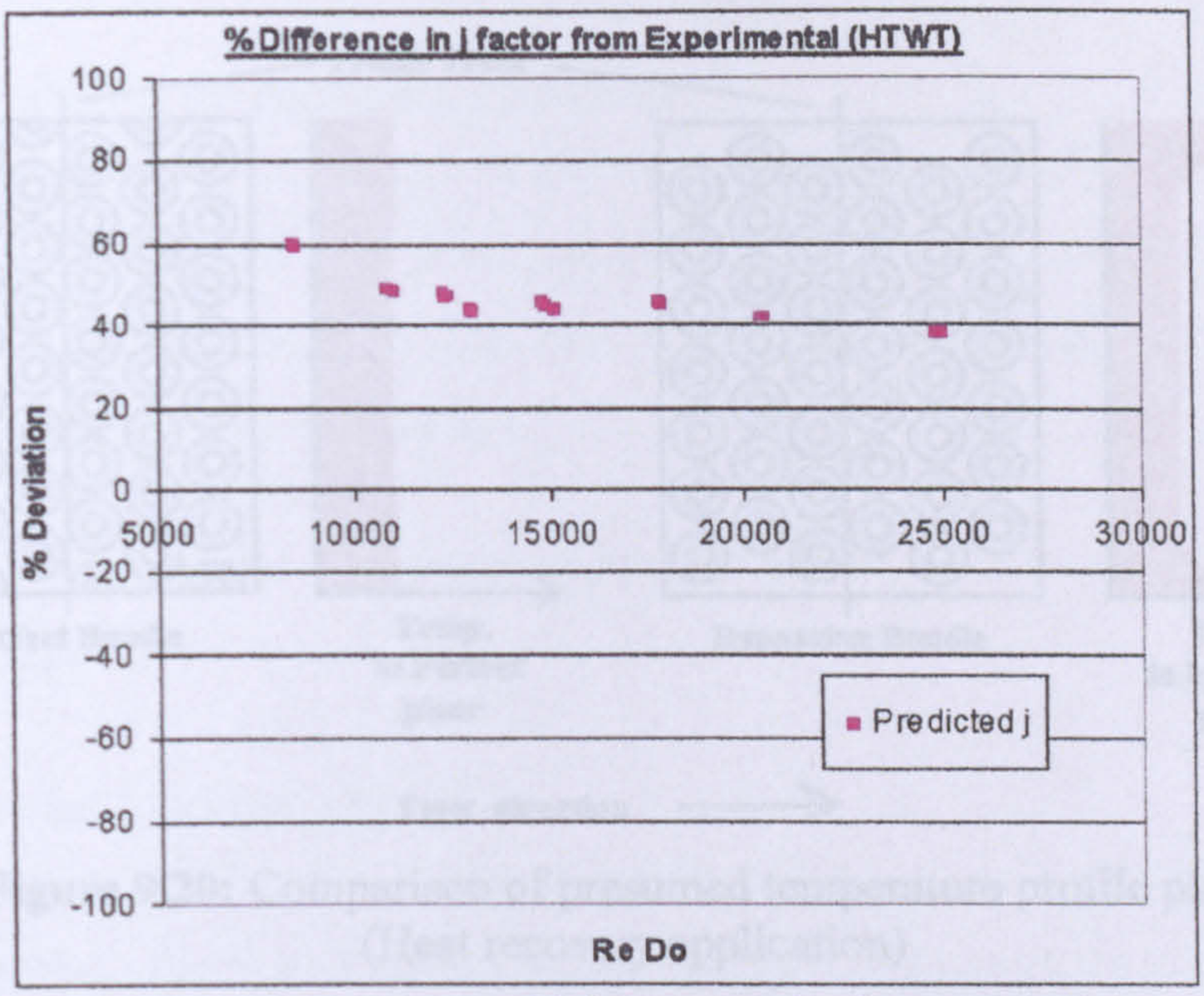

Figure 9.19: Comparison of j factor results for HTWT bypass data

The excess deviation arrives from the fact the calculated j factor decreases with increasing mass flow rate, hence when the smaller bundle mass flow rate is used for the j factor the prediction will be higher..

9.11.4 Further considerations for a bypassing j factor model

It is believed that the poor prediction is caused by the fact that the model does not consider the effects on heat leakage during mass migration. While the pressure drop model considers the two bulk mass flow rates, the process of heat rejection (to or from a finned tube) varies on a row-by-row basis. It has been shown by many researchers, and will be discussed in Chapter 10, that the heat transfer varies with each individual tube row.

In a perfect bundle the corbels maintain the flow pattern and resistance at the wall and remove the heat leakage tendency so a uniform outlet temperature will be reached in the plane behind each tube row. The bypassing bundles outlet temperature profile will always be skewed due to hotter flow in the bypass gaps, and it is believed that a temperature profile will occur, due to the migration effect, as shown in Figure 9.20.

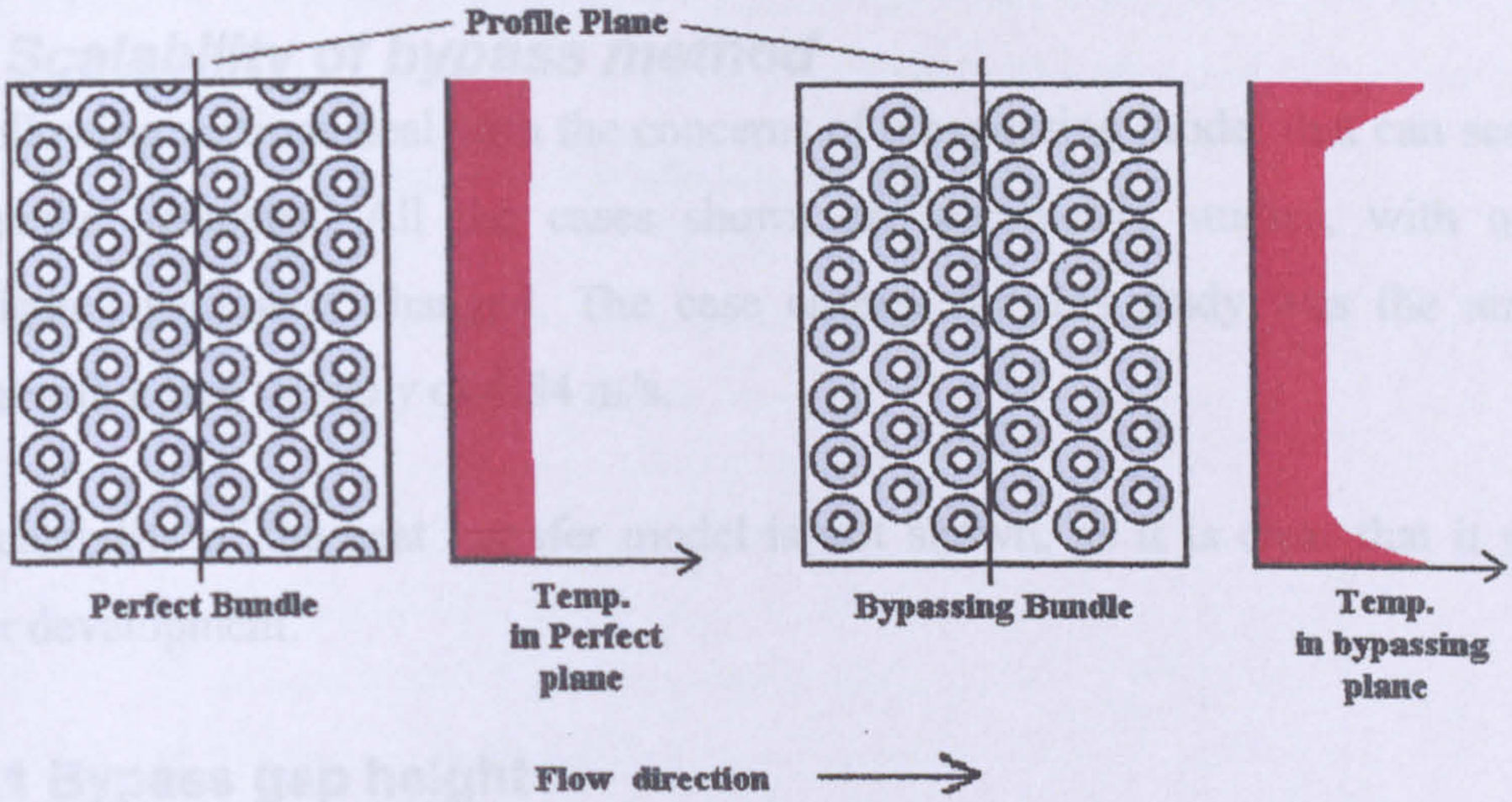

Figure 9.20: Comparison of presumed temperature profile planes
(Heat recovery application)

Therefore the outlet temperature from the bypassing bundle, when averaged using the thermocouple correction noted above, will be closer to the inlet temperature, thus the overall measured heat transfer coefficient (and thus j factor) will be lower than for a similar bundle with no bypassing. The j factor model of Chapter 6 presumes a 'perfect' bundle with no bypass flow, and therefore the straightforward mass split analysis model will overpredict.

It is recommended that any future investigation examines the mass and heat transfer characteristics from the bundle to the bypass lane. Ideally the temperature distribution after each tube row would be known, and from this a heat migration model could be developed to correct the j factor prediction.

9.11.5 Overall Comparison

The above shows that the bypass correction method is necessary, and that while the new standard method is acceptable for both of these bundles the performance is substantially better with the use of the new bypass method. The excellent performance of the air cooler prediction is certainly due in part to the method having been developed from this data, but the HTWT data prediction shows that the model is applicable for other geometries.

It also shows that the heat transfer requires further study to determine a correction for the standard model for the reasons given above in Section 9.11.4.

9.12 Scalability of bypass method

The following sections deal with the concerns of a bypassing model that can scale with the bundle geometry. All the cases shown are parametric studies, with only the investigated parameter changed. The case chosen for this study was the air cooler bundle with a face velocity of 6.84 m/s.

The scalability of the heat transfer model is not shown, as it is clear that it required further development.

9.12.1 Bypass gap height

When the bypass lane height is extended there will be more bypassing flow, and the lower resistance in the bypass region means that there will be more mass leakage from the tube bundle region into the bypass lanes. Hence the mean velocity through the bundle will decrease and the overall pressure drop will reduce. It can be seen in Figure 9.21 that when the bypass lane height is increased, the converged predicted pressure drop decreases. It should be noted that the 'Bundle' and 'Bypass' points overlay, as they are converged, and hence equal. This applies to Figures 9.21 – 9.24.

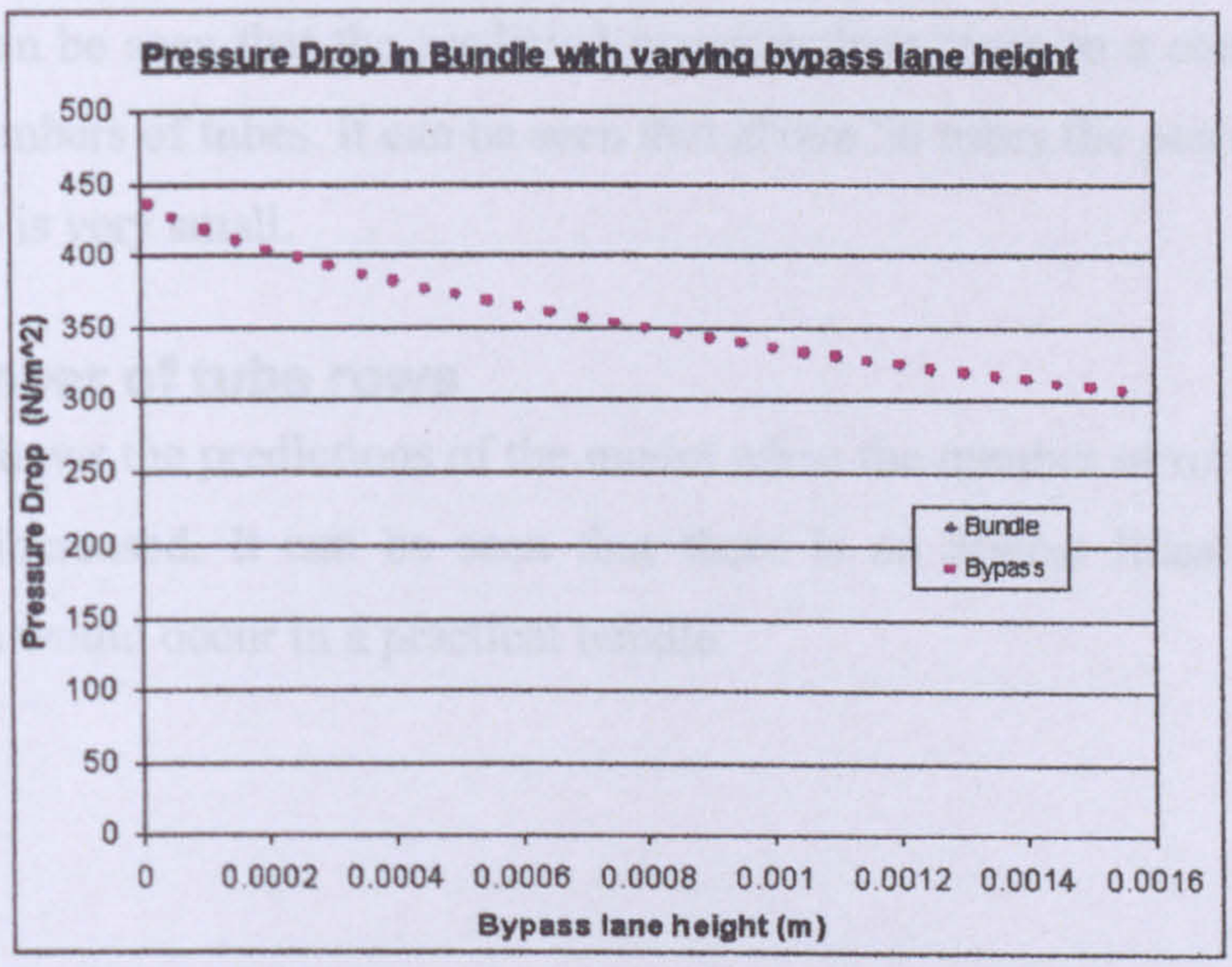

Figure 9.21: Pressure drop with increasing bypass gap height

9.12.2 Number of tubes per row (Duct height)

When the number of tubes per row is increased the effect of the bypassing flow will become less significant. As the number of tubes increases the duct height will increase and the ratio of the bypass lane height to the duct height diminishes. It can be seen in

Figure 9.22 that when the number of tubes per row is increased the converged predicted pressure drop increases, closer to the value predicted by the standard staggered model.

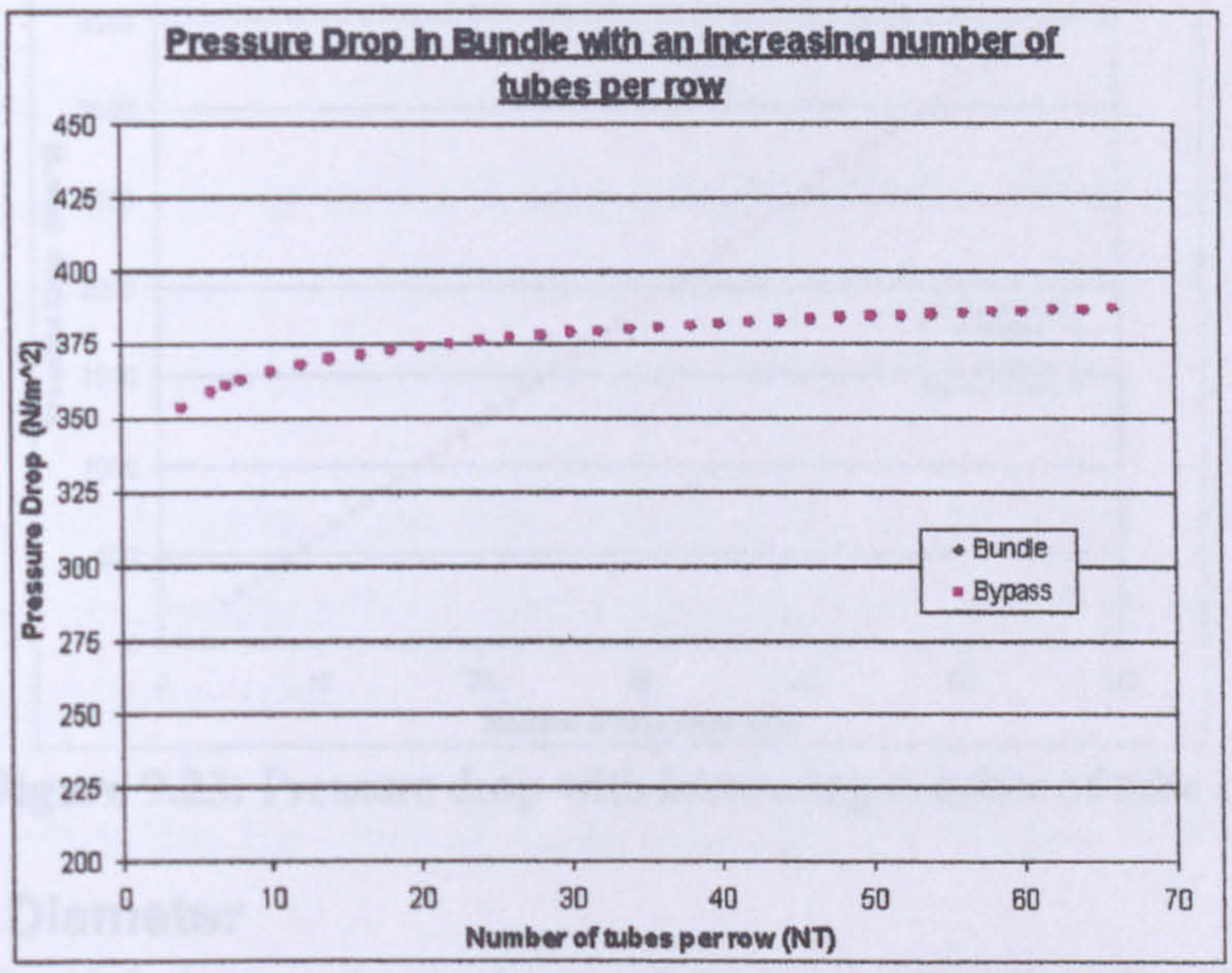

Figure 9.22: Pressure drop with increasing number of tubes per row

Although the processes of bypassing are still occurring, the size of the bundle means that there is a decreased possibility of mass migrating from the centre of the bundle to the bypassing lanes, hence more flow is available to cause drag in the finned tube surfaces. It can be seen that the predicted pressure drop tends to a constant value with increasing numbers of tubes. It can be seen that above 50 tubes the percentage change in pressure drop is very small.

9.12.3 Number of tube rows

Figure 9.23 shows the predictions of the model when the number of tube rows crossed y the flow is increased. It can be seen that there is an almost linear increase in the prediction, as would occur in a practical bundle.

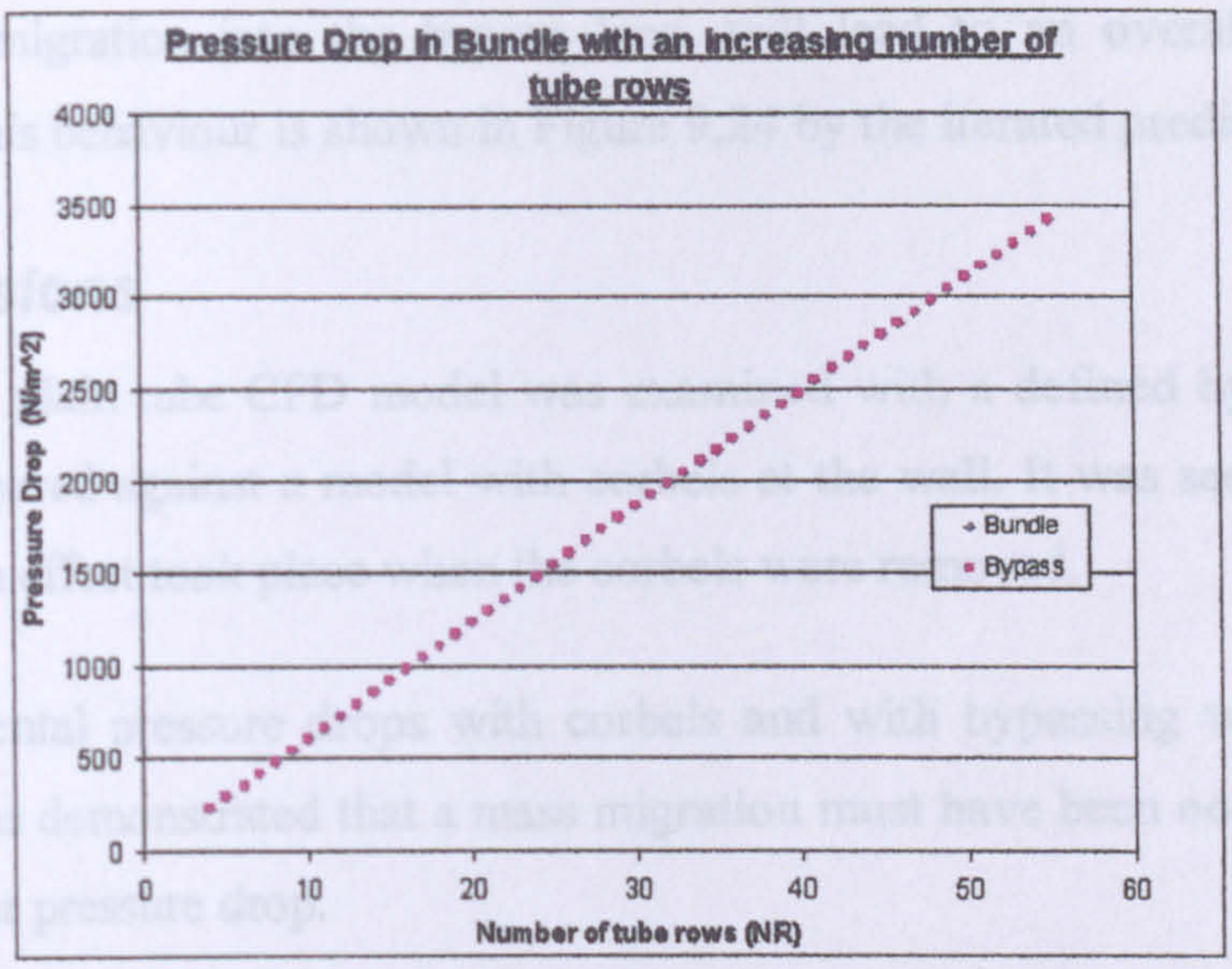

Figure 9.23: Pressure drop with increasing number of tube rows

9.12.4 Fin Diameter

As seen in Equ.9.8 the new bypassing model uses the fin diameter (D_f) as one of its characterising parameters to allow it to scale for varying types of bundles (air coolers, Heat recovery). The fin size affects the extended surface, which typically forms the biggest component of the drag in a finned tube bundle.

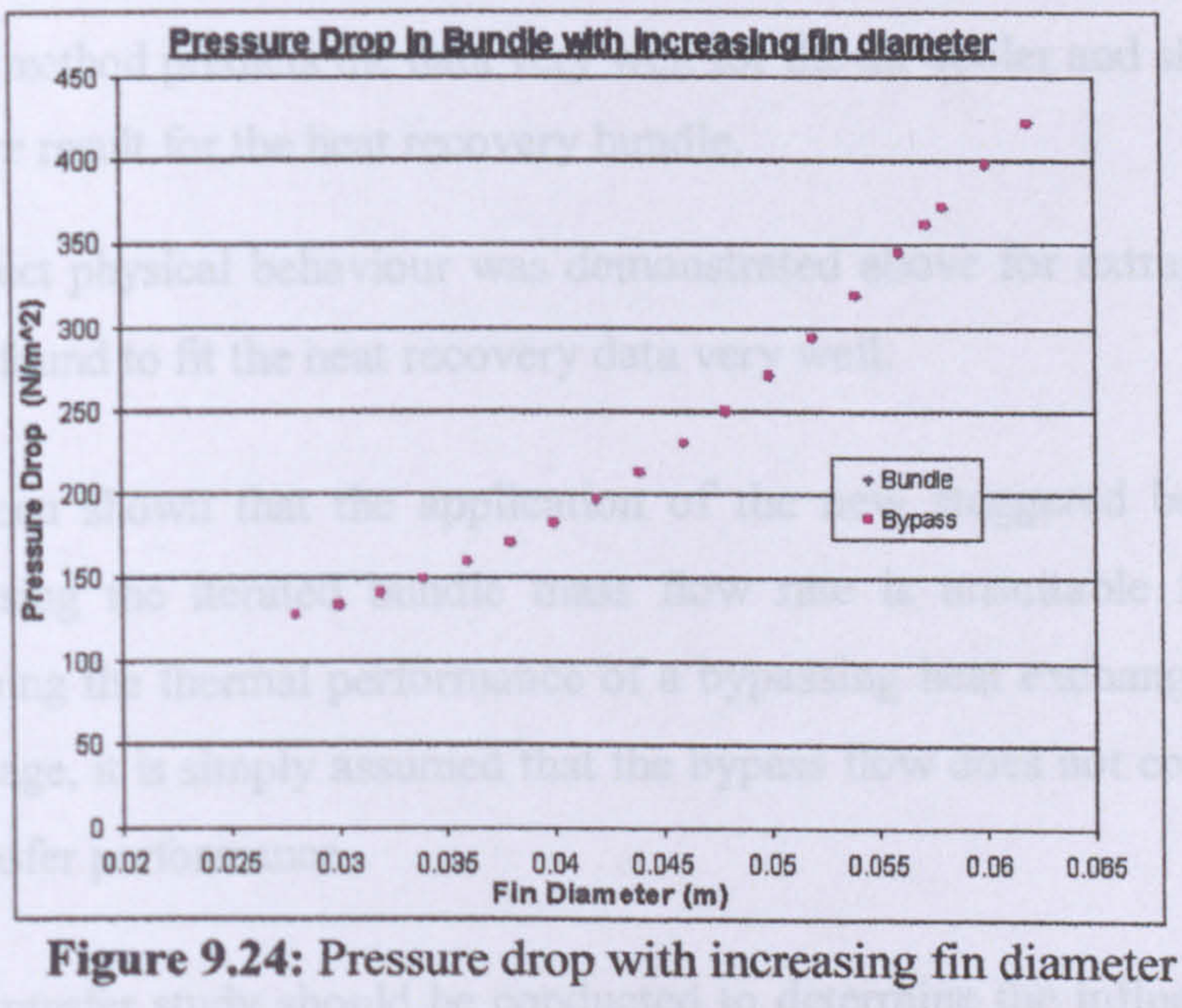

Figure 9.24: Pressure drop with increasing fin diameter

When the fin size is increased for a given pitch arrangement the resistance of the bundle increases, which in turn by the mechanism described in Section 9.6.2 means that more mass will migrate to the bypass lane, increasing the friction in these regions. Cumulatively, the increased resistance and thus pressure drop in the bundle, and the

increased mass migration into the bypass lane, will lead to an overall increase in pressure drop. This behaviour is shown in Figure 9.24 by the iterated predictions.

9.13 Conclusions

- A simple plain tube CFD model was examined with a defined bypassing lane, and compared against a model with corbels at the wall. It was seen that a mass migration effect took place when the corbels were removed.

- Experimental pressure drops with corbels and with bypassing were compared and it was demonstrated that a mass migration must have been occurring to lead to a lower pressure drop.

- It was shown that the level of mass migration increases with increasing flow velocity.

- A new simple method was presented to account for the influence of bypass flow on bundle performance, based on experimental data. This method incorporated a new bypassing component and the staggered bundle model from Chapter 6.

- The new method predicts the data very well for the air cooler and showed a good qualitative result for the heat recovery bundle.

- The correct physical behaviour was demonstrated above for extrapolated cases, and was found to fit the heat recovery data very well.

- It has been shown that the application of the new staggered bundle j factor model using the iterated bundle mass flow rate is unsuitable for accurately determining the thermal performance of a bypassing heat exchanger. Therefore, at this stage, it is simply assumed that the bypass flow does not contribute to the heat transfer performance.

- A heat transfer study should be conducted to determine the influence of bypass on an air-cooler bundle. This would provide data for a j factor correction method in bundles where there is flow bypassing.

- The proposed method is to be incorporated into the HTFS ACOL program in version 6.40, and is considered for inclusion in the next release of the FIHR program.

CHAPTER 10

Modelling the effect of the number of tube rows on heat transfer in inline bundles

10.0 Introduction

This chapter examines the so-called row effect on the heat transfer performance of individual tube rows. The row effect essentially refers to the fact that the heat transfer performance of tubes in subsequent rows in a bundle will be significantly different from that of a single row of tubes, or even the first tube row.

This has two main causes, the most widely quoted is turbulence, but in the reviewed literature little is ever mentioned of its magnitude, or its increase with increasing tube rows. The second factor is temperature difference. A simple example of these concerns would be found in a single pass air-cooler. The elements to this would be as listed below:

1. Cold air approaches the first tube row and is heated. The flow turbulence increases due to encountering the finned tube structure.
2. The heated, more turbulent flow then approaches the second tube row, which has the same tube-side conditions.
3. The thermal effectiveness of the warmed air is slightly decreased. However, the turbulence of the air has increased, so the turbulent thermal transport from the second row's heat transferring surface is increased, compared to that of the first tube.
4. It follows that either temperature variation or turbulence variation will be the controlling effect on what the row-by-row heat transfer variation is. This will be specific to the application.

As discussed in Section 2.5, there have been many studies of the row effect in staggered arrangement bundles, and a few for inline, but both are always hampered by two factors:

- Little credence is paid to the turbulence and its effect on the whole process.
- While conclusions are drawn, no practical prediction method is ever shown.

Also, the efficiency of the fins is often not accounted for in the final calculations, leaving uncertainty about tube duty.

As well as providing data and flow patterns for the inline prediction method described in Chapter 7, the CFD software was also used to provide results for bundles with an extended number of tube rows. This meant that a databank of local and outlet air temperatures, as well as turbulence information, for the four bundles described in

Section 7.1 could be extended, to determine what happens to the heat transfer of each tube row when the number of tubes rows is increased.

This chapter deals specifically with inline arrangement bundles. The approach presented in this chapter could be applied to staggered layout bundles in the future. The chapter will discuss the effects of turbulence both into and within the tube bundle, and then go on to present a new, practical, method of determining the average heat transfer coefficient for each tube row of an exchanger with an inline tube layout. It will be shown that this is done using the heat transfer coefficient predicted using the method in Appendix B and the new inline bundle j factor method given in Chapter 7.

10.1 CFD models

10.1.1 New geometries modelled

This study used the validated three dimensional models presented in Chapter 7 as well as new models created especially for this study.

Given that some researchers report that the heat transfer stabilises with four tube rows whereas some argue for six rows and an occasional few believe it requires eight rows, this spread would allow a reasonable database from which to review the applicability of these beliefs and develop a local heat transfer coefficient correction method. The new geometries are shown in Table 10.1, denoted by the differing number of tube rows.

Bundle	1	3	9
P_t	60	54	60
P_L	60	54	72.7
D_o	25.4	25.4	25.4
D_f	57.2	50.8	50.8
s_f	0.231	0.231	0.231
n_f	433	433	433
Nr	4	8	8
Nr	8	-	-
Nr	10	-	-

Table 10.1: Geometry of new CFD domains for this study (dimensions in mm), with number of row variations tested.

10.1.2 CFD solution scheme

The boundary conditions, solver models and initialisation data were all those as used previously in Chapter 5. Given that the supplied initialisation data was that of the previous models, the CFD output could be scrutinised to determine if the results were those that would be expected. All the pressure drops and overall heat transfer coefficients were compared with the new inline method prediction method given in Chapter 7 and found to be in good agreement.

10.1.3 Boundary conditions

The airside conditions and flow rates for all of these models were the same as for the models in Section 7.1. The tube side conditions were as reported in Section 7.1.

The tube temperature will be shown to be important in the analysis and the final result.

10.2 CFD results

10.2.1 Local temperatures

As CFD records the calculated values of temperature in each of the cells, temperature profiles across the domain could be generated. In inline bundles it is widely believed that the flow, grossly, exists in two distinct streams; the primary stream (immediately around the tubes and fins) and the gap stream (generally between the fin tips, in the transverse direction). To examine this hypothesis planes were set in the CFD models behind the tubes. As shown in Figure 10.1 these planes were placed halfway between the tube centres.

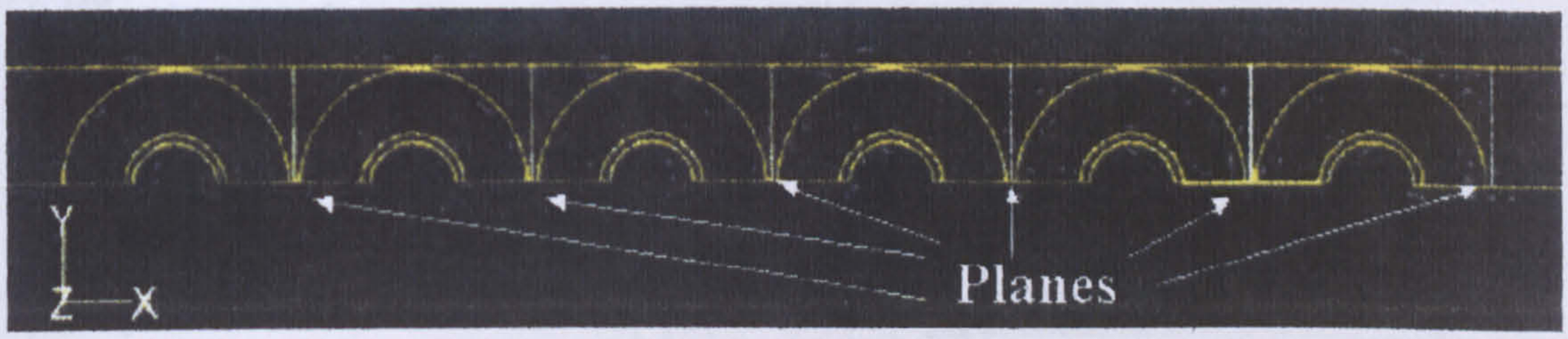

Figure 10.1: Position of planes through bundle for pressure/temperature data

10.2.2 Presentation of row characteristics

All of the temperature profiles are plotted with the temperature on the x-axis and the height from the tube centreline on the y-axis to allow easier understanding with respect to Figure 10.1. It will be seen that for most cases the temperature of the flow in the wake region after the third tube row is near the tube wall temperature.

The overall, mass weighted, turbulence intensity of these planes is also shown. The generation and dissipation of turbulence in a bundle will be shown to be linked to the stability of heat transfer as the row number increases. The percentage turbulence intensity was the chosen parameter for the investigation. This was due to the formulation used in the FLUENT software, as given below, being a measure of intensity with respect to the flow velocity magnitude.

$$I = \frac{\sqrt{\frac{2}{3}k}}{V_{ref}}$$

Where k is the turbulent kinetic energy (m^2/s^2), as calculated locally by FLUENT, and V_{ref} is a reference velocity (m/s), which is the mean velocity magnitude of the flow.

For brevity the results of the bundles based on Bundle 1 and Bundle 4 are shown in full. The models based on Bundles 3 and 9 showed the same patterns as those based on Bundle 1, but, as will be shown, the larger fin spacing of Bundle 4 lead to different characteristics.

10.2.3 CFD results for bundle 1

10.2.3.1 Temperature profiles

Figures 10.2, 10.3, 10.4, and 10.5 show the temperature profiles of the 4, 6, 8 and 10 row configurations of Bundle 1.

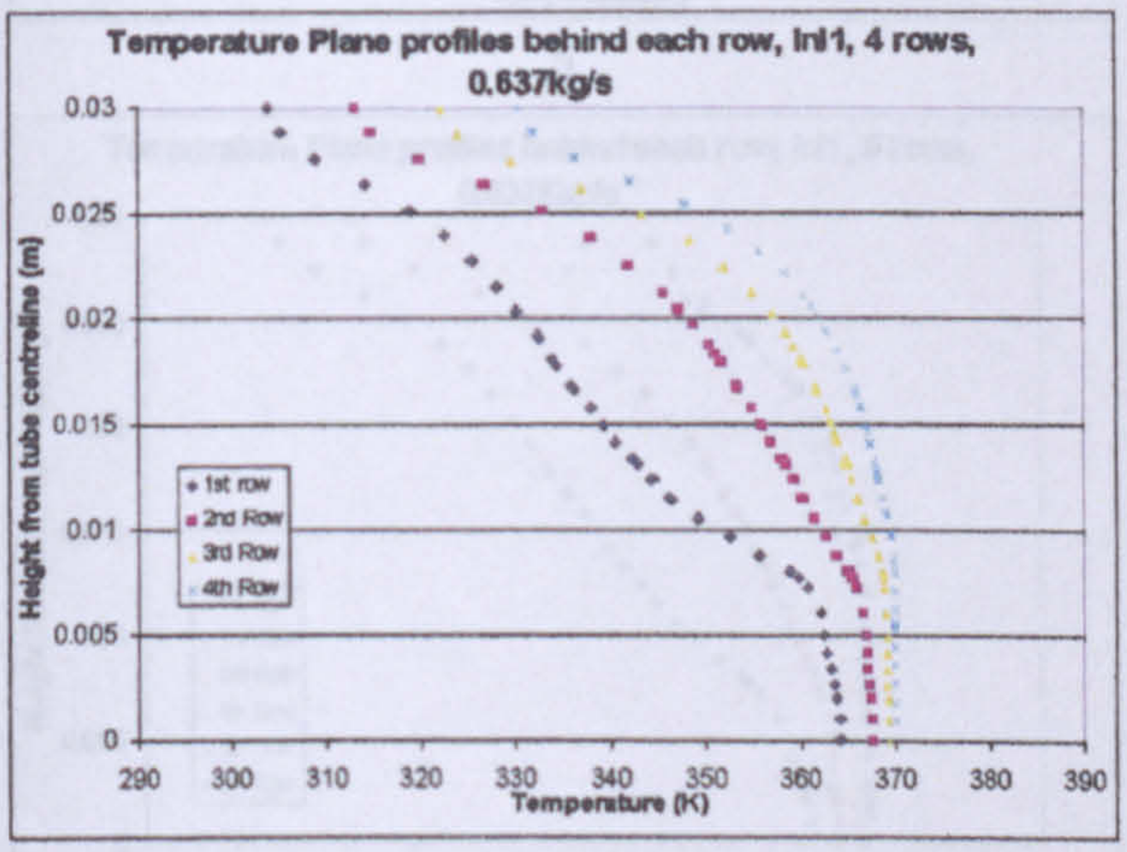

a

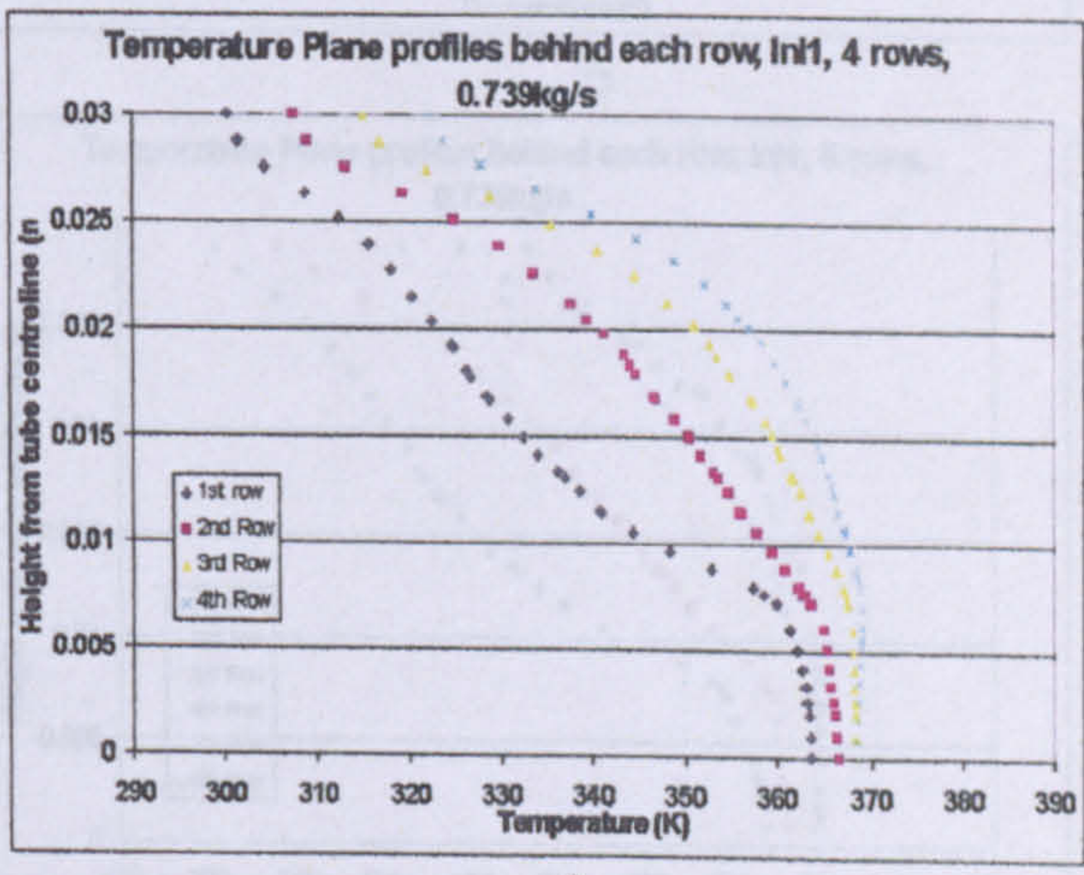

b

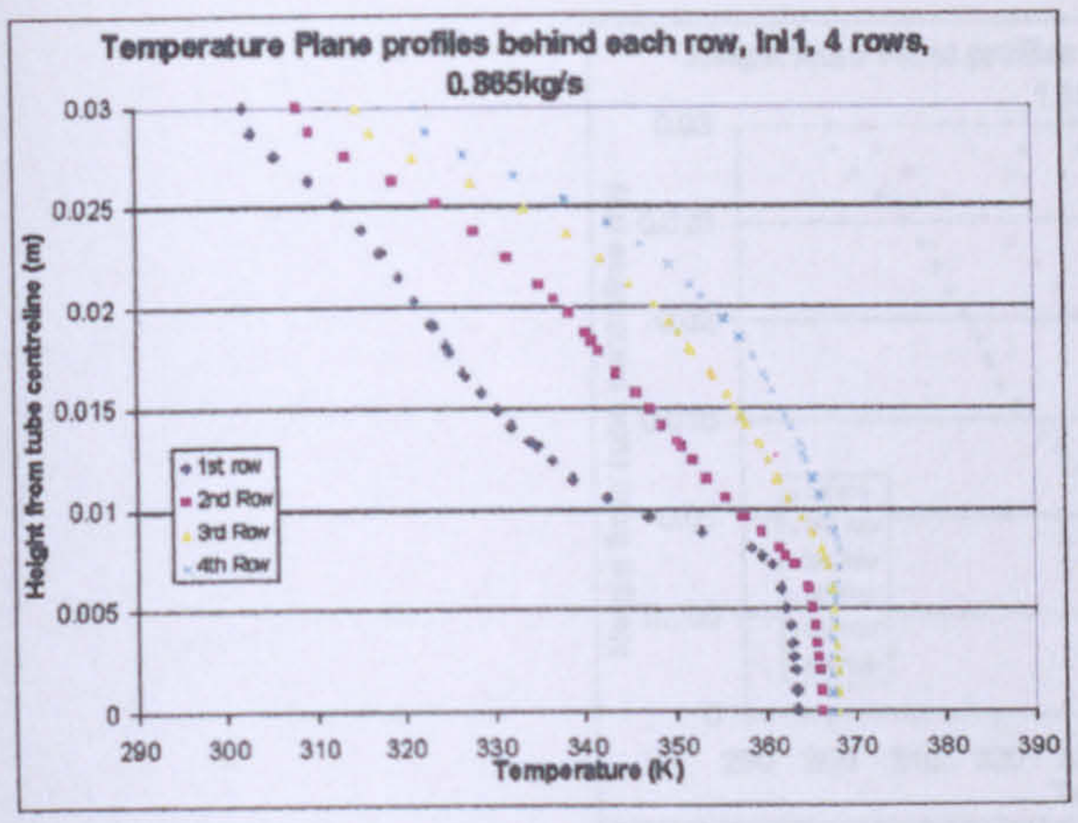

c

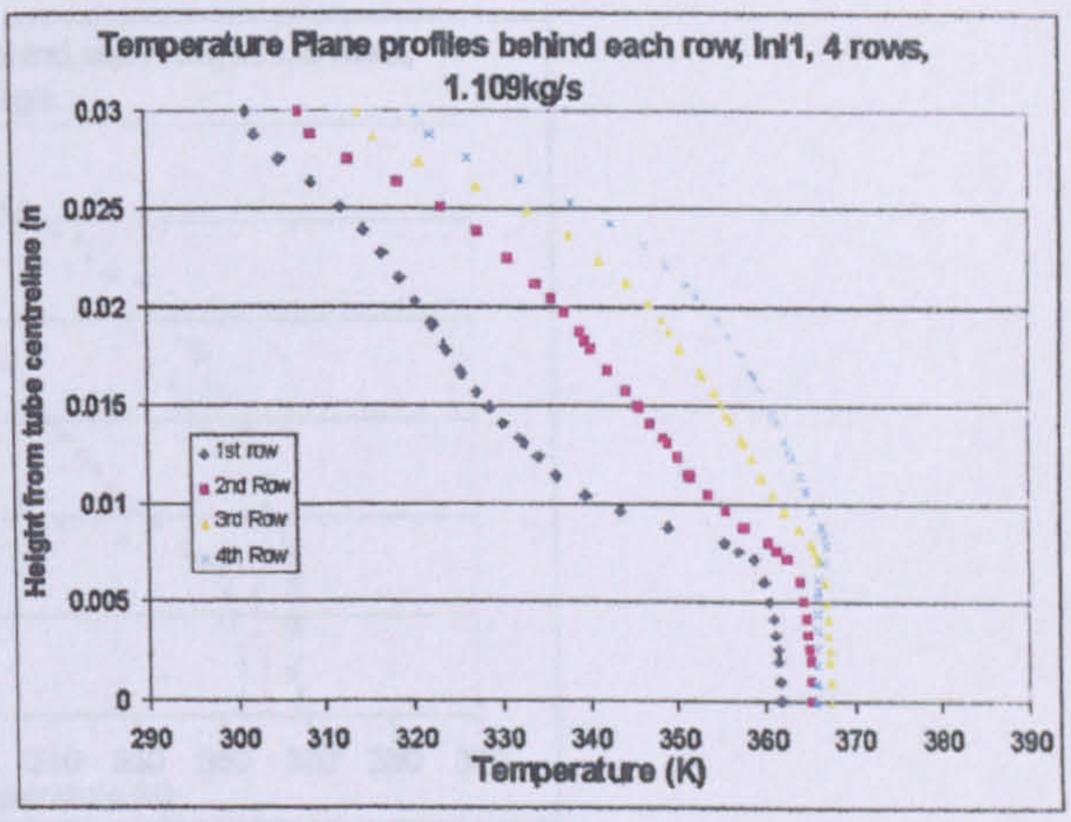

d

Figure 10.2a, b, c, and d: Temperature Profiles on planes of Bundle 1 with 4 rows with varying flow rate

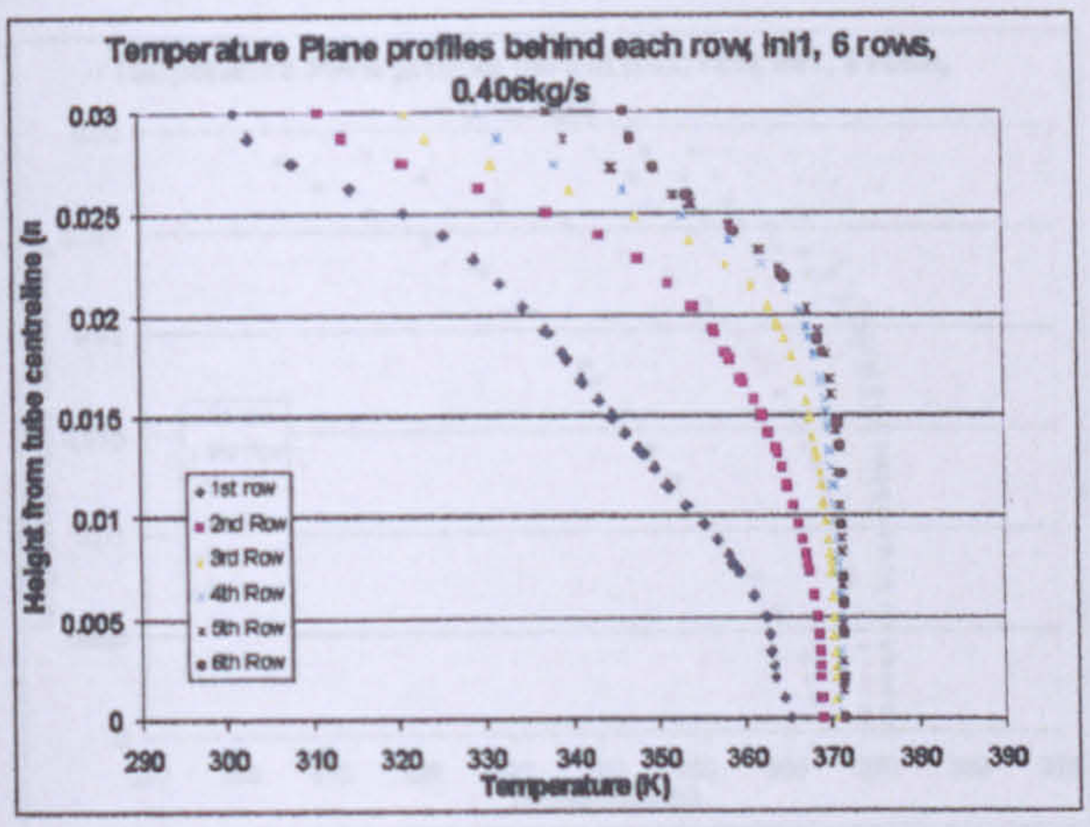

a

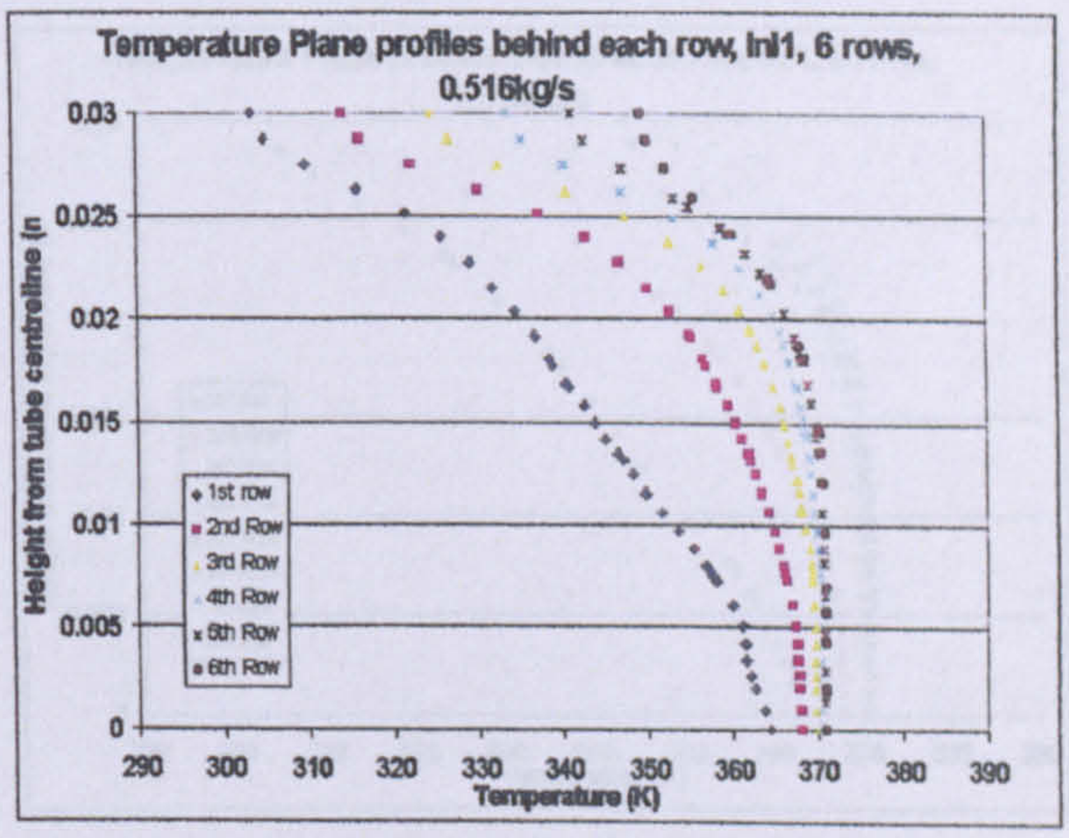

b

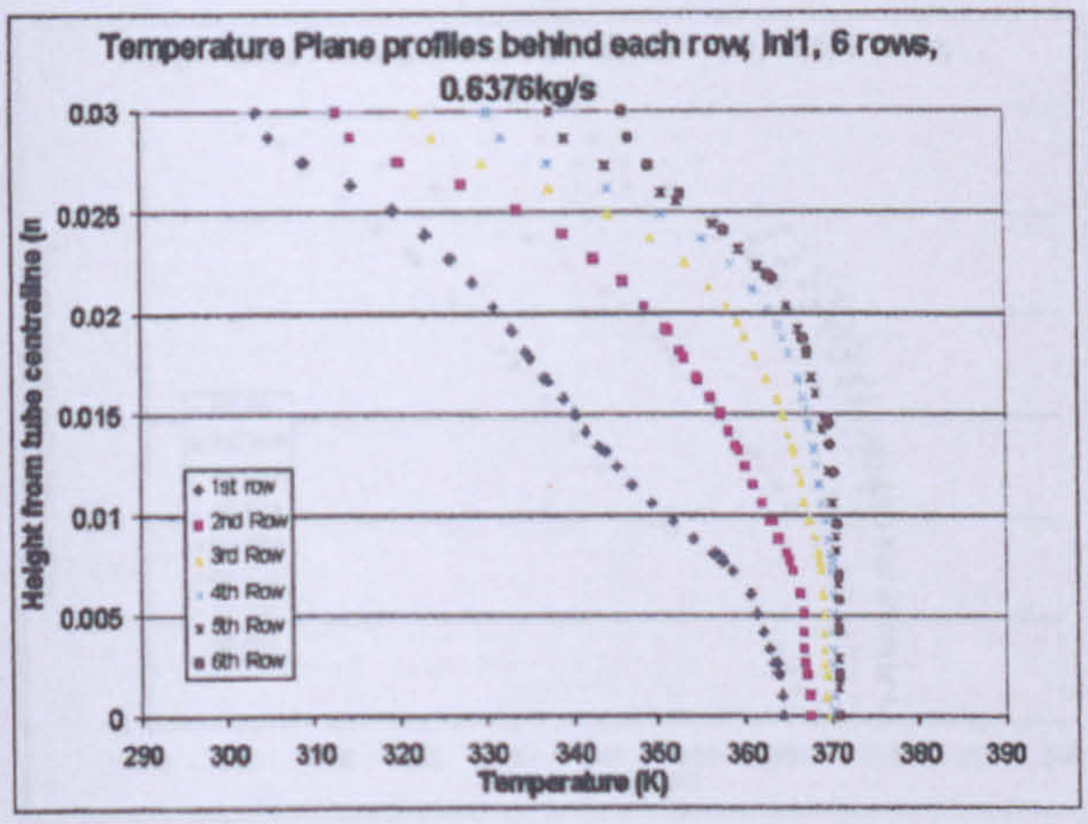

c

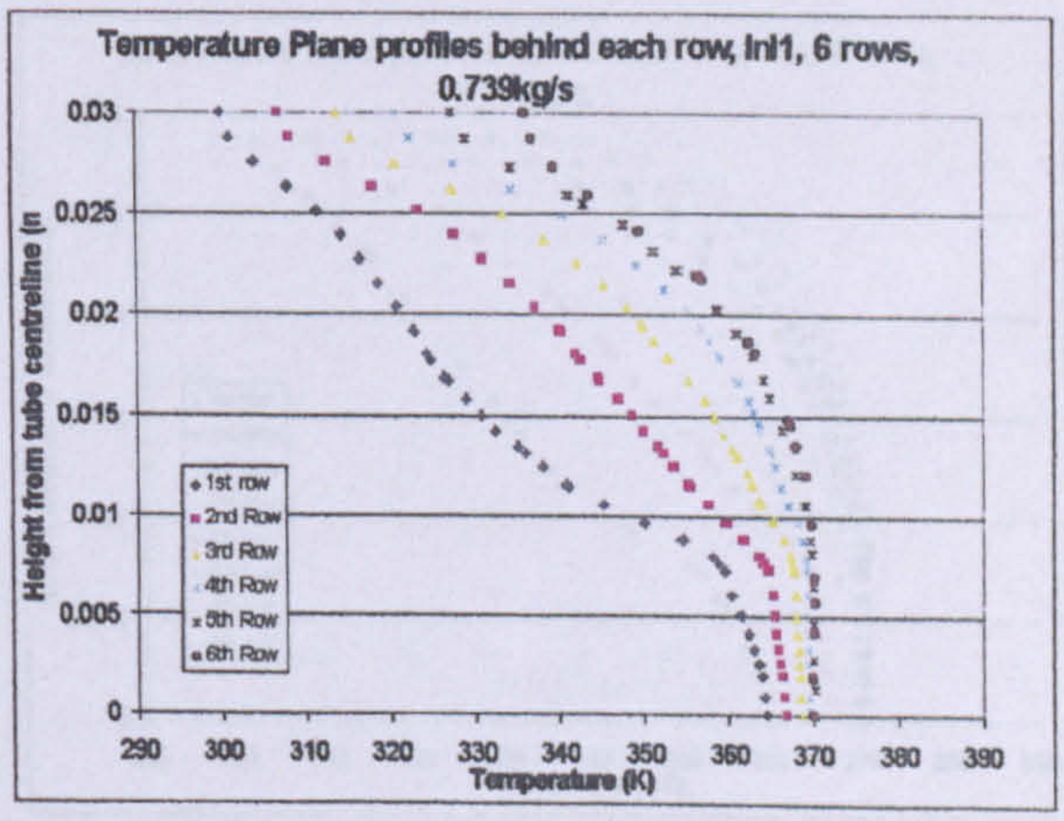

d

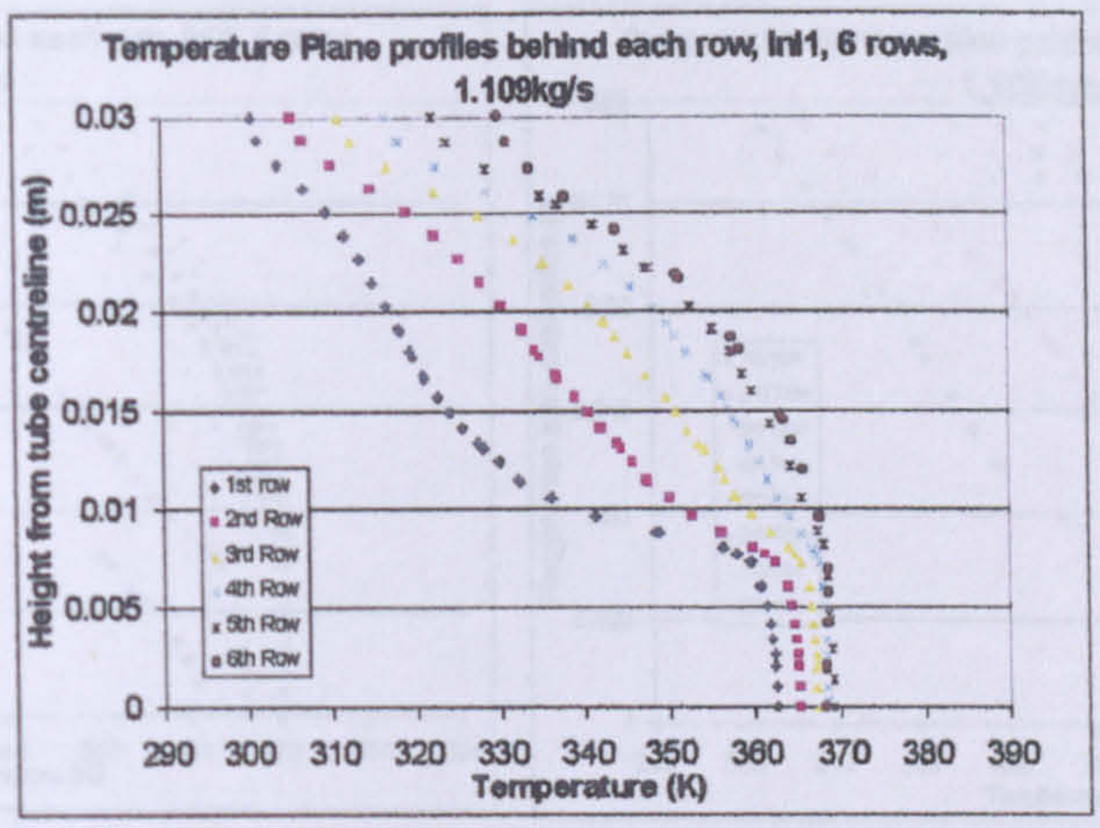

e

Figure 10.3a, b, c, d and e: Temperature Profiles on planes of Bundle 1 with 6 rows with varying flow rate

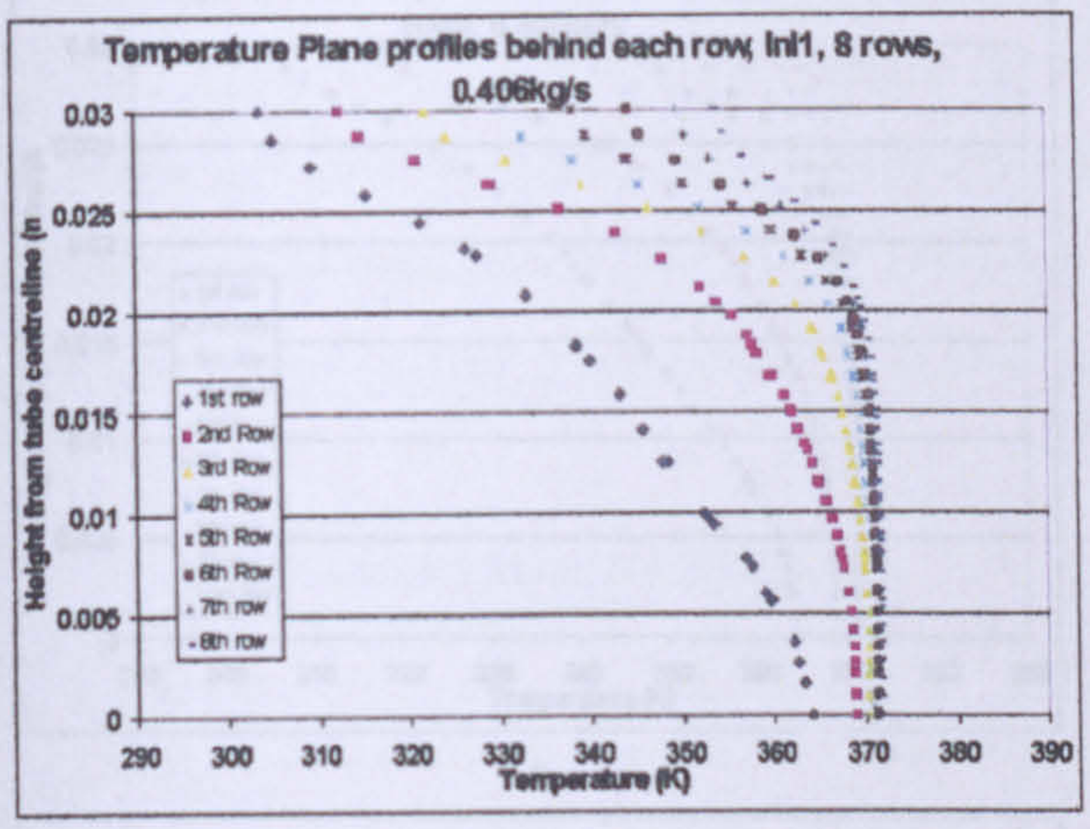

a

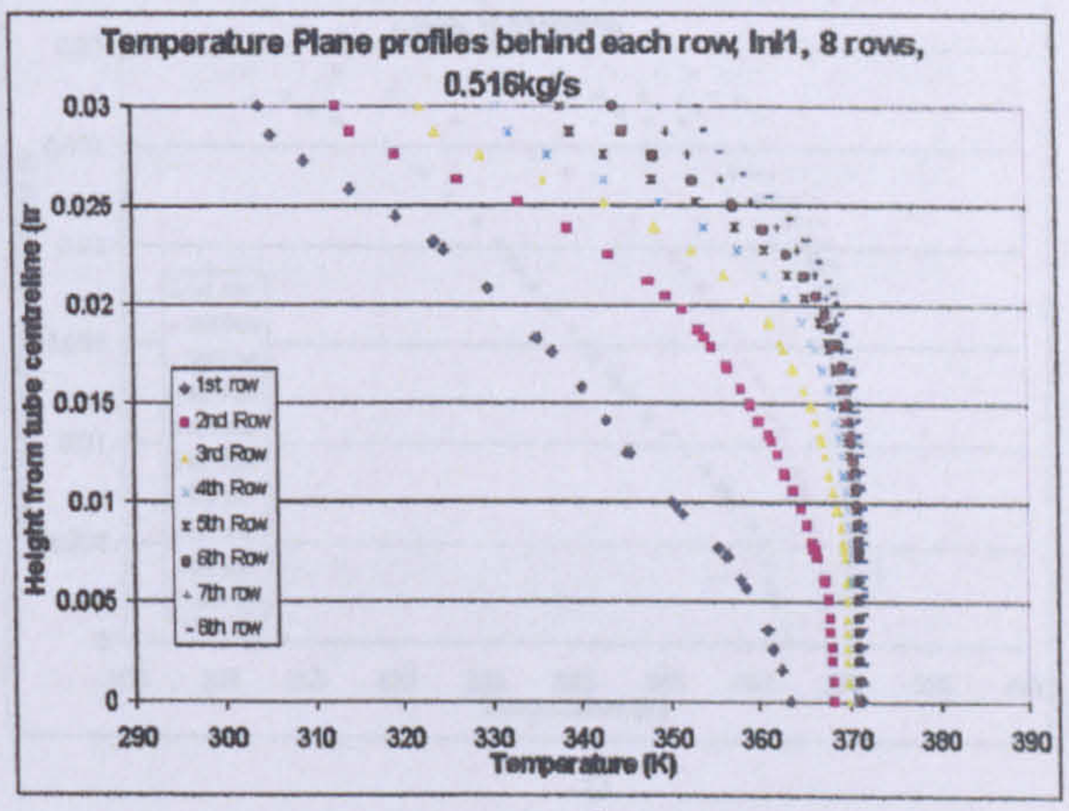

b

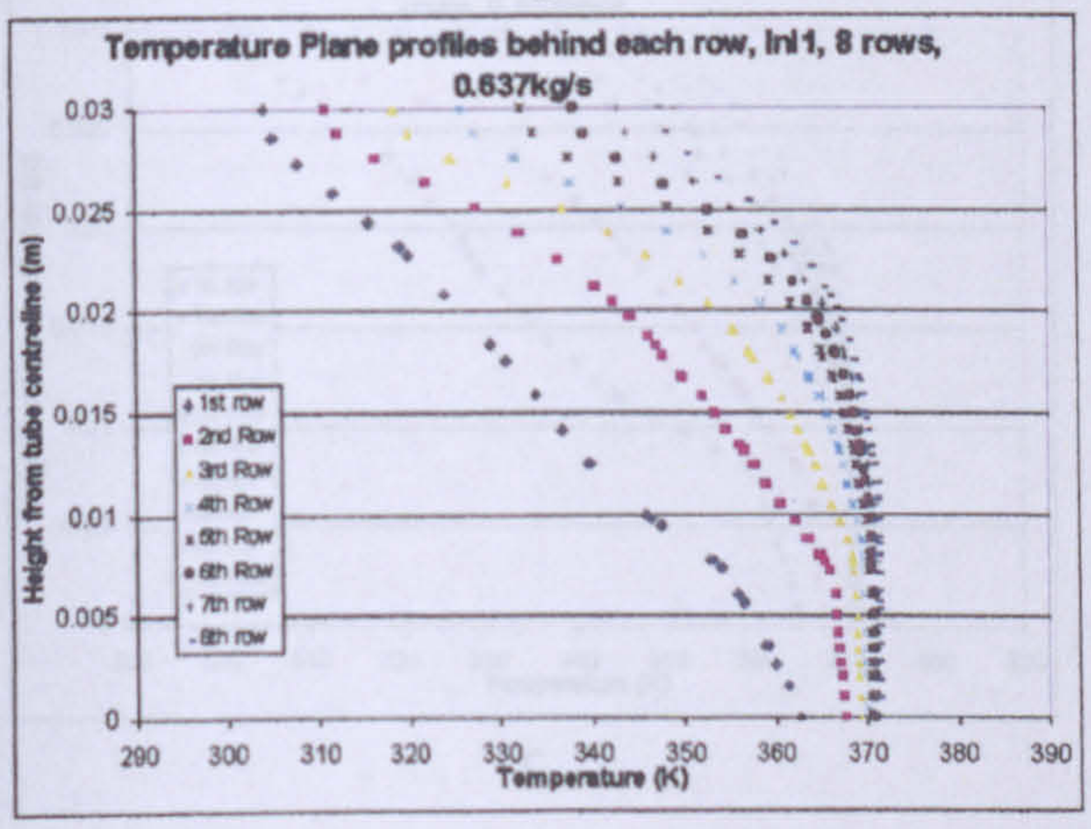

c

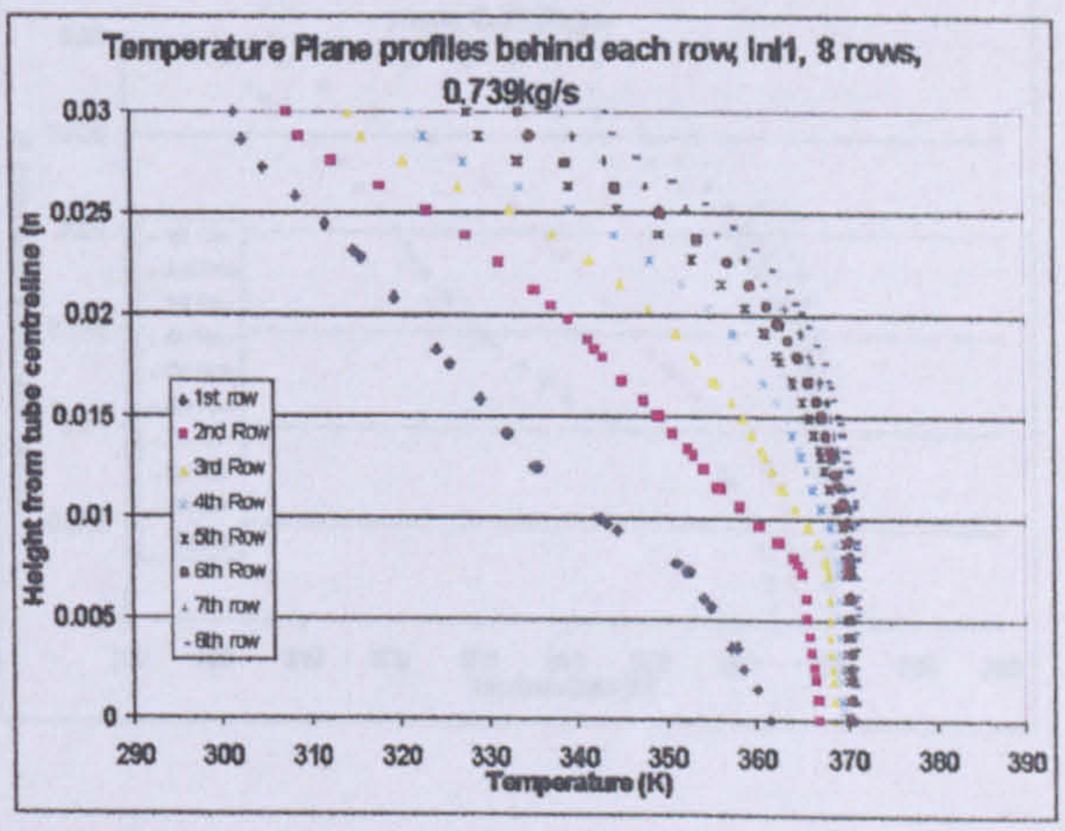

d

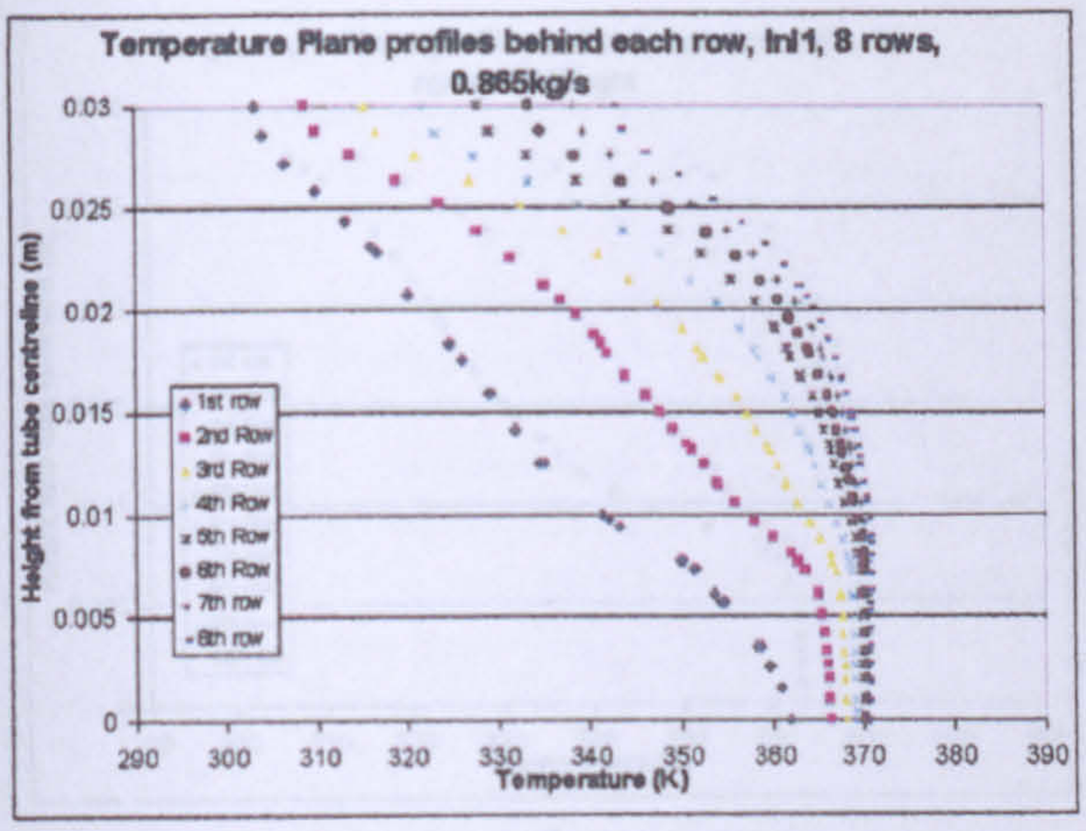

e

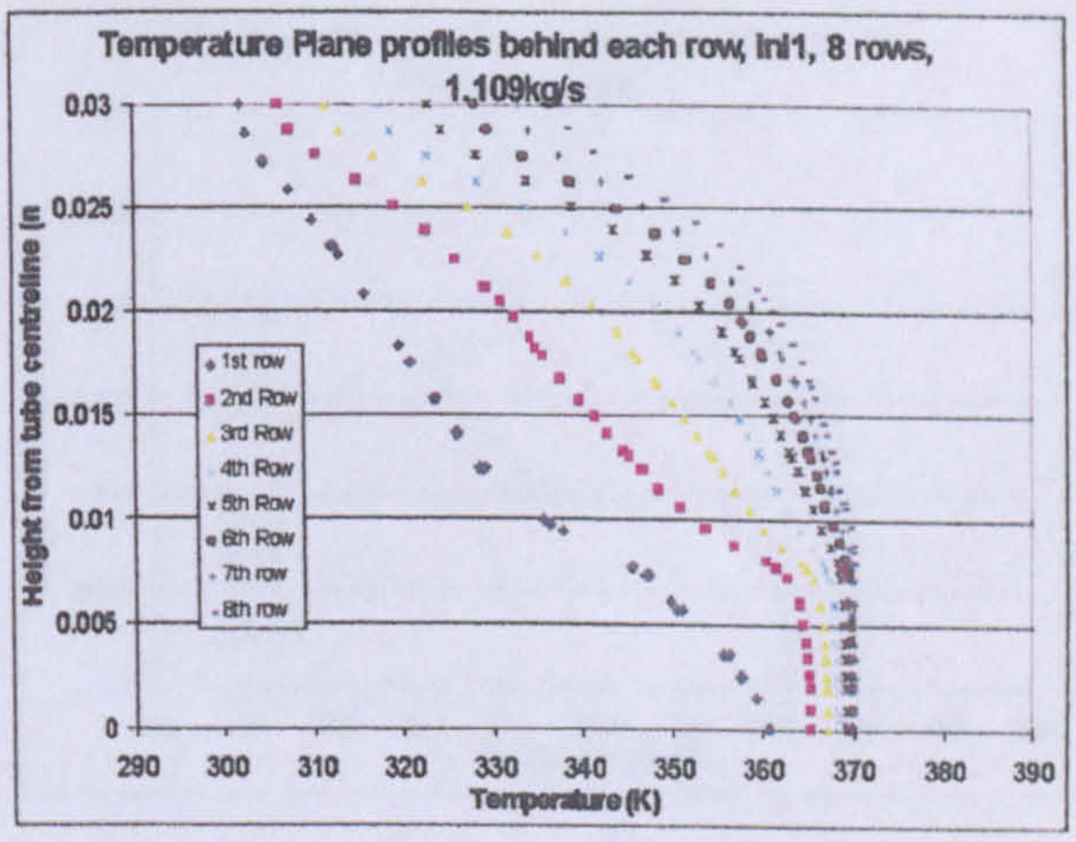

f

Figure 10.4a, b, c and d: Temperature Profiles on planes of Bundle 1 with 8 rows with varying flow rate

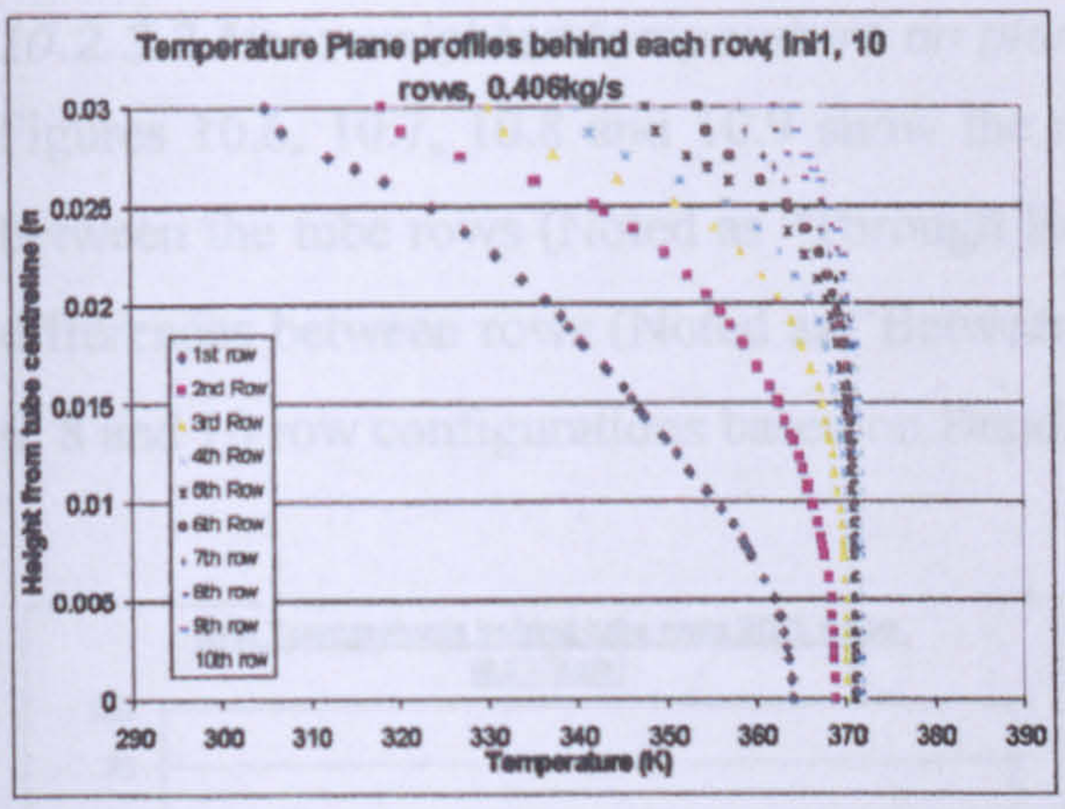

a

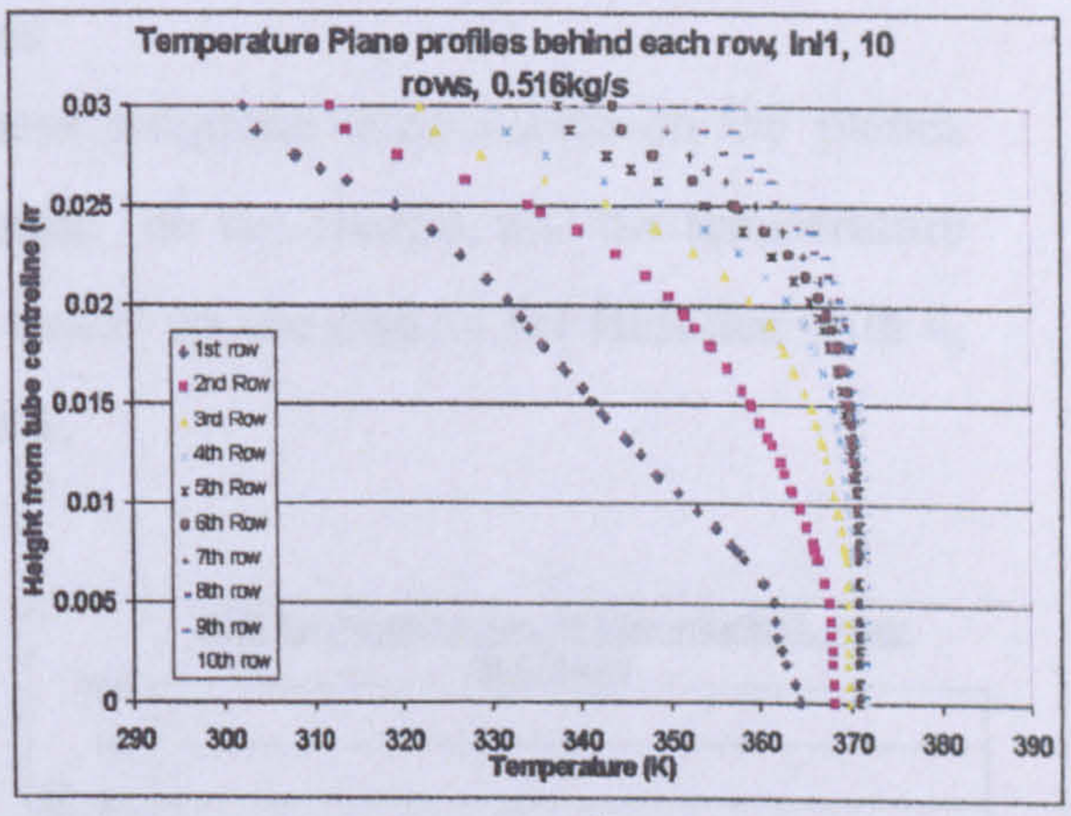

b

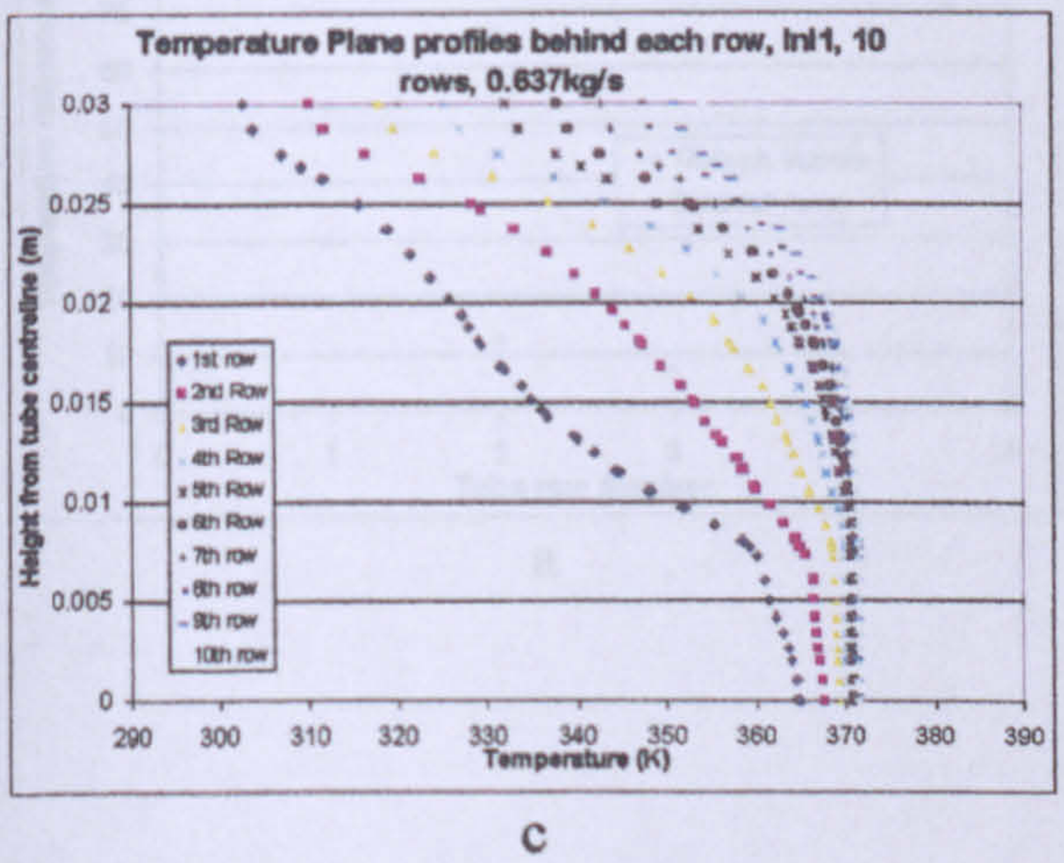

c

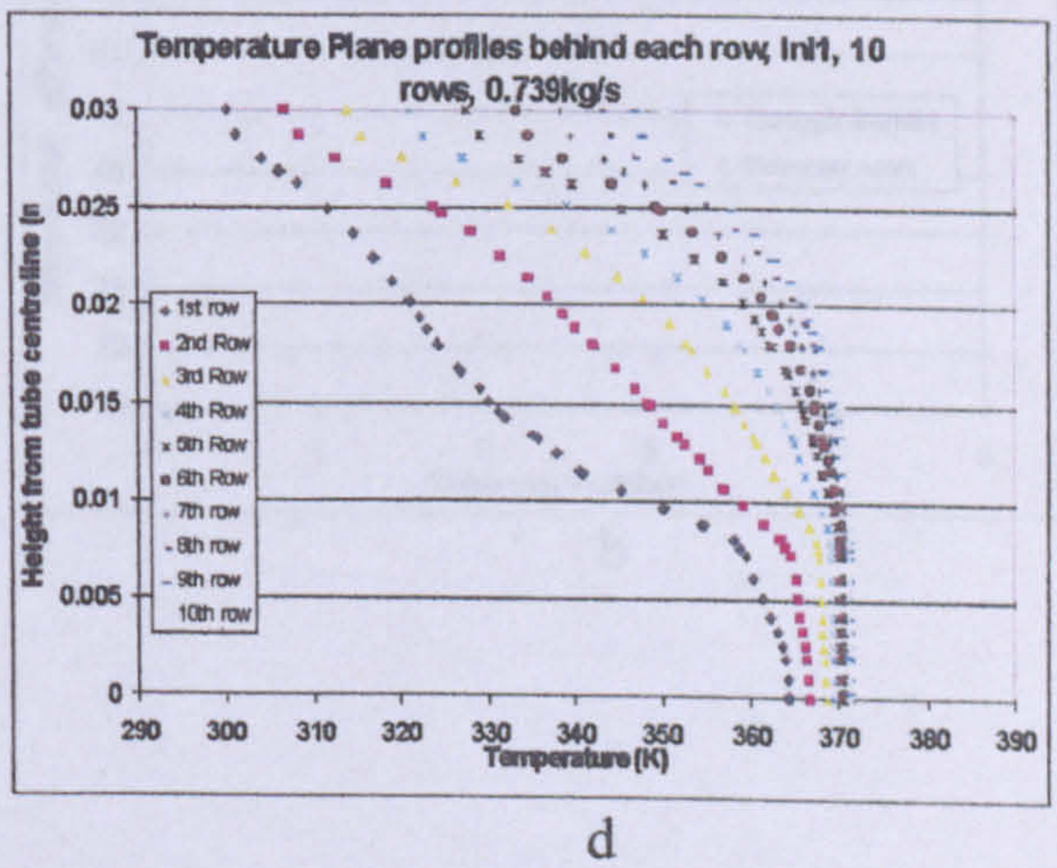

d

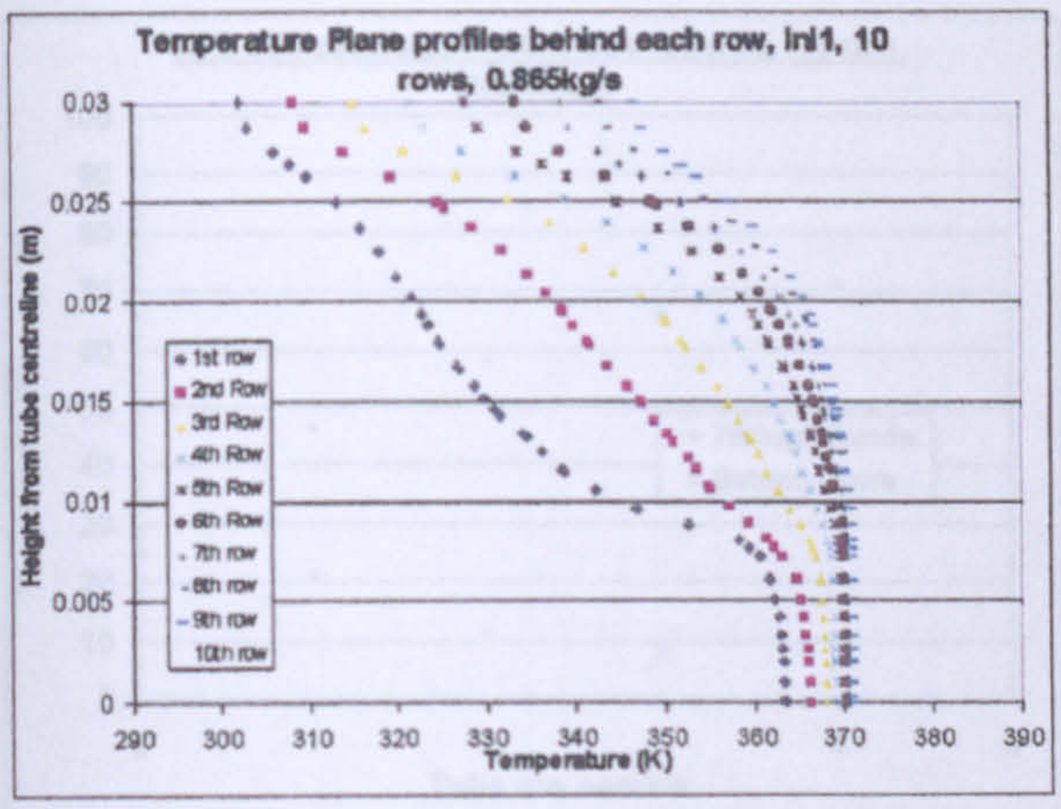

e

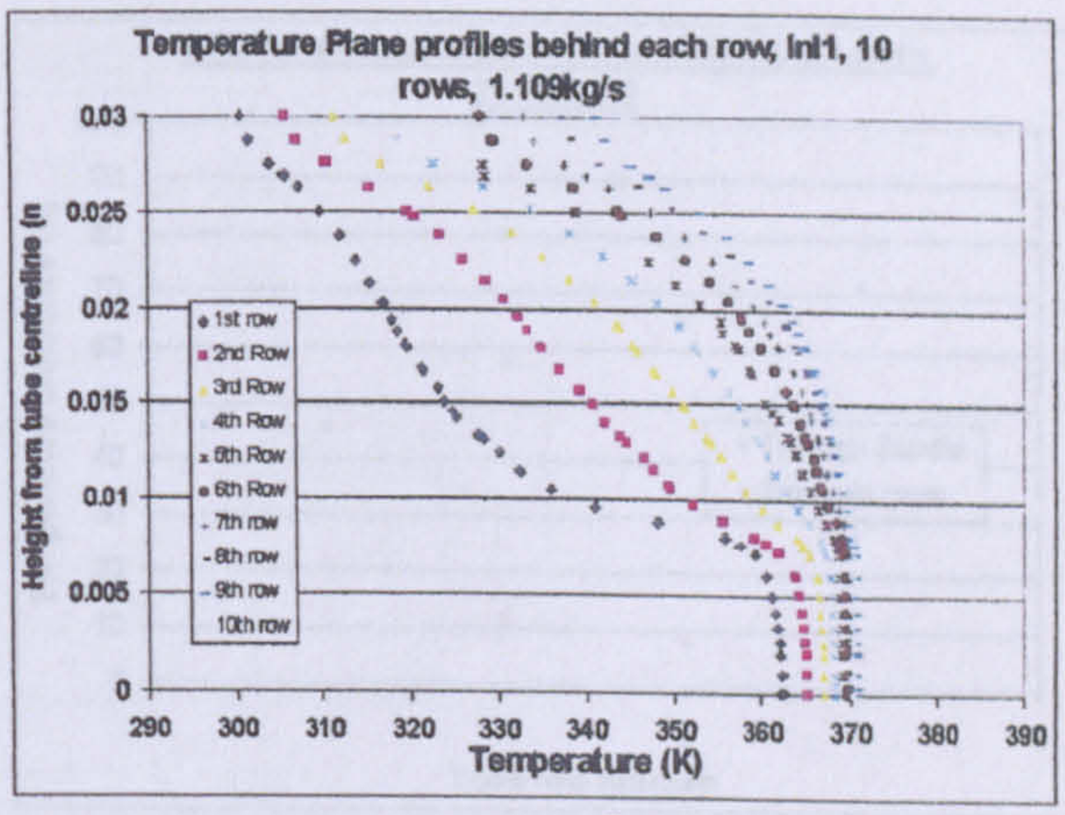

f

Figure 10.5a, b, c, d, e and f: Temperature Profiles on planes of Bundle 1 with 10 rows with varying flow rate

10.2.3.2 Mass weighted temperature on planes

Figures 10.6, 10.7, 10.8 and 10.9 show the mass weighted temperature on the planes between the tube rows (Noted as "Through Bundle" on the charts), and the temperature differences between rows (Noted as "Between rows" on the charts) for Bundles with 4, 6, 8 and 10 row configurations based on Bundle 1.

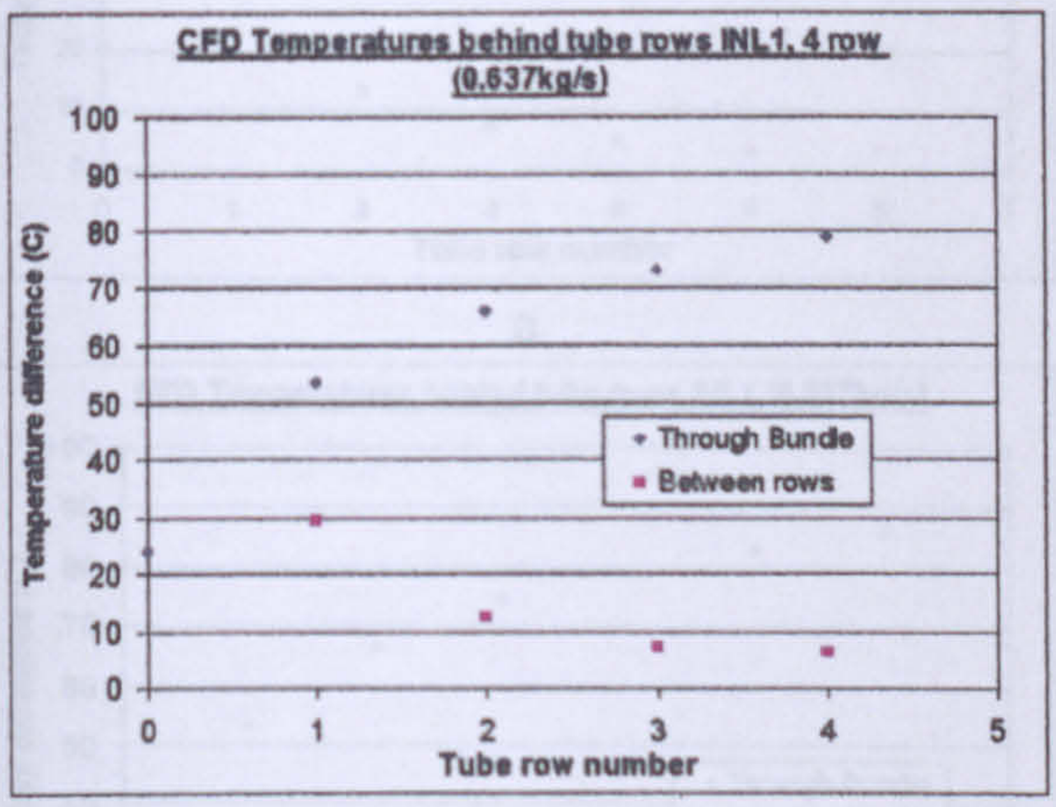

a

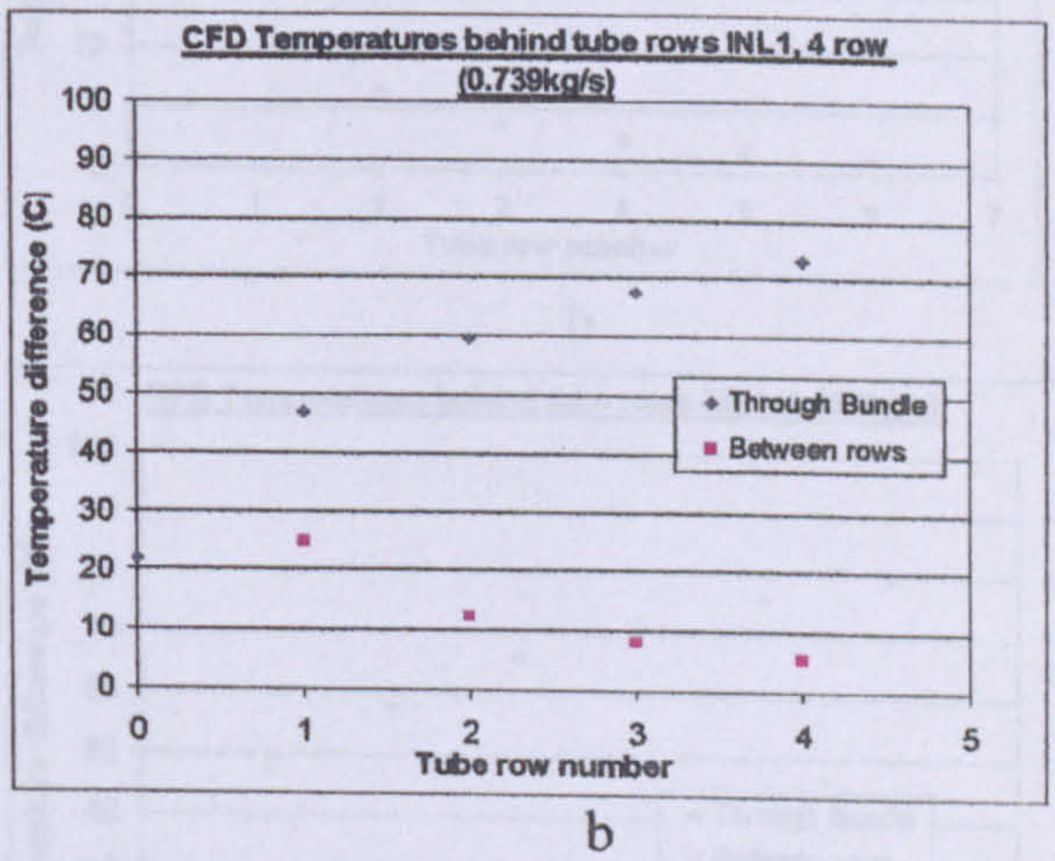

b

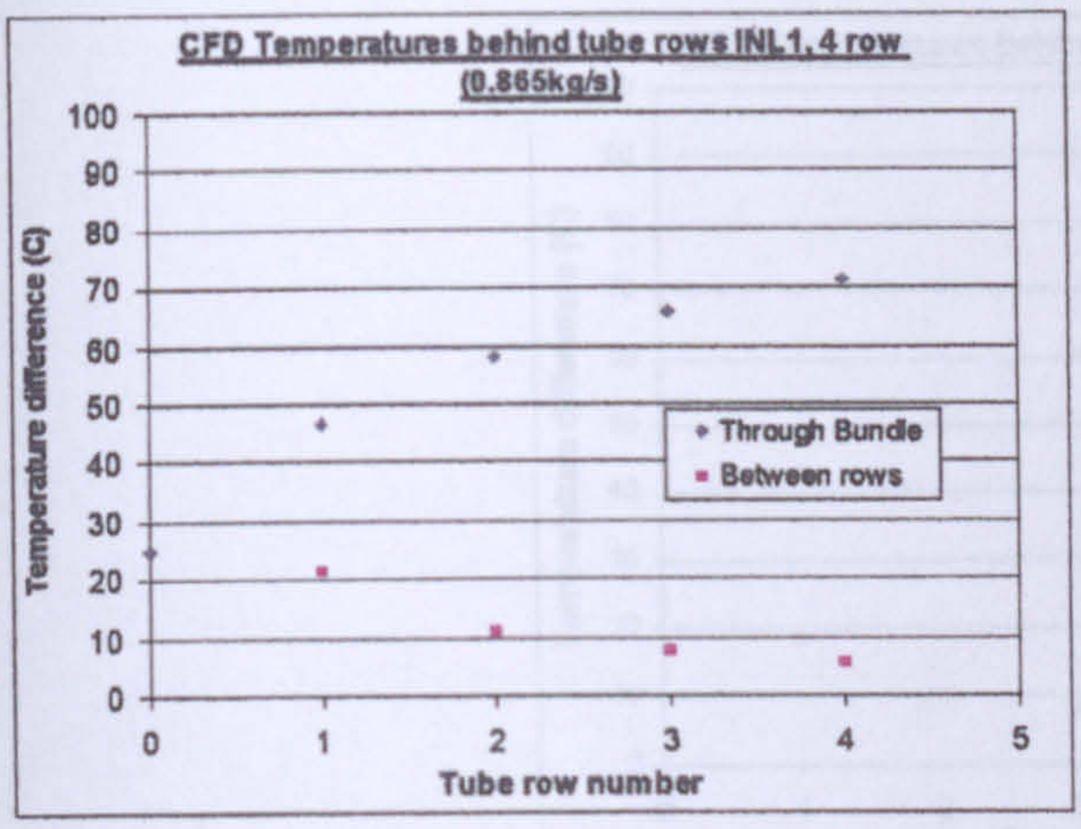

c

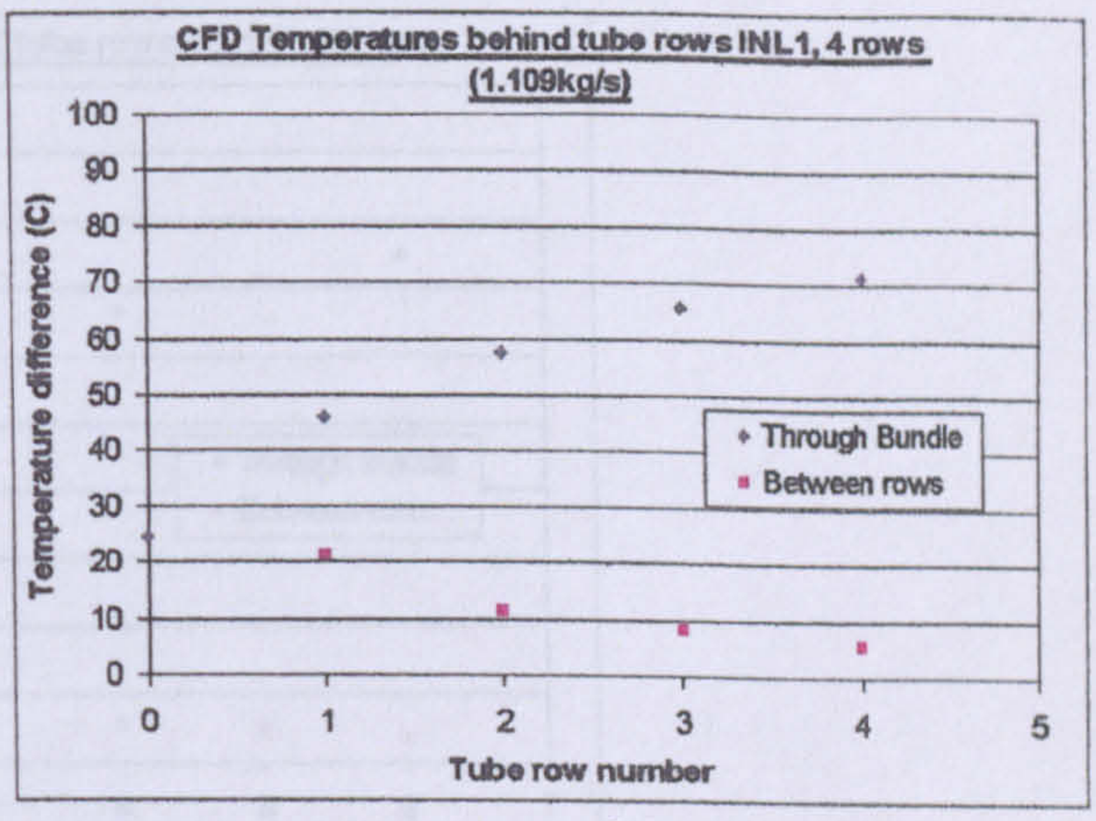

d

Figure 10.6a, b, c and d: Mass averaged plane temperature and temperature difference between tube rows for Bundle 1, 4 rows.

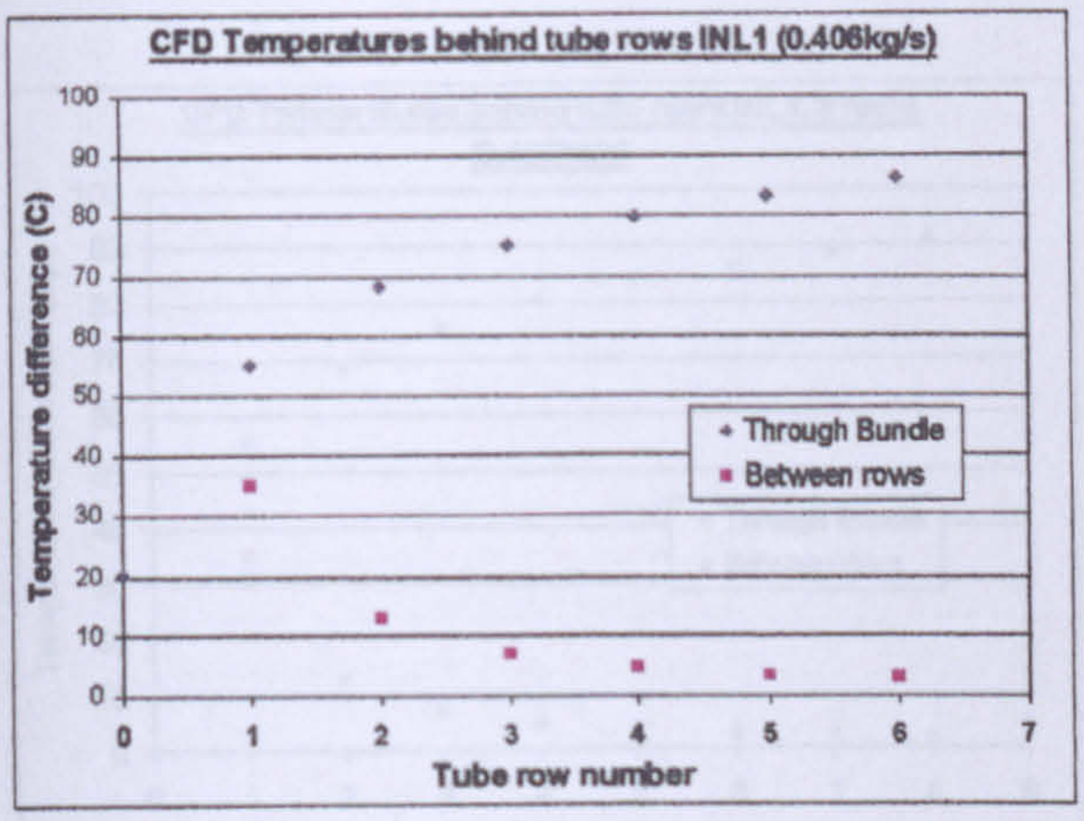

a

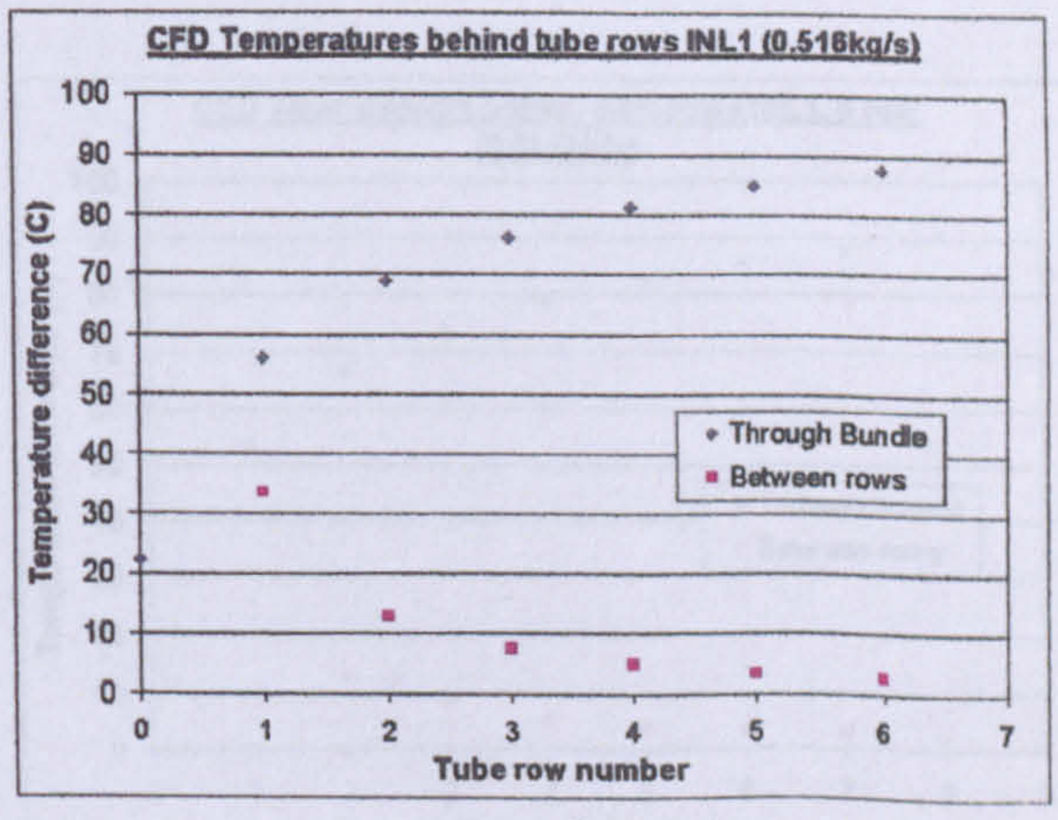

b

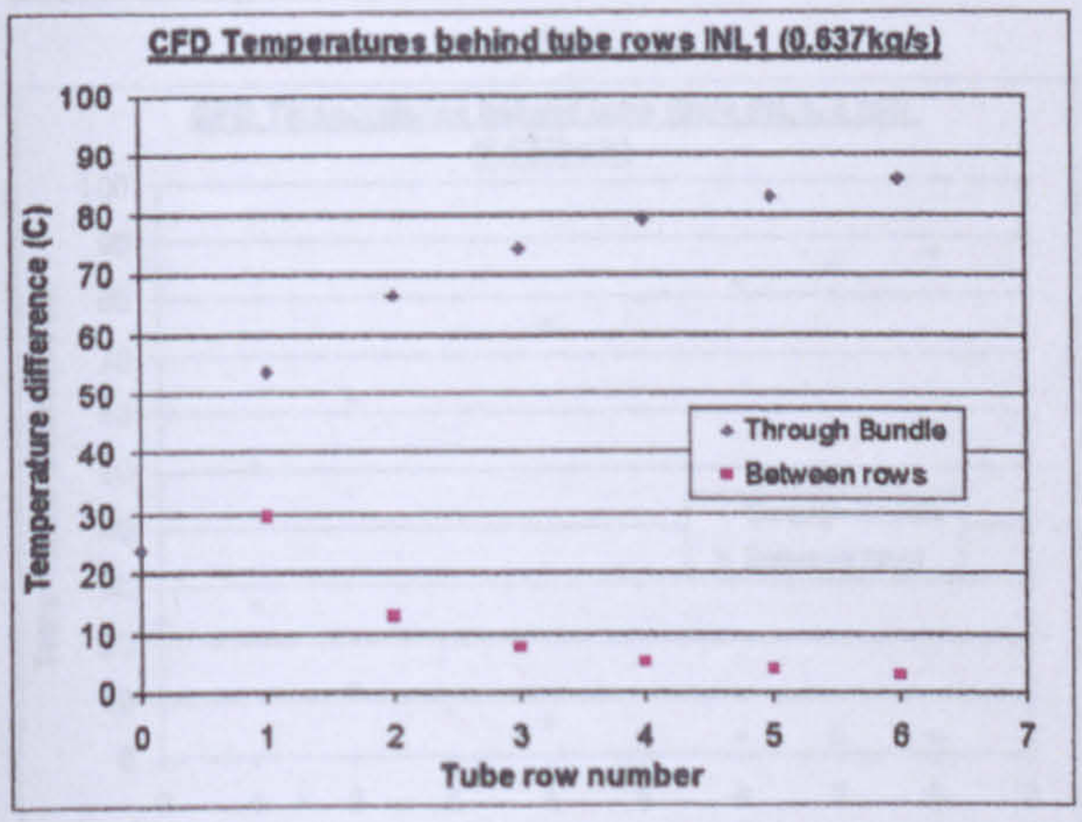

c

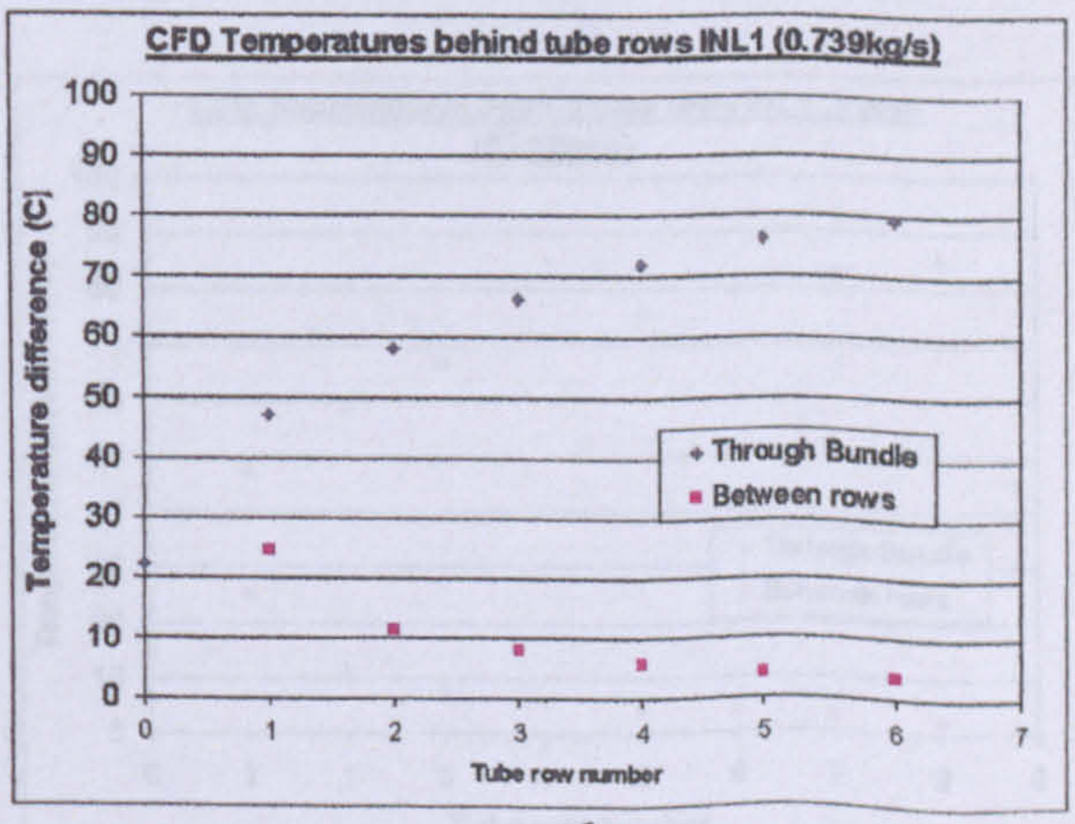

d

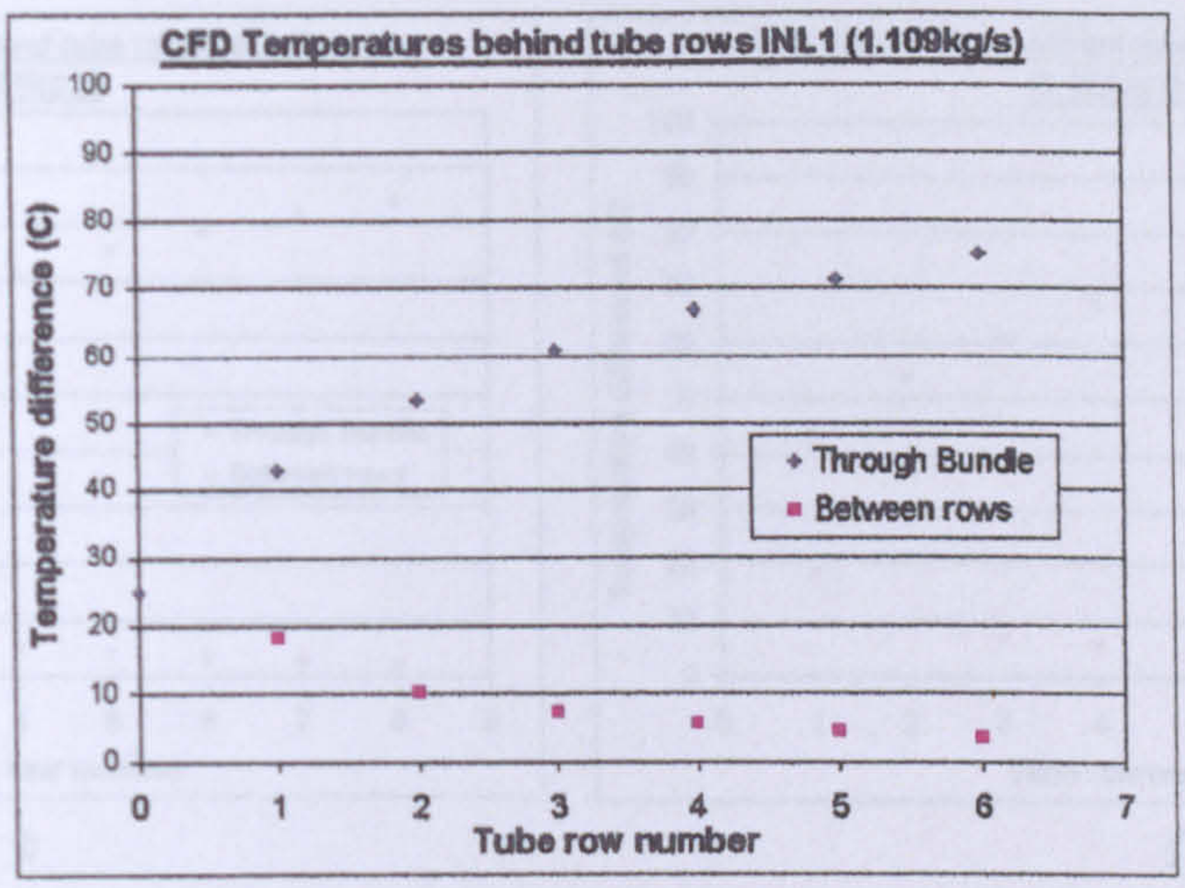

e

Figure 10.7a, b, c, d, and e: Mass averaged plane temperature and temperature difference between tube rows for Bundle 1, 6 rows.

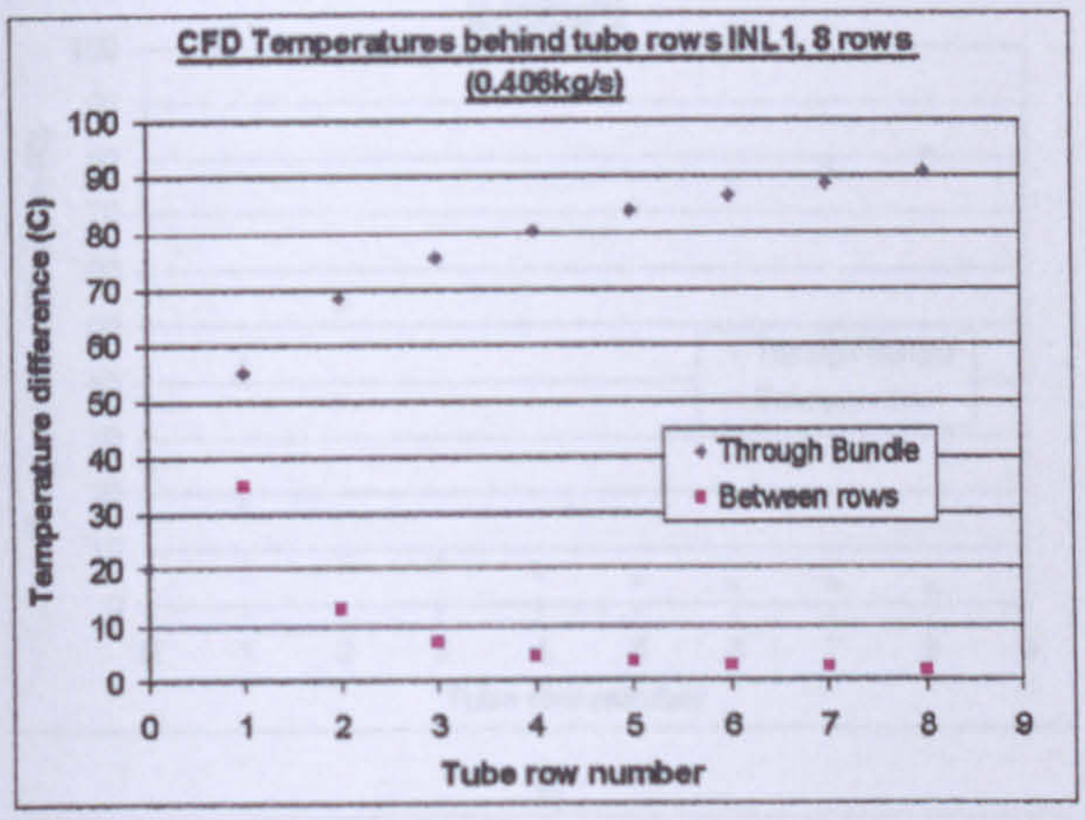

a

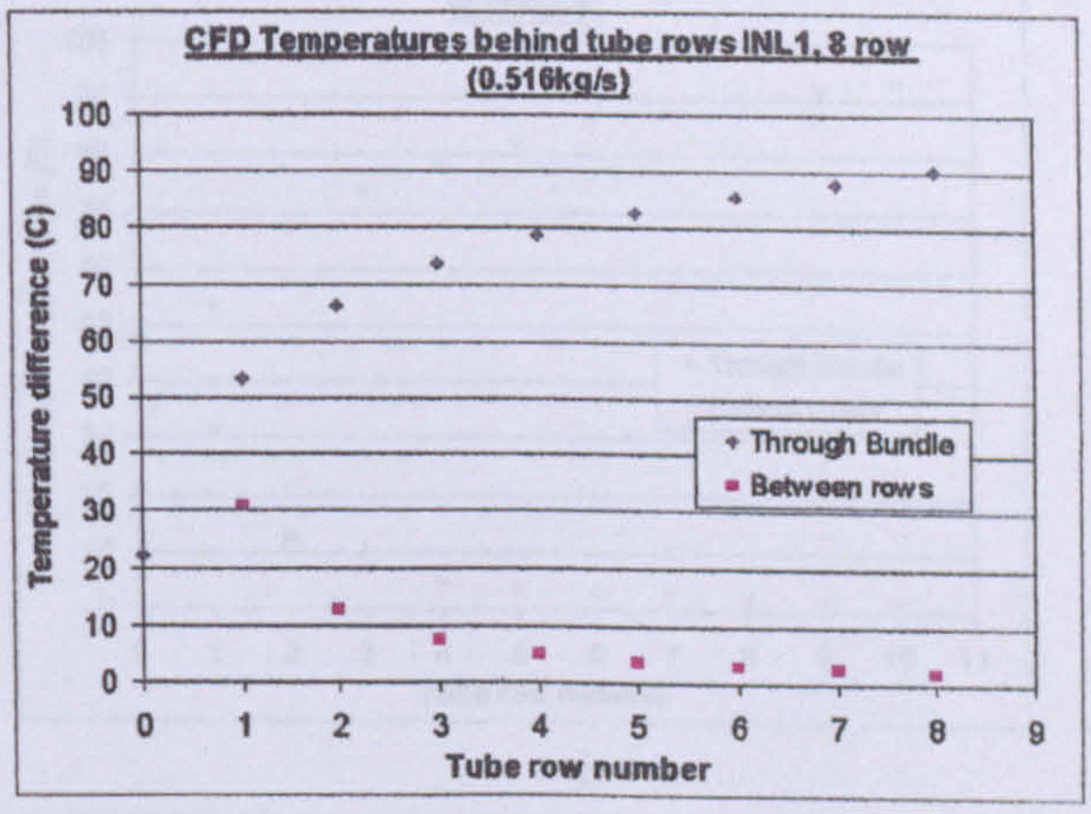

b

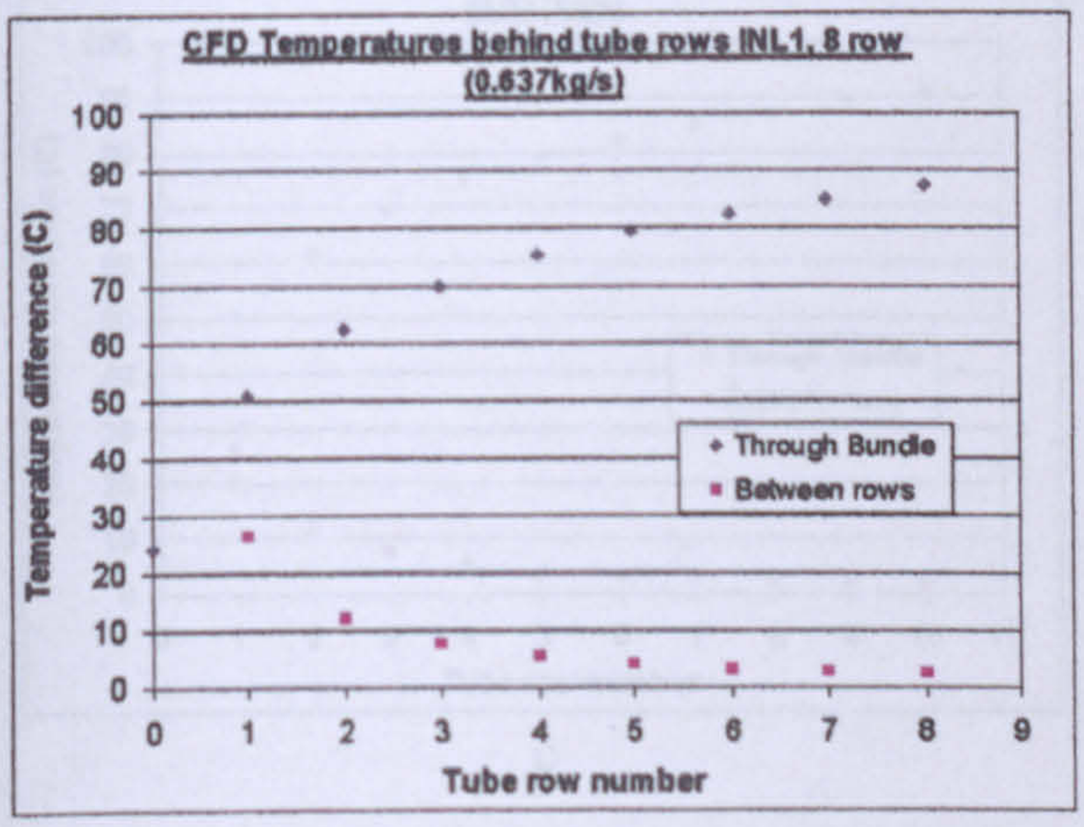

c

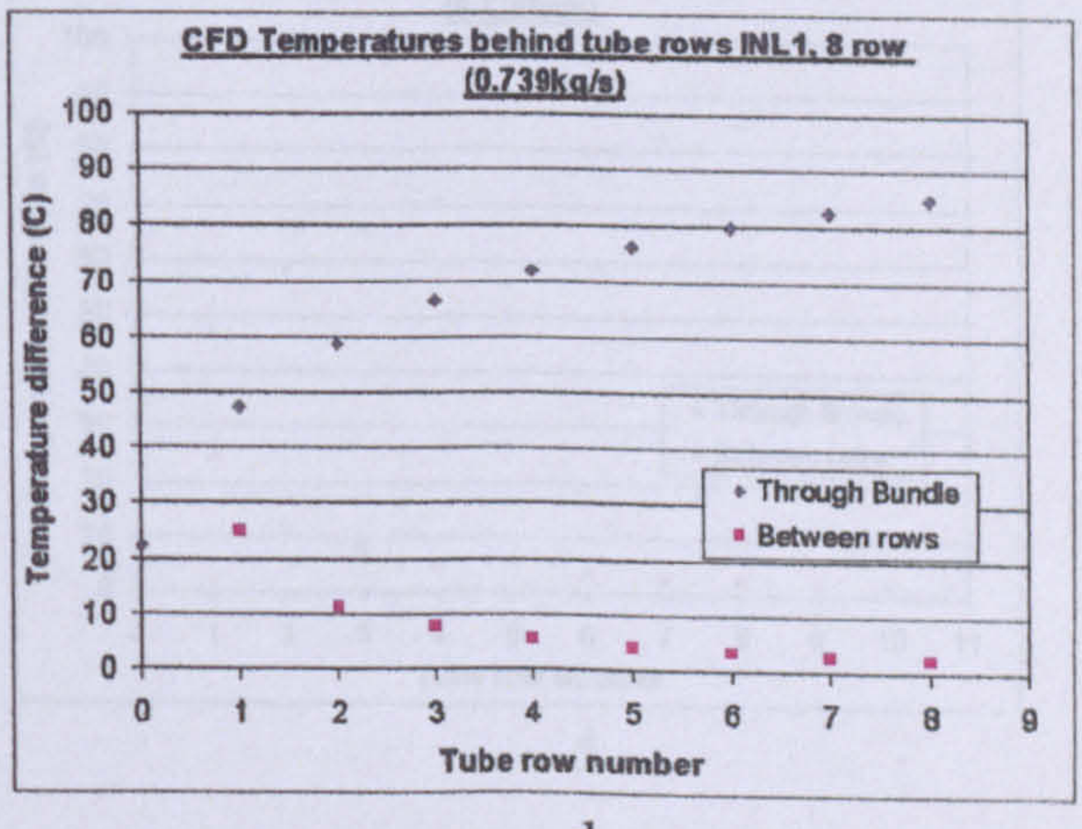

d

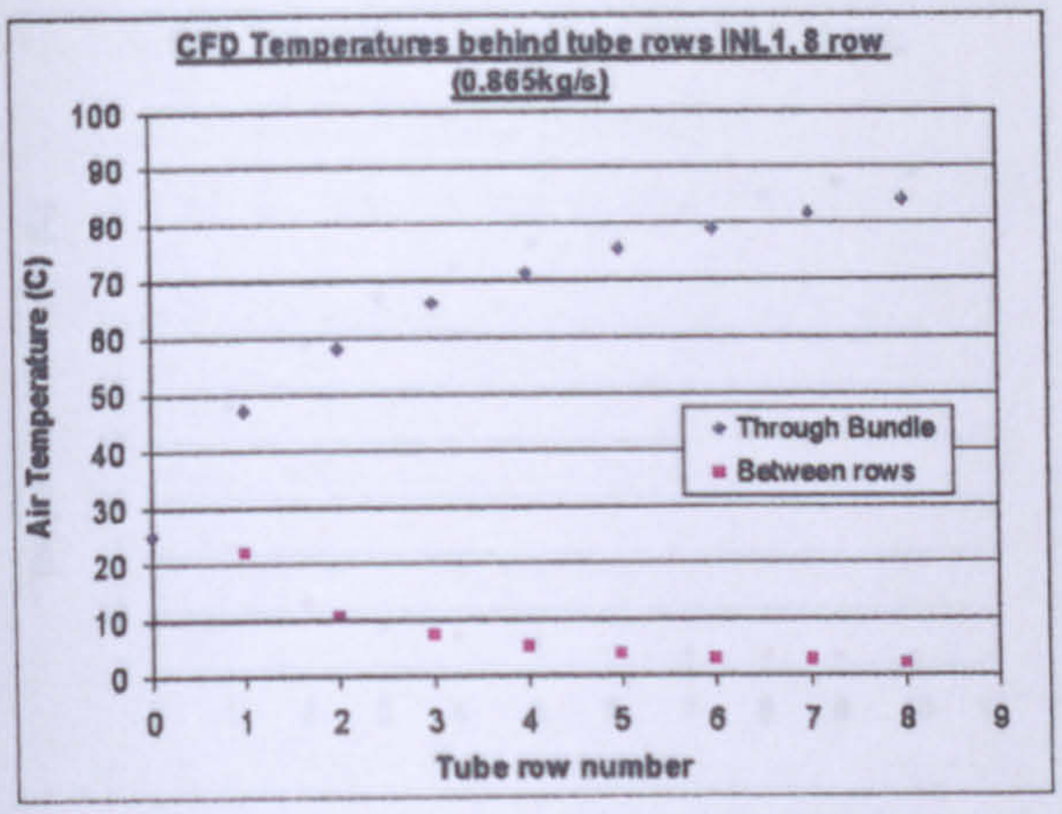

e

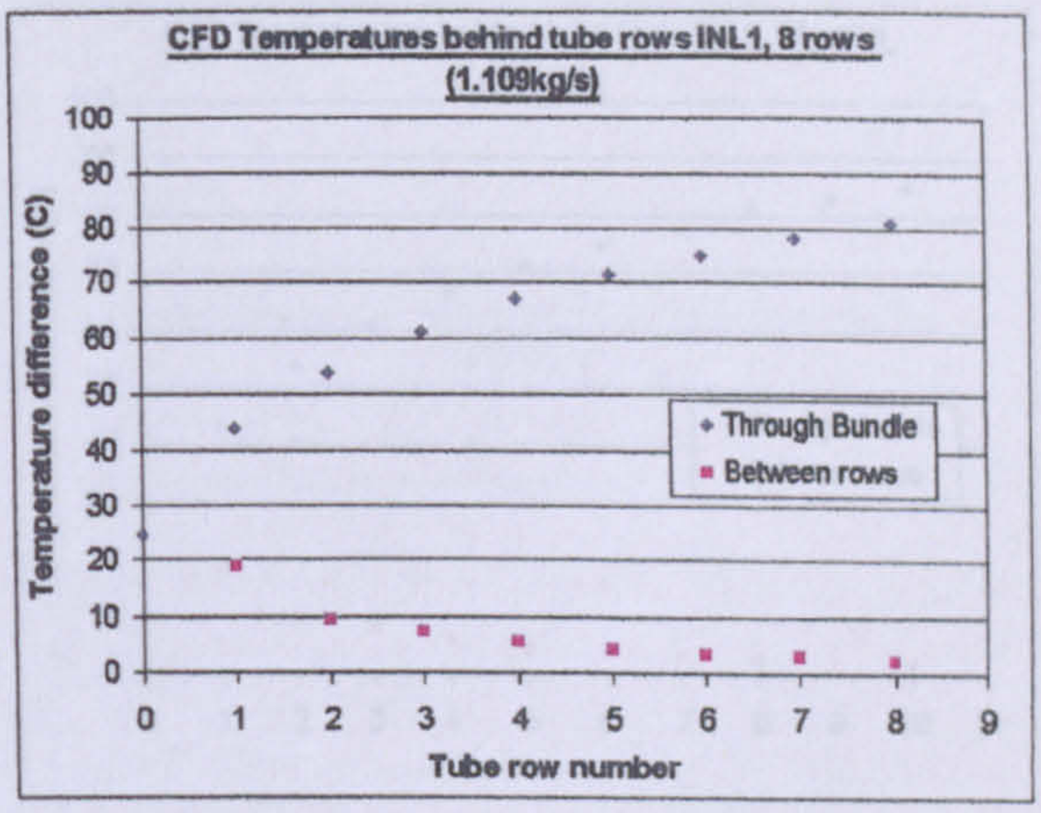

f

Figure 10.8a, b, c, and d: Mass averaged plane temperature and temperature difference between tube rows for Bundle 1, 8 rows.

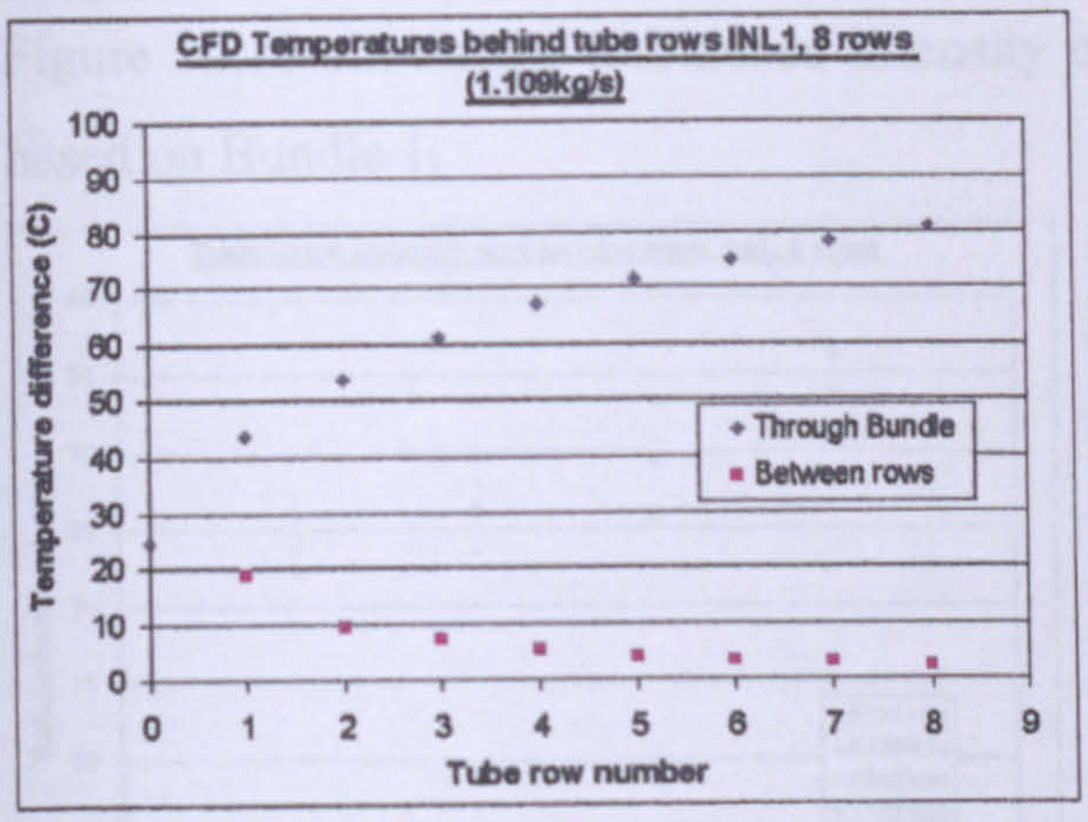

a

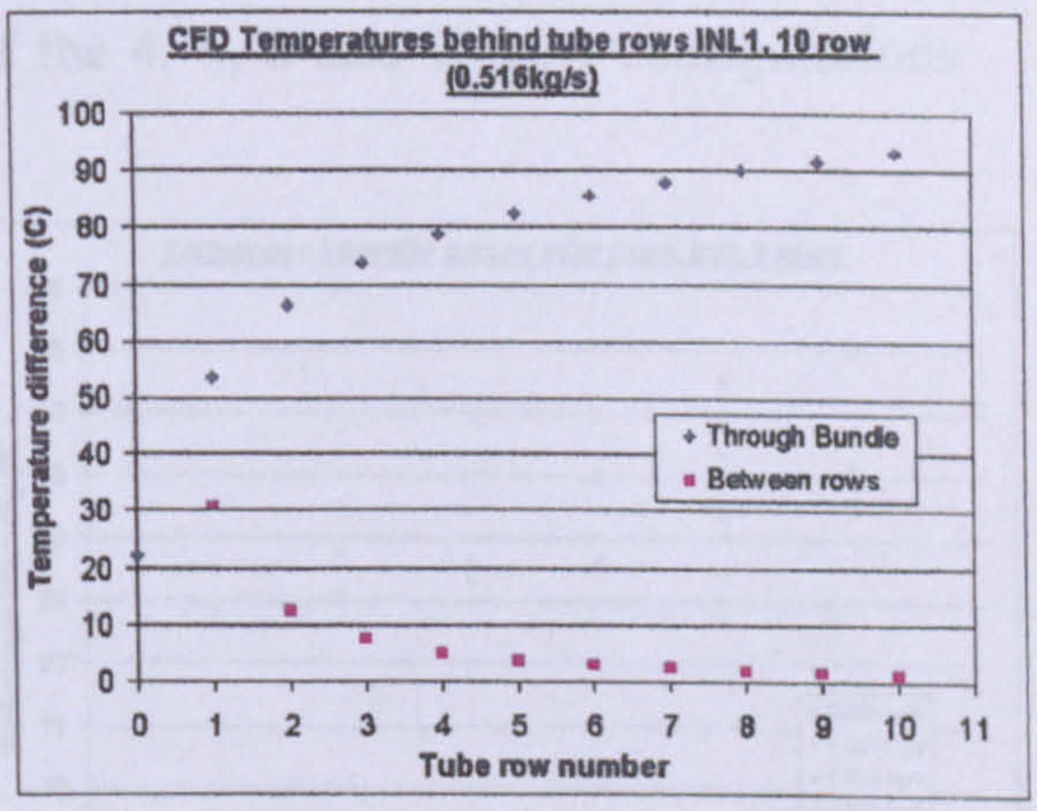

b

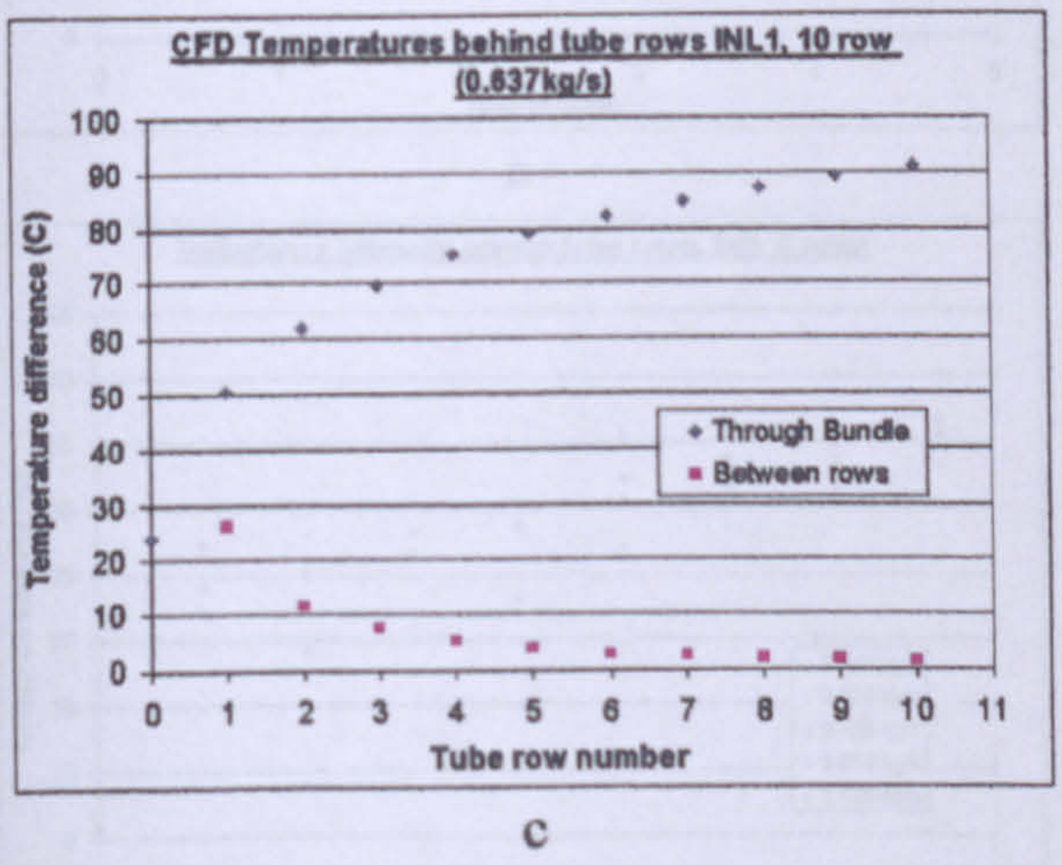

c

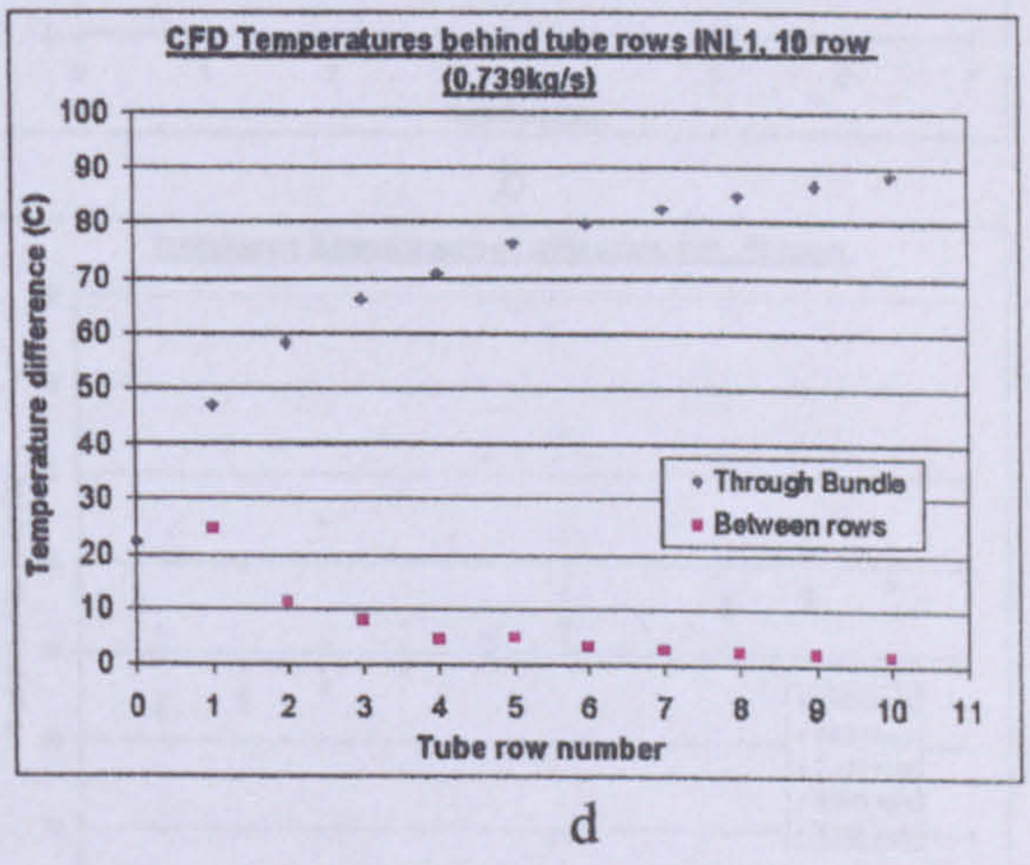

d

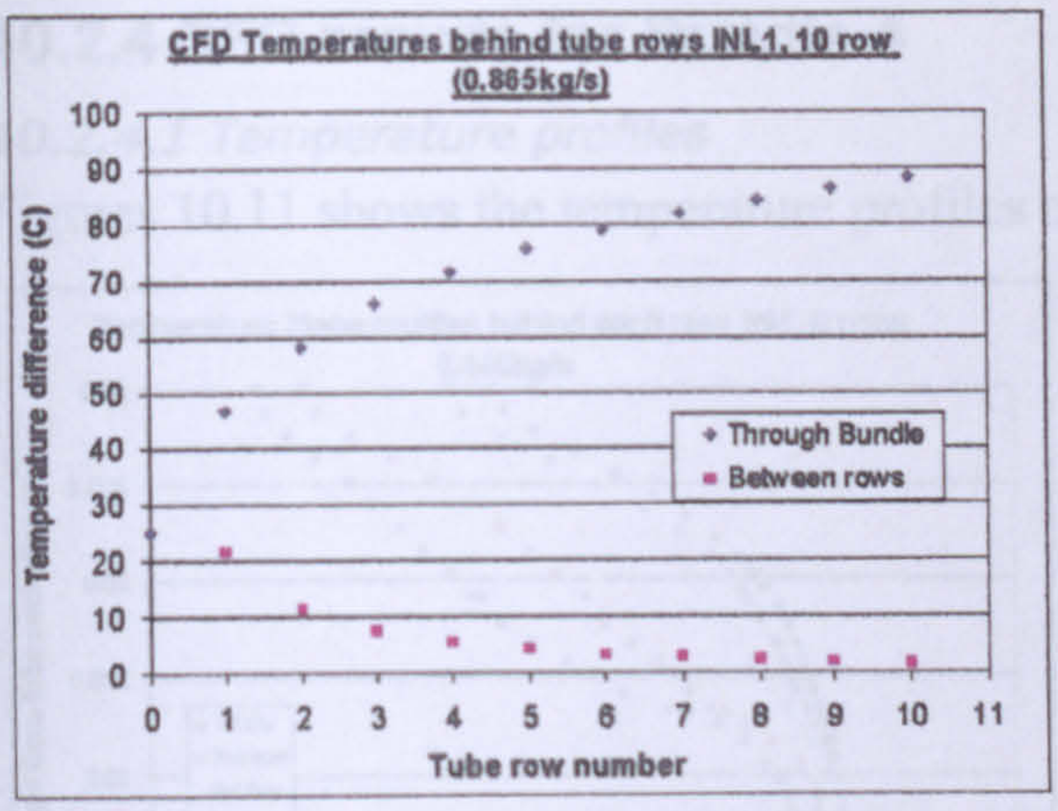

e

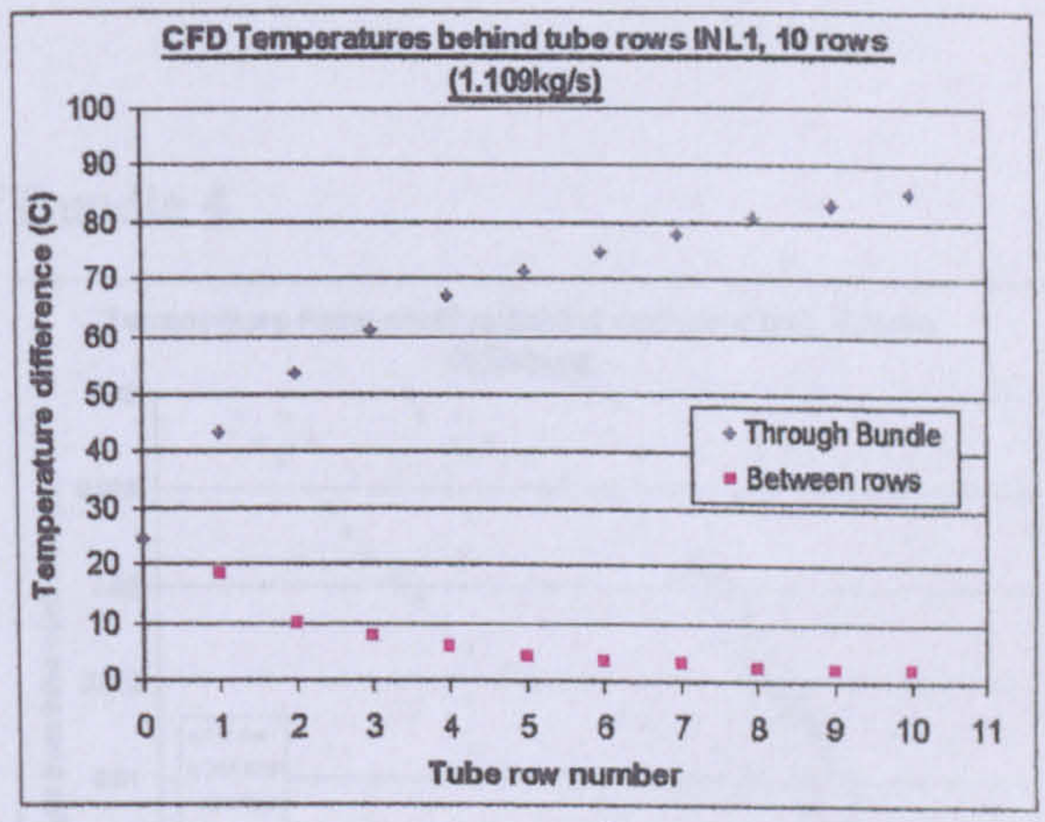

f

Figure 10.9a, b, c, d, e and f: Mass averaged plane temperature and temperature difference between tube rows for Bundle 1, 10 rows.

10.2.3.3 Mass weighted turbulence intensity on planes

Figure 10.10 shows the turbulence intensity of the 4, 6, 8 and 10 row configurations based on Bundle 1.

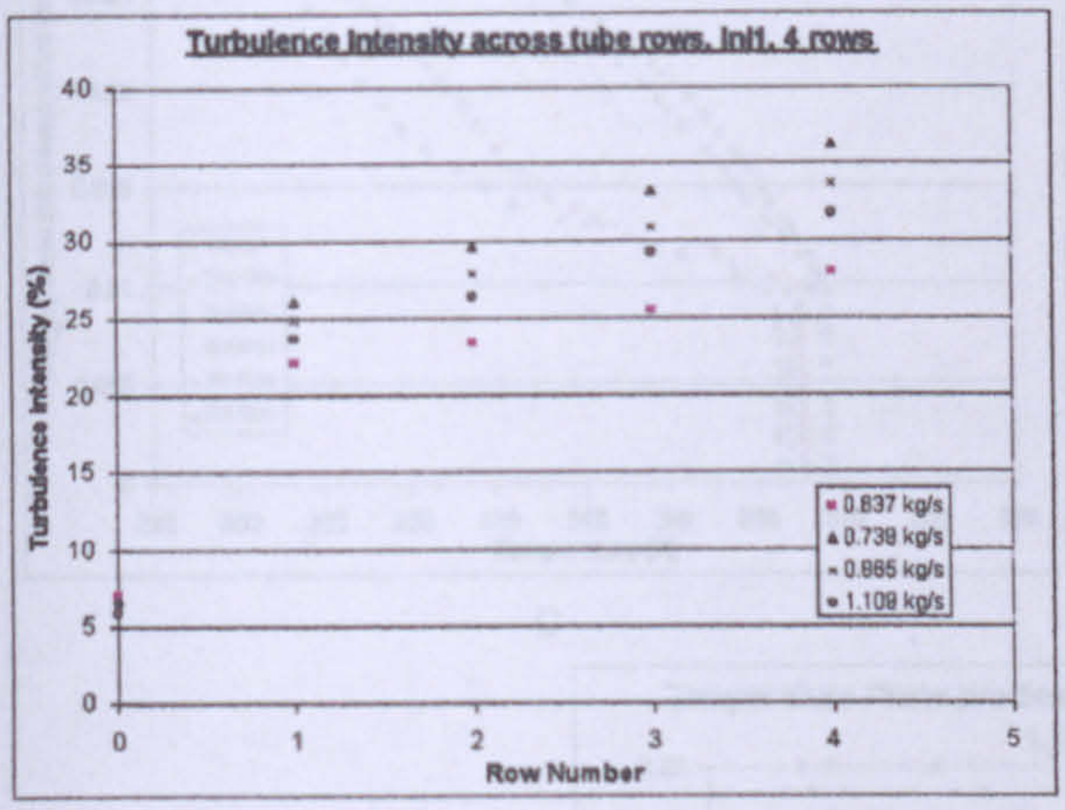

a

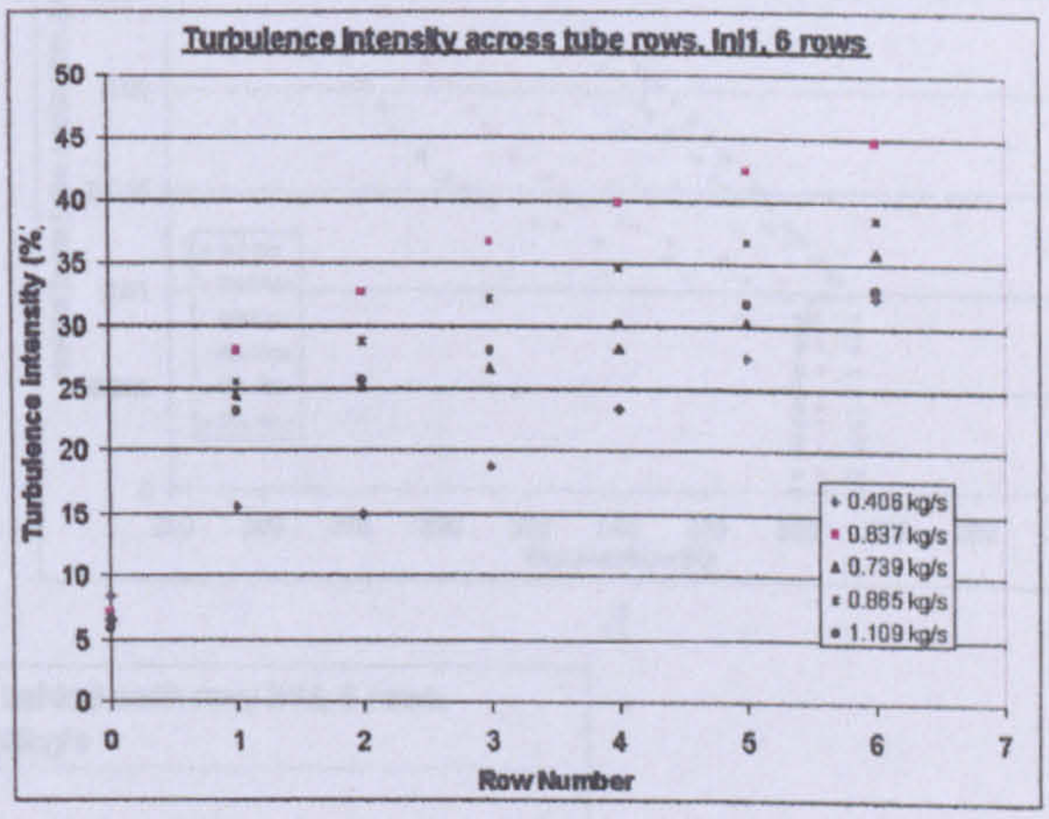

b

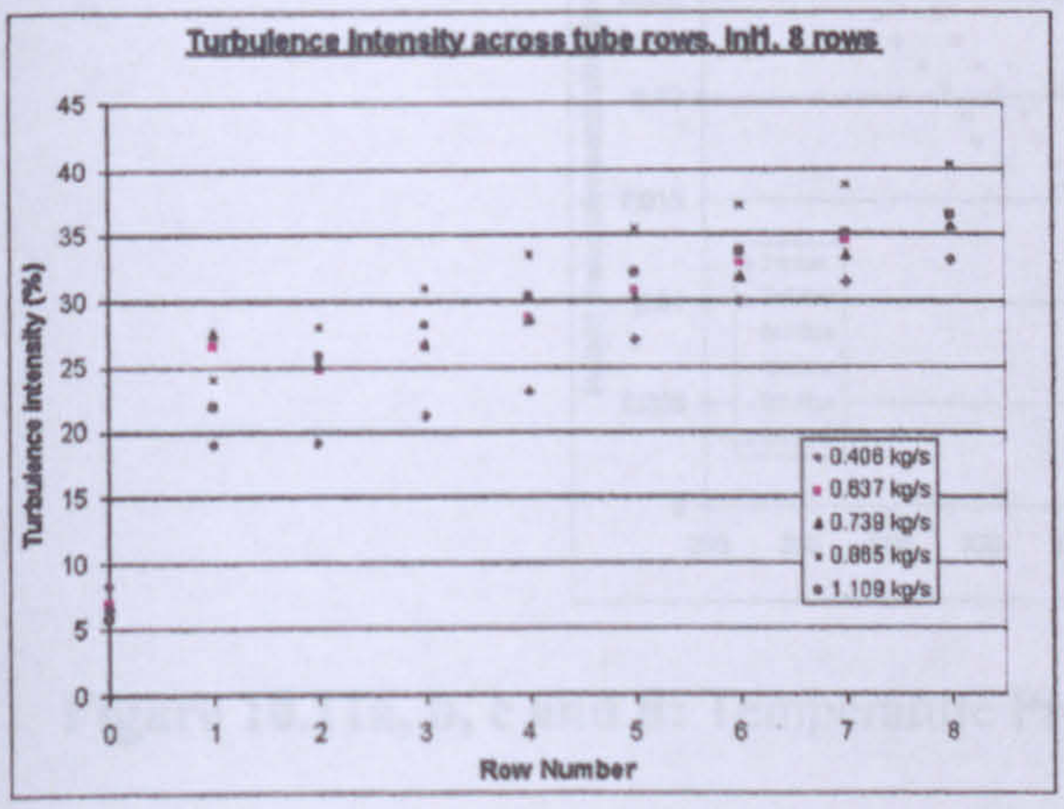

c

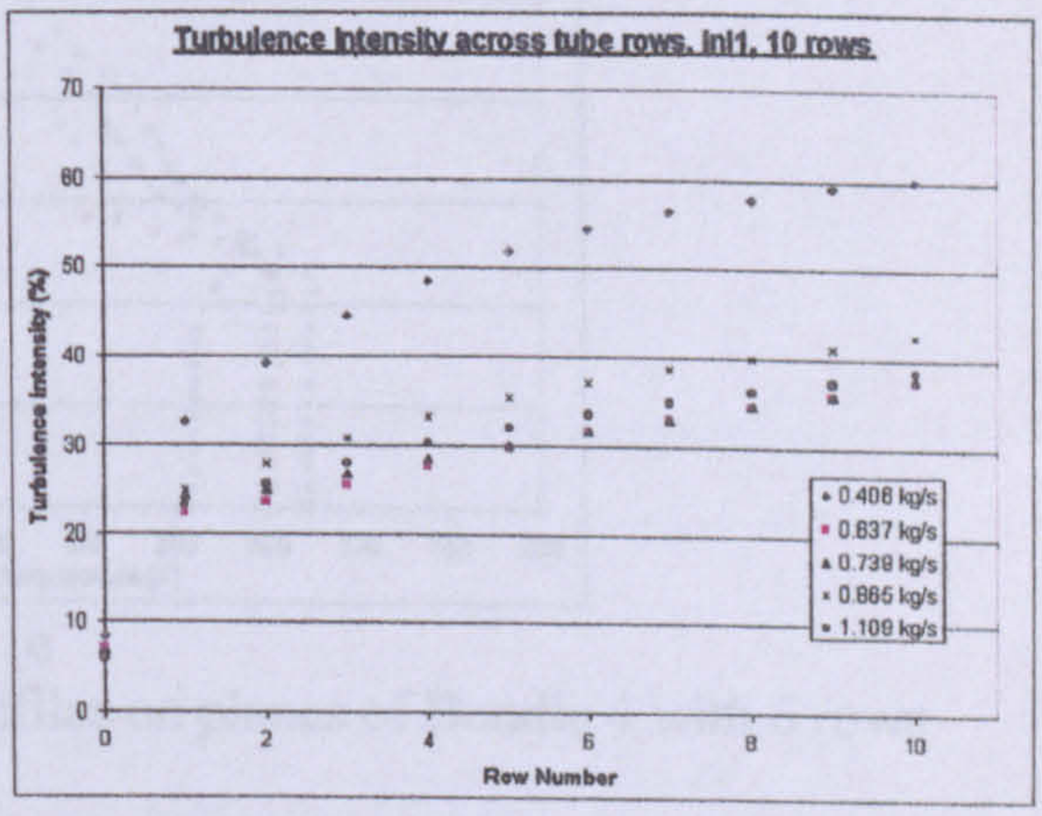

d

Figure 10.10a,b,c and d: Turbulence intensity of Bundle1 with 4 (a), 6 (b), 8(c) and 10 (d) rows

10.2.4 CFD results for Bundle 4

10.2.4.1 Temperature profiles

Figures 10.11 shows the temperature profiles of Bundle 4.

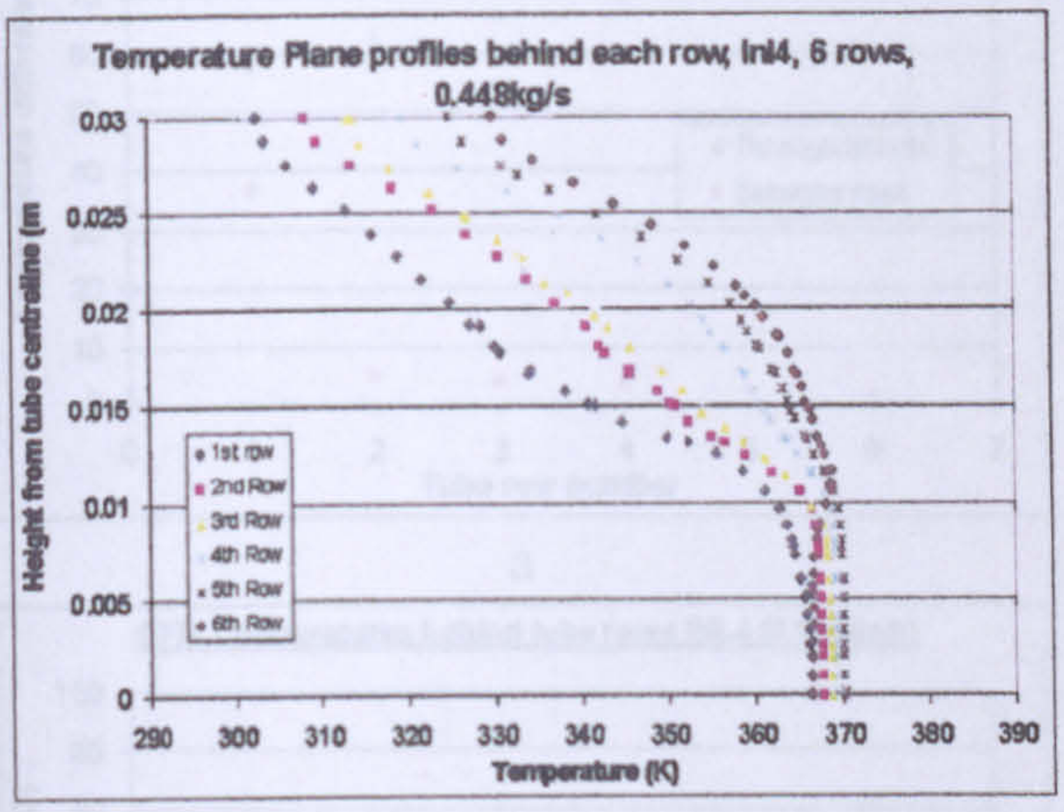

a

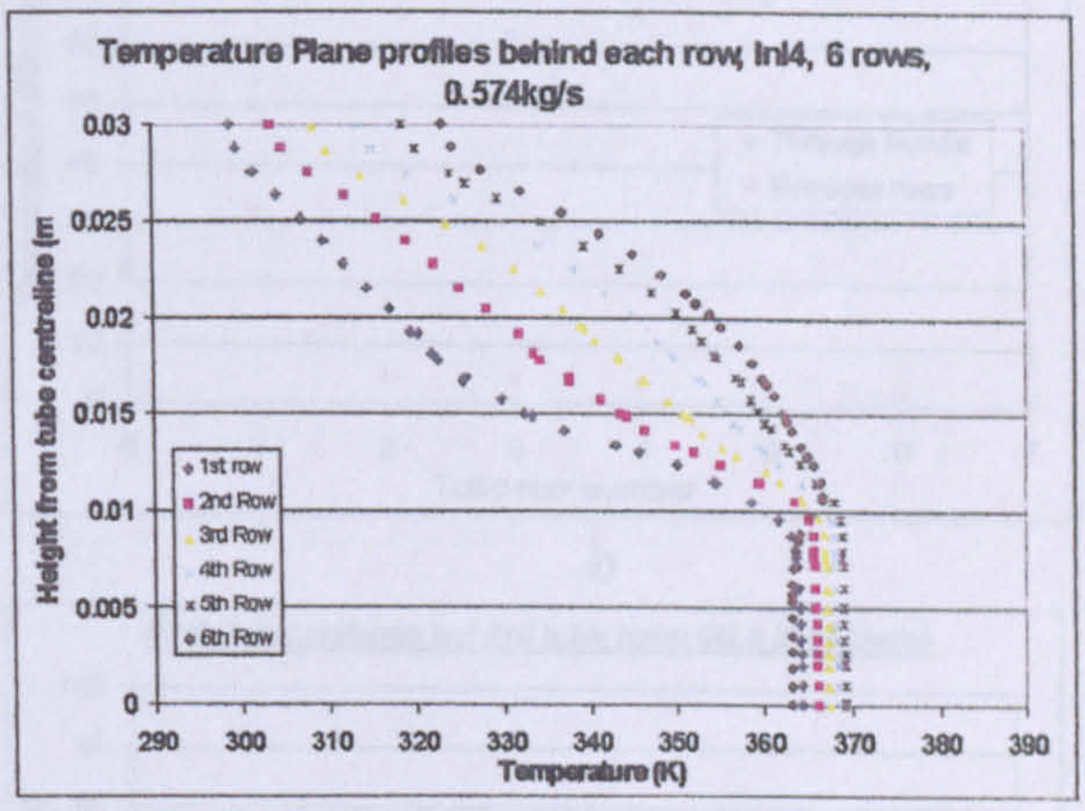

b

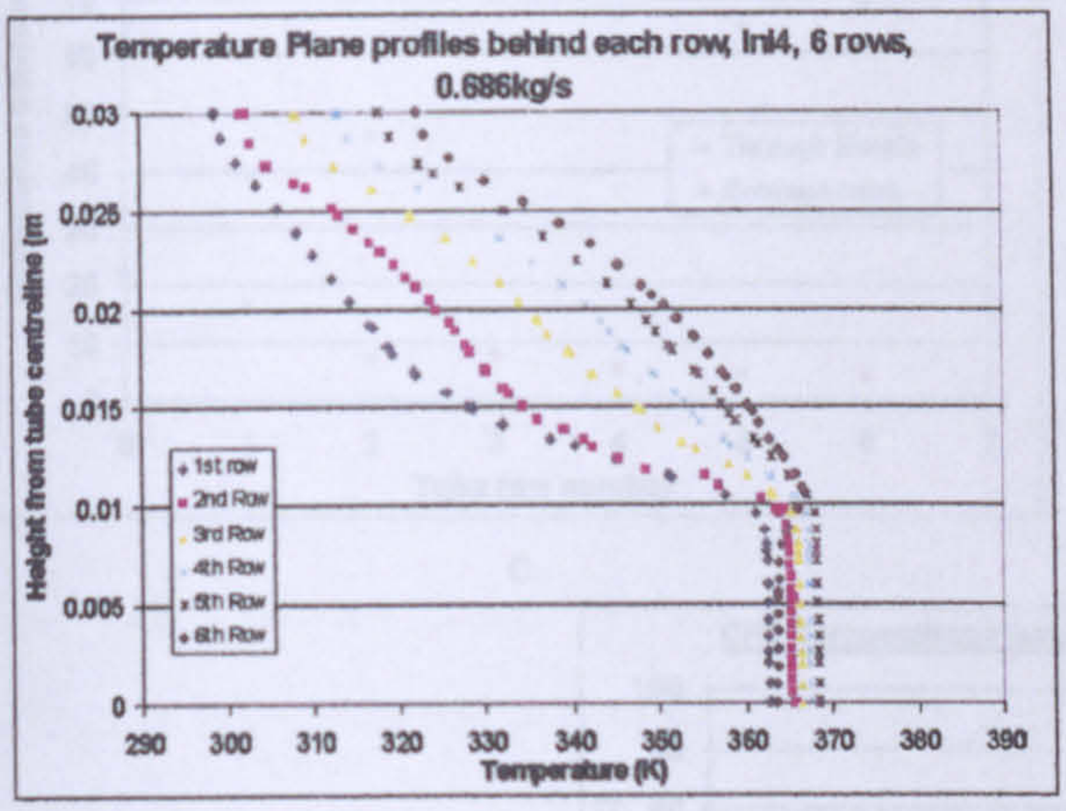

c

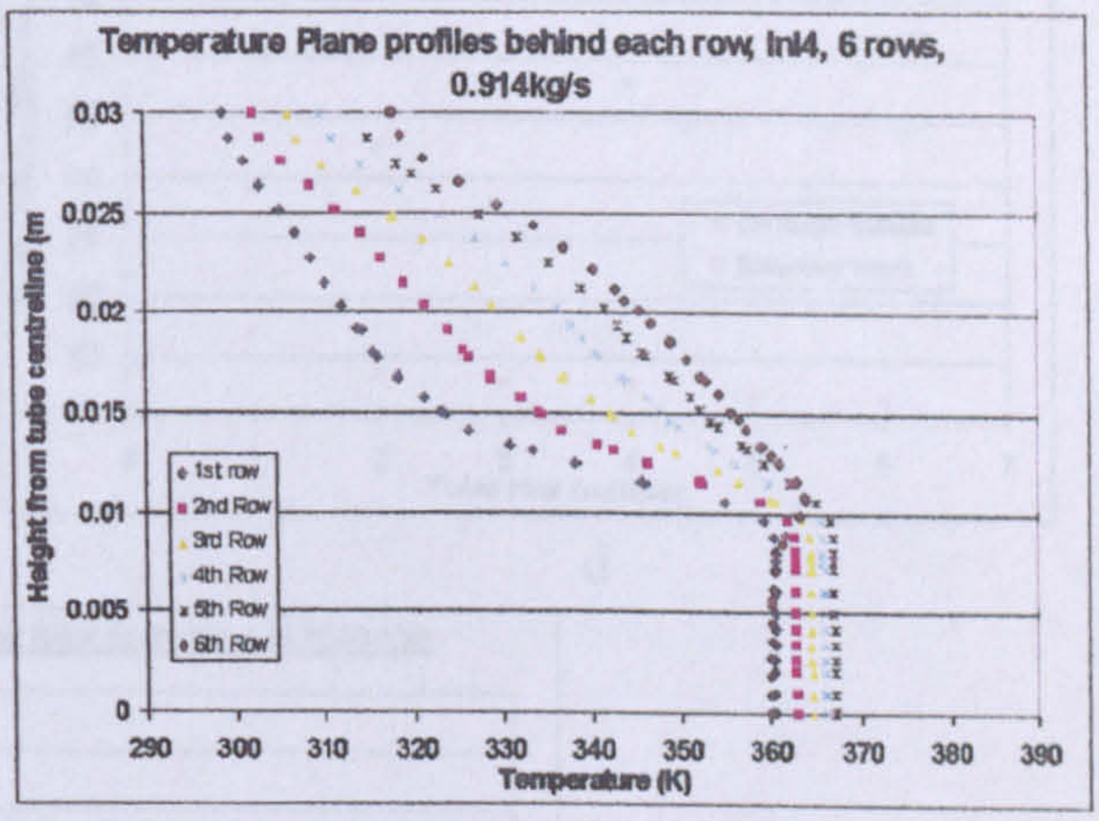

d

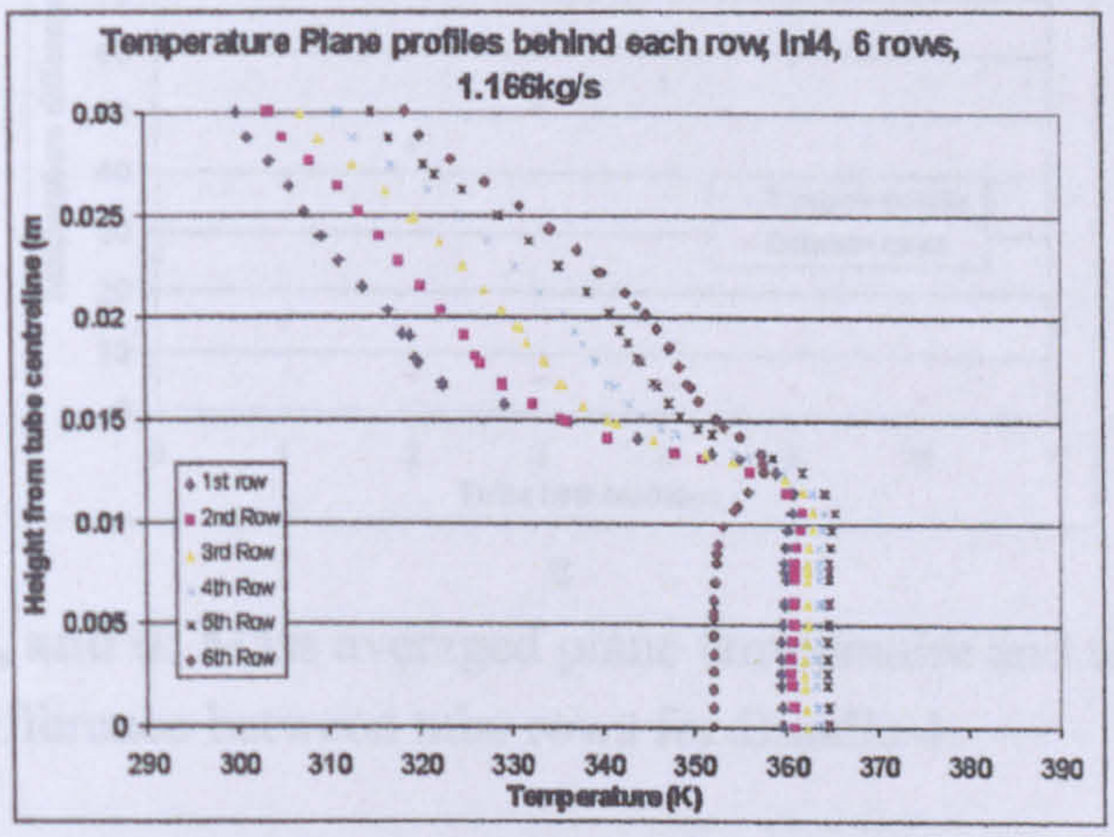

e

Figure 10.11a, b, c and d: Temperature Profiles on planes of Bundle 4 with 6 rows

10.2.4.2 Mass weighted temperature on planes

Figures 10.12 shows the results of the turbulence intensity of Bundle 4.

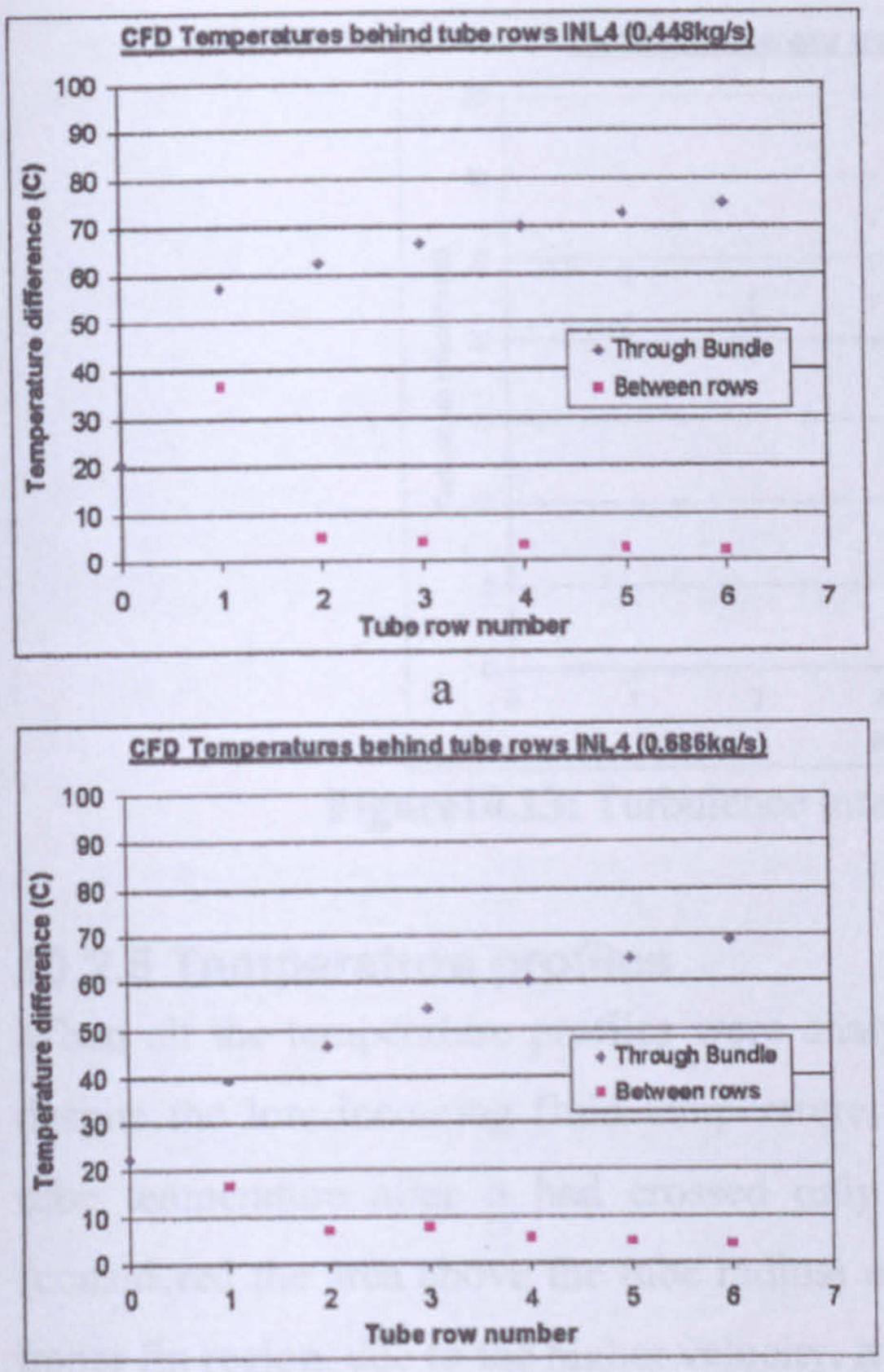

a

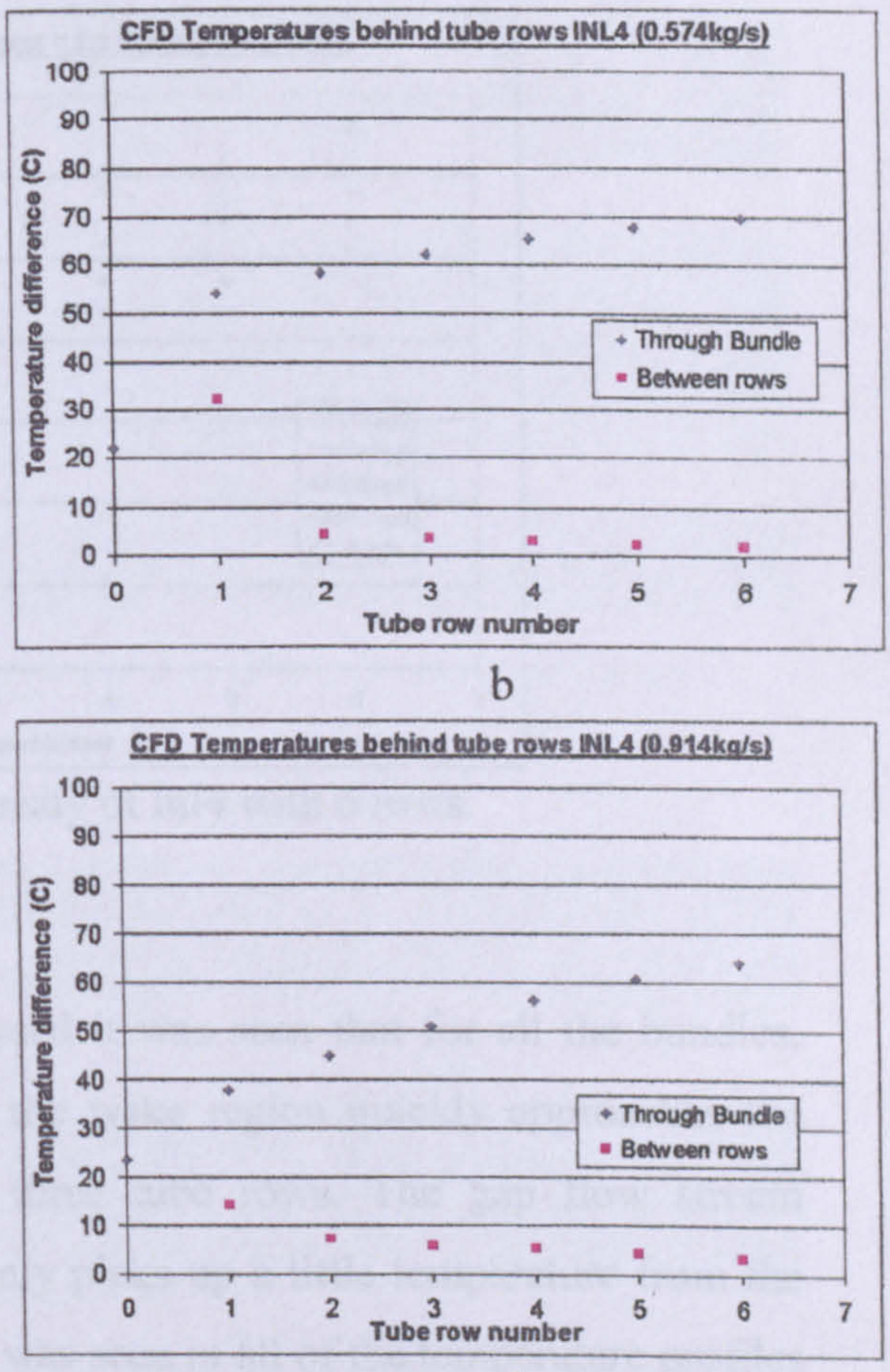

b

c

d

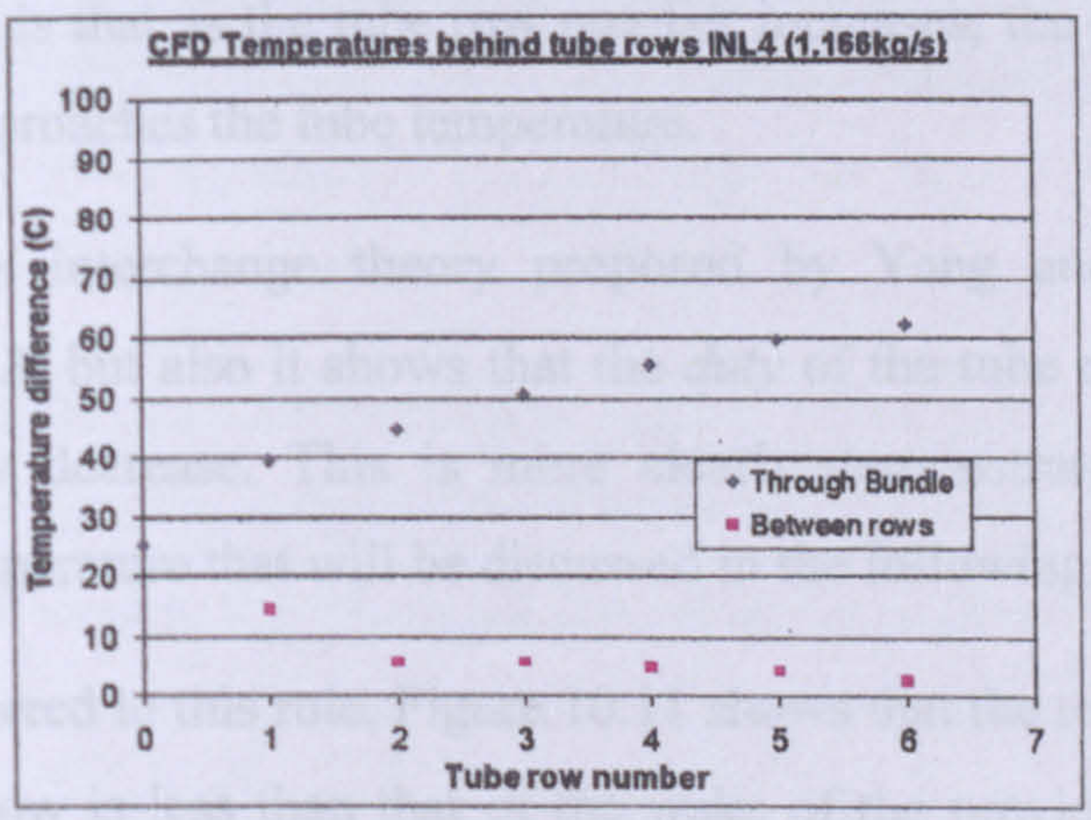

e

Figure 10.12a, b, c, and d: Mass averaged plane temperature and temperature difference between tube rows for Bundle 4

10.2.5.3 Turbulence intensity on planes

Figures 10.13 shows the turbulence intensity of Bundle 4.

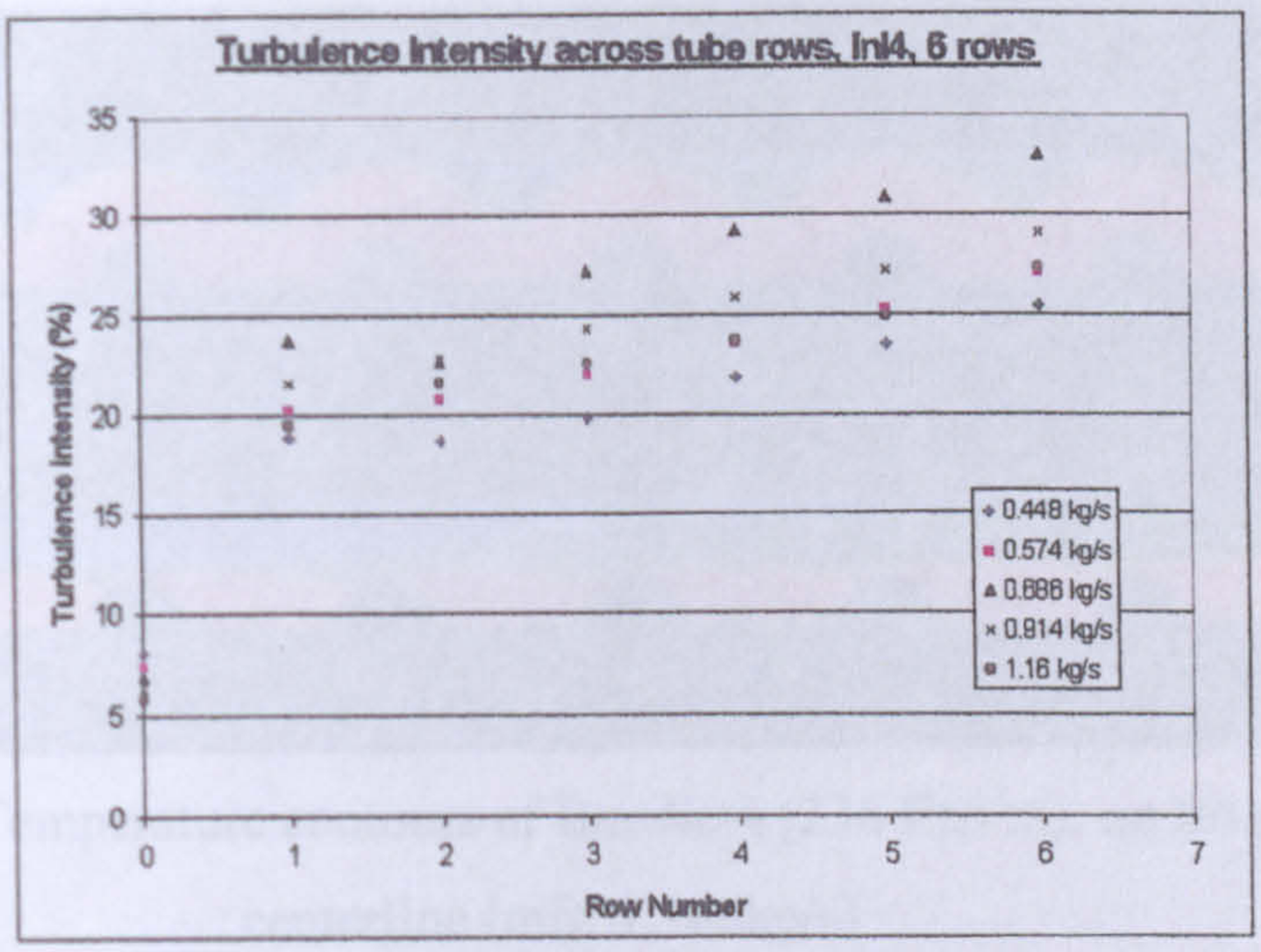

Figure10.13: Turbulence intensity of Inl4 with 6 rows.

10.2.5 Temperature profiles

When all the temperature profiles were analysed it was seen that for all the bundles, despite the low incoming fluid temperature, the wake region quickly approaches the tube temperature after it had crossed only three tube rows. The gap flow stream (considered the area above the tube radius) only picks up a little temperature from the upper fin region, due to the higher velocity. It was seen in all of the temperature profiles that the major difference is that as the tube row number increases, the gap flow stream temperature gradually approaches the tube temperature.

This confirms the mass interchange theory proposed by Yang and Bell [45], as described in Section 2.5.3, but also it shows that the *duty* of the tube rows further into the bundle will actually decrease. This is more clearly demonstrated by the mass weighted average air temperature that will be discussed in the following section.

While Bundle 4 also adhered to this rule, Figure 10.11 shows that the temperature in the wake of the final tube row is less than that of the wake of the previous tubes. Figure 10.14 shows the temperature contours of Bundle 4 and Figure 10.15 shows the temperature contours for Bundle 1 at approximately the same mass flow rate. Bundle 1 had a fin frequency of 433 fins/m whereas Bundle 4 had 236 fins/m.

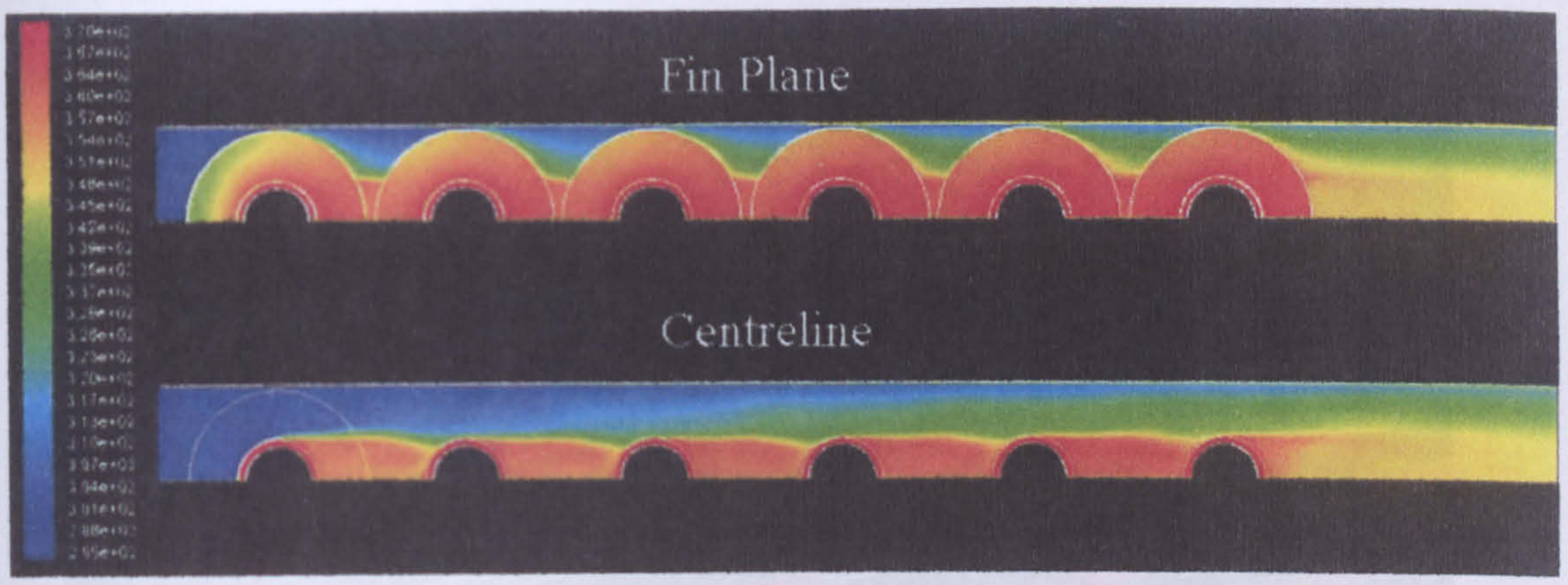

Figure 10.14: Temperature contours of Bundle 4 (236 fins/m), on fin plane and centreline (mfr: 1.166kg/s)

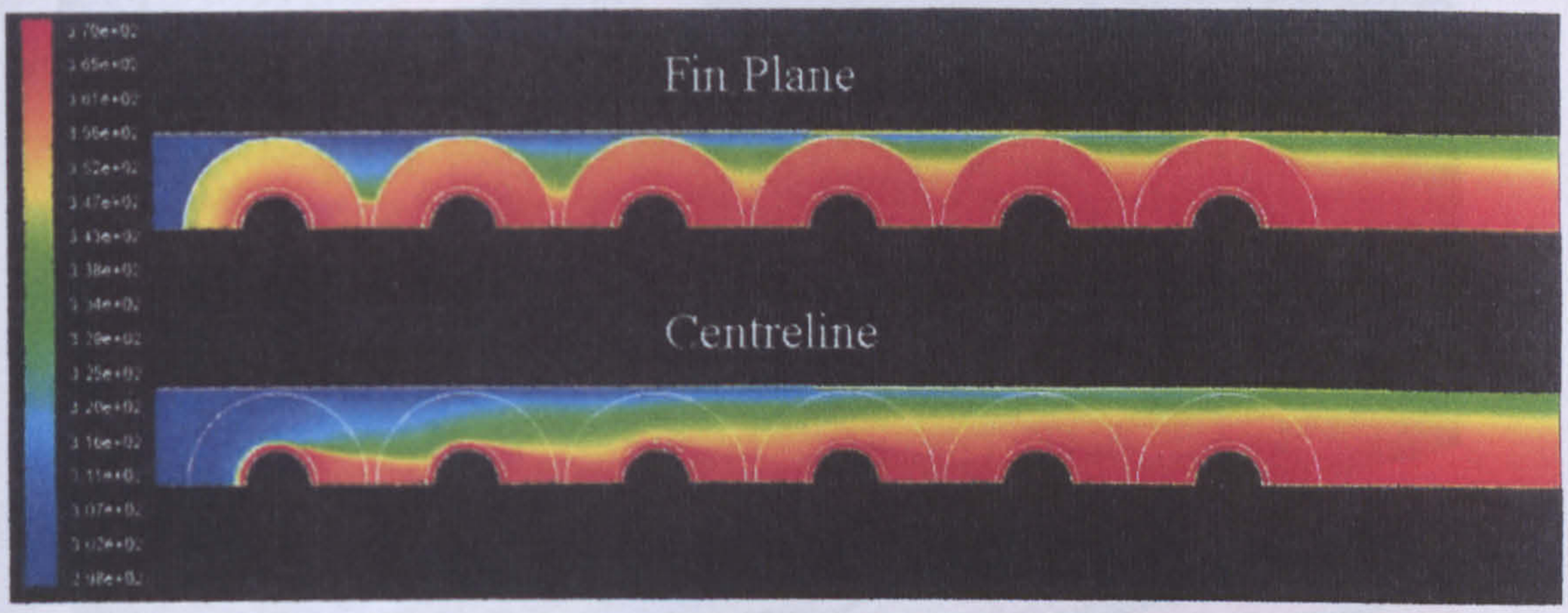

Figure 10.15: Temperature contours of Bundle 1 (433 fins/m), on fin plane and centreline (mfr: 1.109kg/s)

It is postulated that the differences are directly connected with the low fin frequency. If the fin spacing is narrow then the thermal boundary layer on the fins could touch, and this would mean the flow local to the following fins would be heated to a point whereby a smaller duty would be performed on the fins, as there is a reduced temperature difference. It follows from this that when the fin spacing is wider the thermal boundary layers would not touch; thereby a thermal gap flow would exist. This would have the effect of reducing the temperature of the flow at outlet from the fin, hence allowing a cooler flow over the following fins. These effects are seen more clearly in the temperature contours Figures 10.16 and 10.17 where the second and fifth tube rows respectively are compared.

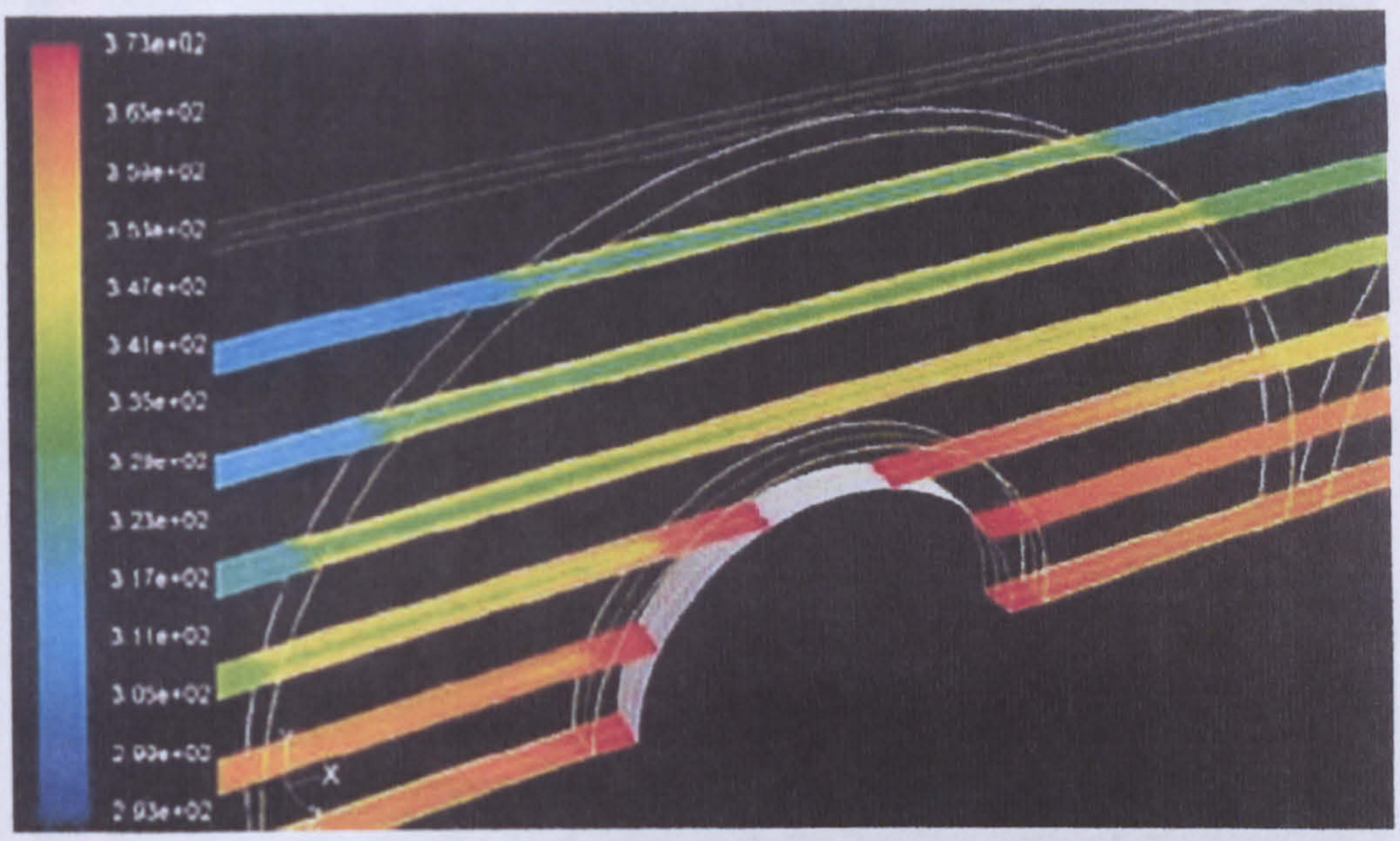

a.

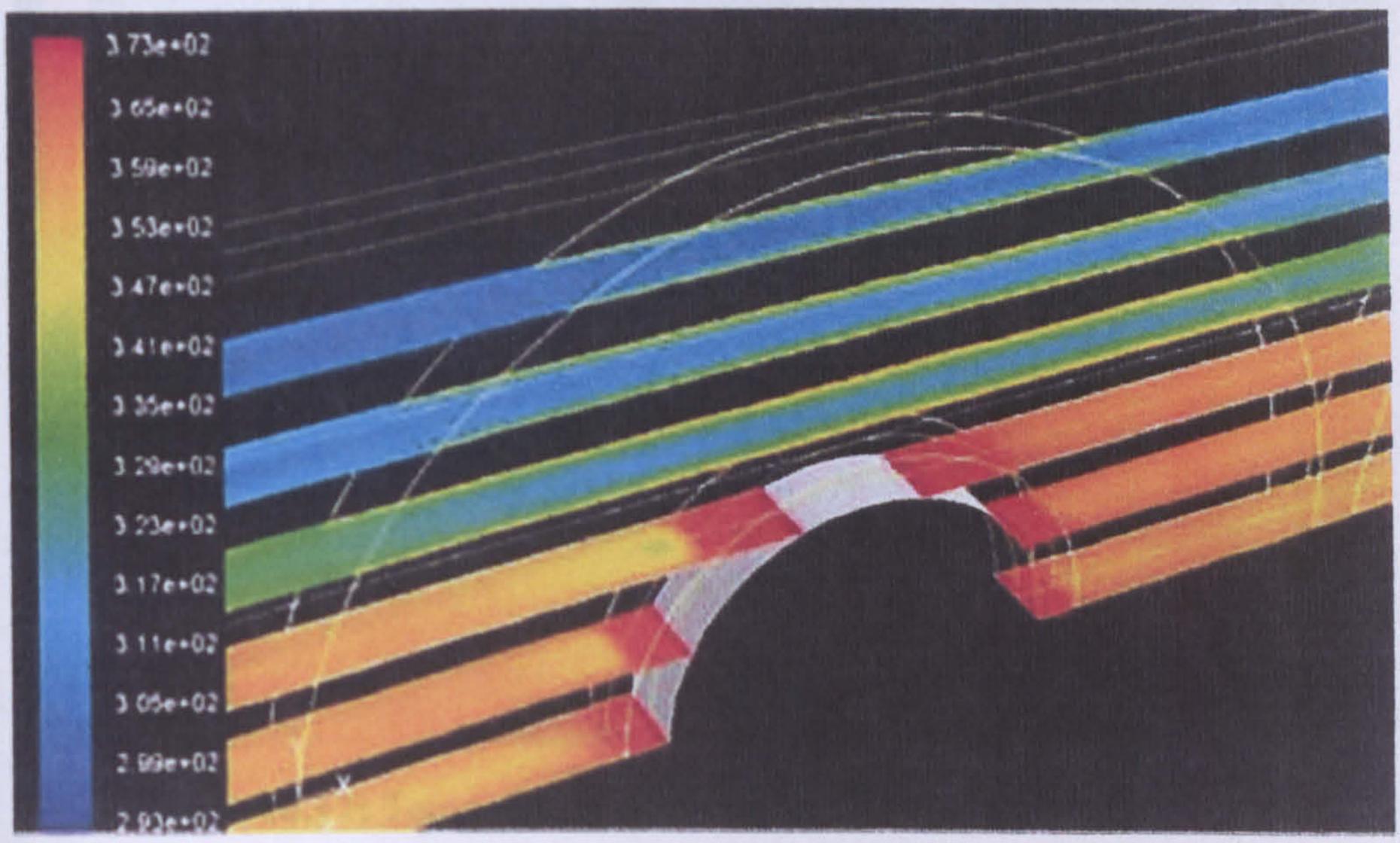

b.

Figure 10.16: Temperature contours between fins on the second row of

a. Bundle 1 mfr=1.109kg/s and b. Bundle 4 mfr=1.166kg/s

It can be seen that there is significantly cooler flow between the fins of b., but that the air temperature behind the tubes in both cases is similar, due to the recirculation. Figure 10.17a shows the air temperature between the fins to have raised substantially, whereas b. still has some relatively cool flow between the fins.

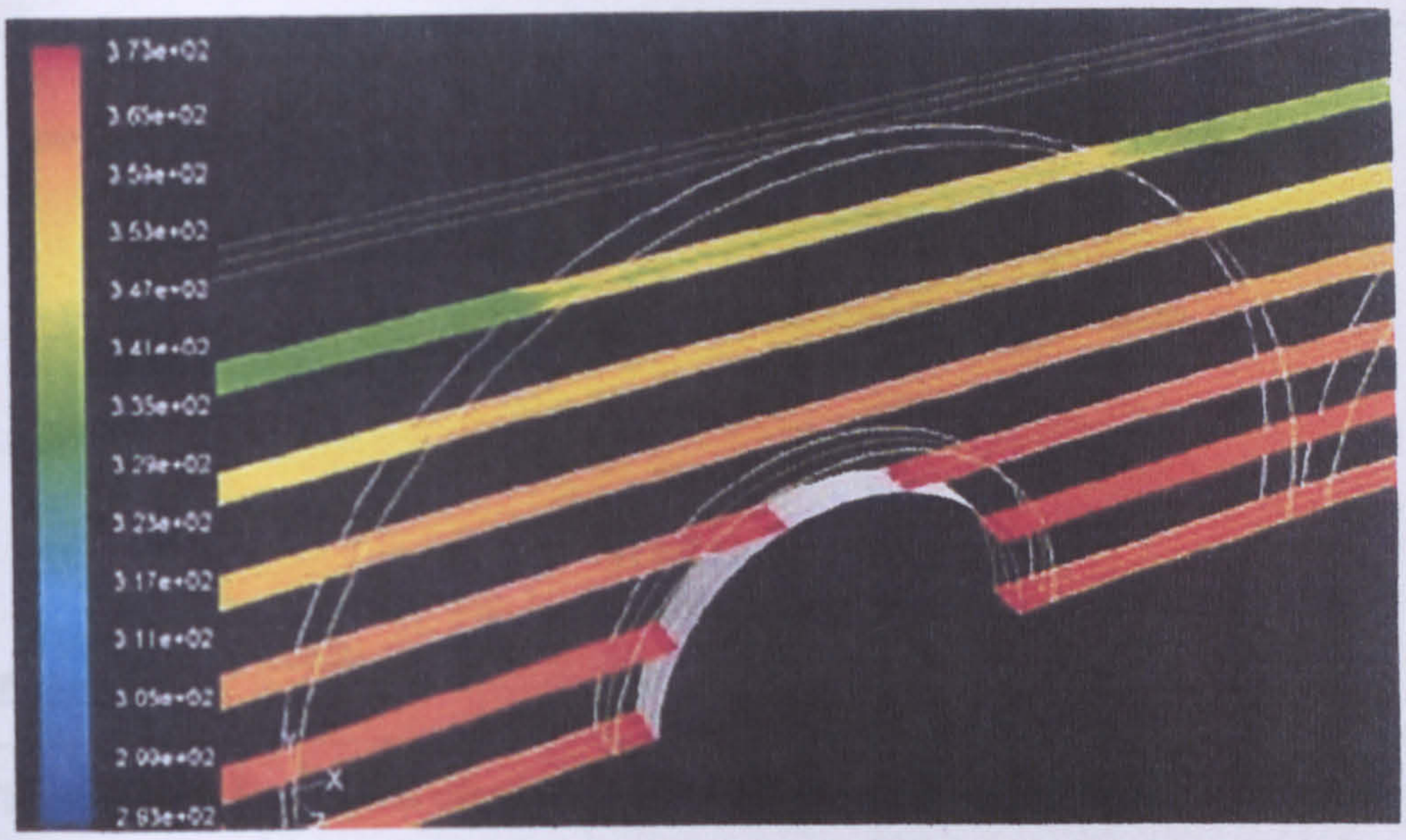

a.

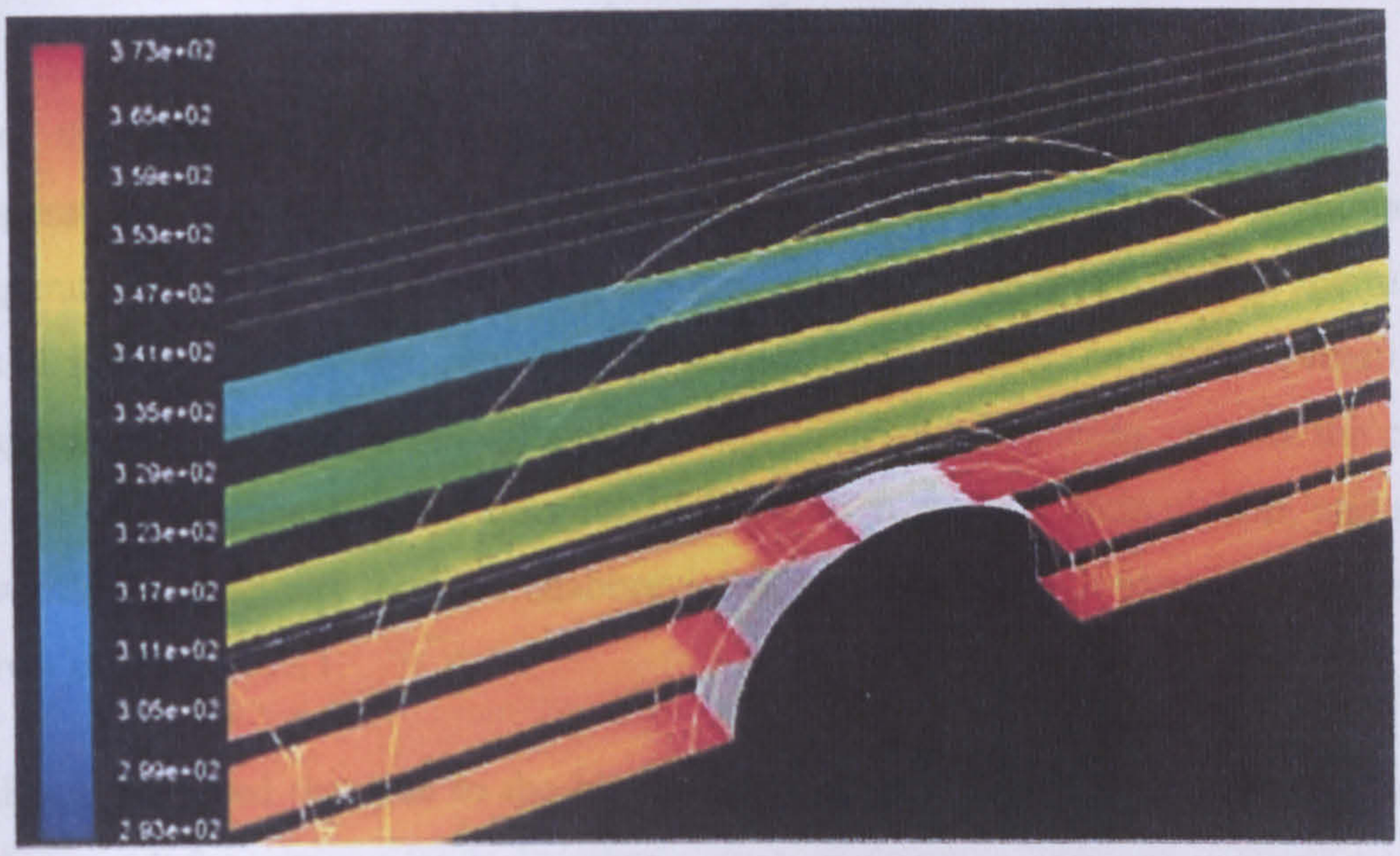

b.

Figure 10.17: Temperature contours between fins on the fifth row of

b. Bundle 1 mfr=1.109kg/s and b.Bundle 4 mfr=1.166kg/s

The temperature of the wake is also believed to be related to the fin frequency, especially the wake from the last tube row. When the fins are widely spaced (Bundle 4) the wake on the centreline is further away from the heated wall affected region, and so the temperature of the wake is not as closely bounded to the fin temperature. This is shown by Figure 10.18 below.

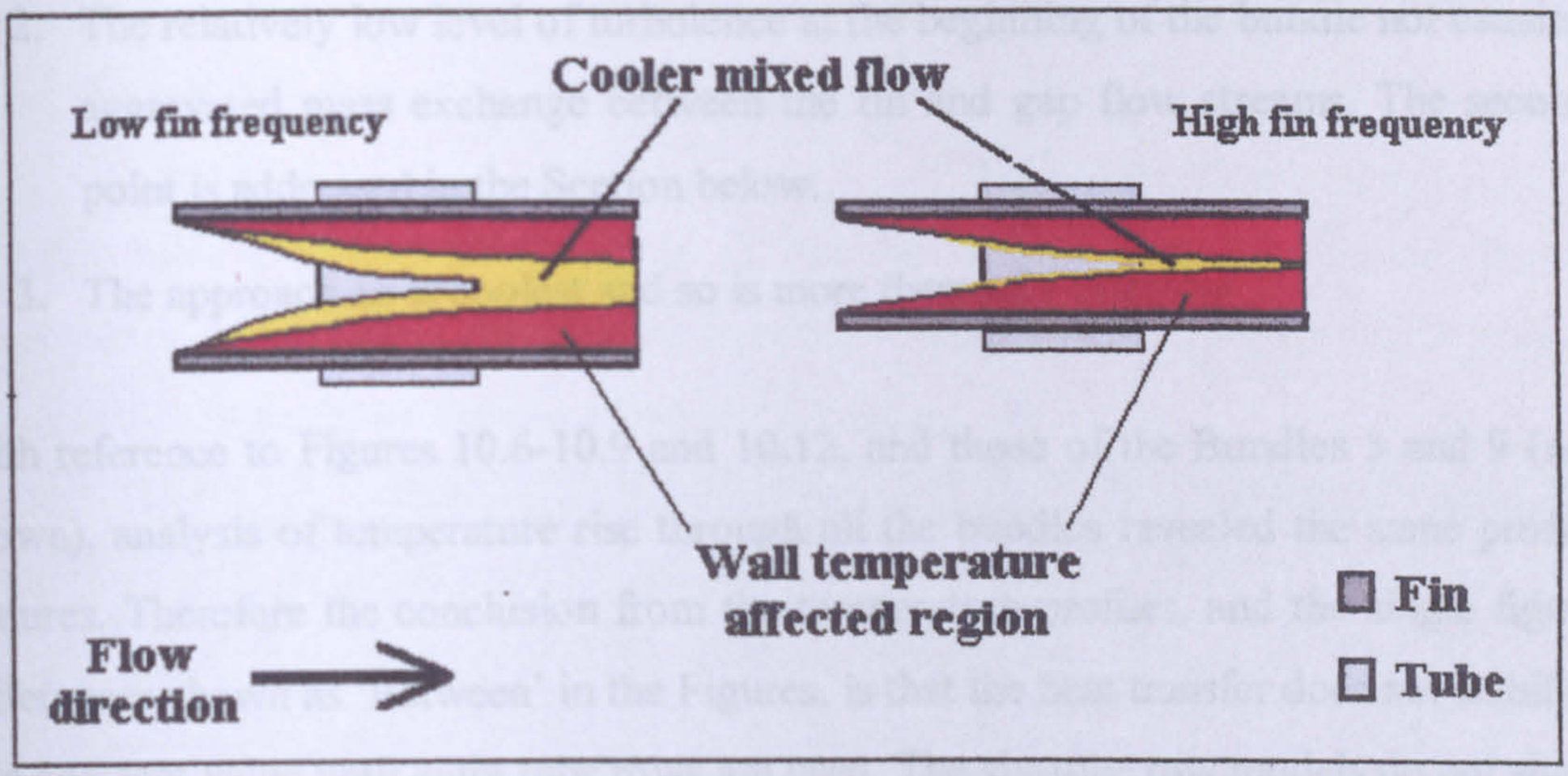

Figure 10.18: Simplified diagram of temperature profiles for an air-cooler case with wide and narrow fin spacing.

From this diagram it can seen how the wakes of Bundle 4 would have lower temperatures, as cooler incoming flow will have a chance to mix with flow in the high temperature, low speed, wall affected region. As it passes over the back of the tube the mixed flow will be pulled into the recirculation wake region, hence the overall wake temperature is reduced, when compared to the higher fin frequency case. In the case of the last tube row there is no cavity flow formation to provide recirculation, and so this flow mixing effect can continue unabbreviated, resulting in the lower wake temperature shown in Figure 10.11.

It should be noted that due to the higher fin frequency Bundle 1 would transfer more heat, per unit face area.

10.2.8 Temperature through bundles and heat transfer stability

It was seen that the temperature of the air rises through all the bundles, as would be expected. However, it can be seen in the temperature Figures 10.9 and 10.12 that the largest temperature rise occurs over the first tube row, then quickly decreases. This decrease is due to three reasons:

1. The 'shadow' effect that occurs from the following tube being caught in the wake of the preceding tube,

2. The relatively low level of turbulence at the beginning of the bundle not causing aggravated mass exchange between the fin and gap flow streams. The second point is addressed in the Section below.

3. The approach air is coolest and so is more thermally effective

With reference to Figures 10.6-10.9 and 10.12, and those of the Bundles 3 and 9 (not shown), analysis of temperature rise through all the bundles revealed the same profile features. Therefore the conclusion from the temperature profiles, and the single figure differences shown as 'Between' in the Figures, is that the heat transfer does not stabilise to a constant value until eight tube rows are used. The six-tube row models do not show a tendency to the smooth temperature profile curve shown by the sixth tube in the eight and ten row models. This indicates that six rows can be considered the point of established, stable, heat transfer in a deeper bundle, where there are more than six rows present. Otherwise a six row bundle in itself cannot be considered to provide a stabilised heat transfer rate.

This is an important result, as it provides a quantified answer to theories and guesses made by previous researchers as to when and where heat transfer stabilises.

10.2.9 Turbulence effects

As discussed above the turbulence through the bundle, at inlet and generated throughout the bundle by combined wake and fin tip splitting effects, is believed to contribute greatly to the overall heat transfer behaviour.

Figures 10.10 and 10.13 show the mass weighted turbulence intensity over the planes of the bundles. The formulation of turbulence intensity is given above in Section 10.2.2, so it can be seen that the magnitude of turbulence intensity is not a reflection on the actual amount of turbulent energy (or any other absolute measure), rather a specific amount relative to the flow velocity magnitude. Therefore the interest is in the trends.

It can be seen in the figures that the turbulence intensity increases throughout the bundle. When considering the total row surface area HTC (h) most studies cite the turbulence argument to support their findings of increasing h. It will be shown that

while this is likely correct it is difficult to arrive at a practical approach for predicting turbulence without recourse to experiments or CFD.

It will have been seen in Figure 10.13 that the low fin frequency bundle, Bundle 4 exhibits a dip in turbulence intensity over the second tube row. Figure 10.19 shows the turbulence intensity on the planes between the fins.

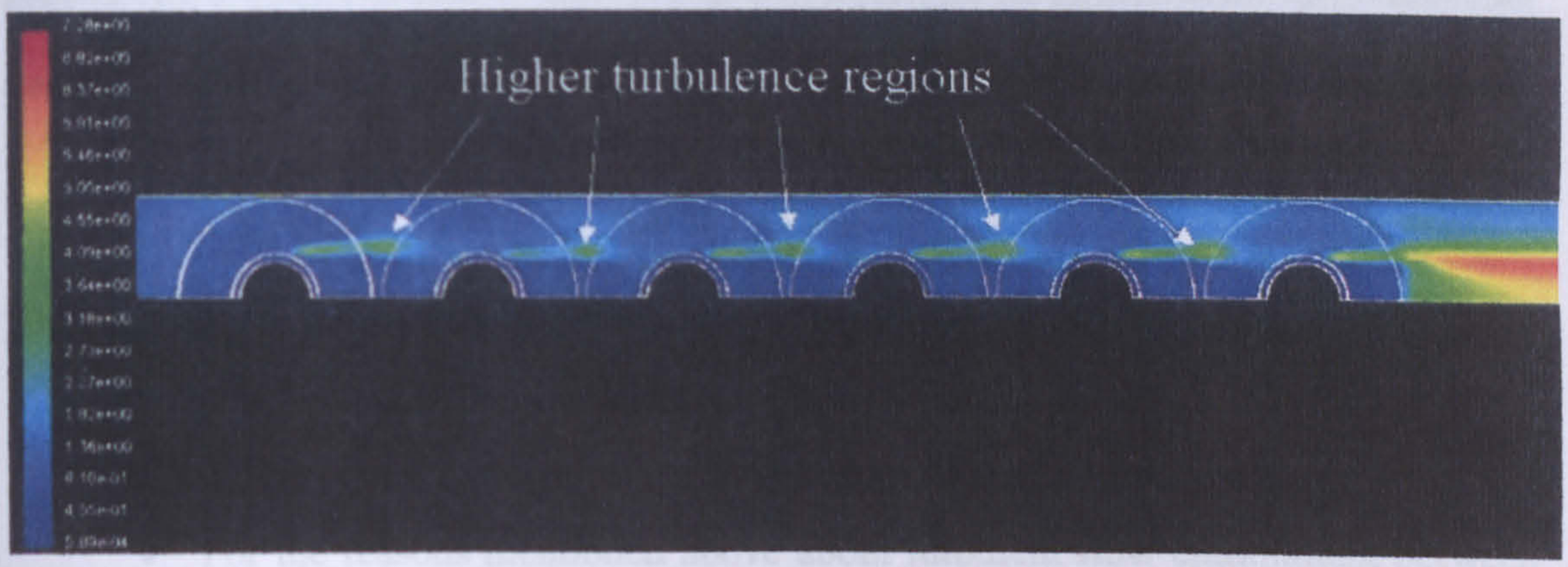

Figure 10.19: Turbulence intensity contours on centreline of Bundle 4 (mfr: 1.166kg/s)

It can be seen that there are higher turbulence regions over the rear of the tubes, from the separation point over the tube top/back. It is therefore believed that only large fin spacings will produce this distinct turbulence pattern.

This is due to the fin tips creating turbulence from the separation effects over their edges. This separation creates boundary layers, which do not merge, on the fins and hence there is relatively low turbulence near the fin wall. The separated turbulent flow becomes entrained in the bulk flow, passes over the top of the tube surface and creates this high speed, high turbulence region, which is charged by both the fin separation turbulence, and turbulence inherent from the separation over the rear of the tube.

Smaller fin gaps do not allow the fin separated flow to move easily away from the wall so the turbulence must remain high around the whole fin and tube unit, as shown in Figure 10.20 below.

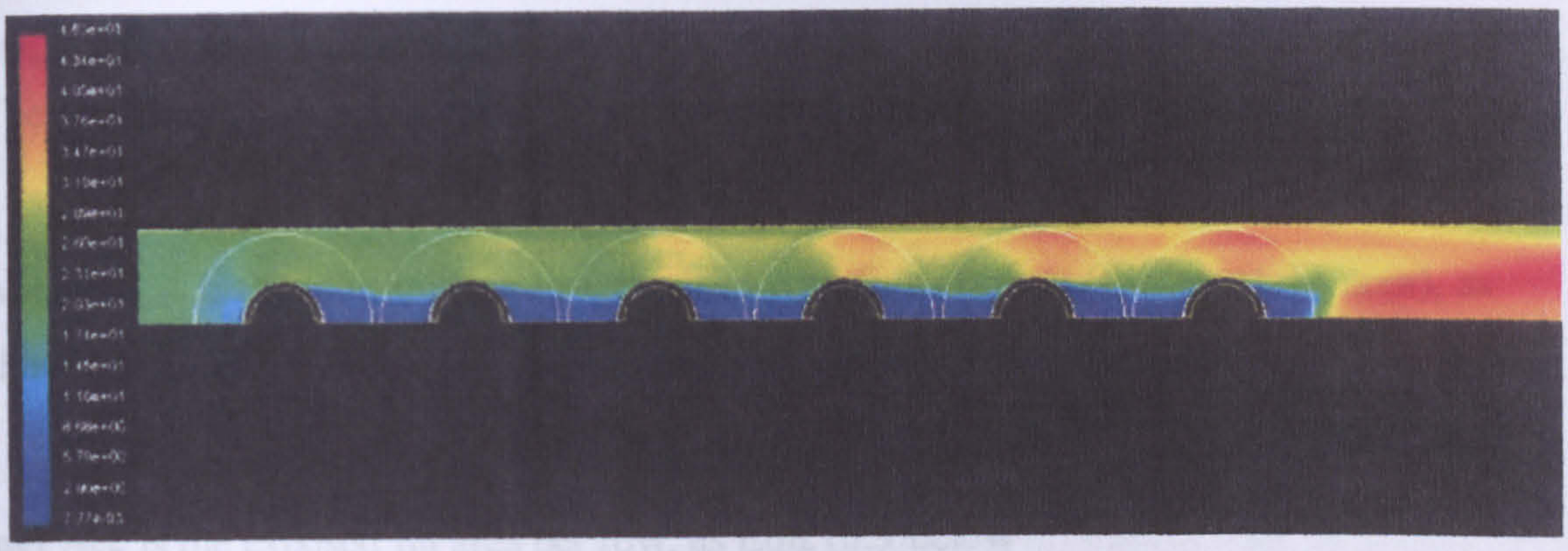

Figure 10.20: Turbulence intensity contours on centreline of Bundle 1

(mfr: 1.109kg/s)

It is not clear why the lower fin frequency bundle shows the second row turbulence intensity dip. It is thought that it occurs as follows:

- The first tube row incites more turbulence from the approach flow.
- For the reasons mentioned above about turbulent flow entrainment between fins, the second row creates a slight damping effect as this highly turbulent flow is marshalled between the fins of the second tube row.
- The separation over the back of the second tube row incites more turbulence than the third tube row can damp.
- This pattern continues through the rest of the tube rows, with the turbulence generation exceeding the damping, hence an overall rise, although smaller than that of the high fin frequency bundles.
- The turbulence intensity increases with increasing tube rows until the damping matches the generation, which although not shown in the results for this bundle is believed would occur in the ninth to tenth tube rows.

Hence low fin frequency has an effect on turbulence stability through the bundle

10.3 Data analysis

The methodology used to determine the local heat transfer was to use the mass weighted integral value of temperature noted above. These plane temperatures were used to treat every tube row as a separate entity using the calculation scheme listed below.

10.3.1 Geometry calculations

The total heat transferring surface area per row was calculated using Equ.10.1

$$A_{TotRow} = N_T \cdot (A_{Tube} + A_{Fin}) \qquad \text{(Equ.10.1)}$$

where A_{Tube} is the tube area per row exposed with fins in place (the bare tube area), as shown in Equ10.2

$$A_{Tube} = \pi D_r \cdot (L_T - s_f \cdot (L_T \cdot n_f)) \qquad \text{(Equ.10.2)}$$

and A_{Fin} is the exposed fin area per row, as Equ.10.3 below

$$A_{Fin} = ((\frac{\pi \cdot D_f^{\,2}}{4} - \frac{\pi \cdot D_r^{\,2}}{4}) \cdot 2 + (\pi \cdot s_f \cdot D_f)) \cdot (L_T \cdot n_f) \qquad \text{(Equ.10.3)}$$

The tube area per row with no fining (the base tube area), was then found from Equ.10.4

$$A_{BTRow} = N_T \cdot L_T \cdot (\pi \cdot D_r) \qquad \text{(Equ.10.4)}$$

10.3.2 Initial data

For the local row duty calculations to be carried out the local specific heat at constant pressure ($C_{p\,Local}$) was required. This was found from HTFS handbook sheet PM20 [94].

The data required to find the $C_{p\,Local}$ is the absolute pressure and the plane temperature. The calculation of properties over a row was taken at the bulk conditions. Therefore the local pressure was calculated from Equ.10.5 below

$$P_{LocalRow} = \frac{P_{In} + P_{Out}}{2} \qquad \text{(Equ.10.5)}$$

Where P_{In} is the pressure in the plane before the tube row in question, and P_{Out} is the pressure in the plane after the row in question.

The bulk temperature was calculated from Equ.10.6.

$$T_{LocalRow} = \frac{T_{In} + T_{Out}}{2} \qquad \text{(Equ.10.6)}$$

Where T_{In} is the temperature in the plane before the tube row in question, and T_{Out} is the temperature in the plane after the row in question.

10.3.3 Determining the row heat transfer coefficient from CFD data

The data from the CFD models was reduced as it would be from experimental results.

The airside duty of each tube row was calculated using Equ.10.7

$$Q_{Row} = Cp_{Local} \cdot mfr \cdot (T_{Out} - T_{In}) \qquad \text{(Equ.10.7)}$$

where mfr is the mass flow rate through the bundle.

The overall heat transfer coefficient per row (U_{Row}), referred to the base tube heat transferring surface was found from Equ.10.8.

$$U_{Row} = \frac{Q_{Row}}{LMTD_{Row} A_{BTRow}} \qquad \text{(Equ.10.8)}$$

The logarithmic mean temperature difference was used as it represents the two driving forces of the exchanger: the heating air and the cooling steam. This is shown in Equ.10.9

$$LMTD_{Row} = \frac{(T_{TubeIn} - T_{Out}) - (T_{TubeOut} - T_{In})}{\ln\left(\frac{T_{TubeIn} - T_{Out}}{T_{TubeOut} - T_{In}}\right)} \qquad \text{(Equ.10.9)}$$

where the equation was based on the preceding (T_{In}) and following (T_{Out}) planes mass weighted temperature value, and the process side temperatures (T_{TubeIn}, $T_{TubeOut}$) were those from the experimental results.

As the LMTD formula is applicable to crossflow only if a correction factor is used, the method and coefficient tables presented by Echarte [99] was investigated. It was found that the for all tube rows in all modelled cases the correction factor, F, over a given row varied between 0.9939 and 0.9994, and thus was considered negligible.

The airside heat transfer coefficient was calculated by removing the tube wall (α_{Wall}) and the tubeside heat transfer coefficient (α_{Tube}) from the overall heat transfer coefficient (U_{Row}) that was given in Equ.10.8. This is shown in Equ.10.10.

$$\alpha_{Row} = \frac{1}{\frac{1}{U_{Row}} - \frac{1}{\alpha_{Wall}} - \frac{1}{\alpha_{Tube}}} \qquad \text{(Equ.10.10)}$$

However, as the boundary conditions of the CFD models for the inside of the tube was set to a constant temperature, assumed to simulate isothermal condensation of steam inside the tubes, there was no tubeside coefficient (α_{Tube}) to be accounted for. Therefore the tubeside coefficient term was removed from Equ.10.10. Using the experimental data it was found that this incurred a maximum of 7% error in the calculation of the airside coefficient.

The tube wall heat transfer coefficient was calculated from Equ.10.11

$$\alpha_{Wall} = \frac{2k_t}{D_o \cdot \ln\left(\frac{D_o}{D_t}\right)} \qquad \text{(Equ.10.11)}$$

Where k_t is the thermal conductivity of the tube material (W/mK) and D_i is the tube internal diameter (m).

The airside coefficient (α_{Row}) was then referred to the base tube area to give the uncorrected airside heat transfer coefficient for the row, α_{Local}, as shown in Equ10.12

$$\alpha_{Local} = \alpha_{Row} \frac{A_{BTRow}}{A_{TotRow}} \qquad \text{(Equ.10.12)}$$

10.3.4 Classic Method

The above shows the method used to calculate the corrected airside row HTC in this study. Previously, researchers have studied the overall HTC based on the total outside surface area per row, so comparative analysis was performed to ensure that the results of this study were similar to those of other workers. Equ.10.13 was used to determine the overall HTC, h. The use of h rather than U in following sections is used to differentiate between previous workers results and the new results, although it is acknowledged they have the same meaning.

$$h = \frac{Q_{row}}{A_{TotRow} \cdot (T_{Out} - T_{In})} \qquad \text{(Equ.10.13)}$$

The parameters for the formula were evaluated from the Equs.10.1 and 10.7. Some results of this method can be seen in Section 10.4 below.

The approach used by previous workers is acceptable for single geometries, but is not suitable for comparisons of bundles of differing geometries, hence the weakness of previous studies for developing a generalised row effect model.

10.4 Heat transfer coefficient results

This section shows the calculated heat transfer coefficients for the bundles. For brevity the results are tabulated. For brevity the HTCs per row referred to the overall surface area (h) are presented only for Bundle 1. While the exact coefficients vary from bundle to bundle all exhibited the same trends. The local coefficient (α_{Local}) is shown for

Bundles 1 and 4, as Bundle 4 showed a turbulence-affected trend, which will be discussed in following sections.

10.4.1 Bundle1

10.4.1.1 Overall coefficient (h)

Tables 10.2 and 10.3 show the row averaged HTC based on the total surface area (h, Equ.10.13). It can be seen in both tables that the coefficient varies only very slightly from the first to last row.

MFR (kg/s)	0.637	0.739	0.865	1.109	0.406	0.637	0.739	0.865	1.109
Row									
1	92.41	107.20	125.37	160.81	58.96	92.41	107.20	125.37	160.80
2	92.47	107.26	125.43	160.89	59.01	92.47	107.26	125.45	160.87
3	92.53	107.32	125.50	160.98	59.05	92.54	107.32	125.53	160.94
4	92.59	107.38	125.56	161.06	59.09	92.59	107.37	125.59	161.01
5	-	-	-	-	59.11	92.63	107.42	125.65	161.08
6	-	-	-	-	59.13	92.67	107.46	125.70	161.13

Table 10.2: Row averaged heat transfer coefficients for Bundle 1 with 4 and 6 rows

MFR (kg/s)	0.406	0.637	0.739	0.865	1.109	0.406	0.637	0.739	0.865	1.109
Row										
1	58.96	92.40	107.20	125.37	160.80	58.97	92.40	107.20	125.37	160.80
2	59.01	92.46	107.26	125.43	160.87	59.02	92.46	107.26	125.43	160.87
3	59.05	92.51	107.32	125.50	160.95	59.07	92.51	107.32	125.50	160.94
4	59.09	92.56	107.37	125.56	161.02	59.11	92.56	107.37	125.56	161.02
5	59.11	92.60	107.42	125.62	161.08	59.14	92.60	107.42	125.62	161.08
6	59.14	92.64	107.46	125.66	161.14	59.16	92.64	107.46	125.66	161.14
7	59.15	92.67	107.49	125.70	161.19	59.18	92.66	107.49	125.70	161.19
8	59.17	92.69	107.52	125.73	161.23	59.19	92.69	107.52	125.73	161.23
9	-	-	-	-	-	59.20	92.71	107.54	125.76	161.27
10	-	-	-	-	-	59.21	92.73	107.56	125.78	161.30

Table 10.3: Overall row heat transfer coefficients for bundle 1 with 8 and 10 rows

10.4.1.2 Airside coefficient referred to bare tube area (α_{Local})

Tables 10.4 and 10.5 show the local row HTC (α_{Local}) derived from Equ.10.12 for the 4 and 6 and 8 and 10 row bundles respectively.

MFR (kg/s)	0.637	0.739	0.865	1.109	0.406	0.637	0.739	0.865	1.109
Row									
1	49.98	45.15	47.07	60.11	36.91	50.56	44.58	55.22	49.32
2	31.14	30.32	32.36	41.65	21.64	32.49	28.13	37.67	34.54
3	23.34	26.09	28.20	36.86	15.79	25.45	24.13	31.33	30.81
4	25.49	21.28	24.10	32.27	13.24	22.29	21.28	28.02	27.87
5	-	-	-	-	11.68	19.75	18.74	23.86	25.71
6	-	-	-	-	12.12	19.28	17.53	23.24	23.73
Bundle	32.48	30.71	32.93	42.72	17.75	25	27.95	31.12	33.66

Table 10.4: Corrected Row Heat transfer coefficients for bundle 1 with 4 and 6 rows with bundle overall HTC

MFR (kg/s)	0.406	0.637	0.739	0.865	1.109	0.406	0.637	0.739	0.865	1.109
Row										
1	36.78	43.32	45.32	48.52	52.28	40.48	43.34	44.59	47.01	49.96
2	21.97	27.33	28.21	31.56	33.57	26.51	26.65	28.04	32.42	35.02
3	16.26	22.57	24.28	27.93	31.36	21.02	22.64	24.41	27.91	31.39
4	13.22	19.21	21.04	24.11	27.96	18.42	19.21	17.71	24.09	28.54
5	12.12	17.41	19.11	21.78	25.48	17.27	17.35	22.38	21.67	24.89
6	11.78	16.29	17.71	20.20	23.73	16.90	16.35	17.80	20.23	23.69
7	12.07	16.15	17.40	19.71	22.96	16.51	16.18	17.36	19.73	23.01
8	11.90	15.64	16.41	19.22	22.80	16.05	15.88	16.91	19.12	22.14
9	-	-	-	-	-	15.08	16.07	16.64	18.79	21.66
10	-	-	-	-	-	14.41	17.69	16.08	18.86	22.08
Bundle	17.01	22.24	23.65	26.62	30.01	20.26	21.13	22.19	24.982	28.23

Table 10.5: Airside row heat transfer coefficients for bundle 1 with 8 and 10 rows with bundle overall HTC

The averaged HTC for the bundle is included at the bottom of each table. It will be shown that is the value from which the comparative correction factor will be derived.

10.4.2 Bundle 4

10.4.2.1 Overall Coefficient (h)

Table 10.6 shows the overall HTC based on the total surface area (h, Equ.10.13). It can be seen in that the coefficient does not vary much.

MFR (kg/s)	0.448	0.574	0.686	0.915	1.167
Row					
1	115.05	147.44	176.04	234.67	299.35
2	115.12	147.52	176.10	234.74	299.43
3	115.17	147.58	176.17	234.81	299.51
4	115.22	147.62	176.23	234.88	299.60
5	115.25	147.66	176.30	234.95	299.68
6	115.28	147.69	176.35	235.02	299.75

Table 10.6: Overall heat transfer coefficients for bundle 4 with 8 and 10 rows

10.4.2.2 Airside coefficient referred to bare tube area (α_{Local})

Table 10.7 shows the local row HTC (α_{Local}) derived from Equ.10.12 for the 6 and 8 row bundles respectively. Bundle 4 had a low fin frequency and it was thought that the wider fin spacing prevents the thermal boundary layers from touching across the fin surface; hence the first tube row demonstrates a very high thermal performance.

MFR (kg/s)	0.448	0.574	0.686	0.915	1.167
Row					
1	75.04	83.62	44.28	49.99	65.52
2	15.05	14.56	23.03	29.30	29.95
3	13.84	13.79	28.95	27.98	33.17
4	12.26	12.35	24.29	26.91	31.78
5	10.46	10.77	22.38	25.16	30.72
6	9.59	9.73	20.92	22.23	19.68
Bundle	22.71	24.14	27.31	30.26	35.14

Table 10.7: Corrected Row Heat transfer coefficients for bundle 4 with 6 rows with bundle overall HTC

10.4.3 Differences in data

It can be seen in the new results for the rows averaged heat transfer coefficient (h) results that they do not follow the same distinct pattern shown in Figure 2.5.2 by Yang and Bell [45] or implied by ESDU's [43] correction factors. The data of ESDU is strictly for plain tubes, however Yang and Bell's data must be examined.

They did not state what fin material they used, but as they were using serrated fins it was assumed they were steel, which would lower the overall transfer coefficient, ceteris paribus, when compared with aluminium, as modelled here. This means that their rise in overall row coefficient would likely be controlled by turbulent effects.

Critically no information on turbulence is present in their report, however it is accepted that serrated fins, by nature of the multiple edges and the aerodynamic excrescence effects that occur because of them, will generate more turbulence than a bundle with plain fins, and this builds quickly through the first few rows. Therefore it is believed that the data of Yang and Bell is correct for their case. The plain fin case treated here, with the turbulence intensity data presented in Section 10.2, is temperature controlled and showed a very slight rise in HTC (h). The comparison between the data of Yang and Bell and new data (Bundle 1, 10 rows) can be seen in Figure 10.21.

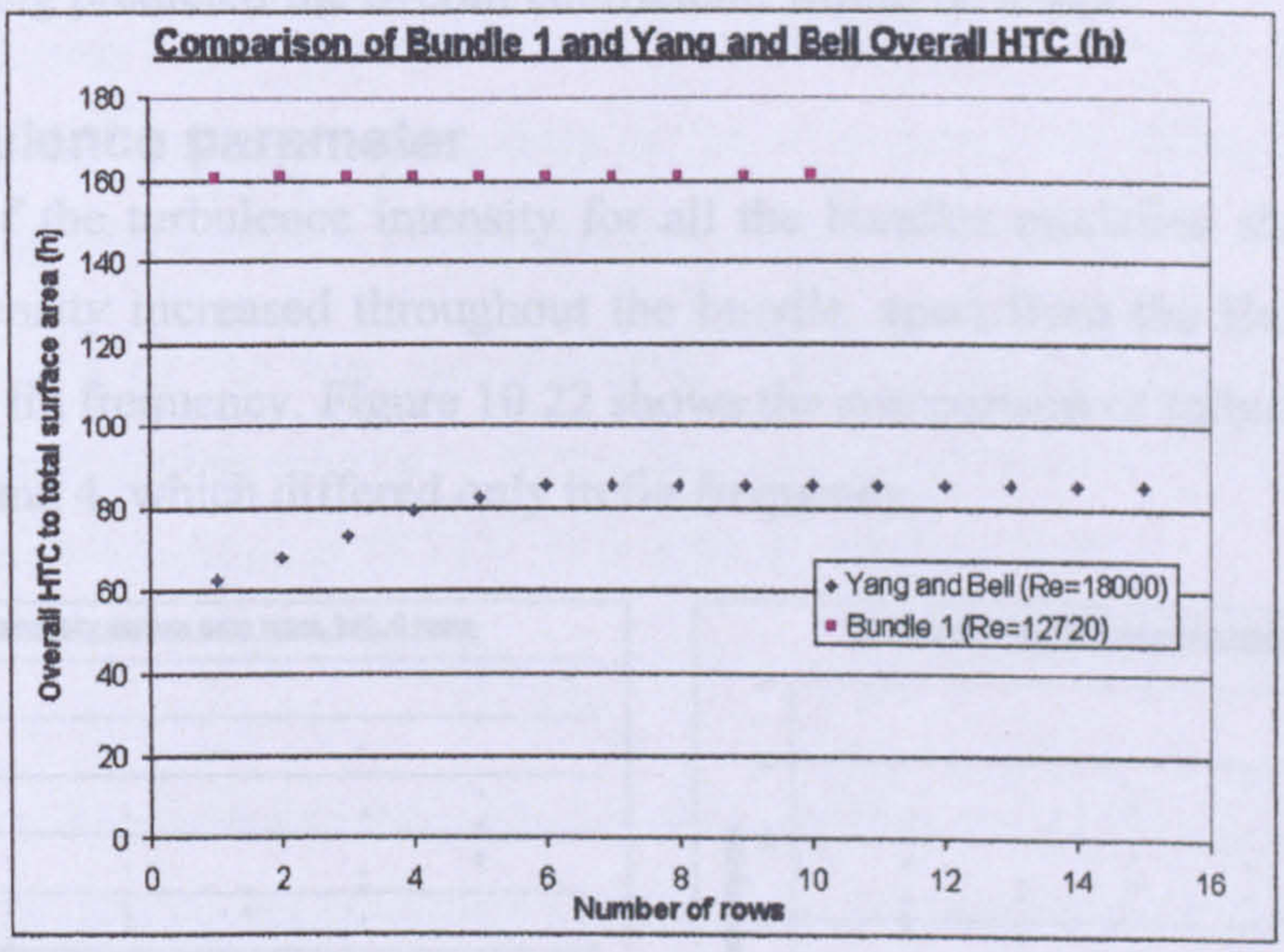

Figure 10.21: Comparison of trends between Bundle1 and the data of Yang and Bell

From all of this it is concluded that, despite the turbulence increase, the controlling factor in these new models is the temperature difference between the incoming air and the tube side steam. Hence the overall HTC (h) does not vary much, and hence any treatment that predicts, or discusses, the overall HTC could be misleading as to the duty of individual tubes, and it appears that the proposed treatment shown in section 10.3.3 is more desirable.

10.5 Prediction model

10.5.1 Model basis

Section 10.2 showed that the turbulence and the temperature difference are key factors. Specifically the turbulence intensity charts show that fin frequency plays an important role in the turbulence development. Therefore the new model uses a turbulence prediction term with respect to fin frequency, and a temperature difference component to predict a factor, by which the bundle airside coefficient needs to be modified by. It will be shown below how this HTC is predicted.

The correction term itself was derived from the difference between the overall bundle and the local coefficient. An example, with reference to Table 10.7, would be the last row for Bundle 4 with the mass flow rate of 0.448kg/s. The local coefficient was 9.59 and the overall coefficient 22.71. Therefore the correction needed to examine the sixth (last) row, having predicted the overall coefficient, would be 0.422.

10.5.2 Turbulence parameter

Examination of the turbulence intensity for all the bundles modelled showed that the turbulence intensity increased throughout the bundle, apart from the Bundle 4, which had the lowest fin frequency. Figure 10.22 shows the comparison of turbulence intensity for Bundles 1 and 4, which differed only in fin frequency.

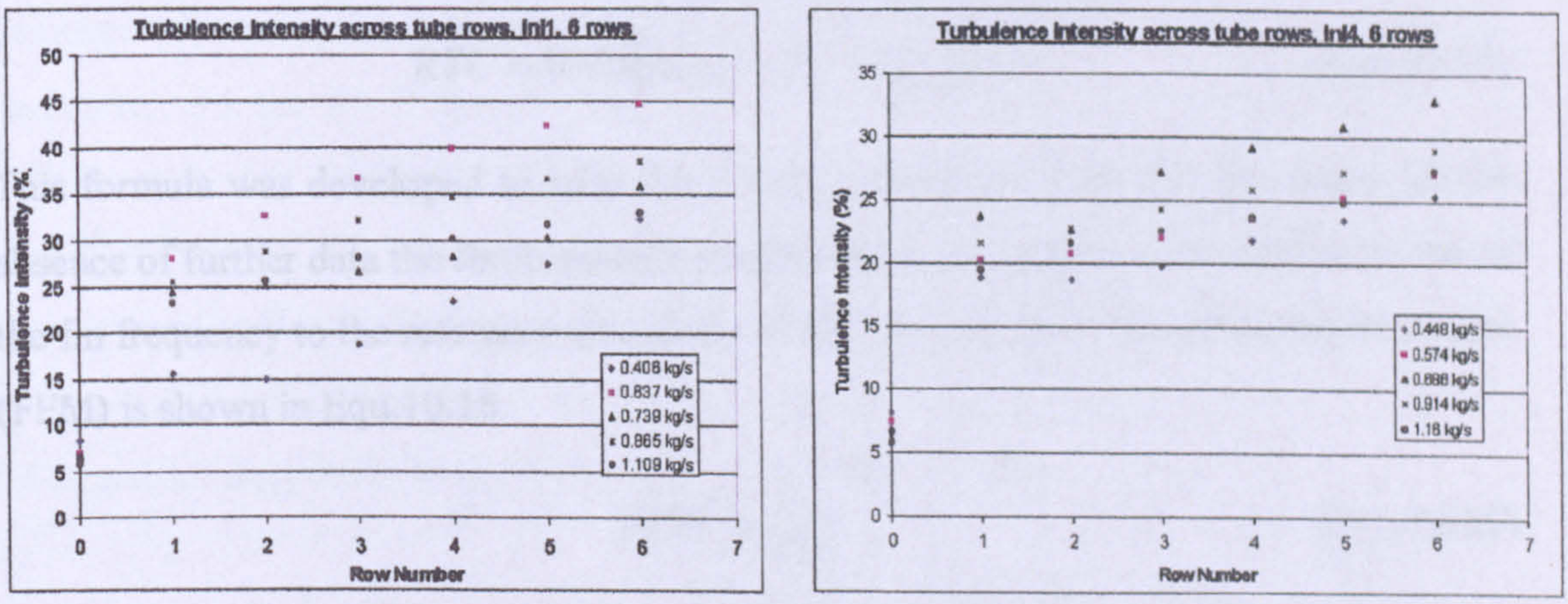

a. b.

Figure 10.22: Comparison of turbulence intensity for a. Bundle 1, 433 fins/m and b. Bundle 4, 236 fins/m

The intensity, as noted in Section 10.2.2, is a function of the turbulent kinetic energy and the magnitude of approach velocity, so the trend is arguably as important as the actual values. This will be shown below in the finished model.

It can be seen in Figure 10.22 that the bundle with 433 fins/m show an increase in turbulence intensity with increasing row number (n_r). The dimensionless turbulence intensity term given in Equ.10.14 was determined to be the optimum fit to predict turbulence intensity for a given row, referred to the freestream inlet intensity. It must be stressed that the denominator figure is a combined average from these tests, and could vary if either a forced draught or induced draught fan system is used, due to differing turbulence intensities.

$$IT_{Pred} = \frac{7.127 \cdot \ln(n_{Row}) + 19.909}{8.5} \qquad \text{(Equ.10.14)}$$

This formulation was found to match the higher fin frequency bundles patterns well, however the low fin frequency with its drop on the second row and differing rise pattern required a modification from this logarithmic rise.

As the second row of the low fin frequency bundle appeared to be causing the difference a formula was developed to fit the intensity pattern based on the row number, the Row Turbulence Coefficient (RTC). This is shown in Equ.10.15

$$RTC = 0.45\left(\left[(n_{Row} - 2)^2 \cdot n_{Row}\right] + 1\right)^{-4.2} \qquad \text{(Equ.10.15)}$$

This formula was developed to raise (or lower) a function of the fin frequency. In the absence of further data the fin frequency function was determined to be simply a ratio of the fin frequency to the reference frequency of 433 fins/m. This Fin Frequency Function (FFM) is shown in Equ.10.16.

$$FFM = \frac{n_f}{433}^{RTC} \qquad \text{(Equ.10.16)}$$

It is recommended that if $n_f \geq 433$ then Equ.10.14 is used as the turbulence intensity prediction in the final model, which will be presented in the following sections. If $n_f < 433$ then Equs.10.14 and 10.16 should be combined, as shown in Equ.10.17.

$$IT_{Pred} = IT_{Pred} \cdot FFM \qquad \text{(Equ.10.17)}$$

During development of the model there was surprisingly no dependence found on the mass flow rate. It will be explained below why, at this stage, this is not critical to the model.

10.5.3 Influence of temperature

In all the cases used for the model development the temperature of the tube is higher than that of the incoming air. As the initial temperature difference between the incoming air and the tubeside temperature was shown to be a driving factor in the heat transfer process, a dimensionless parameter was needed to express this. From the temperature difference plots discussed in Section 10.2.8 it is shown that the temperature difference decreases with increasing row number, and this can be expressed as a power function. Therefore the local row number was combined with the initial temperature difference to produce a new dimensionless parameter. This is shown in Equ.10.18.

$$\frac{T_{Tube}}{T_{AirFace}} \cdot n_{Row} \qquad \text{(Equ.10.18)}$$

where T_{Tube} is the tubeside temperature (K), assuming a constant isothermal condensation, and $T_{AirFace}$ is the temperature (K) of the incoming air.

10.5.4 Fin frequency

It is assumed that the turbulence intensity prediction (Equ.10.14 or 10.17) accounts for the turbulence component of the row effect, and Equ.10.18 is the temperature difference parameter. As the fin frequency has been shown to have a large effect on the row behaviour it was decided to include a direct scaling term. This term is shown in Equ.10.19 to have two components; the fin frequency and the mean fin thickness. These were chosen as the thicker fins used in heat recovery applications, when combined with the typical lower fin frequency, would hopefully provide a scaling parameter that would be of similar magnitude to the air coolers used to develop these models.

$$sf \cdot n_f \qquad \text{(Equ.10.19)}$$

where n_f is the fin frequency (1/m) and s_f is the mean fin thickness (m).

10.5.5 Complete model

The components of the model shown in Equs.10.18 and 10.19 were assembled against the determined correction factor divided by Equ.10.14 (or 10.17 for the low fin frequency bundle) and the exponents derived using a regression. The model was then

compared with the experimental value and a correlation constant determined. The final model is shown in Equ.10.20

$$C_{Row} = 1.089 \cdot \left(\frac{T_{Tube}}{T_{AirFace}} n_{Row} \right)^{-0.702} \left(s_f \cdot n_f \right)^{0.166} IT_{Pred} \qquad \text{(Equ.10.20)}$$

Based on the statements made in Section 10.5.3 it is proposed that Equ.10.20 may be rearranged to be applicable for heat recovery applications (where $T_{AirFace} > T_{Tube}$).

$$C_{Row} = 1.089 \cdot \left(\frac{T_{AirFace}}{T_{Tube}} n_{Row} \right)^{-0.702} \left(s_f \cdot n_f \right)^{0.166} IT_{Pred} \qquad \text{(Equ.10.21)}$$

It must be noted that there is no data available to test this theory.

10.6 Application of the model

To use the proposed correction factor the overall uncorrected bundle heat transfer coefficient (α) must be calculated using the new inline bundle j factor prediction method given in Chapter 7. The procedure for this is given in Appendix B. The coefficient then has the fin efficiency and surface effectiveness removed, as described in Appendix C, to arrive at the corrected coefficient (α_c). The row correction factor can then be calculated as above for the desired row (n_r), using Equ.10.20 (or Equ.10.21). The product of the correction factor (C_{Row}) and the corrected bundle overall coefficient (α_c) will yield the local, corrected HTC, as shown in Equ.10.22.

$$\alpha_{Local} = C_{Row} \cdot \alpha_c \qquad \text{(Equ.10.22)}$$

Using the inline prediction method automatically includes the flow velocity in the overall calculation, and hence removes the need for a mass flow rate (or velocity) based term in the turbulence model.

10.7 Data prediction

10.7.1 Deviations from data

Figure 10.23 shows the percentage deviation of the predicted correction factor (using the new method) from the calculated correction factor, as described in Section 10.5.1.

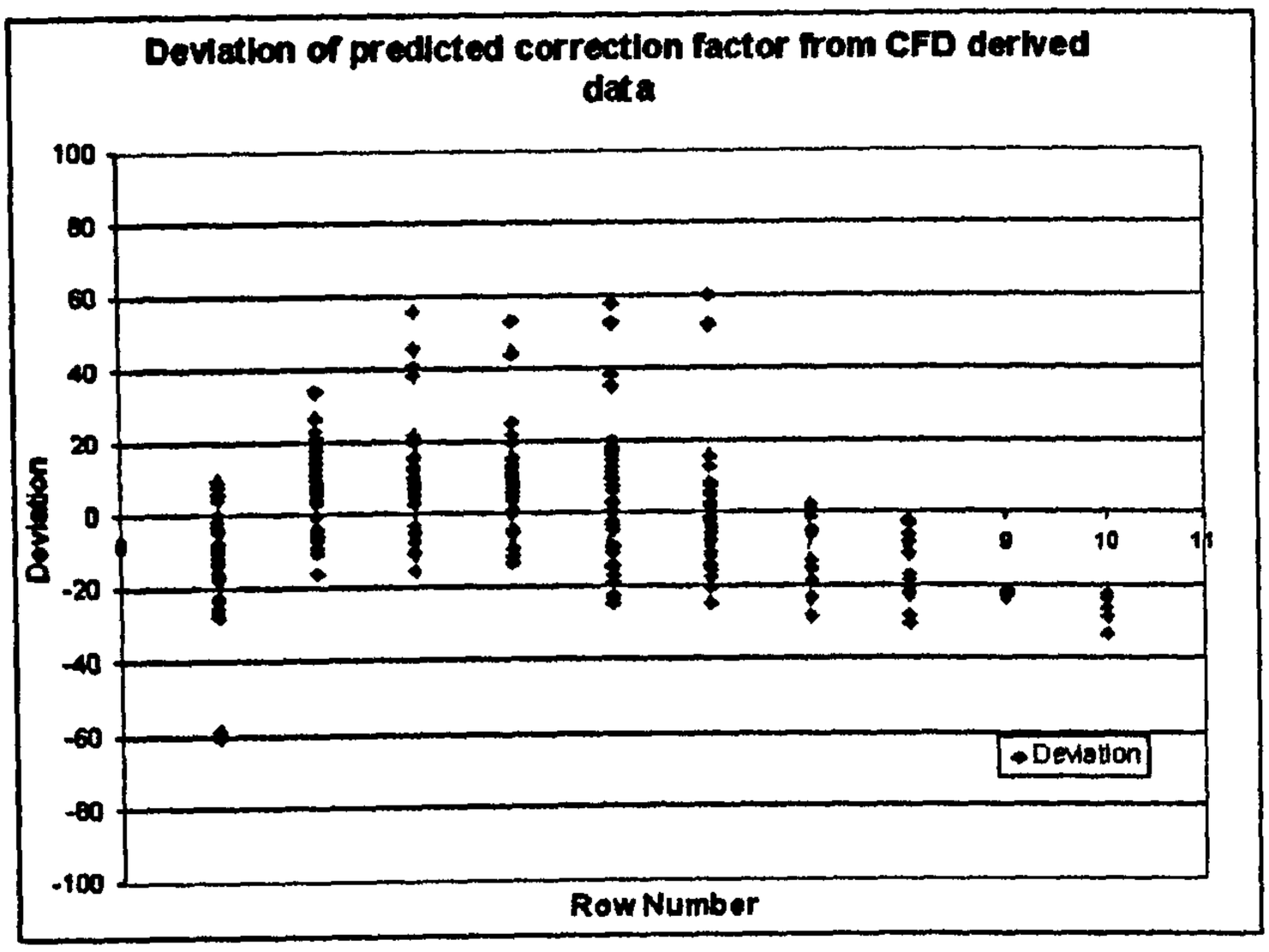

Figure 10.23: Percentage deviations of model predicted correction factor from the CFD derived data

It can be seen that the correction factor is fairly well predicted. 88.9% of all of the data was predicted within ±20% deviation, and 62.1% within ±10%. The standard deviation was 17.99%, skewed by the outlying data, however the spread about the 0 deviation line meant that the RMS deviation was a very low 1.06. The group of –60% deviations on the first row are attributable to Bundle 4, which exhibits a very high first row correction factor, which was difficult to replicate with the model, while adhering to the temperature and turbulence behaviour.

10.7.2 Comparison of calculated correction factors and predicted correction factors

Figure 10.24, 10.25, 10.26 and 10.27 show the comparisons of the calculated correction factors (CFD data) with the predicted correction factors (New model) for Bundles 1, 3, 4 and 9 respectively. The new prediction method is essentially a correlated model and so will only predict one correction factor for a given row number. Whereas, due to the CFD and exact HTCs the calculated data was developed from, the calculated correction factor will vary slightly, hence multiple points on the charts.

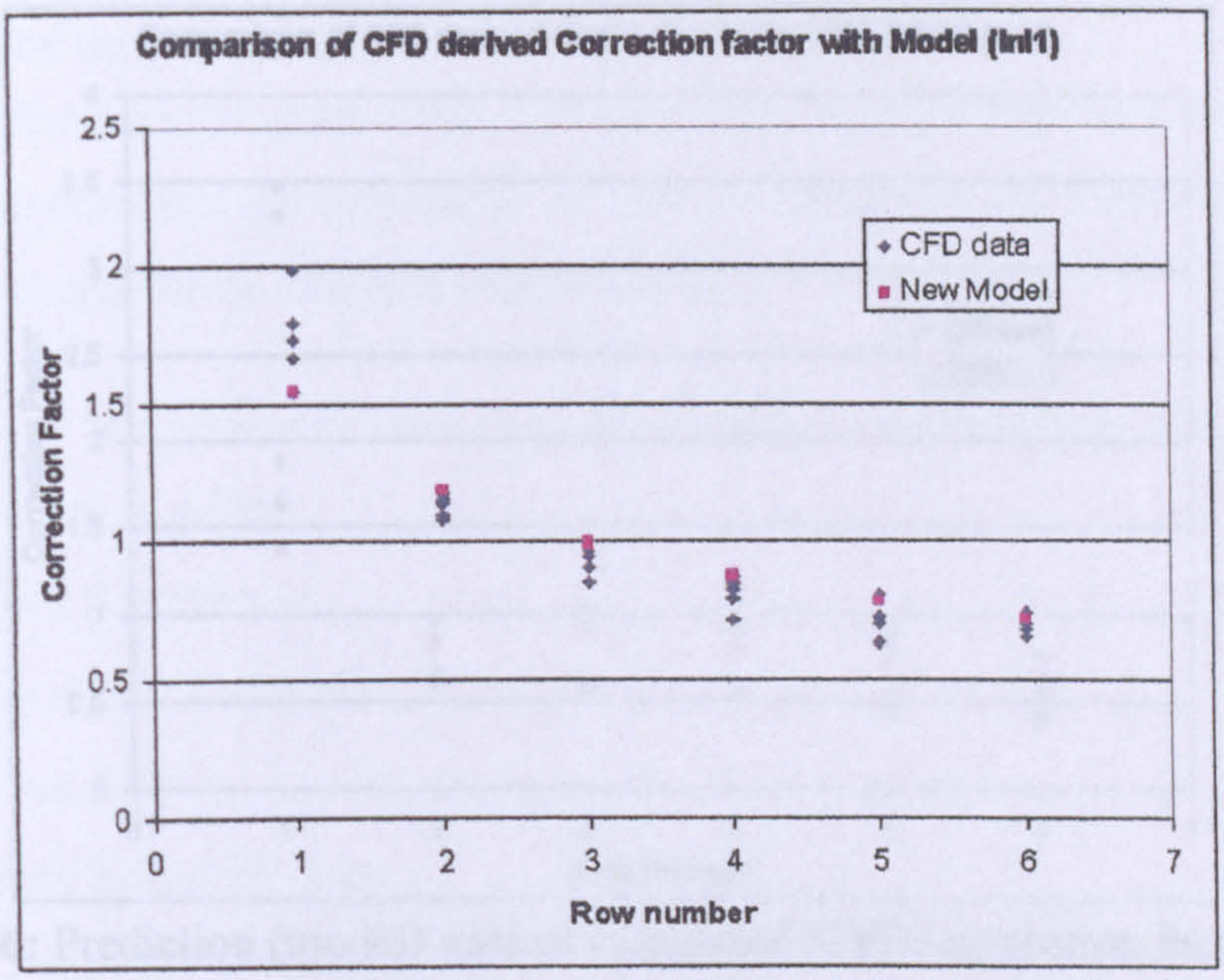

Figure 10.24: Prediction (model) against calculated (CFD) correction factor, Bundle 1

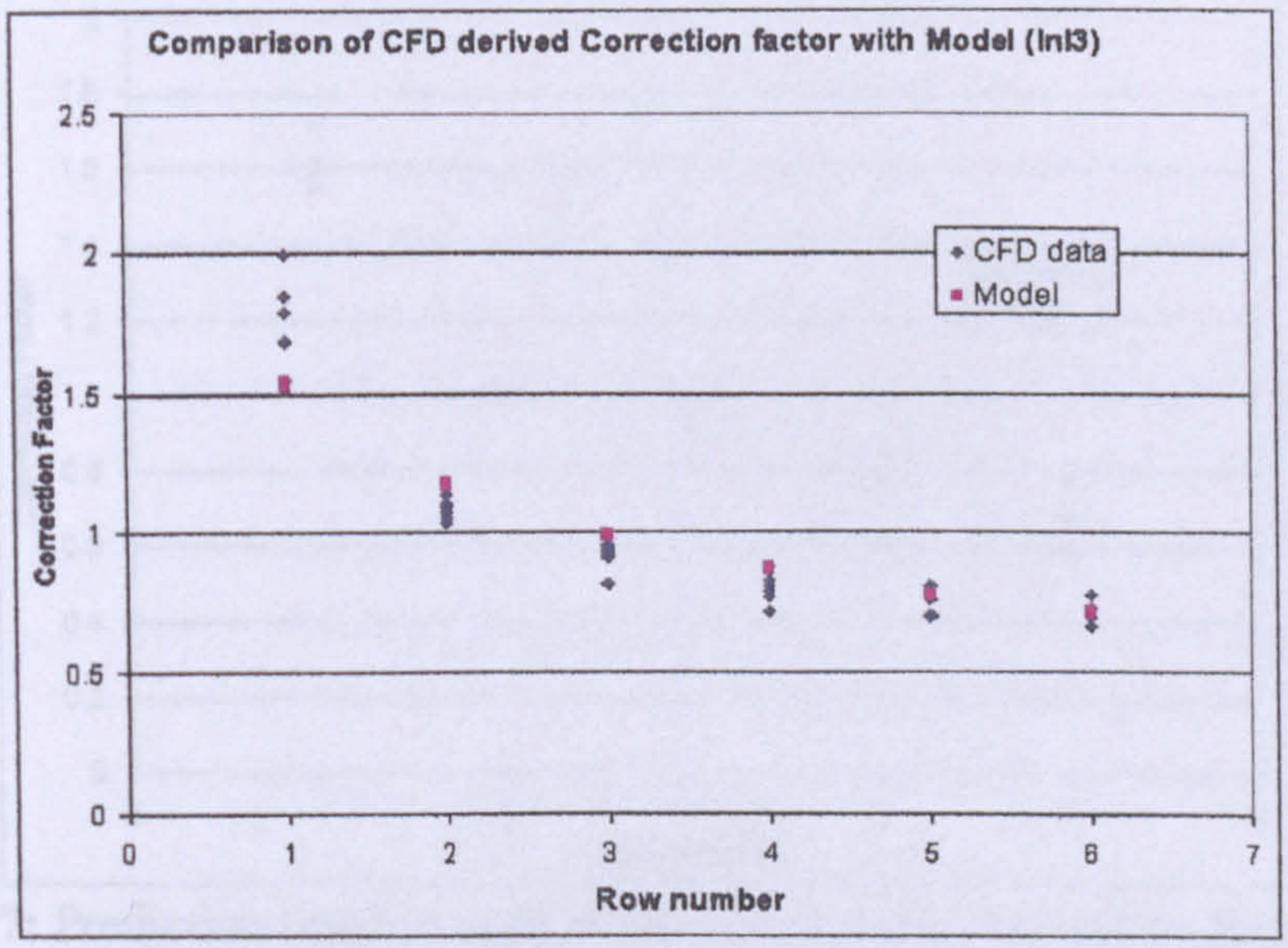

Figure 10.25: Prediction (model) against calculated (CFD) correction factor, Bundle 3

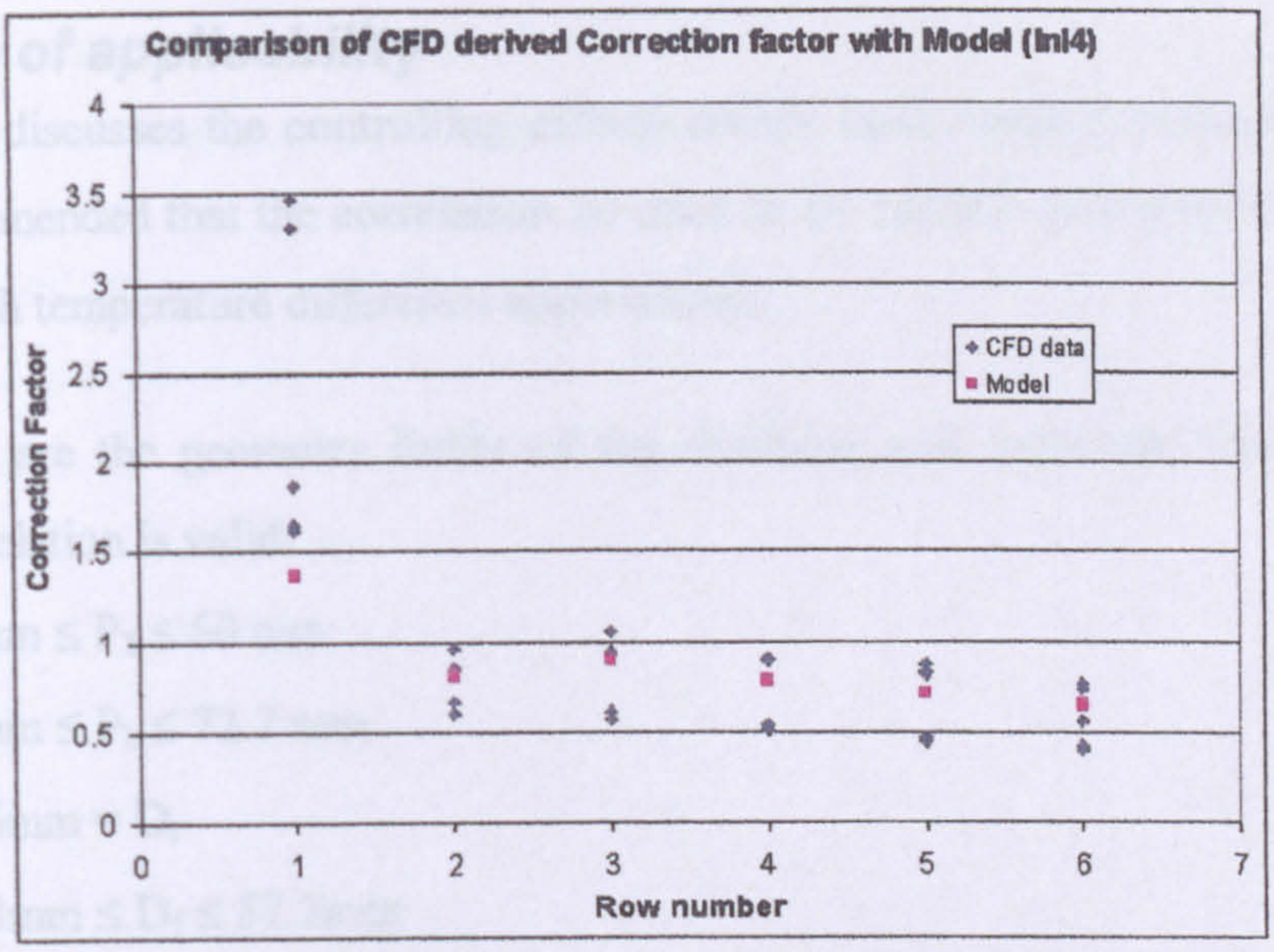

Figure 10.26: Prediction (model) against calculated (CFD) correction factor, Bundle 4

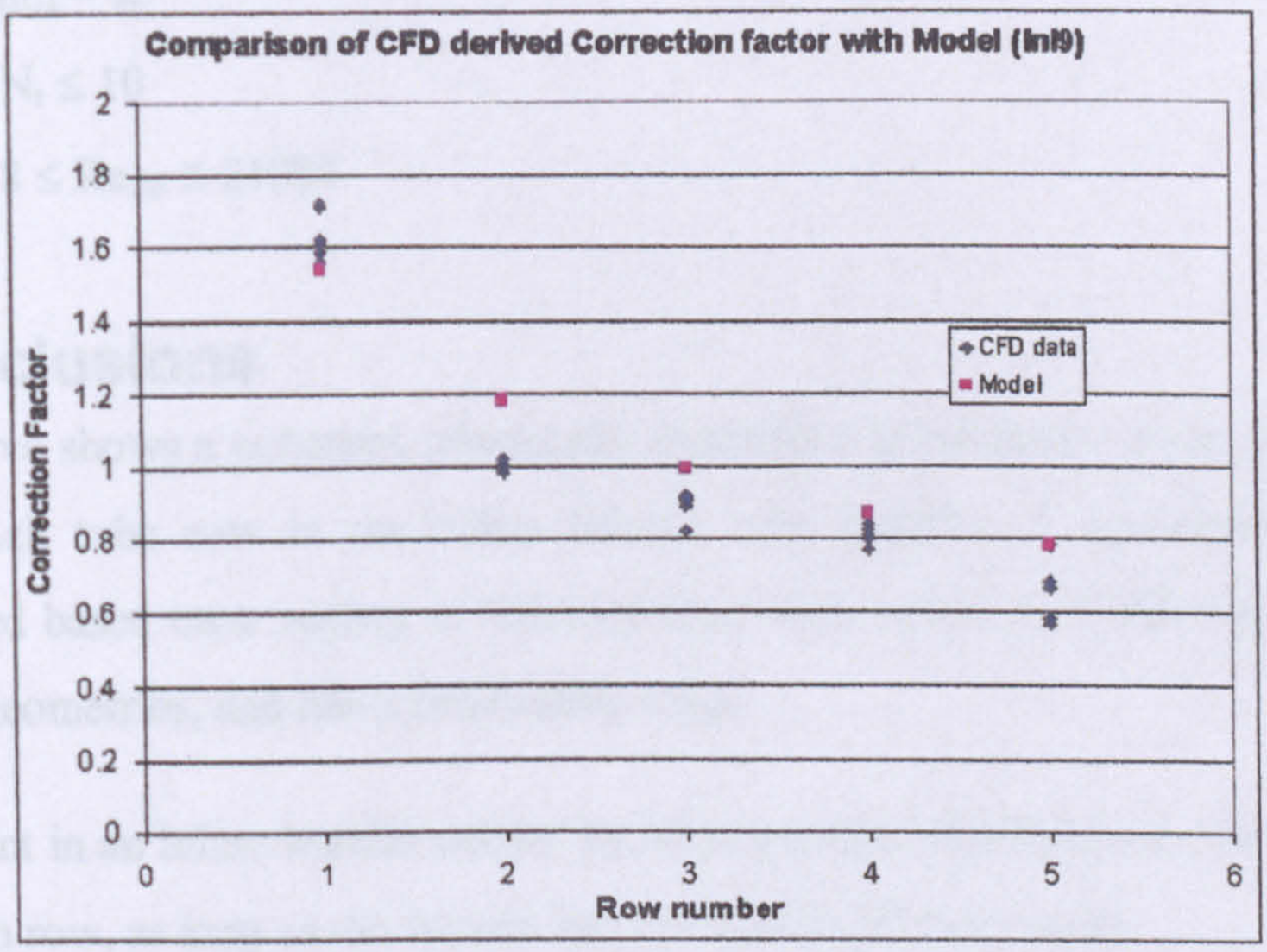

Figure 10.27: Prediction (model) against calculated (CFD) correction factor, Bundle 1

The above Figures show that the correction factor model replicates trends very well and is generally a good fit for the data. The value of the turbulence prediction model can be seen especially well in Figure 10.26.

10.8 Range of applicability

Section 10.4.4 discusses the controlling effects on the heat transfer process, and from this it is recommended that the correlation be used in air-cooled condensation and other isothermal, high temperature difference applications.

The following are the geometry limits of the database and represent the range over which the correlation is valid:

- $54mm \leq P_T \leq 60$ mm
- $54mm \leq P_L \leq 72.7$ mm
- $25.6mm = D_r$
- $50.8mm \leq D_f \leq 57.2mm$
- $236 \leq n_f \leq 433$
- $0.2mm = s_f$
- $4 \leq N_r \leq 10$
- $4618 \leq Re_{Do} \leq 21083$

10.9 Conclusions

- The above shows a coherent, physically explained assessment of the heat transfer from each tube row in an inline finned tube bundle. A correlated model is presented based on a variety of bundles that were tested on CFD using inline air cooler geometries, and has a reasonable range.

- The point in an inline bundle where the heat transfer stabilises was shown to be at the sixth row, as long as the bundle has more than six tube rows.

- Yang and Bell [45] describe their corrections from the standpoint of applying a correction factor to modify the calculated uncorrected coefficient. By their own admission their model "explains everything and predicts nothing", and without detailed, and difficult to collect, information it is believed that their model will be largely useless. Therefore it is suggested that the new method presented above is the only model for determining a single row's HTC in an inline finned tube bundles of practical value.

- The study also shows the value of using CFD to augment experimental testing by providing local examination that can aid method development.

- The method requires experimental validation, and careful consideration of a method to measure and characterise the turbulence both entering and exiting any test bundles.

CHAPTER 11

Conclusions and suggestions for further work

11.0 Conclusions and recommendations for further work

This chapter details the results of the project and possible follow up areas of research that could be conducted to improve on or extend the range of the work presented in the preceding chapters.

11.1 Conclusions

The main conclusions of the thesis is summarised and are in the same order as presented in the thesis.

Model for heat transfer and pressure drop prediction of staggered bundles

A new method for prediction of heat transfer and pressure drop performance of staggered layout finned tube bundles has been developed, and shown to outperform existing open literature methods. It has also solved the problem for deep tube bundles with small fin gaps of the previous best available model, HTFS2.

A new approach is presented to model the flow across staggered tube bundles through the use of an effective gap ratio term. This term seems to accurately represent the change in pressure drop due to change in tube layout arrangement over a wide range of flow Reynolds number

Model for heat transfer and pressure drop prediction of inline bundles

A new method of predicting pressure drop and heat transfer of inline bundles was developed that has strong links to realistic flow processes and observations. The method was shown to out-perform the other available methods. It predicted far more data than the other methods, and proved to behave in a manner that will allow extrapolation outside of the ranges of its database.

The method takes into consideration physical flow behaviour through the bundle and uses a method of calculating a gap loss coefficient that takes account of local boundary layer formation on the extended surface. This approach accurately express the strength of the bypass flow in the fin gap and consequently the influence on pressure drop and heat transfer. The influence of horseshoe vortices was also explored and shown to have little effect on the performance, under most operating conditions.

This model has been developed from a review of the open literature and CFD analysis of data from the NEL Multi-Purpose Wind Tunnel.

Pressure drop prediction method for bundles with bypassing flow

Bypassing of flow around the edges of bundles was examined, and a method of predicting the mass flow split and pressure drop across a bypassing bundle was developed that is applicable to small and large diameter tube bundles

Apparently no method existed to account for the influence of corbel shape on bundle pressure drop. This has been addressed in Chapter 8 and the model presented is simple to use and covers the most widely used wall sealing devices.

The corbel model presented in this study will enhance the accuracy of the new staggered bundle method (Chapter 6) when corbel shapes other than the half tube corbel are used.

The influence of corbel shape will be more significant for bundles with small number of tubes per row, typically the case with heat recovery applications.

Model for the prediction of heat transfer and pressure drop of bundles with bypassing flow

No finned tube bundle bypassing pressure drop calculation method has apparently been reported. The new bypassing model, described in Chapter 9, was developed from air cooler data, but demonstrated that it was applicable to heat recovery bundles.

Experimental pressure drops with half tube corbels and with bypassing were compared and it was demonstrated that a mass migration must have been occurring to lead to a lower pressure drop. It was shown that the level of mass migration increases with increasing flow velocity.

The new method predicts the data very well for the air cooler and showed a good qualitative result for the heat recovery bundle. The expected physical behaviour was demonstrated from the model for extrapolated cases.

Model for the prediction of the heat transfer of individual tube rows

A method of determining the heat transfer of individual tube rows for isothermally condensing inline tube bundles was presented with a two component model that

evaluates the driving force; turbulence or temperature. It has been demonstrated that calculating the airside coefficient, rather than the overall coefficient based on the total surface area improves understanding of the performance of each tube row. Other workers have not done this previously, and therefore it is believed that this makes the new method superior.

The point in an inline bundle where the heat transfer stabilises was shown to be at the sixth row, as long as the bundle has more than six tube rows.

It is not clear whether the method is suitable for bundles where the tubeside fluid is a multi pass arrangement, therefore it is limited to single pass applications. The method is also limited to isothermal condensation applications.

The model is simple to use and is believed to be the only practical method available that covers a range of geometries.

11.2 Recommended improvements/development

This section describes future/continuing research that could be carried out to improve understanding of the thermal and hydraulic processes occurring in finned tube bundles and to improve their modelling.

Staggered bundles

The principles of boundary layer build up on fins and the effects of horseshoe vortices that was discussed and modelled for the inline tube bundles could be applied to the staggered model. The principle of virtual blockages on the fin due to boundary layer appears to have a sound theoretical basis, but does not seem to be treated in any literature. Therefore a study of a scaled up single section of a heated finned tube may provide both pressure loss and heat distribution data. Figure 11.1 below shows a section of finned tube with an electrical resistance heater embedded in it. The surface of the fin and tube would be coated with heat sensitive liquid crystal paint, and the wind tunnel started. The heater would then be activated and the tube would be allowed to reach steady state. The results of temperature contours could then be examined, especially at higher Re flows to look for evidence of temperature effects from horseshoe vortices. Differing fin and/or tube diameters would be used, and following tubes made in the same way would eventually be placed behind this first tube to study the interaction of tube spacing and placement on heat transfer.

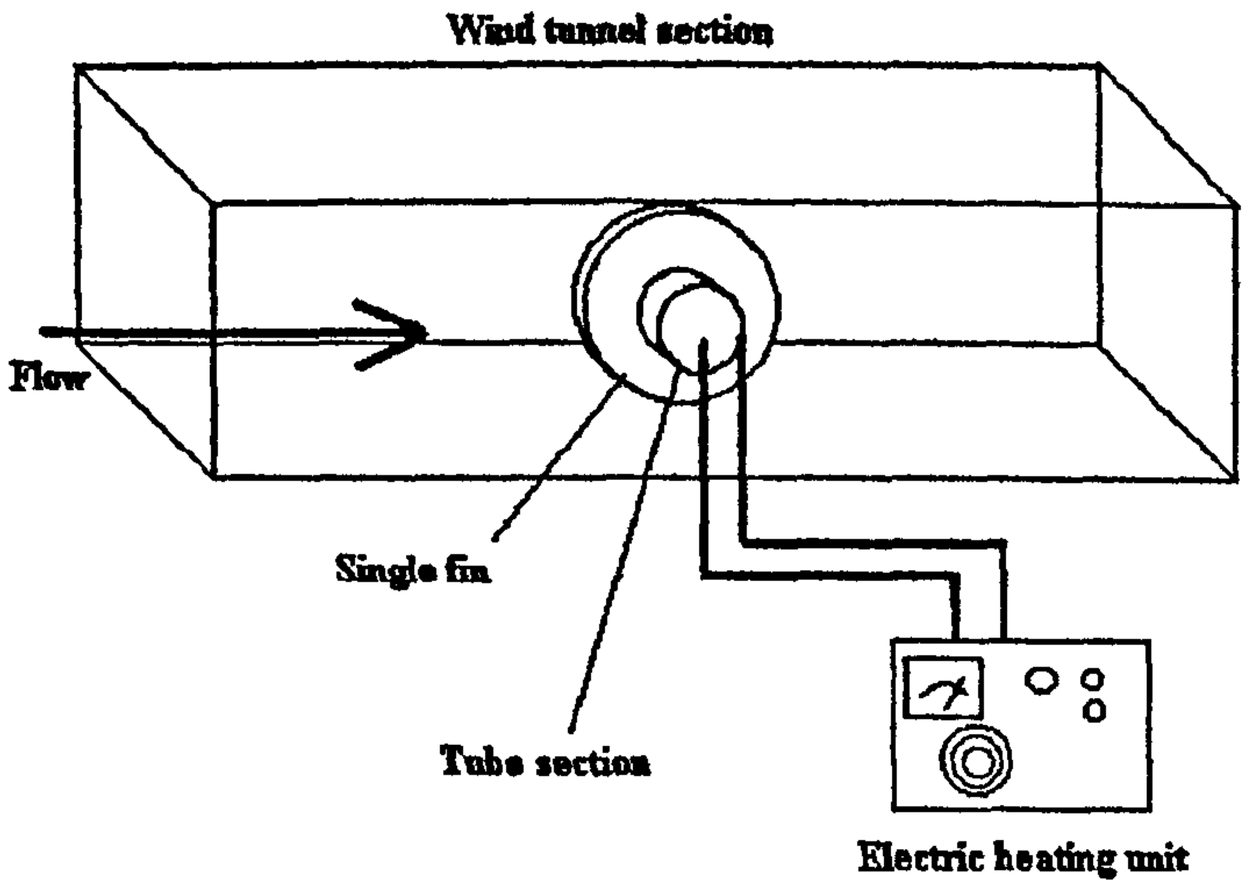

Figure 11.1: Proposed single fin heat transfer experiment.

The drag effects would be determined by the mounting of the tube section on a spring balance, such as that used for aerodynamic scale model testing.

A water tunnel approach could also be used using dye releases in the fin tips and high-speed photography to observe the development of boundary layers over the fin.

Inline bundles

A method to determine the average boundary layer thickness on the fins using more discrete steps should be pursued. The generalised velocities, as shown for the tube centreline, tube top and the high fin region, would need to be found at a few more points, but it is believed that this may improve the average boundary layer thickness, and improve the gap loss coefficient calculation.

Bundles with corbels

- Given the nature of the test apparatus designed for these experiments could be conducted very cost effectively to broaden the range of the presented model, such as an increased number of tube rows.

- The effect of corbels on heat transfer performance was not tested in this study, and it is recommended that bundles be designed to allow measurements to be made on the heat transfer performance. It is acknowledged that if the corbels are performing as expected there should be little or no difference in performance.

- 3D CFD could be used to study the local effects around the fin tips and between the fins at the tubes nearest the floor/roof panels. This would build on the understanding developed from the 2D results shown in Chapter 8, and could potentially lead to a better segregated corbelled bundle model as shown in Figure 11.2.

It is anticipated that a model of this type would allow a perfect bundle pressure drop calculation to take place in parallel with a corbel lane model that includes a more physically based corbel model and a half tube calculation that took into account the specialised flow phenomena that only occurs in the corbel lane. This model would most likely use an iterative procedure to determine the mass flow splits that would allow a specialised heat transfer calculation to take place to account for the thermal flow effects in the near wall region.

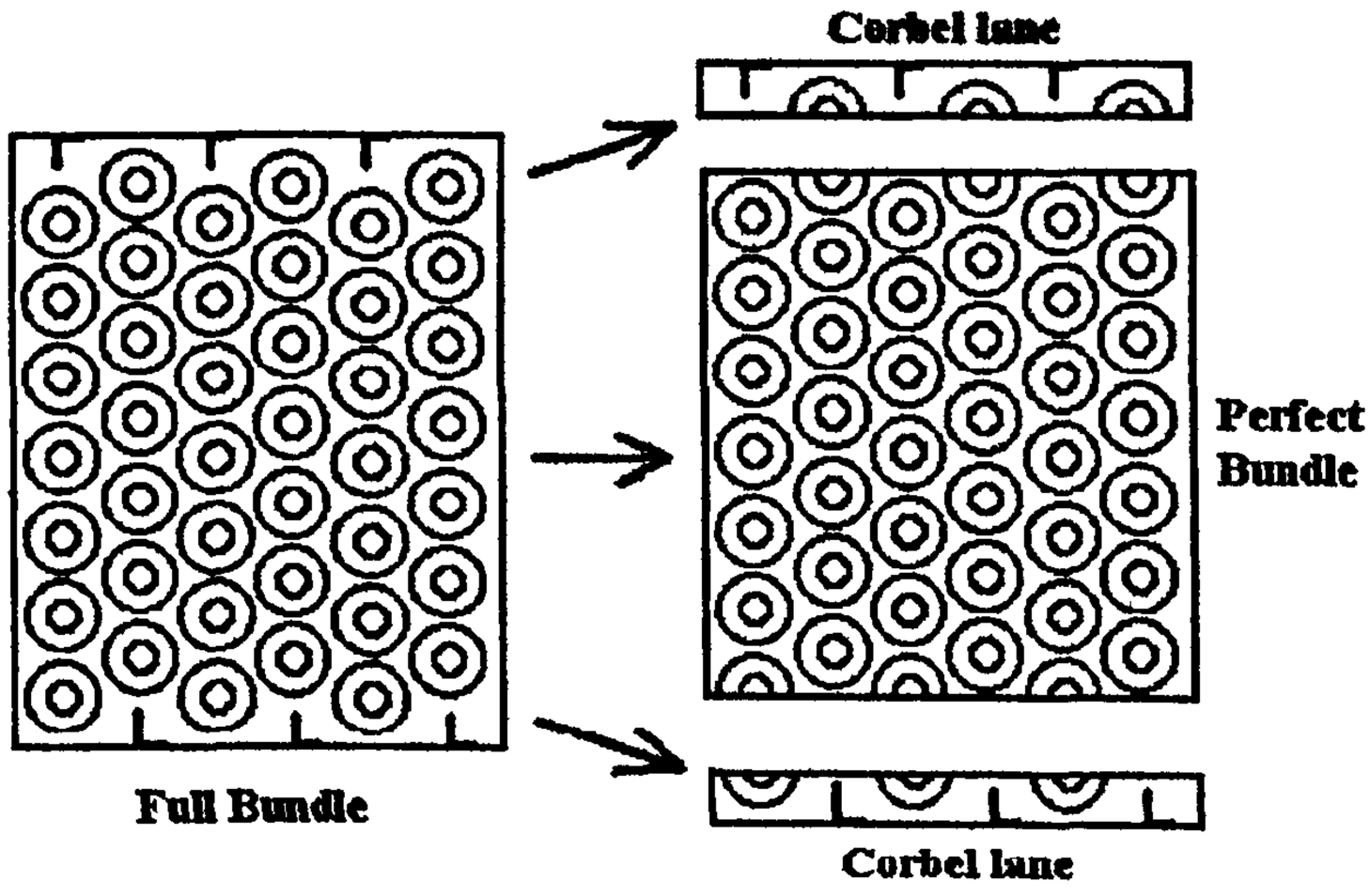

Figure 11.2: Schematic of segregated model

Bundles with bypassing flow

- The results would suggest that a further study involving heat transfer should be carried out. It is suggested that at least two air cooler bundles with differing bypass widths be tested, to verify the assumptions of excluding the bypass mass flow from the heat transfer calculations.
- It is suggested that the flexibility of the current experimental apparatus would allow the tubes and frame to be re-used.
- It was shown in Chapter 9 that the mass transfer from the bundle to the bypass lane may not be linear, and hence the heat transfer from each tube row will vary row-to-row. It is recommended that a *3D CFD* investigation of a test bundle with bypassing be carried out to try and quantify the mass loss. This would aid in the development of a heat transfer prediction method, and it is envisaged that this would take the form of a row weighted mass flow rate that would be used in a j factor prediction.

Examining the row effect and row heat transfer

- A review of work on forced and induced draught operation for ACHEs should be conducted. The approach turbulence has been shown to have a large influence on the bundle turbulence development and hence heat transfer. This could prove critical to the application of the new model.

- A CFD study should be carried out to determine the methods suitability for heat recovery applications, especially at high temperatures where radiant heat transfer may have an influence. The data in the HTWT section of the HTFS databank could provide validation for this.

- It is recommended that turbulence measurements be made upstream and downstream on any future test bundles, as it is clear that this is a topic of great importance in the understanding and construction of a complete model of the row effect on heat transfer.

- The analysis and method shown in Chapter 10 could be performed on staggered arrangement bundles using the data in the HTFS databank to provide validation for the CFD models. The same procedure would be used, and heat recovery bundles should be included to ensure a broad applicability of the resultant method.

- The row effect question for both inline and staggered layout bundles is clouded by the issue of turbulence. To resolve the variation seen by researchers, discussed in Section 2.5.4, tests with varying levels of approach turbulence could be conducted and the local and overall heat transfer measured. Without a study of this nature claims of heat transfer stability can only be made for individual bundles.

References

[1] Kleinschmidt, R.V., Parsons, S.R., "Head resistance of radiator cores", NACA Fifth Annual Report, Report No.61 (1920)

[2] Kays W.M, London, A.L. "Compact heat exchangers", The National Press, Palo Alto, California, (1955)

[3] Briggs, D.E., Young, E.H., "Convection Heat Transfer and Pressure Drop of Air Flowing Across Triangular Pitch Banks of Finned Tubes" ***Chemical Engineering Progress***, Symposium Series, Vol.59, No.41, pp1-9 (1963)

[4] Schmidt, E., "Heat Transfer at Finned Tubes And Computation of Tube Bank Heat Exchangers.", ***Kaltertechnik***, Vol.15, p 98 and Vol.15, p 370 (1963)

[5] Jameson, S.L., "Tube spacing in finned tube banks", ***ASME Transcripts***, Vol.67, No.8, pp 633-642, (1945)

[6] Brauer, H., "Heat and flow investigations on finned tube banks subject to transverse flow Part 1: Experimental systems and results at high pressure", ***Chemie-Ingr-Tech.*** Vol.33, No.5, pp 327-335. (1961)

[7] Brauer, H., "Heat and flow investigations on finned tube banks subject to transverse flow Part 2: influence of fin and tube arrangements", ***Chemie-Ingr-Tech.*** Vol.33, No.6, pp 431-438. (1961)

[8] Brauer, H., "Spiral-fin tubes for crossflow heat exchangers", ***Kaltetechnik,*** Vol. 13, No. 8, pp 274-279 (1961)

[9] Brauer, H, "Heat transfer and flow resistance with inline and staggered finned tubes", ***Dechema Monograph***, Vol.40, No.616-641, pp 41-76, (1962)

[10] Brauer, H, "Studies of flow resistance and heat transfer on inline finned tube", ***Techn. Mittelungen***, Vol.5, No.5, pp214-226, (1962)

[11] Hirschberg, H.G, "Heat transfer and pressure drop on crossflow tube bundles", ***Abhanadl. Deutsh Kaeltech. Ver.*** No.16 (1961)

[12] Robinson, K.K., Briggs, D.E. "Pressure drop of air flowing across triangular pitch banks of finned tubes", ***Chemical Engineering Progress***, Symposium Series, Vol.62, No.64, pp.177-184 (1966)

[13] PFR ENGINEERING SYSTEMS INC., (1976), "Heat transfer and pressure drop characteristics of dry tower extended surfaces. Part II: Data analysis and correlation ", BNWL-PFR-7-102, Marina Del Ray, California, USA.

[14] Weierman, C, "Correlations ease the selection of finned tubes", ***Oil and Gas Journal***, September, (1976)

[15] Rabas, T.J, Eckels, P.W, Sabatino, R.A, "The effect of fin density on the heat transfer and pressure drop performance of low finned tube banks", Chemical Engineering Communications, Vol.10, no1-3, pp 127-147, (1981)

[16] ESDU, "Low fin staggered banks: Heat transfer and pressure loss for turbulent single phase crossflow", ***ESDU Data Item No.84016***, 251-254 Regent St. London, W1R 7AD (1985)

[17] Chu, C.M., "New gas side heat transfer and pressure drop correlations for annular finned tube bundles." ***HTFS RS735***. (1987)

[18] Petukhov, B.S, "Heat transfer and friction in turbulent pipe flow with variable physical properties", ***Advances in Heat Transfer***, Vol.6, pp-503-564, New York, Academic Press. (1970)

[19] Henry, J.A.R., "Effect of fin frequency and tube pitch on bundle pressure loss", ***HTFS RS953*** (1994)

[20] ESDU "Crossflow pressure loss over banks of plain tubes in square and triangular arrays including the effects of flow direction" ***ESDU Data Item No.79039***, 251-254 Regent St. London, W1R 7AD (1980)

[21] Ralston, T, Byskov, R.K., Farrant, P.E., Chu, C.M., "HTFS Models for Heat transfer and pressure drop applied to staggered arrangements of tubes with plain helical fins", ***HTFS RS1016***. (1997)

[22] Ralston, T, Chu, C.M, "HTFS2: Improved models for heat transfer and pressure drop applied to staggered arrangements of tubes with plain helical fins", *HTFS RS1036* (1998)

[23] Chu, C.M., Ralston, T, "Preliminary methods for prediction of pressure drop and heat transfer over helically-finned tube bundles with in-line arrangements" *HTFS RS1037* (1998)

[24] Brauer, H, "Compact heat exchangers", *Chemical and Process Engineering*, Vol.August, pp 451-40, (1964).

[25] Rabas, T.J, Eckels, P.W., "A finned tube heat exchanger side seal study", *Advances in Enhanced heat transfer*, ASME-Heat Transfer Division-18, pp 43-50, Milwaukee, Wisconsin, (1981)

[26] Eckels, P.W., Rabas, T.J., "Heat transfer and pressure drop of typical air cooler finned tubes", *Journal of heat transfer*, Vol.107, pp 198-204, (1985)

[27] Kroger, D.G, "Performance characteristics of industrial finned tubes presented in dimensional form", *Int. Journal of Heat and Mass Transfer*, Vol.29, No.8, pp1119-1125, (1986)

[28] ESDU, "Pressure loss during crossflow of fluids with heat transfer over plain tube banks with baffles" *ESDU Data Item No.74040*, 251-254 Regent St. London, W1R 7AD (1974)

[29] Wills, M.J.N, "Friction pressure drop for plain tube banks in crossflow with or without bypassing", *HTFS Handbook Sheet, SM3* (1984)

[30] Russell, M.A., Wills, M.J.N, "The development of a friction factor relationship for crossflow bypass", AERR-R 11154 (1983)

[31] Martin, D.J., Hasele, L.E., Hollingsworth, M.A., Mayhew, Y.R, "Bypass lanes and sealing strips for flow through tube banks in a duct", *HTFS RS748*. (1988)

[32] Bell, K.J, "Exchanger design", *Petro. Chemical. Engineering*, No.32, pp 26-40 (1960)

[33] Rabas, T.J., Taborek, J, "Survey of turbulent forced convection heat transfer and pressure drop characteristics of low finned tube banks in crossflow", ***Heat Transfer Engineering***, Vol.8, No.2, pp 49-62. (1987)

[34] Mueller, A.C., Chiou, J.P, "Review of various types of flow maldistribution in heat exchangers", ***Heat Transfer Engineering***, Vo.9, No.2, (1988)

[35] Fisher, J, Parker, R.O, "New ideas on heat exchanger design", ***Hydrocarbon Processing***, pp.147-154., July (1969)

[36] Zukauskas, A, Ulinskas, R., "Heat transfer in tube banks in crossflow", Springer-Verlag, Berlin, ISBN 3-540-18865-7. (1988)

[37] Pearce, H.R., "A study of air flow about columns of cylinders with particular *reference to turbulence* and vortex shedding", ***HTFS RS55***. (1972)

[38] Pearce, H.R, "A study of air flow in banks of cylinders with particular *reference to* turbulence and vortex shedding", ***HTFS RS56***. (1973)

[39] Zdravkovich, M.M, "The effects of interference between circular cylinders in cross flow", ***Journal of Fluids and Structures***, No.1, 1987, pp 239-261 (1987)

[40] Lam, K, Fang, X, "The effect of interference of four equispaced cylinders in cross flow on pressure and force coefficients", ***Journal of Fluids and Structures***, No.9, 1995, pp 195-214 (1995)

[41] Neal, S.B.H.C., Hitchcock, J.A, "A study of the heat transfer processes in banks of finned tubes in crossflow using a large scale model technique" ***AIChE Proceedings of the 3rd International Heat Transfer Conference***, August 1966, Chicago, Vol.3, PP 290-298, (1966)

[42] Hashizume, K, "Heat transfer and pressure drop of finned tubes in crossflow", ***Heat Transfer Engineering***, Vol.3, No.2, pp. 15-20 (1981)

[43] ESDU, "Convective Heat Transfer During Crossflow of Fluids over Plain Tube Banks", ***Engineering Sciences Data Unit*** (ESDU), Item No.73013, November, (1973)

[44] Rabas, T.J., Huber, F.V, "Row effects on the heat transfer performance of inline finned tube banks", ***Heat transfer engineering***, vol.10, no.4, pp 19-29 (1989)

[45] Yang, X, Bell, K.J., "Row effect on heat transfer on inline bank with finned tubes", ***Proceedings of the AIChE***, Atlanta, Vol.89, No.295 (1993)

[46] Weierman, C, Taborek, J, Marner, W.J., "Comparison of the performance of inline and staggered banks of tubes with segmented fins", AIChE National Heat Transfer Conference, San Francisco, August 1975 (1975)

[47] Yudin, V.F, Tokhtarova, L.S, "*Influence of number* of transverse finned tubes of staggered and inline banks on heat transfer and resistance", ***Energomashinostroyenie,*** No.4, pp 41-42, (1971)

[48] Kuntiesh, V.B, Iokhvedov, F.M, "Influence of number of rows and arrangement of finned banks in crossflow on local heat transfer of last rows of tubes", *Izv. Vuzov SSSR. **Energetika***, No.3, pp 29-31, (1979)

[49] Yudin, V.F., "Heat transfer of cross finned tubes", Leningrad, Mashinostroyenie, 189pp, (1982)

[50] Henry J.A.R., "Gas temperature measurement downstream of a tube bundle", ***HTFS R880.*** (1991)

[51] ISO GUM, "Guide to the Expression of Uncertainty in Measurement", ISO, Geneva, Switzerland. ISBN 92-67-10188-9, First Edition 1993, corrected and reprinted 1995. (BSI Equivalent: ***BSI PD 6461: 1995***, "Vocabulary of Metrology, Part 3. Guide to the Expression of Uncertainty in Measurement. BSI ISBN 0 580 23482 7.)

[52] Bell, S,, "A Beginner's Guide to Uncertainty of Measurement", ***Measurement Good Practice Guide No. 11***, ISSN 1368-6550, NPL, Teddington, Middlesex, TW11 0LW (1999)

[53] "Measurement of fluid flow – Estimation of uncertainty of a flow-rate measurement" ***ISO/WD 5618.4***

[54] Farrant, P.E., "An Introduction to uncertainty analysis for heat transfer experiments", ***A report for the Thermal Engineering Section, Process and Energy Centre, NEL***, East Kilbride, Scotland, Issue No.1. (2002)

[55] "Uncertainties of measurement during acceptance tests on energy-conversion and power plants – Fundamentals" ***VDI 2048***, October 2000, ICS 17.020; 27.010, VDI Gesellshaft Energietechnik.

[56] Hetz, A.A., Dhaubhadel, M.N., Telionis, D.P, "Vortex shedding over five inline cylinders", ***Journal of Fluids and Structures***, No.5, 1991, pp 243-257 (1991)

[57] Henry, J.A.R., "The HTFS Finned Tube Bundle Data Bank", ***HTFS/P/7/1993***. (1993)

[58] Cox, B, Jallouk, P.A., "Experimental determination of the performance characteristics of eight compact heat transfer surfaces", Oak Ridge Gaseous Diffusion Plant, Union Carbide Corporation, Report K-1832, Oak Ridge, Tennessee, (1972)

[59] Ward, D.J, Young, E.H, "Heat transfer and pressure drop of air in forced convection across triangular pitch banks of finned tubes", ***Chemical Engineering Progress Symposium Series***, Vo.55, No.29, PP 37-44

[60] Cox, B, "Performance of compact heat transfer surfaces-finned and bare tube banks", Oak Ridge Gaseous Diffusion Plant, Union Carbide Corporation, Report K-1847, Oak Ridge, Tennessee, (1973)

[61] Mirkovic, F, "Heat exchangers: design and theory sourcebook", McGraw-Hill Book Company, New York (1974)

[62] McLean, M.S.L., Spence, C.M., "Heat transfer and pressure drop characteristics of eight air-cooled heat exchanger tube bundles", ***HTFS RS733***. (1987)

[63] McLean, M.S.L., Ralston, T, Henry, J.A.R, "The effect of fin and bindle geometry on heat transfer and pressure drop characteristics", ***HTFS RS817*** (1989)

[64] Chu, C.C.M., Farrant, P.E., Spence, C.M., McLean, M.S.L., "Heat transfer and pressure drop of six unusual geometry air cooled heat exchanger tube bundles", ***HTFS RS734***. (1987)

[65] McLean, M.S.L, Barrie, A. and Henry J.A.R, "Heat transfer and pressure drop characteristics of three 5 inch nominal bore heat recovery tube bundles", ***HTFS RS903.*** (1992)

[66] Stasiulivicus, J, Skrinska, A, "Heat transfer of finned tube bundles in crossflow", Hemisphere Publishing Corporation, London (1983)

[67] Lymer, A, Ridal, B.F., "Finned tubes in a crossflow of gas", ***J. British Nuclear Energy Conference***, Vol.6, No.4, pp 307-313 (1961)

[68] Schlichting, H, "Boundary Layer Theory; English Edition", Pergamon Press Ltd, 4&5 Fitzroy Square, London. (1955)

[69] Raudkivi, A.J., Callander, R.A, "Advanced fluid mechanics", Edward Arnold (Publishers), 25 Hill Street, London, (1975)

[70] Blacker, T, "The Cooper Tool", Fluid Dynamics Intl., Davis St, Evanston, Illinois (1996)

[71] Blacker, T, Stephenson, M.B., "Paving: A new approach to automated quadrilateral mesh generation", ***Int. Journal of Numerical Methods***, 32:811-847, (1991)

[72] FLUENT, Fluent Inc, 'Fluent 5, Users Guide Volume 2', Fluent Inc, Lebanon, New Hampshire (1998)

[73] Barnard, R.H, "Road Vehicle Aerodynamic Design", Longman Publishing, ISBN 0-582-24522-2 (1996).

[74] Shaw, C.T., 'Using computational fluid dynamics', Prentice Hall Publishing (1992).

[75] Versteeg, H.K., Malalasekera, W, "An Introduction to computational fluid dynamics", Longman publishing, ISBN 0-582-21884-5 (1999)

[76] Kondjoyan, A, Boisson, H.C, "Comparison of calculated and experimental heat transfer coefficients at the surface of circular cylinders placed in a turbulent cross flow of air", ***Journal of Food Engineering***, No.34, 1997, pp 123-143 (1997)

[77] Rodgers, G.F.C, Mayhew, Y.R, "Thermodynamics and transport properties of fluids", S.I. Units, 5th Edition, Blackwell Publishers (1995)

[78] Webb, R.L., "Air-side heat transfer in finned tube heat exchangers", ***Heat transfer engineering***, Vol. 1, No.3 (1980)

[79] Henry, J. A. R., 'Effect of tube pitch arrangement on air-cooled heat exchanger performance', ***HTFS*** **RS905** (1992)

[80] Sung, H.J., Yang, J.S., Park, T.S, "Local convective mass transfer on circular cylinder with transverse annular fins in crossflow", ***Int. Journal of Heat and Mass Transfer***, Vol.39, No5, pp 1093-1101. (1996)

[81] Fox, T.A., West, G.S., "On the use of end plates with circular cylinders in wind tunnel studies", Research Report No.CE118, August 1990, Dept. of Civil Engineering, University of Queensland. (1990)

[82] Goldstein, R.J., Karni, J, "The effect of a wall boundary layer on local mass transfer from a cylinder in crossflow", ***Journal of Heat Transfer***, Vol.37, pp 2203-2210, (1984)

[83] Lam, K. Fang, X, 'The effect of interference of four equispaced cylinders in crossflow on pressure and force coefficients', ***Journal of Fluids and Structures***, No.9, pp. 195-214 (1995).

[86] Rodgers, G.F.C, Mayhew, Y.R, "Engineering thermodynamics work and heat transfer, 4th Edition, Longman Publishing (1992)

[87] Fisher, E.M., Eibeck, P.A., "The influence of a horseshoe vortex on local convective heat transfer'', ***Journal of Heat Transfer***, Vol.112, May 1990, pp 329-335. (1990)

[88] Bern, M, Plassman, P, "Mesh Generation", ***Handbook of Computational Geometry***, Elsevier Science, (2002)

[89] Bank, R.E, Kent-Smith, R, 'Mesh smoothing using a posteriori error estimates', ***Handbook of Computational Geometry***. Elsevier Science (1997)

[90] Zwinger, T, 'Gambit-CFD oriented preprocessing', CSC Scientific Computing, Espoo, Finland (2001)

[91] Tanner, M, "Reduction of base drag", ***Progressive Aerospace Science***, Vol.16, No.4, pp 369-384. (1975)

[92] Hoerner, S.F, "Fluid dynamic drag", Self Published, Midland Park, New Jersey. (1965)

[93] Sindo, S, "Mini-tufts vs. Tufts made from white cotton", ***Journal of the Visualisation Society of Japan***, Vol.17, No.64, January (1997)

[94] Ambrose, D, Counsell, J.F, Haseler, L, "Heat Capacity and enthalpy of pure gasses" ***HTFS Handbook sheet*** PM20

[95] Gettinby, G, McKenzie, E, "Experimental Design and Taguchi Methods", Lecture Notes, Department of Statistics and Modeling, University of Strathclyde, Glasgow, (2002)

[96] Stanescu, G, Fowler, A.J., Bejan, A, "The optimal spacing of cylinders in free-stream crossflow convection", ***Int. Journal of Heat and Mass Transfer***, Vol.39, No.2, pp 311-317 (1996)

[97] FLUENT Inc, "Turbulent heat transfer in a finned tube heat exchanger", Promotional web page EX50, www.fluent.com, (1998)

[98] Grady, C.J., "Improved heat exchanger designs using vortex generators", Ph.D Thesis, Dept. of Mechanical Engineering, University of Strathclyde, submitted January 2003 (2003)

[99] Echarte, R, "Crossflow correction factors for temperature difference" ***HTFS Handbook sheet*** AM11 (1981)

APPENDICES

APPENDIX A Measurement Uncertainty

A.1 Introduction

According to the ISO 'Guide to the expression of uncertainty in measurement'[51] (ISO GUM) a measurement is not 'complete' unless there is an uncertainty associated with it. A result of a measured flowrate of 7.5 kg/s should be viewed with caution if the uncertainty is ±50%, whereas it can be regarded as trustworthy if the uncertainty is ±2% with a 95% level of confidence.

The sources used in this section are ISO GUM [51], Bell [52], ISO/WD 5618.4 [53] and Farrant [54]. They are mentioned here to save repetition. The figures shown below are taken from Farrant [54].

A.2 Taking measurements

If a flowrate measurement is required using a flowmeter which provides a direct output in kg/s, then the flowrate is the Measurand of interest, which we will be designated as y. The assumption can be made that the flowrate remains constant and that a number of readings are taken. If a histogram of the results is plotted with the y axis showing the

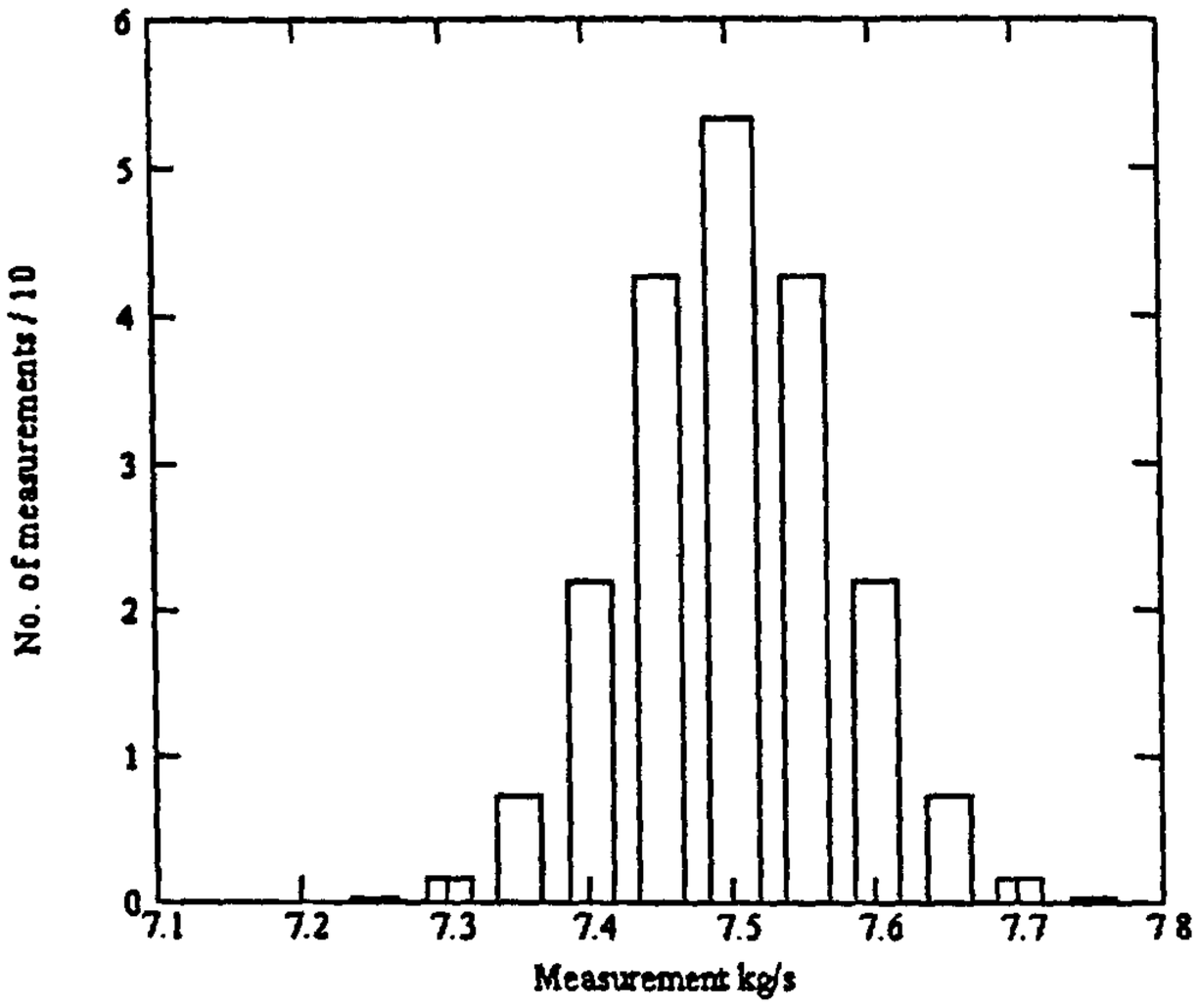

Figure A.1: Histogram showing a typical spread of measurement results

reading of 7.5 kg/s and the number of times we obtained 7.55 kg/s, etc it is likely that a graph similar to Figure A.1 will be obtained.

If more measurements were taken and smaller intervals used on the x axis a graph like Figure A.2 is the likely result. This is an example of a 'normal distribution' and it is usual to assume that experimental measurements are distributed in this manner unless there is information to indicate otherwise. It can be seen that this graph's the peak has been normalised to 1.

We now have many measurements, y_1, y_2,.....y_n and the average value is as shown in Equ.A.1

$$\bar{y} = \frac{1}{n}\sum_{i=1}^{n} y_i \qquad \text{(Equ.A.1)}$$

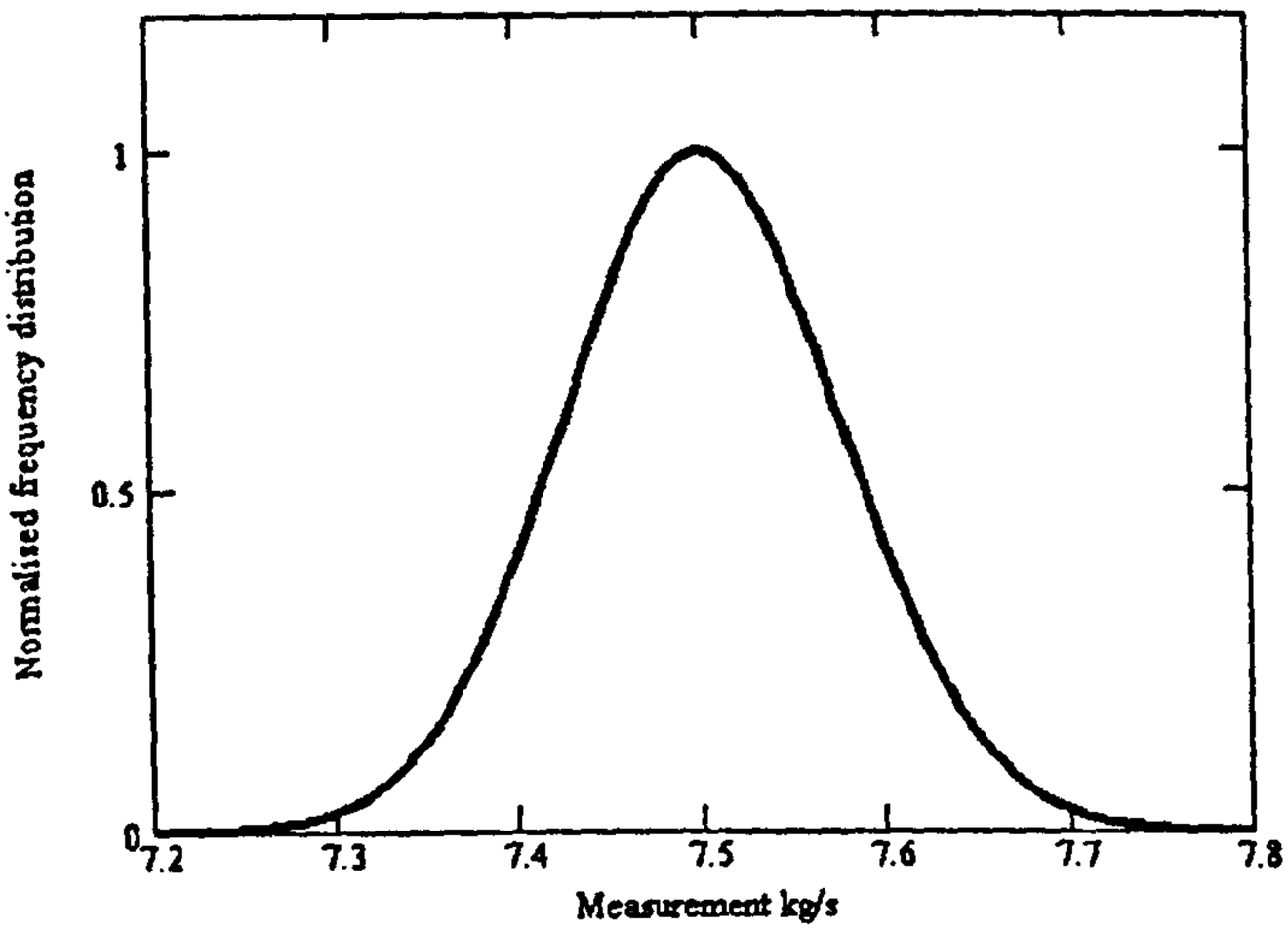

Figure A.2: Frequency distribution of measurement values

We can also obtain an indication of the spread of the measurements from the standard deviation which is shown in Equ.A.2

$$s(y) = \sqrt{\frac{\sum_{i=1}^{n}(y_i - \bar{y})^2}{n-1}} \qquad \text{(Equ.A.2)}$$

It can be seen that this standard deviation has been divided by one less than the number of measurements, n. This is correct if we consider our measurements to be just a sample from what could be a much larger population of measurements. If, however, we consider our measurements to be all we have then the equation Equ.A.3 is correct:

$$s(y) = \sqrt{\frac{\sum_{i=1}^{n}(y_i - \bar{y})^2}{n}} \qquad \text{(Equ.A.3)}$$

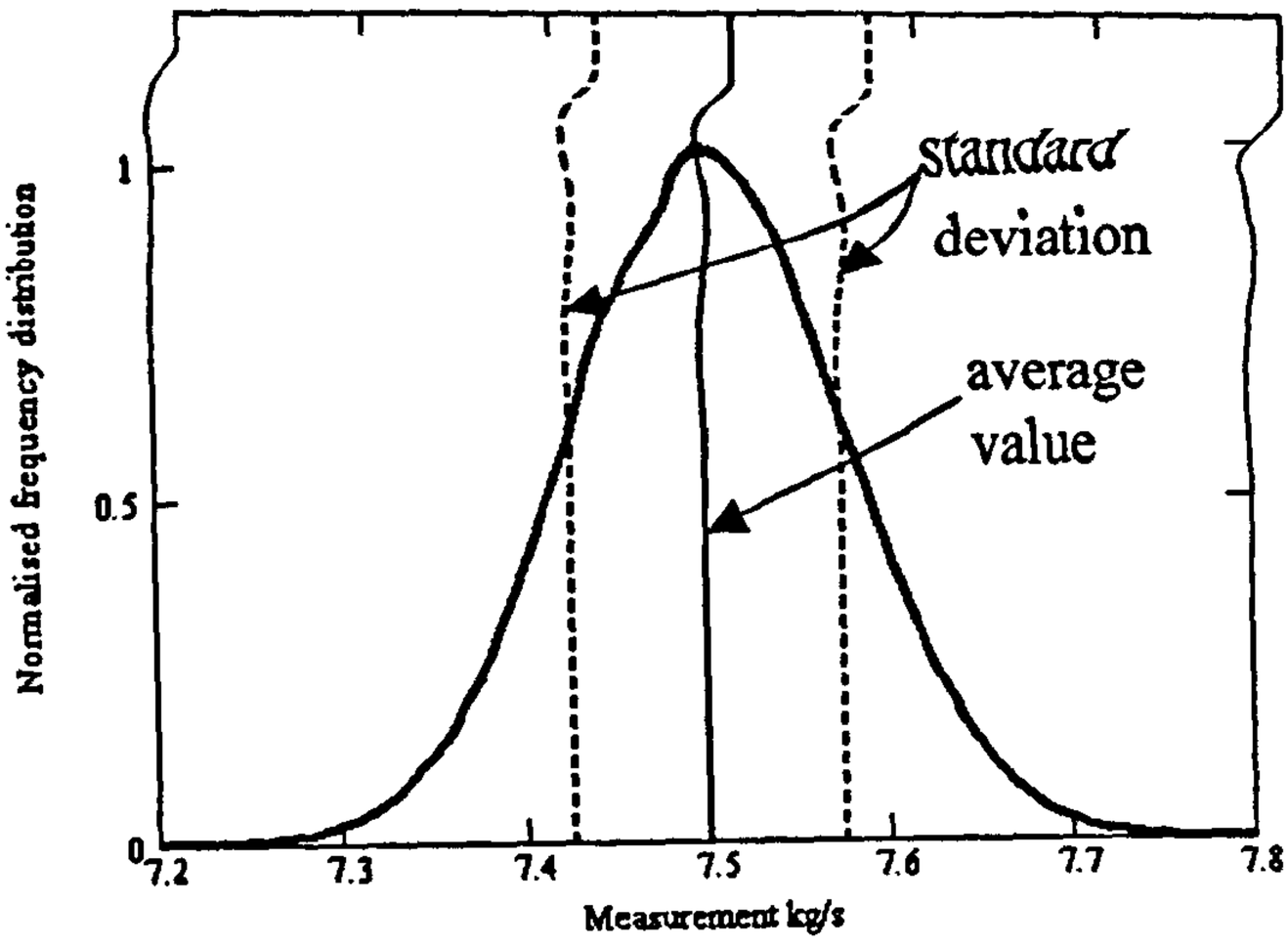

Figure A.3: Average values and standard deviations

The results of equations Equ.A.1 and Equ.A.2 are shown in Figure A.3

The curve shown in figures A.2 and A.3 is such that the standard deviation is 0.075 kg/s, which is ±1% of the mean value 7.5 kg/s. The area enclosed under the curve between the standard deviation lines is 68% of the total area under the curve. So it can be said that the flowrate being measured was 7.5 kg/s ±1% with a level of confidence of 68%. Essentially this translates to, if one more measurement were to be taken which happened to coincide with the 'true value', the probability of that measurement falling in the range 7.5 kg/s ±1% is 68%, and correspondingly the probability that the 'true value' was within this range is 68%.

It can be seen that this level of confidence is quite low. A 95% confidence level is the usually assumed value and this value can be obtained by using a multiplier, the coverage factor, on the standard deviation. A coverage factor of 1.96 would give exactly 95% and this is normally rounded to 2 giving a confidence level of 95.4%. Figure A.4 shows the vertical chained lines at a distance of 2 x standard deviation from the average line.

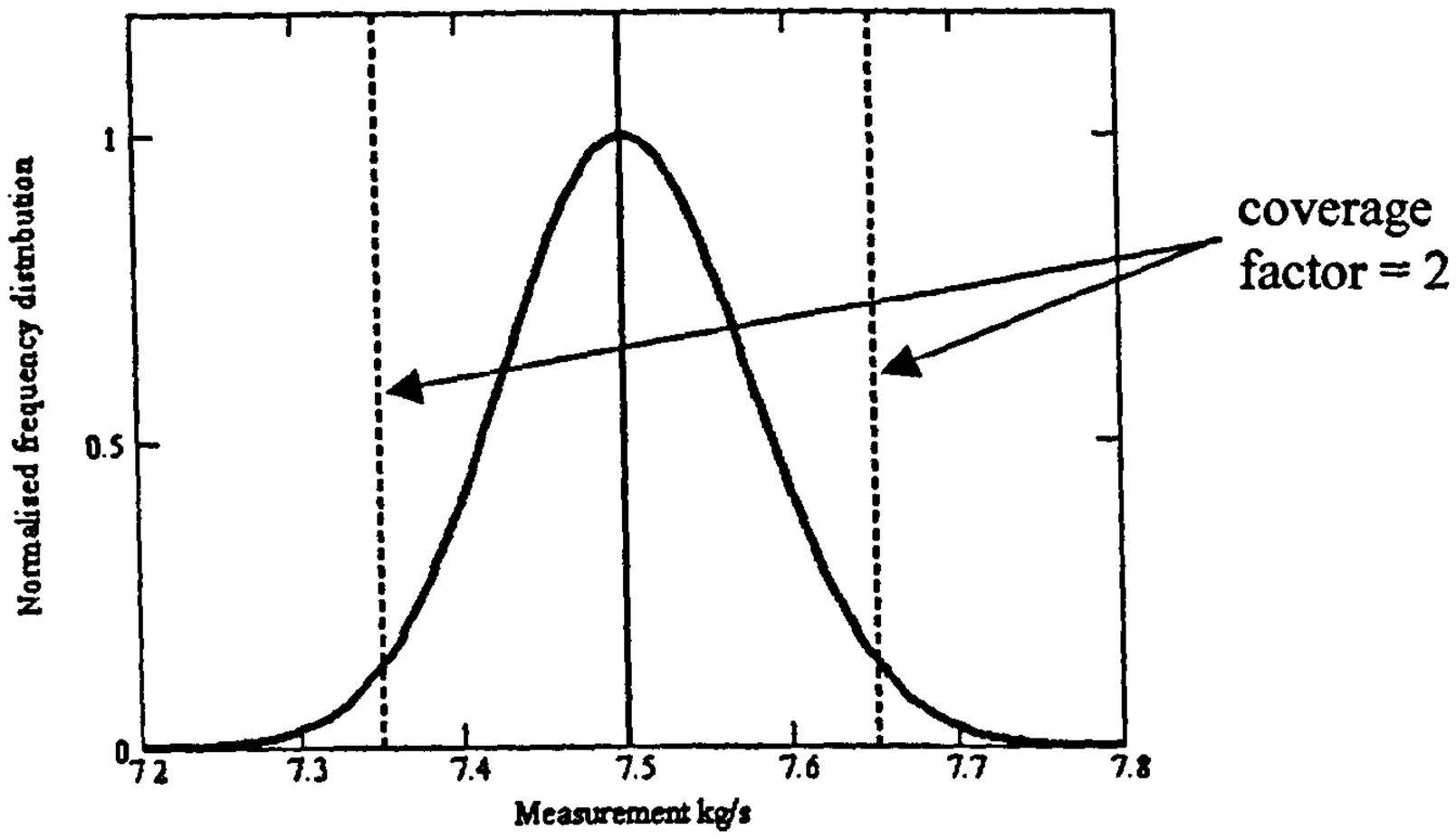

Figure A.4: Average values and 2 x standard deviation

To obtain a confidence level of 99% we need a coverage factor of 2.58. A coverage factor of 3 will provide a confidence level of 99.7%.

A.3 Non-dimensional expanded uncertainty

7.5 kg/s ±2% with a confidence level of 95% is an example of an non-dimensional expanded uncertainty because the uncertainty is expressed as a percentage of the measurand. When performing uncertainty calculations it is considered more correct to work with dimensional uncertainties so that 7.5 kg/s±2% becomes 7.5 kg/s ±0.15 kg/s.

It is an expanded uncertainty, U(y), because the standard uncertainty has been increased to encompass a large fraction of the distribution of values that could reasonably be attributed to the measurand.

The expanded uncertainty is related to the standard uncertainty, u(y), by a multiplier called the coverage factor, k, as shown in Equ.A.4

$$U(y) = k\,u(y) \qquad \text{(Equ.A.4)}$$

The standard uncertainty, u(y), is the uncertainty of the result of a measurement expressed as a standard deviation.

It can be shown that the confidence level associated with particular coverage factors will be reduced when there are small numbers of measurements. For smaller numbers of

measurements the Normal distribution shown in the previous section transforms to a Student t distribution and it can be calculated, for example, for two measurements, a coverage factor of 2 provides a confidence level of only 70.5%. To obtain a 95% confidence level with just two measurements the necessary coverage factor is a very large 12.71. In ordinary situations 10 readings are sufficient to be able to assume a normal distribution. This was the number of readings taken by the data acquisition programs for the instruments used on the MPWT and HTWT, with a few exceptions. Figure A.5 compares the shapes of the distribution curves and shows that, for 10 measurements, the t distribution is close to the Normal distribution.

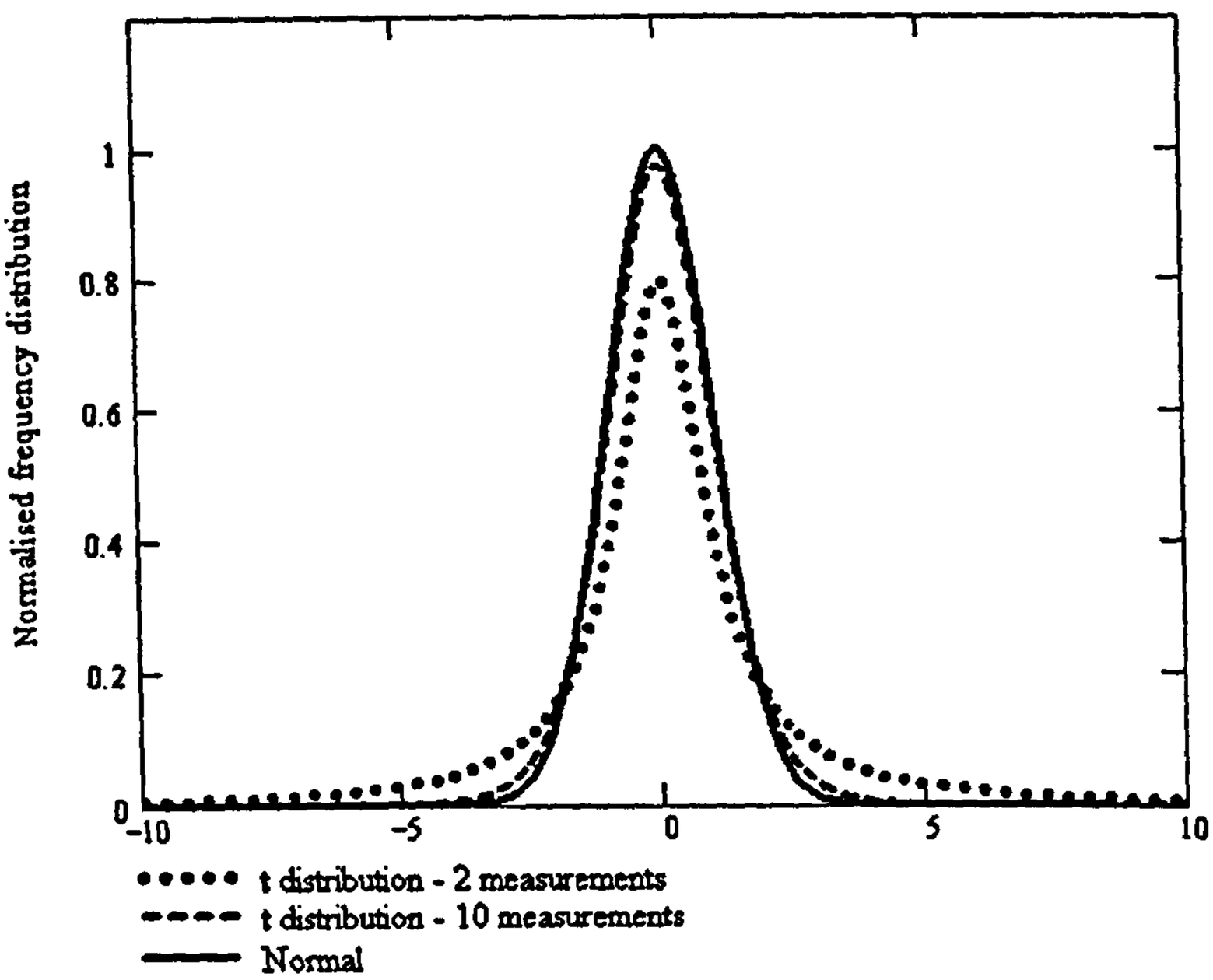

Figure A.5: Comparison of the shapes of the Normal and t distributions

A.4 Uncertainty of the average value

The discussion above was concerned with individual measurements and the uncertainties associated with the measurements. In the experimental results presented in this report were taken at steady state conditions. The n measurements that were taken were typically n = 10. An average value was then calculated from Equ.A.1 and the average used in subsequent calculations. If one extra measurement was taken, a flow measurement, for example, it might have had a value anywhere along the curve shown in Figure A.2. If this value was included with the ten measurements then, even if its

value were much lower or higher than the average, its effect on the average is small. Due to this the standard deviation of the averages of groups of measurements is smaller than the standard deviation of the individual measurements. The estimate of the standard deviation of the average is therefore:

(Equ.A.5)

$$s(\bar{y}) = \frac{s(y)}{\sqrt{n}}$$

Equ.A.2 and Equ.A.5 can be combined as follows:

$$s(\bar{y}) = \sqrt{\frac{\sum_{i=1}^{n}(y_i - \bar{y})^2}{n(n-1)}} \qquad \text{(Equ.A.6)}$$

A comparison of the normalised frequency distribution curves for individual measurements and for averages of 10 measurements is shown in Figure A.6. This is additional evidence for the significant advantage of averaging several readings rather than relying on individual measurements.

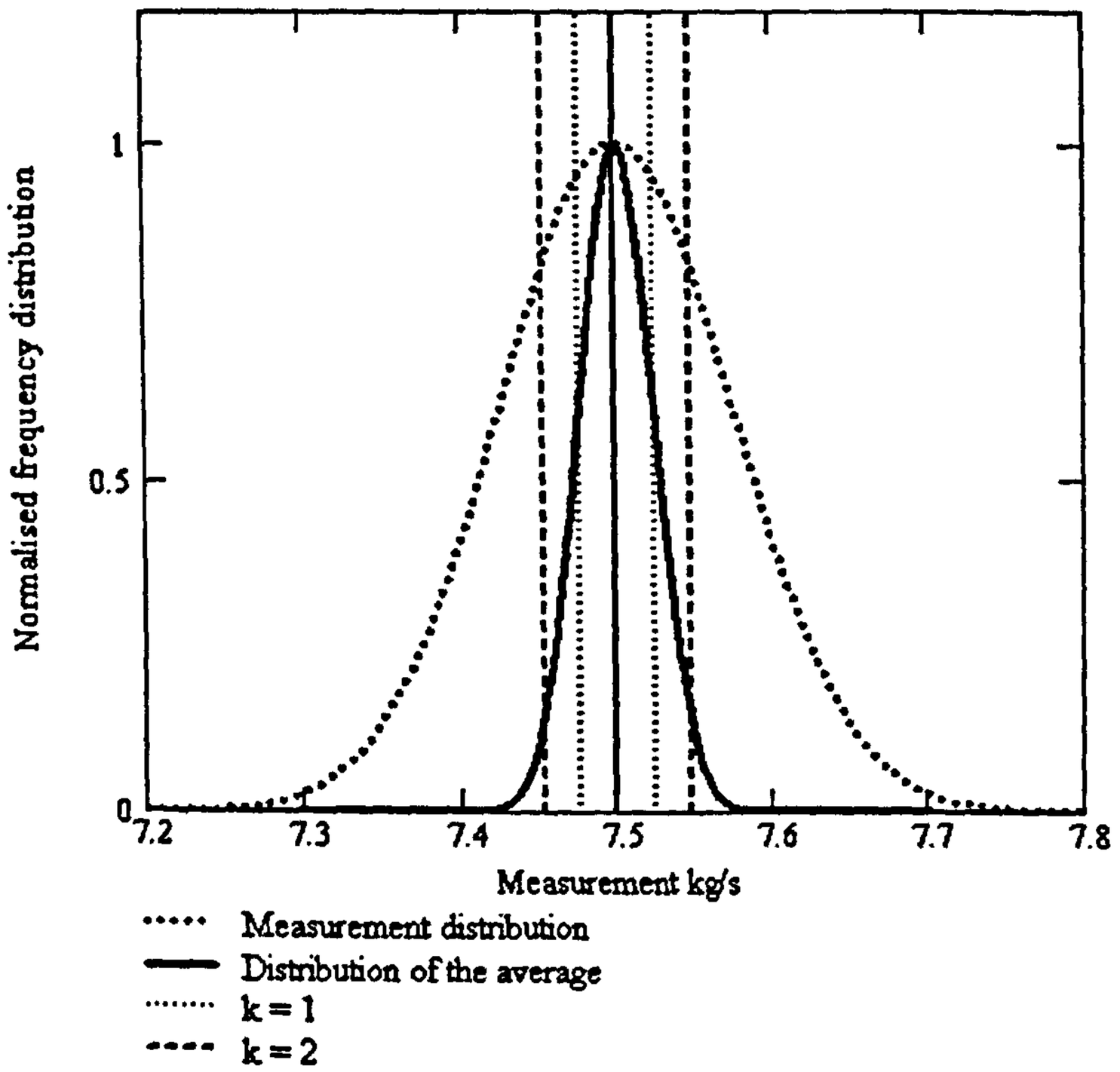

Figure A.6: Comparison of the frequency distributions for measurements and the averages of ten measurements

A.5 Other uncertainty distributions

So far only the Normal and Student t distributions have been discussed. Occasionally another distribution, the rectangular or uniform distribution, is used. It is applied where it is likely that there is equal probability that a measurement will fall anywhere in the range ±a. An example may be taking a measurement, x, to the nearest mm with a rule. The measurement would be x ±0.5 mm. The standard uncertainty for a rectangular distribution is $a/\sqrt{3}$. ISO/WD 5618.4 [44] discusses the reasons for this distribution and others.

3.6.6 Instrument uncertainties

Until now the above sections have dealt with a single measuring instrument producing results directly in the format that was required. The discussion has considered only the scatter associated with taking measurements - no mention has been made of the uncertainties associated with instrument itself.

The instruments used on the MPWT and HTWT were chosen on the basis that they had associated tolerances form their respective manufacturers. The guide used on this project was that is that if no details were given or could be traced then it should be assumed that the instrument uncertainty has a Normal distribution with a confidence level of 95% and a coverage factor of 2. Where the terms 'limit' or 'tolerance limit' or 'maximum instrument drift between calibrations' were used by a manufacturer then a rectangular distribution as described in section 3.6.5 above was assumed.

A manufacturer may state the instrument as having a tolerance of ±1.0%. In the absence of other information the uncertainty was applied to the instrument's full scale reading. Assuming this is applicable to the example flowmeter used for measuring the 7.5 kg/s in the examples above and that the full scale reading for the flowmeter is 10 kg/s then the instrument's expanded uncertainty is therfore $U_i = 0.1$ kg/s.

A.7 Combining uncertainties

It can be seen from the above that there are two defined uncertainties; the instrument uncertainty and the measurement scatter. An approach was needed to determine the combined total uncertainty for each measurement.

With a coverage factor, k (applicable to the measurement, instrument and the combined uncertainties), the measurement, instrument and combined uncertainties are calculated from Equs.A.7 - A.11.

The measurement standard uncertainty is found from the measurement expanded uncertainty divided by the coverage factor, as shown in Equ.A.7.

$$u_m = \frac{U_m}{k} \qquad \text{(Equ.A.7)}$$

The instrument standard uncertainty is the found from the instruments expanded uncertainty divided by the coverage factor, as shown in Equ.A.8.

$$u_i = \frac{U_i}{k} \qquad \text{(Equ.A.8)}$$

Equ.A.9 is used where the instrument standard uncertainty leads us to believe that a rectangular distribution is appropriate.

$$u_i = \frac{U_i}{\sqrt{3}} \qquad \text{(Equ.A.9)}$$

The combined standard uncertainty is then found from the method outlined by Farrant [45], where uncertainties are independent of each other so they are combined by using *the root sum of the squares* method shown in Equ.A.10

$$u_c = \sqrt{u_m^{\,2} + u_i^{\,2}} \qquad \text{(Equ.A.10)}$$

The total combined expanded uncertainty is then the product of the combined standard uncertainty and the coverage factor, as shown in Equ.A.11

$$U_c = k\,u_c \qquad \text{(Equ.A.11)}$$

Continuing the example; For k = 2 for the flowmeter, the measurement standard uncertainty is u_m = 0.075 kg/s the instrument standard uncertainty is $u_i = 0.1/2 = 0.05\,\mathrm{kg/s}$. The standard combined uncertainty and the expanded combined uncertainty are:

$$u_c = \sqrt{0.075^2 + 0.05^2} = 0.090$$

$$U_c = k\,u_c = 0.18\ \text{kg/s}$$

The flowrate is therefore 7.5 kg/s ±0.18 kg/s at the 95% confidence level or alternatively 7.5 kg/s ±2.4%.

A.8 Multi-parameter measurements

In this study the more common situation was that the uncertainties from several sources had to be combined to obtain a combined non-dimensional expanded uncertainty. *For* example, to calculate the friction factor (f factor) for a bundle being tested in the Multi-Purpose Wind Tunnel the following measurements were required:

- Atmospheric pressure
- Air inlet temperature to the cone
- Air pressure in the throat of the cone
- Temperature of the air entering the bundle
- Temperature of the air leaving the bundle
- Air pressure drop across the bundle.

To illustrate this we shall say that the combined standard uncertainty for each instrument is $u(x_i)$, that is the instrument and measurement uncertainties have been combined as in Equ.A.11. It can be imagined that some measurements will have a much bigger influence on the value of the friction factor; the air pressure drop across the bundle compared with the bundle outlet air temperature, for example. Consequently the bundle pressure drop uncertainty will influence the uncertainty of the friction factor to a higher degree than the air outlet temperature uncertainty.

To influence the measurements importance sensitivity coefficients, c_I , were introduced to weight the importance of each standard uncertainty. The overall combined standard uncertainty, $u_c(y)$, is calculated from Equ.A.12

$$u_c(y) = \sqrt{\sum_{i=1}^{n} (c_i u(x_i))^2} \qquad \text{(Equ.A.12)}$$

The sensitivity coefficients were calculated as follows:

For a set of measurements the value of the friction factor, is calculated using equations that were shown in Chapter 3. A small increment, Δx_i, is added to each of the measurements in turn and f is recalculated to give a new value f_i.

To find the sensitivity coefficient Equ.A.13 is used.

$$c_i = \frac{f_i - f}{\Delta x_i} \qquad \text{(Equ.A.13)}$$

An increment is then added to each of the measurements to give the standard uncertainty.

A convenient way of calculating the combined standard uncertainty is to use matrix *notation. The variances (the squares* of the standard deviations) are placed on the leading diagonal of a 'covariance' matrix, S_X. The other elements in the matrix are zero. The sensitivity coefficients are placed in the appropriate places in a sensitivity coefficient vector, F. The combined standard uncertainty can then be calculated as in Equ.A.14.

$$u_c(y) = \sqrt{F^T \cdot S_x \cdot F} \qquad \text{(Equ.A.14)}$$

The matrix algebra approach was originally described in VDI 2048 [45].

The combined expanded uncertainty, $U_c(y)$, is as shown in Equ.A.15

$$U_c(y) = k\, u_c(y) \qquad \text{(Equ.A.15)}$$

A.9 Combining data points

The procedure used on the MPWT and HTWT was to repeat measurements at various flowrates and then to take more measurements at these flowrates in a different order to avoid hysteresis errors. For these experiments five sets of measurements were taken at nominally the same conditions. In this way checks could be made on repeatability, hysteresis and drift. A fictitious exaggerated set of results with uncertainty bars shown only for the ordinates might appear as in Figure A.7a.

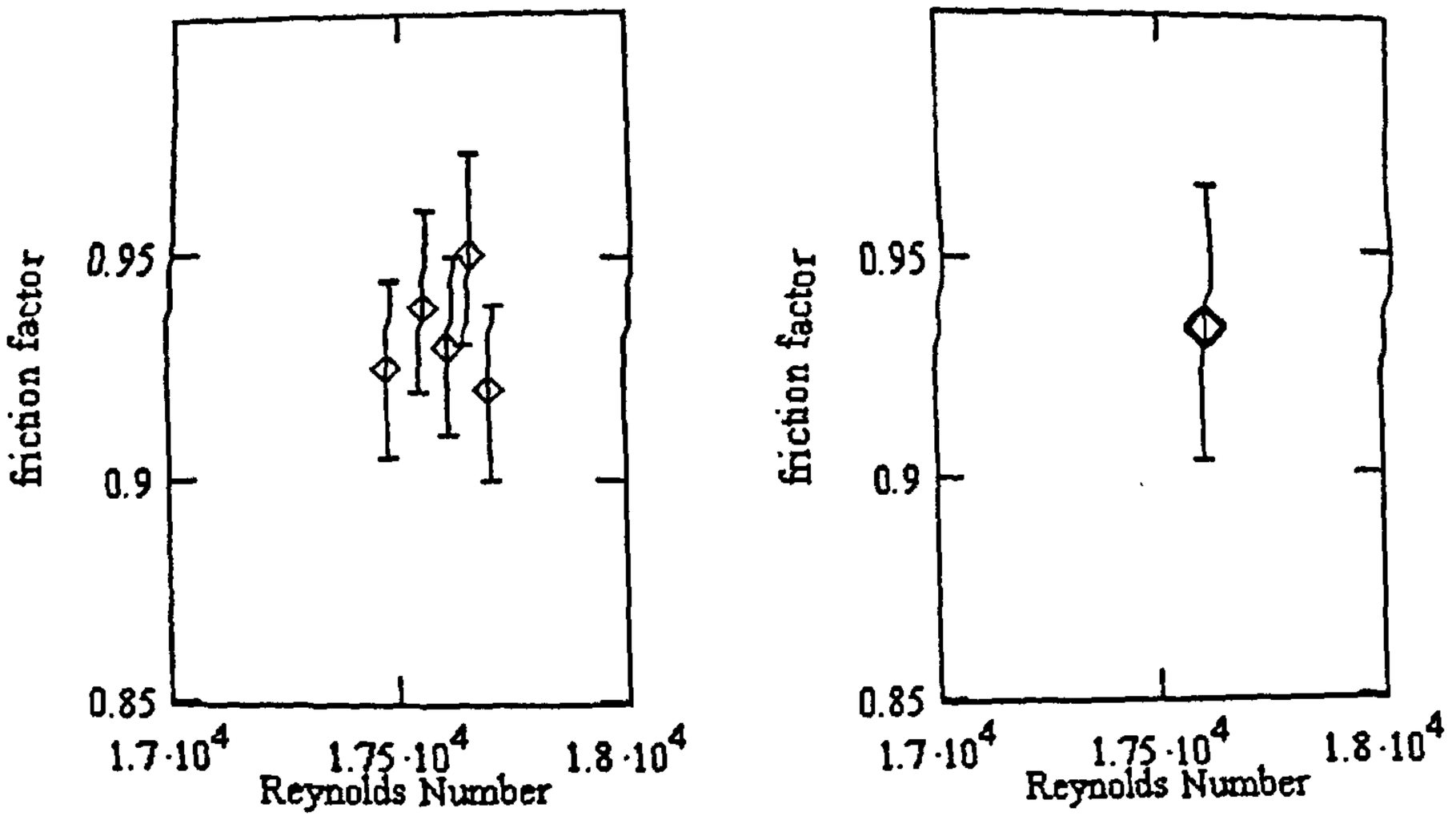

(a) (b)

Figure A.7 (a): A plot of five points taken at nominally the same conditions and **(b)** combined into a single point

To combine these repeat measurements into a single point as shown in Figure A.7b the following equations may be used:

The combined average value, $\bar{y}$, for n ordinate values is:

$$\bar{y} = \frac{\sum_{i=1}^{n} y_i}{n} \qquad \text{(Equ.A.16)}$$

The combined expanded uncertainty, $U_c(\bar{y})$, is:

$$U_c(\bar{y}) = k\sqrt{\frac{\sum_{i=1}^{n}\left[\left(y_i - \bar{y} + \frac{U(y_i)}{k}\right)^2 + \left(y_i - \bar{y} - \frac{U(y_i)}{k}\right)^2\right]}{2n}} \qquad \text{(Equ.A.17)}$$

where k is the coverage factor.

The abscissa values may be treated in the same way.

There now follows a worked example of the process of determining the uncertainty for a combined measurement. The example is of the calculation of the friction (f) factor as used in the MPWT. This example is based on the work presented by Farrant [54].

The value of the f factor was 1.074 and the corresponding Reynolds Number based on the bare tube diameter was 11,580. The bundle was high fin frequency with a bare tube diameter of 18mm.

A.10 Temperature measurements

The temperature measurements in the MPWT were performed using Class 1 Type T thermocouples which for temperatures in the range –40°C to 125°C have a manufacturer's tolerance of ±0.5°C.

Grids of 9 thermocouples were used for measuring the air entering and leaving the tube bundle. It can be shown that the tolerance of the average temperatures entering and leaving the bundle is ±0.5°C. The expanded uncertainty is therefore 0.5°C

A.11 Inlet cone pressure transducer

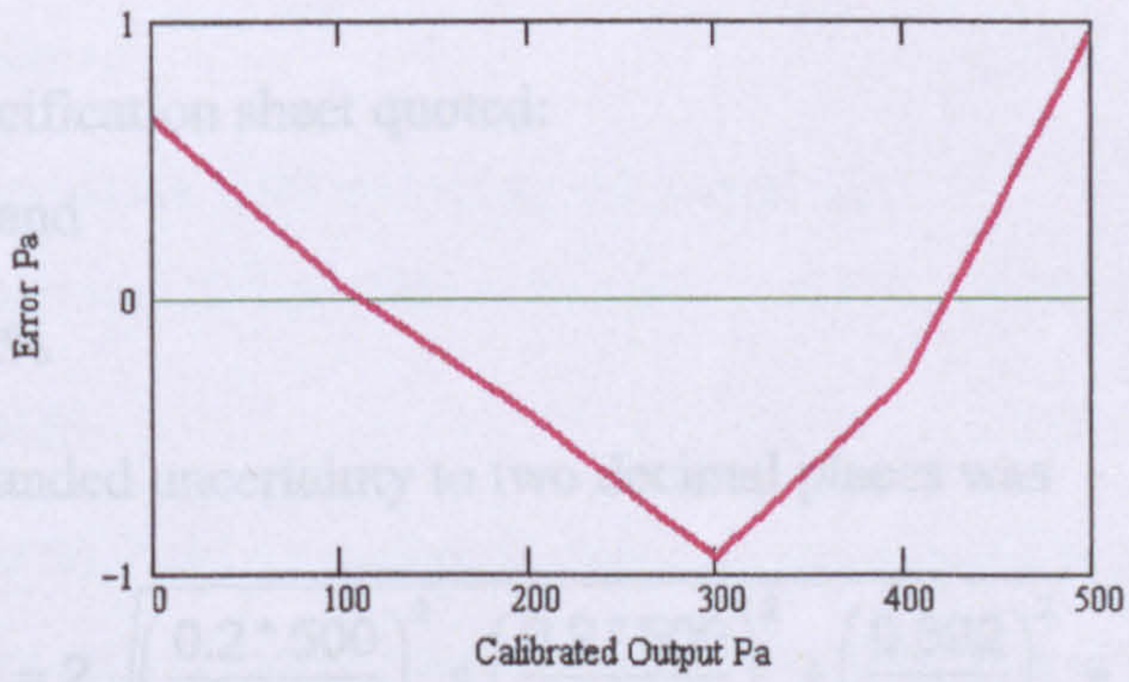

Figure A.8: Inlet Cone Transducer Calibration curve

The graph in figure A.8 shows the errors in the calibration curve for the inlet cone pressure transducer. The maximum error was at 500 Pa when the error is 0.97 Pa.

The transducer specification sheet quoted:

Hysteresis $\leq 0.2\%$ and

Repeatability $\leq 0.2\%$

The combined expanded uncertainty to two decimal places is therefore

$$U_x = 2\sqrt{\left(\frac{0.2*500}{100*2}\right)^2 + \left(\frac{0.2*500}{100*2}\right)^2 + \left(\frac{0.97}{2}\right)^2} = 1.71\,\text{Pa} \qquad \text{(Equ.A.18)}$$

A.12 Bundle pressure drop transducer

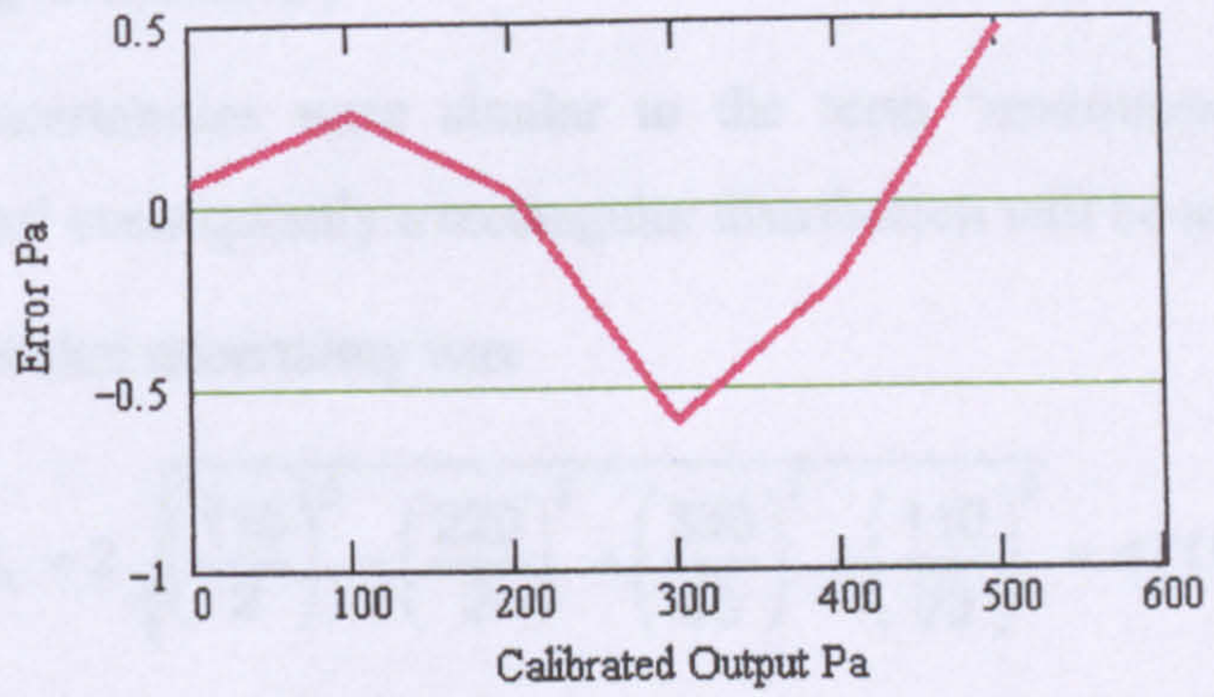

Figure A.92: Bundle pressure drop transducer calibration curve

The graph in Figure A.9 shows the errors in the calibration curve for the bundle pressure drop transducer. The maximum error was at 300 Pa when the error was –0.592 Pa.

The transducer specification sheet quoted:

Hysteresis $\leq 0.2\%$ and

Repeatability $\leq 0.2\%$

The combined expanded uncertainty to two decimal places was

$$U_x = 2\sqrt{\left(\frac{0.2*500}{100*2}\right)^2 + \left(\frac{0.2*500}{100*2}\right)^2 + \left(\frac{0.592}{2}\right)^2} = 1.53\,\text{Pa} \qquad \text{(Equ.A.19)}$$

A.13 Atmospheric pressure transducer

The uncertainties for this instrument were given in terms of the full-scale output of 1100 mbar

Non-linearity and hysteresis	0.1% ≡ 110 Pa
Repeatability	0.2% ≡ 220 Pa

Temperature shift	0.3% / 10°C
(assuming the temperature was never more than 10°C away from the calibration temperature that is assumed to be 20°C the tolerance was	0.3% ≡ 330 Pa
Long term stability	0.1% ≡ 110 Pa

These last two uncertainties were similar to the term 'maximum instrument drift between calibrations' consequently a rectangular distribution will be assumed.

The combined expanded uncertainty was

$$U_x = 2\sqrt{\left(\frac{110}{2}\right)^2 + \left(\frac{220}{2}\right)^2 + \left(\frac{330}{\sqrt{3}}\right)^2 + \left(\frac{110}{\sqrt{3}}\right)^2} = 471\,\text{Pa} \qquad \text{(Equ.A.20)}$$

A.14 Steam pressure transducer

The uncertainties for this instrument were given in terms of the full-scale output which was 1.724 bar abs.

Non-linearity	1.0% ≡ 1724 Pa
Hysteresis	0.25% ≡ 431 Pa
Temperature shift assuming the transducer temperature did not rise above 50°C	0.5% ≡ 862 Pa
Stability	1.0% ≡ 1724 Pa

These last two uncertainties are similar to the term 'maximum instrument drift between calibrations' consequently a rectangular distribution will be assumed.

The combined standard uncertainty was

$$U_x = 2\sqrt{\left(\frac{1724}{2}\right)^2 + \left(\frac{431}{2}\right)^2 + \left(\frac{862}{\sqrt{3}}\right)^2 + \left(\frac{1724}{\sqrt{3}}\right)^2} = 2848\,\text{Pa} \qquad \text{(Equ.A.21)}$$

A.15 Steamside condensate mass

It was assumed that the condensate mass tolerance was ±1 g and this was to the nearest gram and so a rectangular distribution was used.

The standard uncertainty was $u = 1/\sqrt{3} = 0.5774\,g$. The expanded uncertainty (to be consistent with the other expanded uncertainties) was $U_x = 2 \times 0.5774 = 1.15g$

A.16 Condensate collection time

It was assumed that the condensate collection time uncertainty was ±1 s and again this was to the nearest second and so a rectangular distribution was used.

The standard uncertainty was $u = 1/\sqrt{3} = 0.5774\,s$ and, as above, the expanded uncertainty was therefore $U_x = 2 \times 0.5774 = 1.15s$

A.17 Measurements

During an experimental run a data point was taken once the operator was satisfied that the test rig was in a steady state. Condensate from the bundle outlet header was collected for 3 minutes. After the first minute of condensation collection the operator started the data acquisition system from the PC controlling the system. The data acquisition system scaned all the instruments in series ten times. This took approximately one minute. After the three minutes the condensate was weighed and the weight was entered into the PC. The PC calculated the measurement average values and standard deviations using equations (1) and (6) and the data for the experimental point were stored in a file. In general five data points were taken at each air mass flowrate. Later each data point file was read, the uncertainty calculations are performed, and the uncertainty values were added to the file using the a file preprocessor. All the data point files were then read into the analyser spreadsheet program for generating graphs and comparing the experimental with various correlations.

A.18 Combined Uncertainties

An example of the uncertainty calculations is given for the f factor for a NEL customer bundle for the point where the Reynolds Number based on the bare tube OD is 17611

and the f factor is 0.930. The instrument, measurement and combined standard uncertainties were:

$$U_c := \sqrt{U_x^2 + U_m^2}$$

	instrument U_x	measurement U_m	combined U_c
Inlet cone temp. °C	0.5	0.1186	0.514
Inlet cone press. Pa	1.71	0.7359	1.862
Air inlet temp. °C	0.5	0.0208	0.5
Air outlet temp. °C	0.5	0.0933	0.509
Bundle Δp, Pa	1.53	1.3145	2.017
Atmos. Press. Pa	471	0.9731	471.001
Condensate mass, kg	0.0012	0	0.001
Collection time, s	1.15	0	1.15
Steam press. Pa	2848	126.2809	2850.798
Steam inlet temp. °C	0.5	0.0132	0.5
Steam outlet temp. °C	0.5	0.03	0.501

Note the measurement uncertainties for the condensate mass and the collection time were zero because only one measurement was taken for a data point.

A.19 Sensitivity Coefficients

The sensitivity coefficients for the f factor were calculated as described in the report using equation (10).

It will be noticed that the biggest sensitivity coefficient was for the inlet cone pressure from which the air mass flowrate was calculated. The steam side measurements have no effect on the f factor and consequently these measurements have zero sensitivity coefficients.

The coefficients were found to be:

Inlet cone temp.		0.0031
Inlet cone press.		-0.0049
Air inlet temp.		-0.0017
Air outlet temp.		-0.0012
Bundle Δp		0.0015
Atmos. Press.	cf=	$-3.5584 \cdot 10^{-8}$
Condensate mass		0
Collection time		0
Steam press.		0
Steam inlet temp.		0
Steam outlet temp.		0

A.20 f factor Uncertainty

The combined expanded uncertainty can then be calculated from Equ.A.12 and A.15 (or in reality Equs.A.14 and A.15).

The result was the f factor was 0.930 ±0.010 with a confidence limit of 95% or alternatively 0.930 ±1.0% with a confidence limit of 95%.

An identical approach may be used to calculate the uncertainty for the j factor and for the Reynolds Number and for any other measurand of interest.

APPENDIX B Calculation of the heat transfer coefficient from the j factor

The calculation of the heat transfer coefficient from the Colburn j factor is presented below.

1. The first step is to calculate the Prandtl number (Pr) for the crossflow fluid at bulk conditions from Equ.B.1

$$\mathrm{Pr} = \frac{C_p \eta}{\lambda} \qquad \text{(Equ.B.1)}$$

Where C_p is the Specific heat at constant pressure (J/kg K), η is the dynamic viscosity (Ns/m^2) and λ is the thermal conductivity of the fluid (W/m K).

If the calculation is to be performed for an entire bundle then the fluid properties must be those at the bundle bulk condition, which is obtained from by physical property calculations, taken from tables or derived from experimental inlet and outlet temperature and pressure data, using physical property calculations.

2. The maximum mass flux through the bundle is calculated from the mass flow rate divided by the bundle minimum flow area. This is shown in Equ.B.2.

$$M_{Max} = \frac{mfr}{S_{\min}} \qquad \text{(Equ.B.2)}$$

Where mfr is the mass flow rate through the bundle (kg/s) and S_{min} is the minimum flow area through the bundle (m^2), as defined by PFR [13].

3. It is assumed that the j factor of the bundle in question has been calculated using one of the methods from Either Chapter 6 (staggered) or Chapter 7 (inline), so the uncorrected average heat transfer coefficient can be calculated from Equ.B.3.

$$\alpha = jC_p M_{Max} \mathrm{Pr}^{-\frac{2}{3}} \qquad \text{(Equ.B.3)}$$

If the corrected heat transfer coefficient is required then refer to Appendix C.

APPENDIX C Fin efficiency and surface effectiveness calculation method

The calculation of the corrected heat transfer coefficient, taking account of fin efficiency and surface effectiveness, from the uncorrected heat transfer coefficient is presented below. This method was first shown by Schmidt [4].

1. The fin heat transfer number is calculated from Equ.C.1

$$m = \sqrt{\frac{2\alpha}{\lambda_F s_f}} \qquad \text{(Equ.C.1)}$$

Where α is the uncorrected heat transfer coefficient, given in Equ.B.3, λ_F is the thermal conductivity of the fin material and s_f is the mean fin thickness.

2. The corrected fin height is calculated from Equ.C.2.

$$\phi_{Eff} = \frac{D_o}{2}\left[\left(\frac{D_f}{D_o}\right)-1\right]\cdot\left[1+0.35\ln\left(\frac{D_f}{D_o}\right)\right] \qquad \text{(Equ.C.2)}$$

Where D_f is the fin diameter and D_o is the fin root diameter.

3. The fin efficiency is found by Equ.C.3.

$$\varepsilon = \frac{\tanh\left(m\phi_{Eff}\right)}{m\phi_{Eff}} \qquad \text{(Equ.C.3)}$$

4. The surface effectiveness relates the total crossflow-side heat transfer area to an effective heat transfer area at the fin root temperature. It is calculated by Equ.C.4.

$$\gamma = 1-\frac{A_{fin}}{A_f}(1-\varepsilon) \qquad \text{(Equ.C.4)}$$

Where A_{fin} is the fin surface area per unit tube length (m^2/m) and A_f is the total airside heat transfer area per unit length of tube (m^2/m).

5. The corrected overall heat transfer coefficient can now be calculated from Equ.C.5.

$$\alpha_c = \gamma\alpha \qquad \text{(Equ.C.5)}$$

APPENDIX D List of project publications by author

[1] Mcilwain, S.R., Kenbar, A, "Performance characteristics of Air-cooler inline bundles", ***HTFS RS1095***, (2001).

[2] Kenbar, A, Brown, A, Mcilwain, S.R., Farrant, P.E., "Comparing bundle performance with and without corbels", ***HTFS RS1097*** (2001)

[3] Mcilwain, S.R., Kenbar, A, Brisbane, T, "HTFS3: Improvements to HTFS2 method for heat transfer and pressure drop in staggered arrangement of plain high finned tubes", ***HTFS RS1118*** (2002)

[4] Mcilwain, S.R., Kenbar, A, "Performance characteristics of Air-cooler inline bundles with rectangular layouts", ***HTFS RS1119***, (2002).

[5] Mcilwain, S.R., Kenbar, A.M.A, Lee, C.K., "A CFD study of corbel shapes in air-cooled crossflow heat exchangers", ***HTFS RS1124*** (2002)

[6] Mcilwain, S.R., Kenbar, A.M.A, Lee, C.K., "HTFS Inline: Improved method for heat transfer and pressure drop in inline arrangements of plain high finned tubes", ***HTFS RS1137*** (2003)

[7] Mcilwain, S.R., Kenbar, A.M.A, Lee, C.K., "A new method for predicting the pressure drop of finned tube bundles in crossflow with varying corbel shapes", ***HTFS RS1142*** (2003)

[8] Mcilwain, S.R., Kenbar, A.M.A, Lee, C.K., "CFD modeling of inline tube bundles with plain high fins", ***HTFS RS1136*** (2003)

[9] Mcilwain, S.R., Kenbar, A.M.A, Lee, C.K., "A new method to predict pressure drop for staggered finned tube bundles with bypassing flow", ***HTFS RS Report*** (to be published 2004)

[10] Mcilwain, S.R., Kenbar, A, Lee, C.K., "A method to determine the local row heat transfer coefficient in inline finned tube bundles, using CFD derived local data", ***HTFS RS Report*** (to be published 2004)